

Rock Physics and Geomechanics in the Study of Reservoirs and Repositories

Edited by
C. David and M. Le Ravalec-Dupin



Geological Society
Special Publication 284



Rock Physics and Geomechanics in the Study of Reservoirs and Repositories

The Geological Society of London
Books Editorial Committee

Chief Editor

BOB PANKHURST (UK)

Society Books Editors

JOHN GREGORY (UK)

JIM GRIFFITHS (UK)

JOHN HOWE (UK)

PHIL LEAT (UK)

NICK ROBINS (UK)

JONATHAN TURNER (UK)

Society Books Advisors

MIKE BROWN (USA)

ERIC BUFFETAUT (France)

JONATHAN CRAIG (Italy)

RETO GIÉRÉ (Germany)

TOM McCANN (Germany)

DOUG STEAD (Canada)

RANDELL STEPHENSON (The Netherlands)

Geological Society books refereeing procedures

The Society makes every effort to ensure that the scientific and production quality of its books matches that of its journals. Since 1997, all book proposals have been refereed by specialist reviewers as well as by the Society's Books Editorial Committee. If the referees identify weaknesses in the proposal, these must be addressed before the proposal is accepted.

Once the book is accepted, the Society Book Editors ensure that the volume editors follow strict guidelines on refereeing and quality control. We insist that individual papers can only be accepted after satisfactory review by two independent referees. The questions on the review forms are similar to those for *Journal of the Geological Society*. The referees' forms and comments must be available to the Society's Book Editors on request.

Although many of the books result from meetings, the editors are expected to commission papers that were not presented at the meeting to ensure that the book provides a balanced coverage of the subject. Being accepted for presentation at the meeting does not guarantee inclusion in the book.

More information about submitting a proposal and producing a book for the Society can be found on its web site: www.geolsoc.org.uk.

It is recommended that reference to all or part of this book should be made in one of the following ways:

DAVID, C. & LE RAVALEC-DUPIN, M. (eds) 2007. *Rock Physics and Geomechanics in the Study of Reservoirs and Repositories*. Geological Society, London, Special Publications, **284**, 1–14.

FORNEL, A., MEZGHANI, M. & LANGLAIS, V. 2007. Using production data and time domain seismic attributes for history matching. In: DAVID, C. & LE RAVALEC-DUPIN, M. (eds) *Rock Physics and Geomechanics in the Study of Reservoirs and Repositories*. Geological Society, London, Special Publications, **284**, 147–159.

GEOLOGICAL SOCIETY SPECIAL PUBLICATION NO. 284

Rock Physics and Geomechanics in the Study of Reservoirs and Repositories

EDITED BY

C. DAVID

Université de Cergy-Pontoise, France

and

M. LE RAVALEC-DUPIN

Institut Français du Pétrole, France

2007

Published by

The Geological Society

London

THE GEOLOGICAL SOCIETY

The Geological Society of London (GSL) was founded in 1807. It is the oldest national geological society in the world and the largest in Europe. It was incorporated under Royal Charter in 1825 and is Registered Charity 210161.

The Society is the UK national learned and professional society for geology with a worldwide Fellowship (FGS) of over 9000. The Society has the power to confer Chartered status on suitably qualified Fellows, and about 2000 of the Fellowship carry the title (CGeo). Chartered Geologists may also obtain the equivalent European title, European Geologist (EurGeol). One fifth of the Society's fellowship resides outside the UK. To find out more about the Society, log on to www.geolsoc.org.uk.

The Geological Society Publishing House (Bath, UK) produces the Society's international journals and books, and acts as European distributor for selected publications of the American Association of Petroleum Geologists (AAPG), the Indonesian Petroleum Association (IPA), the Geological Society of America (GSA), the Society for Sedimentary Geology (SEPM) and the Geologists' Association (GA). Joint marketing agreements ensure that GSL Fellows may purchase these societies' publications at a discount. The Society's online bookshop (accessible from www.geolsoc.org.uk) offers secure book purchasing with your credit or debit card.

To find out about joining the Society and benefiting from substantial discounts on publications of GSL and other societies worldwide, consult www.geolsoc.org.uk, or contact the Fellowship Department at: The Geological Society, Burlington House, Piccadilly, London W1J 0BG: Tel. +44 (0)20 7434 9944; Fax +44 (0)20 7439 8975; E-mail: enquiries@geolsoc.org.uk.

For information about the Society's meetings, consult *Events* on www.geolsoc.org.uk. To find out more about the Society's Corporate Affiliates Scheme, write to enquiries@geolsoc.org.uk.

Published by The Geological Society from:

The Geological Society Publishing House, Unit 7, Brassmill Enterprise Centre, Brassmill Lane, Bath BA1 3JN, UK

(Orders: Tel. +44 (0)1225 445046, Fax +44 (0)1225 442836)

Online bookshop: www.geolsoc.org.uk/bookshop

The publishers make no representation, express or implied, with regard to the accuracy of the information contained in this book and cannot accept any legal responsibility for any errors or omissions that may be made.

© The Geological Society of London 2007. All rights reserved. No reproduction, copy or transmission of this publication may be made without written permission. No paragraph of this publication may be reproduced, copied or transmitted save with the provisions of the Copyright Licensing Agency, 90 Tottenham Court Road, London W1P 9HE. Users registered with the Copyright Clearance Center, 27 Congress Street, Salem, MA 01970, USA: the item-fee code for this publication is 0305-8719/07/\$15.00.

British Library Cataloguing in Publication Data

A catalogue record for this book is available from the British Library.

ISBN: 978-1-86239-230-4

Typeset by Techset Composition Ltd, Salisbury, UK

Printed by Cromwell Press, Trowbridge, UK

Distributors

North America

For trade and institutional orders:

The Geological Society, c/o AIDC, 82 Winter Sport Lane, Williston, VT 05495, USA

Orders: Tel +1 800-972-9892

Fax +1 802-864-7626

E-mail gsl.orders@aidevt.com

For individual and corporate orders:

AAPG Bookstore, PO Box 979, Tulsa, OK 74101-0979, USA

Orders: Tel +1 918-584-2555

Fax +1 918-560-2652

E-mail bookstore@aapg.org

Website <http://bookstore.aapg.org>

India

Affiliated East-West Press Private Ltd, Marketing Division, G-1/16 Ansari Road, Darya Ganj, New Delhi 110 002, India

Orders: Tel +91 11 2327-9113/2326-4180

Fax +91 11 2326-0538

E-mail affiliat@vsnl.com

Preface

The study of reservoir and repository performance requires the integration of different fields in Earth sciences, including geochemistry, geophysics, structural geology and, in the case of interest here, rock physics and geomechanics. The aim of this Special Publication is to emphasize how rock physics and geomechanics help to obtain a better insight into important issues linked to reservoir management for exploitation of natural resources, and to repository safety assessment for hazardous waste storage in the geological environment. Most of the contributions were originally presented at the Euro-conference on Rock Physics and Geomechanics, which was held on 18–22 September 2005 in Ile d’Oléron, France, focusing on ‘Integration and Application to Reservoirs and Repositories’. This meeting was part of the successful series of Euro-conferences devoted to Rock Physics and Geomechanics, the first of which was held in 1998 in Aussois, France, and it followed the conference in Kijkduin on ‘Micromechanics, Flow and Chemical Reactions’ in 2003 and the conference in Potsdam on ‘Scaling Laws in Space and Time’ in 2004. The specific emphasis of the conference in Oléron was on integrated studies from the areas of hydrocarbon and geothermal recovery, hazardous waste repositories and deep drilling projects. The meeting was attended by 71 scientists from academia and industry from 12 countries, and a total of 66 contributions were presented during the conference. Thanks to the sponsors who supported the conference (IFP, Total, ANDRA, CNRS, University Cergy-Pontoise), 23 young scientists could attend the conference with zero registration fee, and some of them took the opportunity to publish their work in this volume.

The first contribution is an introduction to the subject by **David & Le Ravalec-Dupin**. They present recent advances in the field of rock physics and geomechanics for the characterization of reservoirs and repositories. The following paper, by **Tsang et al.**, presents an overview on the interaction between mechanical deformation and fluid flow in fractured rocks, with examples on borehole injection testing, stress release in a tunnel during excavation, flow anisotropy and channelling in fracture networks, and finally deep CO₂ injection and storage in geological formations. This paper addresses important questions relevant both for reservoir and repository studies, whereas the following contributions have been grouped by common objectives.

In the first group of papers, the focus is on experimental studies for the characterization of

repositories, with three contributions. The first one, by **Bossart**, who is currently the head of the Mont Terri project in Switzerland, presents an overview of key experiments to assess repository performance over realistic time scales, as well as the challenges that scientists have to face in the design and monitoring of underground radioactive waste repositories. In the next contribution, **Damaj et al.**, describe *in situ* experiments at Mont Terri in the Opalinus Clay formation to show the extent and properties of excavated damage zones. The experiments are based on seismic tomography and P-wave velocity estimation during excavation and reloading of a slot cut into the clay formation. The last paper of this group, by **Robion et al.**, deals with the influence of temperature on the elastic and magnetic properties of shales, focusing on the anisotropy evolution. This study was carried out in the laboratory on samples cored in the Callovo–Oxfordian argillite formation that is the host formation of the French underground research laboratory for radioactive waste storage.

In the next group of papers, the emphasis is on reservoir studies. **Blöcher et al.** investigated the poroelastic undrained response of a sandstone to estimate the Skempton coefficient using three methods: laboratory measurements in a pressure vessel, finite-element modelling from thin-section images, and analytical calculation for simple pore geometries. In the next contribution, **Haimson & Klaetsch** present an experimental study showing breakouts in small laboratory drilling tests on St. Peter sandstone, associated with the development of compaction bands under the applied stress. They show that, depending on the porosity range, the compaction bands have different properties, with greater strength and more intragranular cracking for the less porous sandstone samples. Compaction bands have also been studied by **Rudnicki** from a theoretical viewpoint: he presents in the next paper a model for the propagation of compaction bands using a combined anti-crack–dislocation model. In the next contribution, by **Louis et al.**, a review of recent advances in the field of X-ray computed tomography imaging of geomaterials is presented, and the analysis of pore-space heterogeneity and localization of deformation in porous rocks using these methods is discussed. At a larger scale, **Fornel et al.** propose an integrated approach based on rock physics for improved reservoir characterization and modelling using 4D seismic data in combination with production data. In the next contribution, **Kim et al.** present their study on the effect

of rock bridges on the mechanical strength of fractured rock masses, with an insight into the scale effect observed between the strength values of intact rocks and those of the rock mass with discontinuities. A petrophysical study of samples cored at different distances from a fault zone is presented by **Rosener & Géraud** with application to the geothermal project of Soultz-sous-Forêts, eastern France.

The last group of papers includes contributions that cannot be classified in either of the former groups, because they are general studies relevant for both reservoirs and repositories, or are linked to specific applications where rock physics and/or geomechanics play an important role. The contribution by **Bernabé & Evans** deals with the numerical modelling of deformation by pressure solution at asperities subjected to normal load in a fracture, by solving the diffusion equation at the solid–fluid interface in a fluid-filled fracture. In the last contribution, **Wong & Zhu** present a theoretical study on the elastic anisotropy in cracked rocks, in which the anisotropy parameters

are calculated as a function of the crack distribution parameters.

We wish to thank all the participants who attended the 2005 Euro-conference in Oléron and the authors for their contribution to this Special Publication. Many thanks also go to our colleagues who carefully reviewed the manuscripts: E. Aharonov, C. Aubourg, P. Bésuelle, B. Crawford, J. Fortin, J. T. Fredrich, Y. Guéguen, L. Jeannin, R. Katsman, H. J. Kuempel, B. Ledésert, F. Lehner, Y. Leroy, B. Maillot, A. Makurat, P. Rasolofosaon, J. Sarout, S. Shapiro, S. Vidal-Gilbert, C. Viggiani, T. F. Wong, R. Zimmerman and G. Zimmermann.

Finally, our special thanks go to Angharad Hills and Sarah Gibbs at the Geological Society Publishing House for their help and patience during the editorial process. Many thanks go to Kurt Sternlof for providing the photograph for the cover of this book.

C. DAVID
M. LE RAVALEC-DUPIN



Contents

Preface	vii
DAVID, C. & LE RAVALEC-DUPIN, M. Rock physics and geomechanics in the study of reservoirs and repositories	1
TSANG, C.-F., RUTQVIST, J. & MIN, K.-B. Fractured rock hydromechanics: from borehole testing to solute transport and CO ₂ storage	15
BOSSART, P. Overview of key experiments on repository characterization in the Mont Terri Rock Laboratory	35
DAMAJ, J., BALLAND, C., ARMAND, G., VERDEL, T., AMITRANO, D. & HOMAND, F. Velocity survey of an excavation damaged zone: influence of excavation and reloading	41
ROBION, P., DAVID, C. & COLOMBIER, J. C. Temperature-induced evolution of the elastic and magnetic anisotropy in argillite samples from Bure underground research laboratory, eastern France	57
BLÖCHER, G., BRUHN, D., ZIMMERMANN, G., McDERMOTT, C. & HUENGES, E. Investigation of the undrained poroelastic response of sandstones to confining pressure via laboratory experiment, numerical simulation and analytical calculation	71
HAIMSON, B. & KLAETSCH, A. Compaction bands and the formation of slot-shaped breakouts in St. Peter sandstone	89
RUDNICKI, J. W. Model for compaction band propagation	107
LOUIS, L., BAUD, P. & WONG, T.-F. Characterization of pore-space heterogeneity in sandstone by X-ray computed tomography	127
FORNEL, A., MEZGHANI, M. & LANGLAIS, V. Using production data and time domain seismic attributes for history matching	147
KIM, B. H., KAISER, P. K. & GRASSELLI, G. Influence of persistence on behaviour of fractured rock masses	161
ROSENER, M. & GÉRAUD, Y. Using physical properties to understand the porosity network geometry evolution in gradually altered granites in damage zones	175
BERNABÉ, Y. & EVANS, B. Numerical modelling of pressure solution deformation at axisymmetric asperities under normal load	185
WONG, T.-F. & ZHU, W. Weak elastic anisotropy in a cracked rock	207
Index	221

Rock physics and geomechanics in the study of reservoirs and repositories

C. DAVID¹ & M. LE RAVALEC-DUPIN²

¹*Université de Cergy-Pontoise, UMR CNRS 7072, Département des Sciences de la Terre et de l'Environnement, 5, mail Gay-Lussac, Neuville-sur-Oise, F-95031 Cergy-Pontoise, France (e-mail: christian.david@u-cergy.fr)*

²*Institut Français du Pétrole, 1–4 Avenue de Bois-Préau, F-92852 Rueil-Malmaison, France*

Abstract: Reservoir management for hydrocarbon extraction and repositories design for radioactive waste storage are two different areas in which rock physics and geomechanics provide valuable information. Although the targets and objectives are different, similar approaches and common attributes exist in both fields: safety assessment, short- to long-term prediction, integration of various scales of investigation, and remote monitoring, among others. Nevertheless, there are also important differences: reservoirs at depth are investigated through remote geophysical studies, well-logging and/or core samples retrieval, whereas direct access to repositories is possible through excavation in the host formation in which underground research laboratories can be constructed. We review a number of studies focusing on geomechanics and rock physics applied to the characterization of reservoirs and repositories, including laboratory experiments and predictive models, at different scales.

Reservoir management and assessment of repository performance require the integration of different fields in Earth sciences, including geochemistry, geophysics, structural geology, and, in the case of interest here, rock physics and geomechanics. We present recent advances in the studies of reservoirs and repositories with the aim of emphasizing how rock physics and geomechanics help to obtain a better insight into important issues linked to reservoir management for exploitation of natural resources, and to repository safety assessment for hazardous waste storage in the geological environment.

In the area of reservoir management, the importance of geomechanics in problems such as wellbore stability, hydraulic fracturing and subsidence is well known. Recently, there has been a growing interest in the development of a link between fluid flow simulators and geomechanical models. Several approaches have been proposed to incorporate the correct physics and to account for physical phenomena usually neglected in reservoir simulation. New techniques developed in laboratory studies provide relevant data for this integration. The approaches differ in the degree of coupling. The stronger the coupling, the more computationally demanding the simulation. Numerical experiments showed that coupling is of interest for poorly consolidated reservoirs such as chalk reservoirs. In other cases, one may wonder whether a more accurate modelling of production processes

justifies the required computation cost. Complementary sensitivity studies have to be performed to better estimate the conditions in which the coupling is worthwhile.

In the area of underground waste storage, the key issue is to design a repository as safe as possible for human activity and for the environment at the near surface, on time scales of the order of hundreds of years. This challenging task requires us to identify favourable geological targets for the storage, and to develop extensive scientific research in different fields, so as to obtain eventually a predictive model of the repository evolution over large time scales, when high-level radioactive waste packages will be stored underground. Input for these predictive models can only be obtained by thorough experimental research, at different scales (Fig. 1). For that purpose, underground research laboratories (URL) have been constructed in possible host formations in several countries. Two main options are considered. The ‘soft rock’ option consists in storing the radioactive packages at depth in weak rocks such as shales, taking advantage of the retention capacity of clays and the creep capability of the soft rocks. In the ‘hard rock’ option the repository is implemented in low-permeability rocks with a high mechanical strength, such as crystalline rocks.

Whereas the targets are geologically very different (for reservoir rocks, large porosity and permeability are desirable; for waste storage, low permeability and large retention capacity are

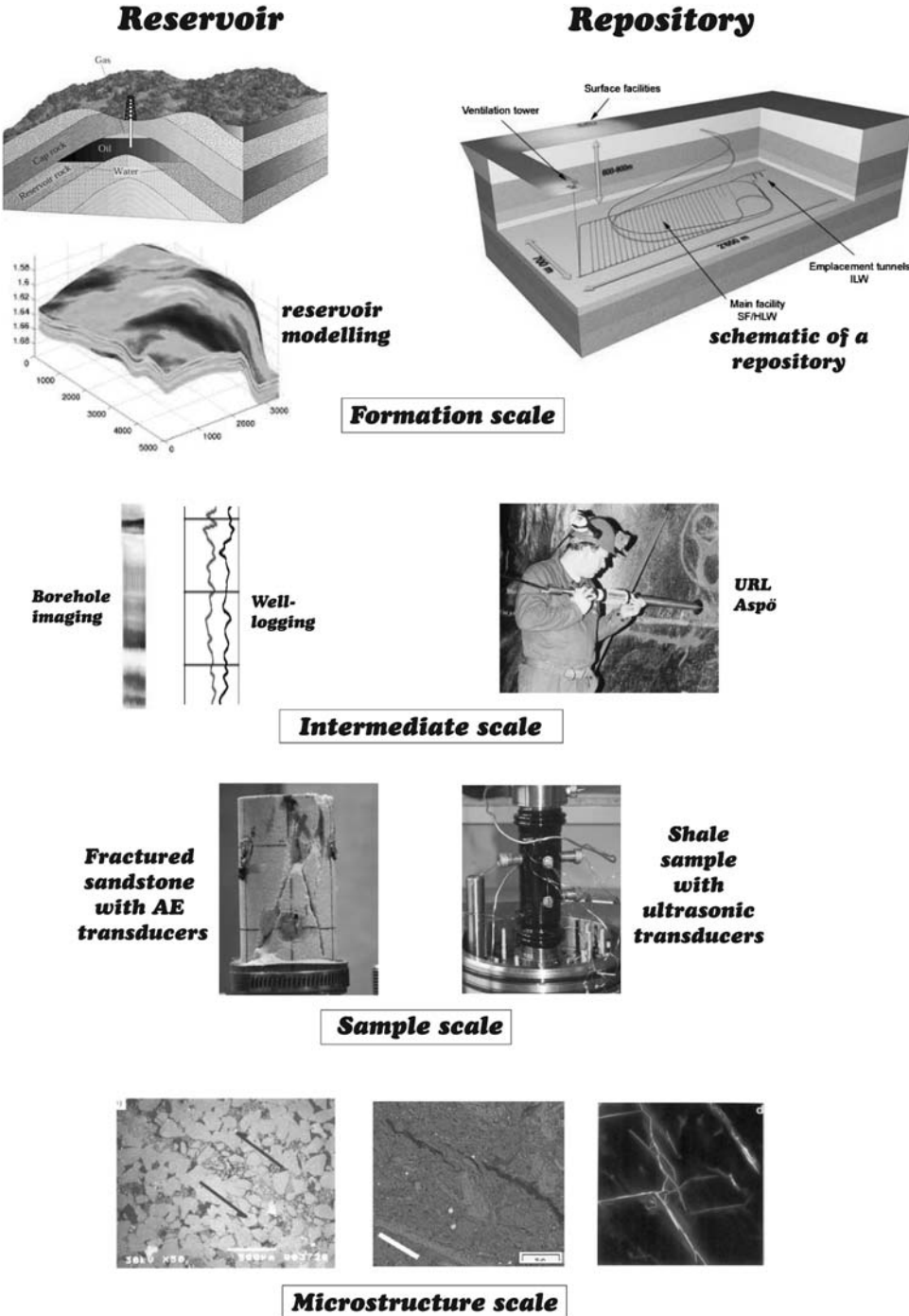


Fig. 1. Synthetic figure showing the different scales that studies in geomechanics and rock physics for reservoir and repository characterization have to deal with. Formation scale: on the left, typical reservoir geometry in an anticline (<http://www.maverickenergy.com/oilgas.htm>) with an example of a reservoir geomechanical simulation (Fornel *et al.* 2007); on the right, a schematic illustration of a repository in a sedimentary formation (http://www.grimsel.com/general/bg_geoldisp.htm). Intermediate scale: for reservoirs, this scale corresponds to borehole

required), there are common interests for the geomechanics and rock physics community to work on these topics. The first one is obviously to characterize the permeability of the formations, which in one case should be high, and in the other case low. Mechanical stability is also needed in both cases, for drilling the borehole into the reservoir, and for the shaft and tunnels in the repository. Studies in geomechanics and rock physics should also be predictive over different time scales, to forecast the evolution in terms of production rate and storage capacity for reservoirs, and in terms of safety assessment for repositories. The scale effect has also to be considered constantly: properties defined at the micro- or sample scale have to be extrapolated (or upscaled) to the formation scale (Guéguen *et al.* 2006). In this regard, underground research laboratories give the opportunity for researchers to work at an intermediate scale, that of the tunnels in which the packages will be stored, a possibility that does not exist for reservoir studies. Finally, there is the need for monitoring the sites (reservoirs or repositories), to anticipate any problem that might occur during production or operation.

Below, we present some recent advances in the area of geomechanics and rock physics applied first to reservoir characterization, and second to repositories in different geological environments.

Reservoir studies for hydrocarbon recovery

Over the past decade, reservoir geomechanics has emerged as a necessary integral part of reservoir simulation studies to better develop and manage oil reservoirs. First, withdrawing or injecting fluid from into the reservoir causes a change in pore pressure, which results in a change in the 3D effective stress state. The stress path followed by the reservoir governs the evolution of the effective stress state; that is, the change in deviatoric stresses, which produces rock deformation and permeability changes. Second, one of the most challenging fields in reservoir engineering is the integration of all

available data for the characterization of reservoirs and the reduction of uncertainties in oil and gas production. These data traditionally include such factors as production history, water cuts and gas/oil ratio. Since the late 1990s, they also consist of 4D seismic data; that is, repeated 3D seismic acquisitions. Four-dimensional seismic data are potentially a powerful tool for monitoring fluid movements throughout the reservoir. The integration of 4D seismic data into reservoir modelling clearly depends on the link between transport and elastic properties. Below, we discuss the issues related to the interplay between geomechanics and flow simulation in produced reservoirs.

Geomechanical effects in produced reservoirs

To date, in conventional flow simulators, the pore volume variation only depends on the pore pressure variation through a pore volume compressibility coefficient (Geertsma 1957). According to this approach, stress changes and strain resulting from reservoir production are not explicitly computed and the pore volume change is directly related to the pressure change through the rock compressibility, which is the only mechanical property considered in conventional reservoir simulations. The use of such a rock compressibility factor implicitly supposes that the stress path followed by the reservoir is known *a priori* and constant during reservoir production. On the other hand, reservoir permeability is unaffected by pore pressure changes. In addition, conventional flow simulators do not account for the interactions between the reservoir and the surrounding regions, such as overburden, underburden and sideburden. Therefore, these simulators are restricted to reservoirs with competent rocks and laterally uniform rock properties: they do not apply to reservoirs where stresses change. However, during reservoir production, many mechanisms generating variations in pressure, saturation and temperature are likely to induce stress changes. The geomechanical contribution is particularly significant for poorly compacted reservoirs and highly compacted rock formations.

(Continued) studies using Formation Microscanner imaging or well-logging tools; for repositories, this scale corresponds to underground research laboratories where scientists have direct access to the host formation for instrumentation (http://www.skb.se/default2____16762.aspx). *Sample scale*: concerns laboratory experiments on rock cores retrieved from boreholes or from URLs. On the left, fractured Bentheim sandstone sample (height 80 mm) with acoustic emission (AE) sensors located at the surface, after a mechanical test; on the right, experimental device for loading a COX argillite sample in a triaxial setup (Sarout 2006) with ultrasonic transducers mounted on the sample surface through a Neoprene sleeve. *Microstructure scale*: this is the scale of grains, pores and cracks. On the left, scanning electron micrograph of a shear band in Berea sandstone (scale bar represents 500 µm); in the middle, scanning electron micrograph of crack patterns in a COX argillite sample after triaxial mechanical testing (scale bar represents 100 µm); on the right, confocal microscopy image of cracks in a granite from Spain (courtesy B. Menéndez & J. Sarout).

Poorly compacted reservoirs. Typical poorly compacted reservoirs consist of chalks and unconsolidated sands. As the reservoir is produced, the pore pressure diminishes, leading to an increase in the effective stress. It triggers grain-scale deformation processes (e.g. Bernabé & Evans 2007) causing elastic (recoverable) and inelastic (permanent) reservoir strain. The increase in the effective stress can be sufficient to enhance reservoir compaction.

Compaction generates an increase in pore pressure (Charlez 1997), which enhances fluid production. For instance, for the Bachaquero field in Venezuela, half of the production was driven by compaction (Merle *et al.* 1976). Depending on rock properties, compaction can propagate to the surrounding sideburden and overburden (Segall 1989). Contraction in the vertical direction is accommodated by subsidence of the free surface. Subsidence can vary from a few centimetres to a few metres. Contraction in the horizontal direction is resisted by the surrounding rock, which is pulled towards the reservoir. Compaction has been recorded in a number of notable case histories. For example, the Wilmington field, located in California, experienced a maximal subsidence of about 9 m as a result of production over 20 years. Horizontal displacements as large as about 4 m were also recorded (Allen 1968). Another example is the Ekofisk field in the North Sea, where a sea-floor subsidence of 42 cm per year was reached in 1990 (Sylte *et al.* 1999). Another consequence of compaction is well failure. At the Belridge diatomite field, California, nearly 1000 wells have experienced severe casing damage during the past 20 years of production.

As stated above, compaction contributes to improve production by squeezing oil from the rock into the borehole. It is also the basis of a contrary effect. Compaction decreases reservoir porosity (Weng *et al.* 2005), thereby reducing reservoir permeability (Wong *et al.* 1997; Ostermeier 2001), and ultimately production.

In addition, recent field and laboratory studies suggest that the overall picture can be much more complicated than simple, uniform compaction. Thin, natural tabular zones of compaction in certain types of sandstone, called compaction bands, were observed in outcrop by Mollema & Antonellini (1996) and Sternlof *et al.* (2005). Similar features were also noticed around boreholes (Haimson 2001). Because of the much reduced porosity in the compaction bands, these structures are potentially important as permeability barriers in reservoirs (Sternlof *et al.* 2006). To avoid the conditions leading to the formation of compaction bands, which can produce destructive compartmentalization of reservoirs, one has to better understand

how the occurrence of localized zones of compaction is related to the stress state and the constitutive properties of the rock. Development of this phenomenon has been investigated in the laboratory, primarily in sandstones with porosities ranging from 13% to 28% (DiGiovanni *et al.* 2000; Olsson & Holcomb 2000; Klein *et al.* 2001; Fortin *et al.* 2006). The data show that localized failure in compactant rock is commonly associated with stress states in the transitional regime from brittle faulting to cataclastic flow (Wong *et al.* 2001), with the mode of localization associated with a broad spectrum of complexity (Baud *et al.* 2004; Ngwenya *et al.* 2003). Simultaneous measurements of stress, strain, acoustic emission locations and permeability during experiments on sandstone samples revealed an up to two-orders-of-magnitude decrease in permeability in the compacted zone (Holcomb & Olsson 2003; Vajdova *et al.* 2004). Theoretical modelling (Katsman *et al.* 2005; Katsman & Aharonov 2006) and microstructural studies (Louis *et al.* 2007) suggest that grain-scale homogeneity played a major role in the development of discrete compaction bands. Rudnicki (2007) has proposed a theoretical model for the propagation of compaction bands. Haimson & Lee (2004) focused on boreholes in Mansfield sandstone, which fail by developing fracture-like breakouts. The Mansfield sandstone contains mainly quartz grains (90%) held together primarily by spot-sutured contacts. Haimson & Lee (2004) observed that the failure mechanism was the removal by the circulating drilling fluid of mainly intact grains loosened during the formation of the compaction band. They concluded that the initial porosity, type of cementation, mineral homogeneity, grain strength, and sphericity appear to be major factors in the formation of compaction bands. Haimson & Klaetsch (2007) performed miniature drilling in St. Peter sandstone samples. They showed that compaction bands precede slot-shaped breakouts, which are formed by flushing off grains from within these bands.

Highly compacted reservoirs. Highly compacted reservoirs include fractured and faulted reservoirs. The main geomechanical effects for these reservoirs is not compaction, but fracturing and changes in fracture conductivities. These effects are related to thermo-poroelastic changes (Gutierrez & Makurat 1997). They can be observed around water injectors, because of the injection of cold water. They also appear around fractures and fault planes: because of the high stiffness of the matrix, strains are localized on fractures and alter their hydraulic conductivities. As a result, preferential flow paths can be

created and change production (Heffer *et al.* 1994; Koutsabeloulis *et al.* 1994).

Coupling between flow simulators and geomechanical models

As mentioned above, for both weakly compacted reservoirs and highly compacted fractured reservoirs, the expected deformation can strongly influence permeability. To account for the geomechanical effects generated by stress changes in and around reservoirs, the fluid flow problem has to be solved in association with a geomechanical model, which accurately predicts the evolution of stress-dependent parameters through time.

Over the past decade, studies focused on the coupling of flow simulators with geomechanical models (Gutierrez & Makurat 1997). However, theoretical and practical difficulties have prevented coupled approaches from being used routinely in simulation studies. Some of these challenges are the complex mechanical behaviour of geomaterials, the strong interplay between mechanical and flow problems, and the fact that reservoir models become very computationally intensive.

As mentioned by numerous researchers, the coupling occurs in various forms, which are listed below. Each coupling technique has its own advantages and disadvantages. Further information has been given by Longuemare *et al.* (2002), Tran *et al.* (2005) and Jeannin *et al.* (2006).

Partial coupling. Partial coupling means that the stress and flow equations are separately solved from two distinct simulators, but intermediate results are passed between the two simulators. Basically, the pore pressure and temperature increments calculated by the flow simulator are given to the geomechanical simulator, which computes the corresponding changes in stresses. These are used to update the permeability values provided to the flow simulator. Partial coupling often uses the finite-difference method for fluid flow simulators and the finite-element method for geomechanical simulators.

Partial coupling may be explicit or iterative. If the information obtained from the geomechanical simulator is not sent back to the flow simulator, the coupling is explicit. If the information is passed back and forth until convergence, the coupling is iterative. Because of its reduced computing cost, explicit coupling is often preferred (e.g. Settari & Mourits 1998). It can be applied to gas reservoirs without significant error, as gas compressibility usually dominates rock compressibility. In such a case, the mass balance is mainly controlled by gas pressure rather than stresses. Iterative coupling requires more CPU time. The computation

needed to achieve an iterative-coupled simulation is around 200 times longer than a conventional reservoir simulation (Samier *et al.* 2006). This approach is preferred when the reservoir behaviour is sensitive to compressibility.

Full coupling. Full coupling is more rigorous: it involves the simultaneous solution of stress and flow equations in the same simulator (e.g. Stone *et al.* 2000), and anisotropy and nonlinearity must be handled. The full coupling usually gives good solutions, but may be extensively CPU-time consuming, especially when dealing with steam-assisted gravity drainage (SAGD) in reservoirs with nonlinear behaviours. Its feasibility and accuracy have yet to be proved for large-scale reservoirs.

Partial iterative and full coupling methods are equally recommended when rock compressibility affects the material balance. Two examples are liquid-filled reservoirs with compaction and subsidence problems and reservoirs with highly nonlinear geomaterials. The iterative coupling approach is considered to be the most flexible, as it can be used without substantial code modifications.

Numerical experiments. The results of a few numerical experiments carried out to investigate the influence of the geomechanical flow simulation coupling are reported in the literature. Jin *et al.* (2000) considered a typical North Sea reservoir. They ran reservoir simulations first with only the flow simulator and second with a flow simulator partially coupled to a geomechanical model. They observed that the evolution of the stress state significantly affects the oil production profile. Longuemare *et al.* (2002) used a partial coupling method to investigate the sensitivity of a highly heterogeneous and compartmentalized limestone reservoir to stress. They showed that the perturbation of the reservoir equilibrium leads to progressive strain localization on a limited number of faults. Samier *et al.* (2006) also carried out a comparative study for two field cases: a large North Sea chalk reservoir and a North Sea HP-HT gas reservoir in a faulted geometry. Samier *et al.* performed different simulations with an increasing coupling. For the chalk reservoir, the results leave no doubt about the importance of using a flow simulator with a geomechanical coupling. The difference in hydrocarbon production and reservoir pressure can reach 25%. For the HP-HT faulted reservoir, the difference in gas and oil production is less than 5% and 1%, respectively. The geomechanical analysis stressed that the three major faults in the central area are not reactivated by the depletion.

Application to 4D seismic data

An example is the integration of 4D seismic data in reservoir models. Four-dimensional seismic data result from the interpretation of repeated seismic surveys over a producing hydrocarbon field. They are used to identify changes in reservoir parameters such as pore pressure, saturation and temperature. To date, the integration of 4D seismic data into reservoir models involves iterative workflows (Landa & Horne 1997; Gosselin *et al.* 2000; Kretz *et al.* 2004; Fornel *et al.* 2007). Briefly, an initial reservoir model is proposed and a flow simulation is performed. The computed pore pressures and saturations are then provided to a petro-elastic model usually built from quantitative relationships, most of them being empirical, to link elastic properties of rocks to pore space, pore fluid, fluid saturation, pore pressure, and rock composition (Mavko *et al.* 1998). In this regard, the theory of poroelasticity provides the right framework to address these problems: Blöcher *et al.* (2007) thoroughly investigated the poroelastic response of Bentheim sandstone samples in undrained conditions and compared their experimental results with finite-elements calculations using detailed information on the rock microstructure. Microtomography techniques have become very powerful in imaging the 3D geometry of porous rocks, from which poroelastic properties can be derived (Arns *et al.* 2002). The petro-elastic model allows for calculating seismic velocities, impedances and time-shifts. The following step consists in comparing the computed seismic answers with the 4D seismic data to be reproduced. Then, the initial model is modified to better match the reference data and the whole process is repeated until 4D seismic data as well as production data are reasonably matched (Le Ravalec-Dupin 2005). In this special case, the coupling is very loose, which means that the computed pore volume changes are derived from pore pressure changes, not stress changes. To our knowledge, the porosity provided to the petro-elastic model is usually the porosity at time zero. In other words, compressibility effects are disregarded, although they are integrated in the flow simulation. In addition, the flow simulation is limited to the reservoir: the overburden and sideburden are not considered. However, as shown by Vidal-Gilbert & Tisseau (2006), the decrease of layer thickness as a result of compaction and the increase in effective stresses result in higher seismic velocities within the reservoir. The seismic travel time is then reduced across the reservoir layer. Above the reservoir, the overburden is stretched and the decrease in effective stresses leads to lower seismic velocities and to an increase in the seismic travel time across the overburden.

Therefore, the time-shifts observed at the reservoir base or top are also affected by the overburden. In their preliminary study, Vidal-Gilbert & Tisseau (2006) concluded that the integration of geomechanical modelling to compute time-lapse seismic velocities and time-shifts shows a moderate effect of the reservoir and the surrounding formations. A careful sensitivity study should be performed to estimate what geomechanical modelling can provide to seismic monitoring.

In addition, including the overburden, sideburden and underburden in the modelling means that additional data have to be collected to feed the coupled simulators, which may be a challenging task. Also, as far as fluid production is the main focus, the relationship between permeability and stress should be the key point of the coupling between flow simulation and geomechanics. However, it is neglected in most coupled reservoir simulations. In some flow simulators, an empirical relation between permeability and pressure can be defined. These relations are generally derived from permeability measurements at various pressures during depletion tests, although uniaxial strain paths are not necessarily representative of the stress state in the reservoir. On the other hand, there is no standard method for determining the changes of fracture conductivities of initially sealing faults. These problems should motivate further laboratory and modelling studies.

Repository studies for radioactive waste storage

The management of radioactive waste is of crucial importance for industrial countries. Underground storage is one of the options on which researchers in many countries are currently working. The principle is to place the waste packages at depth in structures excavated in geological formations known to be impervious to water. The depth at which such structures would be excavated should be at least of the order of 500 m to prevent any disturbance at the Earth's surface and any human intrusion. A geological repository is always based on the concept of multiple barriers that prevent, on different time scales, water coming in contact with the hazardous waste, which would lead to hydrodynamic dispersion into the geological environment. The barriers include the waste packages, the engineered barrier (i.e. the filling material placed between the waste and the rock in the excavated structures) and finally the geological barrier (i.e. the host rock itself) (Schmitz *et al.* 2007). The safety of a repository is assessed by taking all of these barriers into account: they should guarantee that the radioactivity cannot escape for at least

several centuries. Eventually, on a longer time scale, fluids present in the host formation will reach and corrode the packages, and from that time on the radionuclides still present will slowly be released into the geological medium. The retention quality of the geological barrier is then crucial, to delay the migration of radioactive substances and to limit its extension in space. The choice of the host formation is of prime importance, and many countries have put considerable effort and money into studies to find the best location for radioactive waste repositories. To achieve that goal, characterizing the rock properties from cores retrieved from boreholes or at outcrops is far from sufficient. It is necessary to combine scientific investigations at different scales: at the field scale with studies using preferentially geophysical techniques to characterize the extent and potential of the storage area, and at the sample scale to estimate accurately the host-rock properties. However, it is mostly useful to work at an intermediate scale, that of the underground research laboratory (URL) in which real size experiments in galleries and tunnels excavated in the host rock can be run *in situ*, on the host rock as well as on the engineered barriers (Plötze *et al.* 2007). Several URLs are currently operating around the world, in different geological environments: the Meuse Haute-Marne URL in the Callovian–Oxfordian argillite formation (France), the Mont Terri project in the Opalinus clay formation (Switzerland), the Aspö Hard Rock Laboratory in igneous rocks (Sweden), the Lac du Bonnet laboratory in a granite (Canada) and the Yucca Mountain project in ash-flow tuffs (USA), among others. Only one site is in operation, the WIPP site in the USA, where radioactive wastes are stored at about 700 m below the surface in a salt formation. The questions to be addressed when a repository site has to be designed are numerous: Which geological environment is the more relevant? What would be the environmental impact on a long time scale? What kind of technology will be used to store the packages? Will the repository be designed to be reversible (i.e. will there be the possibility to retrieve the packages back to the surface if new technologies for managing radioactive wastes exist at a future date) or not? Which methods will be used for monitoring the site before, during and after operation? To answer these questions, it is necessary to integrate information from many fields in Earth sciences, including geochemistry, geophysics, hydrogeology, structural geology, and of course geomechanics and rock physics. Geomechanical studies are aimed to assess the mechanical stability of the repository in the excavation phase, during operation and in the post-closure period, whereas rock physics studies aim to characterize the physical properties of the host formation as

well as those of the surrounding geological formations, with emphasis on properties related to fluid transfer.

Repositories in soft rock formations

Shales are good candidates for radioactive waste storage because of their mechanical properties (Naumann *et al.* 2006) and very low permeability (Kwon *et al.* 2004a, b): several URLs are currently devoted to the study of shaly formations; for example, in France (ANDRA 2005a) and Switzerland (Bossart & Thury 2007). The Callovian–Oxfordian (COX) argillite formation is extensively studied in the URL that ANDRA (the French agency for radioactive waste management) is operating in the Meuse Haute-Marne region in France. The COX formation is characterized by a low hydraulic conductivity of the order of $10^{-12} \text{ m s}^{-1}$ consistently over the region investigated (Distinguin & Lavanchy 2007), a good homogeneity with virtually no tectonic-induced features such as fractures or joints, and a mineralogical composition that ensures high retention capacity and chemical stability (Gaucher *et al.* 2004). From the mechanical viewpoint, the presence of quartz and carbonates in the rock composition gives the rock a reasonably high mechanical strength (Naumann *et al.* 2007), whereas the clays and especially the swelling properties of smectite make the COX argillite easily deformable with a high potential to creep (Gasc-Barbier *et al.* 2004; Zhang & Rothfuchs 2004; Fabre & Pellet 2006).

The creep capability of shales is a very important property for the evolution of the excavation damaged (or disturbed) zone (EDZ) induced by stress redistribution when galleries or shafts are excavated in the host formation. Indeed, creep will eventually lead to the closure of the excavation-induced fractures in the EDZ, which will help the rock to recover its initial state. This is a very important point, because fractures are highly undesirable in a repository because of their weakening effect on the mechanical stability and most of all their capability to drive fluids much faster than in the pore network of the undisturbed host rock (Bossart *et al.* 2002). Fracture healing or sealing also occurs in hard rocks: Bernabé & Evans (2007) studied the process of fracture closure when pressure solution occurs at asperities. In soft rocks, both *in situ* and laboratory studies show that self-sealing of fractures in the EDZ leads to a significant reduction in the effective hydraulic conductivity with time, thus reducing the potential flow along excavated structures at depth (Blümeling *et al.* 2007). Corkum & Martin (2007) have shown that the mechanical behaviour of the EDZ in the Opalinus clay is not linear

elastic because of the presence of strong diagenetic bonds locking elastic strain energy into the rock microstructure, leading to low mechanical strength. Bossart *et al.* (2006) pointed out that there are still a number of open questions related to the evolution of the EDZ, which need to be addressed by conducting careful experiments like those in progress at Mont Terri. One of these experiments has been described by Damaj *et al.* (2007), who showed that the evolution of the EDZ can be surveyed by means of seismic velocity measurements using a multiple array of sensors combined with tomography techniques to image the disturbed zone. Other key experiments needed for progress have been outlined by Bossart (2007), head of the Mont Terri Rock Laboratory project. Dedecker *et al.* (2007) developed a numerical model (AC/DC; Adaptive Continuum/Discontinuum Code) to predict the variation of permeability close to an excavation in the COX argillite after a few years of its opening: those workers showed that the permeability variations are low, even in the worst scenario that they considered.

Another key issue with the EDZ in repositories is the saturation problem. When drifts or shafts are excavated in a repository, dewatering takes place on the rock wall and the fluid saturation decreases. The effect of excavation on the thermo-hydro-mechanical behaviour of a geological barrier has been studied by Gatmiri & Hoor (2007) using a fully coupled formulation for an unsaturated porous medium subjected to heating in radioactive waste repositories. Rock physical properties and especially mechanical properties are strongly affected by variations in fluid saturation (Mavko *et al.* 1998). An increase in strength and failure strain is generally observed when the saturation decreases (Zhang & Rothfuchs 2004) because most mechanical changes occur along the interlayer space in clays, making the rock softer when saturation increases (Valès *et al.* 2004). Variations in the water content of shales induced by excavation or by heating is also important because it can induce mineralogical transformations, which can be monitored by magnetic measurements (Aubourg pers. comm.).

A common feature in shales is their anisotropy, the origin of which is linked to the depositional conditions of the sediments and the foliated nature of clays. Consequently, most of the physical properties of shales are known to be anisotropic, but the intensity of the anisotropy depends on the rock property. Naumann *et al.* (2007) measured in laboratory experiments the mechanical strength of Opalinus clay samples cored parallel, perpendicular or at 45° to the bedding, and found that the mechanical strength is significantly higher when the loading direction is parallel to the bedding. It is therefore

important to have a good knowledge of the orientation of *in situ* stresses in repositories: Martin & Lanyon (2003) showed that this is especially difficult to achieve in weak rocks such as shales. The long-term deformation estimated in creep experiments by Naumann *et al.* (2007) also showed a strong anisotropy, with larger time-dependent strain observed for the samples loaded perpendicular to the bedding plane, in agreement with the results of Zhang & Rothfuchs (2004) on the COX argillite. Valès *et al.* (2004) showed that the failure mode in Tournemire shale samples depends on the core sample orientation with respect to bedding, but also on the water saturation of the samples. Shales are also well known to be anisotropic with respect to permeability, and it is important to keep this in mind when evaluating the kinetics of fluid and ion transfer in shaly formations. Whereas permeability and hydraulic diffusivity are intrinsically low in shales (Revil *et al.* 2005), the anisotropy of transport properties can be very high: for example, Zhang & Rothfuchs (2004) reported that in the COX argillite the permeability in a direction parallel to bedding is about one order of magnitude higher than that perpendicular to bedding and decreases strongly with increasing water content. The low permeability of shales combined with a high anisotropy and a strong dependence on water content makes it difficult to estimate the mechanical properties and poroelastic parameters of shales in the laboratory (Bemer *et al.* 2004). The elastic anisotropy of shales (Sayers 1994) can also be estimated through the measurement of seismic-wave velocities (Sarout *et al.* 2007). David *et al.* (2007) measured a 20% anisotropy for P-wave velocity in the COX argillite, with a minimum velocity oriented in the direction perpendicular to bedding. Robion *et al.* (2007) showed that the anisotropy of P-wave velocity correlates very well with the anisotropy of magnetic susceptibility (although the latter is less intense) and that it changes when temperature increases. Esteban *et al.* (2006, 2007) have also studied the anisotropy of magnetic susceptibility in the COX argillite, and related the orientation of the eigenvectors of the susceptibility tensor to microstructural observations and pore-size distributions using mercury porosimetry applied to oriented samples. Sarout *et al.* (2007) extended the study of elastic anisotropy with the measurement of S-wave velocity, and their study of seismic velocity evolution with increasing effective stress revealed the interplay between damage and variation of water saturation in the COX argillite samples tested in triaxial experiments. A similar study has been conducted by Popp & Salzer (2007) using a multi-anvil apparatus, to define the dilatancy boundary for the Opalinus clay formation. A theoretical model for the anisotropy of

seismic-wave velocity for a cracked solid with an anisotropic crack distribution has been proposed by Wong & Zhu (2007). The characterization of the anisotropy of physical properties is of great importance for monitoring purposes (Stenhouse & Savage 2004), because large errors can be introduced if it is considered that the rock behaves as an isotropic medium, which is generally far from the reality in shaly formations.

Repositories in hard rock formations

Hard rock formations are potentially good candidates for radioactive waste storage for several reasons: a very low water content (a typical porosity for a granite is of the order of 0.5%), a high mechanical strength, and a high thermal conductivity, which helps in dissipating heat generated by the packages (ANDRA 2005b). Special attention has to be paid to the presence of fractures at all scales in crystalline rocks, as fractures in hard rocks would behave as potential sites for retention of radionuclides, or alternately as preferential paths for the radionuclides to migrate out of the repository. Several URLs are operating in hard rocks: the Aspö Hard Rock Laboratory in Sweden, the Grimsel Underground Testing Facility in Switzerland, and the Lac du Bonnet Laboratory in Canada are good examples. As is the case for URLs in soft rocks discussed above, one has also to deal with the presence of an excavation damage zone in tunnels drilled into hard rock formations. Tsang *et al.* (2007) presented the results of a fully coupled hydromechanical model to understand anomalies in fluid pressure observed during the excavation of the FEBEX (Full-Scale Engineered Barriers Experiment) tunnel in the Grimsel test site (Switzerland): they argued that the fractures created during excavation are strongly affected by the local stress field, which is different from the regional stress field. The FEBEX tunnel experiment was aimed at monitoring continuously the engineered barrier (bentonite) and the surrounding rock during heating–cooling cycles: it was part of the DECOVALEX international programme, the objective of which was to operate a number of full-scale experiments in different URLs (Tsang *et al.* 2005). The formation and/or propagation of fractures in hard rocks during the excavation phase and/or the operating phase in a repository can be monitored by means of acoustic emissions, a technique that was first applied to laboratory studies (e.g. Chang & Lee 2004; Lei *et al.* 2004) and extended to full-scale studies in tunnels or drifts (e.g. Young & Collins 2001; Reyes-Montes *et al.* 2005). Research projects in the Aspö Hard Rock Laboratory have focused, among other aspects, on the estimation of the regional stress field in the

surrounding rock from *in situ* measurements (Ask 2006a, b) and on the development of a real-size prototype of radwaste deposition holes including copper canisters with heaters, bentonite buffers and backfilled deposition tunnels closed by concrete plugs (Johannesson *et al.* 2007). In the latter experiment, a continuous monitoring of temperature and water inflow was conducted, which showed that the system was still drained after several months of operation with water pressure slowly building up in the tunnel. Indeed, fluid circulation is generally enhanced when fractures are present in hard rocks where permeability is intrinsically low: the EDZ provides theoretically possible pathways for fluids to migrate along the tunnels. However, fractures need to be well connected and form a percolating network for fluid or radionuclides to migrate over long distances.

Over recent decades, a number of laboratory experiments have focused on the interplay between mechanical properties and fluid flow in fractured hard rocks, with emphasis on stress-induced elastic closure (Brown & Scholz 1985), effective aperture in fractures with asperities (Brown 1987), and fracture healing driven by pressure solution (Beeler & Hickman 2004). For a review of these aspects, the reader can refer to Guégan & Boutea (2004, chapter 7). Fracture nucleation and propagation in hard rocks can be imaged by means of acoustic emission recording, taking advantage of faster technologies available for signal processing and waveform analysis (Lockner *et al.* 1991; Butt & Calder 1998; Jouniaux *et al.* 2001; Schubnel *et al.* 2006b). Stress-induced damage in hard rocks can be estimated indirectly from the variation of elastic-wave velocities (Takemura & Oda 2005), an important point when monitoring issues have to be addressed. Meglis *et al.* (2005) imaged the extension of the EDZ in the Lac du Bonnet URL (Canada) using ultrasonic velocity tomography: variations in velocity, amplitude and anisotropy correlate well with the variations in the local stress tensor, which results in the presence of regions either in tension or in compression in the vicinity of the excavated tunnel wall. In hard rocks, fracture healing is associated with the development of physico-chemical processes such as pressure solution (Yasubara *et al.* 2004), a mechanism with slower kinetics compared with the development of creep deformation in soft rocks. Jouniaux *et al.* (2001) showed that the presence of healed fractures in a rock mass lowers its mechanical strength and that the acoustic emissions recorded in a triaxial test concentrate along these healed fractures. Kim *et al.* (2007) studied the influence of fracture statistics on the mechanical behaviour of rock masses. At the scale of a fault zone, large variations of physical rock properties are

observed in the fault core, the damaged zone and the protolith (Rosener & Géraud 2007). Theoretical models for fracture nucleation and propagation have to take into account the existence of a process zone at the fracture tip (Zang *et al.* 2000), the crack statistics for stress-induced or temperature-induced damage (David *et al.* 1999) and the coalescence mechanisms, which, starting from a diffuse distribution of damage, lead to fracture localization. Recently, numerical models based on particle mechanics, initially developed for granular media (Potyondy & Cundall 2004), have proven to be very useful for modelling mechanical cracking and fracturing processes in granite (Al-Busaidi *et al.* 2005). For such theoretical or numerical models, data are needed on the crack distributions in hard rocks, which can be investigated either by indirect methods (Kachanov 1993; Schubnel *et al.* 2006a; Wong & Zhu 2007) or by direct observation using various microscopy techniques (Kranz 1983; Menéndez *et al.* 1999; Liu *et al.* 2006).

Conclusion

Geomechanical modelling for reservoir production enhancement requires the integration of information from studies in rock mechanics and rock physics. Depending on the type of coupling, different levels of complexity exist, involving more or less time-consuming numerical codes. There is still potential for improvement of these models; for example, a key point is to better take into account the relationships between permeability and stress both in the matrix and in fractured reservoirs, for different stress paths. Another key point is to account for the possibility of strain localization in compaction bands, in which case modifications in the fluid flow patterns may occur in the reservoir. Enhancement of reservoir production needs to be further developed for obvious economic reasons, in face of the growing demand on energy resources in industrial and emerging countries.

The repository problem is different in the sense that the key issue is to find a site as safe as possible for storing hazardous waste, and the focus is on environmental rather than economic issues. Research by scientists in many fields is necessary to improve our knowledge of the long-term behaviour of geological formations in which radwastes would be stored. The challenging task is to define scenarios that are as precise as possible for the long-term evolution (typically hundreds of years) of repositories either in soft rock or in the hard rock, from experiments run on short time scales. The accuracy and predictability of models depends on the quality of experimental data obtained at

different scales, and the possibility for scientists to work in underground research laboratories is fundamental in this regard. Public acceptance will depend largely on the reliability of the models, on which there is still much work to do. Fortunately, international collaboration is active in making progress on this subject.

We have benefited from discussions with P. Baud on compaction bands in reservoir rocks. P. Lemonnier at IFP and B. Maillet at Cergy-Pontoise University reviewed an early version of the manuscript. J. Sarout (ENS Paris) kindly provided some of the pictures in Figure 1. Many thanks go to B. Menéndez for her help in the design of the graphics in Figure 1.

References

- AL-BUSAIDI, A., HAZZARD, J. F. & YOUNG, R. P. 2005. Distinct element modeling of hydraulically fractured Lac du Bonnet granite. *Journal of Geophysical Research*, **110**, B06302, doi:10.1029/2004JB003297.
- ALLEN, D. R. 1968. Physical changes of reservoir properties caused by subsidence and repressurizing operations, Wilmington field, California. *Journal of Petroleum Technology*, **20**, 23–29, January.
- ANDRA, 2005a. *Dossier 2005 Argile Synthesis report—Evaluation of the feasibility of a geological repository—Meuse/Haute-Marne Site*. Publications ANDRA, coll ‘Les rapports’.
- ANDRA, 2005b. *Dossier 2005 Granite Synthesis report—Interest for granitic formations for geological storage*. Publications ANDRA, coll ‘Les rapports’.
- ARNS, C. H., KNACKSTEDT, M. A., PINCZEWSKIZ, W. V. & GARBOCZI, E. J. 2002. Computation of linear elastic properties from microtomographic images: methodology and agreement between theory and experiment. *Geophysics*, **67**, 1396–1405.
- ASK, D. 2006a. New developments in the Integrated Stress Determination Method and their application to rock stress data at the Aspö HRL, Sweden. *International Journal of Rock Mechanics & Mining Sciences*, **43**, 107–126.
- ASK, D. 2006b. Measurement-related uncertainties in overcoring data at the Aspö HRL, Sweden. Part 2: Biaxial tests of CSIRO HI overcore samples. *International Journal of Rock Mechanics & Mining Sciences*, **43**, 127–138.
- BAUD, P., KLEIN, E. & WONG, T.-F. 2004. Compaction localization in porous sandstones: spatial evolution of damage and acoustic emission activity. *Journal of Structural Geology*, **26**, 603–624.
- BEELER, N. M. & HICKMAN, S. H. 2004. Stress-induced, time-dependent fracture closure at hydrothermal conditions. *Journal of Geophysical Research*, **109**, doi:10.1029/2002JB001782.
- BEMER, E., LONGUIMARE, P. & VINCKÉ, O. 2004. Poroelastic parameters of Meuse/Haute Marne argillites: effect of loading and saturation states. *Applied Clay Science*, **26**, 359–366.
- BERNABÉ, Y. & EVANS, B. 2007. Numerical modelling of pressure solution deformation at axisymmetric

- asperities under normal load. In: DAVID, C. & LE RAVALEC-DUPIN, M. (eds) *Rock Physics and Geomechanics in the Study of Reservoirs and Repositories*. Geological Society, London, Special Publications, **284**, 185–207.
- BLÖCHER, G., BRUHN, D., ZIMMERMANN, G., McDERMOTT, C. & HUENGES, E. 2007. Investigation of the undrained poroelastic response of sandstones to confining pressure via laboratory experiment, numerical simulation and analytical calculation. In: DAVID, C. & LE RAVALEC-DUPIN, M. (eds) *Rock Physics and Geomechanics in the Study of Reservoirs and Repositories*. Geological Society, London, Special Publications, **284**, 71–87.
- BLÜMLING, P., BERNIER, F., LEBON, P. & MARTIN, C. D. 2007. The excavation damaged zone in clay formations time-dependent behaviour and influence on performance assessment. *Physics and Chemistry of the Earth*, **32**, 588–599.
- BOSSART, P. 2007. Overview of key experiments on repository characterization in the Mont Terri Rock Laboratory. In: DAVID, C. & LE RAVALEC-DUPIN, M. (eds) *Rock Physics and Geomechanics in the Study of Reservoirs and Repositories*. Geological Society, London, Special Publications, **284**, 35–40.
- BOSSART, P. & THURY, M. 2007. Research in the Mont Terri Rock laboratory: quo vadis? *Physics and Chemistry of the Earth*, **32**, 19–31.
- BOSSART, P., MEIER, P. M., MOERI, A., TRICK, T. & MAYOR, J. C. 2002. Geological and hydraulic characterisation of the excavation disturbed zone in the Opalinus Clay of the Mont Terri Rock Laboratory. *Engineering Geology*, **66**, 19–38.
- BROWN, S. R. 1987. Fluid flow through rock joints: the effect of surface roughness. *Journal of Geophysical Research*, **92**, 1337–1347.
- BROWN, S. R. & SCHOLZ, C. H. 1985. Closure of random elastic surfaces in contact. *Journal of Geophysical Research*, **90**, 5531–5545.
- BUTT, S. D. & CALDER, P. N. 1998. Experimental procedures to measure volumetric changes and microseismic activity during triaxial compression tests. *International Journal of Rock Mechanics & Mining Sciences*, **35**, 249–254.
- CHANG, S.-H. & LEE, C.-I. 2004. Estimation of cracking and damage mechanisms in rock under triaxial compression by moment tensor analysis of acoustic emission. *International Journal of Rock Mechanics & Mining Sciences*, **41**, 1069–1086.
- CHARLEZ, P. A. 1997. *Rock Mechanics, Petroleum Applications*. **2**. Technip, Paris.
- CORKUM, A. G. & MARTIN, C. D. 2007. The mechanical behaviour of weak mudstone (Opalinus Clay) at low stresses. *International Journal of Rock Mechanics & Mining Sciences*, **44**, 196–209.
- DAMAJ, J., BALLAND, C., ARMAND, G., VERDEL, T., AMITRANO, D. & HOMAND, F. 2007. Velocity survey of an excavation damaged zone: influence of excavation and reloading. In: DAVID, C. & LE RAVALEC-DUPIN, M. (eds) *Rock Physics and Geomechanics in the Study of Reservoirs and Repositories*. Geological Society, London, Special Publications, **284**, 41–55.
- DAVID, C., MENÉNDEZ, B. & DAROT, M. 1999. Influence of stress-induced and thermal cracking on physical properties and microstructure of La Peyratte granite. *International Journal of Rock Mechanics & Mining Sciences*, **36**, 433–448.
- DAVID, C., ROBION, P. & MENÉNDEZ, B. 2007. Anisotropy of elastic, magnetic and microstructural properties of the Callovo-Oxfordian argillite. *Physics and Chemistry of the Earth*, **32**, 145–153.
- DEDECKER, F., CUNDALL, P., BILLAUX, D. & GROEGER, T. 2007. Evaluation of damage-induced permeability using a three-dimensional Adaptive Continuum/Discontinuum Code (AC/DC). *Physics and Chemistry of the Earth*, doi:10.1016/j.pce.2006.01.006.
- DI GIOVANNI, A. A., FREDRICH, J. T., HOLCOMB, D. J. & OLSSON, W. A. 2000. Micromechanics of compaction in an analogue reservoir sandstone. In: GIRAD, J., LIEBMAN, M., BREEDS, C. & DOE, T. (eds) *Proceedings of the North America Rock Mechanics Symposium, July 2000*. Balkema, Rotterdam, 1153–1158.
- DISTINGUIN, M. & LAVANCHY, J. M. 2007. Determination of hydraulic properties of the Callovo-Oxfordian argillite at the Bure site: synthesis of the results obtained in deep boreholes using several *in situ* investigation techniques. *Physics and Chemistry of the Earth*, **32**, 379–392.
- ESTEBAN, L., GÉRAUD, Y. & BOUCHEZ, J. L. 2006. Pore network geometry in low permeability argillites from magnetic fabric data and oriented mercury injections. *Geophysical Research Letters*, **33**, L18311, doi:10.1029/2006GL026908.
- ESTEBAN, L., GÉRAUD, Y. & BOUCHEZ, J. L. 2007. Pore network connectivity anisotropy in Jurassic argillite specimens from eastern Paris Basin (France). *Physics and Chemistry of the Earth*, **32**, 161–169.
- FABRE, G. & PELLET, F. 2006. Creep and time-dependent damage in argillaceous rocks. *International Journal of Rock Mechanics & Mining Sciences*, **43**, 950–960.
- FORTIN, J., SANCHITS, S., DRESEN, G. & GUÉGUEN, Y. 2006. Acoustic emission and velocities associated with the formation of compaction bands in sandstone. *Journal of Geophysical Research*, **111**, doi:10.1029/2005JB003854.
- FORNEL, A., MEZGHANI, M. & LANGLAIS, V. 2007. Using production data and time domain seismic attributes for history matching. In: DAVID, C. & LE RAVALEC-DUPIN, M. (eds) *Rock Physics and Geomechanics in the Study of Reservoirs and Repositories*. Geological Society, London, Special Publications, **284**, 147–159.
- GASC-BARBIER, M., CHANCHOLE, S. & BÉREST, P. 2004. Creep behavior of Bure clayey rock. *Applied Clay Science*, **26**, 449–458.
- GATMIRI, B. & HOOR, A. 2007. Effect of excavation on the thermo-hydro-mechanical behaviour of a geological barrier. *Physics and Chemistry of the Earth*, **32**, 947–956.
- GAUCHER, E., ROBELIN, C., MATRAY, J. M. ET AL. 2004. ANDRA underground research laboratory: interpretation of the mineralogical and geochemical data acquired in the Callovo-Oxfordian

- formation by investigative drilling. *Physics and Chemistry of the Earth*, **29**, 55–77.
- GEERTSMA, J. 1957. The effect of fluid pressure decline on volumetric change of porous rocks. *Transactions of AIME*, **210**, 331.
- GOSSELIN, O., COMINELLI, A., VAN DEN BERG, S. & CHOWDHURY, S. D. 2000. A gradient-based approach for history-matching of both production and 4D seismic data. In: *7th ECMOR, Baveno, Italy V-8*.
- GUÉGUEN, Y. & BOUTÉCA, M. (eds) 2004. *Mechanics of Fluid-Saturated Rocks*. International Geophysics Series, **89**.
- GUÉGUEN, Y., LE RAVALEC, M. & RICARD, L. 2006. Upscaling: effective medium theory, numerical methods and the fractal dream. *Pure and Applied Geophysics*, **163**, 1175–1192.
- GUTTIERREZ, M. & MAKURAT, A. 1997. Coupled HTM modelling of cold water injection in fractured hydrocarbon reservoirs. *International Journal of Rock Mechanics & Mining Sciences*, **34**, 62.
- HAIMSON, B. C. 2001. Fracture-like borehole breakouts in high porosity sandstone: are they caused by compaction bands? *Physics and Chemistry of the Earth (A)*, **26**, 15–20.
- HAIMSON, B. C. & LEE, H. 2004. Borehole breakouts and compaction bands in two high-porosity sandstones. *International Journal of Rock Mechanics & Mining Sciences*, **41**, 287–301.
- HAIMSON, B. & KLAETSCH, A. 2007. Compaction bands and the formation of slot-shaped breakouts in St. Peter sandstone. In: DAVID, C. & LE RAVALEC-DUPIN, M. (eds) *Rock Physics and Geomechanics in the Study of Reservoirs and Repositories*. Geological Society, London, Special Publications, **284**, 89–105.
- HEFFER, K. J., LAST, N. C., KOUTSABELOULIS, N. C., CHAN, H. C. M., GUTTIERREZ, M. & MAKURAT, A. 1994. The influence of natural fractures, faults and earth stresses on reservoir performance, geomechanical analysis by numerical modelling. In: AASEN, J. O., BERG, E. ET AL. (eds) *North Sea Oil and Gas Reservoirs*, III. Kluwer, Dordrecht, 201–211.
- HOLCOMB, D. J. & OLSSON, W. A. 2003. Compaction localization and fluid flow. *Journal of Geophysical Research*, **108**, doi:10.1029/2001JB000813.
- JEANNIN, L., MAINGUY, M., MASSON, R. & VIDAL-GILBERT, S. 2006. Accelerating the convergence of coupled geomechanical-reservoir simulations. *International Journal of Numerical Analysis and Methods in Geomechanics*, in press.
- JIN, M., SOMMERVILLE, J. & SMART, B. G. D. 2000. Coupled reservoir simulation applied to the management of production induced stress-sensitivity. In: *SPE International Oil & Gas Conference and Exhibition, Beijing*, 7–10 November, SPE 64790.
- JOHANNESSON, L.-E., BORGESSON, L., GOUDARZI, R. & SANDEN, T. 2007. Prototype repository: a full scale experiment at Aspö HRL. *Physics and Chemistry of the Earth*, **32**, 58–76.
- JOUNIAUX, L., MASUDA, K., LEI, X., NISHIZAWA, O. & KUSUNOSE, K. 2001. Comparison of the microfracture localization in granite between fracturation slip of a preexisting macroscopic healed joint by acoustic emission measurements. *Journal of Geophysical Research*, **106**, 8687–8698.
- KACHANOV, M. 1993. Elastic solids with many cracks and related problems. *Advances in Applied Geophysics*, **30**, 259–445.
- KATSMAN, R., AHARONOV, E. & SCHER, H. 2005. Numerical simulation of compaction bands in high-porosity sedimentary rock. *Mechanics of Materials*, **37**, 143–162.
- KATSMAN, R. & AHARONOV, E. 2006. A study of compaction bands originating from cracks, notches, and compacted defects. *Journal of Structural Geology*, **28**, 508–518.
- KIM, B. H., KAISER, P. K. & GRASSELLI, G. 2007. Influence of persistence on behaviour of fractured rock masses. In: DAVID, C. & LE RAVALEC-DUPIN, M. (eds) *Rock Physics and Geomechanics in the Study of Reservoirs and Repositories*. Geological Society, London, Special Publications, **284**, 161–173.
- KLEIN, E., BAUD, P., REUSCHLÉ, T. & WONG, T.-F. 2001. Mechanical behaviour and failure mode of Bentheim sandstone under triaxial compression. *Physics and Chemistry of the Earth (A)*, **26**(1–2), 21–25.
- KOUTSABELOULIS, N. C., HEFFER, K. J. & WONG, S. 1994. Numerical geomechanics in reservoir engineering. In: SIRIWARDANE, H. J. & ZAMAN, M. M. (eds) *Computer Methods and Advances in Geomechanics*. Balkema, Rotterdam, 2097–2104.
- KRANZ, R. L. 1983. Microcracks in rocks: a review. *Tectonophysics*, **100**, 449–480.
- KRETZ, V., LE RAVALEC-DUPIN, M. & ROGGERO, F. 2004. An integrated reservoir characterization study matching production data and 4D-seismic. *SPE Reservoir Evaluation and Engineering*, April, 116–122.
- KWON, O., HERBERT, B. E. & KRONENBERG, A. K. 2004a. Permeability of illite-bearing shale: 2. Influence of fluid chemistry on flow and functionally connected pores. *Journal of Geophysical Research*, **109**, B10206, doi:10.1029/2004JB003055.
- KWON, O., KRONENBERG, A. K., GANGI, A. F., JOHNSON, B. & HERBERT, B. E. 2004b. Permeability of illite-bearing shale: 1. Anisotropy and effects of clay content and loading. *Journal of Geophysical Research*, **109**, B10205, doi:10.1029/2004JB003052.
- LANDA, J. & HORNE, R. 1997. A procedure to integrate well test data, reservoir performance history and 4-D seismic information into a reservoir description. In: *SPE Annual Technical Conference and Exhibition, San Antonio, TX*, 5–8 October. SPE 38653.
- LEI, X., MASUDA, K., NISHIZAWA, O. ET AL. 2004. Detailed analysis of acoustic emission activity during catastrophic fracture of faults in rock. *Journal of Structural Geology*, **26**, 247–258.
- LE RAVALEC-DUPIN, M. 2005. *Inverse Stochastic Modeling of Flow in Porous Media—Application to Reservoir Characterization*. Technip, Paris.
- LIU, S., FAISAL ANWAR, A. H. M., KIM, B. C. & ICHIKAWA, Y. 2006. Observation of microcracks in granite using a confocal laser scanning microscope. *International Journal of Rock Mechanics & Mining Sciences*, **43**, 1293–1305.
- LOCKNER, D. A., BYERLEE, J. D., KUKSENKO, V., PONOMAREV, A. & SIDORIN, A. 1991. Quasi-static fault growth and shear fracture energy in granite. *Nature*, **350**, 39–42.

- LONGUEMARE, P., MAINGUY, M., LEMONNIER, P., ONAISI, A., GÉRARD, Ch. & KOUTSABELOULIS, N. 2002. Geomechanics in reservoir simulation: overview of coupling methods and field case study. *Oil and Gas Science and Technology*, **57**, 471–483.
- MARTIN, C. D. & LANYON, G. W. 2003. Measurement of in-situ stress in weak rocks at Mont Terri Rock Laboratory, Switzerland. *International Journal of Rock Mechanics & Mining Sciences*, **40**, 1077–1088.
- MAVKO, G., MUKERJI, T. & DVORKIN, J. 1998. *The Rock Physics Handbook: Tools for Seismic Analysis in Porous Media*. Cambridge University Press, Cambridge.
- MEGLIS, I. L., CHOW, T., MARTIN, C. D. & YOUNG, R. P. 2005. Assessing *in situ* microcrack damage using ultrasonic velocity tomography. *International Journal of Rock Mechanics & Mining Sciences*, **42**, 25–34.
- MENÉNDEZ, B., DAVID, C. & DAROT, M. 1999. A study of the crack network in thermally and mechanically cracked granite samples using confocal scanning laser microscopy. *Physics and Chemistry of the Earth, A*, **24**, 627–632.
- MERLE, H. A., KENTIE, C. J. P., VAN OPSTAL, G. H. C. & SCHNEIDER, G. M. G. 1976. The Bachaquero study—a composite analysis of the behavior of a compaction drive/solution gas drive reservoir. *Journal of Petroleum Technology*, September, 1107–1115.
- MOLLEMA, P. N. & ANTONELLINI, M. A. 1996. Compaction bands: a structural analog for anti-mode I cracks in aeolian sandstone. *Tectonophysics*, **32**, 889–895.
- NAUMANN, M., HUNSCHE, U. & SCHULZE, O. 2007. Experimental investigations on anisotropy in dilatancy, failure and creep of Opalinus Clay. *Physics and Chemistry of the Earth*, **32**, 889–895.
- NGWENYA, B. T., KWON, O., ELPHICK, S. C. & MAIN, I. G. 2003. Permeability evolution during progressive development of deformation bands in porous sandstones. *Journal of Geophysical Research*, **108**, 2343, doi:10.1029/2002JB001854.
- OLSSON, W. A. & HOLCOMB, D. J. 2000. Compaction localization in porous rock. *Geophysical Research Letters*, **27**, 3537–3540.
- OSTERMEIER, R. M. 2001. Compaction effects on porosity and permeability: deepwater Gulf of Mexico turbidites. *Journal of Petroleum Technology*, February, 68–74.
- PLÖTZE, M., KAHR, G., DOHRMANN, R. & WEBER, H. 2007. Hydro-mechanical, geochemical and mineralogical characteristics of the bentonite buffer in a heater experiment: the HE-B project at the Mont Terri Rock Laboratory. *Physics and Chemistry of the Earth*, **32**, 730–740.
- POPP, T. & SALZER, K. 2007. Anisotropy of seismic and mechanical properties of Opalinus clay during triaxial deformation in a multi-anvil apparatus. *Physics and Chemistry of the Earth*, **32**, 879–888.
- POTYONDY, D. O. & CUNDALL, P. A. 2004. A bonded-particle model for rock. *International Journal of Rock Mechanics & Mining Sciences*, **41**, 1329–1364.
- REVIL, A., LEROY, P. & TITOV, K. 2005. Characterization of transport properties of argillaceous sediments: application to the Callovo-Oxfordian argillite. *Journal of Geophysical Research*, **110**, B06202, doi:10.1029/2004JB003442.
- REYES-MONTES, J. M., RIETBROCK, A., COLLINS, D. S. & YOUNG, R. P. 2005. Relative location of excavation induced microseismicity at the Underground Research Laboratory (AECL, Canada) using surveyed reference events. *Geophysical Research Letters*, **32**, L05308, doi:10.1029/2004GL021733.
- ROBION, P., DAVID, C. & COLOMBIER, J. C. 2007. Temperature-induced evolution of the elastic and magnetic anisotropy in argillite samples from Bure underground research laboratory, eastern France. In: DAVID, C. & LE RAVALEC-DUPIN, M. (eds) *Rock Physics and Geomechanics in the Study of Reservoirs and Repositories*. Geological Society, London, Special Publications, **284**, 57–69.
- ROSENER, M. & GÉRAUD, Y. 2007. Using physical properties to understand the porosity network geometry evolution in gradually altered granites in damage zones. In: DAVID, C. & LE RAVALEC-DUPIN, M. (eds) *Rock Physics and Geomechanics in the Study of Reservoirs and Repositories*. Geological Society, London, Special Publications, **284**, 175–184.
- RUDNICKI, J. W. 2007. Models for compaction band propagation. In: DAVID, C. & LE RAVALEC-DUPIN, M. (eds) *Rock Physics and Geomechanics in the Study of Reservoirs and Repositories*. Geological Society, London, Special Publications, **284**, 107–125.
- SAMIER, P., ONAISI, A. & FONTAINE, G. 2006. Comparisons of uncoupled and various coupling techniques for practical field examples. *SPE Journal*, March, 89–102.
- SAROUT, J. 2006. *Propriétés physiques et anisotropie des roches argileuses: Modélisation micromécanique et expériences triaxiales*. PhD thesis, Ecole Normale Supérieure de Paris.
- SAROUT, J., MOLEZ, L., GUÉGUEN, Y. & HOTEIT, N. 2007. Shale dynamic properties and anisotropy under triaxial loading: experimental and theoretical investigations. *Physics and Chemistry of the Earth*, **32**, 896–906.
- SAYERS, C. M. 1994. The elastic anisotropy of shales. *Journal of Geophysical Research*, **99**, 767–774.
- SCHMITZ, R. M., SCHROEDER, C. & CHARLIER, R. 2007. A general approach to assess hydro-mechanical changes of natural clay barriers due to physico-chemical interactions with radwaste in deep disposal sites. *Physics and Chemistry of the Earth*, **32**, 922–928.
- SCHUBNEL, A., BENSON, P. M., THOMPSON, B. D., HAZZARD, J. F. & YOUNG, R. P. 2006a. Quantifying damage, saturation and anisotropy in cracked rocks by inverting elastic wave velocities. *Pure and Applied Geophysics*, **163**, 947–973.
- SCHUBNEL, A., WALKER, E., THOMPSON, B. D., FORTIN, J., GUÉGUEN, Y. & YOUNG, R. P. 2006b. Transient creep, aseismic damage and slow failure in Carrara marble. *Geophysical Research Letters*, **33**, doi:10.1029/2006GL026619.
- SEGALL, P. 1989. Earthquakes triggered by fluid extraction. *Geology*, **17**, 942–946.

- SETTARI, A. & MOURITS, F. M. 1998. A coupled reservoir and geomechanical simulation system. *SPE Journal*, 219–226.
- STENHOUSE, M. J. & SAVAGE, D. 2004. Monitoring experience associated with nuclear waste disposal and its application to CO₂ sequestration projects. In: BAINES, S. J. & WORDEN, R. H. (eds) *Geological Storage of Carbon Dioxide*. Geological Society, London, Special Publications, **223**, 235–247.
- STERNLOF, K. R., RUDNICKI, J. W. & POLLARD, D. D. 2005. Anticrack inclusion model for compaction bands in sandstone. *Journal of Geophysical Research*, **110**, B11403, doi:10.1029/2005JB003764.
- STERNLOF, K. R., KARIMI-FARD, M., POLLARD, D. D. & DURLOFSKY, L. J. 2006. Flow and transport effects of compaction bands in sandstone at scales relevant to aquifer and reservoir management. *Water Resources Research*, **42**, W07425, doi:10.1029/2005WR004664.
- STONE, T., GARFIELD, B. & PAPANASTASIOU, P. 2000. Fully coupled geomechanics in a commercial reservoir simulator. In: *SPE European Petroleum Conference, Paris, 24–25 October*, 45–52.
- SYLTE, J. E., THOMAS, D. K., RHETT, D. W., BRUNNING, D. D. & NAGEL, N. B. 1999. Water induced compaction in the Ekofisk field. In: *Annual Technical Conference and Exhibition, Houston, TX, 3–6 October*, SPE 56246.
- TAKEMURA, T. & ODA, M. 2005. Changes in crack density and wave velocity in association with crack growth in triaxial tests of Inada granite. *Journal of Geophysical Research*, **110**, B05401, doi:10.1029/2004JB003395.
- TRAN, D., NGHIEM, L. & BUCHANAN, L. 2005. Improved iterative coupling of geomechanics with reservoir simulation. In: *SPE Reservoir Simulation Symposium, Houston, TX, 31 January–2 February*, SPE 93244.
- TSANG, C. F., JING, L., STEPHANSSON, O. & KAUTSKY, F. 2005. The DECOVALEX III project: a summary of activities and lessons learned. *International Journal of Rock Mechanics & Mining Sciences*, **42**, 593–610.
- TSANG, C.-F., RUTQVIST, J. & MIN, K.-B. 2007. Fractured rock hydromechanics: from borehole testing to solute transport and CO₂ storage. In: DAVID, C. & LE RAVALEC-DUPIN, M. (eds) *Rock Physics and Geomechanics in the Study of Reservoirs and Repositories*. Geological Society, London, Special Publications, **284**, 15–34.
- VAJDOVA, V., BAUD, P. & WONG, T.-F. 2004. Permeability evolution during localized deformation in Bentheim sandstone. *Journal of Geophysical Research*, **109**, B10406, doi:10.1029/2003JB002942.
- VALÈS, F., NGUYEN MINH, D., GHARBI, H. & REJEB, A. 2004. Experimental study of the influence of the degree of saturation on physical and mechanical properties in Tournemire shale (France). *Applied Clay Science*, **26**, 197–207.
- VIDAL-GILBERT, S. & TISSEAU, E. 2006. Sensitivity analysis of geomechanical behavior on time-lapse seismic velocity modeling. In: *SPE Europe/EAGE ACE, Vienna*, SPE 100142.
- WENG, M. C., JENG, F. S., HUANG, T. H. & LIN, M. L. 2005. Characterizing the deformation behavior of Tertiary sandstones. *International Journal of Rock Mechanics & Mining Sciences*, **42**, 388–401.
- WONG, T.-F., DAVID, C. & ZHU, W. 1997. The transition from brittle to cataclastic flow: mechanical deformation. *Journal of Geophysical Research*, **102**, 3009–3025.
- WONG, T.-F., BAUD, P. & KLEIN, E. 2001. Localized failure modes in a compactant porous rock. *Geophysical Research Letters*, **28**, 2521–2524.
- WONG, T.-F. & ZHU, W. 2007. Weak elastic anisotropy in a cracked rock. In: DAVID, C. & LE RAVALEC-DUPIN, M. (eds) *Rock Physics and Geomechanics in the Study of Reservoirs and Repositories*. Geological Society, London, Special Publications, **284**, 207–220.
- YASUHARA, H., ELSWORTH, D. & POLAK, A. 2004. The evolution of permeability in a natural fracture: the significant role of pressure solution. *Journal of Geophysical Research*, **109**, doi:10.1029/2003JB002663.
- YOUNG, R. P. & COLLINS, D. S. 2001. Seismic studies of rock fracture at the Underground Research Laboratory, Canada. *International Journal of Rock Mechanics & Mining Sciences*, **38**, 787–799.
- ZANG, A., WAGNER, F. C., STANCHITS, S., JANSEN, C. & DRESEN, G. 2000. Fracture process zone in granite. *Journal of Geophysical Research*, **105**, 23651–23661.
- ZHANG, C. & ROTHFUCHS, T. 2004. Experimental study of the hydro-mechanical behaviour of the Callovo-Oxfordian argillite. *Applied Clay Science*, **26**, 325–336.

Fractured rock hydromechanics: from borehole testing to solute transport and CO₂ storage

C.-F. TSANG¹, J. RUTQVIST¹ & K.-B. MIN²

¹*Earth Sciences Division, Lawrence Berkeley National Laboratory, 1 Cyclotron Road, Berkeley, CA 94720, USA (e-mail: cftang@lbl.gov)*

²*Department of Energy and Geo-Environmental Engineering, Pennsylvania State University, University Park, PA 16802, USA*

Abstract: The interaction between mechanical deformation and fluid flow in fractured rock gives rise to a host of coupled hydromechanical processes, which form the basis of a number of interesting research questions with practical implications. This paper will first discuss these processes in general, describing two numerical models that have been developed to analyse these processes. Then, four very different studies will be presented to illustrate the richness of this field. The first study has to do with borehole injection testing to determine fracture parameters and how hydromechanical effects will modify test results. The second study is on stress changes (caused by stress release) in rock near a tunnel during excavation, which cause significant changes in fluid pressures in the region. The third study is on the relationship between mechanical effects and flow anisotropy and channelling in a rock block with a fracture network. The fourth study pertains to the hydromechanical effects associated with deep CO₂ injection and storage. These examples serve to demonstrate the various interesting research problems in fractured rock hydromechanics. In the coming years, we expect intensified activity and further advances in this exciting field of research.

Hydromechanical coupling in fractured rock masses is an important issue for many rock mechanics and hydrogeology applications (Rutqvist & Stephansson 2003). Fractured rock masses are composed of continuum rock matrix with embedded fractures, and the latter act as the main pathways of fluid flow. Hydromechanical coupling can be direct or indirect (Rutqvist & Stephansson 2003). A direct coupling occurs when applied stresses produce a change in hydraulic pressure, or vice versa. An indirect coupling occurs when mechanical changes affect hydraulic property parameters, or when hydraulic conditions affect mechanical properties. For example, apertures of fractures can change as a result of normal stress-induced closures or openings, and also as a result of shear stress-induced dilations. Hence, the permeability of fractured rock masses, which is strongly dependent on fracture apertures, is stress dependent. The indirect coupling is particularly important, as stress-induced changes in permeability can be large (several orders of magnitude) and irreversible under perturbations resulting from various natural and human activities. These activities include underground construction, causing stress redistributions close to rock openings, as well as geothermal energy and oil or gas reservoir productions, where injection and extraction of fluids entail significant changes in fluid pressures and effective stresses underground.

In the early and mid-1980s, coupled processes associated with nuclear waste repositories were

discussed in a series of workshops, concluded with an edited book on the subject (Tsang 1987). More general discussions on coupled processes in geological systems were given by Tsang (1991, 1999). Numerical models capable of simulating coupled thermo-hydromechanical processes in fractured rock masses have been in existence since the early 1980s. However, it is only in the last few years that models capable of simulating coupled thermo-hydromechanical processes under multi-phase flow conditions (such as those of unsaturated geological formations) have come into being. Reviews of state-of-the-art numerical methods and modelling were presented by Rutqvist *et al.* (2001), and Jing & Hudson (2002).

In the next section, we describe two numerical simulators, the ROCMAS and TOUGH-FLAC codes, which are used in the studies presented in this paper. They also serve to provide some insight into the complexity needed for coupling hydrological or rock mechanics models. Following this, four very different studies of coupled hydromechanical processes are presented: (1) hydromechanical effects in injection well testing, a field and modelling study of indirect coupling, involving one fracture intercepted by a well; (2) hydromechanical effects in tunnel drilling, a field and modelling study of direct coupling in rock mass around a tunnel under excavation, involving effects of stress release and redistribution; (3) hydromechanical effects on flow in fracture

networks, a modelling study of indirect coupling in rock mass, involving many fractures in a network; (4) hydromechanical effects in CO_2 injection and storage, a modelling study of direct coupling in rock mass, involving potential fracture opening under injection and buoyancy pressures in a multiphase system.

Some brief remarks will conclude the paper.

Two numerical simulators for modelling coupled hydromechanical processes

The first simulator is the ROCKMAS code (ROCK Mass Analysis Scheme), a finite-element code for analysis of coupled thermal–hydrological–mechanical (THM) processes in saturated–unsaturated fractured porous media. It has been gradually developed and extended since the early 1980s by J. Noorishad and coworkers. A hydromechanical formulation for fractured rock, based on Biot's general effective stress theory (Biot 1941), was developed (Noorishad *et al.* 1982) and then extended to nonisothermal conditions (Noorishad *et al.* 1984, 1992).

Noorishad & Tsang (1996) and Rutqvist *et al.* (2001) extended the original formulation of coupled thermohydroelasticity in terms of Biot's theory of consolidation to partially saturated media through the Philip & de Vries theory for heat and moisture flow in soil. In this theory, the three phases, solid, liquid, and gas, are present. However, it is assumed that the gas pressure P_g is

constant and equal to atmospheric pressure throughout the porous medium. Vapour transport occurs only through molecular diffusion driven by a gradient in vapour concentration (density), and advection of vapour with bulk gas flow is neglected. As in the general case, the vapour density in the medium is governed by Kelvin's relation, which assumes thermodynamic equilibrium for pore liquid in contact with its vapour, with phase changes occurring as evaporation–condensation processes.

The second simulator is the TOUGH–FLAC code (Rutqvist *et al.* 2002), based on a coupling of the two existing computer codes TOUGH2 (Pruess *et al.* 1999) and FLAC3D (Itasca Consulting Group 1997). TOUGH2 is a well-established simulator for geohydrological analysis with multiphase, multicomponent fluid flow and heat transport, and FLAC3D is a widely used commercial code designed for rock and soil mechanics. For analysis of coupled THM problems, TOUGH2 and FLAC3D are executed on compatible numerical grids and linked through external coupling modules, which serve to pass relevant information between the field equations solved in the respective codes (Fig. 1). A TOUGH-to-FLAC link takes multiphase pressures, saturation, and temperature from the TOUGH2 simulation and provides the updated temperature and pore-pressure information to FLAC3D (Fig. 1). Because the TOUGH2 mesh uses one grid point within each element, and FLAC3D nodes are located in element corners, data have to be interpolated from mid-element (TOUGH2) to corner locations (FLAC3D).

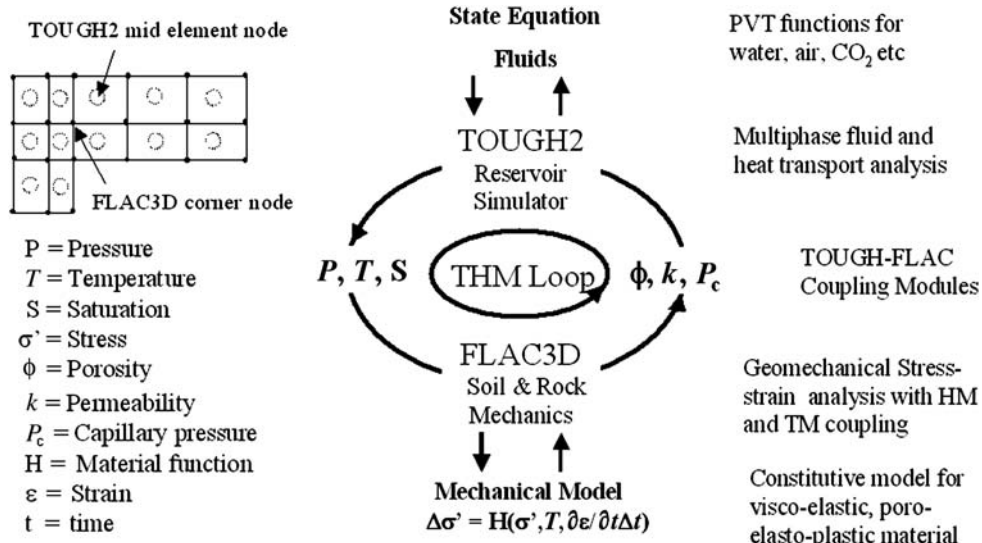


Fig. 1. TOUGH–FLAC simulator coupled THM analysis with multiphase fluid flow.

After data transfer, FLAC3D internally calculates thermal expansion and effective stress according to

$$\Delta\epsilon^T = \mathbf{I}\beta_T\Delta T \quad (1)$$

$$\boldsymbol{\sigma}' = \boldsymbol{\sigma} - \mathbf{I}\alpha P \quad (2)$$

where ϵ^T is thermal strain, β_T is the linear thermal expansion coefficient, \mathbf{I} is the unit tensor, T is temperature, $\boldsymbol{\sigma}'$ is effective stress, $\boldsymbol{\sigma}$ is total stress, α is the Biot effective stress parameter, and P is pore fluid pressure. In a multiphase flow calculation, the value of P transferred to FLAC3D could represent an average pore pressure calculated from the pressures of the various phases (Rutqvist *et al.* 2002).

A FLAC-to-TOUGH link takes the element stress and deformation from FLAC3D and updates the corresponding element porosity, permeability, and capillary pressure to be used by TOUGH2, according to the following general expressions:

$$\phi = \phi(\boldsymbol{\sigma}', \boldsymbol{\epsilon}) \quad (3)$$

$$\mathbf{k} = \mathbf{k}(\boldsymbol{\sigma}', \boldsymbol{\epsilon}) \quad (4)$$

$$P_c = P_c(\boldsymbol{\sigma}', \boldsymbol{\epsilon}). \quad (5)$$

No interpolation in space is required for this data transfer because stress and strain are defined in FLAC3D elements, which are identical to TOUGH2 elements. A TOUGH–FLAC coupling module for this link would then calculate the hydraulic property changes, based on material-specific theoretical or empirical functions.

A separate batch program controls the coupling and execution of TOUGH2 and FLAC3D for the linked TOUGH–FLAC simulator. It was done within the FLAC3D input file using the FLAC–FISH programming language (Itasca Consulting Group 1997). The calculation is then stepped forward with the transient thermo-hydrological (TH) analysis in TOUGH2, by conducting, at each time step or at the TOUGH2 Newton iteration level, a quasi-static mechanical analysis with FLAC3D, to calculate stress-induced changes in porosity and intrinsic permeability. By limiting to cases with small strain conditions, there is no change in mesh dimension during the simulations.

Hydromechanical effects in injection well testing

In this study, *in situ* hydromechanical properties (Fig. 2) were determined on fractures intersecting a 1700 m deep borehole, KLX02, at the Laxemar area near Åspö Hard Rock Laboratory in Sweden (Rutqvist *et al.* 1997). The fractures were located at three highly conductive zones at depths of 270, 315, and 340 m. The hydromechanical properties were back-calculated by coupled numerical modelling of single-borehole multiple-pressure injection tests.

The KLX02 borehole is cased to 200 m depth and has a diameter of 76 mm for depth greater than 200 m. The bedrock consists mainly of granite and diorite, and the fracture frequency is in general low, especially down to 700 m and between 1100 and 1500 m. The three test zones

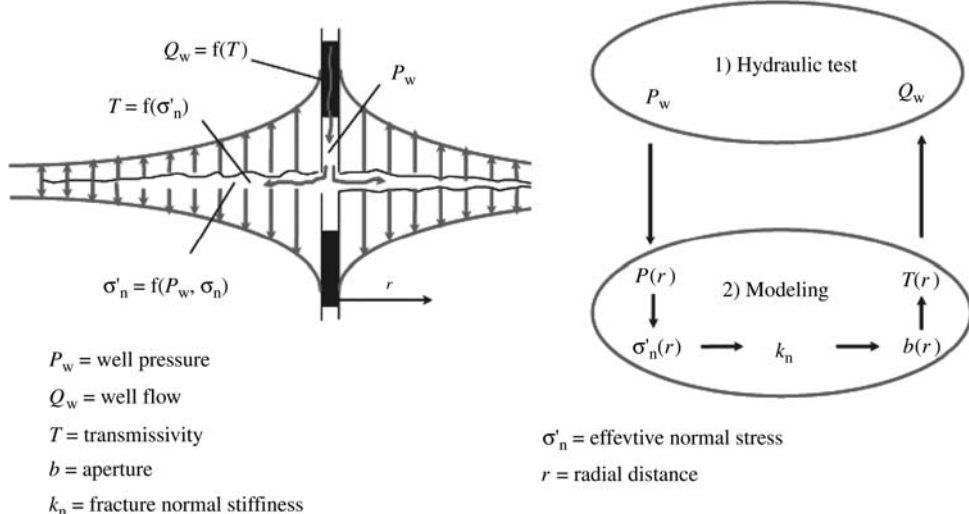


Fig. 2. *In situ* determination of hydromechanical properties of rock joints.

could be identified from flow, temperature, and electrical resistivity logging as the most hydraulic conductive zones in the upper 700 m of the borehole (Ekman 1997). The zones at 270 and 340 m coincide with the intersection of fracture zones a few metres wide, which also were identified by borehole radar. The rock in these zones was reported to be crushed and fractured granite, with a frequency of 10–20 fractures per metre. Pulse-injection tests, together with images from a high-resolution TV system, showed that the transmissivity in each zone was dominated by flow through a few open fractures. The most hydraulic conducting fractures appear to have very rough surfaces with open channels between contact points and parts filled or coated with calcite or chlorite. The orientation of the fractures at 270 and 340 m is oblique to the fracture zone, and they may be strike-slip shear fractures. In the discussion below, we describe the study of the fracture zone at 270 m.

During injection well testing, the fracture of interest is isolated in the well by the use of one packer above and another one below the section with the fracture. An increase in pressure P_w in the packered interval will be accompanied by an increase in flow rate Q_w (Fig. 2). Through modelling, in this case using the ROCMAS code, the pressure profile $P(r)$ in the fracture, as a function of radial distance from the well, can be calculated from P_w . The effective normal stress σ'_n is then calculated using $P(r)$, and the corresponding fracture aperture changes $b(r)$ are evaluated if one assumes a fracture normal stiffness k_n . Transmissivity T of the fracture is calculated from $b(r)$ and provides the parameter needed to obtain injection flow rate, which can be compared with the measured Q_w . Parameters are adjusted to ensure a good match between simulated and measured data, thus yielding their optimal values.

Below, we shall consider the use of the hydraulic jacking test, which is conducted by a stepwise increase of the fluid pressure. At each step, the well pressure is kept constant for a few minutes until the flow is steady (Fig. 3). The technique was first applied by Londe & Sabarly (1966) and

Louis *et al.* (1977) to study pressure-sensitive permeability under dam foundations. Rutqvist (1995) and Rutqvist *et al.* (1997) used hydraulic jacking tests, combined with coupled numerical modelling, to determine the *in situ* hydromechanical (HM) properties of fractures in crystalline rock. The numerical analysis of these injection tests shows that the flow rate at each pressure step is strongly dependent on the fracture aperture and normal stiffness of the fracture in the vicinity of the borehole, where the pressure changes the most (Fig. 4). Figure 5 shows field-test results for the successive pressure at each step plotted against the flow rate attained at that step, in the case of the fracture intercepted by the Laxemar KLX02 borehole at 270 m depth (Rutqvist *et al.* 1997). For the early part of the stepwise increasing pressure, the flow rate increases as a nonlinear function of pressure. A temporal peak-pressure is obtained at a flow rate of 1.3 l min^{-1} before the pressure begins to decrease with an increasing flow rate. A shear-slip analysis of this fracture, which was inclined to the principal *in situ* stresses, indicated that these irreversible fracture responses could be caused by shear slip, as the fluid pressure reduced the shear strength of the fracture. The subsequent step-down of pressures took a different path because of the change in hydromechanical properties resulting from shearing and fracturing.

The overall results from the hydraulic jacking tests conducted at Laxemar showed that the pressure sensitivity of the fractures is strongly dependent on the initial hydraulic permeability. The permeability of the most conductive fractures is relatively insensitive to injection pressure, whereas the permeability of the least conductive fractures can be strongly dependent on the injection pressure. From the borehole-television image, the most conductive fractures appear to be open fractures that are incompletely cemented, indicating flow channels in a fracture that are 'locked open' by shear dislocation or mineral filling (Rutqvist *et al.* 1997).

In addition, we note that if a pulse injection test, instead of the hydraulic-jacking test, is made on the fracture (see first peak at about 4 min in Fig. 3), the pressure increase $P(r)$ is very much limited to a small area around the well (Fig. 4). In this case, the induced changes in σ'_n , $b(r)$, and fracture transmissivity are also very small. Thus, the coupled hydromechanical effect is expected not to be significant, so that a conventional hydrological analysis method would apply. This observation presents the interesting possibility that a hydraulic jacking test and pulse injection test combined, on the same fracture, could be analysed simultaneously to optimally determine the fracture hydraulic and mechanical parameters.

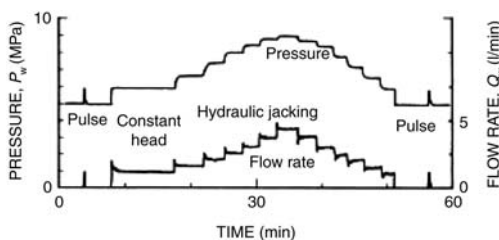


Fig. 3. Hydraulic jacking test: pressure and flow-rate data.

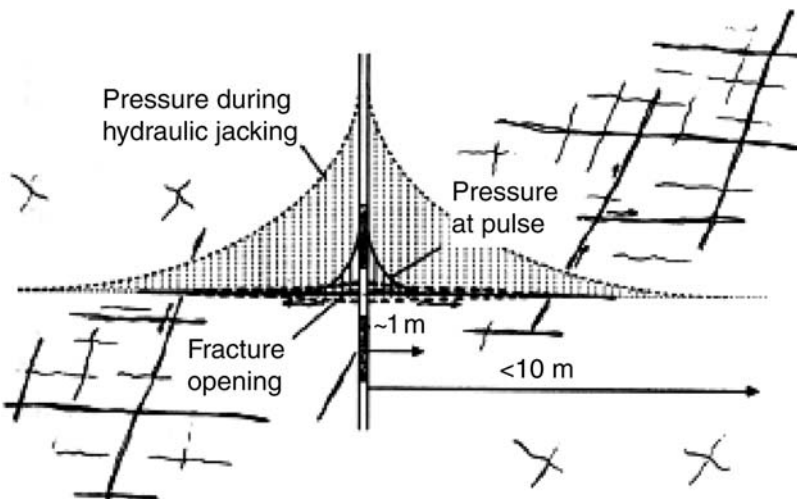


Fig. 4. Schematic picture of pressure profiles in a fractured rock during a hydraulic jacking test and a pulse injection test.

Hydromechanical effects during tunnel drilling

During the excavation of the FEBEX tunnel, located in fractured crystalline rock at the Grimsel Test Site in Switzerland, peculiar responses in fluid pressure were observed in the surrounding rocks (McKinley *et al.* 1996). A borehole was first drilled 3 m away from and parallel to a planned tunnel and then packed into two 10 m sections, P3 and P4. During tunnel drilling using a tunnel

boring machine (TBM), the water pressures in P3 and P4 were monitored. Figure 6 shows the drilling and resting cycles of the TBM (the line next to the shaded area) and the P3 and P4 pressure responses. The front end of the tunnel passed P4, but just reached P3. Thus, the pressure behaviour in P3 was not as clear as one would expect, but the P4 pressure showed a distinct response, with two peaks corresponding to two drilling-and-resting cycles (Fig. 6). It is believed that during tunnel drilling directly across from P4 interval, the pore pressure in P4 increased because of the induced stress concentration near P4. Then, during the resting period between drilling, water leaked away because of rock permeability, and thus the pore pressure decreased (Fig. 2).

To understand the data, a fully coupled 3D HM modelling of the tunnel-drilling procedure was performed (Rutqvist *et al.* 2004) using the finite-element code ROCMAS (Rutqvist *et al.* 2001). The mesh used for the simulation is shown in Figure 7. An initial stress field was assigned according to the range of stress measurements in the Grimsel area (Pahl *et al.* 1989): $\sigma_v = 10$ MPa, $\sigma_h = 15$ MPa and $\sigma_{\text{H}} = 30$ MPa, where σ_{H} is oriented at 45° to the tunnel axis.

The FEBEX tunnel was modelled according to the actual TBM schedule. The boring was conducted in 10 h shifts, with no activities during nights and weekends, and, in the modelling, uniform excavation during each 10 h shift is assumed. Figure 8 presents the simulated changes in mean stress at 18:00 h on October 25 (see Fig. 6, which shows excavation at 61 m directly opposite zone P4). Figure 9 shows the

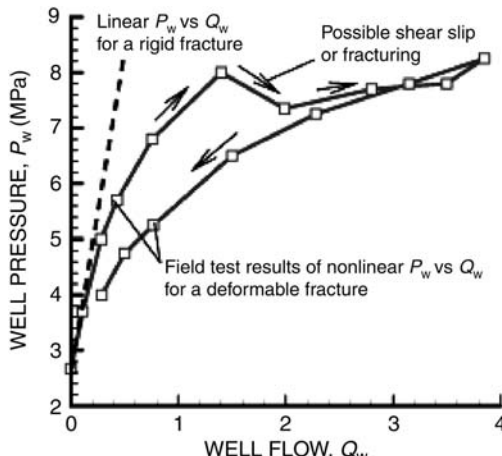


Fig. 5. Numerical modelling and field experiment data for a hydraulic jacking test involving increasing and decreasing pressure steps. For comparison, the expected result for a rigid fracture is shown as the dashed line.

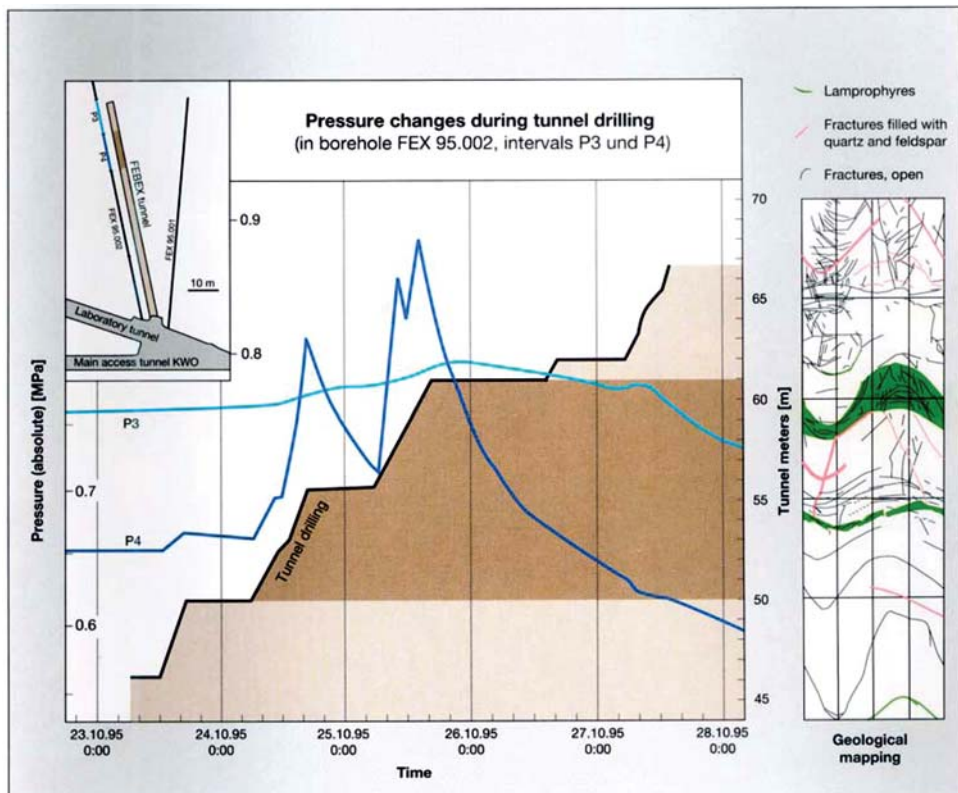


Fig. 6. During TBM excavation of the FEBEX tunnel, distinct increases in fluid pressure were observed in a borehole interval (P4) located a few metres away from the drift wall (from McKinley *et al.* 1996).

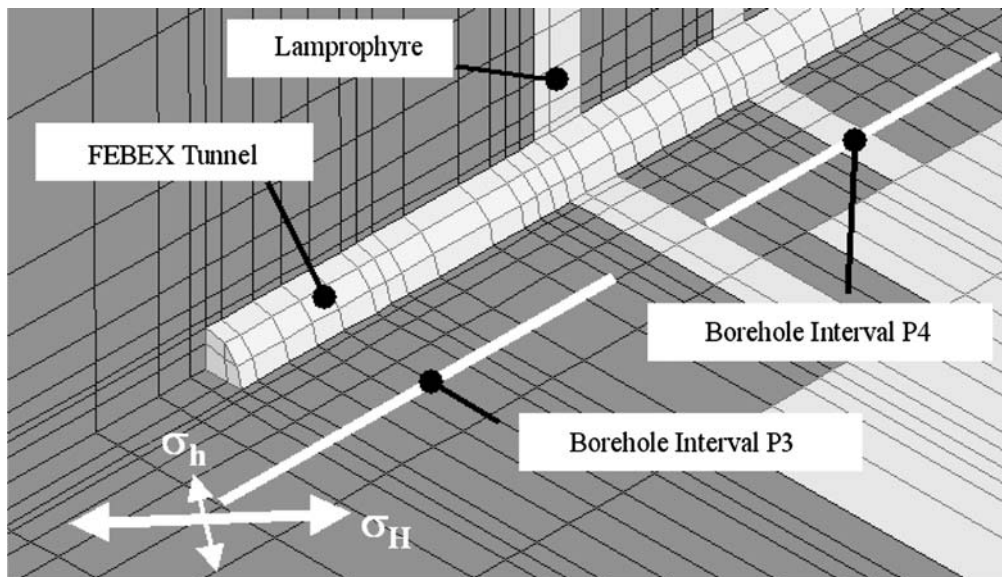


Fig. 7. Mesh design for simulating stress and pore-pressure changes around the FEBEX tunnel.

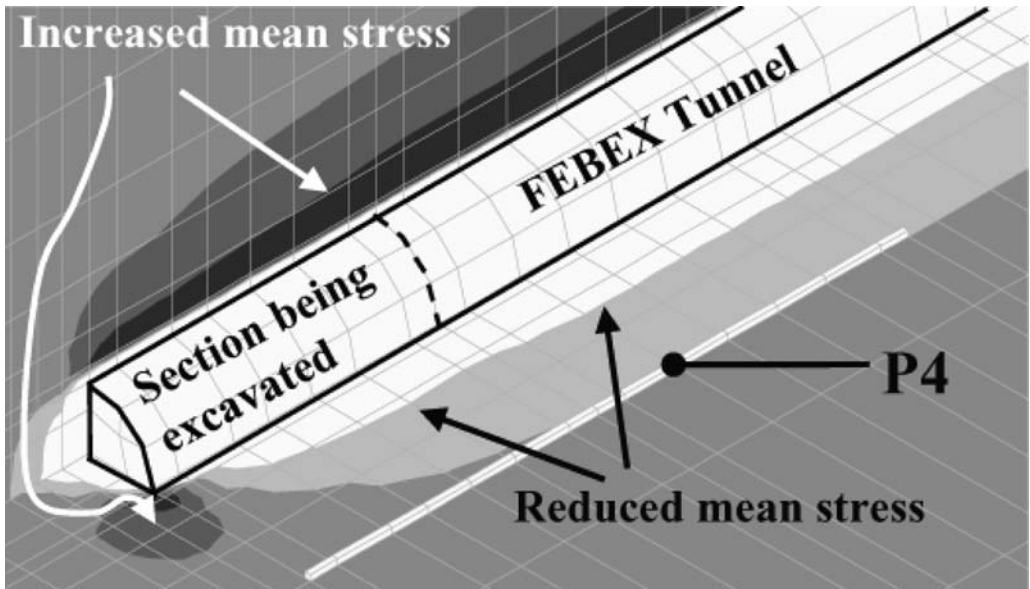


Fig. 8. Calculated changes in mean stress at the end of the second step of excavating the FEBEX tunnel (see Fig. 6, 61 m on the right axis).

corresponding fluid pressure, with two zones of increased values, one around the front-left side of the excavation and one above it, near its front. Figure 8 shows that near these two zones of pressure increase, the mean stress has increased as a result of

the excavation. In contrast, the fluid pressure on the side of the drift is decreased where the mean stress has decreased. The figures also show that the HM-induced changes in fluid pressures are temporal. For example, the HM-induced fluid-pressure

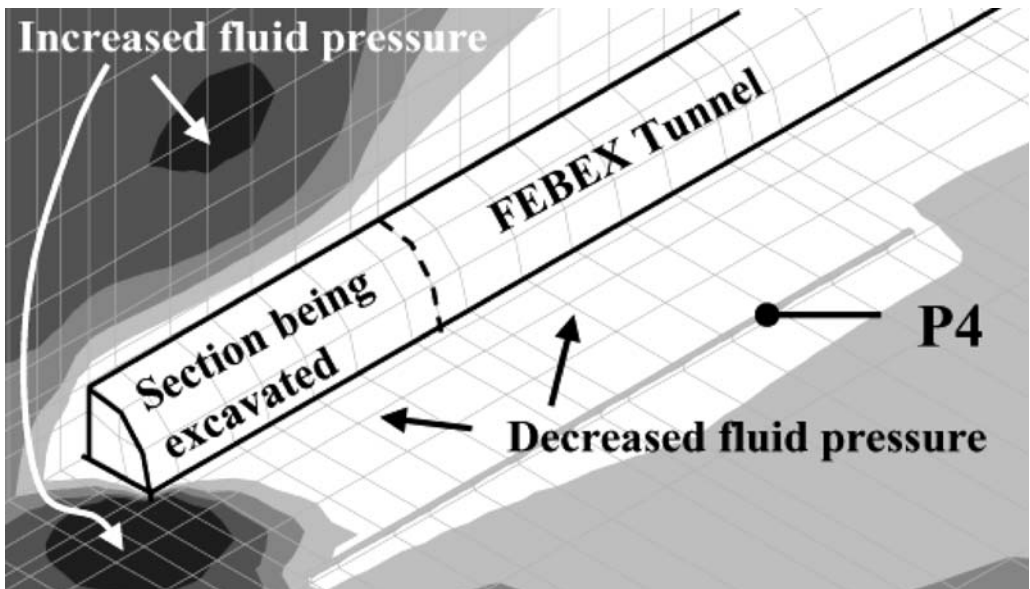


Fig. 9. Calculated change in pore pressure at the end of the second step in excavating the FEBEX tunnel (see Fig. 6, 61 m on the right axis).

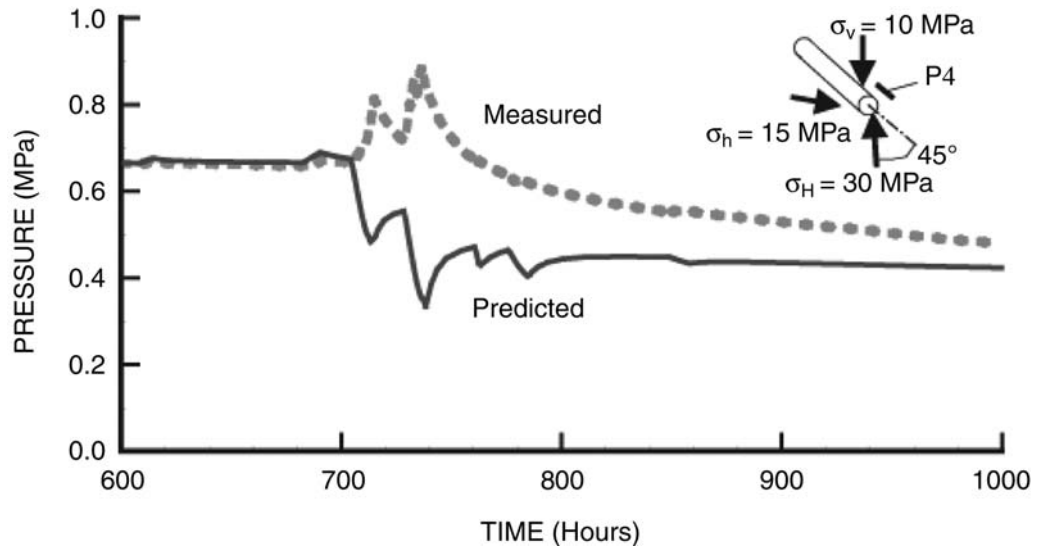


Fig. 10. Predicted and measured pore-pressure evolution for the estimated regional stress field.

rise above the tunnel diminishes 5–10 m behind the tunnel face, because of drainage into the tunnel.

Figure 10 presents the predicted and measured pressure responses in P4. Whereas the timing of pressure response is about right, the predicted values are opposite to what were measured; that is, pressure drops instead of peaks. The reason for the discrepancy was found in the assumed *in situ* stress field, which is an important factor that

controls the fluid-pressure changes. It was found in a variation study that the measured pressure changes can be reproduced by changing the orientation and magnitude of the stress field. An example of a much-improved match is shown in Figure 11, together with the adjusted stress field shown in the upper-right corner. The main point of this example is to show the high sensitivity of pore-pressure changes to local *in situ* stress fields.

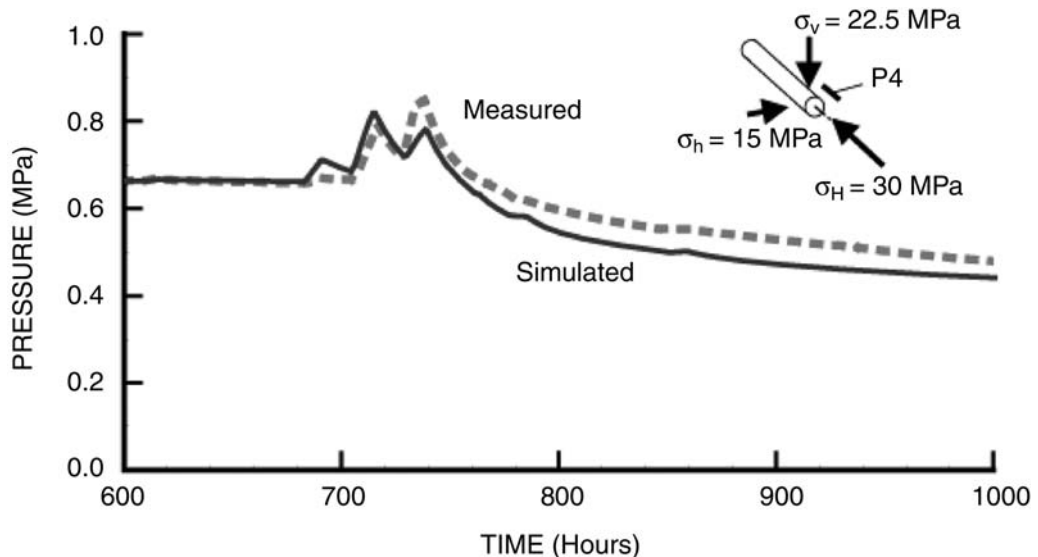


Fig. 11. Simulated and measured pore-pressure evolution for the adjusted local stress field.

It was shown in a more general study that the measured pressure responses can be captured if the stress field is rotated such that contraction (compressive strain rate) and corresponding increases in mean stress occur near the P4 borehole on the side of the drift. Good agreement between measured and simulated evolution of fluid pressure could be obtained if the maximum principal stress were rotated about 40° from the horizontal. Such a rotation of the local *in situ* stress field is not unrealistic, especially considering the presence of the lamprophyre zones and other geological features.

Thus, one conclusion from the study is that significant pore-pressure responses can be expected in the rock during tunnel excavation, and these responses are very sensitive to the local stress field. The local stress field could well be different from the regional stress field, especially if there is a major fault zone or other geological features in the vicinity of the tunnel. Perhaps the study described in this section suggests a way to study the local stress field.

Hydromechanical effects on flow in fracture networks

The objective of the study is to investigate the stress-dependent permeability in fractured rock masses considering a realistic representation of a fracture-network system and stress–deformation behaviour. The geometric basis for this study is a discrete fracture network (DFN) generated in a square region, 5 m × 5 m in size (Fig. 12), based on statistical information on fractures from a site characterization programme at Sellafield, UK

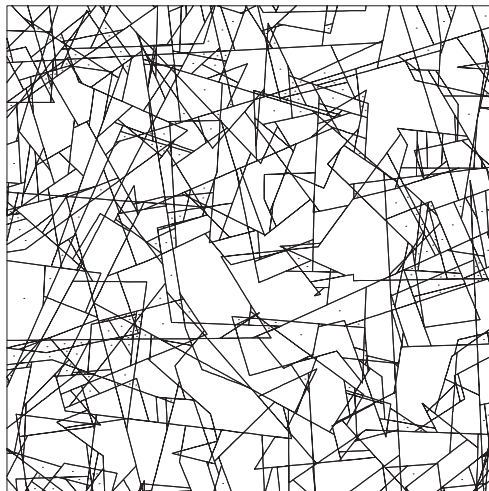


Fig. 12. Geometry of fracture system in the DFN model.

(Andersson & Knight 2000). The size of 5 m × 5 m is selected for the model, based on previous investigations for the calculations of the equivalent mechanical and hydraulic properties. This scale was shown (Min *et al.* 2004a; Min & Jing 2003) to represent both the initial mechanical and hydraulic representative elementary volumes (REVs).

After the generation of the DFN model, various boundary stresses σ_x and σ_y were applied to generate deformed models for flow analysis (Fig. 13). Each rock block between fractures was modelled as continuous, homogeneous, isotropic, linear, elastic, and impermeable media. The application of σ_x and σ_y is carried out in two ways. The first is to keep their ratio the same at $\sigma_x/\sigma_y = 1.3$. The second is to keep σ_y constant at 5.0 MPa and vary σ_x , so that their ratio ranges from 0.5 to 5.0. For each case, after the mechanical calculations are completed and the aperture value of each fracture is revised, flows in the x and y direction are calculated by applying a pressure step in the x and y direction, respectively. From the calculated flows, the permeabilities of the fracture network in the two directions are then calculated as k_x and k_y .

Key factors affecting the hydraulic behaviour of fractures, such as opening, closing, sliding and dilation, were modelled by incorporating relevant fracture constitutive models. A stepwise nonlinear normal stress–normal closure relation is adopted to approximate a hyperbolic normal deformation process. The stress–shear displacement fracture behaviour was modelled by an elastic–perfectly plastic constitutive model, with a Mohr–Coulomb failure criterion, and fracture dilation occurs when it starts to slide. This dilation continues until a predefined critical shear displacement (U_{cs}) value, beyond which the dilation stops (Min *et al.* 2004b).

Figure 14 shows the aperture changes with the increase of both horizontal and vertical boundary stresses while keeping a constant stress ratio of 1.3 between them. Because the stress ratio is close to unity, the stress states in most of the fractures do not cause shear failure, and normal stress is the main cause for the aperture change, basically closure. The initial aperture (30 mm) at a zero stress level decreased to 8.8 mm (mean values) when the mean stress magnitude was increased to 23 MPa. The changes in fracture apertures occur almost uniformly within the model region with the increase of stresses. This is because the fracture-normal closure resulting from normal stress increases is the dominant mechanism that controls fracture deformation, as significant shear dilation does not occur with the stress ratio equal to 1.3. Aperture anomalies can be observed in a few isolated places in the model region, mainly in the sharp corners of the blocks, where fracture failure

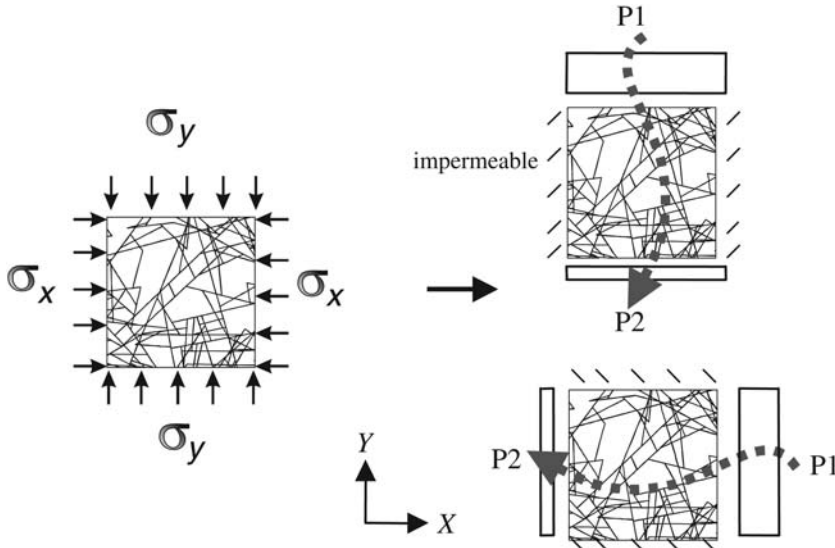


Fig. 13. Applications of stress boundary conditions and calculation of equivalent permeability in the x and y directions. σ_x and σ_y indicate the boundary stresses applied in horizontal and vertical directions, respectively. P1 and P2 indicate the hydraulic pressure applied in the boundaries, with P1 > P2.

occurs as a result of stress concentration. However, these were observed only locally and did not extend to the entire fracture length, and therefore their influence on the overall fluid flow field is minor for this 2D analysis.

Figure 15 shows the aperture changes when the horizontal boundary stress is increased in steps from 2.5 to 25 MPa, with a fixed vertical boundary stress of 5 MPa (the k ratio changing from 0.5 to 5), to investigate the influence of shear failure in fractures induced by larger differential stresses. In contrast to Figure 14, fracture aperture changes are not uniform. At a stress ratio of 3.0, large apertures can be observed in the critically oriented and well-connected fractures, thus affecting the flow paths significantly. This tendency becomes increasingly clear at a stress ratio of five. An examination of the results suggests the following reasons for this phenomenon.

(1) Critically oriented fractures continue to dilate under increasing differential stresses, which leads to much larger apertures of these fractures compared with their less critically oriented neighbouring fractures. The critical orientation is the orientation that is prone to shear failure as a result of applied stresses: it is calculated to be about 33° (Min *et al.* 2004b) in our example.

(2) It is not only the orientation of fractures, but also the connectivity of fractures that is needed for the formation of sufficient fracture dilation by stress change. Because the neighbouring fractures can hinder further plastic shear

development in fractures of critical orientation, many critically oriented fractures with poor connectivity could not produce large apertures, because of their poor connection to the fractures with similar orientation.

(3) The trace length of fractures is another important factor in forming clustered fractures conducting fluid flow with large apertures. This is natural with respect to connectivity, since longer fractures have a higher degree of connectivity compared with short ones, which are prone to being hindered by the neighbouring fractures and rock blocks. The figure shows that the long fractures are much more dilated than the shorter fractures (among the critically oriented fractures), which is also in line with field observations (e.g., Renshaw & Park 1997).

Figure 16 presents the calculated equivalent permeability changes with the increasing stress ratio. To evaluate the effect of shear dilation, the results with a pure elastic fracture model that excludes failure and dilation are shown as dashed lines in Figure 16. The pure elastic and the elasto-plastic models show a similar response until the stress ratio k reaches c. 2.5, which is the starting point of shear failure for fractures inclined at about 33° from the horizontal plane. At this point and afterwards, some fractures in the fractured rock masses start to fail and, with continued shear dilation, notable differences between the models are observed. At a stress ratio of five, the additional contribution from shear dilations of fractures is

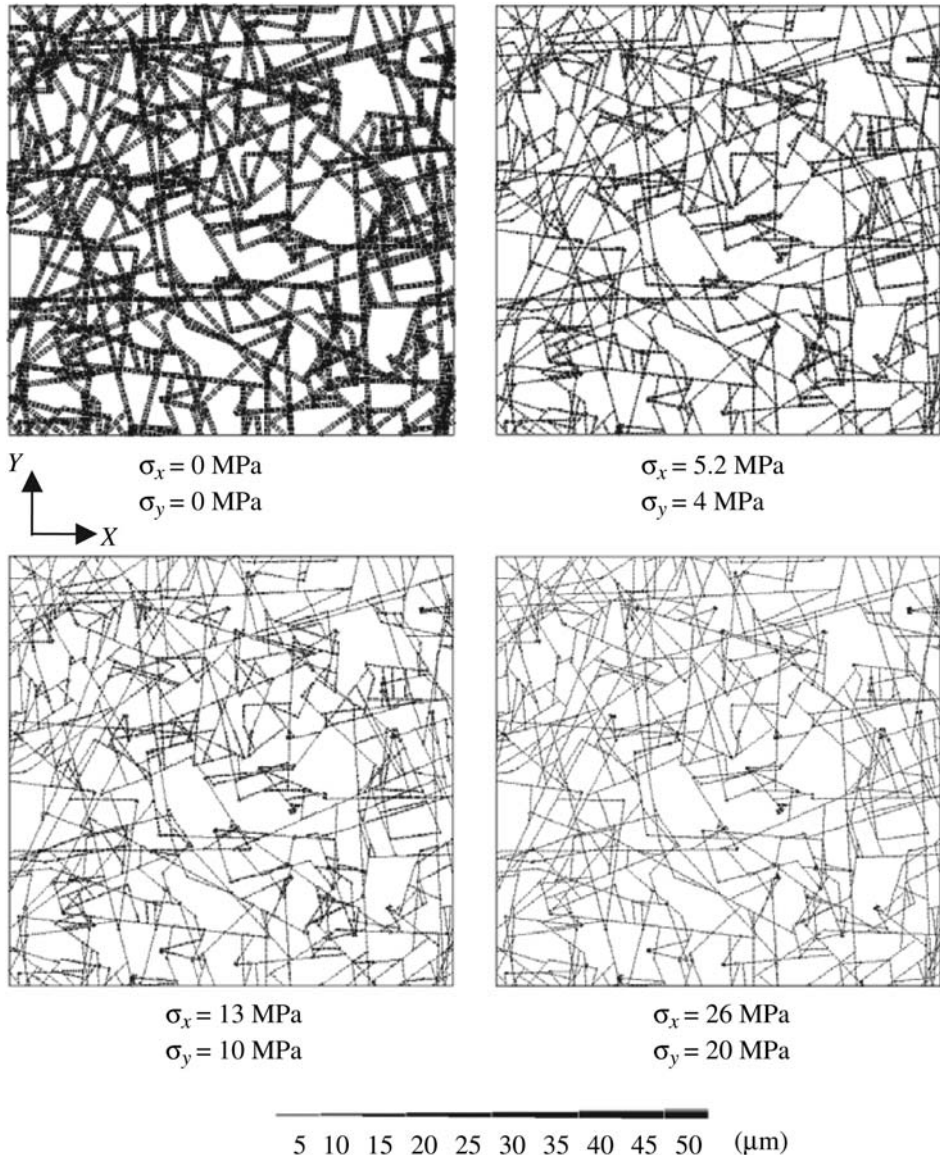


Fig. 14. Change of fracture apertures with the increase of stresses for the fixed stress ratio of 1.3. The thickness of lines indicates the magnitude of apertures. Mean apertures for the four cases were 30, 16.8, 11.9, and 8.8 μm , respectively.

more than one order of magnitude for k_x and a factor of four for k_y . On the other hand, the fractures that are not critically oriented continue to close with an increase in stresses; this makes their apertures smaller, and fluid flow is reduced. However, the dilation of fractures caused by shear is abrupt (with larger gradients) when shear failure starts to develop, and this dominates the process. As the horizontal boundary stress σ_x increases, the range of fracture orientation angles for possible shear

failure also increases, with resulting increased permeability. The increase of permeability stabilizes after a certain stress ratio, because the shear dilation of a fracture does not continue after the critical shear displacement is reached. Interestingly, this increased permeability is analogous to experimental results on the intact rocks, which show a similar decrease and increase in permeability with increasing differential stresses (Lee & Chang 1995).

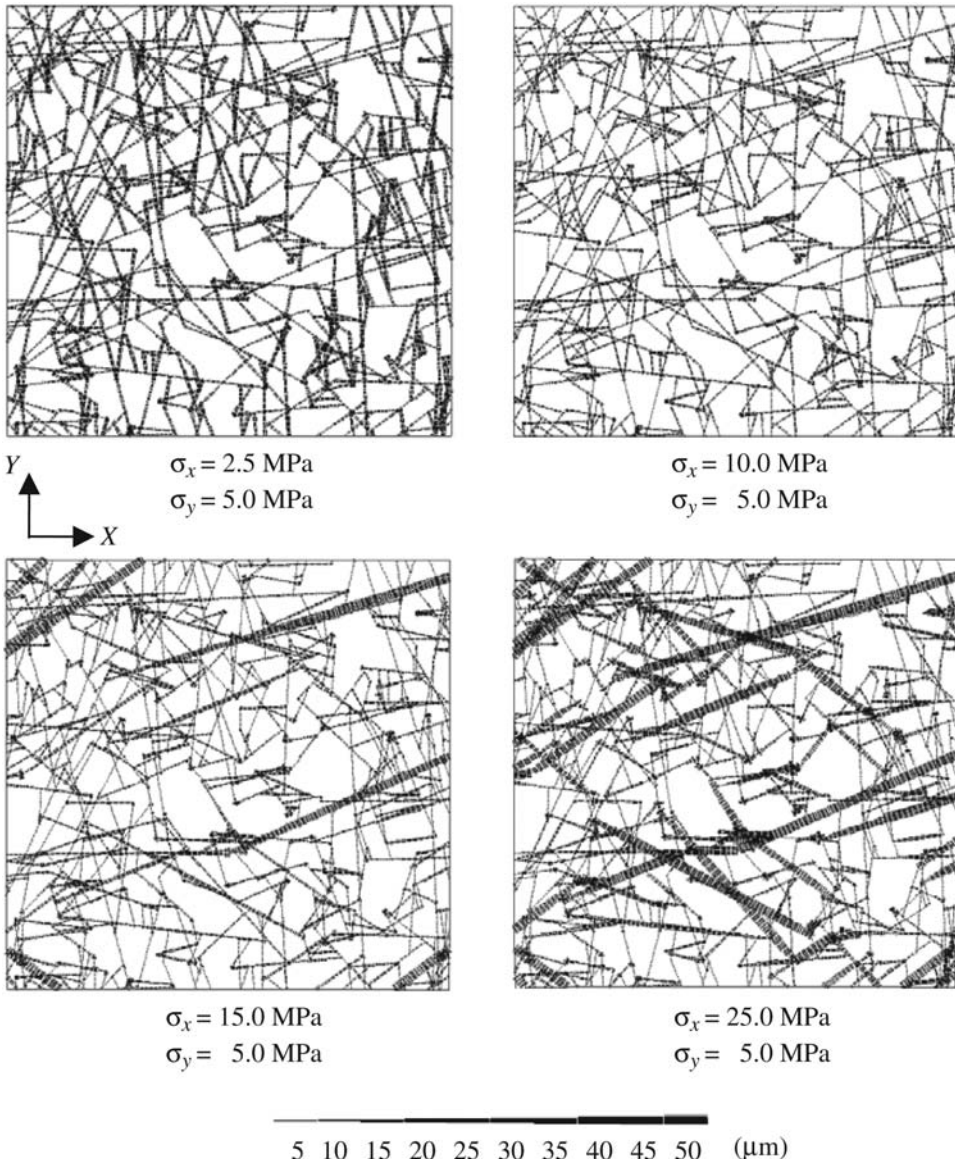


Fig. 15. Changes in fracture apertures with the increase in stress ratio, with a fixed vertical stress of 5 MPa. The thickness of the line indicates the magnitude of apertures.

Figure 17 shows the normalized flow rates in each fracture intersecting the left vertical boundary of the model. The initial uniform flow pattern changes when fracture dilation starts to develop, at a stress ratio of about three and beyond. Only 10% of fractures (four out of 40 fractures) carry about 50% and 70% of the fluid flow across the boundary, at a stress ratio of three and five, respectively, which demonstrates the channelling effect induced by stresses. This is a very dramatic effect.

Hydromechanical effects involved in CO₂ injection and storage

Disposal or storage of pressurized CO₂ from fossil-fired power plants in deep saline aquifers has been suggested as one of the promising concepts for reducing emission of greenhouse gases into the atmosphere (Reichle *et al.* 1999). The injection would take place at a depth below 800 m, so that the CO₂ would be within the temperature and

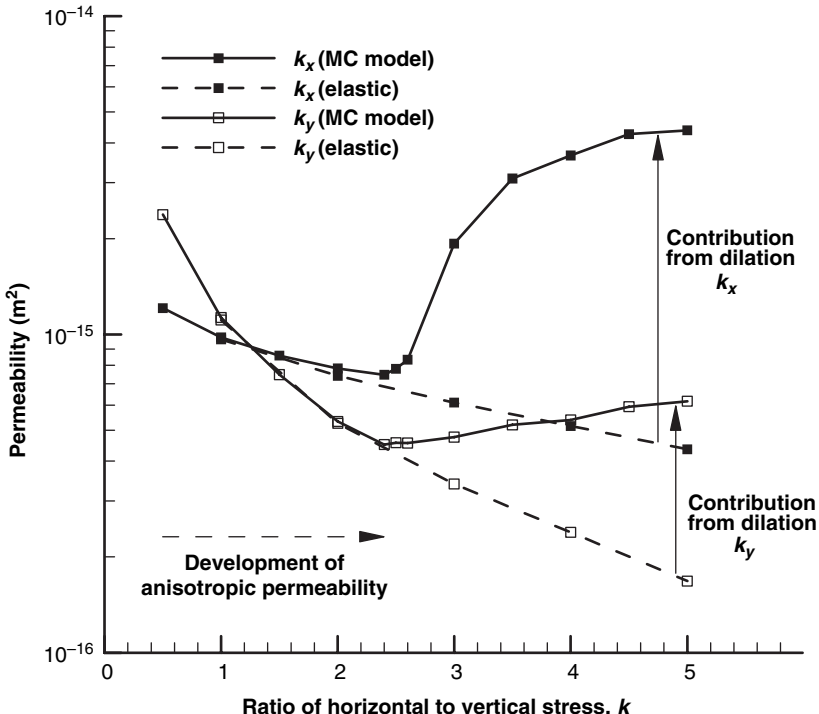


Fig. 16. Equivalent permeability (k_x and k_y) change as a result of the change in stress ratio. Differential stress is increased while keeping the magnitude of vertical stress constant. The Mohr–Coulomb (MC) model (continuous lines) is compared with the pure elastic model with no shear failure (dashed lines).

pressure range for it to be a supercritical fluid. As a supercritical fluid, the CO₂ behaves like a gas with low viscosity, but with a liquid-like density approximately half that of the formation brine, depending on pressure and temperature. Thus, large volumes of CO₂ gas would be compressed to a higher-density supercritical fluid and stored in a much smaller volume in the brine formation.

In this section, caprock mechanical and HM changes are studied during CO₂ injection into a hypothetical sandstone aquifer covered by

semipermeable shale (Rutqvist & Tsang 2005). The problem is analysed using the coupled computer codes TOUGH2–FLAC3D (Rutqvist *et al.* 2002), which simulate multiphase flow, in this case supercritical CO₂, water and salt, coupled with heat transfer and rock deformation.

For general discussion, it is useful to consider a basic injection-and-storage scenario and storage of CO₂ in brine formations, as presented in Figure 18, which shows a storage injection zone overlain by a caprock greater than 800 m in depth.

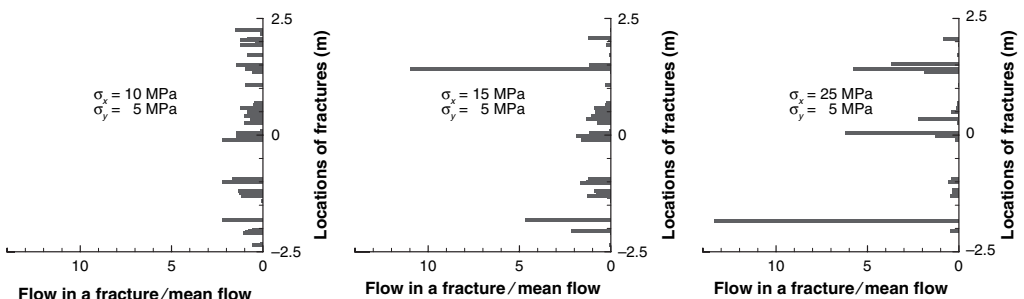


Fig. 17. Normalized flow rates at the left vertical boundary of the model at points where the boundary is intercepted by fractures. The three plots show the normalized flow rates for stress ratios of 2, 3, and 5, respectively.

Three main physico-chemical processes are indicated. First, we note the hydrological process of CO₂ buoyancy flow, with its factor-of-two lower density and an order-of-magnitude lower viscosity. Thus, by buoyancy, the plume of injected CO₂ will migrate outwards from the injection well and upwards towards the caprock. Other hydrological factors also come into play, which will be discussed below. Second, both injection and buoyancy provide additional pressure on the rock matrix of the formation, which may thus be deformed, with changes in matrix porosity or fracture apertures. They in turn cause changes in flow permeability and, consequently, the flow field. Finally, the injected CO₂ plume will, in general, chemically react with the formation minerals. This could give rise to porosity changes near the injection well, but, positively, such chemical changes reactions involving the injected CO₂ can form new minerals in the rock matrix, thus trapping CO₂ chemically. This is the mineral trapping process for sequestration of CO₂.

Because supercritical CO₂ is less dense than water, deep underground disposal requires a sufficiently impermeable seal (caprock) above an underground storage zone to trap the injected CO₂. However, disposal from one standard-size 1000 MW coal-fired power plant for 30 years could occupy more than 100 km² of a 100 m thick zone (Pruess *et al.* 2001). Over such a vast area, it is not likely that we would find a caprock that is perfectly homogeneous and impermeable (Fig. 19). A

caprock may be discontinuous and may contain imperfections such as faults and fractures of various sizes (from metre-scale fractures to kilometre-scale faults). Further, the hydraulic properties of a fault may change with injection-induced hydraulic pressure. Thus, the performance assessment of CO₂ storage in an underground brine formation requires the analysis of a number of simultaneously interacting processes, including multiphase flow, heat transfer, and mechanical deformation. Rock deformation and stresses are important because the injection of CO₂, in general, produces an increased pore pressure, which in turn will change the stress field and cause deformations in the rock mass (Fig. 19). Changes in the stress field can affect the performance of an injection site in several ways. First, if sufficiently large, they could cause failure, giving rise to a high-permeability leakage path through fractured rock. Second, the induced stresses will act upon pre-existing faults and fractures, and cause opening or slip displacement with associated permeability changes. Such hydromechanical changes in a caprock could damage the sealing characteristics for a safe long-term containment of the CO₂. Third, it is well known that extraction of fluid from an underground reservoir (e.g., oil and gas) causes subsidence of the ground surface. By the same processes, an underground injection of compressed CO₂ can cause the ground surface to heave (uplift) because of a reduction in effective stress in the aquifer.

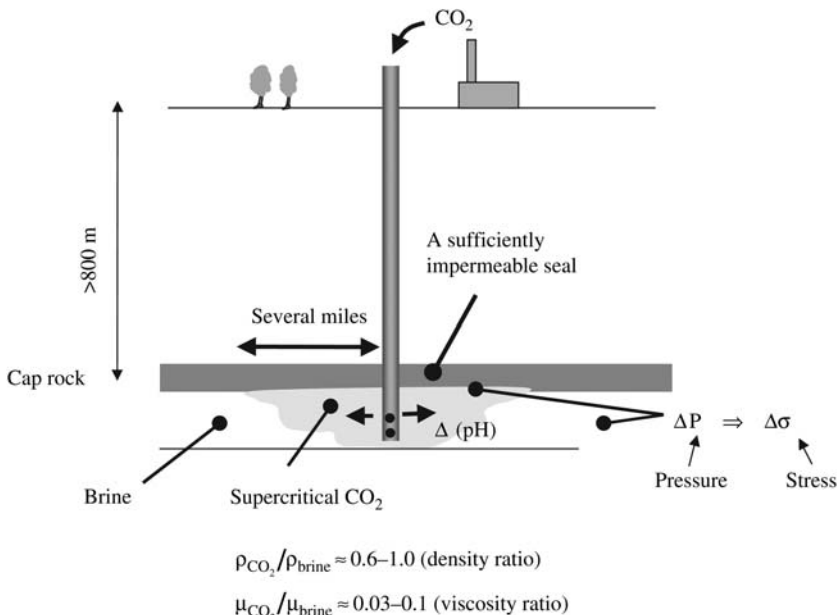


Fig. 18. A basic scenario for CO₂ injection and storage in a brine formation.

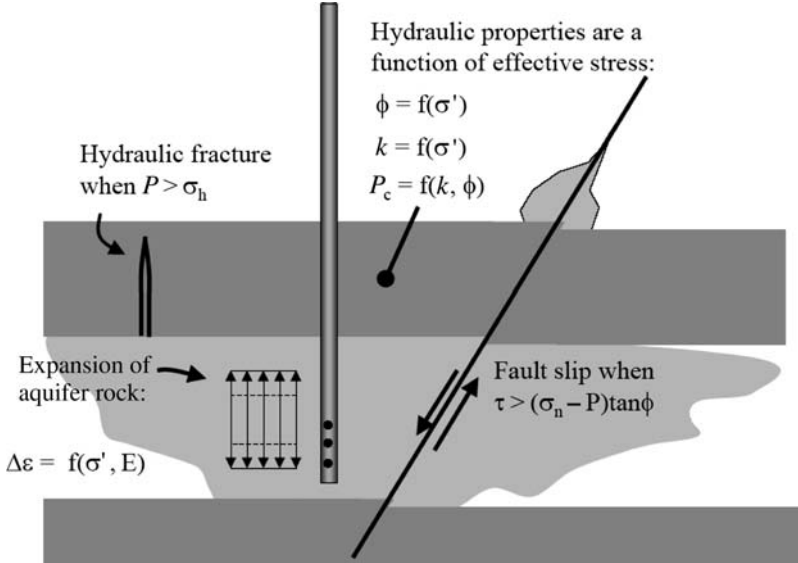


Fig. 19. Hydromechanical processes associated with CO_2 injection. Here, ϕ is the porosity of the caprock.

Figure 20 presents the injection pressure during a 30 year period with or without consideration of the stress-dependent rock-mass permeability. At constant injection rate, the injection pressure increases continuously during the injection and tends to 37 or 43 MPa, depending on whether stress-dependent permeability changes are considered. The difference in peak pressure is explained by the fact that the permeability in the injection zone in the former case increases because of a general reduction in effective stresses during injection. Thus, the stress-dependent permeability changes in the aquifer would have a positive effect on the CO_2 injection operation, because a higher flow rate can be maintained without increasing the injection pressure over the lithostatic pressure for a

longer time. In this modelling, the injection pressure would exceed the lithostatic pressure (or the minimum compressive principal stress) after about 10 years of injection. Because we are not modelling the nonlinear stress-deformation behaviour of hydraulic fracturing or plastic shear, our calculations will be performed for up to 10 years of injection. In practice, the injection rate would be reduced after a number of years to ensure that the injection pressure is not close to the lithostatic value.

Coupled HM interactions in a caprock-reservoir system are studied with a view to evaluating the integrity of the caprock system and reservoir leakage. We will analyse the possibilities of caprock failure by looking at the critical pressure that could induce hydraulic fracturing or the critical pressure that could induce shear slip of pre-existing faults. A conservative assumption is that a hydraulic fracture could develop as soon as the fluid pressure exceeds the least compressive principal stress, and hence, the critical pressure for fracturing is

$$P_{fc} = -\sigma_3. \quad (6)$$

We define a pressure margin to the onset of hydraulic fracturing as

$$P_{fm} = P - P_{fc} < 0 \quad (7)$$

which should be kept negative to prevent fracturing. Thus, P_{fm} tells us how much further the pressure can be increased before fracturing is initiated.

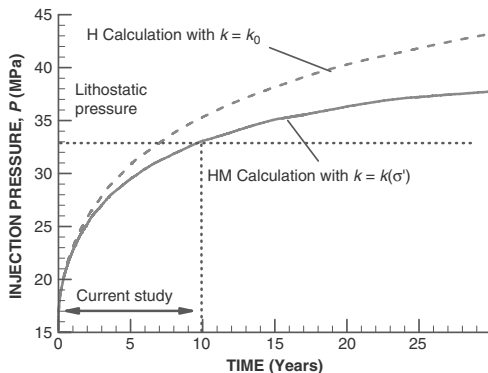


Fig. 20. Injection pressure as a function of time.

A conservative assumption for the onset of fault slip is to assume that a fault could exist at any point and have any orientation. For such a case, the Coulomb failure criteria can be written in the following form:

$$\tau_{m2} = (\sigma_{m2} - P) \sin \phi + S_0 \cos \phi \quad (8)$$

where τ_{m2} and σ_{m2} are the 2D maximum shear stress and mean stress in the σ_1, σ_3 -plane, respectively, and are defined as

$$\tau_{m2} = \frac{1}{2}(\sigma_1 - \sigma_3) \quad (9)$$

$$\sigma_{m2} = \frac{1}{2}(\sigma_1 + \sigma_3) \quad (10)$$

and S_0 and ϕ are the fault's coefficient of internal cohesion and angle of internal friction, respectively.

In analogy with the criterion for hydraulic fracturing, we can define the critical pressure for the onset of slip as

$$P_{sc} = \sigma_{m2} + S_0 \cot \phi - \frac{\tau_{m2}}{\sin \phi}. \quad (11)$$

For faults, a zero cohesion may be assumed and a typical range for ϕ is 25–35°. In this calculation, we test for slip using a zero cohesion and a friction angle of 30°, leading to the following pressure margin for the onset of slip:

$$P_{sm} = P - P_{sc} < 0. \quad (12)$$

Figures 21 and 22 show the zones of possible fault slip and hydraulic fracturing for two stress regimes, defined in terms of the relationship between the horizontal and vertical stresses (σ_h and σ_v , respectively): an isotropic stress regime ($\sigma_h = \sigma_v$); a normal fault stress regime ($\sigma_h = 0.7\sigma_v$).

In these figures, the potential for hydraulic fracturing and for fault slip was evaluated using equations (7) and (12). For the isotropic stress regime, mechanical failure would probably initiate at the interface between the caprock and injection zone, where the reduction in vertical effective stress can lead to the formation of horizontal hydraulic fractures (Fig. 21, lower part). Furthermore, a larger zone of possible slip on pre-existing fractures occurs at the upper and lower part of the injection zone (Fig. 21, upper part). This implies that an unfavourably oriented fault could be reactivated with possible permeability change. However, even if fracturing or fault reactivation were to take place in the lower part of the caprock, the simulation indicates that reactivation would be contained within this area and not propagate through the upper part of the cap.

Figure 22 shows that, for the normal faulting stress regime, the zones of potential shear slip and hydraulic fracturing are more extensive is, in this case, the initial, far-field horizontal stress is lower. Importantly, in the case of a normal faulting stress regime, shear slip and hydraulic fracturing would preferentially occur on vertical fractures. Furthermore, the shear slip could occur in the entire caprock and not just in its lower part. In other words, there is a potential for slip on a pre-existing fault crossing the entire caprock, and hence CO₂ leakage along it.

As a general presentation of coupled hydro-mechanical changes during a CO₂ disposal operation, the present analysis is somewhat simplified, and the results should be taken only qualitatively for any particular site, because quantitative results are very sensitive to local rock properties. At a real injection site, the parameters for these empirical relationships should be calibrated against *in situ* measurements at an appropriate scale and over an appropriate range of conditions.

Overall, the analysis shows that the magnitude and the anisotropy of the initial stress field is an important factor in determining where and how failure could occur. In the case of an isotropic stress field, with both stresses equal to the weight of the overburden, shear slip along low-angle faults and the formation of horizontal hydraulic fractures are the most likely failure modes. In the case of relatively low horizontal stress (the normal fault stress regime, which might be the most common case in storage formations), shear slip along steep faults and formation of vertical fractures are the most likely failure modes.

The study was extended to include injection into a reservoir–caprock system bounded by two sealing faults. Figure 23 shows an example of fault reactivation analysis using this model. In this example, CO₂ is injected within a permeable injection zone laterally confined between two sealing (low-permeability) faults. An internal friction angle of 25° is assumed for the faults. In this case, CO₂ was injected at high pressure until slip was triggered along the two bounding faults. A maximum fault slip of about 5 cm was predicted along fault sections intersecting the injection zone (Fig. 23, right). However, analysis shows that shear failure is limited to a zone of substantially increased fluid pressure and does not propagate further than about 100 m above and below the injection zone. In general, the stress evolution around the faults and the injection zone is more complex in this case than for the homogeneous caprock case. Localized concentration of stresses (including shear stresses), as well as localized stress releases, is more likely, and this could lead to additional damage, particularly in areas where

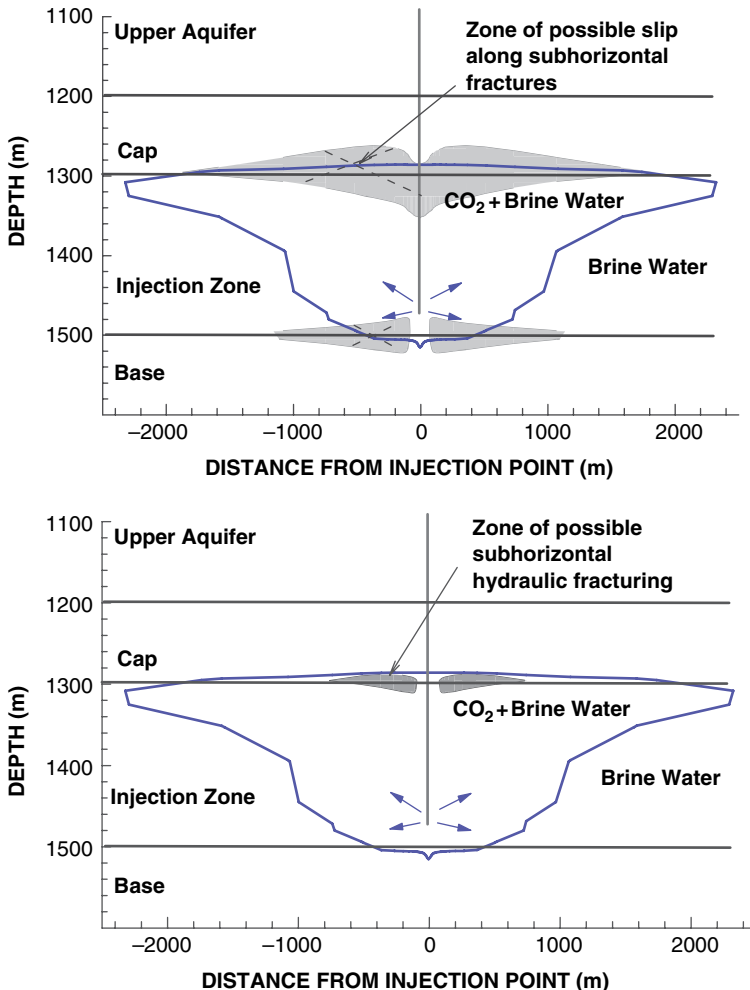


Fig. 21. Calculated zones of possible shear slip (upper plot) and hydraulic fracturing (lower plot) after 10 years of injection for the case of isotropic stress regime ($\sigma_h = \sigma_v$).

the fault intersects the caprock. Such damage may induce increased permeability along the fault. However, this possibility was not considered in this initial study.

In general, slip on pre-existing faults and other discontinuities intersecting the caprock are viewed as a likely scenario for generation of possible CO₂ leakage paths. However, further analysis is required to evaluate whether fluid flow will occur in conjunction with the slip. Shear tests on single fractures in shale indicate that permeability can increase or decrease depending on the current stress normal to the fractures (Gutierrez *et al.* 2000). At high normal stresses, shear slip is accompanied by significant gouge production, and the permeability can actually decrease by several orders of

magnitude. However, geological studies indicate that local stresses and the presence of faults control containment and release of deep overpressured fluids. Further research is needed for a realistic modelling of complex fault structures and for modelling of potential changes in fault permeability and mechanical properties.

In summary, the following points on coupled hydromechanical effects in CO₂ injection may be emphasized.

(1) A general reduction in the effective mean stress induces strongly coupled hydromechanical changes in the lower part of the caprock. Therefore, the strongest hydromechanical changes and the greatest risk of rock failure occur in the lower part of the caprock.

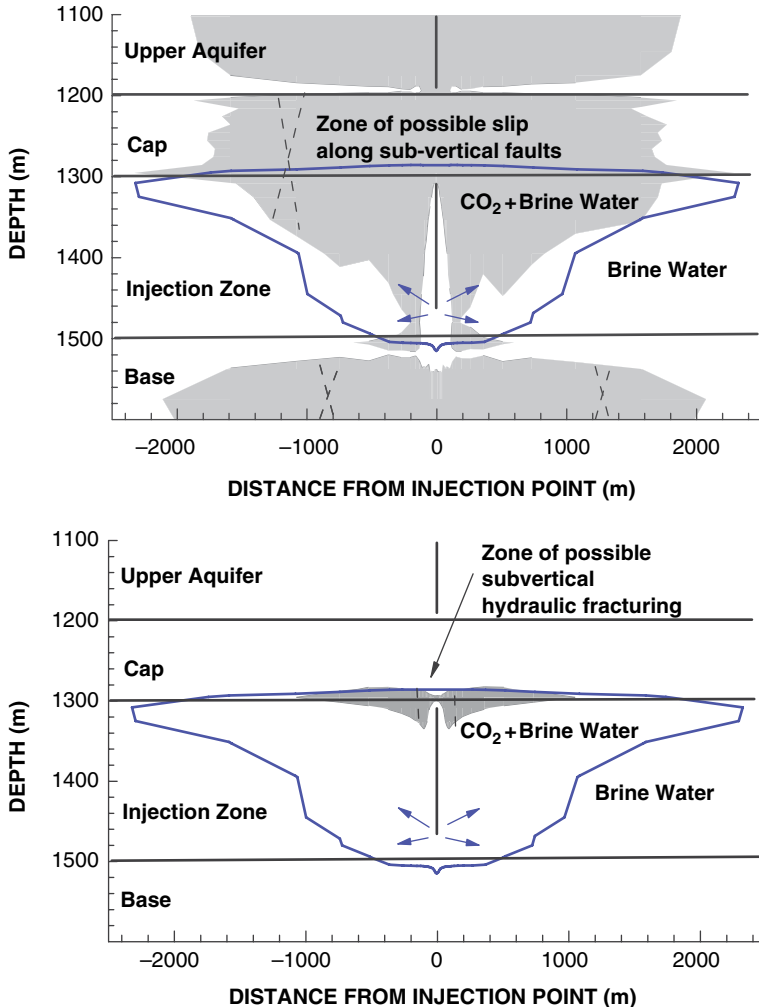


Fig. 22. Calculated zones of possible shear slip (upper plot) and hydraulic fracturing (lower plot) after 10 years of injection for the case of normal faulting stress regime ($\sigma_h = 0.7\sigma_v$).

(2) Because the aquifer pressure slowly increases during the injection period, fluid has time to diffuse into the rock and create horizontal poroelastic stresses. These events will decrease the probability of fracturing and shear of subvertical fractures, but also make the shear reactivation along subhorizontal fractures more likely. Thus, shear reactivation of existing fractures is the primary failure mode of concern in CO₂ injection.

(3) The analysis indicates that shear reactivation in the lower part of the caprock could take place at an injection pressure well below the lithostatic pressure. However, depending on the initial *in situ* stress field, this fault slip reactivation may or may not be confined to the lower parts of the caprock.

(4) The type of stress regime (e.g., isotropic or normal fault types) is a key parameter that determines whether fracturing and shear slip are likely to take place along subhorizontal or subvertical fractures. For a common normal fault type of stress regime, fracture slip would preferentially take place along subvertical fractures, so that hydraulic fracturing would be vertical.

(5) Once the CO₂ fluid reaches the upper part of the caprock (for example, through a permeable fault), the upward CO₂ migration is accelerated because of the combined effects of relative permeability and viscosity changes, and changes in intrinsic permeability caused by pressure-induced hydromechanical effects.

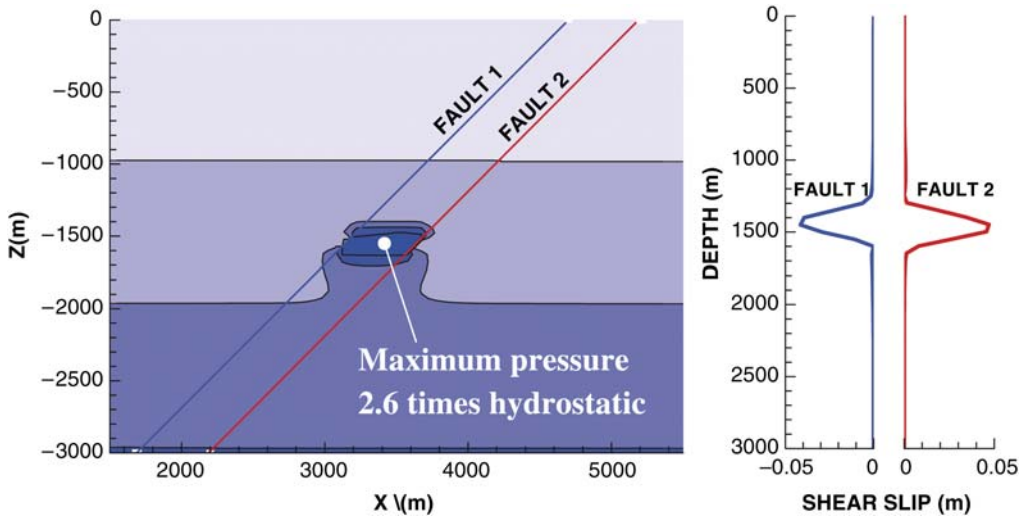


Fig. 23. Fault slip during CO_2 injection. Right figure shows contours of fluid pressure; left figure shows the magnitude of shear displacement along faults 1 and 2.

Concluding remarks

Fractured rock hydromechanics is a rich field of research, as exemplified by the four studies described in some detail above. These studies demonstrate the intricate interactions and couplings of hydrological and mechanical effects in four very different problems. The results of these problems have significant implications for practical issues of interest to society, such as contaminant transport, tunnel stability, sequestration of greenhouse gases, and site characterization of a geological system.

There are a number of outstanding challenges in this field. They include the following.

(1) Hydromechanical effects involving multiple fractures and faults. Except for the first study, the examples covered in this paper all require, to varying degrees, the consideration of the interference between neighbouring fractures or faults to understand the hydromechanical behaviour of the system. More field and modelling investigations are needed on such multifracture systems.

(2) Constitutive relationships and equations of state. In the discussion within this paper, we have assumed that the constitutive relationships for mechanical processes and the equations of state of fluids are available for modelling studies. Although much information is available, the state-of-art is still lacking for shear processes on certain rock materials and for certain fluid mixtures.

(3) Hydromechanical processes for a broad range of space and time scales. The concern is how to relate the pore-scale behaviour all the way up to the basin scale, and similarly how to relate

the time scale of a typical field or laboratory experiment to that of the natural geological system. For this, knowledge of, and treatment techniques for, heterogeneities in geological media are needed.

(4) Key parameters from site characterization. All problems of practical importance concern a site, and how to obtain key parameters associated with hydromechanical processes at the site is still an open problem. Definition of these key parameters depends on the issues of concern for the site. Research is needed not only on new site measurement techniques, but also on modelling methods that integrate the data and reflect an understanding of how these data relate to the parameters that are critical to the issues.

The authors would like to thank many collaborators over the years on studies described in this paper. In particular, they would like to acknowledge helpful discussions with members of the DECOVALEX project, especially with O. Stephansson, J. Hudson, and L. Jing. The paper was prepared with partial support of the US Department of Energy under Contract No. DE-AC02-05CH11231 with the Lawrence Berkeley National Laboratory.

References

- ANDERSSON, J. & KNIGHT, L. 2000. *DECOVALEX III Project, TASK 3, BMT2 protocol, Understanding the impact of upscaling THM processes on performance assessment. Version 6.0*. Swedish Nuclear Power Inspectorate, Stockholm.
- BIOT, M. A. 1941. General theory of three-dimensional consolidation. *Journal of Applied Physics*, **12**, 155–164.

- EKMAN, D. 1997. *Rock stress, hydraulic conductivity and stiffness of fracture zones in the Laxemar Borehole, Småland, Sweden*. MSc thesis, Royal Institute of Technology, Stockholm, Sweden.
- GUTIERREZ, M., OINO, L. E. & NYGÅRD, R. 2000. Stress-dependent permeability of a de-mineralised fracture in shale. *Marine and Petroleum Geology*, **17**, 895–907.
- ITASCA CONSULTING GROUP, 1997. *FLAC 3D, Fast Lagrangian Analysis of Continua in 3 Dimensions. Version 2.0*. Itasca Consulting Group, Minneapolis, MN.
- JING, L. & HUDSON, J. A. 2002. Numerical methods in rock mechanics. *International Journal of Rock Mechanics & Mining Sciences*, **39**, 409–427.
- LEE, C. I. & CHANG, K. M. 1995. Analysis of permeability change and groundwater flow around underground oil storage cavern in Korea. In: FUJII, T. (ed.) *Proceedings of the Eighth ISRM Congress, Tokyo, Japan*. Balkema, Rotterdam, 779–782.
- LONDE, P. & SABARLY, F. 1966. La distribution des perméabilités dans la fondation des barrages voûtes en fonction du champ de contrainte. In: *Proceedings of the 1st International Congress on Rock Mechanics, Lisbon Vol. II*. Bertrand Ida, Lisbon, 517–522.
- LOUIS, C., DESSENNE, J.-L. & FEUGA, B. 1977. Interaction between water flow phenomena and the mechanical behavior of soil or rock masses. In: GUDEHUS, G. (ed.) *Finite Elements in Geomechanics*. Wiley, New York, 479–511.
- MCKINLEY, L., KICKAIAIR, W., DEL OLMO, C. & HUERTAS, F. 1996. The FEBEX Project: full-scale simulation of engineered barriers for a HLW repository. *NAGRA Bulletin*, **27**, 56–67.
- MIN, K. B. & JING, L. 2003. Numerical determination of the equivalent elastic compliance tensor for fractured rock masses using the distinct element method. *International Journal of Rock Mechanics & Mining Sciences*, **40**, 795–816.
- MIN, K. B., RUTQVIST, J., TSANG, C.-F. & JING, L. 2004a. A block-scale stress–permeability relationship of fractured rock determined by numerical experiments. In: STEPHANSSON, O., HUDSON, J. A. & JING, L. (eds) *Coupled T–H–M–C Processes in Geo-systems. Geo-engineering Book Series*, **2**. Elsevier, Amsterdam, 269–274.
- MIN, K. B., RUTQVIST, J., TSANG, C.-F. & JING, L. 2004b. Stress-dependent permeability of fractured & rock masses: a numerical study. *International Journal of Rock Mechanics & Mining Sciences*, **41**, 1191–1210.
- NOORISHAD, J. & TSANG, C.-F. 1996. Coupled thermo-hydroelasticity phenomena in variable saturated fractured porous rocks—Formulation and numerical solution. In: STEPHANSSON, O., JING, L. & TSANG, C.-F. (eds) *Coupled Thermo-Hydro-Mechanical Processes of Fractured Media*. Developments in Geotechnical Engineering, **79**, 93–134.
- NOORISHAD, J., AYATOLLAHI, M. S. & WITHERSPOON, P. A. 1982. A finite element method for coupled stress and fluid flow analysis of fractured rocks. *International Journal of Rock Mechanics & Mining Sciences & Geomechanics Abstracts*, **19**, 185–193.
- NOORISHAD, J., TSANG, C.-F. & WITHERSPOON, P. A. 1984. Coupled thermal–hydraulic–mechanical phenomena in saturated fractured porous rocks: numerical approach. *Journal of Geophysical Research*, **89**, 10365–10373.
- NOORISHAD, J., TSANG, C.-F. & WITHERSPOON, P. A. 1992. Theoretical and field studies of coupled hydro-mechanical behavior of fractured rocks I. Development and verification of a numerical simulator. *International Journal of Rock Mechanics and Mining Sciences*, **29**, 401–409.
- PAHL, A., HEUSSERMANN, S., BRAÜER, V. & GLOGGLER, W. 1989. *Grimsel Test Site. Rock stress investigations*. NAGRA, NTB, **88-39E**.
- PRUESS, K., OLDENBURG, C. & MORIDIS, G. 1999. *TOUGH2 User's Guide, Version 2.0*. Lawrence Berkeley National Laboratory Report **LBNL-43134**.
- PRUESS, K., XU, T., APPS, J. & GARCIA, J. 2001. *Numerical modeling of aquifer disposal of CO₂*. Society of Petroleum Engineers, Paper **66537**.
- REICHLE, D., ET AL. 1999. *Carbon sequestration research and development*. US Department of Energy Report **DOE/SC/FE-1**.
- RENshaw, C. E. & PARK, J. C. 1997. Effect of mechanical interactions on the scaling of fracture length and aperture. *Nature*, **386**, 482–484.
- RUTQVIST, J. 1995. Determination of hydraulic normal stiffness of fractures in hard rock from hydraulic well testing. *International Journal of Rock Mechanics & Mining Sciences & Geomechanics Abstracts*, **32**, 513–523.
- RUTQVIST, J. & STEPHANSSON, O. 2003. The role of hydromechanical coupling in fractured rock engineering. *Hydrogeology Journal*, **11**, 7–40.
- RUTQVIST, J. & TSANG, C. F. 2005. Coupled hydro-mechanical effects in CO₂ injection. In: TSANG, C. F. & APPS, J. A. (eds) *Underground Injection Science and Technology. Developments in Water Science*, **52**, 651–680.
- RUTQVIST, J., TSANG, C.-F., EKMAN, D. & STEPHANSSON, O. 1997. Evaluation of *in situ* hydromechanical properties of rock fractures at Laxemar in Sweden. In: LEE, H.-K., YANG, H.-S. & CHUNG, S. K. (eds) *Proceedings of 1st Asian Rock Mechanics Symposium, ARMS 97, Seoul*. A. A. Balkema, Rotterdam, 619–624.
- RUTQVIST, J., BÖRGESSON, L., CHIJIMATSU, M., ET AL. 2001. Thermohydromechanics of partially saturated geological media—governing equations and formulation of four finite element models. *International Journal of Rock Mechanics & Mining Sciences*, **38**, 105–127.
- RUTQVIST, J., WU, Y.-S., TSANG, C.-F. & BODVARSSON, G. S. 2002. A modeling approach for analysis of coupled multiphase fluid flow, heat transfer, and deformation in fractured porous rock. *International Journal of Rock Mechanics & Mining Sciences*, **39**, 429–442.
- RUTQVIST, J., REJEB, A., TIJANI, M. & TSANG, C. F. 2004. Analyses of coupled hydrological–mechanical effects during drilling of the FEBEX tunnel at Grimsel. In: STEPHANSSON, O., HUDSON, J. A. & JING, L. (eds) *Coupled T–H–M–C Processes in Geo-Systems: Fundamentals, Modelling, Experiments and Applications*. Elsevier Geo-Engineering Book Series, **2**, 131–136.
- TSANG, C.-F. (ed.) 1987. *Coupled Processes Associated with Nuclear Waste Repositories*. Academic Press, New York.
- TSANG, C.-F. 1991. Coupled thermomechanical hydro-chemical processes in rock fractures. *Review of Geophysics*, **29**, 537–551.
- TSANG, C.-F. 1999. Linking thermal, hydrological and mechanical processes in fractured rocks. *Annual Review of Earth and Planetary Sciences*, **27**, 359–384.

Overview of key experiments on repository characterization in the Mont Terri Rock Laboratory

P. BOSSART

Swisstopo—Mont Terri Project direction, Fabrique des Chaux, 2882 St-Ursanne, Switzerland (e-mail: paul.bossart@swisstopo.ch)

Abstract: Repositories for radioactive waste are designed as disposal systems that perform a number of functions relevant to long-term safety and security, including (1) isolation of waste from the human environment, (2) long-term confinement and radioactive decay within the disposal system and (3) attenuation of radionuclide releases to the environment. The generic rock laboratory at Mont Terri plays an important role in the characterization of such repositories. The experimental results gained in this underground facility are used, together with information from natural analogues, deep drilling programmes and modelling, to assess the evolution and performance of a repository. A time scale for processes affecting repository performance is outlined. A transient phase in the first 10–20 ka is followed by an equilibrium phase. Key experiments cover processes observed over relevant time scales, feasibility experiments and experiments focusing on long-term process understanding. The last can only be partly investigated over realistic time scales in direct experiments because of the long time frame required. Key experiments are briefly outlined and key references are provided.

Over the past 10 years, 12 partner organizations (ANDRA, BGR, CRIEPI, ENRESA, FOWG (now swisstopo), GRS, HSK, IRSN, JNC (now JAEA), NAGRA, OBAYASHI and SCK-CEN) have jointly carried out and financed a research programme in the generic Mont Terri Rock Laboratory. The Rock Laboratory is located in the Canton of Jura in northwestern Switzerland. The experiments can be assigned to the following three categories: (1) process and mechanism understanding in undisturbed Opalinus Clay; (2) experiments related to repository-induced perturbations; (3) experiments related to repository performance during the operational and post-closure phases.

Repository performance

Experimental results provide input for assessing different phases of repository evolution and performance. General repository evolution is shown in Figure 1, with a transient and an equilibrium phase being distinguished. During the construction of a repository (time period of 5–15 years), stress redistributions may lead to the formation of an excavation damaged zone (EDZ) around the tunnels. During the operational phase (waste emplacement and backfilling; time period of several years to around 50 years), an unsaturated zone will evolve in the near field as a result of ventilation and redox conditions will become oxidizing (Traber 2004). In the first few hundred years after closure, significant changes in repository evolution will occur, including tunnel convergence and compaction, and

saturation and swelling of the bentonite backfill (NAGRA 2002). These processes take place concurrently with the saturation and closure of open discontinuities in the EDZ (self-sealing). Redox conditions in the near field start to become reducing. Increased temperatures as a result of the decay heat from the waste may reach about 90 °C at the bentonite–rock interface within around 100 years and temperatures will then gradually decrease (Johnson *et al.* 2002). Hydrogen production as a result of steel canister corrosion, and subsequent gas transport through the backfill, along interfaces and in the host rock, starts after saturation of the backfill (some 100 years after closure of the repository). Steel canister failure is expected to occur after about 10 ka. This is the earliest time at which radionuclides will be released into the backfill and host rock. Diffusion is the major transport process for radionuclides (geosphere transport times between 10⁴ and 10⁶ years). Transport by advection is limited because of the low hydraulic conductivity of the intact Opalinus Clay host rock and its self-sealing capacity.

Key experiments

Key experiments on repository characterization and performance assessment are outlined in Figure 2. These experiments can be divided into observations over relevant time scales, feasibility experiments and experiments designed to investigate long-term processes on time scales that are not directly accessible through conventional laboratory work.

Repository Evolution and Performance

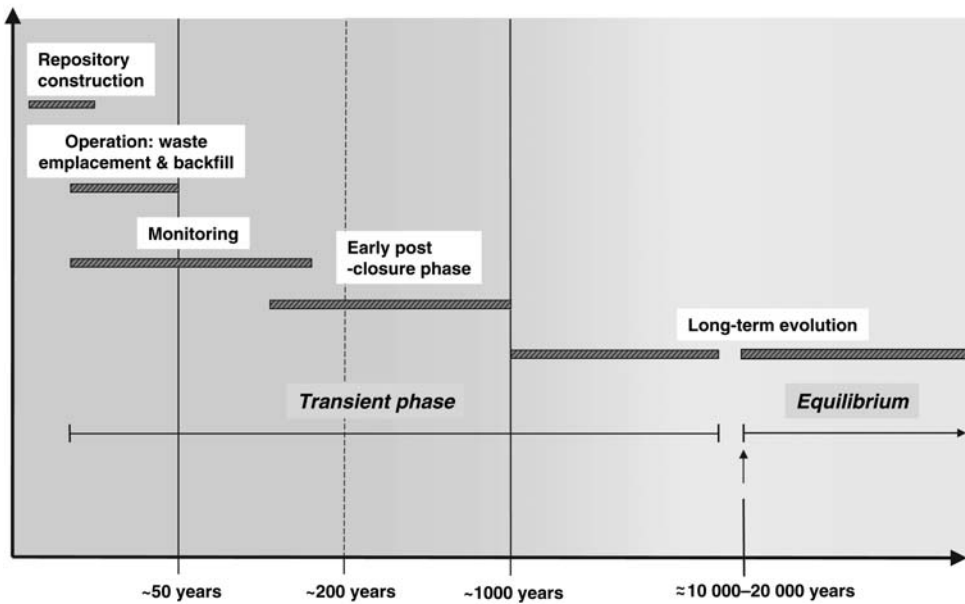


Fig. 1. Main steps in the transient and equilibrium phases of repository evolution and performance. Processes such as resaturation and heat transfer, as well as chemical reactions such as pyrite oxidation, plot into the early post-closure phase. After about 10–20 ka, the repository system becomes equilibrated; the bentonite backfill is saturated (swelled), the excavation damaged zone is sealed and pore pressures have recovered (no pressure gradients). Radionuclides start to enter the backfill and host rock at about 10 ka at the earliest.

Key Experiments

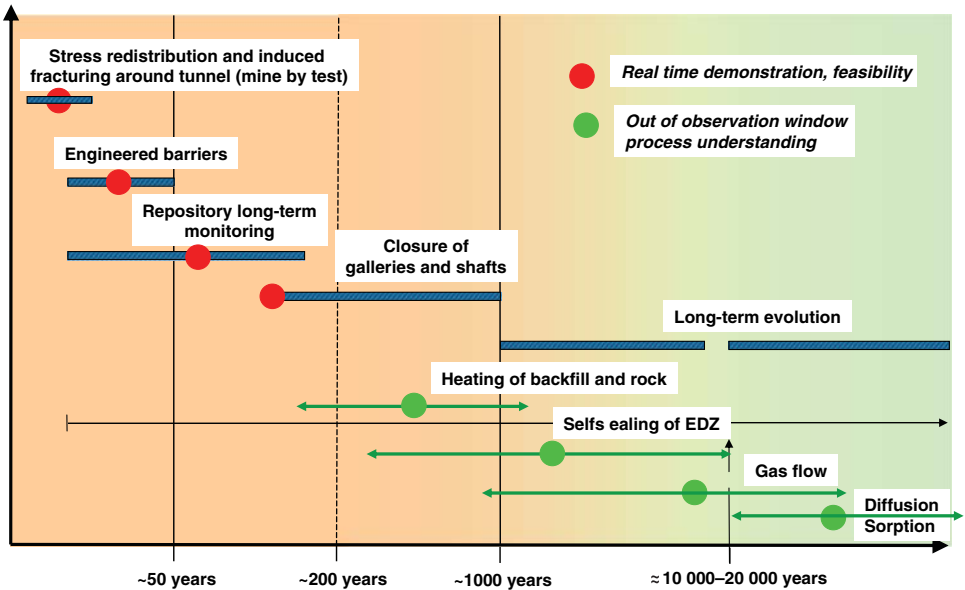


Fig. 2. Key experiments on repository evolution and performance, with real-time demonstration and feasibility experiments and experiments dealing with process understanding. Superimposed on the time bars of Fig. 1 are the key experiments that are outlined in the text.

The most important experiments are briefly outlined, and key references that provide details of the technical and scientific work being performed in the underground laboratory are given.

Stress redistribution and induced fracturing around tunnels (mine-by test)

During the construction of underground facilities, the *in situ* stress field is altered and a secondary stress field develops around the openings. Depending on the host-rock properties, this stress redistribution leads to the development of an EDZ around the tunnel, where changes (e.g. fracturing) lead to a significant increase in the hydraulic conductivity around the tunnel. A mine-by test was carried out in a 35 m long section of the Mont Terri Rock Laboratory (ED-B experiment), using a road header for excavation. The mechanical and hydraulic responses were monitored with an array of instruments measuring deformations, pore pressures, acoustic emissions and geophysical properties. Field results and their interpretation using rock mechanical modelling have been presented by Martin *et al.* (2004).

Engineered barriers

The engineered barriers (EB) experiment aims to demonstrate a new concept for buffer construction and emplacement of high-level waste and spent fuel in horizontal drifts in a clay formation such as the Opalinus Clay. The principle of the new method is based on the combined use of a lower bed made of compacted bentonite blocks and an upper backfill made of highly compacted granular bentonite material that can be emplaced remotely. A dummy canister with the same dimensions and weight as the reference canister was placed on top of a bed of bentonite blocks and the upper part of the drift was backfilled with granular bentonite material using an auger technique. The drift was sealed with a concrete plug and the evolution of various hydromechanical parameters, both in the barrier and the rock, and particularly in the EDZ, is being monitored for a period of about 5 years. Because of the small amount of free water available in this formation, an artificial hydration system was installed to accelerate the saturation of the buffer. The first steps of this experiment have been described by Mayor *et al.* (2005). The experiment is still continuing.

Long-term repository monitoring

Although the concept of a geological repository is based on passive safety, which does not require monitoring and maintenance, public demand for a

certain observation period of the disposal system is very high. The long-term monitoring project addresses this issue and is designed to provide basic information as input for the decision to finally seal the repository. In the Swiss concept, this step should be taken only after an extended monitoring phase in a pilot repository (NAGRA 2002). The feasibility of such a pilot repository has to be demonstrated, together with the development of a long-term monitoring programme (e.g. definition of key parameters, measurement criteria and methods, as well as quality assurance and data management for the long-term monitoring system). Of special interest are the following questions: Which parameters should be measured, when, how often and for how long? Are sensors, cables and/or wireless transmission systems or non-destructive monitoring techniques feasible and reliable (e.g. over a period of 100 years)? What are the measurement criteria and what are the requirements regarding quality assurance and data management for monitoring?

Long-term monitoring experiments are now in the planning phase and may be carried out in the Rock Laboratory during a later phase.

Closure of tunnels and shafts

After the waste canisters have been emplaced in a repository and the disposal tunnels have been back-filled, the access tunnels and shafts need to be back-filled and closed. Moderately compacted clay–sand mixtures may represent an appropriate solution. Besides the economic advantages, such clay–sand mixtures may be advantageous with respect to gas transport. After saturation, gas transport through the bentonite–sand backfill is still possible, but this would not be the case if a pure bentonite backfill were used. Furthermore, clay–sand mixtures would still ensure the self-sealing capability of the backfill. The main aim of this experiment is to determine the sealing capacity of different clay–sand mixtures at different compaction densities and water saturations in interaction with the Opalinus Clay and to improve existing THM (thermo-hydro-mechanical) models by comparing the results of numerical simulations with *in situ* and laboratory test data. An overview of laboratory tests has been given by Rothfuchs *et al.* (2005). *In situ* investigations in the Mont Terri Rock Laboratory started in 2004 within the framework of the SB experiment (self-sealing barriers of clay–sand mixtures) and first results are expected in 2007.

Heating of backfill and rock

The heating (HE-B) experiment aims to understand the coupled thermo-hydro-mechanical processes in

a clay formation around a heat source similar to those in a potential repository. Special emphasis is placed on the interaction between the clay host rock and the bentonite buffer, which is part of the engineered barrier system, under saturated conditions. For this purpose, a vertical borehole with a diameter of 300 mm and a length of 7 m was drilled and an electrical heater surrounded with bentonite rings (Spanish Serrata bentonite was used) was installed. About 20 boreholes were instrumented to measure temperatures, total pressures, radial displacements and gas–water release, and to perform geoelectric tomography. Finally, the whole test site was dismantled and the installations and buffer materials were analysed. Measurement results and interpretations have been described by Goebel *et al.* (2006).

Self-sealing of the EDZ

After closure, the repository will slowly resaturate. The interaction of the water with the clay, the swelling of the bentonite and the creep of the host rock will eventually lead to self-sealing of the fracture network in the EDZ. This self-sealing has been demonstrated by long-term hydrotesting, where a decrease in the transmissivity of the fracture network was observed with time during resaturation (Meier *et al.* 2002). The relevant processes leading to this self-sealing are now being investigated in more detail. This is being carried out for tectonic faults in the host rock as well as for EDZ fractures that formed during construction of an underground gallery.

Gas flow

In a repository, hydrogen gas will be produced by corrosion of the steel canisters containing the spent fuel and long-lived high-level waste. In addition to gas flow through the intact rock mass, repository seals, interfaces between engineered barriers and reactivation of sealed structures such as (closed) fractures in the EDZ will represent potential gas flow paths. The objective of gas flow experiments is to identify the relevant gas transport processes and mechanisms in the Opalinus Clay, such as advective-dispersive and diffusive transport of dissolved gases in the porewater, two-phase flow, flow as a result of pathway dilatation, or even gas flow through induced fractures. First results of gas tests have been given by Croisé *et al.* (2006). A further large-scale experiment in the Mont Terri Rock Laboratory, the so-called ‘gaspath through host rock and along sealed sections (HG-A)

experiment’, has just started. An overview of this experiment has been given by Marschall *et al.* (2006).

Diffusion and sorption

A key issue for the performance assessment of a repository is the understanding of dominant solute transport processes of radionuclides. As clay formations generally exhibit very low hydraulic conductivities, the dominant transport process is molecular diffusion combined with sorption of the solutes on clay mineral surfaces. Parameters such as the diffusion-accessible porosity and the effective diffusion coefficients normal and parallel to bedding are derived from field experiments. In the Mont Terri Rock Laboratory, a method has been developed to obtain these diffusion parameters *in situ* and to validate them with parameters obtained from diffusion experiments carried out on drillcore samples in the laboratory. The concept for such a diffusion and sorption experiment consists of circulating a tracer cocktail in a packed-off borehole interval for one to several years. After this, the diffusion borehole is overcored and the tracer distribution in the overcore is measured. These experiments are carefully planned by design and scoping calculations and by interpretation modelling after completion of the *in situ* tests. So far, several radioactive tracers have been used (e.g. tritium, ^{22}Na , ^{60}Co , ^{75}Se , ^{85}Sr , ^{133}Ba , ^{137}Cs and ^{152}Eu), with cocktail concentrations always below exemption limits. Results and interpretations of the first diffusion experiments have been presented mainly by Palut *et al.* (2002) and Tevissen *et al.* (2004). Diffusion and sorption experiments are continuing in the long term.

Discussion

A rock laboratory generally provides direct access to the geological environment under realistic repository conditions. The generic Mont Terri Rock Laboratory is purely for research purposes and no waste will ever be disposed of there. The experiments being carried out provide the basis for understanding the hydrogeological, rock mechanical and geochemical characteristics and coupled processes that control the performance of the natural (rock) and engineered barriers (canister, bentonite backfill) of a geological repository. Furthermore, rock laboratories are ideal locations for developing the technologies required for the construction, operation, monitoring and closure of a repository. In addition, they are essential in providing information on the long-term

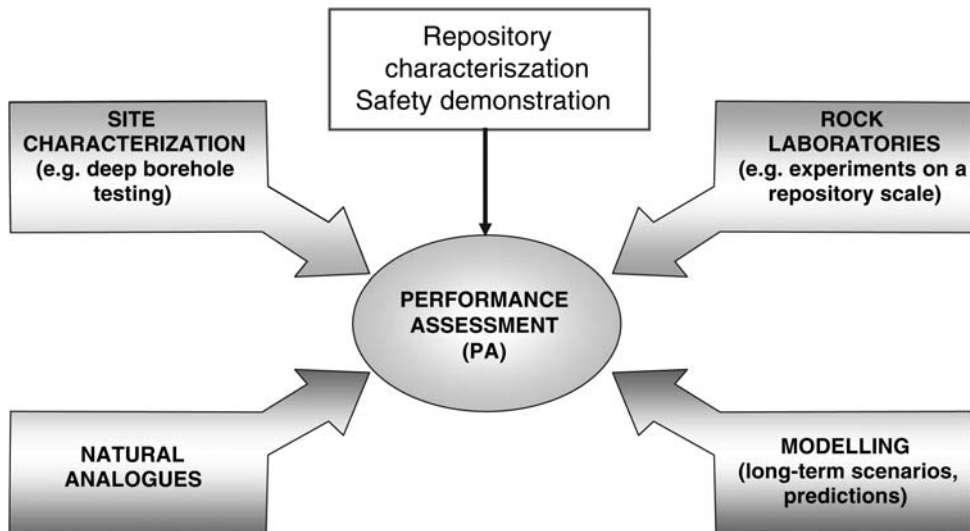


Fig. 3. Integration of information derived from rock laboratories, site characterization, natural analogues and modelling into performance assessment.

performance of engineered barriers and monitoring systems. Finally, a key role of a rock laboratory is enhancing public confidence. By opening the facility to the public, technological developments can be demonstrated and a platform for discussions with scientists and technicians can be provided, helping to create and improve confidence and acceptance for a repository programme.

The question of whether a generic rock laboratory such as Mont Terri alone is sufficient for the performance assessment of a geological repository at a real site can clearly be answered in the negative. Additional site-specific information and investigations are needed for repository characterization and demonstration of safety. As outlined in Figure 3, this additional information consists of the study of natural analogues, the testing of specific sites (with the intention of realizing a repository) and the entire palette of modelling with which long-term scenarios can be assessed and system performance can be evaluated. (A natural analogue is an occurrence of materials or processes that resemble those expected in a proposed geological repository (Côme & Chapman 1986). In essence, natural analogue studies use information from the closest possible approximations, or direct analogies, of the long-term behaviour of materials and processes found in a repository, or caused to develop by it, and test models appropriate to performance assessment work. For example, the migration history of radionuclides from radioactive mineral deposits over very long times can be

analysed and the results used in forecasting the potential behaviour of similar radionuclides in a repository over a long time period.) The integration of all available information from the real site, the analogues and the experimental results obtained from site-specific and generic rock laboratories will lead to an appropriate and reliable safety demonstration for geological disposal.

References

- CÔME, B. & CHAPMAN, N. A. (eds) 1986. *Natural analogue working group; first meeting, Brussels, November 1985*. Commission of the European Communities, Nuclear Science and Technology Report, EUR 10315.
 CROISÉ, J., MAYER, G., MARSHALL, P., MATRAY, J.-M., TANAKA, T. & VOGEL, P. 2006. Gas threshold pressure test performed at the Mont Terri rock laboratory. Experimental data and analyses. *Oil & Gas Science and Technology – Revue de l’IFP*, **61**, 631–645.
 GOEBEL, I., ALHEID, H.-J., JOCKWER, N. ET AL. 2006. *Heater Experiment: rock and bentonite thermo-hydro-mechanical (THM) processes in the near field of a thermal source for development of deep underground high level radioactive waste repositories*. EC report, 5th Euratom Framework Programme (1998–2002), Project FIS5-2001-00024.
 JOHNSON, L. H., NIEMEYER, M., KLUBERTANZ, G., SIEGEL, P. & GRIBI, P. 2002. *Calculations of the temperature evolution of a repository for spent fuel, vitrified high-level waste and intermediate level*

- waste in Opalinus Clay. NAGRA Technical Report **NTB 01-04**.
- MARSCHALL, P., DISTINGUIN, M., SHAO, H., BOSSART, P., ERNACHESCU, C. & TRICK, T. 2006. Creation and evolution of damaged zones around a microtunnel in a claystone formation of the Swiss Jura Mountains. *SPE International Symposium and Exhibition on Formation Damage Control, in Lafayette, LA, 15–17 February 2006* SPE 98537-MS.
- MARTIN, C. C., LANYON, G. W., BLÜMLING, P. & BOSSART, P. 2004. Excavation disturbed zone in clay shale: Mont Terri. swisstopo Technical Report **TR 2001-01**.
- MAYOR, J.-C., GARCIA-SINERIZ, J.-L., ALONSO, E., ALHEID, H.-J. & BLÜMLING, P. 2005. Engineered barrier emplacement experiment in Opalinus Clay for the disposal of radioactive waste in underground repositories. Euratom Programme 1998–2002. EC-Report ‘EB’, **FIS5-1999-00121**.
- MEIER, P., TRICK, T., BLÜMLING, P. & VOLCKAERT, G. 2002. Self-sealing of fractures within the excavation damaged zone at the Mont Terri rock laboratory. Results after one year of experimental work. In: HOTEIT, N., SU, K., TIJANI, M. & SHAO, J.-F. (eds) *Proceedings of International Workshop on Geomechanics. Hydromechanical and Thermohydro-mechanical Behaviour of Deep Argillaceous Rocks, Paris, 11–12 October 2000*. Swets & Zeitlinger, Lisse.
- NAGRA 2002. *Opalinus Clay Project. Demonstration of feasibility of disposal for spent fuel, vitrified high-level waste and long-lived intermediate-level waste. Summary Overview*. Swiss National Cooperative for the Disposal of Radioactive Waste, Wettingen.
- PALUT, J.-M., FIERZ, T., EIKENBERG, J. ET AL. 2002. *Diffusion in-situ experiment DI. Field activity and data report*. swisstopo Technical Report **TR 2000-03**.
- ROTHFUCHS, T., JOCKWER, N., MIEHE, R. & JHANG, C.-L. 2005. Self-sealing barriers of clay/mineral mixtures in a clay repository. Gesellschaft für Anlagen-und Reattorsicherheit mbh, Report **GRS-212**.
- TEVISSEN, E., SOLER, M. J., MONTARNAL, P., GAUTSCHI, A. & VAN LOON, L. R. 2004. Comparison between *in situ* and laboratory diffusion studies of HTO and halides in the Opalinus Clay from the Mont Terri. *Radiochimica Acta*, **92**, 781–786.
- TRABER, D. 2004. *Studies on weathered Opalinus Clay in a 130 year old railway tunnel (Col de La Croix). Part III: Geochemical investigations on drillcore BBC-3*. Internal Technical Note, Federal Office of Topography, swisstopo, Wabern.

Velocity survey of an excavation damaged zone: influence of excavation and reloading

J. DAMAJ¹, C. BALLAND¹, G. ARMAND², T. VERDEL¹,
D. AMITRANO³ & F. HOMAND⁴

¹LAEGO-INERIS, Ecole des Mines de Nancy, Parc Saurupt, F-54042 Nancy Cedex,
France (e-mail: cyrille.balland@ineris.fr)

²ANDRA, CD 960, Voie Gasselle, 55290 Bure, France

³LIRIGM, Université J. Fourier, BP 53, 38041 Grenoble, France

⁴LAEGO-ENSG, bât. E, rue du Doyen-Marcel-Roubault, 54501
Vandœuvre-les-Nancy cedex, France

Abstract: During gallery excavation, regardless of the method chosen, the surrounding rock is mechanically disturbed in the case of underground disposal of chemical or radioactive wastes, and such mechanical changes to the rock state can create preferential pathways for the release of material from the waste inside the excavation (e.g. chemical waste gases, brine or dissolved radionuclide) up to the biosphere. The mechanical characterization of this disturbed zone is thus essential in assessing the rock capacity necessary to form an impermeable geological rock barrier. The key to this effort lies in determining the nature, extent and change to this disturbed zone. A survey by ultrasonic wave analysis is particularly appropriate for these purposes, as it provides information on the zone left undisturbed by the boreholes. The main aim of this paper is to describe a recent *in situ* experiment (called EZ-A) conducted in Opalinus clay at the Mont Terri Rock Laboratory in Switzerland. This experimental campaign successfully studied the possibility of improving the properties of rocks forming the excavation damaged zone (EDZ). The experiments consisted of three stages: the first entailed locating the EDZ caused by the construction of gallery EZ-A at the Mont Terri laboratory; the second traced the evolution of the EDZ arising from a 20 cm thick and 150 cm deep slot excavation in the EZ-A gallery floor; and the third stage focused on the P-wave velocity evolution surrounding the slot during a pressure loading at the slot walls, which serves to characterize the EDZ evolution in the slot. These three stages were carried out using seismic tomography and then recording the wave propagations during the excavation and reloading stages. The measurement of velocity before and after slot excavation reloading, together with the survey during slot excavation, showed a decrease in P-wave velocity underneath the slot floor down to a 0.2 m depth. Reloading clearly improves P-wave propagation along the sidewall and slightly decreases it under the slot.

The excavation of underground openings generally damages rock in the vicinity of the openings. This damage level depends, among other factors, on the excavation method (Sato *et al.* 2000), rock properties (Zimmerman & King 1985), stress field, geometry of the opening, and the age of excavation (Schuster *et al.* 2001). This zone is known as the excavation damaged zone (EDZ), as defined at the CLUSTER conference of Luxembourg in 2003.

Over the past 20 years, geophysical, geotechnical and geological methods have been utilized to search for fundamental answers regarding both the assessment of rock mass properties following an excavation process and the estimation of time-dependent effects over longer periods. Determining the extent and properties of the EDZ is essential in designing and constructing seals and plugs for radioactive waste repositories (Maxwell & Young

1995; Maxwell *et al.* 1997; Schuster *et al.* 2001; Young & Collins 2001).

It is a well-known fact that seismic velocities in rocks change considerably with the progressive onset of failure. Seismic survey methods can therefore help in analysing changes in rock properties in the EDZ around underground openings. In this paper, we study EDZ extension using an integrated interpretation of two geophysical methods: seismic tomography and velocity surveying.

One approach to severing fracture network connectivity along a seal could consist of excavating slots and filling them with a low-permeability material that has the potential to swell perpendicular to the gallery. To verify this concept, ANDRA performed *in situ* experiments on slots.

The primary objective of this paper is to present the velocity survey and seismic tomography results

for one of the *in situ* experiments, focusing on the effects of filling material swelling. Complete saturation of bentonite in a slot takes time, which is why the pressure on slot walls, in this case caused by the swelling of bentonite, is applied by means of a hydraulic flat jack.

Geology of the EZ-A gallery

A new gallery (EZ-A) was excavated in the Opalinus clay layer located in the shaly facies at the Mont Terri Underground Research Laboratory (URL) (Nussbaum *et al.* 2004). In this gallery, a new experiment (EDZ cut-off) was carried out (Bossart *et al.* 2002) to study the following points: (1) EDZ evolution before and after excavation of a slot in the floor of the EZ-A gallery; (2) EDZ evolution as a result of reloading the slot walls using a flat jack.

Figure 1 shows EDZ evolution during the three steps of the EDZ cut-off experiment. Evolution of the EDZ is presented here during slot excavation and slot wall reloading. The EZ-A gallery was excavated in the shaly facies at the URL. Nussbaum *et al.* (2004) carried out structural and geological mapping of the EZ-A gallery; they identified at the URL two sets of fault planes along the axis of the EZ-A niche. The dominant system, subparallel to the bedding planes, plunges towards the SE (azimuth range 140–150°) at a medium angle (mean dip 45–50°). The minor system dips at a small angle (10–20°) towards the SW (azimuth range 200–220°). Figure 2 shows vertical cross-sections at 4 and 6 m from the EZ-A gallery entrance. In this figure, major fault systems have been indicated in red and minor systems in blue.

Experimental description: EDZ cut-off

In the new EZ-A gallery, several experiments were carried out including EDZ cut-off, which entailed the three following stages: Stage 1: determination of the EDZ under the EZ-A gallery floor (related to the presence of the gallery itself); Stage 2: tracking the evolution in the EDZ as a result of advances of the 20 cm thick, 150 cm deep slot excavation into the gallery floor; Stage 3: tracking the evolution in the EDZ as a result of reloading of slot sidewalls by means of a hydraulic flat jack to simulate the swelling of compacted bentonite filling (this filling would apply loading also on the slot base, which is not possible with this layout).

Executing these three stages necessitated the following: boreholes were drilled to perform the initial tomography and position the ultrasonic sensors and geotechnical tools (extensometer, inclinometer); the slot was excavated (by BGR) using a saw, with slot dimensions of 1.5 m depth, 3 m width and 0.2 m thickness; the hydraulic flat jack was placed in the slot and loading–unloading cycles were carried out; the maximum loading was fixed at 1.98 MPa, which is compatible with the swelling pressure of compacted bentonite (ANDRA 2005).

The INERIS Institute was responsible for tomography measurements and velocity survey setup, in addition to data analysis. The slot excavation and geotechnical measurements are not described in this paper, which focuses on the ultrasonic measurement methods.

The following two measurement techniques were used: seismic tomography to determine the EDZ caused by the existence of the gallery (Stage 1); a velocity survey to track the evolution of the EDZ during both slot excavation (Stage 2) and

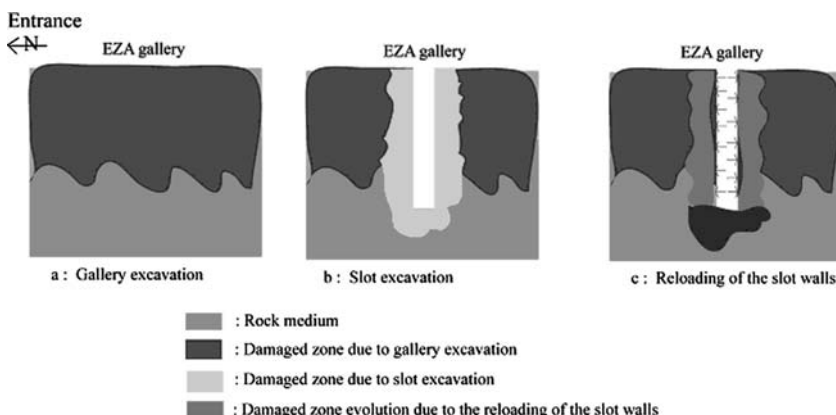


Fig. 1. Principle applied for the various stages of the EDZ cutoff experiment: EDZ evolution during slot excavation and slot wall reloading.

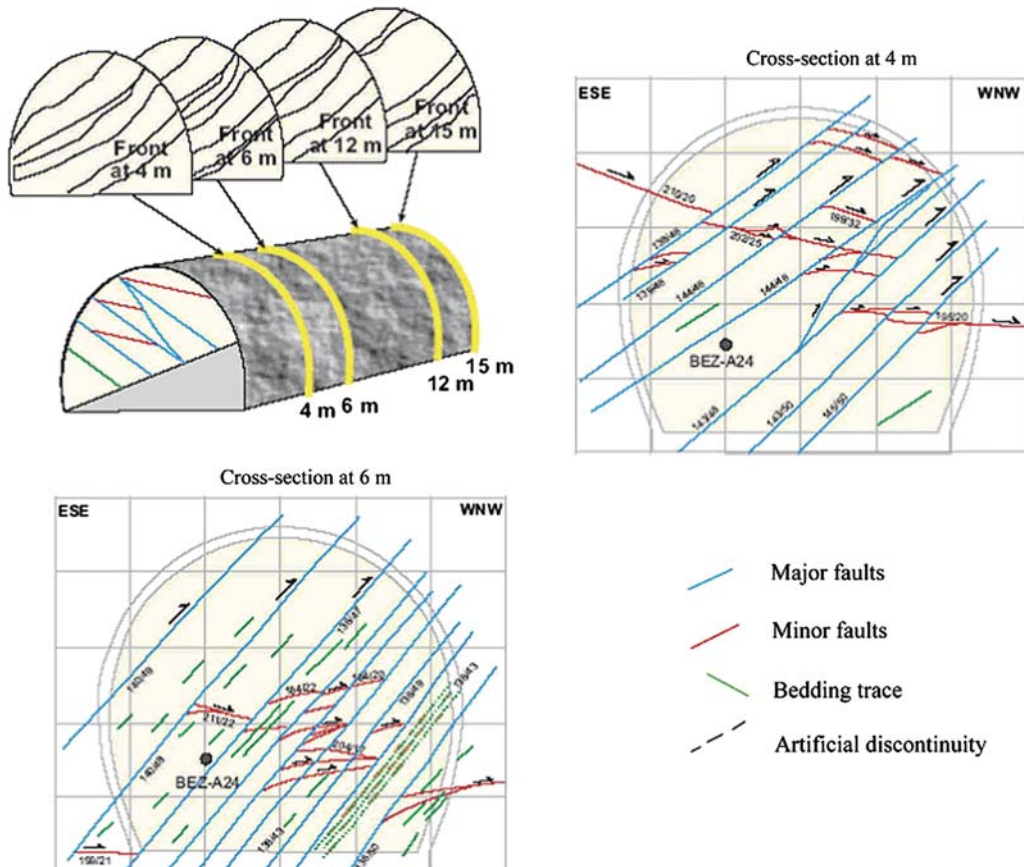


Fig. 2. Geological and structural mapping of the EZ-A niche extension (Nussbaum *et al.* 2004).

pressure reloading of the slot sidewalls (Stage 3). The acquisition system used during the experiment was adapted to the expected signal frequency range (i.e. 10 MHz per channel) to be captured and recorded, following a 14-bit digital conversion on a ± 2 V electrical input signal. The maximum number of channels is 16 and the transducers used are R6 sensor types from the Physical Acoustics Corporation (PAC, USA).

The devices used during these three stages are described below.

Seismic tomography

Two probes were used to conduct the seismic tomography. The first carried eight sources placed 10 cm apart, and the second carried 12 receivers. The two probes were installed in two borings (EZA-18 and EZA-19), 66 mm in diameter and 170 cm in depth, respectively. These two probes were vertically moved in accordance with nine configurations, to investigate the zone between the two borings by

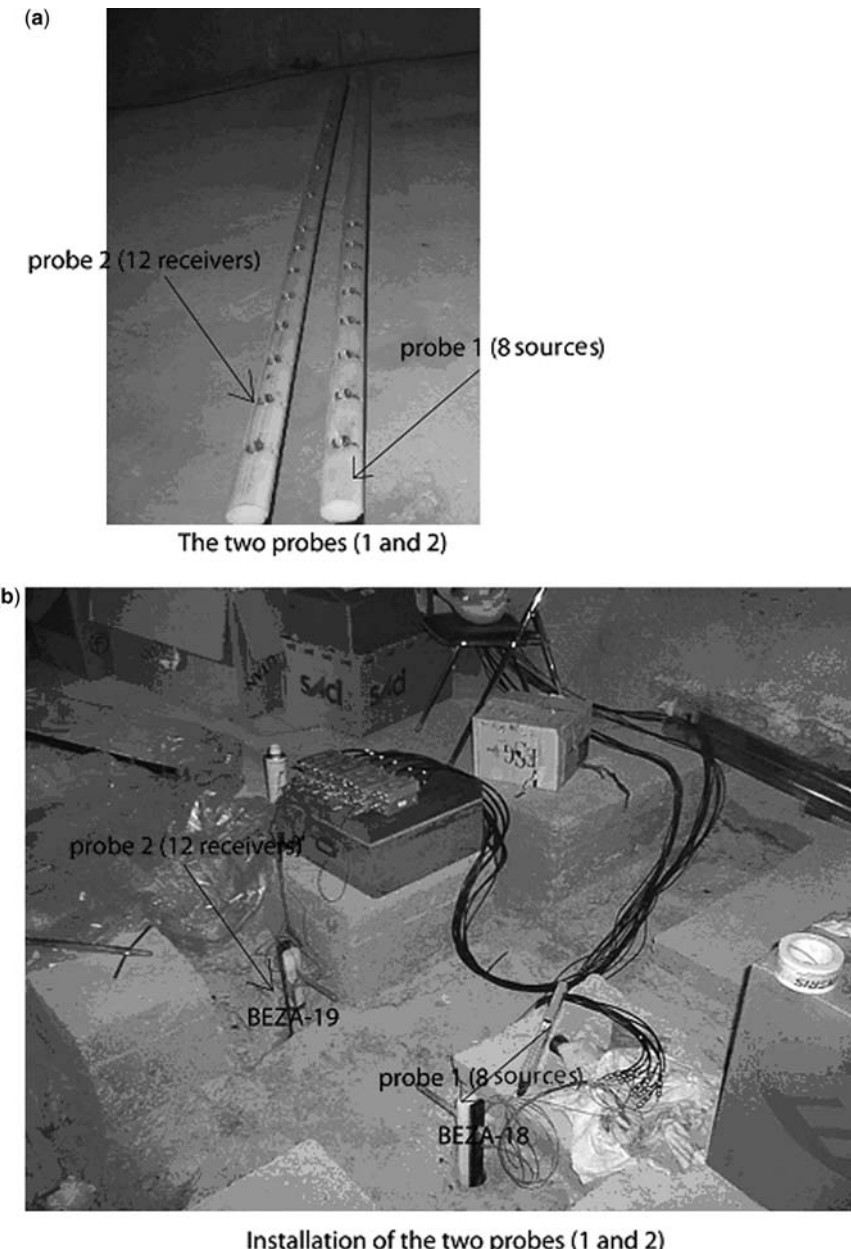
means of seismic signals. Figure 3 shows the positions of the two probes within the slot. This setup allowed estimation of the EDZ extension as a result of the presence of the gallery.

Velocity survey during slot excavation

The two probes were installed in borings EZA-18 and EZA-19 to investigate the zone damaged during slot excavation. The setup allowed study of the velocity variations at the slot base (see Fig. 4). Figure 4 also shows the devices used with the two probes intended for the slot excavation. As can be observed, such a setup allows investigation of the variation in P-wave arrival time as the slot advances.

Velocity survey during slot sidewall reloading

The main objective during this stage was to study the effect of pressure on the slot walls, by observing



Installation of the two probes (1 and 2)

Fig. 3. (a) Details of the two probes: Probe 1 has eight sources; Probe 2 has 12 receivers. (b) Installation of the two probes in the EZ-A gallery slot.

changes in rock velocity around the slot. An increase in velocity as a result of pressure loading reveals an improvement in mechanical parameters near the slot, as correlated with microcrack closing.

A hydraulic flat jack was installed in the slot to reload the slot walls under pressure. The reloading cycle was introduced over an 18 h period with

nine incremental loading steps lasting 2 h each. Figure 5 depicts the reloading cycle (pressure in MPa v. time in minutes).

A third probe was necessary to explore the zone opposite the slot. For this purpose, a new probe carrying five sources was installed in the jack in contact with the slot sidewalls. Figure 6

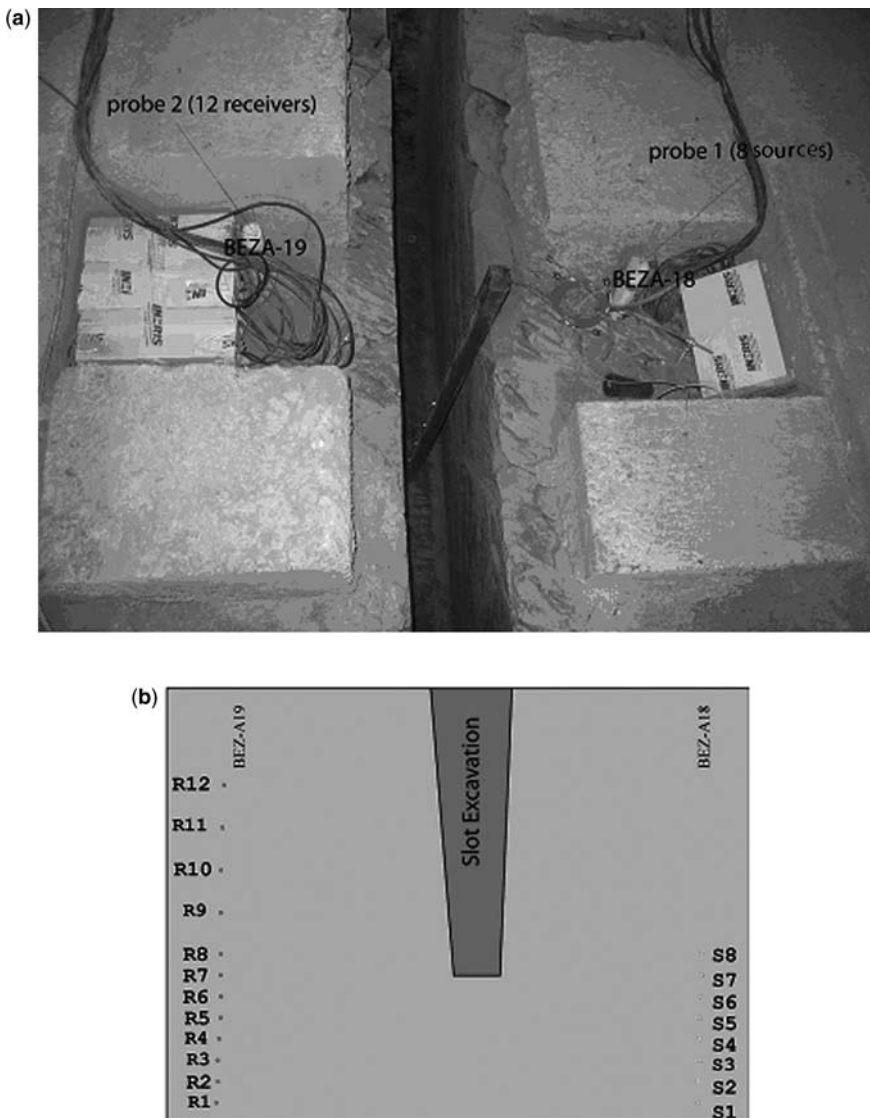


Fig. 4. (a) Excavation of the slot; (b) position of sources and receivers during slot excavation (S, sources; R, receivers).

shows the various positions of the sources and receivers, from which two zones could be investigated: a zone at the base (Zone A in Fig. 6) and another facing the slot (Zone B). This setup enabled us to monitor the evolution of the EDZ during slot wall reloading.

In contrast, crack locks developed in the EDZ during slot sidewall reloading can explain the decrease in permeability. Moreover, crack locks generate (or enhance) an increase in P-wave velocity (Bourbié & Zinszner 1985; Sato *et al.* 2000; Kahraman 2002; Pyrak-Nolte 2002; Levin *et al.* 2004).

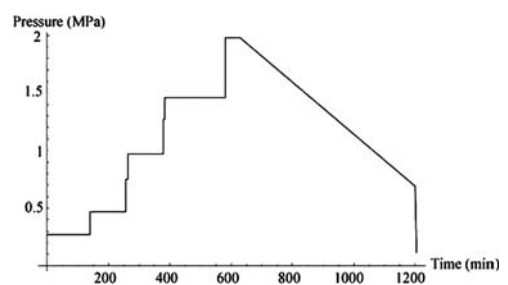


Fig. 5. The applied pressure cycle (MPa) v. time (minutes).

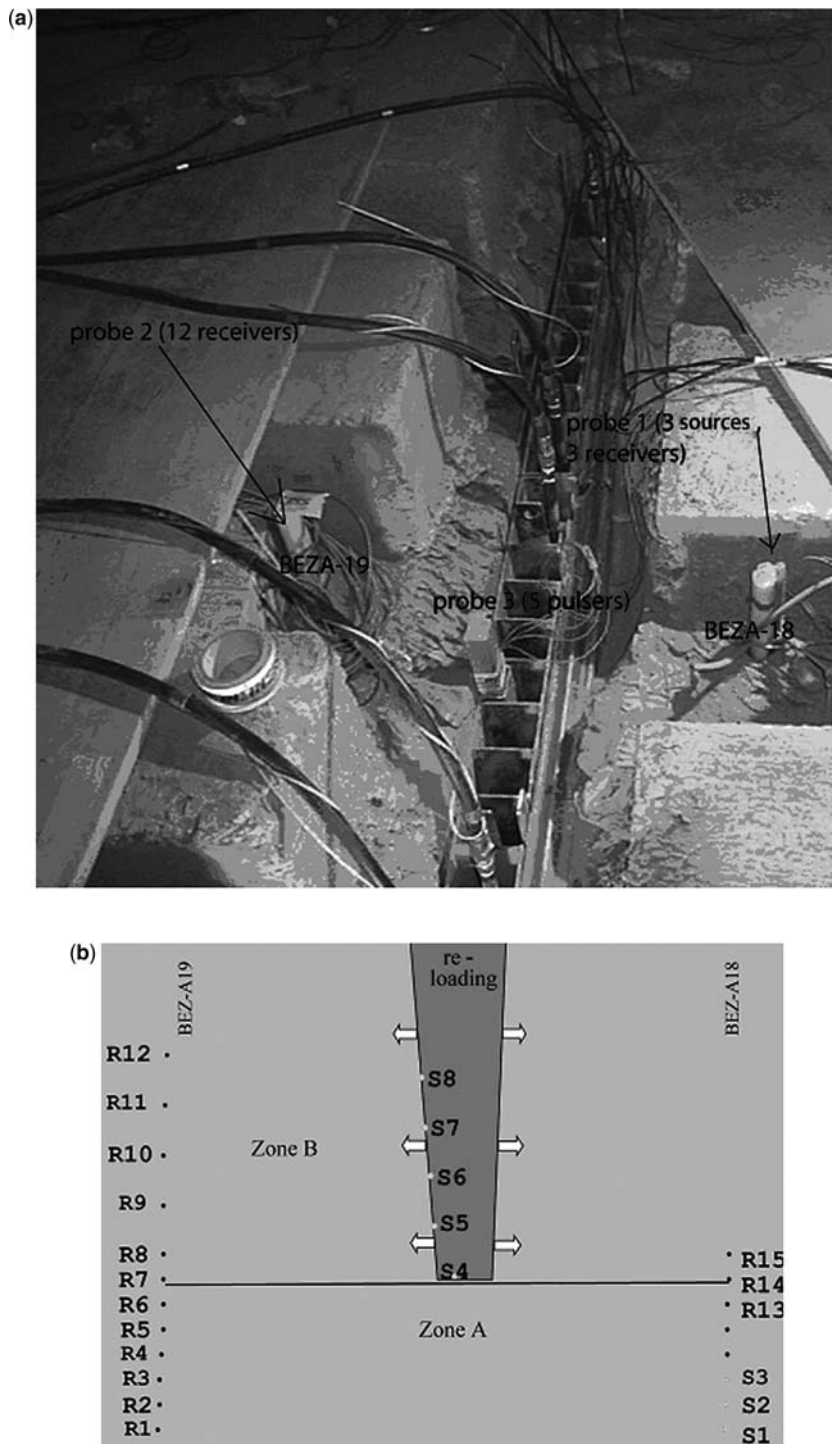


Fig. 6. The third step of the experiment: (a) shows the position of the three probes and the hydraulic flat jack installed in the slot excavation; (b) shows source and receiver positions (S, sources; R, receivers) for the two zones (A and B).

Methods and results

Tomography

The tomography study was carried out by moving the probes 1 and 2 vertically in accordance with nine configurations. Theoretically, it would be possible to derive 598 rays from these nine configurations. The array of source and receiver points was designed to obtain good angular coverage of the investigated area and optimum system stability during tomographic inversion. We were only able, however, to determine 222 seismic rays. Figure 7 indicates the number of seismic rays depending on the numerical model and experimental findings. The density of rays is observed to be low within the zone close to the gallery wall, whereas it starts to increase in the zone further from the slot wall. This may explain the difficulty encountered, as seismic waves crossed through the EDZ as a result of the existence of this gallery.

After recording signals from the nine configurations, we determined the travel time of P-wave propagation. This inversion procedure was performed using the TOMSIS software package (Verdel 2001; Damaj 2002; Damaj & Balland 2004; Damaj *et al.* 2004). This software was developed by a team from the INERIS Institute and runs in the Mathematica environment. The method adopted in this application is based on the least-squares inversion (linear problem resolution) with variable damping (Cote & Lagabrielle 1986; Bernabini & Cardarelli 1997; Cardarelli *et al.* 2003) and features the use of *a priori* information on mean slowness:

$$X = (G^T G + \lambda^T) - 1(G^T b + \lambda^T I_m)$$

where X is the slowness vector of the considered cell; G is the tomographic matrix, constructed from either straight or bent ray paths (Um & Thurber 1987); b is the data vector (in this case,

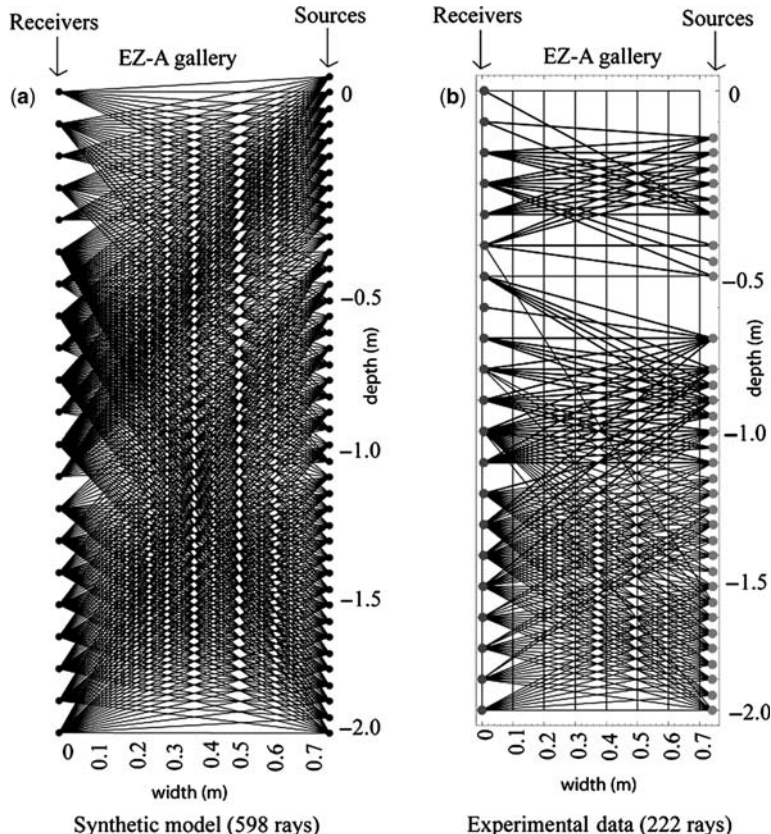


Fig. 7. Ray density: (a) synthetic model; (b) experimental model.

travel time); λ is the diagonal matrix of the variable damping factors; and I_m is the mean slowness.

Because of the low density of rays over the zone spanning the 50–80 cm depth range, the tomographic inversion diverges. To improve this inversion, we undertook partial inversions; that is, we carried out the tomographic inversion in two parts: Part 1 from 0 to -0.5 m; Part 2 from -0.8 m to -2 m. This inversion procedure was performed using bending rays by integrating the Um & Thurber (1987) algorithm within TOMSIS. Various grids were tested to identify the optimum, taking into account the maximum resolution obtainable with the geometry and frequencies employed. In addition, the unitary covariance matrix (Tarantola & Valette 1982) was examined for each grid, to determine the degree of amplitude error associated with each cell, and the influence of such error on other cell values (i.e. the degree of correlation between cells). The optimum mesh is shown in Figure 8.

The results of this inversion exercise allowed us to identify two zones (Parts 1 and 2), characterized by differences in P-wave velocity. Part 1 features a P-wave velocity of $<3.000 \text{ km s}^{-1}$, whereas the P-wave velocity in Part 2 varies between 2.500 and 3.400 km s^{-1} (see Fig. 8). Estimated P-wave velocity errors related to source and receiver positions as well as the picking of first arrivals are less than 50 m s^{-1} . Figure 8 also shows the P-wave velocities of Parts 1 and 2 together with the structural geology of the rock medium. The zone of low ray density (Part 1) is traversed by some minor faults (indicated in red) and influenced by perturbations caused by EZ-A gallery excavation. Moreover, the zone between depths of 0.5 and 0.8 m is crossed by three minor fault systems, which may explain the low ray density.

Similarly, the plot of mean P-wave velocity v. source depth reveals a zone of low velocity (around 2.500 km s^{-1}) over at least the first 0.5 m depth from the gallery surface. Below 0.8 m

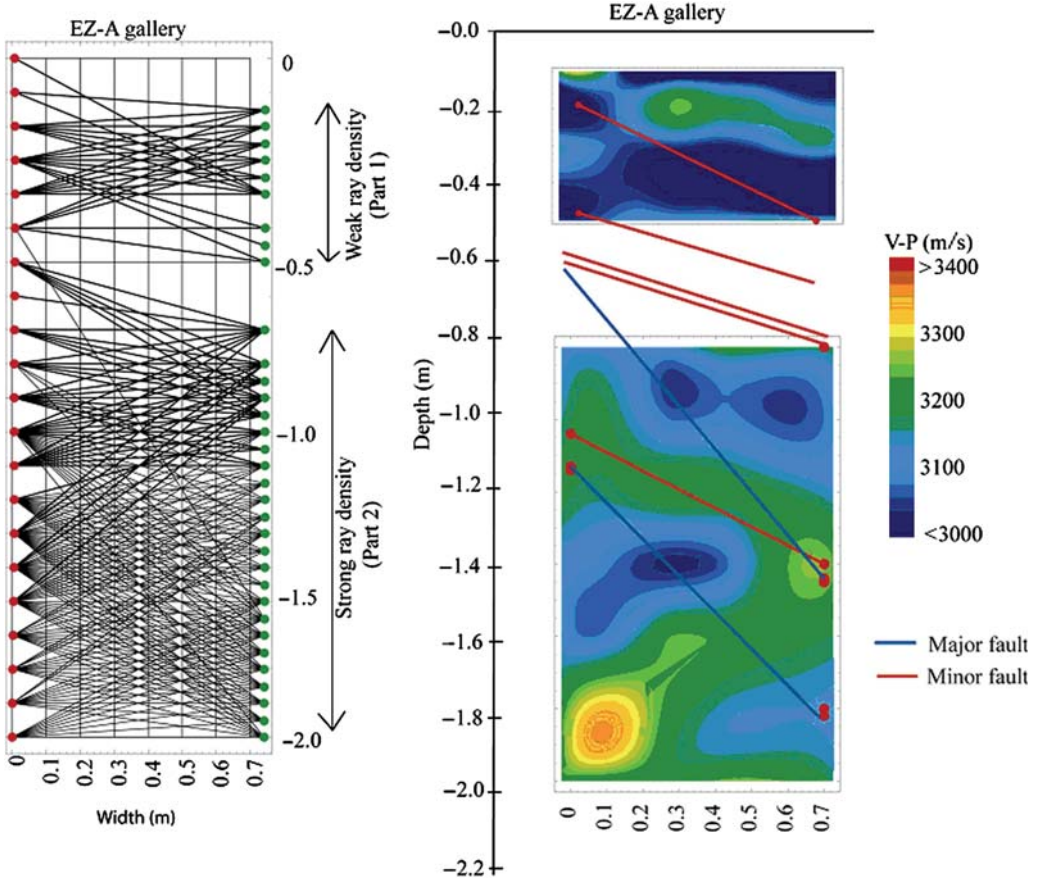


Fig. 8. Tomographic inversion, Parts 1 and 2 (green, sources; red, receivers). The colour bar shows the magnitude of the P-wave velocity (m s^{-1}).

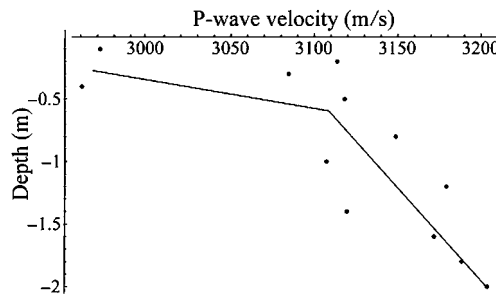


Fig. 9. Mean P-wave velocity v. source depth.

depth, the P-wave velocity of most rays is c. 3.100 km s⁻¹ (see Fig. 9).

The conclusions reached are as follows: Part 1 is a zone of low seismic ray density and low P-wave velocity; Part 2 is a zone of high ray density and a field of high P-wave velocity. The EDZ caused by presence of the gallery thus extends to a depth of 50 cm, with respect to wall distance from the gallery.

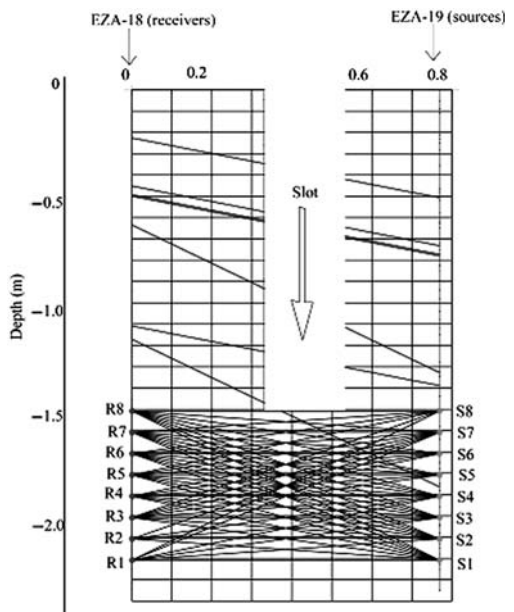


Fig. 10. Zone located under the slot (S, sources; R, receivers).

Velocity survey during excavation

The excavation of a slot will create a damaged zone; is it possible to estimate the dimension of this zone through an analysis of P-wave propagation? To answer this question, signals were recorded during slot excavation. The velocity survey allows us to

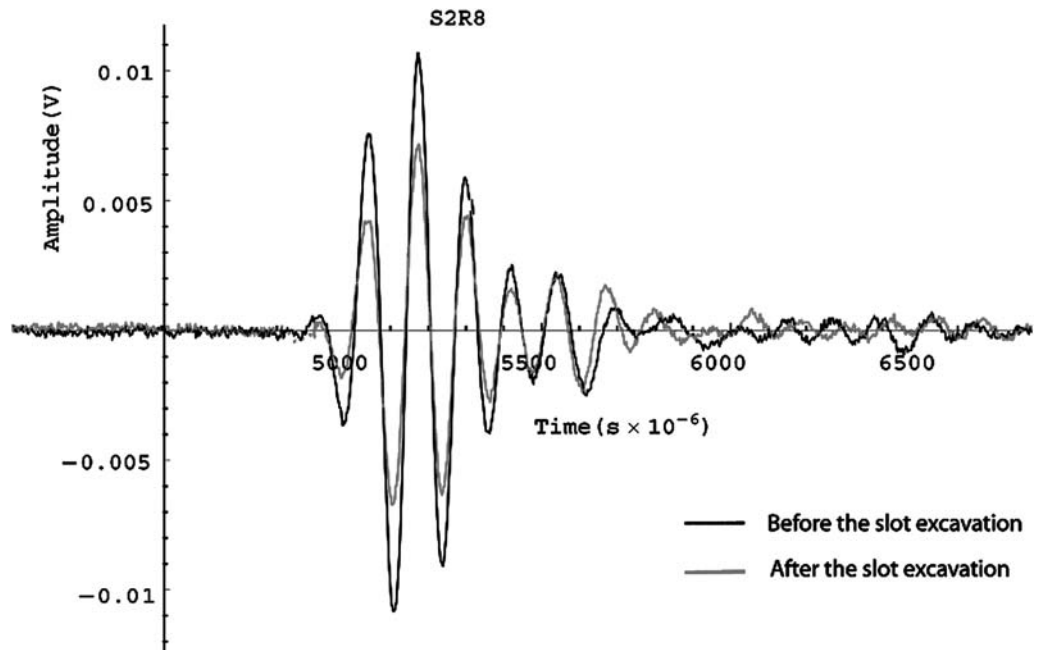


Fig. 11. Superimposition signals: ray S2R8 before and after slot excavation.

trace the evolution of waves crossing the zone underneath the slot base. Figure 10 shows the zone over which this study was conducted as a function of the structural geology (blue indicates the minor fault system, and red the major system).

Figure 11 presents the example of superimposed signals before and after slot excavation for ray path S2R8. This figure shows an increase in P-wave arrival time and a decrease in maximum amplitude. The variation amplitude (magnitude and travel time) depends heavily on both ray path direction and source position.

The location of the damaged zone caused by slot excavation was estimated by generating a chart showing the layout of the mean velocity values. The method adopted consists of: (1) discretizing

the medium studied using a regular grid; (2) determining the rays crossing each cell; (3) calculating the P-wave velocity corresponding to each ray, assuming that all rays are straight lines, and the mean velocity values in each cell.

Once these stages have been completed, the P-wave velocity can be plotted versus the slot advance rate. Similarly, we have estimated the errors arising in the P-wave velocity calculation. The results are as follows: a reduction in the number of rays following slot excavation was noted in the zone close to the slot base (58 rays before excavation, 49 after); an increase in dimensions of the low P-wave velocity zone at the slot base was observed. Figure 12 shows both the location of the damaged zone caused by slot

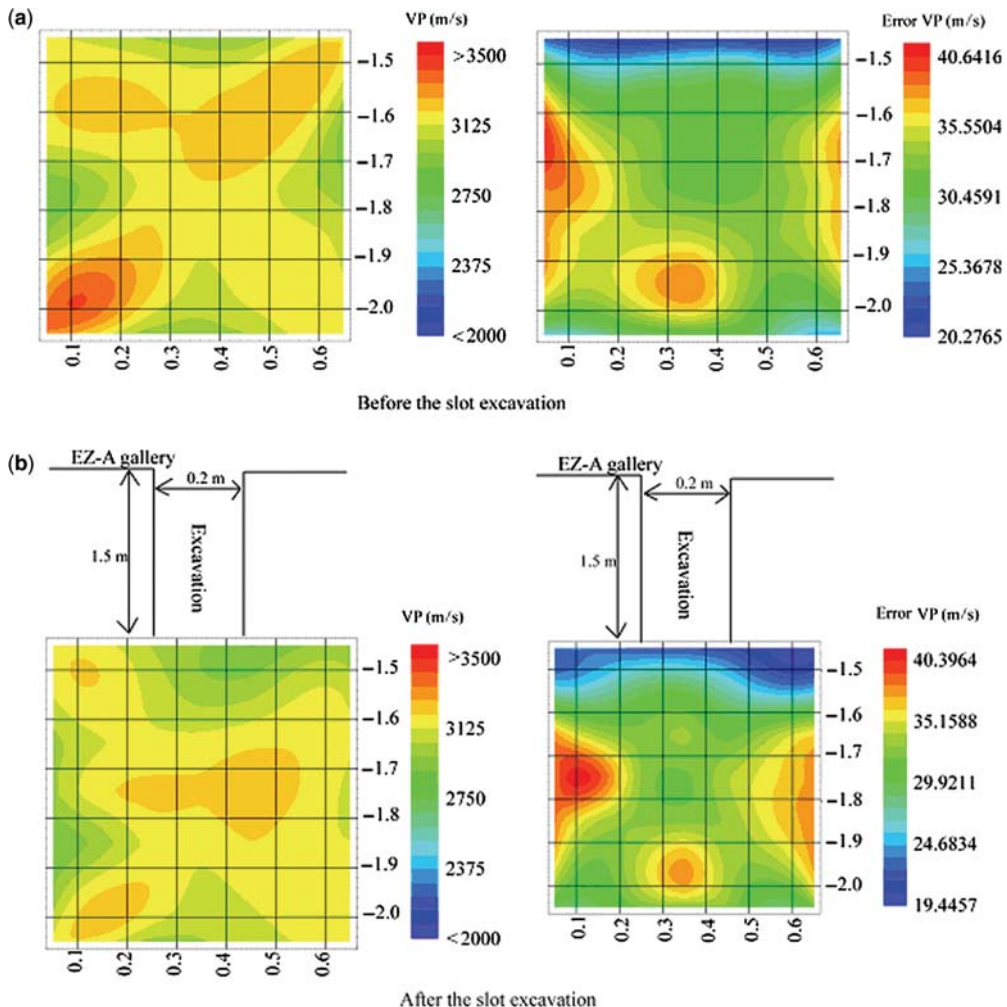


Fig. 12. Spatial variation in P-wave velocity and error velocity: (a) before and (b) after slot excavation. The colour bar shows the magnitude of the P-wave velocity (left-hand column) and the error velocity (right-hand column) (m s^{-1}). The vertical and horizontal axes represent the position (in metres).

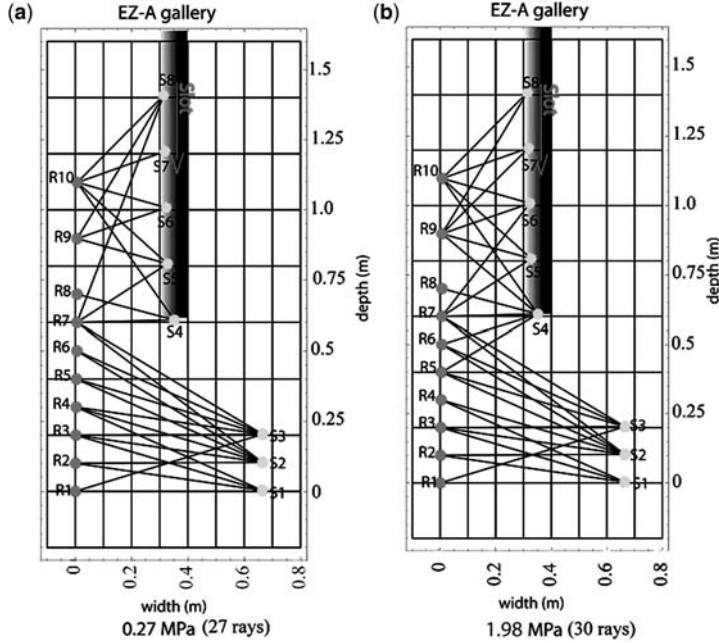


Fig. 13. Ray density: (a) at 0.27 MPa, and (b) at 1.98 MPa (sources, S; receivers, R).

excavation and the errors arising from both source positions and P-wave arrival time determination.

Velocity survey during reloading

The P-wave velocity was automatically measured every 15 min during the pressure cycle (see Fig. 5). To track EDZ evolution during slot wall reloading, the two extreme stages of the pressure cycle (0.27 and 1.98 MPa) were studied. Figure 13 shows the number of rays at these two pressure levels. This figure indicates an increase in the number of rays with rising pressure (27 rays at 0.27 MPa, increasing to 30 rays at 1.98 MPa). This increase corresponds to the appearance of

three rays in Zone B (Fig. 6b), which implies the presence of a crack lock parallel to the pressure.

Figure 14 provides two examples of signal superimposition at the same two pressure levels (0.27 and 1.98 MPa). In this figure, we present the difference between the signals propagating opposite to the slot (Zone B) and those propagating below the slot base (Zone A). Figure 14a shows the evolution in ray S2R4, which propagates under the slot base (Zone A). A decrease in amplitude coupled with an increase in travel time can be seen. Figure 14b shows the evolution in ray S7R10, which propagates opposite to the slot (Zone B). The ray S7R10 reveals an increase in amplitude and a decrease in travel time (Fig. 14b) with rising pressure.

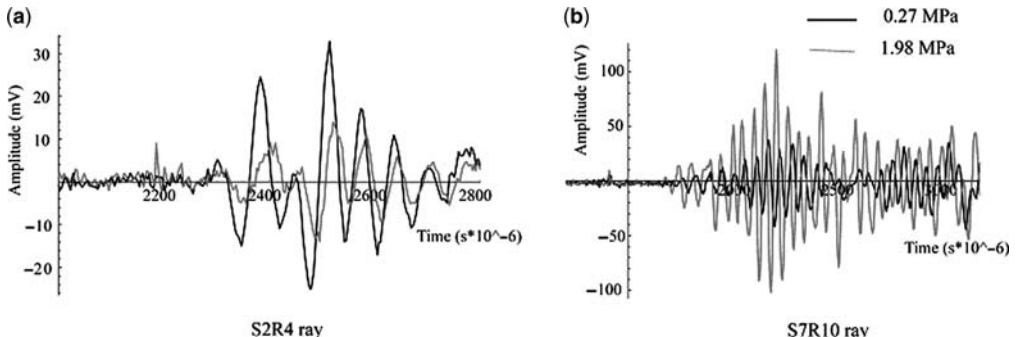


Fig. 14. Superimposition signals at 0.27 and 1.98 MPa: (a) ray S2R4; (b) ray S7R10.

Figure 15 illustrates the P-wave velocity evolution for rays S2R2 and S5R10. S2R2 propagates below the slot base and demonstrates both a decrease in P-wave velocity during slot reloading and an increase during pressure relaxation, whereas for ray S5R10 a positive correlation between P-wave velocity and pressure was derived. The rate of P-wave velocity variation depends upon ray direction. To examine this correlation more closely, a P-wave velocity plan is essential for quantifying the damaged zone evolution.

Figure 16 shows the evolution in P-wave velocity at 0.27 MPa and 1.98 MPa with respect to the structural geology map. A smaller increase in P-wave velocity in areas facing slot walls (Zone B in Fig. 5) was found, with an uncertainty lower than 70 m s^{-1} . Figure 16 also shows a decrease in P-wave velocity underneath the slot (Zone A in Fig. 5), with an uncertainty again lower than 70 m s^{-1} . Furthermore, a strong increase in P-wave velocity was recorded over the fractured zone (cracks between 0.75 and 1.25 m deep). A strong increase in P-wave velocity also developed in the zone with structural fractures (again between 0.75 and 1.25 m deep).

Figure 17 shows the differences in P-wave velocity between 1.98 and 0.27 MPa. The velocity survey method allows us to distinguish four P-wave velocity evolution zones: Zone 1 (0–0.8 m) is characterized by low speed variation (60 m s^{-1}); Zone 2 (0.8–1.4 m) is characterized by a strong increase in P-wave velocity (715 m s^{-1}); Zone 3 (1.4–1.6 m) is characterized by a strong decrease in P-wave velocity and is located beneath the slot base (590 m s^{-1}); Zone 4 (1.6–2.0 m) is once again characterized by low speed variation (60 m s^{-1}).

Along the same lines, the plot of mean P-wave velocity v. source depth shows good correlation between P-wave velocity and the pressure cycle for rays located in the immediate vicinity of slot sidewalls (i.e. at a distance of 0.5–1.5 m). In contrast, a small reduction in P-wave velocity arises for rays existing within the slot base (Fig. 18), as a result of the uniaxial loading of the experimental layout.

The method of reloading sidewalls proves significant for improving the mechanical characteristics of the damaged zone opposite the slot. Results can be summarized as follows: (1) considerable improvement in the quality of seismic rays coupled with an increase in ray number for the

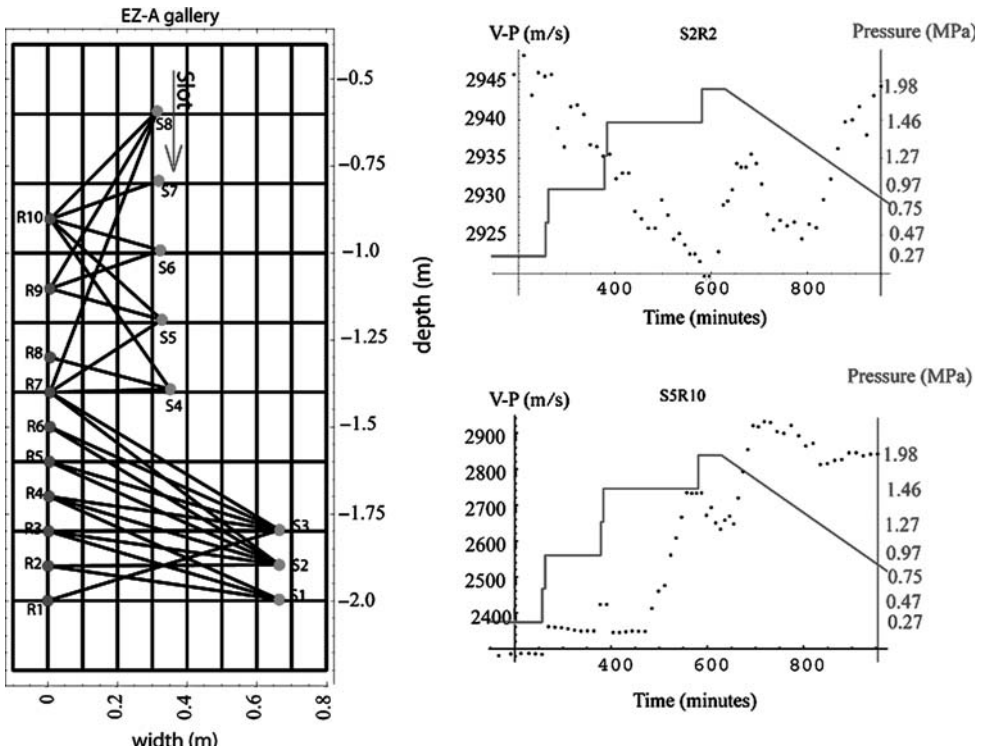


Fig. 15. Two sample curves of P-wave velocity (m s^{-1}) v. pressure (MPa): S2R2 shows weak damage for the existing zone at the slot base; S5R10, on the other hand, shows good improvement in the existing zone opposite the wall slot (sources, S; receivers, R).

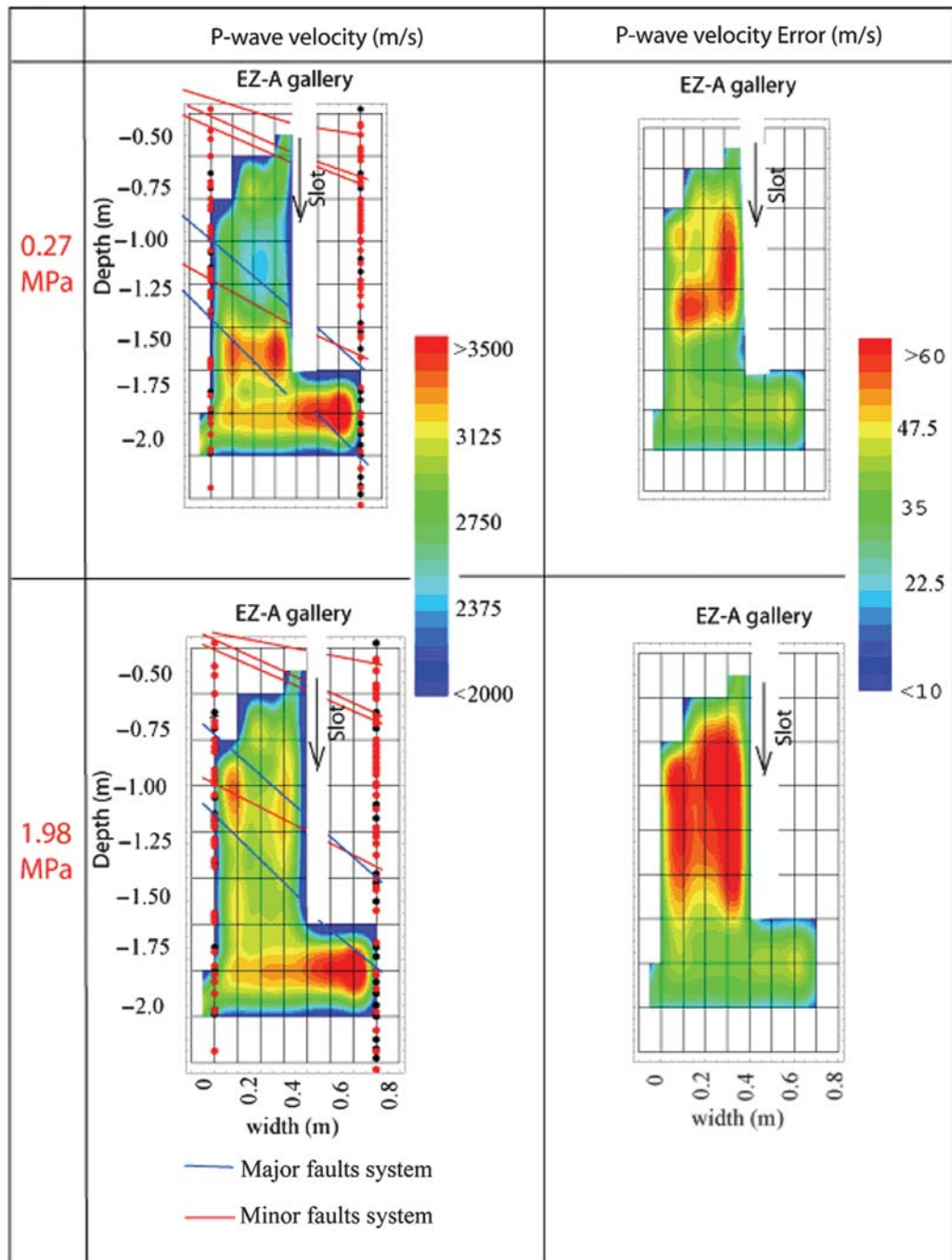


Fig. 16. P-wave velocity and error: (a) at 0.27 MPa and (b) at 1.98 MPa of slot excavation pressure. The colour bar shows the magnitude of P-wave velocity (left-hand column) and error velocity (m s^{-1}) (right-hand column).

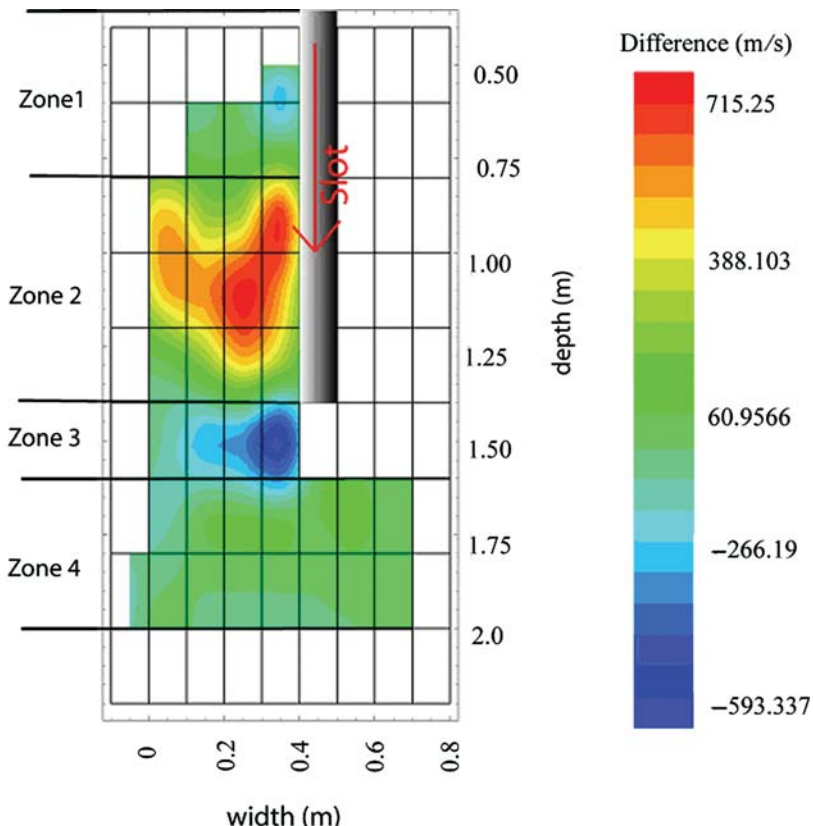


Fig. 17. Difference between P-wave velocities at the two pressure steps (0.27 and 1.98 MPa). The colour bar shows the magnitude of the difference in P-wave velocity values (m s^{-1}).

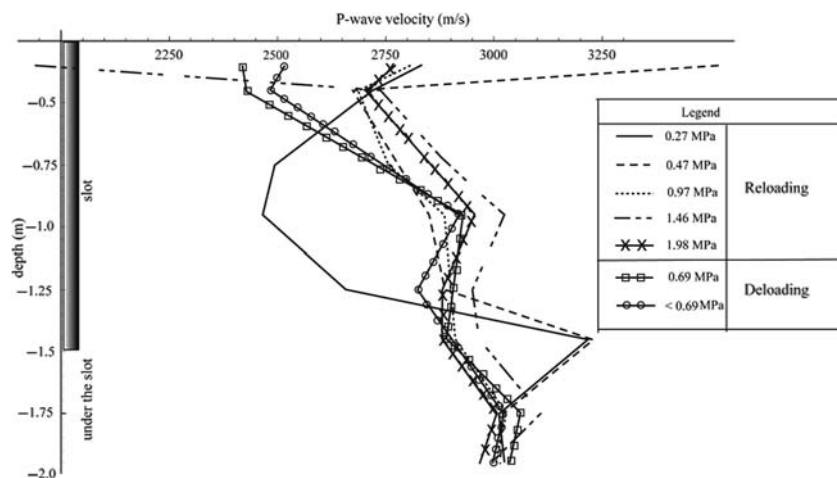


Fig. 18. Evolution in P-wave velocity (m s^{-1}) v. depth and pressure (MPa).

zone lying in the vicinity of the slot wall (Fig. 14); (2) an increase in P-wave velocity strongly dependent upon ray direction (Figs 15 and 16); (3) an increase in P-wave velocity over the zone located beside the slot, and a limited impact over the zone located beneath it (Figs 17 and 18).

Conclusion

An *in situ* EDZ cutoff experiment was performed to determine the EDZ width and the influence of reloading. The conclusions drawn may be summarized as follows.

(1) Tomographic inversion using the damped least-squares method showed the presence of a low P-wave velocity zone with low ray density, extending to -0.5 m at the gallery wall.

(2) Recording signals during trench excavation is used for locating the EDZ at the slot base (which extends down to -0.2 m from the slot base) and decreasing ray density at the slot base.

(3) Recording signals during reloading served to highlight Good improvement in the EDZ opposite the slot, as shown by the remarkable increase in P-wave velocity (700 m s^{-1}); a deterioration in the EDZ beneath the slot, as shown by the significant decrease in P-wave velocity (500 m s^{-1}); a strong correlation found between P-wave velocity and applied pressure.

(4) The evolution in velocity v. pressure is dependent on ray direction (assumed here to be straight).

The authors are grateful to the Mont Terri Project and to the EZ-A experiment team of partners ANDRA, BGR and NAGRA, which have supported all experimental work.

References

- ANDRA 2005. *Dossier 2005 Argile—Tome Evolution phénoménologique du stockage*, 394–523.
- BERNABINI, M. & CARDARELLI, E. 1997. Variable damping factor in travel time tomography. *Journal of Applied Geophysics*, **38**, 131–141.
- BOSSART, P., MEIR, P. M., MOERI, A., TRICK, T. & MAYOR, J. C. 2002. Geological and hydraulic characterisation of the excavation disturbed zone in the Opalinus Clay of the Mont Terri Rock Laboratory. *Engineering Geology*, **66**, 19–38.
- BOURBIÉ, T. & ZINSZNER, B. 1985. Hydraulic and acoustic properties as a function of porosity in Fontainebleau sandstone. *Journal of Geophysical Research*, **90**, 11524–11532.
- CARDARELLI, E., MARRONE, C. & ORLANDO, L. 2003. Evaluation of tunnel stability using integrated geophysical methods. *Journal of Applied Geophysics*, **52**, 93–102.
- COTE, Ph. & LAGABRIELLE, R. 1986. La tomographie sismique comme méthode de reconnaissance détaillée du sous-sol. *Revue Française de Géotechnique*, **36**, 47–53.
- DAMAJ, J. 2002. *Techniques d'auscultation microseismique d'ouvrages miniers abandonnés*. Projet de DEA (PAE3S), INERIS/Laego—Ecole des Mines de Nancy.
- DAMAJ, J. & BALLAND, C. 2004. *EZ-A Experiment: velocity survey around a cross-cut slot*. Report INERIS DRS-04-51272/RN01.
- DAMAJ, J., BALLAND, C., VERDEL, T., AMITRANO, D. & HOMAND, F. 2004. Auscultation et surveillance des perturbations hydromécaniques d'ouvrages souterrains par la mesure et l'analyse de la propagation d'ondes dans les roches. In: *Proceedings of the International Conference on Geotechnical Engineering*, Beirut, 19–22 May 2004, 791–798.
- KAHRAMAN, S. 2002. The effects of fracture roughness on P-wave velocity. *Engineering Geology*, **63**, 347–350.
- LEVIN, V., MARKOV, M. & KANAUN, S. 2004. Effective field method for seismic properties of cracked rocks. *Journal of Geophysical Research*, **109**, doi: 10.1029/2003JB002718.
- MAXWELL, S. C. & YOUNG, R. P. 1995. Seismic imaging of rock mass responses to excavation. *International Journal of Rock Mechanics & Mining Sciences & Geomechanics Abstracts*, **33**, 713–724.
- MAXWELL, S. C., YOUNG, R. P. & READ, R. S. 1997. A micro-velocity tool to assess the excavation damaged zone. *International Journal of Mechanical Sciences*, **35**, 235–247.
- NUSSBAUM, C., GRAF, A., BADERTSCHER, N. & BOSSART, P. 2004. *EDZ cut-off (EZ-A) experiment: structural and geological mapping of the EZ-A niche including mapping of reconnaissance boreholes, floor slot and EDZ around the Gallery 98 (EH section)*. Mont Terri Project, TN 2004-09.
- PYRAK-NOLTE, L. J. 2002. Seismic imaging of fractured media. In: *Proceedings of 5th International Workshop on the Application of Geophysics in Rock Engineering*, Toronto, Canada, 7 July 2002, 5–13.
- SATO, T., KIKUCHI, T. & SUGIHARA, K. 2000. In-situ experiments on an excavation disturbed zone induced by mechanical excavation in Neogene sedimentary rock at Tono mine, central Japan. *Engineering Geology*, **56**, 97–108.
- SCHUSTER, K., ALHEID, H.-J. & BÖDDNER, D. 2001. Seismic investigation of the excavation damaged zone in Opalinus Clay. *Engineering Geology*, **61**, 189–197.
- TARANTOLA, A. & VALETTE, B. 1982. Generalized non-linear inverse problems solved using least squares criterion. *Review of Geophysics*, **20**, 219–232.
- UM, J. & THURBER, C. 1987. A fast algorithm for two-point seismic ray tracing. *Bulletin of the Seismological Society of America*, **77**, 972–986.
- VERDEL, T. 2001. *Logiciel TOMI, version 1.2.0*. Documentation électronique Laego-Ineris, Ecole des Mines de Nancy.
- YOUNG, R. P. & COLLINS, D. S. 2001. Seismic studies of rock fracture at the Underground Research Laboratory, Canada. *International Journal of Rock Mechanics & Mining Sciences*, **38**, 787–799.
- ZIMMERMAN, R. W. & KING, M. S. 1985. Propagation of acoustic waves through cracked rock. In: *Proceedings of 26th US Symposium on Rock Mechanics*, Rapid City, SD, 26–28 June 1985, 739–745.

Temperature-induced evolution of the elastic and magnetic anisotropy in argillite samples from Bure underground research laboratory, eastern France

P. ROBION, C. DAVID & J. C. COLOMBIER

GdR FORPRO 0788–UMR 7072, Université de Cergy-Pontoise, Département des Sciences de la Terre et de l’Environnement, 5, mail Gay-Lussac, Neuville-sur-Oise, F-95031 Cergy-Pontoise, France (e-mail: philippe.robion@u-cergy.fr)

Abstract: The influence of temperature on magnetic and elastic properties of the Callovian–Oxfordian argillite formation, host of the French underground research laboratory for studying radioactive waste repository, has been investigated following two types of experiments. In the first experiment, rock samples were heated at 95 °C in an oven for 41 days, and in the second, heating–cooling cycles at increasing maximum temperatures were applied. Magnetic susceptibility and P-wave velocity measurements were conducted to investigate the effect of heating not only on the absolute values but also on the anisotropy. Whereas little variation was observed in the first experiment, the results of the heating–cooling cycles showed that different stages can be identified in the evolution of P-wave velocity and magnetic susceptibility with maximum temperature applied. At temperatures below 200 °C, the velocity increases sharply whereas the magnetic susceptibility remains unchanged: this is interpreted as being the result of mineralogical transformations, probably associated with dewatering of the clays. Above 200 °C, a large increase in susceptibility associated with a levelling off (or even a decreasing trend) of the velocity results from the competition between thermal cracking processes and another kind of mineralogical transformation affecting both properties. A magnetic mineralogical study showed that the main ferromagnetic mineral present is magnetite. An interesting result of the study is that in the temperature range investigated, the elastic properties are enhanced and the anisotropy is increased by raising the temperature, which has important consequences for the seismic monitoring of the storage site.

The French national radioactive waste management agency (ANDRA) has been developing for many years an extensive scientific programme to characterize the Callovian–Oxfordian (COX) argillite formation in eastern France, a possible candidate for an underground repository of radioactive waste. For that purpose an underground research laboratory has been built at Bure in the Meuse–Haute Marne region. In underground research laboratories such as those of Mont Terri or Bure, a major issue is the characterization of the extent and properties of the excavated disturbed or damaged zone (EDZ) as well as the investigation of the effects of a temperature rise in the host formation (Bossart *et al.* 2002). A good knowledge of the rock properties is also of primary importance (Madsen 1998; Esteban *et al.* 2006).

To highlight the effect of damage and its evolution with time, an obvious preliminary step was the estimation of the properties of the undisturbed host rock. This was done in a previous study (David *et al.* 2007) on the magnetic susceptibility and the P-wave velocity of the COX argillite, which focused on the anisotropy of both properties. Louis *et al.* (2005) showed by combining magnetic, elastic and microstructural properties that a better

insight into the source of anisotropy of sedimentary rocks can be achieved. In the present study, we investigate the temperature effect on the magnetic susceptibility and the P-wave velocity, as well as on the magnetic mineralogy, to identify the nature of the ferromagnetic minerals. The following questions are addressed: What is the evolution of the physical properties investigated with increasing temperature? Is there any change in the anisotropy parameters as a result of temperature variations? What is the effect of time on long-term experiments at fixed temperature compared with short-term experiments?

Physical properties of the COX argillite

The anisotropy of magnetic susceptibility and P-wave velocity in the COX argillite has been studied in a recent paper (David *et al.* 2006). The main results can be summarized as follows. The starting material for the study was a core provided by ANDRA, retrieved in the COX argillite formation at 460 m depth in the EST204 well. The mineralogy was assumed to be similar to that of cores retrieved at comparable depths in adjacent

wells (EST205 and EST103) that were investigated by Gaucher *et al.* (2004): 30% quartz + feldspar, 40% clay minerals and 25% carbonates. The low field anisotropy of the magnetic susceptibility (AMS) was measured using an impedance bridge KLY3S designed by AGICO, which allows the determination of the magnetic susceptibility second rank tensor with principal axes K_{\max} , K_{int} and K_{\min} . The P-wave velocity was measured using ultrasonic transducers with dominant frequency 1 MHz, a Panametrics 5058 PR pulser and a digital oscilloscope. The velocity is classically calculated from the time of flight for a wave travelling from transmitter to receiver. For both properties, the minimum axes were close to the bedding pole, whereas the intermediate and maximum axes, in the bedding plane, were nearly isotropic. The anisotropy factor, defined as the difference between extreme principal values normalized to the mean value, was larger for the P-wave velocity (26%) than for the magnetic susceptibility (3.3%). To derive the principal directions for the variation of P-wave velocity, the pseudo-tensorial approach of Louis *et al.* (2003, 2004) was used. The principal axes for both properties were obtained from measurements on 17 small samples, of 25 mm diameter and 22.5 mm length, that were cored in a direction either perpendicular or parallel to the bedding plane. Details on the sample preparation and the measurement scheme have been given by David *et al.* (2006).

Analysis of the sample shape effect

One aspect that was unsolved in the work of David *et al.* (2007) was whether there might be a sample-shape effect in the sense that the principal axes were found in the coring direction of the samples. To address this question, a new set of samples was cored in three perpendicular directions oblique with respect to the bedding plane. The results for this new set of samples are presented and compared with the previous results. We call hereafter set 1 the original sample collection (core axes either parallel or perpendicular to the bedding) and set 2 the new set of samples, with oblique orientations with respect to bedding. The resulting P-wave velocities for both sets are compared in Figure 1. The angular evolution of the mean velocity across eight diameters is plotted in Figure 1a for samples from sets 1 and 2. Whereas the curves are perfectly symmetrical with respect of the 90° vertical line for the original set (set 1), such symmetry is no longer the rule for the oblique set (set 2). If the stereoplot for the new set is drafted in the reference frame linked to the oblique coring directions, we obtain Figure 1b. To compare with the original dataset, we need to rotate the vectors in the reference

frame linked to the horizontal bedding plane and vertical pole; the results then become comparable in both direction and magnitude for the two sets of samples (Fig. 1c). Similar conclusions are drawn from the magnetic susceptibility data. The minimum axis is located very close to the bedding pole, and the bedding plane again appears to be isotropic. Although this test does not provide a definitive indication that there is no sample-shape effect in the technique used here, it validates the data presented in both the former and the present study. Below, a collection of samples from both sets were used to investigate the effect of heating on the evolution of magnetic and acoustic properties and their respective anisotropy.

Influence of temperature on the magnetic and acoustic properties

The objective was to analyse the temperature effect on the magnetic and elastic properties of the COX argillite, and more specifically on the evolution in magnitude and orientation of the anisotropy. Two types of experiments were conducted. In the first experiment, argillite samples were heated to a constant temperature and the properties were measured as a function of time. In the second experiment, the samples were heated to a maximum temperature and then cooled, with the evolution of the properties investigated relative to the maximum temperature imposed in each cycle.

Evolution with time at constant temperature

One set of three oblique samples (set 2) was selected. The samples were put in an oven at a constant temperature (95 °C) for more than 1 month, and the P-wave velocity and magnetic susceptibility were measured at given time intervals, following the standard procedure (David *et al.* 2007). Unfortunately, for technical reasons, there was a large gap in the sequence of measurements between 8 and 32 days after the beginning of the experiment. The choice of temperature was motivated by the fact that among the dimensioning criteria used by ANDRA for radioactive waste disposal is a temperature set below 100 °C over several centuries and a return to a temperature under 70 °C after less than 1000 years, to avoid major disturbance in the host rock (ANDRA 2005). Figure 2 shows the evolution of the mean values for the magnetic susceptibility and the P-wave velocity as well as the corresponding anisotropy factors relative to time. The open symbols at time zero give the reference values at room temperature before the experiments started. The variations observed for

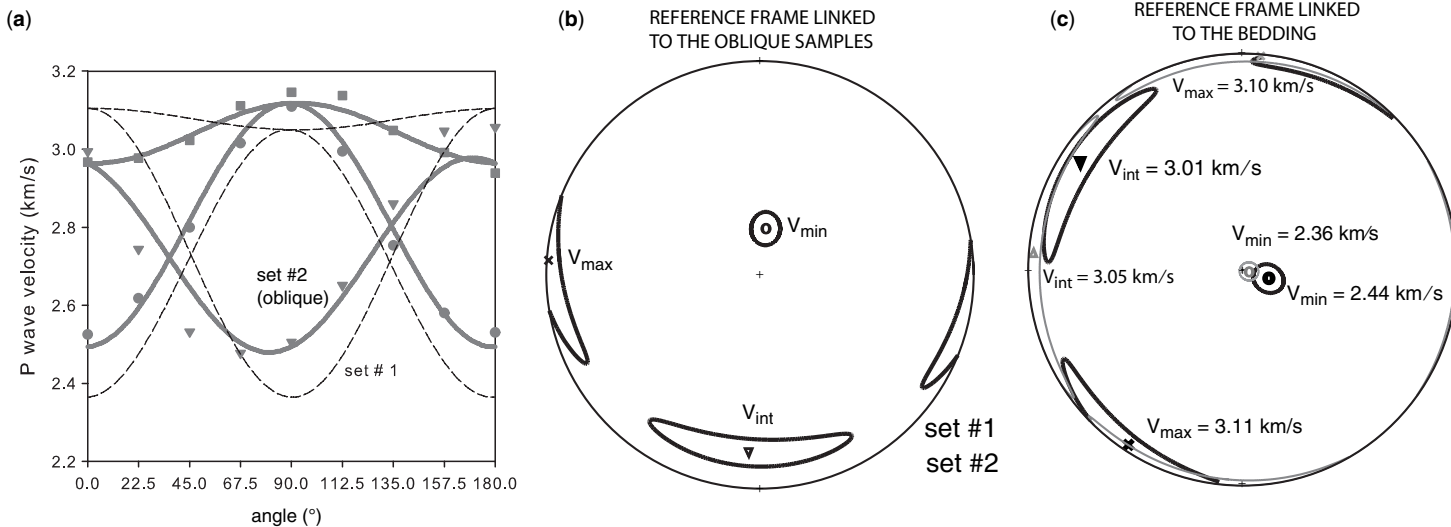


Fig. 1. Evolution of the P-wave velocity for sets 1 and 2. **(a)** Angular evolution of the mean velocity across eight diameters on three orthogonal samples X (●), Y (▽) and Z (■), and fitting curves using an elliptical model; bold lines, set 2; fine dashed lines, set 1. **(b)** Velocity stereoplot for set 2 in the reference frame linked to the sampling scheme. **(c)** Velocity stereoplot linked to the bedding for set 1 (grey) and set 2 (black).

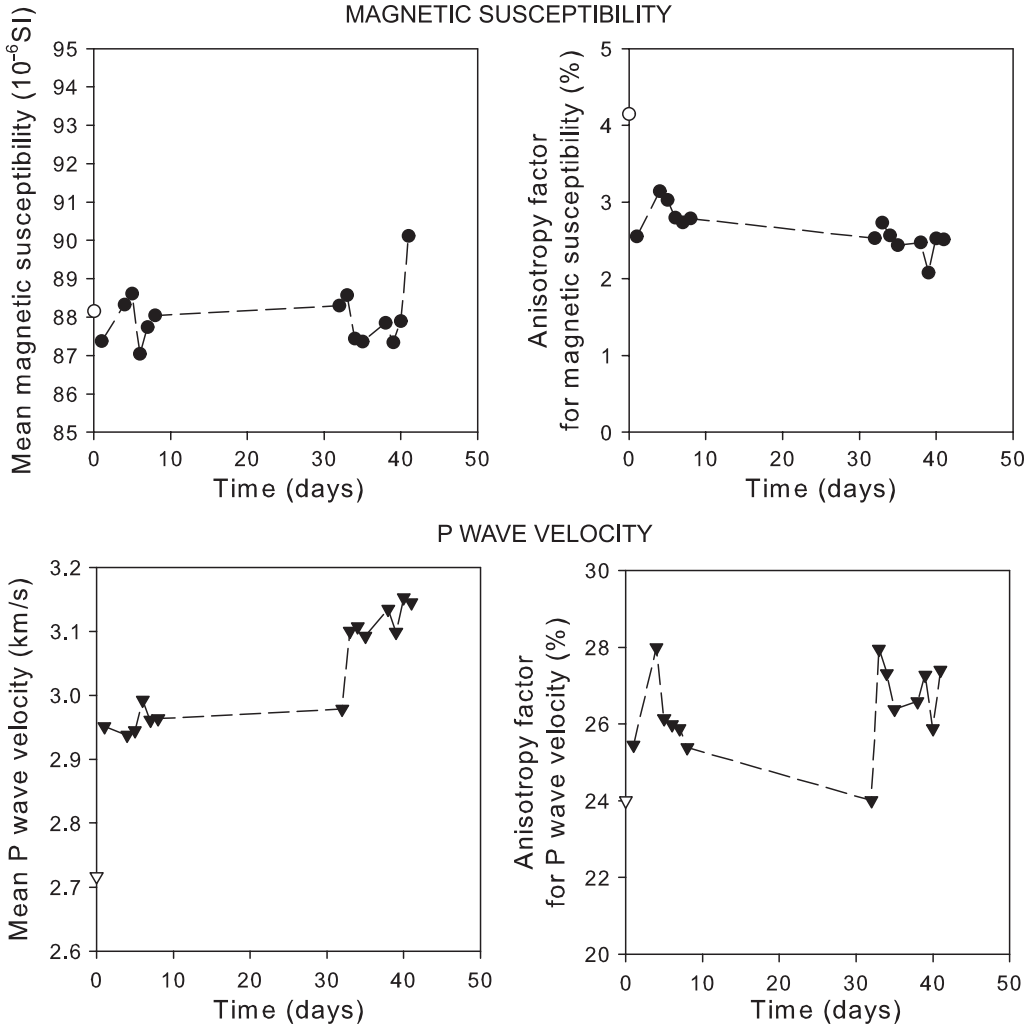


Fig. 2. Evolution of the mean values for the magnetic susceptibility (top) and P-wave velocity (bottom) and the corresponding anisotropy factor v. time. Open symbols correspond to the reference values at room temperature.

the magnetic susceptibility are small, within the range of experimental error. However, it may be noted that the anisotropy factor decreases by about 1.5% between time zero (reference state before heating) and 1 day, then after a short increase it continues to decrease slightly with time. For the P-wave velocity, the average variations observed are also rather small, but a significant increase in both the mean velocity and the anisotropy factor is observed between 32 and 33 days. Such a sudden jump was not observed for the magnetic susceptibility. This jump might be an artefact, as it cannot be ruled out that the measurement on day 32 was flawed and that the sample experienced a slow evolution while it stayed untouched in the

oven for 24 days. The results show that the P-wave velocity is generally more sensitive to long-term heating at 95 °C than is the magnetic susceptibility, although the variations remain small.

Evolution with temperature in heating–cooling cycles

In the second study on evolution with heating and cooling cycles, two sets of three orthogonal samples were subjected to several heating–cooling cycles at increasing temperatures. The objective was here to characterize the material properties in a temperature range larger than the dimensioning criteria used by ANDRA for

radioactive waste storage. It is also interesting to study the properties of the argillite at much higher temperatures, which would induce significant mineralogical changes. Starting from room conditions, the oven temperature was increased at a rate of $1\text{ }^{\circ}\text{C min}^{-1}$, slowly enough to prevent any significant thermal gradient that could damage the samples. When the selected temperature was reached, the oven was maintained at this maximum temperature for 1 h, before normal and slow cooling to room temperature. Twelve cycles were performed with successively the following maximum temperatures: 60, 80, 100, 120, 140, 160, 200, 250, 300, 350, 400 and 450 $^{\circ}\text{C}$. The

results show that the magnetic susceptibility and the acoustic velocity behave very differently (Fig. 3). The magnetic susceptibility does not exhibit any significant variation until 200 $^{\circ}\text{C}$: above this temperature, a sharp increase is observed, to 10^{-3} SI at 450 $^{\circ}\text{C}$; that is, three orders of magnitude higher than at the beginning of the experiment. Interestingly, this dramatic increase in susceptibility takes place without any significant change in the anisotropy, indicating that the newly formed minerals have a weak magnetic fabric. At high temperature, a change in the colour of the samples from grey to reddish indicates that some oxidation took place. The P-wave

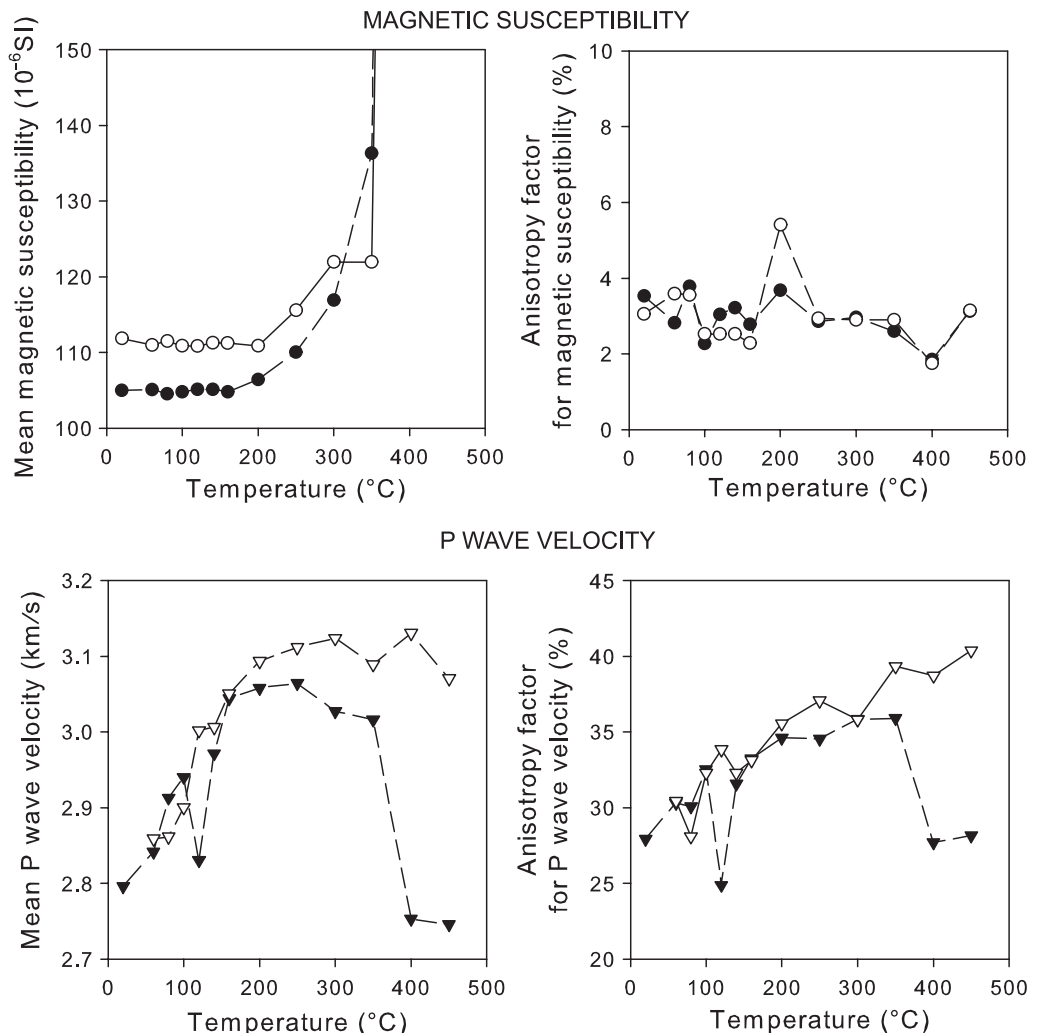


Fig. 3. Evolution of the mean values for the magnetic susceptibility (top) and P-wave velocity (bottom) and the corresponding anisotropy factor v. Temperature in heating–cooling cycles. Two sets (open and closed symbols) of three orthogonal samples were used in this experiment.

velocities show a significant increase, of the order of 10%, between 20 °C and 200 °C, followed by a stable trend around 3.1 km s⁻¹ at higher temperature. In contrast, the anisotropy factor increases continuously to 40% at 450 °C for one sample set, corresponding to a relative increase of 35% from the initial value, whereas for the other set a sharp drop is observed above 350 °C to the initial values for both the mean velocity and the anisotropy factor. So far there is no satisfactory explanation for this contrasting behaviour of samples tested under the same conditions. Taking into account the fact that the ellipsoid derived for the P-wave velocity is an approximation (Louis *et al.* 2004), the method used here was compared with Thomsen's weak anisotropy theory (Thomsen 1986). The ellipsoidal model predicts the following evolution of the P-wave velocity with θ , the directional angle measured with respect to the bedding pole:

$$V_P = V_o(1 + \psi \cdot \sin^2 \theta) \quad (1)$$

where V_o and ψ are the parameters of the ellipsoidal model. The P-wave velocity is given by the following relation for the weak anisotropy model:

$$V_P = \alpha(1 + \delta \cdot \sin^2 \theta \cdot \cos^2 \theta + \epsilon \cdot \sin^4 \theta) \quad (2)$$

where α is the velocity in the bedding pole direction, and ϵ and δ are Thomsen's parameters characterizing the magnitude of the anisotropy. It is easy to show from equation (2) that the two models are equivalent if ϵ is equal to δ . The parameters for both models were estimated using a least-squares fitting method. The evolution of all these parameters is plotted in Figure 4 as a function of temperature, as well as the r.m.s. error for each method.

The model velocities α and V_o mimic the mean velocity evolution shown in Figure 3. Whereas the r.m.s. error for Thomsen's model is slightly better than that for the ellipsoidal model (0.11 km s⁻¹ on average compared with 0.15 km s⁻¹), both models give an equally good fit to the experimental data. However, the two models are not equivalent, as the difference $\epsilon - \delta$ is significantly different from zero and increases slightly with temperature (between 0.12 and 0.20). Interestingly, there is an increasing trend for the evolution of the ψ parameter with heating temperature, similar to the evolution of the ϵ parameter, in agreement with the fact that the anisotropy of the P-wave velocity increases with temperature.

To obtain a deeper insight into the evolution of the anisotropy for both properties, a Flinn diagram (Jelinek 1981) has been drawn, which helps to represent both the strength and the shape of ellipsoids using ratios of their principal axes (Fig. 5): for a given property X , the lineation index $L = X_{\max}/X_{\text{int}}$ is plotted as a function of the foliation index $F = X_{\text{int}}/X_{\min}$, where X_{\max} , X_{int} and X_{\min} are the maximum, intermediate and minimum eigenvalues of the tensor representing the property X , respectively. The pseudo-tensor approach (Louis *et al.* 2003) has been used for the P-wave velocity. This representation confirms that the elastic anisotropies are much larger than the magnetic ones (David *et al.* 2007), and it shows that the ellipsoids of both properties are highly oblate (parallel to the bedding) at all temperatures. In the Flinn representation, the magnetic data for both sample sets are scattered, whereas the data for the P-wave velocity clearly follow a systematic trend. This trend is confirmed by plotting the foliation index of the P-wave velocity ellipsoid, which clearly increases with temperature (Fig. 6).

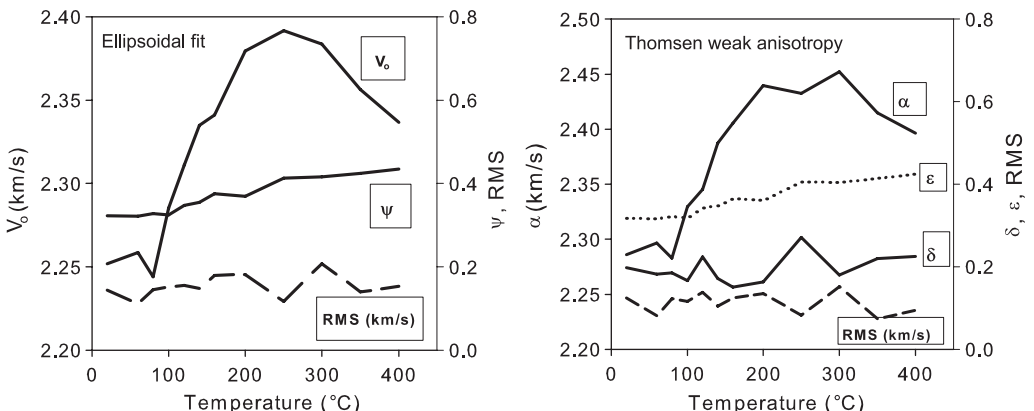


Fig. 4. Evolution of the fitting parameters for the ellipsoidal method (on the left) and for Thomsen's weak anisotropy parameters (on the right) as a function of temperature (see text for details).

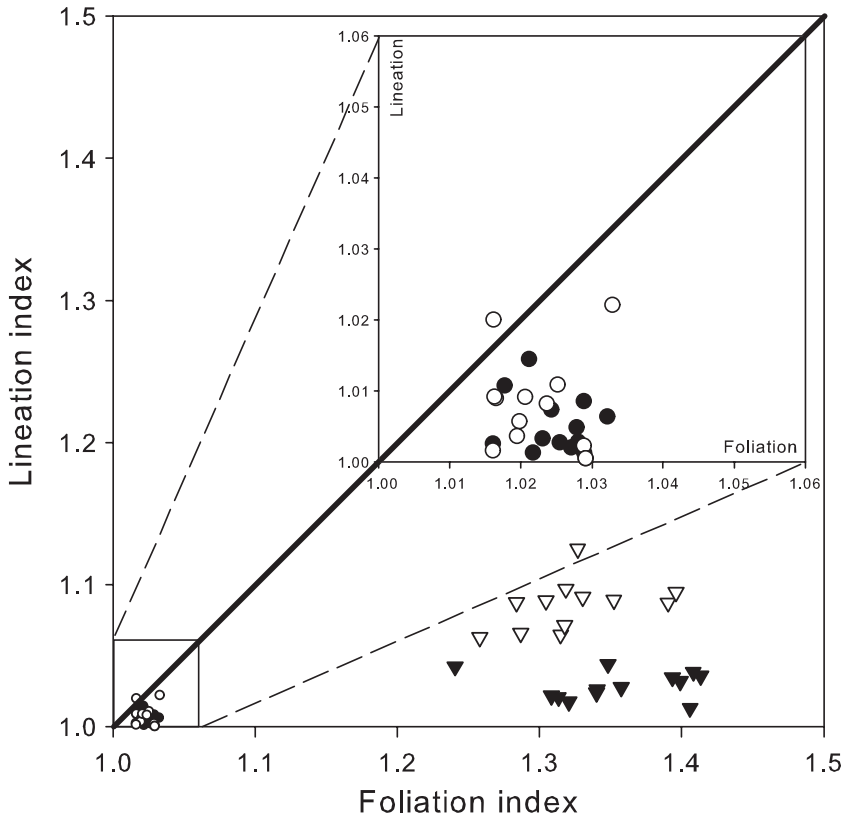


Fig. 5. Flinn diagrams for magnetic susceptibility (circle) and P-wave velocity (triangle). Open and closed symbols correspond to the two sets of three orthogonal samples used in the heating–cooling cycles.

In contrast, the foliation index of the susceptibility is virtually constant over the investigated temperature range. Finally, we investigated the directional aspects of the anisotropy for both properties and we found no significant variations in the positions of the principal axes with increasing temperature (Fig. 7). For instance, the minimum axes always plot very close to the bedding pole. Interestingly, in the bedding plane the maximum axes of the acoustic velocities are generally located at right angles to the maximum susceptibility axes. It should be noted that the confidence ellipses of the magnetic susceptibility data become very large with increasing temperature.

Magnetic mineralogy

The ferromagnetic mineralogy was investigated by using stepwise demagnetization of a ‘three-axis’ isothermal remanent magnetization (IRM) following the procedure of Lowrie (1990), who analysed the decrease of saturation magnetization with

increasing temperature. The maximum unblocking temperature corresponds to the temperature at which magnetization becomes zero. Iron oxides such as hematite (Fe_2O_3) and magnetite (Fe_3O_4) are characterized by maximum unblocking temperatures of about 675 °C and 580 °C, respectively, whereas ferromagnetic iron sulphides have much lower unblocking temperatures (<325 °C). Coercivity represents the ability of a ferromagnetic mineral to align in an increasing external direct magnetic field. Magnetization is constant when saturation is reached. Magnetite is considered as a soft coercivity mineral, with a saturation field lower than 0.3 T, whereas hematite is a hard coercivity mineral, with a saturation field higher than 1.5 T. Pyrrhotite’s coercivity is between these values, with a saturation field lower than 1 T. Lowrie (1990) proposed the induction of three magnetization fields (1.5, 0.5 and 0.1 T) along three perpendicular directions on a sample before application of a stepwise thermal demagnetization. This procedure leads to separate ferromagnetic minerals with different coercivities and blocking

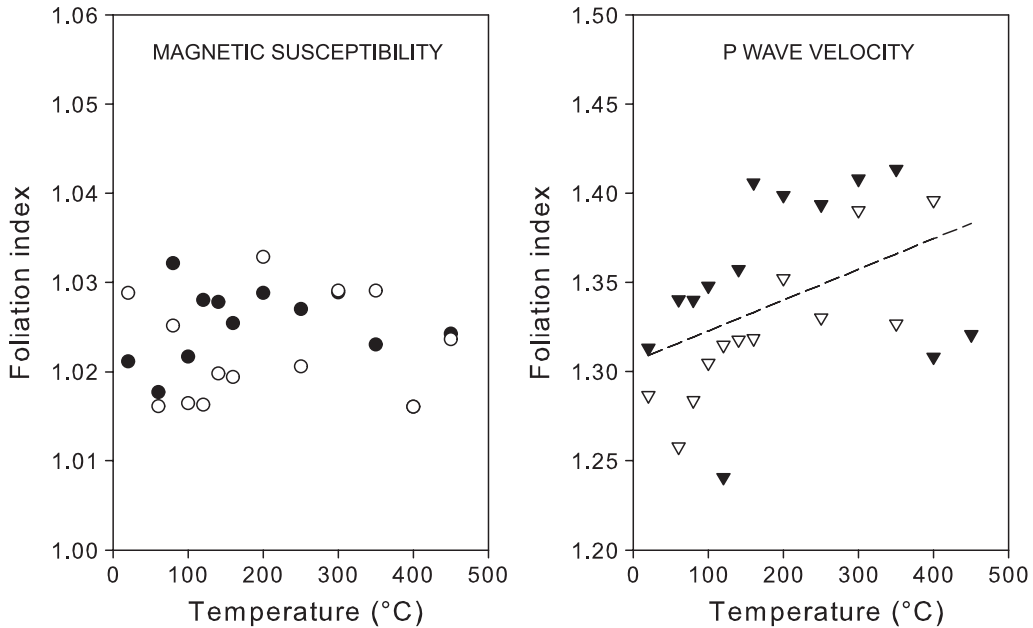


Fig. 6. Evolution of magnetic and acoustic foliation index v. temperature. Open and closed symbols correspond to the two sets of three orthogonal samples used in the heating–cooling cycles. The dashed line indicates the best linear fit on the complete velocity dataset.

temperature spectra. Here we used steps of 50 °C with finer steps near 325 °C, which corresponds to the pyrrhotite maximum unblocking temperature. The samples were heated to 600 °C.

The thermal treatment was conducted with the same device as for the cooling–heating cycle experiments. The samples were heated for 1 h to the selected step temperature and then cooled to room temperature in non-magnetic conditions to avoid spurious remagnetization of the samples. The magnetization was then measured at room temperature with a JR6 spinner magnetometer (AGICO). The magnetic susceptibility was also monitored with a KLY3S susceptometer to detect changes in magnetic properties induced by heating.

Stepwise demagnetization was carried out on three representative samples: a non-heated sample (A), a sample heated to 95 °C (B), and a sample heated to 450 °C with heating–cooling cycles (C). Magnetite was identified in the three samples along the soft and medium coercivity curves with characteristic unblocking temperatures between 550 and 600 °C. The hard coercivity fraction does not present any significant contribution to the total magnetization. The initial magnetization in sample C is roughly three times that measured in samples A and B (Fig. 8). This difference means that magnetite is the only ferromagnetic phase created during heating to 450 °C. In contrast, no significant

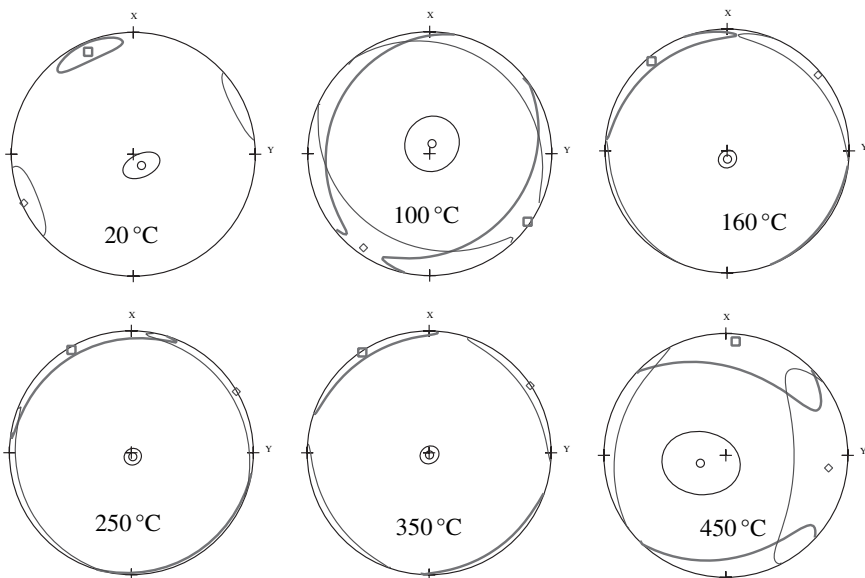
difference was observed between A and B coercivity–temperature spectra, proving that no ferromagnetic phase was created. These results are consistent with the magnetic susceptibility measured during constant temperature and heating–cooling cycle experiments.

In conclusion, the analysis of the coercivity–temperature spectra indicates that the main carrier of remanent magnetization in natural argillite is magnetite (Fig. 8). The sharp increase of susceptibility after heating above 200 °C is also due to magnetite. Samples heated at constant temperature (95 °C) do not show any significant modification of the ferromagnetic mineralogy before and after the experiments.

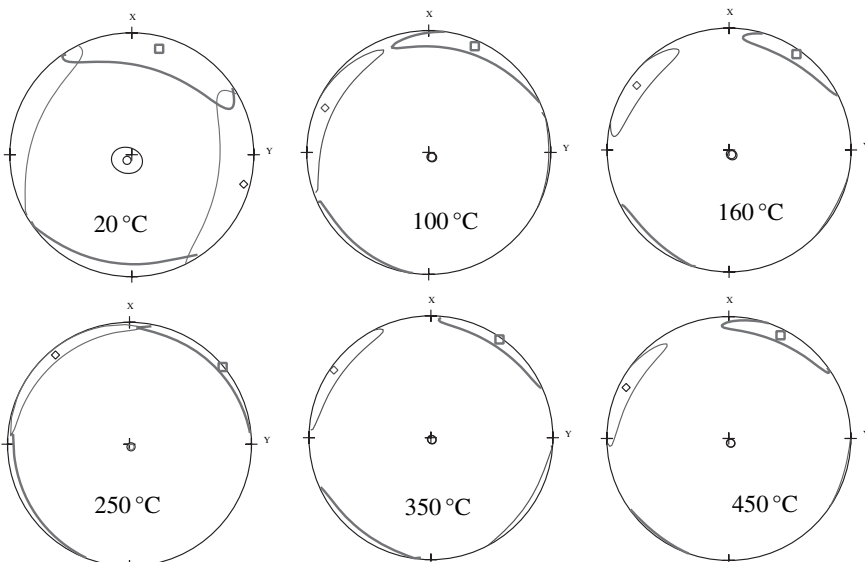
Discussion and conclusions

To summarize our main results, we observe that heating argillite samples to 95 °C for 41 days produces no significant variation in the magnetic susceptibility or its anisotropy. However, the P-wave velocity seems to increase with time: the increase observed after 41 days is equivalent to that obtained after heating at a temperature of about 200 °C. For the experiments in which argillite samples were slowly heated to increasing maximum temperatures, contrasting results were obtained

MAGNETIC SUSCEPTIBILITY



P WAVE VELOCITY



□ maximum ◇ intermediate ○ minimum ⚡ 95% confidence ellipses

Fig. 7. Stereoplots at selected temperatures for magnetic susceptibility (top) and P-wave velocity (bottom). The bedding plane is horizontal.

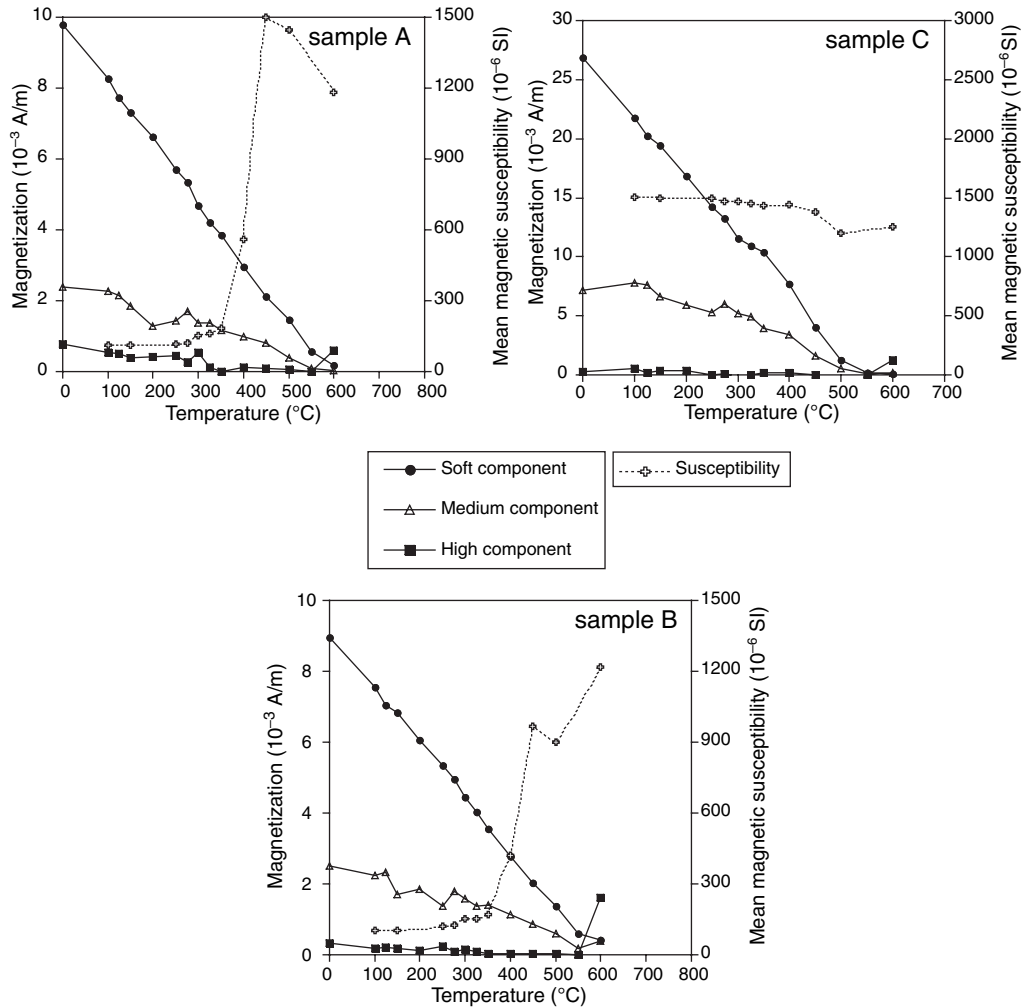


Fig. 8. Thermal demagnetization of a three-component IRM produced by magnetizing the samples with a 1.5 T field along the z -axis (hard component), followed by 0.5 T along the y -axis, and finally 0.1 T along the x -axis. Sample A was not heated; sample B was heated at 95°C ; sample C was subjected to heating–cooling cycles to 450°C .

for the evolution of magnetic susceptibility and P-wave velocity as a function of temperature.

In the $20\text{--}200^{\circ}\text{C}$ temperature range the magnetic susceptibilities do not change, whereas both the mean P-wave velocity and the elastic anisotropy increase significantly. This latter result is of importance because it shows that an increase of temperature will induce an enhancement of the elastic parameters of the COX argillite that is attributed to dehydration by removal of interstitial water, either absorbed or in an interlayer position of the smectite-type clay minerals (Huang *et al.* 1994). It is difficult to say if mineralogical

transformations took place in this temperature range because no significant change of the magnetic susceptibility is observed. Mobility of absorbed water in clay particles is the more likely mechanism inducing the change in the elastic properties. Modification of the clay structure by water mobility might create tighter contacts between particles, inducing a porosity reduction and enhanced elastic moduli.

At temperatures above 200°C , a sharp increase in magnetic susceptibility is obtained with no effect on the anisotropy, the origin of which is linked to mineralogical transformations (Pytte &

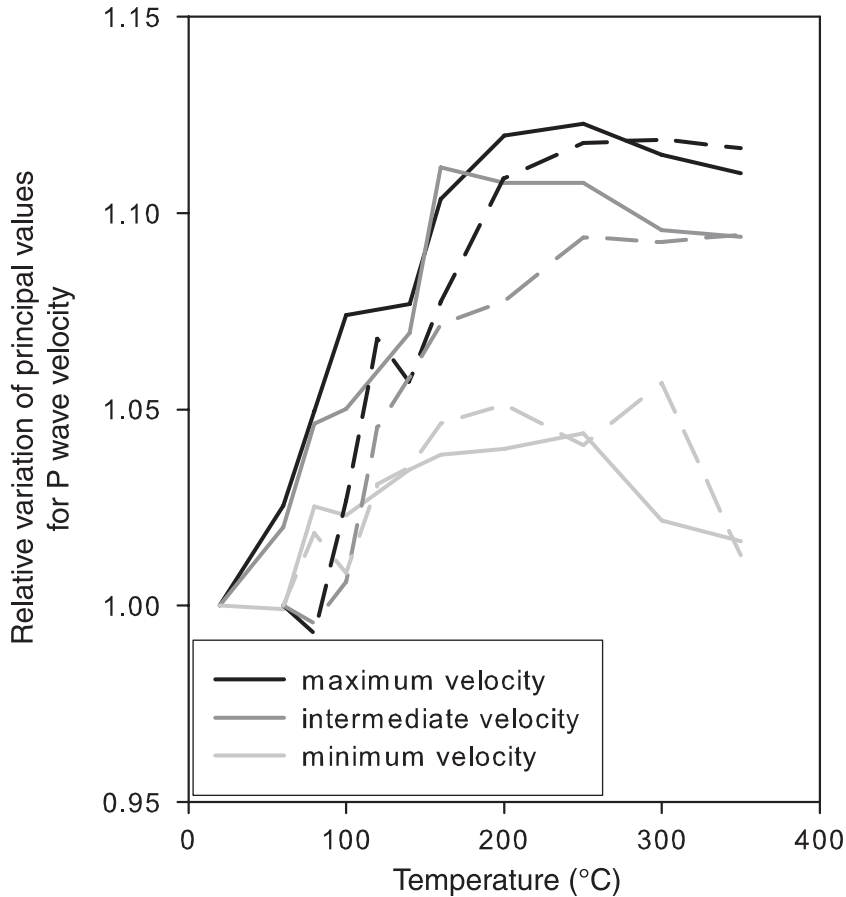


Fig. 9. Evolution of the relative variation of principal values for the P-wave velocity during heating–cooling cycles to 350 °C. Mean velocities are normalized to their initial value. Dashed and continuous lines correspond to the two sets of samples used in the experiments.

Reynolds 1989; Yates & Rosenberg 1998; Guillaume *et al.* 2004). This may be attributed to the transformation of iron sulphides, as we know that the COX argillite contains about 1% of pyrite (Rimstidt & Vaughan 2003). In contrast, the mean P-wave velocity levels off, whereas the anisotropy keeps increasing, although for one sample set a sharp decrease in both the mean velocity and the anisotropy was found at 350 °C. We attribute this levelling off to the occurrence of thermal cracking in the rock, which makes the material more compliant. However, we cannot rule out the fact that the mineralogical transformation mentioned above also has some influence on the velocity evolution. The increase in the anisotropy factor is mainly due to the decrease of the minimum velocity (Fig. 9), which can be interpreted as the result of

anisotropy of the induced thermal cracks. As the relative variation of the velocity is smaller in the direction parallel to the bedding pole (minimum velocity in Fig. 9), the thermal cracks induced by heating above 200 °C are preferentially oriented parallel to the bedding plane (Fig. 10). It is well known that in a solid in which the crack distribution is anisotropic, the compliance is larger in the direction corresponding to the normal of the cracks (Mavko *et al.* 1998). In the case of the COX argillite, we conclude that the anisotropy associated with bedding has a strong control on the orientation of the cracks generated by thermal processes. This is consistent with the fact that the foliation index increases with temperature and therefore, with an increasing oblateness of the pseudo P-wave velocity ellipsoid.

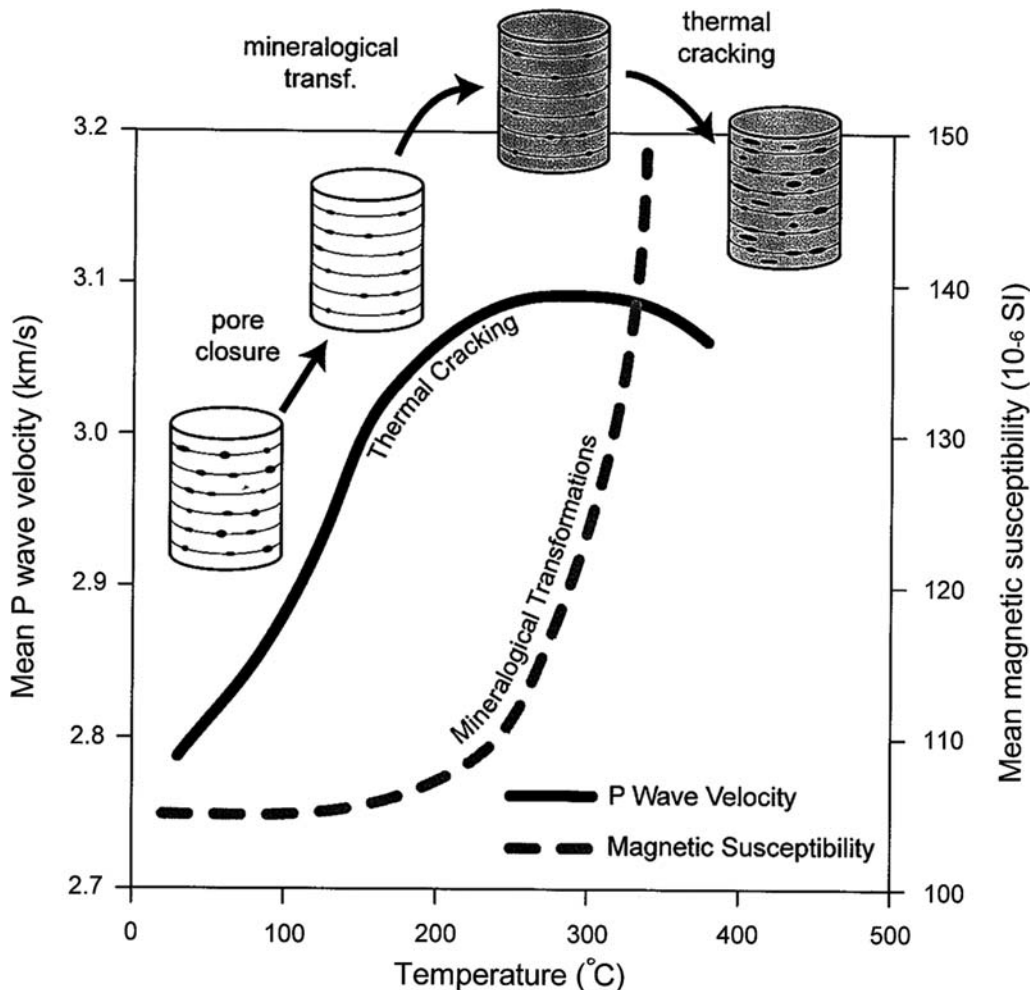


Fig. 10. Microstructural sketches interpreting the evolution of mean P-wave velocity and magnetic susceptibility properties with increasing temperature. Cracks induced by heating and mineralogical transformations are the dominant mechanisms above 200 °C.

Our interpretation of the evolution of the investigated properties with temperature needs to be confirmed by chemical analyses by SEM (or other microscope techniques) as well as a thorough analysis of the microstructures for samples corresponding to the different stages identified in Figure 9. This is a challenging task in the COX argillite because of the shaly nature of the rock.

This work was financially supported by the CNRS and ANDRA through the GdR FORPRO (Research action number 2003.II) and corresponds to GdR FORPRO contribution 2006/09A. The authors thank J.-M. Siffre, C. Aubourg and B. Menéndez for technical assistance

and scientific contribution. We have benefited from comments on an early version of the manuscript by P. Lebon and A. Trouiller (ANDRA). Many thanks go to J.-L. Bouchez, who thoroughly reviewed the manuscript, and to an anonymous reviewer. ANDRA (Agence Nationale pour la Gestion des Déchets Radioactifs) kindly provided the argillite cores.

References

- ANDRA 2005. *Dossier 2005 Argile Synthesis report—Evaluation of the feasibility of a geological repository—Meuse/Haute-Marne Site*. Publications ANDRA, coll. ‘Les rapports’.

- BOSSART, P., MEIER, P. M., MOERI, A., TRICK, T. & MAYOR, J. C. 2002. Geological and hydraulic characterisation of the excavation disturbed zone in the Opalinus Clay of the Mont Terri Rock Laboratory. *Engineering Geology*, **66**, 19–38.
- DAVID, C., ROBION, P. & MENÉNDEZ, B. 2007. Anisotropy of elastic, magnetic and microstructural properties of the Callovo–Oxfordian argillite. *Physics and Chemistry of the Earth*, **32**, 145–153.
- ESTEBAN, L., BOUCHEZ, J. L. & TROUILLER, A. 2006. The Callovo–Oxfordian argillites from the eastern Paris basin: magnetic data and petrofabrics. *Comptes Rendus Géoscience*, **338**, 867–881.
- GAUCHER, E., ROBELIN, C., MATRAY, J. M. ET AL. 2004. ANDRA underground research laboratory: interpretation of the mineralogical and geochemical data acquired in the Callovo–Oxfordian formation by investigative drilling. *Physics and Chemistry of the Earth*, **29**, 55–77.
- GUILLAUME, D., NEAMAN, A., CATHELINEAU, M. ET AL. 2004. Experimental study of the transformation of smectite at 80 and 300 °C in the presence of Fe oxides. *Clay Minerals*, **39**(1), 17–34.
- HUANG, W. L., BASSETT, W. A. & WU, T. C. 1994. Dehydration and hydration of montmorillonite at elevated temperatures and pressures monitored using synchrotron radiation. *American Mineralogist*, **79**, 683–691.
- JELINEK, V. 1981. Characterization of the magnetic fabric of the rocks. *Tectonophysics*, **79**, 63–67.
- LOUIS, L., DAVID, C. & ROBION, P. 2003. Comparison of the anisotropic behaviour of undeformed sandstones under dry and saturated conditions. *Tectonophysics*, **370**, 193–212.
- LOUIS, L., ROBION, P. & DAVID, C. 2004. A single method for the inversion of anisotropic data sets with application to structural studies. *Journal of Structural Geology*, **26**, 2065–2072.
- LOUIS, L., DAVID, C., METZ, V., ROBION, P., MENÉNDEZ, B. & KISSEL, C. 2005. Microstructural control on the anisotropy and transport properties in undeformed sandstones. *International Journal of Rock Mechanics & Mining Sciences*, **42**, 911–923.
- LOWRIE, W. 1990. Identification of ferromagnetic minerals in rock by coercivity and unblocking temperature properties. *Geophysical Research Letters*, **17**, 159–162.
- MADSEN, F. T. 1998. Clay mineralogical investigations related to nuclear waste disposal. *Clay Minerals*, **33**, 109–129.
- MAVKO, G., MUKERJI, T. & DVORKIN, J. 1998. *The Rock Physics Handbook—Tools for Seismic Analysis in Porous Media*. Cambridge University Press, Cambridge.
- PYTTE, A. M. & REYNOLDS, R. C. 1989. The thermal transformation of smectite to illite. In: NAEGER, N. D. & MCCULLOH, T. H. (eds) *The Thermal History of Sedimentary Basins*. Springer, Berlin, 133–140.
- RIMSTIDT, J. D. & VAUGHAN, D. J. 2003. Pyrite oxidation: a state-of-the-art assessment of the reaction mechanism. *Geochimica et Cosmochimica Acta*, **67**, 873–880.
- THOMSEN, L. 1986. Weak elastic anisotropy. *Geophysics*, **51**, 1954–1966.
- YATES, D. M. & ROSENBERG, P. E. 1998. Characterization of neoformed illite from hydrothermal experiments at 250 °C and $P_{v,\text{soln}}$: An HRTEM/ATEM study. *American Mineralogist*, **83**, 1199–1208.

Investigation of the undrained poroelastic response of sandstones to confining pressure via laboratory experiment, numerical simulation and analytical calculation

G. BLÖCHER¹, D. BRUHN¹, G. ZIMMERMANN¹, C. McDERMOTT² & E. HUENGES¹

¹*GeoForschungsZentrum Potsdam, Telegrafenberg, D-14473 Potsdam, Germany*

(e-mail: bloech@gfz-potsdam.de)

²*Centre for Applied Geoscience (ZAG), University of Tuebingen, Sigwartstr. 10, D-72076 Tuebingen, Germany*

Abstract: To describe the poroelastic behaviour of sandstones, two factors have to be considered: the grain structure and the pore volume included. Changes in these two factors through diagenetic processes, tectonic loading or other forces lead to different results. Often external stresses induce a compaction of the rock and, therefore, a reduction of pore volume and an increased fluid pressure. Under undrained conditions, the largest pore pressure response can be observed. Besides the Biot coefficient, the Skempton coefficient (B) is one of the most important variables of elastic rock deformation, as it describes the pore pressure change related to the acting stresses. This study shows three ways of determining the Skempton coefficient and gives evidence of its pressure dependence. First, the undrained poroelastic response of a Bentheimer sandstone sample to confining pressure change was measured. Second, a thin-section micrograph was transferred into a finite-element model, including a discretization of the grain structure and the pore space. Finally, the Skempton coefficient of a linear elastic hollow sphere was calculated to prove the laboratory experiment and the numerical simulation.

This study investigates the undrained pore pressure change as a result of confining pressure change. The ambient stresses of rocks can change in response to tectonic loading or, for example, near seismic epicentres (Lockner & Stanchits 2002). If these stress changes cause pore volume loss or gain, then the resulting compression or decompression can significantly influence the rock strength. This can, for instance, induce earthquakes and other tectonic processes.

For saturated rocks the pore volume loss or gain directly results in pore pressure (P_p) change and therefore influences the effective stress σ_e (Terzaghi 1923):

$$\sigma_e = \sigma - P_p,$$

where σ is the total stress. For consolidated sandstones, with a higher stiffness, the grain contact area counteracts the applied stresses. This effect can be measured and expressed in terms of Biot's coefficient α (Biot 1941):

$$\sigma_e = \sigma - \alpha P_p.$$

For fully saturated rocks under undrained conditions, the pore pressure P_u change is a function of the mean stress. Under hydrostatic conditions the mean stress is equal to the confining pressure

P_c , and the ratio of pore pressure change to the applied confining pressure is known as the isotropic Skempton coefficient B (Brown & Korringa 1975; Green & Wang 1986). The pore pressure change is related to confining pressure change by the following equation (Skempton 1954):

$$B = \frac{dP_u}{dP_c}$$

The isotropic Skempton coefficient can also be expressed in terms of the bulk module (K) and the porosity ϕ (Detournay & Cheng 1993):

$$B = \frac{\frac{K_f}{\phi} \left(1 - \frac{K_{fr}}{K_s} \right)}{\frac{K_f}{\phi} \left(1 - \frac{K_{fr}}{K_s} \right) + K_{fr} \left(1 - \frac{K_f}{K_s} \right)}$$

where the subscripts f, fr and s stand for fluid, framework and solid, respectively.

Other studies investigated the development of the Skempton coefficient under different experimental conditions. These studies showed that B is nearly independent of deviatoric stress change, but decreases as a result of the stiffening effect of increasing confining pressure (Lockner & Stanchits 2002), under axisymmetric loading (Lockner &

Beeler 2003) and as a function of effective stress (Zimmerman 1991). Furthermore, an additional content of clay particles inside the pore spaces has also been shown to cause the Skempton coefficient to decrease (Al-Wardy & Zimmerman 2004). The stiffer bulk modulus and framework can be explained by closure of open micro-cracks at high confining pressure levels (Mesri *et al.* 1976). In addition to these previous studies, we show here how the confining pressure changes affect differently shaped pore space geometries; this effect leads to a higher stiffness and results in change of the Skempton coefficient for isotropic and hydrostatically loaded rock.

Geological laboratory observations often show that most rocks and soils have anisotropic and heterogeneous material properties. This means for the elastic anisotropic response that the axial Skempton coefficients (B_x , B_y and B_z) vary with the different principal stress directions (σ_x , σ_y , σ_z). In the general case an anisotropic stress tensor ($\sigma_x \neq \sigma_y \neq \sigma_z$) is given. Under undrained conditions (no flow across the boundaries of the sample) a change in one of the axial stresses will directly induce changes in pore pressure P_u (Wang 2000).

For layered sediment displaying anisotropy, the material properties can be strongly anisotropic depending on orientation. For a homogeneous isotropic sandstone, the properties are equal in the principal stress directions, therefore the axial Skempton coefficients can be expressed as $B_x = B_y = B_z = B$. Stress fields can vary in the principal directions. Under hydrostatic conditions, the three principal stresses are equal to the confining

pressure $P_c = \sigma_x = \sigma_y = \sigma_z$. With an additional axial load in the z -direction, the vertical stress is increased, leading to the typical triaxial test scenario where $\sigma_x = \sigma_y < \sigma_z$.

Laboratory experiment

Two samples of Bentheimer sandstone were examined. Bentheimer sandstone has been used in numerous studies, and has been described in detail by Brown (2002). In preparation for the experiment, the sandstone samples were completely saturated in a hydraulic system. The samples underwent a 2 day flow of distilled water before the shut-off valves of the hydraulic system were closed to ensure the maximum saturation of more than 95%, determined after Smith & Smith (1998).

Both samples were cylinder shaped with a diameter of 5 cm, a length of 10 cm and a porosity of c. 20%. The total volume of the sandstone cylinder was 196.36 cm³ and the pore volume was c. 39 cm³. For measuring the axial and lateral strains of the sandstone samples, two axial extensometers and one radial chain extensometer were installed (MTS 2004). In each of the experiments the sample was situated inside the pressure chamber (Fig. 1). This test system allows stresses up to 140 MPa. To implement hydrostatic conditions, the chamber was filled with a pressure fluid, and to keep the sample from being contaminated, it was surrounded by a silicon jacket. Besides the mechanical system, a hydraulic system was connected to the Bentheimer sandstone. To minimize the wake space of the hydraulic system, all capillaries were plugged by wires and the remaining

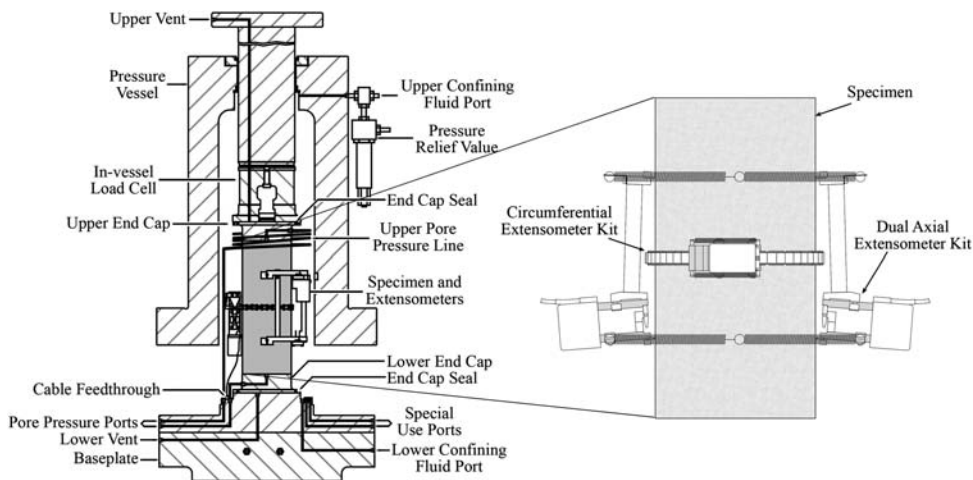


Fig. 1. Laboratory test configuration showing Bentheimer sandstone sample in the pressure chamber (MTS 2004). Pore pressure change was measured with the hydraulic shut-off valves closed to minimize external pore pressure system volume.

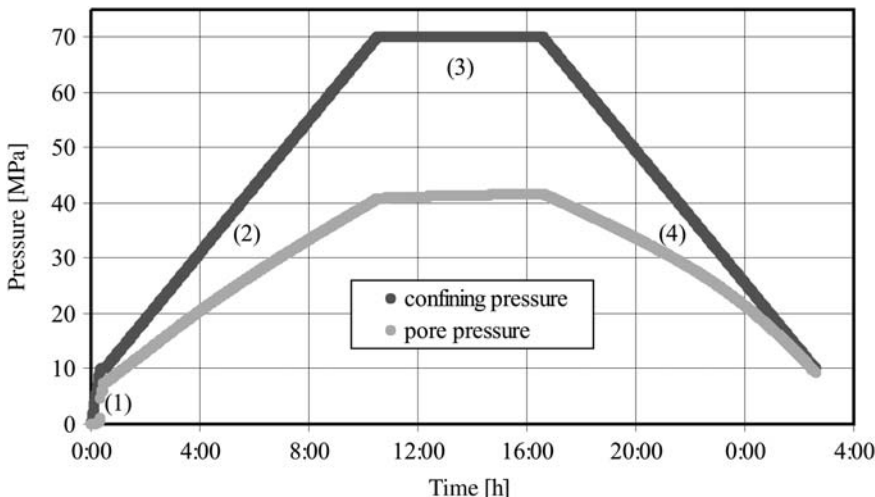


Fig. 2. Time-dependent progression of confining pressure and undrained pore pressure throughout the experiment. (1) Adjustment of the initial conditions; (2) increase of the confining pressure from 10 to 70 MPa and responding pore pressure; (3) hold phase; (4) decrease of confining pressure down to its initial conditions and measured pore pressure.

dead volume was measured to 5 ml; this is equivalent to 13% of pore volume.

In the first experiment we measured the elastic, elasto-plastic and poroelastic properties (all undrained) of an intact (without visible damage) Bentheimer sandstone at confining pressures from 10 to 70 MPa. The experiment was carried out at hydrostatic conditions so that sample properties are related to changes in confining pressure P_c . To show the reversibility of the induced pore pressure P_u , the confining pressure was increased to the maximum (70 MPa) and then reduced to the initial conditions. We measured the elastic deformation of the sandstone given by axial and radial extension, as well as the pore pressure during the entire time of the experiment. By means of the pore pressure, we determined the isotropic Skempton coefficient, defined by $B = dP_u/dP_c$ (Lockner & Beeler 2003).

The experiment started with the adjustment of the initial conditions, which were 10 MPa for confining pressure and 7.44 MPa for pore pressure. After closing the shut-off valves, the confining pressure was increased at a constant rate of 0.1 MPa min^{-1} , to its highest level of 70 MPa. At this level, the confining pressure was kept constant for 6 h and was then decreased to its initial condition, again at a constant rate of 0.1 MPa min^{-1} . The controlled confining pressure and the undrained pore pressure response for the whole experiment are shown in Figure 2. It can be seen that, at the end of the experiment, the pore pressure does not regain its initial value. This implies that irreversible

deformation, such as micro-cracks, flattening of grain contacts, grain crushing and pore collapse, is caused by high ambient stresses.

The influence of confining pressure during the hold phase can best be shown by the continuing increase of pore pressure and deformation in both the axial and transverse direction (Fig. 3). The change in volumetric strain, which is calculated as the sum of axial strain and two times lateral strain, was highest at the beginning of the hold phase. After c. 2 h the graph shows a more linear behaviour with time. The development of the pore pressure, which depends on the deformation of the pore space, is similar to that of the volumetric strain. Therefore, the pore pressure change during the hold phase must be related to a continuing deformation of the rock. The reduction of the confining pressure to its initial value shows that deformation was not reversible. To determine the amount of irreversible deformation, we compared the measurement of strain and pore pressure before and after the experiment. The volumetric strain started at 0.94×10^{-3} at 10 MPa confining pressure and the pore pressure was set to 7.44 MPa. Shortly after the experiment, the value for volumetric strain reached 1.35×10^{-3} and pore pressure was 9.28 MPa. After an additional waiting time of 70 h the volumetric strain did not change significantly, and reached its final value of 1.31×10^{-3} . In comparison with the starting value, a residual gap of 0.37×10^{-3} was observed. The final level of the pore pressure was 8.79 MPa, so the difference from the initial value was 1.35 MPa.

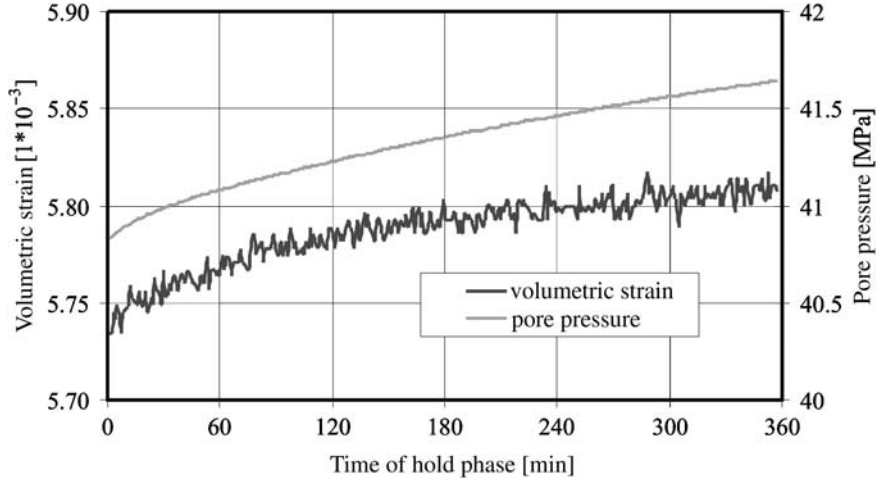


Fig. 3. Development of volumetric strain and pore pressure over a period of 6 h. The confining pressure was kept constant at 70 MPa during this hold phase.

These residual differences were 2–4 times larger than the changes during the high-pressure hold phase, therefore we assume that irreversible deformation occurred throughout the experiment.

The further increase of volumetric strain confirms the irreversible deformation during the hold phase. For purely elastic deformation and under the experimental conditions only changes in confining pressure can cause changes in the size of the sample. The observed amount of irreversible deformation (irreversible changes/total

changes) is 4%, and is neglected in the following calculation of the Skempton coefficient. For a hydrostatically pressurized sample the isotropic Skempton coefficient is calculated from the ratio of changes in pore pressure to changes in confining pressure, $B = dP_u/dP_c$. The data were collected at a sampling interval of 1 min. To smooth the curve and minimize the noise, a sliding average over 10 min was taken to calculate the isotropic Skempton coefficient shown in Figure 4.

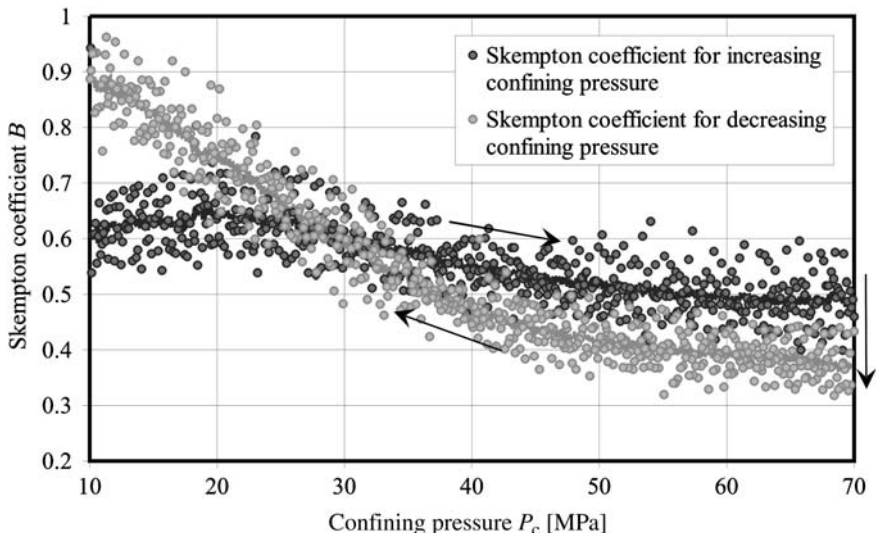


Fig. 4. Calculated isotropic Skempton coefficient for the first experiment for an increasing (dark grey spots) and for a decreasing (light grey spots) confining pressure. The black arrows represent the time flow of the laboratory experiment.

At the beginning of the experiment, the isotropic Skempton coefficient increased with increasing confining pressure to 20 MPa. This could be due to adjustment of the initial conditions and possible dissolution of gas in the fluid. The Skempton coefficient then decreased with increasing confining pressure to a minimum value of 0.49 at 70 MPa. After the hold phase, and a delayed deformation of the rock, the isotropic Skempton coefficient was 0.37 and increased to 0.9 at 10 MPa confining pressure.

There are two limiting boundaries for the isotropic Skempton coefficient: if the confining pressure affects only the grain structure it should be zero, and if the confining pressure affects only the fluid inside the pore spaces it should be one. We assume that the decrease of the Skempton coefficient from 20 to 70 MPa confining pressure results from the changing ratio of pore volume to grain volume as well as from a change of the pore-space geometry. This leads to a higher bulk modulus of the sample. On the one hand, the water is more compressible than the grains (Table 1), therefore the pore volume decreases with increasing confining pressure. On the other hand, irregular pore spaces were more susceptible to the confining pressure, therefore their shapes became more rounded, and pore throats and micro-cracks were closed. This geometry change, caused by closing of micro-cracks and elastic deformation of grains, results in a more stable structure. In the hold phase, the deformation continued, which resulted in a further loss of pore volume and a stabilization of the grain structure. Consequently, the Skempton coefficient decreased.

In the first part of the down-ramp (from 70 MPa to 40 MPa), the run of the curve was similar to that for the up-ramp. However, at lower pressures the Skempton coefficient increased to 0.9. This shows a stronger reaction of the pore fluid to the confining

pressure than before; this is due to irreversible deformation, which led to an increasing compactness of the grain structure, and a consolidation of the rock as the experiment proceeded. Under these new experimental conditions, the fluid was now the dominant linear elastic component. The irreversible deformation of the sandstone remained and prevented it from reaching its initial volume.

The second experiment was also carried out at hydrostatic conditions, so that sample properties were related to changes in confining pressure. To show the reversibility of the induced pore pressure, the confining pressure was increased to the maximum and then reduced to the initial conditions twice. To reduce the irreversible deformation and to minimize the non-linear effects, we introduced two new factors. First, we increased the confining pressure during the experiment only to a maximum of 60 MPa. Second, we preconditioned the Bentheimer sandstone sample by applying a pressure cycle from 5 to 70 MPa, and repeated this procedure four times (Hart & Wang 1995). In the first cycle, the raising of the confining pressure from 5 to 70 MPa and its lowering was done in 10 min; in the three following cycles, it took about 2 min each. To maintain quasi-elastic conditions, the absolute value of the preconditioning was 16.7% higher than the projected confining pressure in the experiment. Throughout the preconditioning, the pore system was open to the atmosphere to achieve drained conditions. The design of the total experiment including the preconditioning and the measured pore pressure is shown in Figure 5.

During the four preconditioning cycles the volumetric strain increased from 0.0 before loading to 6.1×10^{-3} after loading at 0 MPa confining pressure. This remaining volumetric strain was irreversible and is used as a starting value for the experiment. After closing the shut-off valves, we applied a confining pressure of 10 MPa and a pore pressure of 5.08 MPa, and the volumetric strain further increased to 7.8×10^{-3} . After the experiment the volumetric strain at 10 MPa confining pressure was 8.7×10^{-3} , so an additional irreversible volumetric strain of 0.9×10^{-3} occurred as a result of the loading of the experiment. The volumetric strain indicates that 80–85% off all irreversible deformation occurred during the preconditioning. The remaining irreversible deformation of 15–20% occurred in the course of the experiment, especially during the high-pressure parts. The comparison of volumetric strain and pore pressure of the first and second confining loops shows that the second one was less affected by irreversible deformation. During the hold phase of loop 1 the volumetric strain increased from

Table 1. Mechanical input parameters for the numerical model of both material groups

Parameter	Material group 1: grains	Material group 2: fluid
Young's modulus E (GPa)	35	0
Poisson's ratio ν	0.23	0.5
Shear modulus G (GPa)	14.2	0
Bulk modulus k (GPa)	21.6	2.2
Lamé's constant λ (GPa)	12.1	2.2
Lamé's constant μ (GPa)	14.2	0

The Young's modulus and the Poisson's ratio for the grains were chosen according to properties of other low-permeability rocks (Woolley 2004) and for the fluid equal to water.

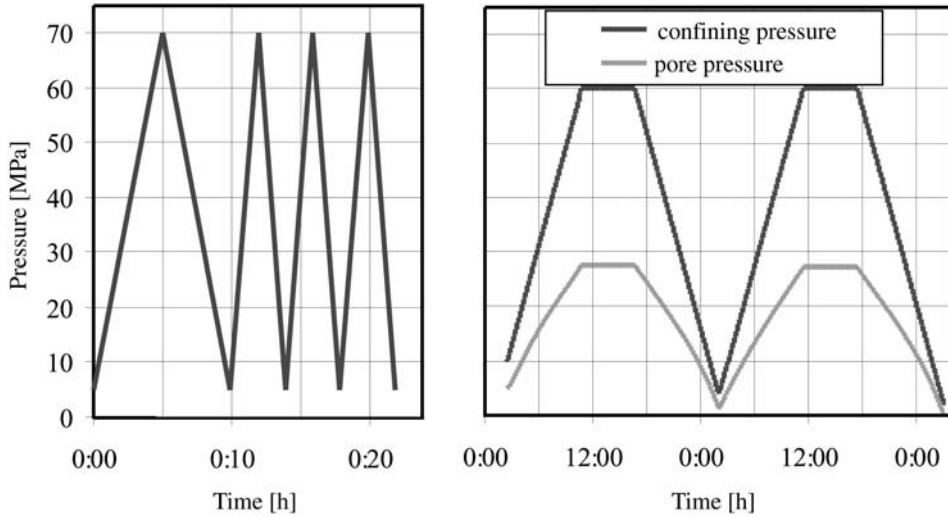


Fig. 5. Changes in confining pressure and pore pressure over the period of preconditioning (left side) and the experiment (right side).

12.04×10^{-3} to 12.12×10^{-3} , and within loop 2 from 12.12×10^{-3} to 12.16×10^{-3} . Here the curves were similar to those for the first experiment. A significant increase of pore pressure over the hold phases as in the first experiment could not be observed. The effect of preconditioning on the hold phase of confining loop 2 is shown in Figure 6. There, after reaching the 60 MPa level for confining pressure, the pore pressure increased for a period of 20 min depending on changes in volumetric strain. Then the pore pressure decreased, probably as a result of a temperature drop of the hydraulic system, or caused by forcing pore fluid into unsaturated

and badly connected pores, until the effect of deformation dominated again and induced a small increase of pore pressure. The final value for pore pressure was 27.17 MPa and in this case was equal to the starting value of the hold phase.

Under these more elastic conditions the calculated isotropic Skempton coefficient can be taken as more accurate than in the first experiment (Fig. 7), because the influence of irreversible deformation was minimized. Nevertheless, in the range of 12–35 MPa confining pressure, the calculated Skempton coefficient of the first up-ramp was a little higher than that for the following ones, and

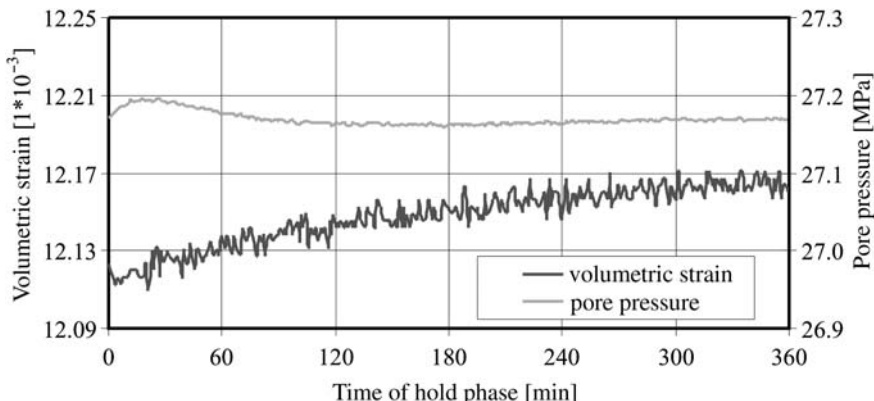


Fig. 6. Evolution of volumetric strain and pore pressure over a period of 6 h. The confining pressure was kept constant at 60 MPa during this second hold phase.

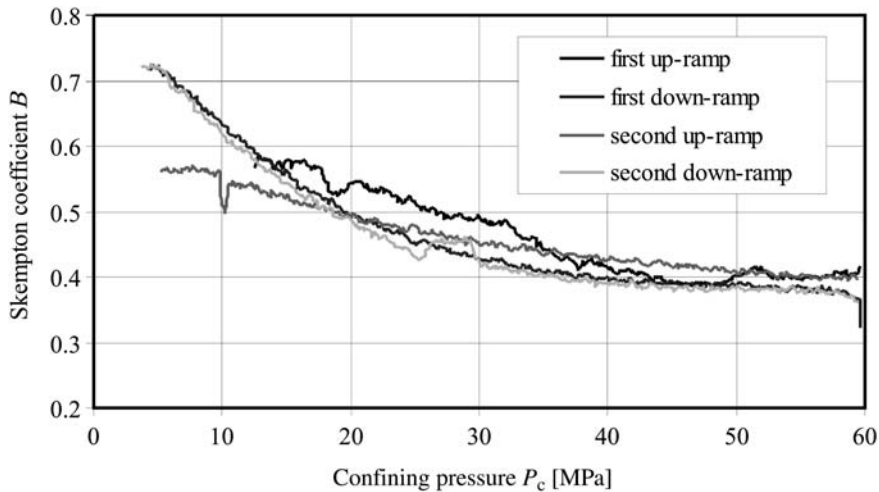


Fig. 7. Sliding average (nine values) of calculated Skempton coefficient for the four confining pressure ramps, first loop (dark grey) and second loop (light grey) are plotted together.

was possibly influenced by an irreversible deformation. The following curves were close together; also, the offset, which occurred during the hold phases, was minimized from 0.1 in the first experiment to 0.02 in the second one. Therefore, all the Skempton coefficients determined in this laboratory test could be taken as an elastic response of the sandstone sample. With this new setup of the experiment, the isotropic Skempton coefficient started at $c.$ 0.7 at 5 MPa and decreased to 0.4 at confining pressure 60 MPa. To investigate the dependence of the Skempton coefficient on confining pressure change, we differentiated the isotropic Skempton

coefficient with respect to confining pressure (Fig. 8). For this purpose a trend curve was added to the measurements of each confining pressure ramp except the first one. In all cases an exponential function gave the best results: for the first down-ramp $y = 0.55e^{-0.076x} + 0.373$, for the second up-ramp $y = 0.27e^{-0.04x} + 0.372$ and for the second down-ramp $y = 0.54e^{-0.078x} + 0.37$. The first derivatives of these equations must be exponential functions too, which shows that the change of the Skempton coefficient was highest at low pressure and was reduced by an increasing confining pressure.

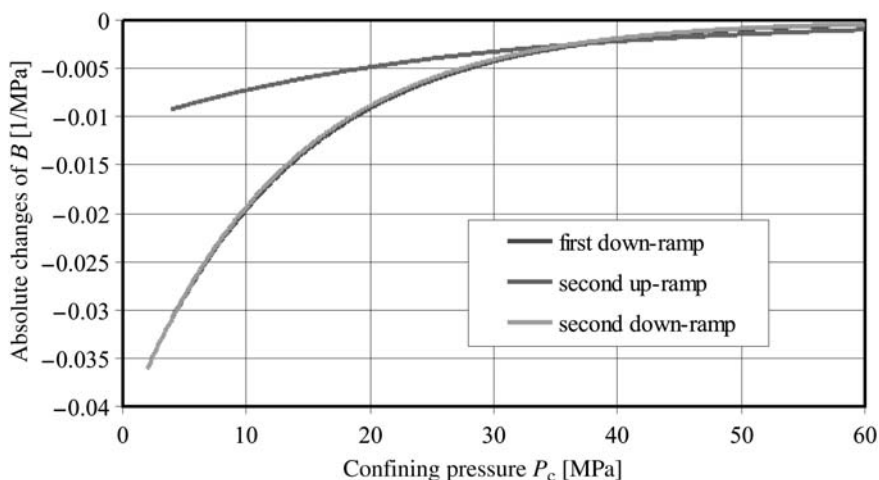


Fig. 8. First derivative of Skempton coefficient with respect to confining pressure; the influence of the ambient pressure on the Skempton coefficient decreases at high-pressure levels.

Numerical simulation

We modelled the mechanical behaviour and the related hydraulic properties of the Bentheimer sandstone sample, to compare the results with the experiments. For this purpose, we used a thin-section micrograph of the undeformed sandstone as input microstructure. The model simulates similar conditions to those of the experimental study, which means that the geometric, hydraulic and mechanical properties are the same as those in the experiment. To realize these requirements a finite-element (FE) model is used, which defines each grain and each pore space and their typical attributes in a discrete way. It also models the deformation of the rock using deformation and displacement of the model grid. The resulting pore pressures were used to determine the isotropic Skempton coefficient.

In preparation for the model, the geometry of the intact Bentheimer sandstone sample had to be rebuilt. For this purpose the cut-out of a thin-section micrograph (Fig. 9) was analysed to separate the pore spaces from the grain structure. The sum of areas of each single pore space A_p related to total image area A_{tot} is defined as the optical porosity ϕ of the image cut-out, which is 19.6% for this case. For an isometric distribution of pore spaces, the 2D area-fraction of pore space ϕ coincides with the 3D pore-space fraction of the porous medium (Trautwein 2005). Therefore, the modelled undrained poroelastic response of the thin-section micrograph should be comparable with the experimentally determined rock behaviour. Based on the image data a suitable input geometry, including differentiation between pore spaces and grains, was created for the numerical model. It started

with a conversion of the given grey-scaled or red–green–blue (rgb)-coloured image into a binary image, by using colour thresholding across the image. Here, the bimodal distribution of grey tones is used to differentiate between pore spaces and grains (Fig. 10a). Through this relatively simple conversion into a binary image a couple of misclassifications occurred, which have to be removed from the first classification. For this removal, a C++ code was written, which counted the number of pixels for each white or black pixel cluster. If this value was below a defined threshold, then the pixel cluster was in all likelihood misclassified and was removed. The chosen algorithm was bidirectional and deleted both white and black bad spots, as well as pore spaces that intersected with the model boundary (Fig. 10b).

Based on this cleared binary image a second algorithm was applied, which referenced the image to its original dimensions ($1.3 \text{ mm} \times 1.3 \text{ mm}$) and vectorized the geometry. For this purpose the function took the position of each pore–grain contact and saved the coordinates of the determined points and lines into a geometric input file for the open-source 3D FE mesh generator Gmsh (Geuzaine & Remacle 2006), as shown in Figure 10c. By using this geometry file, the surfaces for pores and grains can be defined inside the Gmsh environment. The refinement of the mesh along the boundaries between grains and pore spaces was achieved by a combination of characteristic length definition and a triangle mesh algorithm. The characteristic length or the size of one mesh element is defined as the radius of the circumscribed circle for the triangle and was set to 10 length units for each point of the geometry.

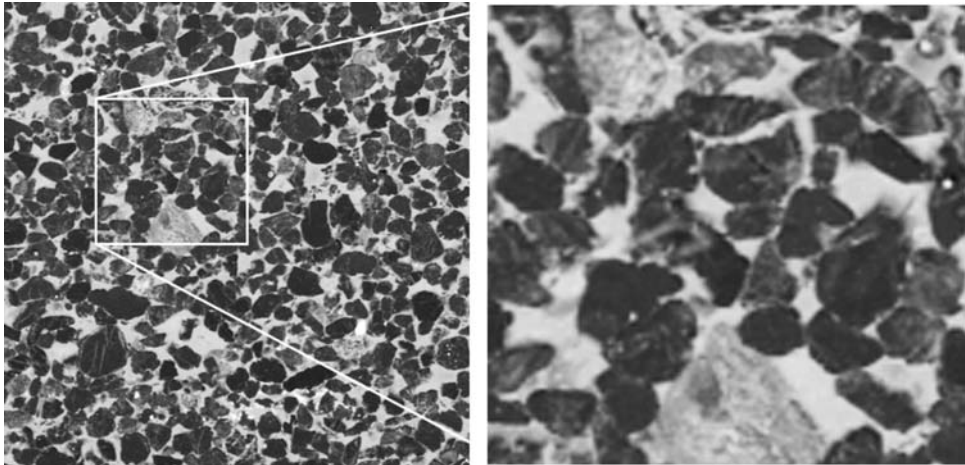


Fig. 9. Thin-section micrograph of an intact Bentheimer sandstone sample; on the right is shown an enlarged cut-out used for the FE model.

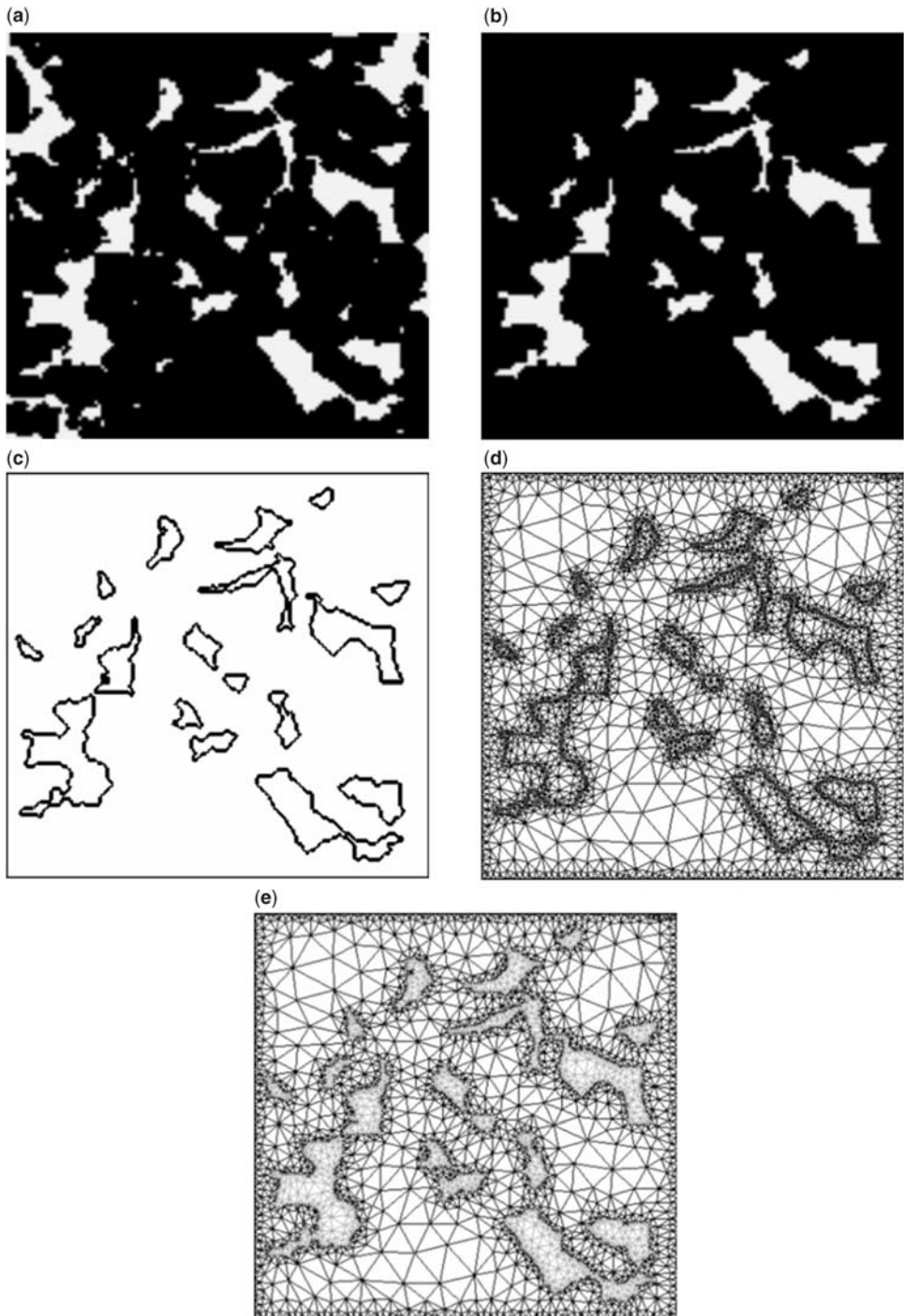


Fig. 10. Pre-processing of a thin-section micrograph; (a) direct conversion of the grey-scale image into a binary image; (b) removal of bad spots and marginal pore spaces; (c) vectorization and referencing of the image to the original dimensions; (d) meshing with refinement of the pore–grain boundaries; (e) allocation of material groups to the elements.

The contrast of material properties and the gradient for stress, strain and displacement is generally highest at the pore–grain interfaces. To represent these property changes we refined the relevant areas. Because the interspace between the input single points is one and therefore smaller than the characteristic length, and by choosing the triangle mesh algorithm, the boundaries were automatically refined by a factor of 10 (Fig. 10d). At the end of the pre-processing, the material groups were assigned to the mesh geometry. For this assignment a colour mapping for the two groups was accomplished inside Gmsh (Fig. 10e), which can be interpreted by the modelling software.

The following numerical modelling of the mechanical behaviour was carried out with the FE program GeoSys/RockFlow (Korsawe *et al.* 2003; Wang & Kolditz 2005). This simulation software combines the four basic processes (thermal, mechanical, hydraulic and chemical) that dominate the hydrogeological behaviour of porous media. In the present model a combination of liquid flow (hydraulic process) for the fluid inside the pores and deformation (mechanical process) for the grains as well as the fluid were linked. Furthermore, different requirements of the model, such as initial conditions, boundary conditions, source terms, etc., had to be defined. First, we defined the elementary structure of the model area by using points, lines, polylines, surfaces and volumes. This is necessary for subsequent specification of other parameters. In addition to the basic structure the above-described mesh was implemented in the model. For this purpose it had been converted into a GeoSys/RockFlow format. Different types of boundary conditions were implemented. The first was applied to the borders of the model area, to simulate the increase of the confining pressure from 0 to 70 MPa as in the experiment, and the second was a horizontal and a vertical line, where the displacements normal to the lines were set to zero, as shown in Figure 11. This was necessary to keep the model-mesh in place. Both types of boundary conditions were of the first kind and therefore are Dirichlet boundary conditions.

At the beginning of the laboratory experiment, the confining and the pore pressures were set to their initial conditions, which were 10 MPa and 7.44 MPa, respectively. In the current state of Rockflow in combination with the present mechanical problem, it is impossible to set up different initial conditions for the two material groups, therefore both the confining pressure and the pore pressure were set to zero. This deviation from the laboratory values is not significant, as the definition of the Skempton coefficient under linear elastic conditions used only the changes of the pressures, $B = dP_u/dP_c$.

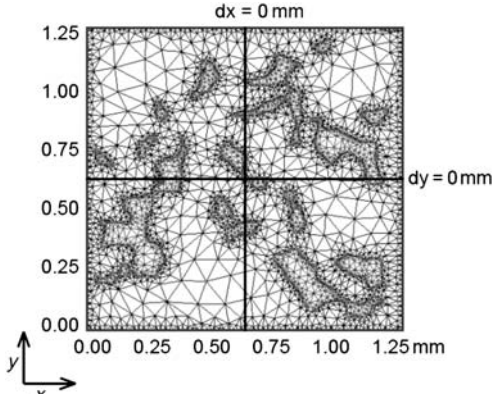


Fig. 11. Boundary conditions of the numerical model; the outer border simulated the increase of the confining pressure by imposing normal pressure and the bold crossed lines fixed the model-mesh by setting the normal displacement to zero.

For modelling the mechanical behaviour of porous media, especially under undrained conditions, we assume that all strains are small. With a pore–grain separation, the fluid properties such as viscosity, heat conductivity, and density are not required. Also, the porous media properties such as tortuosity, permeability and storage coefficient are not needed, because they are given by the model geometry. Therefore only the solid properties for an elastic deformation were specified inside the model; these are the Young's modulus E and the Poisson's ratio ν . The shear modulus G and the bulk modulus K can be expressed in terms of E and ν :

$$G = \frac{E}{2(1+\nu)}, \quad K = \frac{E}{3(1-2\nu)}.$$

The quantities λ and μ known as Lamé's constants are related to E , ν and K by the following equations (Telford *et al.* 1976):

$$E = \frac{\mu(3\lambda + 2\mu)}{(\lambda + \mu)}, \quad \nu = \frac{\lambda}{2(\lambda + \mu)}$$

$$\text{and} \quad K = \frac{3\lambda + 2\mu}{3}.$$

For a discrete model, where the distribution of the solid properties takes place in a single mesh and without flow across the grains, the fluid can be taken as a solid medium with the mechanical properties of a fluid. The effect of this consideration is that the model calculates stress values for the fluid, which correspond to the pore pressure. The mechanical input parameter E and ν , as well as

the resultant shear modulus, bulk modulus and Lame's constants for both material groups, are listed in Table 1, where the shear modulus for the fluid is calculated as zero. This causes numerically based deformations of the mesh elements near the pore spaces, which is atypical for a fluid. To stabilize the model a shear modulus 100 times smaller than that of the grain was used for the fluid.

Finally, the time discretization has to be defined for the model. Here the constant time step method was used, and the period of each step was set to 20 min. The total number of time steps was given by the increasing rate of the confining pressure, which should be 0.1 MPa min^{-1} , similar to that in the laboratory experiment, and its end-level was at 70 MPa. To increase the confining pressure from 0 MPa to 70 MPa, a discretization of 35 time steps (20 min each) was implemented. After each time step the results for displacement, strain and stress were saved to a file to post-process their changes depending on the confining pressure.

We modelled only the elastic behaviour of porous media, because simulation of irreversible deformation at single grain level would involve a restructuring of the grain matrix, which is not possible at present. Through the chosen deformation process only the purely elastic deformation of the thin-section micrograph can be modelled, so a decrease of the confining pressure is unnecessary, because no hysteresis can be expected.

The resulting stresses inside the grains and the induced pore pressures at a confining pressure level of 70 MPa are shown in Figure 12. For the

grains the induced stresses vary approximately from 40 to 100 MPa and the average weighted by volume is identical to the applied confining pressure. Near the grain contacts and between neighbouring pores, the stresses in the grains can be observed to be highest. In the protected parts such as inside the grains the stress does not reach the applied confining pressure.

Much more interesting than the induced stresses in the grains is the resulting pressure inside the pore spaces. For each single pore the pressure is uniformly distributed, because it is under hydrostatic conditions, but the pressure differs from pore space to pore space. This effect may be due to the disconnection of the pores given by the cross-section geometry. In the future, this problem could be solved by an iterative adjustment of the pore pressures by the weighted average during modelling or by connection of pore spaces through fluid-transmissible 1D elements, or of course by a real 3D model, where the pathways are geometrically defined.

First, we calculate the pressure of each single pore and then the resulting pore pressure of the thin section by using the volume-weighted average of all pore spaces. By means of the pressures determined after each time step and the corresponding confining pressure, the isotropic Skempton coefficient is computed for the total simulated time. It is found that the Skempton coefficient is constant over the total range of confining pressure for each single pore space, but decreases with increasing confining pressure for the weighted

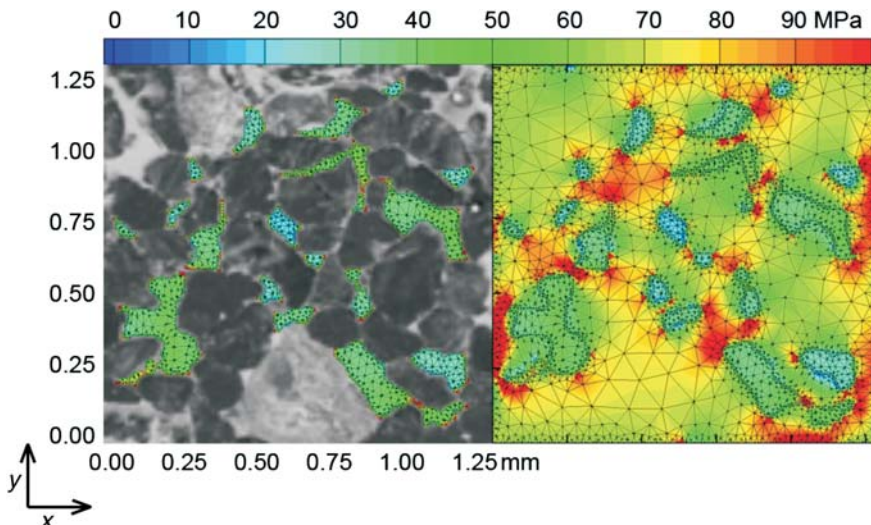


Fig. 12. Calculated stresses across the model area as a result of a confining pressure of 70 MPa. The magnitude is shown by the colour scale at the top of the figure. On the left side the model results are overlaid by the original grain structure, so only the pore pressure responses are visible.

average. We also observe that the Skempton coefficient of irregularly shaped pore spaces is up to two times higher than that of the rounded ones. To explain this effect, we consider that the ratio between the surface area of an irregular pore space S_i and the included volume V_i is higher than for a rounded pore space:

$$\frac{S_i}{V_i} > \frac{S_r}{V_r}.$$

Therefore the forces that act on an irregular pore space are higher than those on a round pore space, and so is the resulting volume loss. Thus increasing the confining pressure from 0 MPa to 70 MPa results in a decreasing ratio between an irregular volume and a rounded one:

$$\frac{V(0 \text{ MPa})_i}{V(0 \text{ MPa})_r} > \frac{V(70 \text{ MPa})_i}{V(70 \text{ MPa})_r}.$$

Hence, this higher compressibility causes a higher pore pressure and therefore a higher Skempton coefficient.

$$B_i > B_r.$$

Although the Skempton coefficient is constant for each single pore, the weighted average for the isotropic Skempton coefficient

$$B = \sum_{k=1}^n B_k V_k$$

where n is the number of pores must decrease with an increasing confining pressure under these assumptions (Fig. 13).

By means of the results of the numerical FE model and the laboratory experiment, we are now able to compare the displacements, strains, stresses and isotropic Skempton coefficients. The applied stresses in both the laboratory experiment and the model are the same, but in the simulation the distribution of the resulting stresses across the thin section can be observed. This shows a stress concentration up to 100 MPa, which is not visible and cannot be measured in the laboratory experiment. The induced pore pressure at 60 MPa confining pressure ranges from 20 MPa in round pores to 40 MPa in irregular pores, and at 70 MPa confining pressure the pore pressure ranges from 23 MPa to 47 MPa, respectively. The weighted average at these stress levels for the numerical model are 33.1 MPa (at $P_c = 60$ MPa) and 38.4 MPa (at $P_c = 70$ MPa). The comparison of the calculated pore pressures over the entire range of confining pressure with the two laboratory experiments (Fig. 14) shows that the difference between the two sandstone samples is higher than the discrepancy between laboratory data and numerical simulation.

Besides the pore pressures, the strain values are good indicators of the correctness of the numerical simulation. The strain values measured during the experiment represent the displacement of the core sample surface related to the dimensions of the sandstone cylinder. To make these measurements comparable with the numerical calculations, we used the axial extension data and estimated the strain values in the x - and y -directions of the upper-left and the lower-right corner from the thin section. The measured magnitude and increase of strain with the confining pressure matches the model calculated values very well, as shown in Figure 15. One important observation is that in the

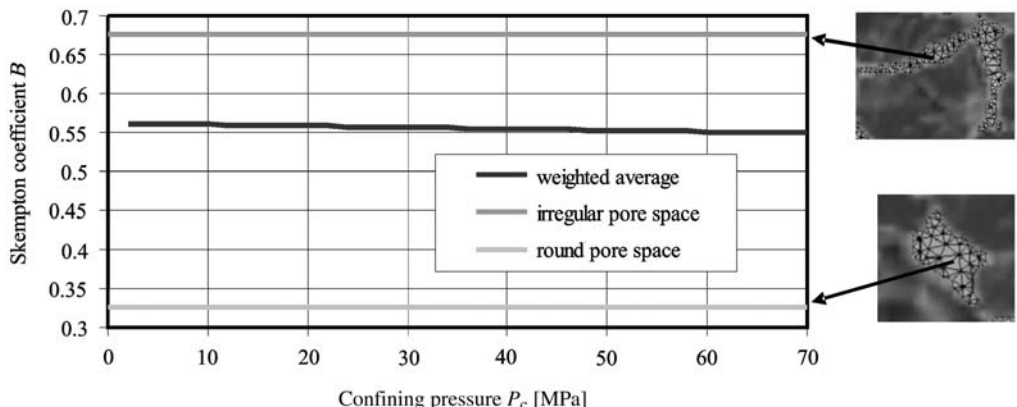


Fig. 13. Skempton coefficient, for rounded pore space, irregular pore space and the weighted average as a function of confining pressure.

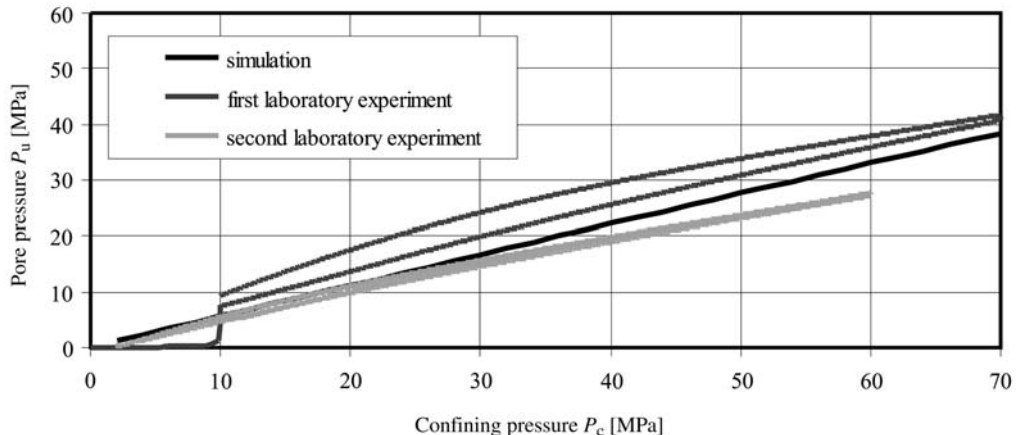


Fig. 14. Induced pore pressure v. confining pressure of the numerical simulation (dark grey), the first laboratory experiment (medium grey) and the second laboratory experiment (light grey). The preconditioning at the beginning of the second experiment results in a minimization of the pore pressure hysteresis.

vicinity of the pore spaces the strain is highest. This can be explained by higher compressibility of the pore spaces, with a corresponding higher deformation of the surrounding grains.

We refrain from making a comparison of displacements at this point, because this is similar to the strains. In both the laboratory experiment and the numerical simulation the isotropic Skempton coefficient decreases with increasing confining pressure. The only difference is that the Skempton coefficient for the laboratory experiment is close to an exponential function of the confining pressure, whereas in the numerical simulation it is a linear function. Until now the isotropic Skempton coefficient was

taken as a constant value under these conditions, but the two completely different methods show that it is dependent on the confining pressure. To prove these results we will finally calculate the Skempton coefficient analytically for a purely elastic hollow sphere.

Analytical calculation

In this section, we derive an exact solution of a spherically symmetrical problem. We consider a solid hollow sphere, which is subjected to spherically symmetrical loading. This means that internal body forces, tractions and displacements are

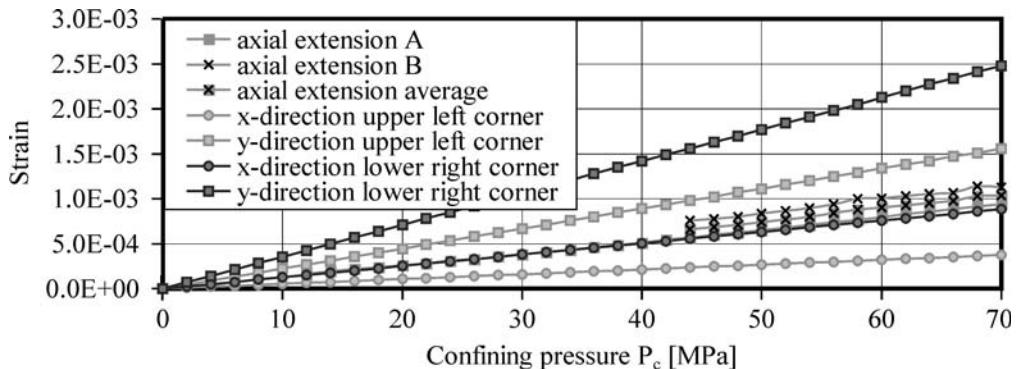


Fig. 15. Strains measured by axial extensometer A and axial extensometer B and mean values of the first laboratory experiment and calculated strains of the upper left corner and lower right corner in the x- and y-direction. The determination of the axial extension (B) and therefore the average extension started at 44 MPa, because some problems of the wire line lead-through caused inaccurate measurements at the range from 0 to 44 MPa.

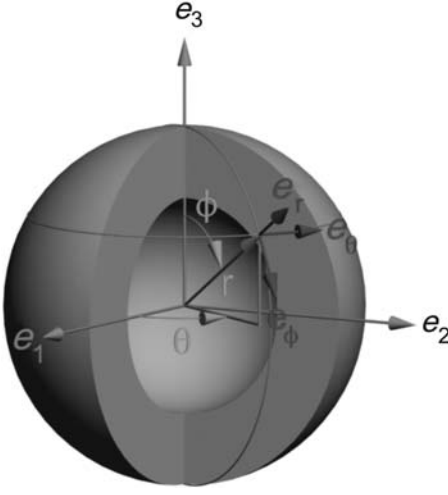


Fig. 16. Hollow sphere, with a Cartesian and spherical coordinate system.

independent of θ and ϕ , and act in the radial direction only. The solution of this problem is most suitably expressed using a spherical polar coordinate system, as shown in Figure 16.

To simplify the problem we make a couple of assumptions and follow the procedure outlined by Lubliner (1998). The material of the hollow sphere is isotropic and a linear elastic solid, with Young's modulus E and Poisson ratio v . Furthermore, no body forces act on the sphere, the temperature is uniform and all displacements are small. In these circumstances, the displacement, strain and stress fields are spherically symmetrical. The displacement u is a scalar function of the radial coordinate r only, $u = u(r)$, because for a radial deformation the circumferential displacements are zero. The strain and stress tensors can be written as components in $\{e_r, e_\theta, e_\phi\}$:

$$\boldsymbol{\varepsilon} = \begin{bmatrix} \varepsilon_r & 0 & 0 \\ 0 & \varepsilon_\theta & 0 \\ 0 & 0 & \varepsilon_\phi \end{bmatrix}, \quad \boldsymbol{\sigma} = \begin{bmatrix} \sigma_r & 0 & 0 \\ 0 & \sigma_\theta & 0 \\ 0 & 0 & \sigma_\phi \end{bmatrix}.$$

Inside the strain tensor the only non-zero entries are the radial strain $\varepsilon_r = du/dr$ and the circumferential strains $\varepsilon_\theta = \varepsilon_\phi = u/r$.

For our particular questions, the solution of the pressurized linear elastic hollow sphere containing a fluid inclusion has already been derived (Timoshenko & Goodier 1934), as shown in equation (1) below. There the pore pressure p_u affecting the inner surface of the hollow sphere with $r = r_1$ and the outer surface at $r = r_2$ is stressed by only the confining pressure p_c , as shown in Figure 17.

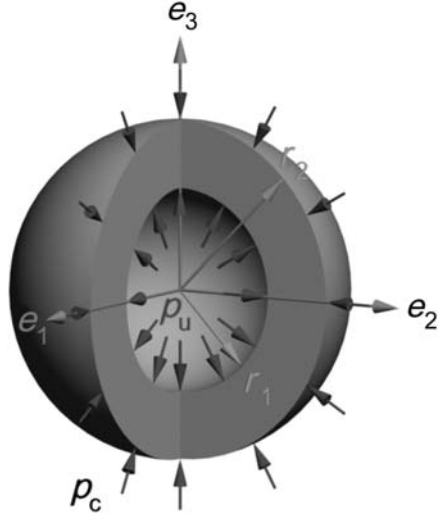


Fig. 17. Linear elastic hollow sphere, filled with a spherical fluid inclusion. Pore pressure p_u acts on the interior surface and confining pressure p_c acts on the exterior surface.

As $\varepsilon_\theta = \varepsilon_\phi = u/r$, the displacement u in a radial direction is

$$u(r) = \frac{2(p_u r_1^3 - p_c r_2^3)(1-2v)r^3 + (p_u - p_c)(1+v)r_2^3 r_1^3}{2E(r_2^3 - r_1^3)r^2}. \quad (1)$$

With this equation for radial displacement we obtain an exact solution for known boundary conditions, but the pore pressure should be a dependent value. Therefore we look at the fluid inclusion, to find a pore pressure dependent equilibrium relationship on the inner surface for stress, strain or displacement. For this purpose we use the converted definition of the bulk modulus K (Gueguen & Palciauskas 1994):

$$\frac{\Delta V}{V} = \frac{-p_u}{K} \quad (2)$$

where the volumetric strain can be expressed in terms of the radius:

$$\frac{\Delta V}{V} = \frac{\frac{4}{3}\pi r_1^3 - \frac{4}{3}\pi r_1^3}{\frac{4}{3}\pi r_1^3}. \quad (3)$$

To find an equilibrium for displacements, we substitute the resulting radius r'_1 in terms of its original length and an additional displacement

$$r'_1 = r_1 + u(r_1). \quad (4)$$

Therefore the volumetric strain for small displacements is a function of r and $u(r)$:

$$\frac{\Delta V}{V} = \frac{3r_1^2 u(r_1) + 3r_1 u(r_1)^2 + u(r_1)^3}{r_1^3} \approx \frac{3u(r_1)}{r_1} \quad (5)$$

and the pore pressure p_u can be expressed dependent on the bulk modulus, the radius and the displacement:

$$\frac{-p_u}{K} = \frac{3r_1^2 u(r_1) + 3r_1 u(r_1)^2 + u(r_1)^3}{r_1^3} \approx \frac{3u(r_1)}{r_1}. \quad (6)$$

With equation (1), the displacement at the inner surface $u(r_1)$ can be calculated by

$$u(r_1) = \frac{2(p_u r_1^3 - p_c r_2^3)(1 - 2v)r_1 + (p_u - p_c)(1 + v)r_2^3 r_1}{2E(r_2^3 - r_1^3)}$$

and with the simplification of (6) the corresponding pore pressure for a fluid inclusion inside the hollow sphere can be calculated by

$$p_u = \frac{9Kr_2^3 p_c(1 - v)}{3K(2r_1^3(1 - 2v) + r_2^3(1 + v)) + 2E(r_2^3 - r_1^3)}. \quad (7)$$

This simplified solution leads to a linear dependence of pore pressure and confining pressure, and

also to a constant isotropic Skempton coefficient. The laboratory experiment and the numerical simulation show that the Skempton coefficient is not constant, therefore the simplification is inappropriate. Without simplification of (6) the pore pressure of the fluid inclusion can be calculated by

$$p_u = -K \frac{3r_1^2 u(r_1) + 3r_1 u(r_1)^2 + u(r_1)^3}{r_1^3} \quad (8)$$

and the equilibrium condition for the outer sphere is

$$p_u = \frac{2E(r_2^3 - r_1^3)u(r_1) + 3r_1 r_2^3 p_c(1 - v)}{2r_1^4(1 - 2v) + r_1 r_2^3(1 + v)}. \quad (9)$$

In this case the pore pressure p_u has to be calculated numerically.

For this purpose we used a small, self-written C++ code, which calculates the pore pressure that results at different confining pressure levels. The bulk modulus K for the fluid inclusion was set to 2.2 GPa as for the numerical simulation, and the Poisson's ratio v and Young's modulus E for the hollow sphere were set to 0.25 and 35 GPa, respectively. Furthermore, the inner radius r_1 was set to 0.6 mm and the outer radius r_2 to 1 mm, so that the volume of the inclusion is equivalent to a porosity of 21.6%. During the calculation, the confining pressure was increased from 0 MPa to 70 MPa in 1 MPa steps. At each confining pressure level, the pore pressure was determined with a precision of 23 decimal places. At the confining pressure level of 70 MPa, the analytically

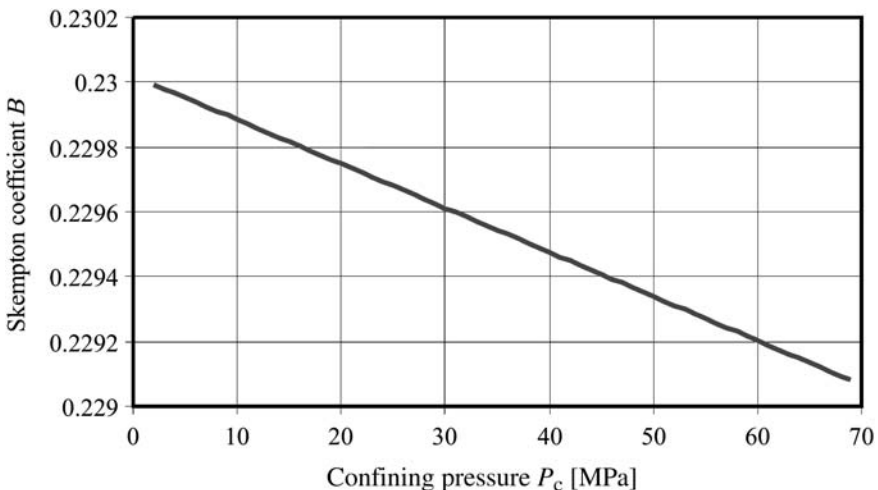


Fig. 18. Isotropic Skempton coefficient of the analytical calculation dependent on the confining pressure. As in the laboratory experiment and the numerical simulation, B decreases with increasing confining pressure.

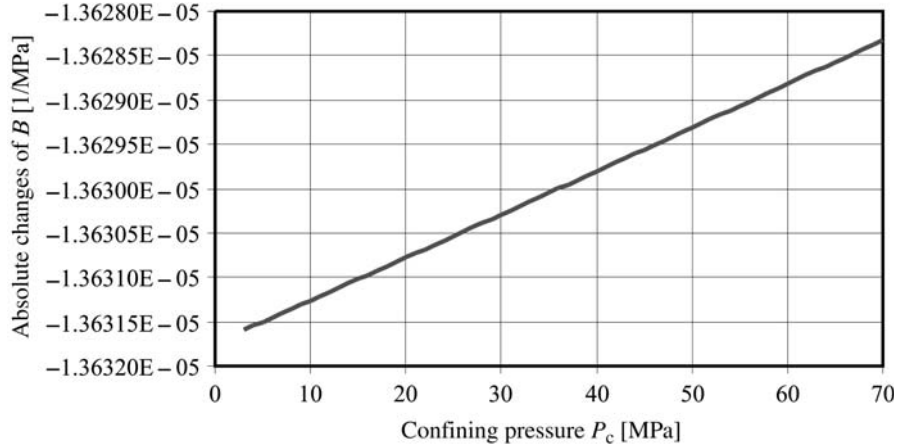


Fig. 19. First derivative of Skempton coefficient with respect to confining pressure. The influence of the confining pressure on the Skempton coefficient decreases at high ambient stress levels, as in the laboratory experiment.

calculated pore pressure reaches a value of 22.9 MPa and is similar to the numerically simulated results for round pore spaces. In combination with the numerical results, we conclude that rounded and spherical geometries are most resistant to the applied confining pressure and that the induced pore pressure and the derived Skempton coefficient of such pore spaces are a lower boundary value of the complete grain–pore system. The evolution of the isotropic Skempton coefficient as a result of the confining pressure change (Fig. 18) shows the same behaviour as in the laboratory experiment and in the numerical simulation, and the first derivative of Skempton coefficient with respect to confining pressure (Fig. 19) confirmed this trend.

Conclusions

Until now the isotropic Skempton coefficient has been taken as a constant value, independent of confining pressure. In contrast, laboratory experiments as well as numerical simulations and analytical calculation show that the isotropic Skempton coefficient decreases with increasing confining pressure. Both the laboratory experiment and the analytical calculation show an exponential relation of the isotropic Skempton coefficient with the confining pressure. We propose that this relationship is due to the change in pore-space geometry: the overall pore space changes to a stiffer structure with increasing confining pressure. The analytically calculated Skempton coefficient is a limiting value of the numerically and experimentally determined Skempton coefficients, and it also decreases with confining pressure. The linear dependence of the Skempton coefficient on confining pressure in the

numerical simulation is explained by the fact that the pore spaces are not connected. With connected pore spaces, as in a sandstone sample or in a real 3D model, the pressure equalization of irregular and rounded pore spaces would amplify the effect of a decreasing Skempton coefficient at low confining pressure levels, because the geometric pore-space change is highest. Therefore the Skempton coefficient would also be an exponential function of confining pressure.

The experimentally specified variation of the isotropic Skempton coefficient of more than 0.3 represents the true Bentheimer sandstone response. In the numerical simulation the variation of the volume-weighted average is only 0.02, but the difference between the Skempton coefficient of a crack-like pore space and a rounded pore is also slightly more than 0.3. A complete change of the Skempton coefficient from one extreme to another depending on the confining pressure change cannot be simulated without flow, because of the limitation presented by the 2D geometry of the thin-section micrograph. Therefore the 2D model shows only the upper and lower limits and the trend of the isotropic Skempton coefficient. With the analytical calculation we show only the decreasing trend of the Skempton coefficient as a result of confining pressure change and the lower limit for the Bentheimer sandstone represented by a nearly incompressible hollow sphere. Therefore the variation of B within the analytical calculation is only 0.001.

The analytical calculation shows that, in addition to the confining pressure and the pore-space geometry, the bulk modulus of the fluid and the Young's modulus as well as the Poisson's ratio of the solid influence the resulting pore pressure and therefore the isotropic Skempton

coefficient. Under linear elastic conditions, these three rock properties can be taken as constant, therefore the isotropic Skempton coefficient is an exponential function of the confining pressure and the pore-space geometry only. The exact change of pore-space geometry as a result of confining pressure change needs further investigation.

The results of this work can help to reinterpret data of existing studies that investigated the poroelastic behaviour of porous media. This work shows that different stress fields affect the geometry of porous media and therefore the poroelastic response in a nonlinear way. By using a variable Skempton coefficient, we can improve the accuracy of prediction of the behaviour of porous media in different stress fields. Furthermore, we can use this knowledge to calculate the pore pressure change in different stress fields, implementing the change of effective stress. The effective stress strongly affects hydromechanically linked processes of rocks; for example, a change of Coulomb failure stress (Arnadottir *et al.* 2003) or stress-dependent permeability.

The authors thank the Center of Applied Geoscience at the University of Tübingen for close collaboration in Geosys/RockFlow related questions. L. Liebeskind is acknowledged for assistance with the laboratory experiment, R. Becker for preparation of the Bentheimer sandstone sample, and E. Spangenberg and S. Raab for valuable discussions. Both anonymous reviewers are acknowledged for constructive comments, which improved the paper. This work was funded by the German Ministry of Environment and Nature (BMU) and supported by the GeoForschungsZentrum Potsdam (GFZ).

References

- AL-WARDY, W. & ZIMMERMAN, R. 2004. Skempton coefficient of clean and clay-rich sandstones. In: *Proceedings of 17th ASCE Engineering Mechanics Conference*, University of Delaware, Newark, DE, 6.
- ARNADOTTIR, T., JONSSON, S., PEDERSEN, R. & GUDMUNDSSON, G. B. 2003. Coulomb stress changes in the south Iceland seismic zone due to two large earthquakes in June 2000. *Geophysical Research Letters*, **30**, 4.
- BIOT, M. A. 1941. General theory of three dimensional consolidation. *Journal of Applied Physics*, **12**, 155–164.
- BROWN, P. J. II. 2002. *Shock tube experiments for the determination of petrophysical parameters*. MSc thesis, Colorado School of Mines, Golden, CO.
- BROWN, R. J. S. & KORRINGA, J. 1975. On the dependence of the elastic properties of a porous rock on the compressibility of the pore fluid. *Geophysics*, **40**, 608–616.
- DETOURNAY, E. & CHENG, A. H. D. 1993. *Fundamentals of Poroelasticity, Analysis and Design Methods*. Pergamon, Oxford.
- GEUZAIN, C. & REMACLE, J. F. 2006. *Gmsh: a three-dimensional finite element mesh generator with built-in pre- and post-processing facilities*. Case Western Reserve University, Cleveland, OH.
- GREEN, D. H. & WANG, H. F. 1986. Fluid pressure response to undrained compression in saturated sedimentary rock. *Geophysics*, **51**, 948–956.
- GUEGUEN, Y. & PALCIAUSKAS, V. 1994. *Introduction to the Physics of Rocks*. Princeton University Press, Princeton, NJ.
- HART, D. J. & WANG, H. F. 1995. Laboratory measurements of a complete set of poroelastic moduli for Berea Sandstone and Indiana Limestone. *Journal of Geophysical Research, B, Solid Earth and Planets*, **100**, 17741–17751.
- KORSawe, J., STARKE, G., WANG, W. & KOLDITZ, O. 2003. *Finite element analysis of poroelastic consolidation in porous media: mixed and standard approaches*. University of Hannover–Center for Applied Geosciences, University of Tübingen.
- LOCKNER, D. A. & BEELER, N. M. 2003. Stress-induced anisotropic poroelasticity response in sandstone. In: *Proceedings of 16th ASCE Engineering Mechanics Conference*, University of Washington, Seattle, 13.
- LOCKNER, D. A. & STANCHITS, S. A. 2002. Undrained poroelastic response of sandstones to deviatoric stress change. *Journal of Geophysical Research, B, Solid Earth and Planets*, **107**, 30.
- LUBLINER, J. 1998. *Plasticity Theory*. Prentice-Hall, Englewood Cliffs, NJ.
- MESRI, G., ADACHI, K. & ULLRICH, C. R. 1976. Pore-pressure response in rock to undrained change in all-round stress. *Géotechnique*, **26**, 317–330.
- MTS 2004. *MTS Rock and concrete mechanics testing systems*. MTS Systems Corp., Eden Prairie, MN.
- SKEMPTON, A. W. 1954. The pore pressure coefficient A and B. *Géotechnique*, **4**, 143–147.
- SMITH, I. & SMITH, G. N. 1998. *Elements of Soil Mechanics*. Blackwell, Oxford.
- TELFORD, W. M., GELDART, L. P., SHERIFF, R. E. & KEYS, D. A. 1976. *Applied geophysics*. Cambridge University Press, Cambridge.
- TERZAGHI, K. 1923. Die Berechnung der Durchlassigkeitsziffer des Tonens aus dem Verlauf der hydrodynamischen Spannungsscheinungen. *Sitzungsberichte der Akademie der Wissenschaften in Wien, Mathematisch-Naturwissenschaftliche Klasse, Abteilung IIa*, **132**, 105–124.
- TIMOSHENKO, S. P. & GOODIER, J. N. 1934. *Theory of Elasticity*. McGraw-Hill, Kogakusha, Tokyo.
- TRAUTWEIN, U. 2005. *Poroelastische Verformung und petrophysikalische Eigenschaften von Rotliegend Sandsteinen*. PhD thesis, Technischen Universität, Berlin.
- WANG, H. F. 2000. *Theory of Linear Poroelasticity with Applications to Geomechanics and Hydrogeology*. Princeton University Press, Princeton, NJ.
- WANG, W. & KOLDITZ, O. 2005. *Object-oriented finite element analysis of thermo-hydro-mechanical (THM) problems in porous media*. Center for Applied Geosciences, University of Tübingen.
- WOOLLEY, J. A. 2004. *Shock tube experiments measuring and modeling the slow P-wave in low permeability rock cores*. Colorado School of Mines, Golden, CO.
- ZIMMERMAN, R. W. 1991. *Compressibility of Sandstones: SOURCE*. Developments in Petroleum Science, **29**.

Compaction bands and the formation of slot-shaped breakouts in St. Peter sandstone

B. HAIMSON¹ & A. KLAETSCH^{1,2}

¹*Department of Materials Science and Engineering and Geological Engineering Program,
University of Wisconsin, Madison, WI 53706-1595, USA (e-mail: baimson@wisc.edu)*

²*Present address: Mueser Rutledge Consulting Engineers, New York, NY 10122-0002, USA*

Abstract: Drilling of vertical wellbores in sandstone often results in stress-induced failed zones called breakouts. In the laboratory, miniature drilling under simulated far-field crustal stress conditions above a certain threshold produces breakouts that can be studied to enhance our understanding of deformation and failure mechanisms in rock. We report on drilling experiments in St. Peter sandstone, an Ordovician aeolian rock consisting of well-rounded bimodal quartz grains held together by sutured contacts. Breakouts here are slot-shaped and oriented at right angles to the far-field maximum stress direction (σ_H), resembling emptied compaction bands. We distinguish between two porosity ranges in this rock. In the high-porosity variety (16–22%), grains are bonded through narrow sutures. In the vicinity of the borehole at points aligned with the far-field least horizontal principal stress (σ_h) direction, where the maximum compressive stress concentrates, grain sutures sever at relatively low stress levels, leading to intergranular cracking. Debonded intact grains repack and produce a reduced-porosity narrow compaction band. Loose grains in the band abutting the borehole wall are then flushed out, assisted by the circulating drilling fluid. This intensifies the stress concentration ahead of the breakout tip, advancing the compaction band and lengthening the slot-shaped breakout. The process continues sequentially. Grains in the lower-porosity sandstone (11–12%) are more substantially sutured over much larger surface areas. This makes the sutures nearly as strong as the grains themselves; hence, failure requires considerably higher stresses, sufficient to bring about intragranular cracking. Consequently, and in contrast to the high-porosity sandstone, breakouts here are preceded by compaction bands of shattered and crushed grains. Both types of compaction bands have been encountered in the field and in independent laboratory experiments.

Stress-induced breakouts in vertical boreholes, as viewed in cross-section, are elongations resulting from compressive failure at and behind the borehole wall in the zones of highest stress concentration; that is, along the diameter aligned with the far-field least horizontal *in situ* stress (σ_h) direction (we will refer to it as the ‘ σ_h springline’). Gough & Bell (1981) were among the first to recognize the interrelationship between breakouts and the far-field state of stress. They analysed four-arm dipmeter logs in many Alberta oil wells and discovered a surprisingly consistent alignment of borehole breakouts with the regional σ_h direction. Gough & Bell also proposed a mechanism of failure, dependent on the state of stress, leading to breakout formation.

Several laboratory studies have shown that breakout geometries in crystalline and carbonate rocks are nearly identical to those described by Gough & Bell (Haimson & Herrick 1986; Haimson & Song 1993; Lee & Haimson 1993). Typically, these breakouts have a dog-eared shape extending in the direction of the least principal far-field horizontal stress. Optical microscopy as

well as SEM reveal that the failure mechanism leading to breakouts involves the initiation of a series of dilatant tensile microcracks simultaneously subparallel to the borehole wall and to the maximum far-field horizontal stress σ_H . Between the extended microcracks thin rock flakes develop parallel to the borehole wall, which at critical stress conditions fail and spall off sequentially into the borehole, giving rise to the typical dog-eared shaped breakouts.

A major departure from the expected borehole breakout shape and mechanism was discovered in Berea sandstone (Haimson & Song 1998). Samples of medium-porosity ($n = 17\%$) Berea sandstone developed typical shallow and broad dog-eared shaped breakouts. However, Berea sandstone of higher porosity ($n = 22\text{--}25\%$) gave rise to very long and narrow slot-shaped breakouts, oriented perpendicular to σ_H , suggesting that they had formed by a mechanism different from that previously observed. A similar type of tabular failure zones around circular holes was documented in lightly sintered glass bead bricks subjected to uniaxial stress (Bessinger *et al.* 1997).

A thorough investigation of slot-shaped borehole breakouts in high-porosity Berea sandstone (Haimson 2001, 2003; Haimson & Kovacich 2003) focused on their possible mechanisms of formation as well as on various stress and drilling parameters that could affect their development. It was shown that the high-porosity Berea sandstone developed a narrow band ahead of the tip of slot-shaped breakouts, along the σ_h springline, within which grains were debonded and compacted, reducing rock porosity. This finding supported speculations that slot-shaped breakouts are created by emptying compaction bands (Olsson 1999).

Compaction bands (CBs) are tabular zones of localized deformation that accommodate pure compaction with negligible shear offset. They were first discovered in outcrops of the Navajo sandstone, in the Kaibab monocline, Utah (Mollema & Antonellini 1996). Later, they were also identified in the Aztec sandstone, Valley of Fire State Park, Nevada (Sternlof *et al.* 2004, 2005). Both rocks are Jurassic, aeolian, highly porous ($n = 20\text{--}25\%$), and consist almost entirely of quartz grains that are relatively large (0.2–0.5 mm) and weakly bonded through suturing. Compaction bands appear to develop perpendicular to the maximum principal stress, and can extend for tens of metres, creating a thin curtain of low porosity–low permeability, which can suppress the flow of fluids through the sandstones.

In this paper we report on a series of drilling experiments conducted in St. Peter sandstone, which was selected because of its similarity to the two sandstone formations in which CBs had been discovered. The objective of the research was to study the micromechanics leading to the formation of slot-shaped breakouts. We describe the relationship between borehole breakout dimensions and *in situ* stress, and the grain-scale properties that contribute to their formation. We present evidence coupling the formation of slot-shaped borehole breakouts to compaction bands.

St. Peter sandstone properties

St. Peter sandstone extracted from a quarry in Verona, Wisconsin, USA, is an Ordovician aeolian sandstone, composed of nearly 100% well-rounded quartz grains, with a bimodal size distribution of 0.1–0.2 mm and 0.35–0.45 mm. Quartz overgrowth grain sutures, with little or no iron oxide cement, hold the sandstone skeletal structure together. The porosity of the St. Peter sandstone studied here varies from block to block, but can be summarized as being either 11–12% ('low porosity') or 16–22% ('high porosity'). The

uniaxial compressive strength averages 55 MPa, but varies from as high as 80 MPa for low-porosity samples to as low as 40 MPa for high-porosity ones.

The properties of grain size, sphericity, and composition remain unchanged regardless of porosity. On the other hand, there is a clear difference between the high- and low-porosity samples in the amount of grain suturing. The high-porosity samples have narrow, and sometimes nearly pointwise sutured contacts between grains, giving the sutured grains a characteristic hourglass appearance, and allowing for relatively large pore spaces (Fig. 1a). The low-porosity samples invariably contain broad, uneven sutures that envelop much of the grain boundaries, leaving room for smaller pore spaces between grains (Fig. 1b). This grain bonding difference proved to be crucial to understanding the difference between the breakout micromechanisms in the two porosity ranges.

Experimental setup and procedure

Irregular blocks of St. Peter sandstone were cut and surface ground into right rectangular prisms having dimensions of either 130 mm \times 130 mm \times 180 mm or 152 mm \times 152 mm \times 229 mm, depending on the available block size. Each sample was prepared with the long axis perpendicular to bedding planes. Samples were then placed into the University of Wisconsin high-capacity (3.8 MN each direction) biaxial loading apparatus, used to apply independent maximum and minimum horizontal principal stresses, σ_H and σ_h , respectively (Fig. 2). Independent servo-controlled hydraulic boosters monitored by pressure transducers supplied pressure to the two pairs of horizontal loading pistons. Thin copper shims cut to the approximate dimensions of the specimen faces and coated with a mixture of stearic acid and petroleum jelly were placed between the specimen and steel loading platens to minimize friction during loading (Labuz & Bridell 1993).

The biaxial loading apparatus was centred within a loading frame equipped with a vertically mounted hydraulic cylinder of 1.34 MN capacity, for the application of the vertical principal stress, σ_v (Fig. 2). A laboratory testing software package was used to control the servo-hydraulic system and record pressure transducer and load cell outputs. An electric drill affixed to the loading frame crosshead was used to drill a borehole through a hole in the upper loading platen. A pneumatic cylinder supplied downward drilling pressure. Penetration of the diamond coring bit

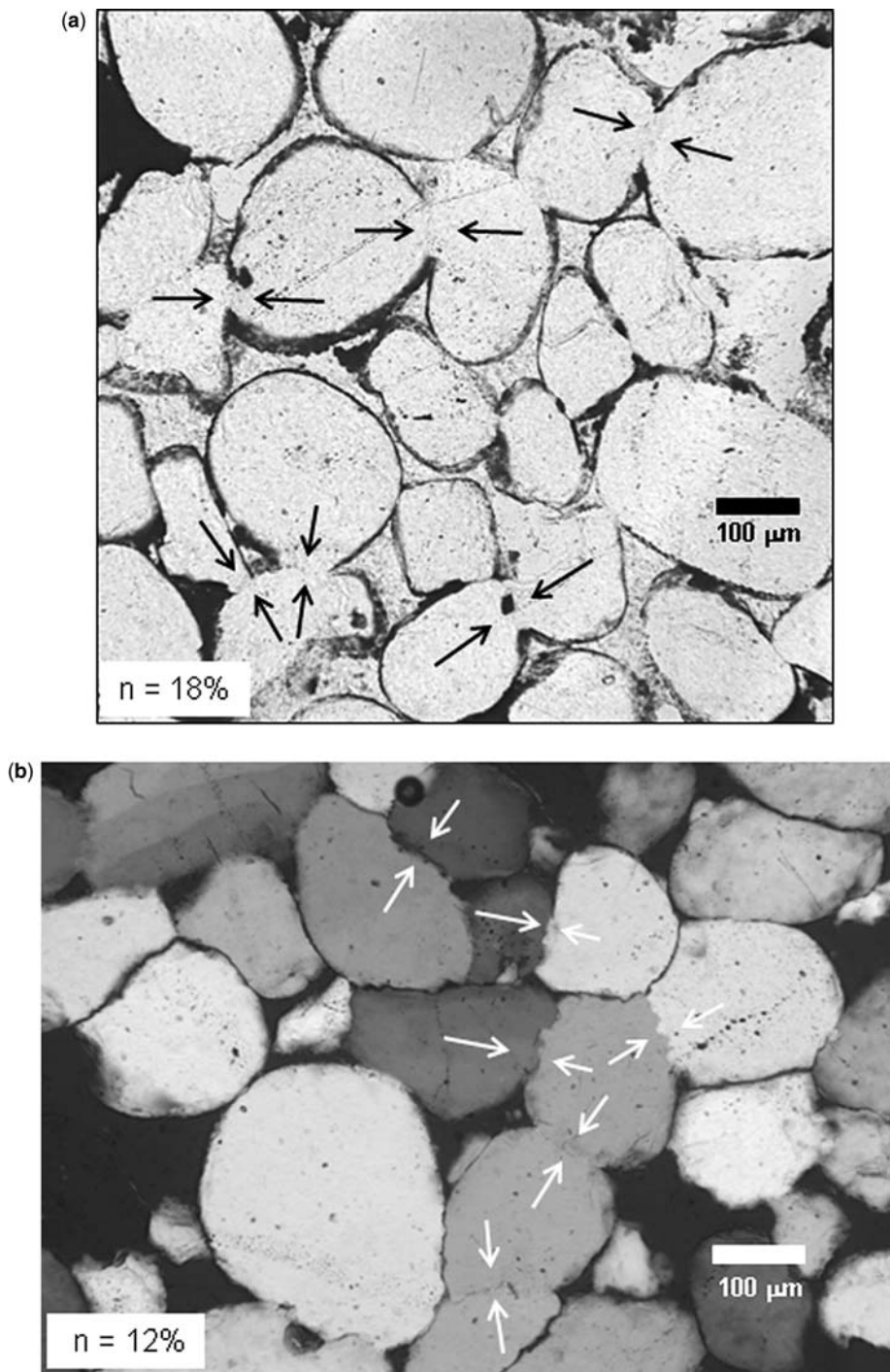


Fig. 1. (a) Plane-polarized light image of narrow, nearly pointwise grain sutures (examples indicated by arrows) in high-porosity St. Peter sandstone. (b) Cross-polarized light image of broad grain sutures (examples indicated by arrows) in low-porosity St. Peter sandstone.

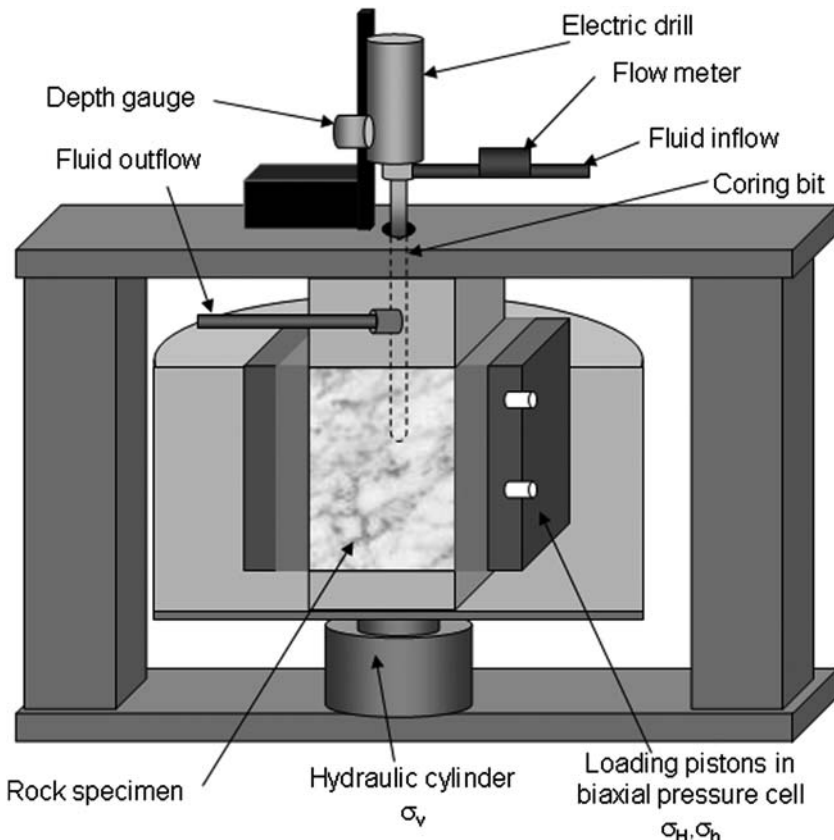


Fig. 2. Schematic illustration of the University of Wisconsin borehole stability testing assembly. Rectangular prismatic specimens are first loaded in three mutually perpendicular directions using three independent servo-control systems. Drilling is conducted while the specimen is under true triaxial stress, simulating real field conditions.

was recorded from a potentiometer depth gauge attached to the drill (Fig. 2).

Testing procedure was designed to provide a realistic simulation of *in situ* drilling, where rock is subjected to crustal stresses before drilling is conducted. Thus, testing began by first applying the pre-determined stresses to the intact specimen. All three principal stresses were increased at a constant rate of 0.1 MPa s^{-1} until they reached their prescribed magnitudes. While all three unequal principal stresses were held constant, an axial (vertical) borehole was drilled into the centre of each sandstone specimen. Water was used as drilling fluid to keep the bit cool and remove debris. Drill bit penetration was held at a constant rate for each test. Once the borehole extended to the desired depth (typically 25 mm from the bottom of the specimen), the coring bit was retracted and the drilling fluid valve was turned off. The specimen was kept

under the same far-field stresses for an additional 15–30 min, to allow for the completion of breakout formation.

As soon as a test was completed, the specimen was removed from the biaxial cell and allowed to dry in an oven at a temperature below 50°C . The borehole was then filled with epoxy to preserve its shape. Once cured, the specimen was dissected into 10 mm thick slices, to allow the measurement of breakout dimensions at different depths within the borehole. Out of selected slices, thin sections containing the breakout tips were prepared for optical microscope viewing. Breakout zones to be analysed by SEM were cut into $25 \text{ mm} \times 25 \text{ mm}$ chips, surface ground, polished with $0.1 \mu\text{m}$ diamond paste, and gold coated. Magnified optical and SEM images were used to better characterize grain size, composition, cementation, microcracking, and 2D porosity (using the commercial OptimusTM software).

Breakouts in high-porosity St. Peter sandstone

Shape, dimensions, and relationship to far-field stress conditions

Under a sufficiently high state of far-field stress, high-porosity St. Peter sandstone develops very narrow tabular or slot-shaped (nearly fracture-like) breakouts that can reach several borehole diameters in length (Fig. 3). At the borehole wall, the breakouts are invariably aligned with the least horizontal far-field stress springline. This alignment renders slot-shaped breakouts important indicators of *in situ* principal stress directions in field situations. Moreover, slot-shaped breakouts extend in the same σ_h direction. As these tabular breakouts are in a plane perpendicular to the maximum horizontal far-field stress (Fig. 3), it is expected that shear is not associated with this failure process.

A significant finding has been the discovery that slot-shaped breakouts in St. Peter sandstone extend for some distance below the bottom of the advancing hole, all along remaining orthogonal to σ_H direction (Fig. 4). This unexpected behaviour suggests that breakout initiation occurs at or near the advancing drill-bit cutting tip, along the σ_h springline. The implication here is that the stress concentration responsible for the breakout formation might be considerably more complex than that under the typically assumed plane strain conditions. (In this paper, however, we follow the currently accepted approach of employing the plane strain solution whenever stresses around boreholes are discussed.) The slot cut into the bottom of the hole could also serve as an alternative indicator of the *in situ* principal stress directions, detectable by such methods as logging-while-drilling (LWD), a tool that could potentially give a continuous record of stress direction variation with depth.

Slot-shaped breakouts have parallel edges, and an approximately constant width (1–2 mm) equal to several grain diameters, regardless of the far-field stresses applied (Fig. 3). The span of breakouts at the borehole wall is also independent of the applied stress, and only slightly larger than the breakout width. We infer that the width of slot-shaped breakouts is a material property, unrelated to the stress conditions that created the breakout.

On the other hand, the length of breakouts is highly dependent on the magnitude of the far-field horizontal principal stresses, as illustrated by Figure 3. In general, for test specimens taken from the same block of St. Peter sandstone, breakouts are observed to grow in length approximately linearly as the ratio of σ_H/σ_h increases, for either constant σ_H and σ_v or constant σ_h and σ_v (Fig. 5). The

relationship differs depending on the block porosity and grain bonding condition. The effect of σ_v appears to be minor, and has not been studied in detail.

The strong dependence of the breakout length in high-porosity St. Peter sandstone on the far-field stress ratio suggests that it could be used as an *in situ* stress magnitude indicator. To accomplish this goal for sandstone of known material properties, breakout length in field situations would have to be determined accurately, and estimates of two of the *in situ* principal stresses would have to be known. For example, the vertical stress can typically be approximated from the weight of the overlying rock at the depth of breakout, and the minimum horizontal stress can often be estimated from leak-off tests that are routinely run in oilfield wells (Zoback *et al.* 2003). The all important maximum horizontal stress is, however, not known unless specific stress measurements are undertaken, or (potentially) borehole breakout length–stress relationship is established. For now, there are at least two major difficulties with direct use of our results in field situations: the lack of known logging tools that can reliably determine breakout length, and the unknown scale effect needed to interpret our laboratory relationships in terms of *in situ* conditions. In fact, there is a paucity of field data revealing slot-shaped breakouts, for the very reason that present logging tools are not equipped to identify narrow deep radial indentations in the wellbore wall.

Micromechanics of slot-shaped breakout formation

Thin-section analysis of the breakout tip area in high-porosity St. Peter sandstone reveals one striking feature: the grains ahead of the breakout tip are predominantly intact, with little evidence of intragranular splitting or shattering. Some micro-cracking is noticeable within the grains, but not sufficient to affect their integrity. However, grains in front of the breakout tip appear to be debonded by grain boundary cracks (Fig. 6). The general lack of grain splitting suggests that the concentrated high compressive stress tangent to the breakout tip along the σ_h springline was not sufficient to cause the strong quartz grains to fail, but was adequate to break up the narrow sutured grain contacts. Once debonded, the well-rounded grains are mobile and able to repack into a tighter, less porous configuration. We infer that breakout initiates when debonded grains along the σ_h springline at the borehole wall are washed off by the circulating drilling fluid. The new shape of the borehole + breakout enhances the stress concentration at the breakout

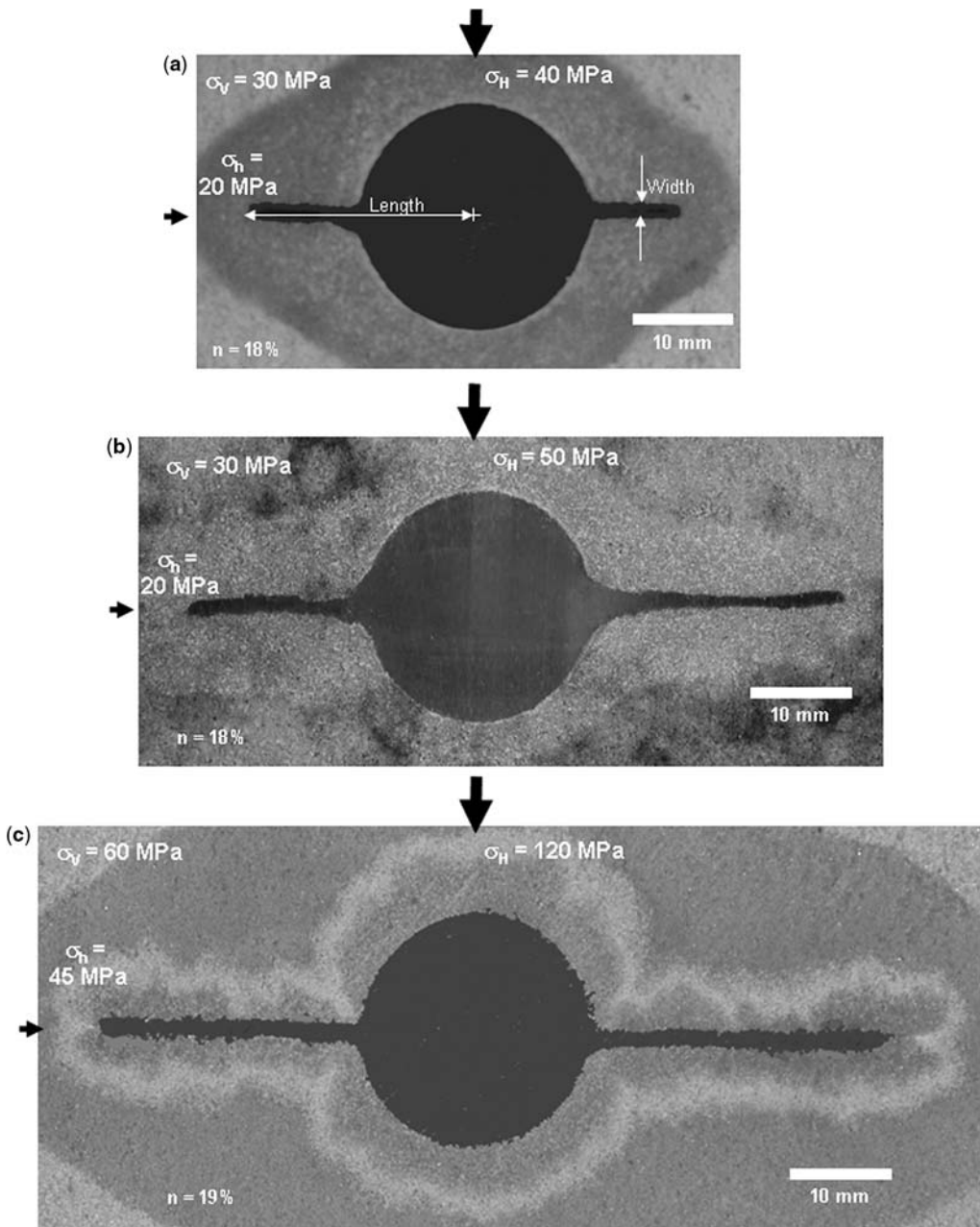


Fig. 3. (a–c) Photographs of truncated cross-sections of tested specimens showing three examples of slot-shaped borehole breakouts in high-porosity St. Peter sandstone. Porosity and specific far-field principal stresses are marked for each case. The increase in breakout length as the ratio σ_H/σ_h increases should be noted. Length and width of breakouts are defined in (a). Length is measured from the centre of the borehole to facilitate its use in dimensionless length v. far-field stress in Figure 5. The penetration into the rock of the epoxy poured in the hole to preserve the breakout (see the light-colour contouring of the penetration in (c)) shows that the narrow zones aligned with and ahead of the breakout tips are less permeable than the rest of the rock surrounding the hole and breakout. This is interpreted as a sign of reduced porosity there resulting from localized compaction.

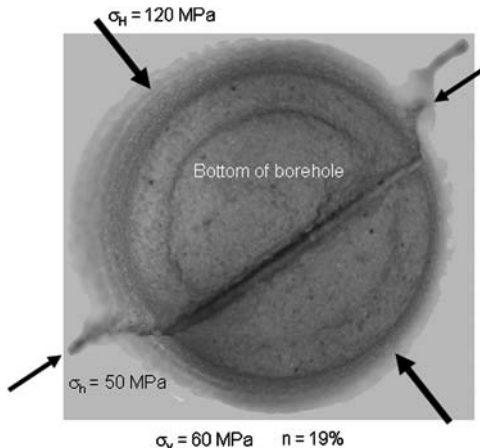


Fig. 4. Photograph, taken from above, of the lower section of the borehole in a tested specimen of high-porosity St. Peter sandstone, showing that the breakout cuts not only through diametrically opposed points along the σ_h springline along the vertical wall of the borehole, but also through the bottom of the hole.

tip, thus extending the zone of debonded grains. This process continues sequentially, creating the slot-shaped breakout. A conceptual model of the micro-mechanics of slot-shaped breakout formation is described in the Discussion.

The role of the circulating fluid (tap water in our tests) in flushing out loosened grains from the

breakout tip and thus creating the unusual shape of these breakouts was verified by testing two samples taken from the same block and subjected to identical far-field stresses, except that one was first drilled under no external pressure and only then loaded, whereas the other was drilled under far-field stress conditions like the rest of the tests described in this paper. The pre-drilled specimen did not require any circulating fluid during the application of the far-field loading, resulting in a rather short breakout; the pre-stressed specimen, in which fluid was circulated during drilling, yielded a typical slot-shaped breakout of significant length (Fig. 7).

Evidence of grain repacking in the narrow zone ahead of the breakout was obtained by determining the 2D porosity of specified areas on backscattered electron images of breakout tips. An example is shown in Figure 8. The rectangular area just ahead of a breakout tip was found to have a porosity of 15.9% (Fig. 8a; pores are the black areas). Similar rectangular zones in the same sample away from the borehole and the breakout had an average porosity of 18.1% (Fig. 8b), suggesting that the grains in the narrow zone ahead of the breakout tip have been repacked to form a reduced-porosity compacted zone or band. It should be noted that the SEM image of the reduced-porosity band ahead of the breakout tip (Fig. 8a) reveals under higher magnification that although intact, some grains do show signs of microcracking as a result of the high stress concentration, albeit not sufficient to create splitting.

Additional indication of reduced porosity ahead of the breakout tip came from an unexpected source. Some cross-sections of breakouts showed that the thin epoxy, used to fill the boreholes after testing so as to preserve the induced breakouts, penetrated some distance into the rock before solidifying, but the amount of penetration in the zone ahead of the breakout tip was clearly limited. An example is shown in Figure 3c. The extent of epoxy penetration is contoured by the light colour boundary. The epoxy coming out of the breakout tip flows to the left and to the right, with only a minimal amount straight ahead in the σ_h direction. We interpret this flow pattern as an indication of the loss of permeability ahead of the breakout tip, resulting from the reduced porosity within the compacted band.

Olsson (1999) suggested that slot-shaped breakouts are emptied CBs, a geological structure that had been discovered in outcrops of the Navajo sandstone, a high-porosity, medium to large grain size, aeolian rock composed almost exclusively of quartz grains held together by sutured contacts (Mollema & Antonellini 1996). Compaction bands are planar features that stand in positive relief in the outcrops as a result of their increased resistance

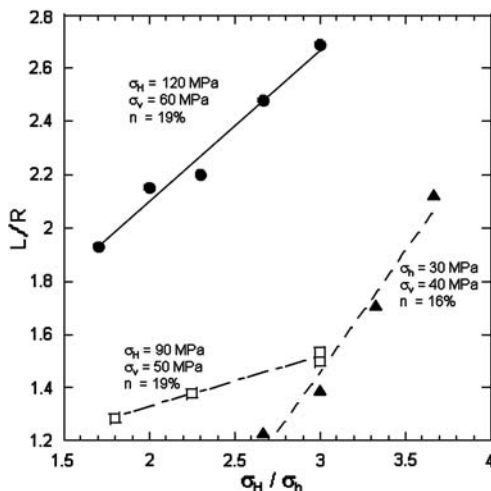


Fig. 5. Dimensionless plot showing the variation of the normalized breakout length (L) with respect to borehole radius (R) as a function of the horizontal stress ratio σ_H / σ_h for given conditions of porosity (n), σ_v and either constant σ_H or constant σ_h , in high-porosity St. Peter sandstone.

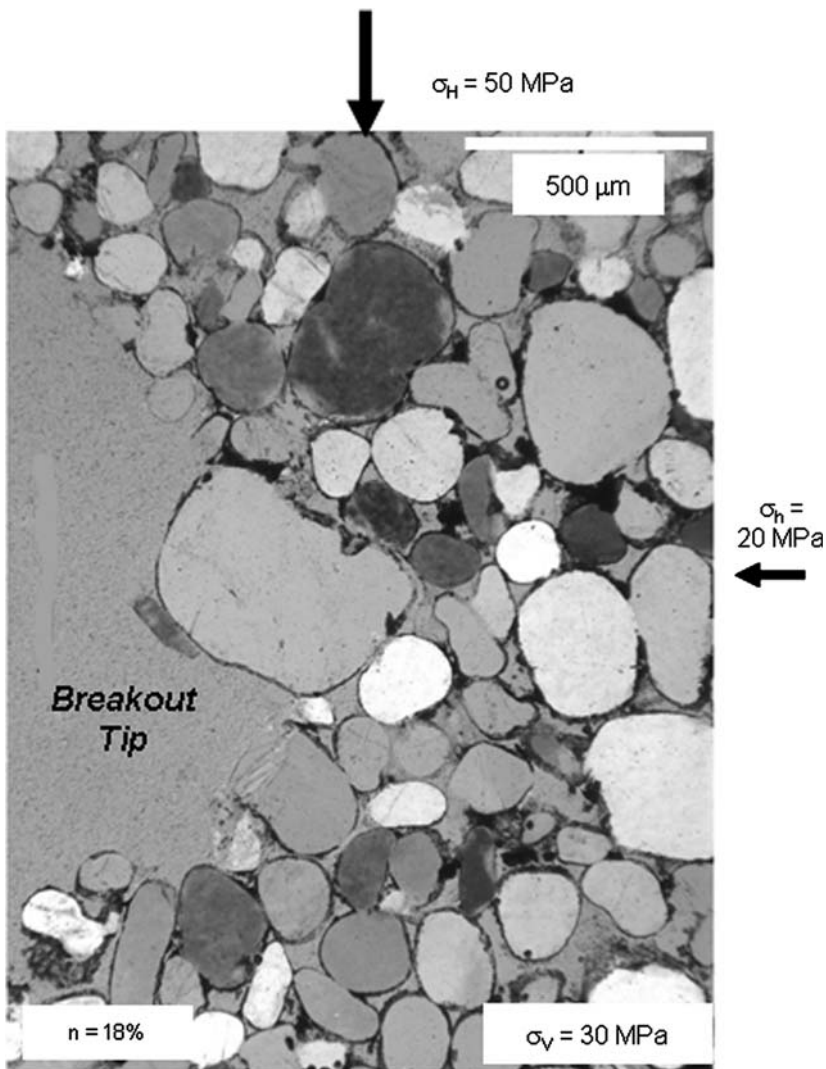


Fig. 6. Cross-polarized light image of a breakout tip in high-porosity St. Peter sandstone, showing that grains ahead of the tip appear to be intact.

to weathering. Mollema & Antonellini defined CBs as tabular zones of localized deformation that accommodate pure compaction, leading to reduced porosity. Compaction bands are thought to have been formed perpendicular to the major principal stress, as no shear offset is observed.

St. Peter sandstone is similar to the Navajo sandstone, in that it is also aeolian, and it consists almost 100% of medium to large quartz grains bonded by sutured contacts. We found planar features of positive relief in blocks of St. Peter sandstone as they were retrieved from the quarry (Fig. 9). These suspected CBs are perpendicular to bedding

planes, and therefore assumed to have been vertical upon formation. From the sample photographed in Figure 9 we prepared a section for backscattered electron imaging. The projected area of the narrow positive relief feature showed that its porosity (17.2%) was substantially lower than in the areas adjacent to it on either side (20.6% and 21.1%, respectively, Fig. 10a), a strong indication that the zone is indeed a compaction band. In addition, by magnifying a small section of the compacted zone (Fig. 10b) grains appear intact, just as in Figure 6 or 8. Comparing Figure 8 with Figure 10, we note in each a similar zone of localized deformation

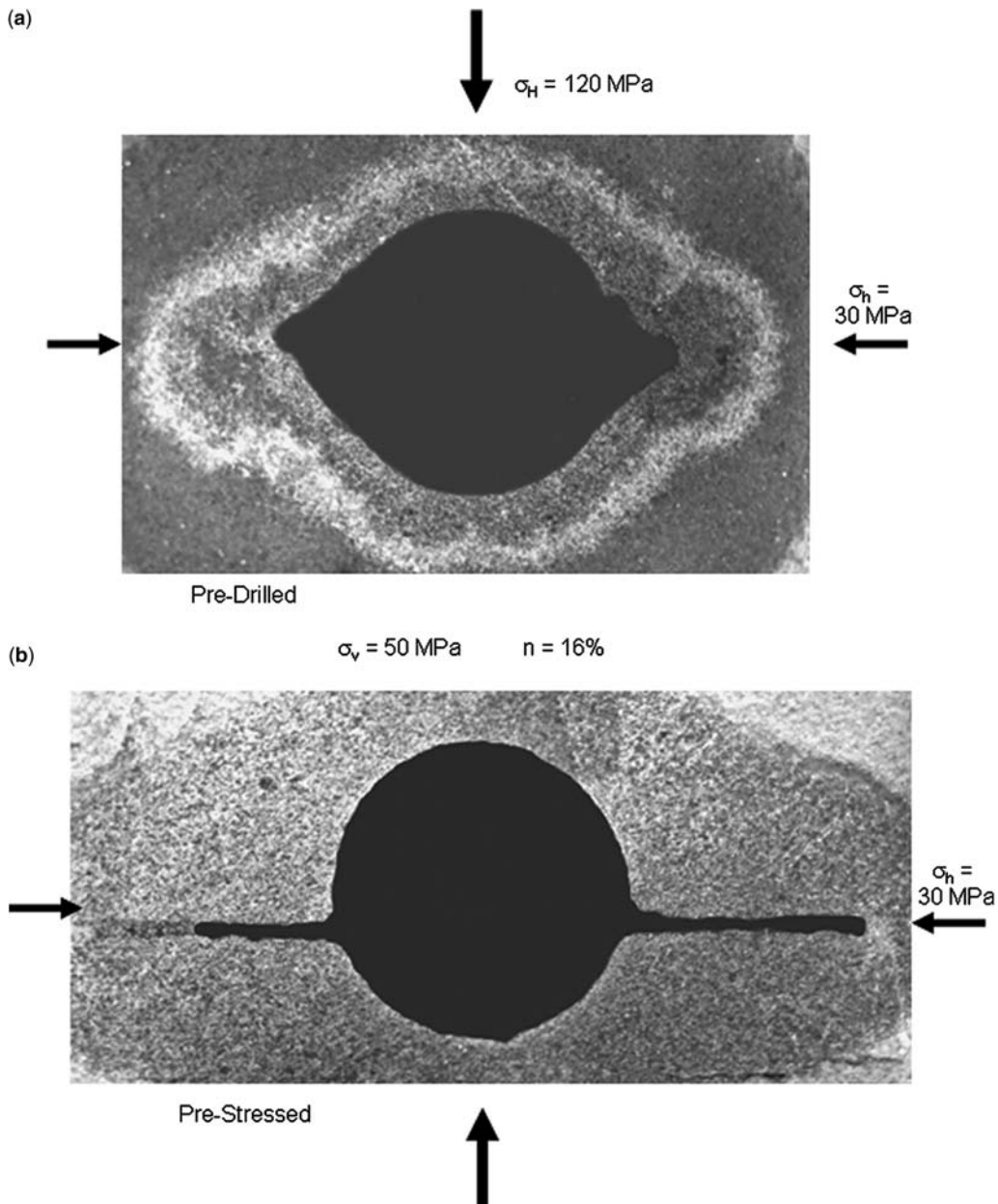


Fig. 7. Photographs of truncated cross-sections of tested specimens, showing borehole breakouts in two high-porosity St. Peter sandstone samples taken from the same block and subjected to identical far-field stresses. (a) Breakout in a sample that was first drilled through, and thereafter subjected to far-field stresses while the hole was dry (pre-drilled). (b) Breakout in a sample that was first subjected to the far-field stresses, and only then was drilled into using water as circulation fluid.

within a narrow band, analogous to the compaction bands in Navajo sandstone (Mollema & Antonellini 1996). In both the breakout tip area and the natural CB we observe localized compaction, which in

these high-porosity (*c.* 20%) St. Peter sandstone samples is formed by loosening of grain contacts that allows repacking with very little grain cracking or crushing.

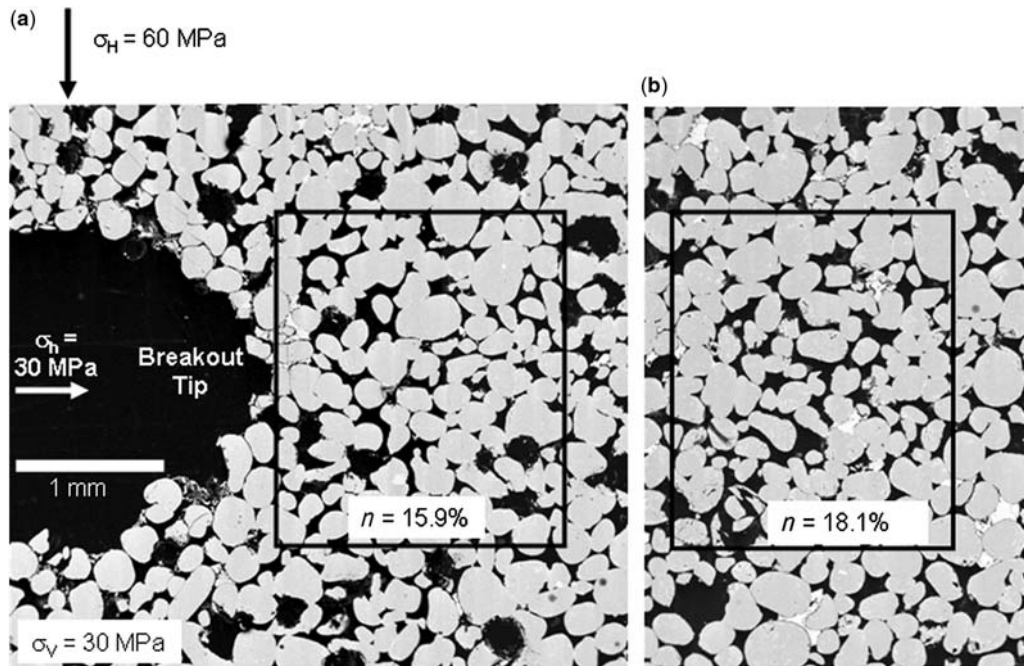


Fig. 8. (a) Backscattered electron image of the area ahead of the breakout tip in a high-porosity sample of St. Peter sandstone reveals mainly intact grains. Far-field stresses are marked on the image. The 2D porosity (obtained by using commercial software that measures and computes the percentage of the black areas, representing pores, out of the total area of the marked rectangle,) is 15.9%. (b) Similar rectangular areas of the tested sample away from the breakout tip, like the one shown, indicate an average 2D porosity of 18.1%.

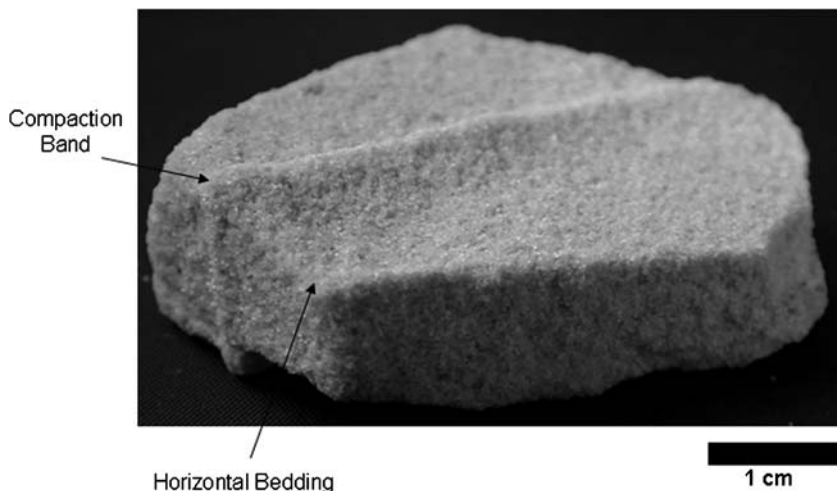


Fig. 9. Photograph of a vertically oriented band of apparently compacted grains in positive relief with respect to horizontal bedding in a hand sample of St. Peter sandstone.

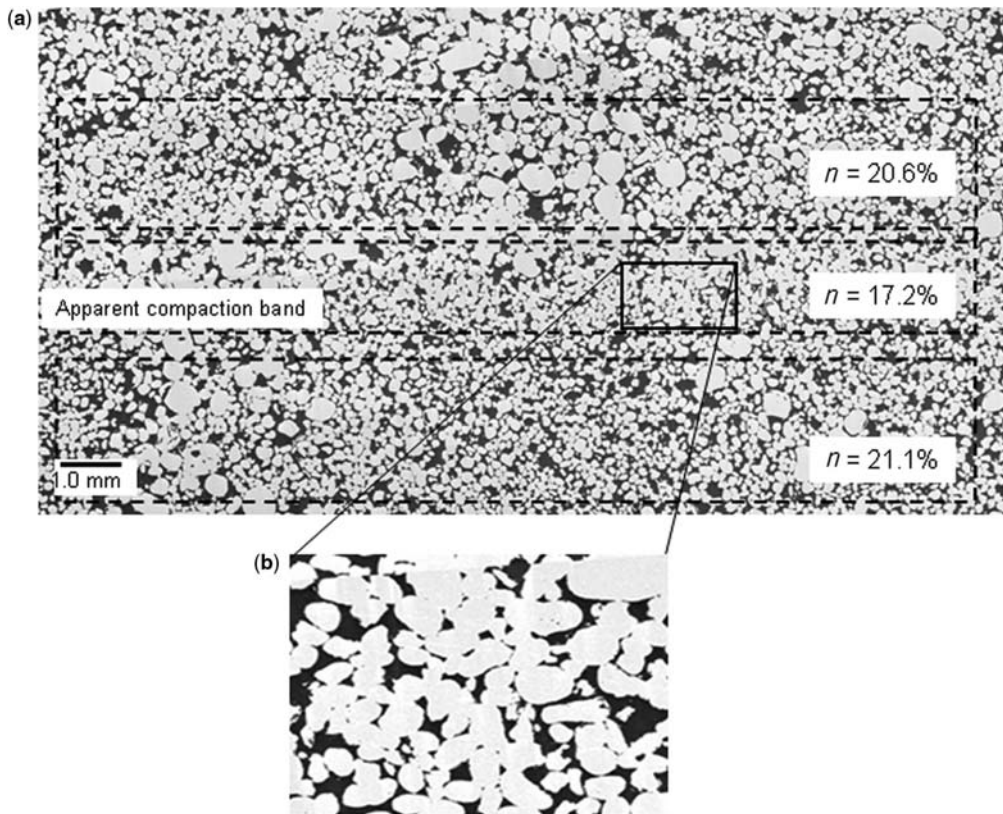


Fig. 10. (a) Backscattered electron image of an apparent natural compaction band in a St. Peter sandstone hand sample in horizontal cross-section. Three zones are shown, each framed by a dashed-line box. The 2D porosity within the band (middle box) is 17.2%; adjacent zones on both sides of the band have an average porosity of 21%. (b) A close-up view of a representative small section of the compacted band shows mainly intact grains.

Breakouts in low-porosity St. Peter sandstone

Shape, dimensions, and relationship to far-field stress conditions

Breakouts in low-porosity St. Peter sandstone are nearly identical in shape to those of the high-porosity rock. They are narrow and tabular, and have an equally narrow span at the borehole wall (Fig. 11). The breakouts increase in length with the level of the stress ratio σ_H/σ_h for given σ_H and σ_v (Fig. 12). However, for similar far-field stress conditions breakout lengths in the low-porosity rock are much shorter than in the high-porosity variety. A comparison of Figures 6 and 13 reveals, for example, that for the stress ratio of σ_H/σ_h of 3 : 1, and $\sigma_H = 100$ MPa and $\sigma_v = 50$ MPa, the normalized breakout length in low-porosity St. Peter sandstone is about 1.2 : 1; for the same stress ratio in high-porosity rock, for

which $\sigma_H = 90$ MPa and $\sigma_v = 50$ MPa, the normalized breakout length averages 1.52 : 1, whereas for $\sigma_H = 120$ MPa and $\sigma_v = 60$ MPa, it is 2.7 : 1. The shorter breakout length in low-porosity St. Peter sandstone is attributed to the higher resistance to failure resulting from the increased density, enhanced grain contact suturing (Fig. 1), and greater compressive strength (see the section describing the St. Peter sandstone properties).

As in the case of the higher-porosity St. Peter sandstone, breakouts are *c.* 1–2 mm in width over the entire breakout regardless of stress condition, and breakout length decreases near the end of the borehole, extending a short distance below the bottom of the hole.

Micromechanics of slot-shaped breakout formation

Although the macroscopic appearance of breakouts in the low-porosity St. Peter sandstone is similar to

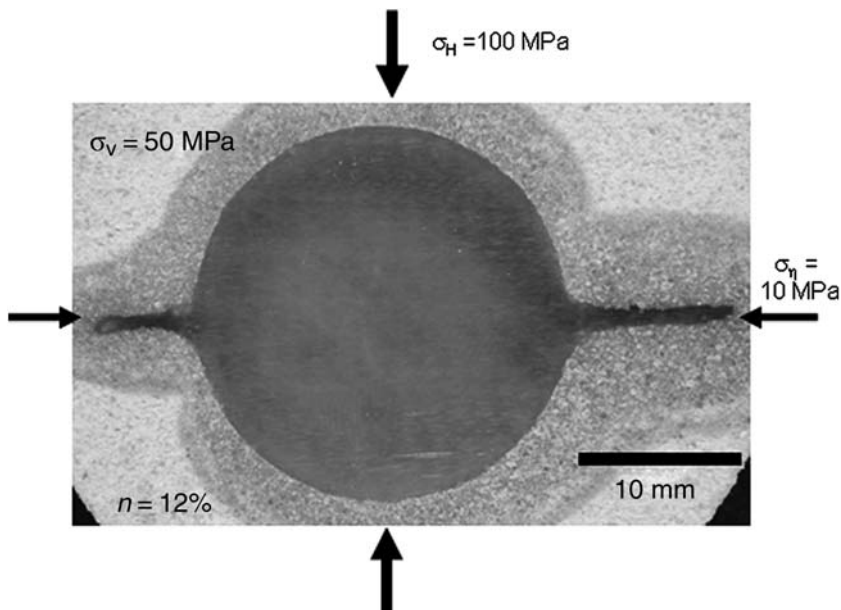


Fig. 11. Photograph of a truncated cross-section of a tested specimen showing a typical slot-shaped borehole breakout in a low-porosity St. Peter sandstone sample. Far-field principal stresses are marked in the figure. A rough comparison with Figure 3 suggests that to achieve the same breakout length a low-porosity sample would require considerably higher far-field stress ratios.

that in high-porosity samples, thin-section analysis reveals a striking difference. Whereas little evidence of intragranular microcracking is exhibited in high-porosity samples, the low-porosity

sandstone reveals a long and narrow band of cracked and crushed grains ahead of the breakout tip. The crushed zone has the same width as the breakout, and can extend for a considerable distance (Figs 13 & 14). This is in stark contrast to the intact compacted grains observed ahead of breakouts in high-porosity St. Peter sandstone. Figure 13b demonstrates in greater detail the localized characteristic of grain crushing, with many of the adjacent grains on both sides being merely cracked. Within a distance of a few grain diameters even the cracking disappears and the condition there is seemingly unaffected by the forces that formed the crushed band.

The extensive grain crushing observed along the σ_h springline indicates that failure is not restricted to the grain contact sutures as was the case in the high-porosity St. Peter sandstone. One explanation for the marked difference in the grain-scale behaviour is the extent to which grains are sutured in low-porosity St. Peter sandstone. Unlike the high-porosity samples, in which grains are bonded by narrow, nearly point-wise grain sutures (Fig. 1a), the low-porosity St. Peter sandstone is held together by broad grain sutures created by greater amounts of pressure solution and quartz recrystallization (Fig. 1b). As the sutures are composed of quartz, and as they encompass much of the grain surface area, they are nearly identical in strength to the grains themselves. Thus, sufficiently

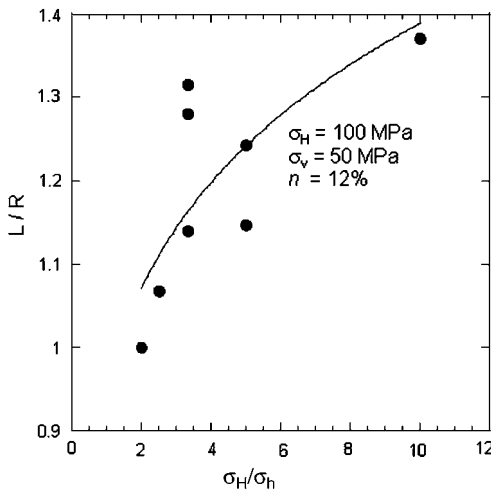


Fig. 12. Dimensionless plot showing the variation of the normalized breakout length (L) with respect to borehole radius (R) as a function of the horizontal stress ratio σ_H/σ_h for constant porosity (n), σ_v and σ_H in low-porosity St. Peter sandstone.

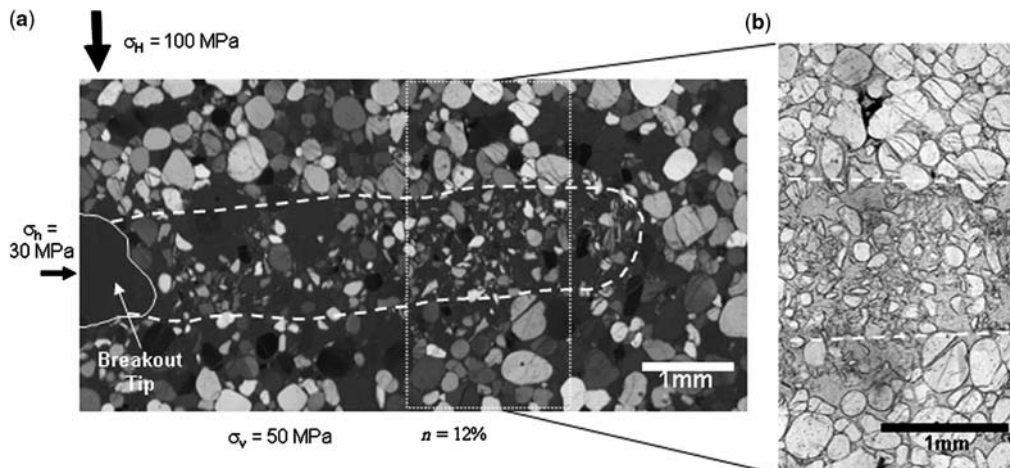


Fig. 13. (a) Cross-polarized light image of the area ahead of a slot-shaped breakout in low-porosity St. Peter sandstone. An extended zone, along the σ_h springline, of similar width to that of the breakout, and consisting of mainly crushed grains, presumably caused by localized compaction, is contoured by a dashed line. Around this zone grains are predominantly intact, although some are cracked. (b) Plane-polarized light image of an enlarged segment (marked by dotted line) of (a). The difference in grain condition between the compacted and crushed zone (contoured by dashed lines) and the two adjacent areas is striking. In the adjacent areas this image reveals the extent of cracking in the mainly intact grains.

high tangential stress acting normal to the σ_h springline brings about cracking and crushing of both grains and grain sutures ahead of the breakout tip. Crushed material is removed by the circulating drilling fluid, forming and then extending sequentially slot-shaped breakouts in low-porosity St. Peter sandstone.

A backscattered electron image of a breakout in low-porosity St. Peter sandstone (Fig. 14a) depicts an entire tabular narrow breakout and an equally narrow and long band of crushed grains just ahead of its tip. Details of the crushed-grain compaction band are shown in Figure 14b. Some of the grains within the band are intact, but most are shattered or crushed. On the outside of the band, even in its immediate vicinity, grains are intact, illustrating the extent to which the compaction band is localized.

The examples shown in Figures 13 and 14 provide perhaps the strongest visual evidence that compaction bands develop ahead of the advancing breakout tip. The zone of intensely fractured grains ahead of the breakout tip may be analogous to the grain crushing and collapse of porosity in laboratory-induced compaction bands observed, for example, in Bentheim sandstone (Klein *et al.* 2001; Vajdova & Wong 2003).

Figure 14 reveals no discernible fracturing pattern within the crushed zone, because of the severe grain damage. However, near the end of the crushed zone farthest from the borehole,

individual tensile cracks perpendicular to the σ_h springline are visible, an indication of how grain crushing occurs within the band: high compressive tangential stress in the σ_h direction along the σ_h springline splits the grains, some of which may then crack again several times as grain fragments crowd into each other within the narrow band.

Owing to the significant reduction in grain size within the crushed zone, removal of some fine-grained material even during the most careful preparation of thin sections or SEM specimens was inevitable. Hence, no 2D porosity measurements would have been valid within the compaction bands ahead of breakouts in low-porosity St. Peter sandstone.

Discussion

Our experimental results lead us to suggest a conceptual model of the micromechanical process that results in slot-shaped breakouts (Fig. 15). Drilling of a vertical borehole, under a state of far-field stress beyond a certain threshold, brings about the break-up of grain contact sutures within a narrow band straddling the σ_h springline (Fig. 15a). This allows the now debonded and loosened rounded quartz grains to repack, forming a reduced-porosity compaction band (Fig. 15b). The debonded grains close to the borehole wall are ejected and more are removed by the drilling circulating water,

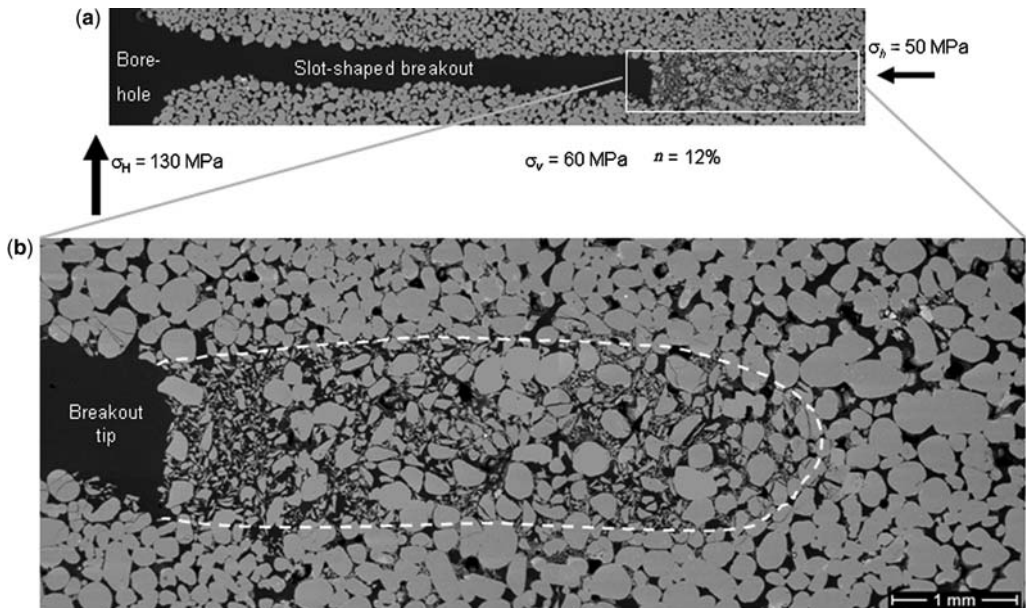


Fig. 14. (a) Backscattered electron image of an entire slot-shaped breakout in low-porosity St. Peter sandstone. (b) A close-up image of the breakout tip area reveals a zone (contoured by dashed line) of mainly crushed or shattered grains just ahead of the tip and in line with the breakout. The grains in the surrounding rock are mainly intact.

carving a slot-like opening or breakout (Fig. 15c). The enhanced high stress concentration at the tip of the initial breakout causes additional grains to debond, extending the compaction band. Thus, additional debonded grains are evacuated, causing the breakout to grow. The sequential process continues until, as the narrow breakout deepens and the drilling advances sufficiently far from the cross-section considered, the circulating fluid loses its capacity to remove debonded grains, especially when they interlock in a stable arch. This, we speculate, brings about the final breakout length.

We have identified two types of CBs that precede and shape slot-like breakouts in St. Peter sandstone. In the high-porosity variety, CBs appear to consist of predominantly whole grains, some of which may be microcracked but still intact. Grains have been debonded and rearranged to yield a localized compacted zone. In the low-porosity case, CBs are narrow zones of cracked and crushed grains. How do these two types of CBs compare with other observations? Field compaction bands in the Navajo and the Aztec sandstones are zones of localized deformation of intact grains, some of which may be microfractured (Mollema & Antonellini 1996; Sternlöffel *et al.* 2005). Compaction bands found in high-porosity St. Peter sandstone are largely in agreement with

these field observations. However, laboratory-induced compaction bands in triaxial tests of Castlegate and Bentheim sandstones are predominantly zones of crushed grains (Olsson 1999; Klein *et al.* 2001; Vajdova & Wong 2003). These are similar to compaction bands ahead of breakout tips in low-porosity St. Peter sandstone.

Vajdova & Wong (2003) conducted triaxial tests on notched samples of Bentheim sandstone. The notches closely resemble initial breakouts in boreholes. Vajdova & Wong found that as the maximum compressive stress perpendicular to the notch reaches a threshold magnitude a short compaction band develops at the notch tip. As loading continues the CB advances sequentially in a direction normal to the maximum stress until it covers the entire cross-section of the specimen. The CB is thin, only a few grain diameters in width, and consists of cracked and crushed grains. Vajdova & Wong's experiments provide strong support for our findings both with respect to CB initiation and its episodic elongation.

Katsman & Aharonov (2006) conducted a theoretical investigation of the compaction band phenomenon using a version of the spring network model. Among simulations conducted was one representing a homogeneous sample with a thin hollow opening, an attempted 2D

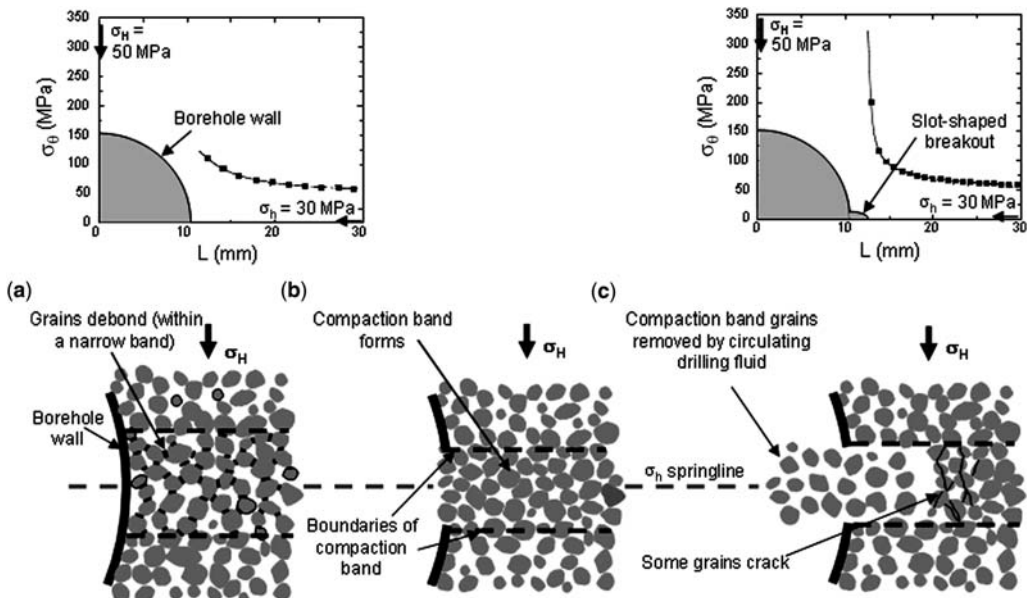


Fig. 15. A conceptual model of the micromechanism leading to slot-shaped breakouts in quartz-rich sandstones (after Lee 2005). (a) Upon the drilling of a vertical borehole the horizontal far-field state of stress (such as shown in the upper diagram) creates a high tangential stress (σ_0) concentration along the σ_h springline. If σ_0 along that line and in the vicinity of the borehole wall is sufficiently high, sutured contacts between quartz grains within a narrow band fail and grains are debonded. (In the low-porosity St. Peter sandstone sutures cover most of the surface areas of the grains, making them practically as strong as the grains themselves. In that case higher σ_0 will be required to debond grains, but in the process the grains will also crack and shatter.) (b) The debonded and loose quartz grains within the band are now free to repack and form a reduced-porosity compaction band. (c) The debonded grains adjacent to the borehole wall are removed with the help of the drilling circulating fluid. This forms the initial breakout, which intensifies the tangential stress concentration ahead of its tip (see upper diagram), and that causes additional layers of grains within the narrow band to debond. Some grains crack owing to the higher σ_0 , but still maintain their integrity. Circulating fluid assists in evacuating the newly debonded grains, lengthening the slot-shaped breakout. The process continues sequentially until, we speculate, a balance is reached between the stress condition at the breakout tip, the efficiency of the circulating fluid flowing into the narrow deep opening as the drilling bit advances away from the cross-section considered, and the tendency of grains to form stable arches within the compaction band, at which point the breakout growth comes to an end.

replica of our experiments involving a borehole in a uniform sandstone block. Uniaxial compressive loading was increased incrementally. Beyond a certain stress magnitude, a compaction band initiated and propagated stepwise in a direction perpendicular to the applied stress. Although the far-field stress in our tests was held constant throughout the experiment, the maximum stress at the breakout tip did increase incrementally as the breakout length grew. Hence, we consider the experimental and the simulated loading conditions to be similar. The results of Katsman & Aharonov reinforce our interpretation of the CB initiation and growth ahead of the breakout tip. A spring network model simulation of a notched specimen under uniaxial loading similarly resulted in a CB initiation and incremental propagation scenario, in support of the experimental findings of

Vajdova & Wong (2003), and indirectly of the borehole breakout case.

The observation that slot-shaped breakouts are found not only on opposite sides of boreholes, along the σ_h springline, but also under the bottom of the hole, connecting the two sides, is not simply a surprising feature of this failure process. It is also potentially an important finding that may require a reanalysis of the stress conditions controlling breakouts. It appears now that slot-shaped breakouts initiate right at the bottom of the hole, where stresses are concentrated differently from anywhere outside of the hole-bottom influence. Currently, stresses at a point around a borehole in elastic rock are assumed to be defined by the well-known Kirsch solution (Jaeger & Cook 1979), in which the assumption is made that the point in question is well away from the bottom of the hole

and that a 2D (plane strain) approach is applicable. If breakouts initiate near or at the bottom of the hole the stresses there cannot be reduced to a 2D domain and cannot be obtained analytically; they have to be estimated numerically. At present, there is no experimental evidence that the dog-eared breakouts that are typically induced in crystalline rocks also originate at the bottom of the hole. If this were the case, however, some existing models relating *in situ* stress to breakout dimensions based on the Kirsch solution (e.g. Haimson & Chang 2002) would have to be reassessed.

Conclusions

Breakouts in vertical holes drilled into St. Peter sandstone are long, tabular, and very narrow (several grain diameters), and perpendicular to the maximum horizontal stress σ_h . Ahead of the breakout tip a zone is observed that is similar in width to the breakout, and that registers substantially lower 2D porosity than the host rock. We infer that the high stress concentration along the σ_h springline breaks the sutured-grain contacts, allowing them to repack and reduce porosity without noticeable shear. The long and narrow zone matches the description of field CBs, and appears to precede the breakout formation and extension. Loosened grains in the compacted band at the borehole wall are flushed off in episodic fashion, aided by the circulating water, creating the slot-shaped breakout, which can better be described as an emptied CB. We identify two grain conditions within the CB ahead of the breakout tip. In the higher-porosity St. Peter Sandstone (16–22%) the bimodal rounded grains are spot-sutured. Far-field stresses that bring about grain debonding and repacking are at levels lower than those required to induce grain damage, forming a CB that is almost free of grain cracking. In the lower-porosity St. Peter sandstone (11–12%), grains are sutured over large surface areas (which is the reason for the lower porosity), so that the stress level required to debond them is also sufficient to crack and crush the grains themselves. Here the CB is dominated by split and crushed grains. Both types of compaction bands have been observed either in the field or in the laboratory. Experiments by others with notched samples under triaxial testing, and a powerful simulation approach, support our finding that compaction bands in St. Peter sandstone precede slot-shaped breakouts, which are formed by flushing off grains from within these bands.

This work was supported by the US Department of Energy, Office of Basic Energy Science, Geosciences Research Program grant DE-FG02-98ER14850. Some of the work

reported here was published in the informal *Proceedings of the 5th North American Rock Mechanics Symposium* (University of Toronto Press, pp. 1365–1371, 2002).

References

- BESSINGER, B. A., LIU, Z., COOK, N. G. W. & MYER, L. R. 1997. A new fracturing mechanism for granular media. *Geophysics Research Letters*, **24**, 2065–2068.
- GOUGH, D. I. & BELL, J. S. 1981. Stress orientations from oil-well fractures in Alberta and Texas. *Canadian Journal of Earth Sciences*, **18**, 638–645.
- HAIMSON, B. C. 2001. Fracture-like borehole breakouts in high-porosity sandstone: are they caused by compaction bands? *Physics and Chemistry of the Earth (A)*, **26**, 15–20.
- HAIMSON, B. C. 2003. Borehole breakouts in Berea sandstone reveal a new fracture mechanism. *PAGEOPH*, **160**, 813–831.
- HAIMSON, B. C. & CHANG, C. 2002. True triaxial strength of the KTB amphibolite under borehole wall conditions and its use to estimate the maximum horizontal *in situ* stress. *Journal of Geophysical Research*, **107**, 2257–2270.
- HAIMSON, B. C. & HERRICK, C. G. 1986. Borehole breakouts—a new tool for estimating *in situ* stress? In: STEPHANSSON, O. (ed.) *Rock Stresses and Rock Stress Measurement. Proceedings of International Symposium on Rock Stress*. CENTEK, Luleå, Sweden, 271–281.
- HAIMSON, B. C. & KOVACICH, J. 2003. Borehole instability in high-porosity Berea sandstone and factors affecting dimensions and shape of fracture-like breakouts. *Engineering Geology*, **69**, 219–231.
- HAIMSON, B. C. & SONG, I. 1993. Laboratory study of borehole breakouts in Cordova Cream: a case of shear failure. *International Journal of Rock Mechanics & Mining Sciences & Geomechanics Abstracts*, **30**, 1047–1056.
- HAIMSON, B. C. & SONG, I. 1998. Borehole breakouts in Berea sandstone: two porosity-dependent distinct shapes and mechanisms of formation. In: *Proceedings SPE/ISRM Rock Mechanics in Petroleum Engineering*, Vol. 1. Society of Petroleum Engineers, Richardson, TX, 229–238.
- JAEGER, J. C. & COOK, N. G. W. 1979. *Fundamentals of Rock Mechanics*, 3rd edn. Chapman and Hall, New York.
- KATSMAN, R. & AHARONOV, E. 2006. A study of compaction bands originating from cracks, notches, and compacted defects. *Journal of Structural Geology*, **28**, 508–518.
- KLEIN, E., BAUD, P., REUSCHLÉ, T. & WONG, T.-F. 2001. Mechanical behavior and failure mode of Bentheim sandstone under triaxial compression. *Physics and Chemistry of the Earth, Part A*, **26**, 21–25.
- LABUZ, J. F. & BRIDELL, J. M. 1993. Reducing frictional constraints in compression testing through lubrication. *International Journal of Rock Mechanics & Mining Sciences & Geomechanics Abstracts*, **30**, 451–455.

- LEE, H.-K. 2005. *Borehole breakouts in arkosic sandstones and quartz-rich sandstones*. PhD thesis, University of Wisconsin.
- LEE, M. Y. & HAIMSON, B. C. 1993. Laboratory study of borehole breakouts in Lac du Bonnet granite: a case of extensile failure mechanism. *International Journal of Rock Mechanics & Mining Sciences & Geomechanics Abstracts*, **30**, 1839–1845.
- MOLLEMA, P. N. & ANTONELLINI, M. A. 1996. Compaction bands: a structural analog for anti-mode I cracks in aeolian sandstone. *Tectonophysics*, **267**, 209–228.
- OLSSON, W. A. 1999. Theoretical and experimental investigation of compaction bands in porous rock. *Journal of Geophysical Research*, **104**, 7219–7228.
- STERNLOF, K. R., CHAPIN, J. R., POLLARD, D. D. & DURLOFSKY, L. J. 2004. Permeability effects of deformation band arrays in sandstone. *AAPG Bulletin*, **88**, 1315–1329.
- STERNLOF, K. R., RUDNICKI, J. W. & POLLARD, D. D. 2005. Anti-crack inclusion model for compaction bands in sandstone. *Journal of Geophysical Research*, **110**, B11403, doi:10.1029/2005JB003764.
- VAJDOVA, V. & WONG, T.-F. 2003. Incremental propagation of discrete compaction bands: acoustic emission and microstructural observations on circumferentially notched samples of Bentheim. *Geophysics Research Letters*, **30**, 14, article 1775.
- ZOBACK, M. D., BARTON, C. A., BRUDY, M. ET AL., 2003. Determination of stress orientation and magnitude in deep wells. *International Journal of Rock Mechanics & Mining Sciences*, **40**, 1049–1076.

Models for compaction band propagation

J. W. RUDNICKI

Department of Civil and Environmental Engineering, Northwestern University, Evanston,
IL 60208-3109, USA (e-mail: jwrudn@northwestern.edu)

Abstract: A compaction band is modelled as a thin, ellipsoidal heterogeneity with an imposed inelastic compactive strain and different elastic moduli from the surrounding matrix. Previously published results are used to determine the stress state in the band. For a wide variation of properties, stress conditions, and inelastic strain, the stress state in the band for aspect ratios observed in the field, 10^{-3} – 10^{-4} , is indistinguishable from the result in the zero aspect ratio limit. In this limit, the compressive stress immediately adjacent to the band tip is roughly 10–100 times the far-field stress for parameters representative of field conditions. This value is relatively insensitive to the elastic mismatch between the band and the surrounding material, and is primarily controlled by the ratio of the far-field stress to twice the shear modulus times the inelastic compactive strain. This ratio is inferred to be about 0.02–0.05 from published field results, but may be several times larger for laboratory specimens. The ratio of tip to far-field stress increases with decrease of band shear modulus and becomes unbounded if both the shear modulus and aspect ratio go to zero. A combined anti-crack-dislocation model, in which a compactive relative displacement $2h$ is specified in the centre of the band and uniform traction elsewhere, predicts that for growth at constant energy release rate h is proportional to \sqrt{L} where L is the half-length of the band. For an energy release rate of 40 kJ m^{-2} , inferred in an earlier study from field observations and comparable with compaction energies inferred from laboratory tests on circumferentially notched compression samples, the constant of proportionality is consistent with that inferred from laboratory observations and earlier field data.

In brittle rocks, shear deformation in localized zones is typically accompanied by dilation (porosity increase) or compaction (porosity decrease). In a limiting case, localized, roughly planar zones of solely compaction, without shear, can occur perpendicular to the maximum compressive stress. Such structures, called compaction bands, have been identified in porous sandstone formations in the field (Mollema & Antonellini 1996; Sternlof *et al.* 2005; Sternlof 2006), in axisymmetric compression experiments on several porous sandstones (Olsson 1999; Olsson & Holcomb 2000; Wong *et al.* 2001; Holcomb & Olsson 2003; Baud *et al.* 2004; Förtin *et al.* 2006) and emanating from borehole breakouts in laboratory experiments on porous sandstone (Haimson & Song 1998; Haimson 2001, 2003; Klaetsch & Haimson 2002; Haimson & Lee 2004). Although this mode of localized deformation has attracted attention in rocks only recently, it has been observed in a variety of other porous materials, including metal foams (Bastawros *et al.* 2000; Park & Nutt 2001), polycarbonate honeycomb (Papka & Kyriakides 1998), snow (J. Desrues, pers. comm.), ice (Kirby *et al.* 1992) and large deformation of porous elastomers (Kinney *et al.* 2001). Both laboratory (Holcomb & Olsson 2003; Vajdova *et al.* 2004) and field studies (Antonellini & Aydin 1994, 1995; Sternlof *et al.* 2004; Sternlof 2006) have shown that compaction bands can inhibit flow across them. The porous rocks in which these

bands have been observed are typical of reservoir rocks. The presence of compaction bands in such formations can form impermeable barriers and adversely affect the use of these rocks for a variety of applications, such as aquifer management, hydrocarbon recovery and storage, and CO₂ sequestration (Wawersik *et al.* 2001).

There are many differences between the structures observed in the laboratory and in the field but an obvious one is their length. The lengths of bands observed in the field (Mollema & Antonellini 1996; Sternlof *et al.* 2005; Sternlof 2006) are of the order of tens of metres. In contrast, the lengths of the bands in the experiments are limited to the width of the specimen, a few centimetres. In addition, the bands in the experiments appear suddenly across the entire width, or, at least, extend across the width rapidly in comparison with the rate of loading (Wong *et al.* 2001; Baud *et al.* 2004; Förtin *et al.* 2006). The constraint created by the larger amount of material surrounding the bands in the field is certainly one factor in the differences in extension. In an effort to understand better the conditions for extension of compaction bands, Vajdova & Wong (2003) and Tembe *et al.* (2006) conducted axisymmetric compression tests on circumferentially notched specimens. They observed incremental propagation of compaction bands from the notch edge that coincided with bursts of acoustic emission activity.

One possible mechanism for band extension is that the presence of the band increases the compressive stress ahead of the band (the component perpendicular to the plane of the band or, possibly, the hydrostatic stress) to a level that favours band extension. A second, more complex possibility is that the presence of the compaction band alters the stress and deformation field just ahead of the band in a way that makes it more favourable for localized compaction according to the criterion that has been used with some success to model the onset of band formation (Issen & Rudnicki 2000; Rudnicki 2003, 2004; Béuelle & Rudnicki 2004; Challa & Issen 2004; Grueschow & Rudnicki 2005). Essential to evaluation of either mechanism is knowledge of the stress state ahead of the band. Here we calculate the stress within the band and adjacent to the band tip using a model of the band as a flat, ellipsoidal inclusion subjected to an inelastic compactive strain and having different elastic moduli from the surrounding matrix material.

Although knowledge of the stress state ahead of the band tip is necessary to evaluate propagation, it is not sufficient. Extension of the band by localization depends on the inelastic properties of the material. For extension by elevation of the stress ahead of the band, the level of the stress needed must be known. Furthermore, the stress field at the tip of the band depends on the detailed structure there. In a later section, we summarize an energy release criterion for propagation suggested by Rudnicki & Sternlof (2005) that does not depend on the details of the near-tip field.

Finally, we examine a combined anti-crack-dislocation model motivated by a suggestion by Sternlof (2006) and by the observed variation of midpoint band width with length reported by Sternlof *et al.* (2005). The model has a closing mode dislocation, representing inelastic compaction specified over the central portion of the band and uniform traction, equal to the difference between far-field compressive normal stress and a resistive band stress, specified over the remainder. The magnitude of this traction is specified by the requirement that the relative displacement should vary smoothly at the ends of the central dislocation.

Compaction band as ellipsoidal inhomogeneity

At present, the only detailed study of compaction bands in the field is that of Sternlof (2006) on the Aztec Sandstone of the Valley of Fire, Nevada. A striking feature of these data is that profiles of the width of the bands v. length are very nearly elliptical, although the aspect ratio is very small, 10^{-3} – 10^{-4} . Sternlof *et al.* (2005) figure 4a shows

1700 measurements of thickness v. length for 16 band traces. The measurements have a correlation index of 0.79 with an ellipse drawn through the data. Sternlof *et al.* figure 4c shows data for a single band 24.75 m long with a correlation index of 0.87. These data strongly suggest modelling the bands as ellipsoidal inhomogeneities, which makes it possible to take advantage of the well-known results of Eshelby (1957).

The compaction band is idealized as an ellipsoidal region with different elastic properties from the surrounding material (Fig. 1). The surrounding material is assumed to be of infinite extent (that is, of extent much greater than that of the compaction band) and loaded at infinity by compressive normal stresses in directions coinciding with the principal axes of the ellipsoid. Eshelby (1957) showed that the stress and strain in the ellipsoidal region are uniform (as long as the properties of the region are uniform). Because of the uniform interior strain and the ellipsoidal shape, the displacements of the boundary are also ellipsoidal. This supports the use of the measured width of the bands as a surrogate for the displacements in the observations of Sternlof *et al.* (2005) and Sternlof (2006).

A further implication of Eshelby's (1957) result is that the difference between the stress state in the band σ_{ij}^B and the stress state in the far field σ_{ij}^∞ is related to the corresponding difference in strain states $\varepsilon_{ij}^B - \varepsilon_{ij}^\infty$ by

$$S_{mnkl} C_{kl} \left\{ \sigma_{ij}^B - \sigma_{ij}^\infty \right\} = (S_{mnkl} - \delta_{mk} \delta_{nl}) \times \left\{ \varepsilon_{kl}^B - \varepsilon_{kl}^\infty \right\} \quad (1)$$

where δ_{ij} is the Kronecker delta ($\delta_{ij} = 1$, if $i = j$; $\delta_{ij} = 0$, if $i \neq j$). Here and throughout the paper, repeated indices imply summation over values 1, 2, and 3. In equation (1) the S_{mnkl} are components of a tensor that depends only on the geometry of the ellipsoid and the Poisson's ratio v of the matrix. The tensor possesses the symmetries $S_{mnkl} = S_{nmkl}$ and $S_{mnkl} = S_{mnlk}$ but, in general, $S_{mnkl} \neq S_{klmn}$. The C_{kl} are the elastic compliances of the matrix, i.e.

$$\varepsilon_{ij}^\infty = C_{ijkl} \sigma_{kl}^\infty. \quad (2)$$

(The result (1) was not cited explicitly by Eshelby (1957) but follows from the results of that study and has been discussed by Rudnicki (1977, 2002).) The band material is also assumed to be elastic, possibly with different properties from the matrix, but subjected to an inelastic strain ε_{ij}^p . Thus, the relation between the stress and strain in the band is given by

$$\varepsilon_{ij}^B = C_{ijkl}^B \sigma_{kl}^B + \varepsilon_{ij}^p \quad (3)$$

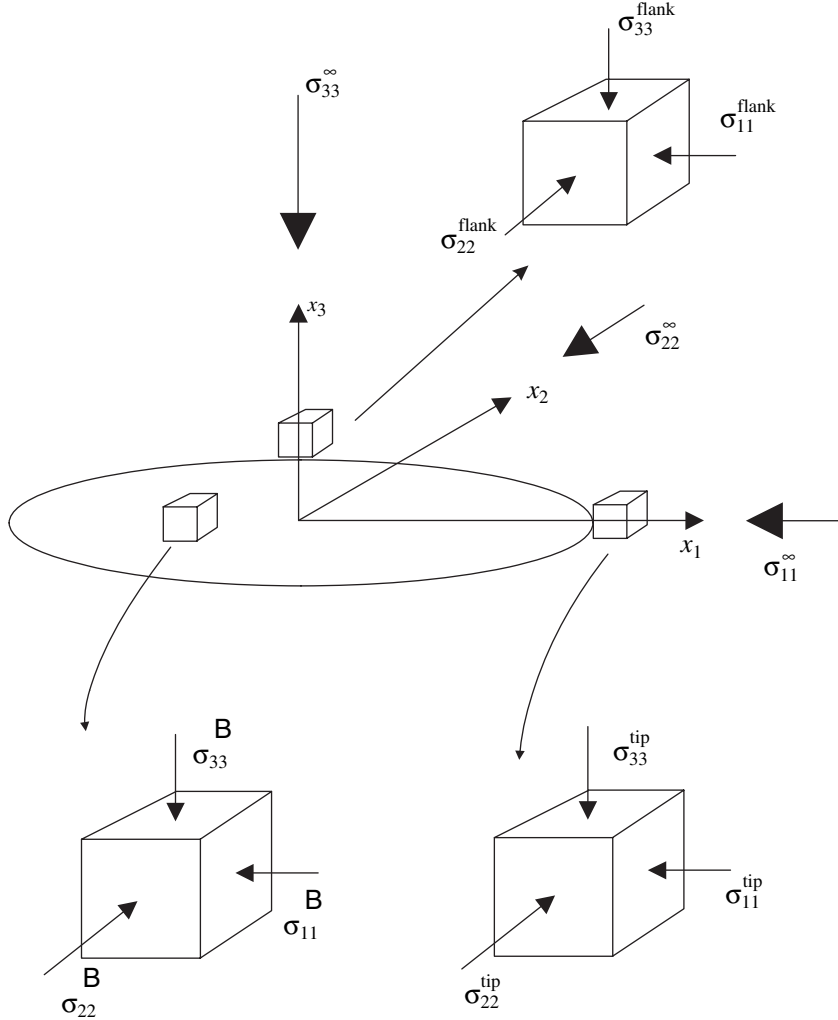


Fig. 1. Model of a compaction band as a thin, axisymmetric ellipsoidal inclusion showing far-field stresses σ_{ij}^∞ , uniform stresses in the band σ_{ij}^B , stresses at the tip of the band σ_{ij}^{tip} and stresses at the flank $\sigma_{ij}^{\text{flank}}$.

where the C_{ijkl}^B are the elastic compliances of the band. The elasticities of both the band and the matrix are assumed to be isotropic so that the C_{ijkl} have the form

$$C_{ijkl} = \frac{1}{2\mu} \left\{ \frac{1}{2} (\delta_{ik}\delta_{jl} + \delta_{il}\delta_{jk}) - \frac{\nu}{1+\nu} \delta_{ij}\delta_{kl} \right\} \quad (4)$$

where μ is the shear modulus and ν is Poisson's ratio. The corresponding array of moduli is

$$L_{ijkl} = (\kappa - 2\mu/3)\delta_{ij}\delta_{kl} + \mu(\delta_{ik}\delta_{jl} + \delta_{il}\delta_{jk}) \quad (5)$$

where $\kappa = 2\mu(1+\nu)/3(1-2\nu)$ is the bulk modulus and

$$L_{ijkl} C_{klmn} = C_{ijkl} L_{klmn} = \frac{1}{2} (\delta_{im}\delta_{jn} + \delta_{in}\delta_{jm}). \quad (6)$$

Equations (2) and (3) can be used to eliminate the stress or the strain from (1). Doing the latter gives

$$\begin{aligned} \sigma_{pq}^B + L_{pqmn}^B S_{mnkl} \left\{ C_{klji} - C_{klji}^B \right\} \sigma_{ij}^B \\ = L_{pqmn}^B \left\{ C_{mnij} \sigma_{ij}^\infty - (\varepsilon_{mn}^p - S_{mnkl} \varepsilon_{kl}^p) \right\}. \end{aligned} \quad (7)$$

If $\epsilon_{ij}^p = -\zeta^1 p^1 C_{ijk}^1$, then equation (7) reduces to equation (13) of Rudnicki (2002), where p is pore pressure in the inhomogeneity and ζ^1 is a porous media constant; Rudnicki (2002) used the superscript I for B, G and K for the moduli denoted here by μ and κ , respectively, and labelled matrix elasticity tensors with the superscript ∞ . In addition, the matrix C_{mnpq} in the first term on the right-hand side of equation (13) of Rudnicki (2002) should have the superscript I replaced by ∞ . Specializing to isotropic materials, separating the stress and inelastic strain into deviatoric and spherical parts, i.e.

$$\sigma_{ij} = s_{ij} + \sigma \delta_{ij} \quad (8a)$$

$$\epsilon_{ij}^p = e_{ij}^p + \frac{1}{3} \epsilon^p \delta_{ij} \quad (8b)$$

and substituting into (7) gives the following two equations:

$$\begin{aligned} \sigma^B(1 + \alpha k) &= (k + 1)\sigma^\infty - \kappa_B(1 - \alpha)\epsilon^p \\ &\quad + \kappa_B S_{mmkl}(e_{kl}^p - g s_{kl}^B/2\mu_B) \end{aligned} \quad (9)$$

and

$$\begin{aligned} s_{pq}^B + (g s_{kl}^B - 2\mu_B e_{kl}^p) \\ \times \left\{ S'_{pqkl} - \frac{k}{3(1 + \alpha k)} S'_{pqkk} S_{mmkl} \right\} \\ = (1 + g)s_{pq}^\infty - 2\mu_B e_{pq}^p + \frac{2\mu_B}{3\kappa_B} \frac{S'_{pqkk}}{(1 + \alpha k)} \\ \times (\kappa_B \epsilon^p - k\sigma^\infty) \end{aligned} \quad (10)$$

where

$$S'_{pqkl} = S_{pqkl} - \frac{1}{3} \delta_{pq} S_{mmkl} \quad (11)$$

$$g = \mu_B/\mu - 1, \quad k = \kappa_B/\kappa - 1, \quad \text{and}$$

$$S_{mmkk} = 3\alpha = (1 + v)/(1 - v). \quad (12)$$

If $\epsilon_{ij}^p = -\zeta^1 p^1 K_I \delta_{ij}$, then (9) and (10) reduce to equations (15) of Rudnicki (2002) with the changes in notation noted following (7).

Stress state in an axisymmetric band

Although it is possible to carry out the analysis for an arbitrarily shaped ellipsoid, the planform of compaction bands is not well constrained by observation and the analysis simplifies considerably if the ellipsoid is axisymmetric. Hence, the lengths of the

semi-axes of the ellipsoid in the x_1 and x_2 directions are assumed to be equal to a and greater than the length c of the distinguished short axis in the x_3 direction (Fig. 1). If, in addition, the far-field stress state is axisymmetric with principal directions aligned with the band axes, and only $\sigma_{22}^\infty = \sigma_{11}^\infty$ and σ_{33}^∞ are nonzero, then the stress state in the band is also axisymmetric, and only $\sigma_{22}^B = \sigma_{11}^B$ and σ_{33}^B are nonzero. In this case, for both the band and the far-field, the mean stress is related to the components by $\sigma = (2\sigma_{11} + \sigma_{33})/3$ and there is only a single distinguished deviatoric component,

$$\sigma_{33} = -2\sigma_{22} = -2\sigma_{11} = 2(\sigma_{33} - \sigma_{11})/3. \quad (13)$$

Similarly, we assume that the inelastic strain is also axisymmetric so that there is only one distinguished deviatoric component

$$e_{33}^p = -2e_{22}^p = -2e_{11}^p = 2(e_{33}^p - e_{11}^p)/3. \quad (14)$$

Setting $p = q = 3$ in (10) yields

$$\begin{aligned} s_{33}^B &= \frac{1}{1 + gA} \{ (1 + g)s_{33}^\infty + 2\mu_B e_{33}^p (A - 1) \\ &\quad + (2\mu_B/\kappa_\infty)B(\kappa_B \epsilon^p - k\sigma^\infty) \} \end{aligned} \quad (15)$$

where

$$\begin{aligned} A &= S_{3333} - S_{3311} \\ &\quad - \frac{(1 + kS_{33kk})(S_{mm33} - \alpha)}{2(1 + \alpha k)} \end{aligned} \quad (16)$$

and

$$B = \frac{(S_{33kk} - \alpha)}{3(1 + \alpha k)} \quad (17)$$

and, for axisymmetry the indices '1' and '2' may be interchanged on the S_{ijkl} . Expressions for the relevant S_{ijkl} have been given by Mura (1987) and Rudnicki (2002) and, for convenience, are also listed in the Appendix. Evaluating (9) for axisymmetry then gives

$$\begin{aligned} \sigma^B(1 + \alpha k) &= (k + 1)\sigma^\infty - \kappa_B(1 - \alpha)\epsilon^p \\ &\quad + \kappa_B 2S_{mm11}(e_{11}^p - g s_{11}^B/2\mu_B) \\ &\quad + \kappa_B S_{mm33}(e_{33}^p - g s_{33}^B/2\mu_B) \end{aligned} \quad (18)$$

where $S_{mm11} = S_{mm22}$. Using (13) and (14) gives

$$\begin{aligned}\sigma^B(1 + \alpha k) &= (k + 1)\sigma^\infty - \kappa_B(1 - \alpha)\epsilon^P \\ &+ \kappa_B(S_{mm33} - S_{mm11}) \\ &\times (e_{33}^P - g s_{33}^B/2\mu_B).\end{aligned}\quad (19)$$

However,

$$S_{mm11} = \frac{1}{2}(S_{mmkk} - S_{mm33})$$

and therefore

$$S_{mm33} - S_{mm11} = \frac{3}{2}(S_{mm33} - \alpha).$$

Determining s_{33}^B from (15), substituting into (19) and dividing by $(1 + \alpha k)$ gives σ^B . Stress components perpendicular and parallel to the short axis of the band are given by

$$\begin{aligned}\sigma_{33}^B &= \sigma^B + s_{33}^B \\ \sigma_{11}^B &= \sigma^B - s_{33}^B/2.\end{aligned}\quad (20)$$

The expressions for the stress reduce correctly to the proper results in the limit of a sphere (although this is not a realistic shape for a compaction band). If the shear modulus of the band is finite (neither zero nor unbounded), then expansion of the general expressions for small aspect ratio reveals that the zero aspect ratio limit yields results identical to those for a planar layer considered by Cocco & Rice (2002) and used by Sternlof *et al.* (2005). If the 3-axis is the short axis of the ellipsoid, then Cocco & Rice (2002) noted that $\epsilon_{ij}^B = \epsilon_{ij}^\infty$ if neither i nor j is three and that $\sigma_{ij}^B = \sigma_{ij}^\infty$ if either i or j is three. The particular relations relevant here are

$$\sigma_{33}^B = \sigma_{33}^\infty \quad (21a)$$

$$\epsilon_{11}^B = \epsilon_{11}^\infty, \quad \epsilon_{22}^B = \epsilon_{22}^\infty. \quad (21b)$$

Using (21a), and (3) and (2) to eliminate the elastic strains from (21b) yields

$$\begin{aligned}\sigma_{11}^B &= \frac{(1 + v_B)}{(1 - v_B)} \left\{ \frac{(1 - v)}{\mu} \mu_B \sigma_{11}^\infty \right. \\ &+ \left. \sigma_{33}^\infty \left[\frac{v_B}{(1 + v_B)} - \frac{\mu_B}{\mu} \frac{v}{(1 + v)} \right] - 2\mu_B \epsilon_{11}^P \right\} \\ &\quad (22)\end{aligned}$$

where $\sigma_{22} = \sigma_{11}$ in both the band and the far field for axisymmetry (identical to equations (4b) and

(4c) of Sternlof *et al.* (2005) for axisymmetry and slightly different notation).

If the shear modulus is zero, then the band reduces to a void and the stresses in the band are zero. In the limit of the short axis of the ellipsoid, c , approaching zero, the products of c and the strains ϵ_{3j}^B equal the crack (or anti-crack) surface displacements predicted by fracture mechanics (Rudnicki 1977; Hoenig 1978). In the case of compressive loading the crack surfaces are predicted to interpenetrate. This analogue of a tensile crack with the signs of the stresses and displacements reversed has been termed an ‘anti-crack’ (Fletcher & Pollard 1981) and applied to compaction bands by Sternlof & Pollard (2002) and Sternlof *et al.* (2005). In the application to compaction bands, this interpenetration is interpreted as inelastic compaction of a narrow, but finite width band.

If the shear modulus of the band is unbounded, then the ellipsoid is rigid and has a shape change specified by ϵ_{mn}^P (without alteration by the constraint of the matrix). In the limit of the short axis of the ellipsoid, c , approaching zero, the products of c and the strains ϵ_{3j}^B become equal to the specified relative displacements (which are interpenetration for a compaction band), as in a dislocation (or anti-dislocation) model (Katsman *et al.* 2006). Hence, the Eshelby inclusion model encompasses both a crack (or anti-crack) and a dislocation (or anti-dislocation) in the limits of a vanishingly thin zone and either zero or unbounded moduli.

Typically, the aspect ratio, $e = c/a$, of compaction bands is very small. Values from data of Sternlof *et al.* (2005) range from 10^{-3} to 10^{-4} and, consequently, those workers argued that the zero aspect ratio limit is a good approximation. Here we will provide additional quantitative support for this approximation and extend the conditions for which it applies by comparing the results for the zero aspect ratio limit with those obtained using the general expressions for a flat, but finite aspect ratio axisymmetric ellipsoid.

Figure 2 plots the stress normal to the plane of the band σ_{33}^B , divided by σ_{33}^∞ , the far-field normal stress, and Figure 3 plots the stress parallel to the plane of the band σ_{11}^B , divided by σ_{33}^∞ , against the aspect ratios ranging from 10^{-4} – 10^{-1} for fixed values of other parameters. The other parameters are varied about a set similar to those inferred by Sternlof *et al.* (2005) for the Valley of Fire. These are only the normal inelastic strain ϵ_{33}^P nonzero, identical elastic constants for the band and matrix, $\mu_B = \mu$ and $v_B = v = 0.2$, lateral far-field stress equal to half the normal stress (i.e. $\sigma_{11}^\infty = \sigma_{22}^\infty = 0.5\sigma_{33}^\infty$) and the ratio $\sigma_{33}^\infty/2\mu\epsilon_{33}^P$ equal to 0.05.

Figures 2a and 3a show the effect of varying the ratio $\sigma_{33}^\infty/2\mu\epsilon_{33}^P$ on $\sigma_{33}^B/\sigma_{33}^\infty$ and $\sigma_{11}^B/\sigma_{33}^\infty$. Sternlof

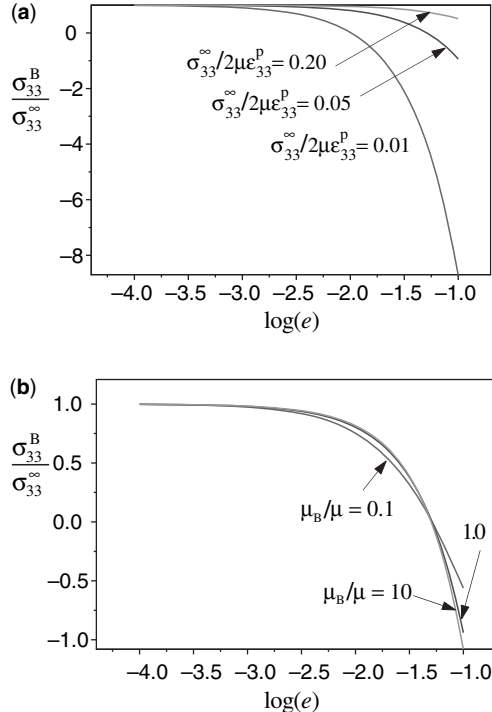


Fig. 2. Stress normal to the plane of the band σ_{33}^B , divided by σ_{33}^∞ , the far-field normal stress, against aspect ratios ranging from 10^{-4} to 10^{-1} . (a) Results for three values of $\sigma_{33}^\infty/2\mu\epsilon_{33}^P$ and fixed values of other parameters: $\epsilon_{11} = \epsilon_{22} = 0$, $\mu_B = \mu$, $v_B = v = 0.2$, and $\sigma_{11}^\infty = \sigma_{22}^\infty = 0.5\sigma_{33}^\infty$. (b) Results for $\sigma_{33}^\infty/2\mu\epsilon_{33}^P = 0.05$ and three values of μ_B/μ with other parameters the same as in (a).

et al. (2005) used $\epsilon_{33}^P = 0.1$, corresponding to a roughly 10% porosity loss in the band. For the value of Young's modulus $E = 20$ GPa and Poisson's ratio $v = 0.2$ estimated by Sternlof *et al.* (2005), the corresponding shear modulus is $\mu = 8.3$ GPa. Their best estimate of the maximum principal compressive stress at the time of band formation was 40 MPa, although they noted a possible range of 13–54 MPa. For $\sigma_{33}^\infty = 40$ MPa the ratio $\sigma_{33}^\infty/2\mu\epsilon_{33}^P$ is about 0.02, and Figures 2a and 3a show results for the values 0.01, 0.05, and 0.20. For aspect ratios less than about $10^{-2.5}$, the results from (21a) and (21b), corresponding to $\sigma_{33}^B = \sigma_{33}^\infty$ and $\sigma_{11}^B = \sigma_{11}^\infty$, are a very good approximation. The approach to this limit is slower for larger values of ϵ_{33}^P . Nevertheless, the ratio $\sigma_{33}^\infty/2\mu\epsilon_{33}^P$ would have to be much smaller for there to be any significant deviation from the zero aspect ratio limit in the range of aspect ratios reported by Sternlof *et al.* (2005). It is, however, interesting to note that the signs of σ_{11}^B and σ_{33}^B

differ from that of σ_{33}^∞ for larger aspect ratios and the value at which the change of sign occurs decreases with decreasing $\sigma_{33}^\infty/2\mu\epsilon_{33}^P$. This occurs because of competition between the effects of the far-field compressive stress and the inelastic compaction. If inelastic compaction occurred in the absence of far-field stress, the stresses in the band would need to be tensile for the total band deformation to be compatible with the matrix. This effect is, however, countered by the effect of the far-field compressive stress, which is amplified as the aspect ratio of the band decreases.

A 10% porosity loss in the band, corresponding to $\epsilon_{33}^P = 0.1$, is also representative of compaction bands formed in axisymmetric compression experiments (Olsson 1999; Olsson & Holcomb 2000; Wong *et al.* 2001; Holcomb & Olsson 2003; Baud *et al.* 2004; Förtin *et al.* 2006), although there is some evidence in Castlegate sandstone (Olsson 1999; Olsson & Holcomb 2000; Holcomb & Olsson 2003) that the compaction is not purely uniaxial and that $\epsilon_{11}^P = \epsilon_{22}^P$ is extensile (dilatant) (D. Holcomb, pers. comm.). Whether this is a general feature of band formation or is due to the limited lateral constraint in the laboratory is not clear. Values of the axial stress at which compaction bands form in the laboratory tend to be much higher than the 13–54 MPa estimated by Sternlof *et al.* (2005) for field conditions at the time of band formation in the Valley of Fire. Typically, the axial stress at band formation in the laboratory ranges from more than 100 MPa (e.g. Olsson & Holcomb 2000) to several hundred MPa (e.g. Baud *et al.* 2004). Estimates of the shear modulus from axial stress v. strain curves of Olsson & Holcomb (2000) and Baud *et al.* (2004) yield values in the range of 5–10 GPa, similar to that estimated from Sternlof *et al.* (2005). Thus, the ratio $\sigma_{33}^\infty/2\mu\epsilon_{33}^P$ appropriate for laboratory conditions may be c. 2–10 times larger than estimated from Sternlof *et al.* (2005).

Figures 2b and 3b show the effect of decreasing and increasing the band shear modulus by a factor of 10 (in Fig. 3b the zero aspect ratio limit is shown by a dashed horizontal line). The effect on σ_{33}^B is small and the effect on σ_{11}^B corresponds well to the prediction of equation (22) for aspect ratios less than $10^{-2.5}$. Figure 3(c and d) shows that variation of σ_{11}^B as a result of changes in the band Poisson's ratio and the lateral far-field stress are also predicted well by equation (22) for small aspect ratios. Changing these parameters has virtually no effect on σ_{33}^B and, hence, is not shown.

These results confirm that the simplified layer solution, analogous to that of Cocco & Rice (2002) and used by Sternlof *et al.* (2005), is

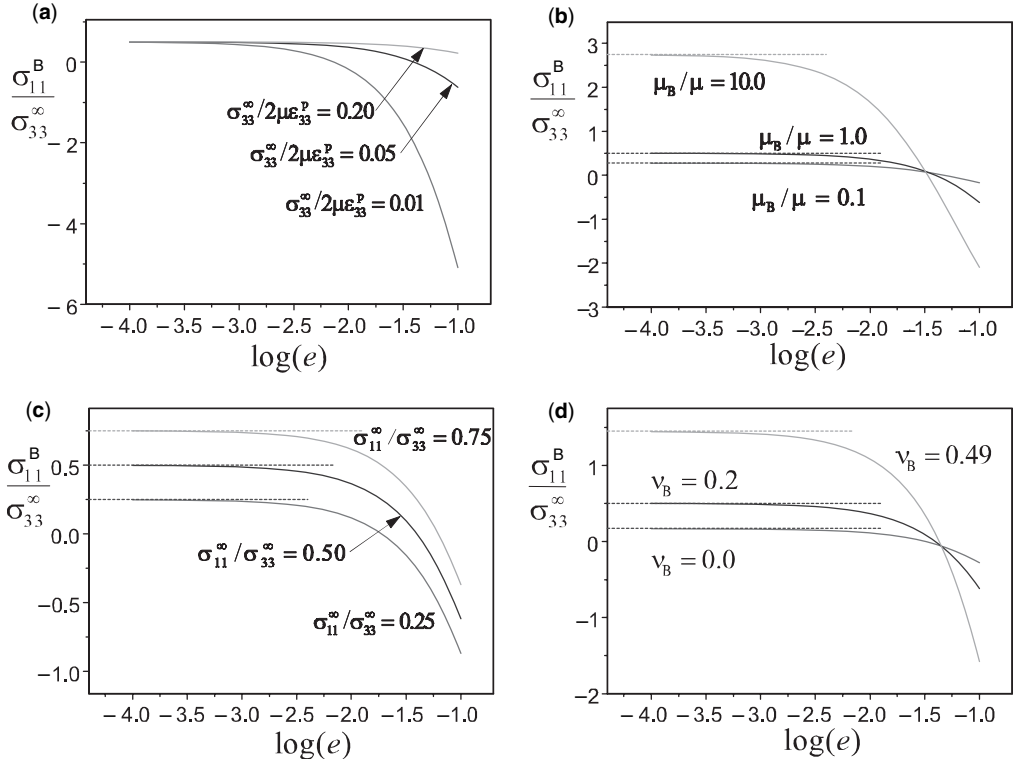


Fig. 3. Stress parallel to the plane of the band σ_{11}^B , divided by σ_{33}^∞ , against the aspect ratios ranging from 10^{-4} to 10^{-1} for fixed values of other parameters: $\varepsilon_{11}^p = \varepsilon_{22}^p = 0$, $\mu_B = \mu$, $v_B = v = 0.2$, $\sigma_{11}^\infty = \sigma_{22}^\infty = 0.5\sigma_{33}^\infty$ and $\sigma_{33}^\infty/2\mu\varepsilon_{33}^p = 0.05$. (a), (b), (c) and (d) show the effects of changing $\sigma_{33}^\infty/2\mu\varepsilon_{33}^p$, μ_B/μ , $\sigma_{11}^\infty/\sigma_{33}^\infty$ and v_B , respectively.

indeed a good approximation for the very small aspect ratios that have been observed, but there is no impediment to similar calculations for larger aspect ratios. Therefore, in the next section we will adopt this approximation and examine the effects of elastic property mismatch, far-field stress ratio and inelastic compactive strain on the stress state immediately adjacent to the band.

Stress state adjacent to the band

The stress immediately outside the band can be obtained from conditions of continuity of traction and displacement across the band–matrix interface. If, as depicted in Figure 1, the midplane of the ellipsoid lies in the x_1x_2 -plane and the short axis is in the x_3 direction, then continuity of normal traction on the x_1 -axis requires

$$\sigma_{11}^{\text{tip}} = \sigma_{11}^B. \quad (23)$$

Continuity of displacement requires that $u_2^{\text{tip}} = u_2^B$ and $u_3^{\text{tip}} = u_3^B$. Consequently, the derivatives

tangent to the band–matrix boundary must also be continuous, requiring that

$$\varepsilon_{22}^{\text{tip}} = \varepsilon_{22}^B, \quad \varepsilon_{33}^{\text{tip}} = \varepsilon_{33}^B. \quad (24)$$

Using the elasticity relations (2) and (3) to eliminate the strains gives

$$\begin{aligned} \sigma_{22}^{\text{tip}} &= \frac{\mu}{\mu_B} \sigma_{22}^B + \frac{v}{(1-v)} \sigma_{11}^B \left(1 - \frac{\mu}{\mu_B}\right) \\ &\quad + \frac{\mu}{\mu_B} \sigma_{kk}^B \frac{v - v_B}{(1-v)(1+v_B)} \\ &\quad + \frac{2\mu}{(1-v)} (\varepsilon_{22}^p + v\varepsilon_{33}^p) \end{aligned} \quad (25a)$$

$$\begin{aligned} \sigma_{33}^{\text{tip}} &= \frac{\mu}{\mu_B} \sigma_{33}^B + \frac{v}{(1-v)} \sigma_{11}^B \left(1 - \frac{\mu}{\mu_B}\right) \\ &\quad + \frac{\mu}{\mu_B} \sigma_{kk}^B \frac{v - v_B}{(1-v)(1+v_B)} \\ &\quad + \frac{2\mu}{(1-v)} (\varepsilon_{33}^p + v\varepsilon_{22}^p) \end{aligned} \quad (25b)$$

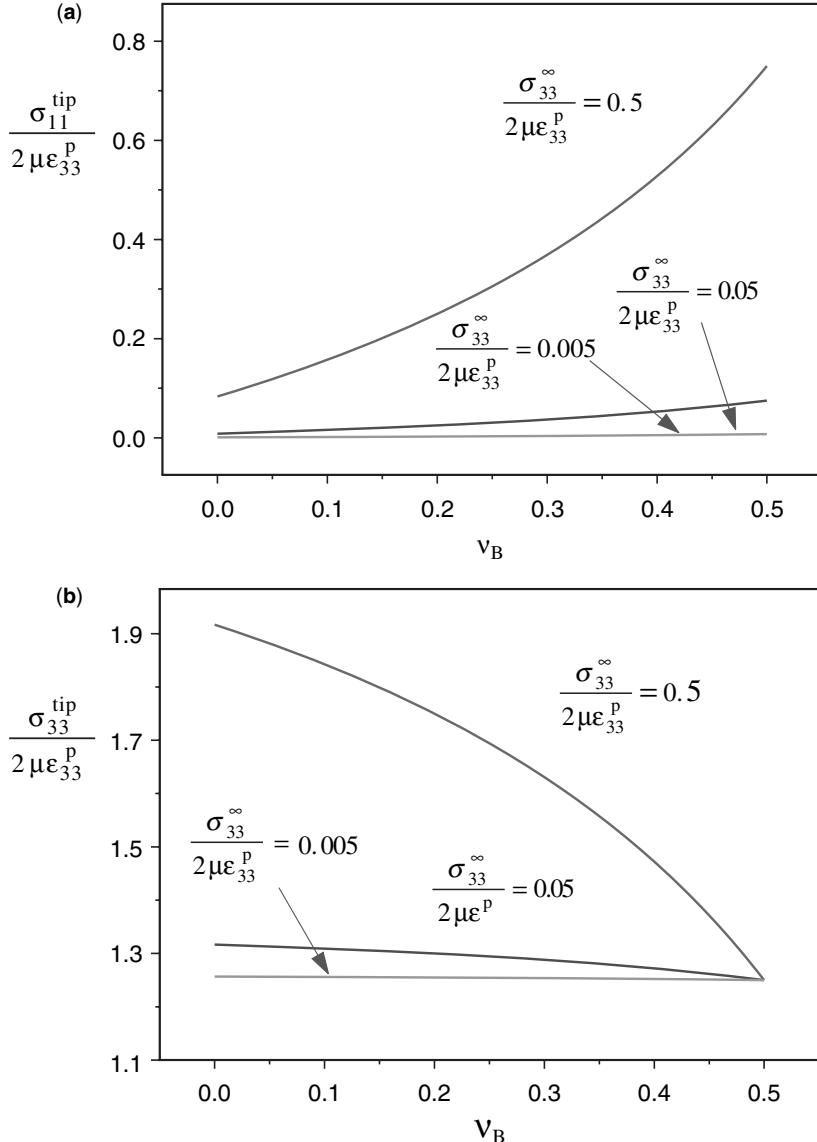


Fig. 4. Stress components σ_{33}^{tip} (b) and σ_{11}^{tip} (a), divided by $2\mu\varepsilon_{33}^p$, against the band Poisson's ratio v_B for values of $\sigma_{33}^{\infty}/2\mu\varepsilon_{33}$ an order of magnitude smaller (0.005) and larger (0.5) than for the base set (0.05). Other parameters are $\varepsilon_{11}^p = \varepsilon_{22}^p = 0$, $v = 0.2$, $\mu_B = \mu$, and $\sigma_{11}^{\infty} = \sigma_{22}^{\infty} = 0.5\sigma_{33}^{\infty}$.

which are the same as equations (6) of Sternlof *et al.* (2005) (with slightly different notation). It should be noted that even if the ellipsoid and far-field stress state are axisymmetric, the stress state adjacent to the band is not. Because the localization criterion for compaction band formation (Issen & Rudnicki 2000) indicates that axisymmetric

compression stress states are most favourable, the departure from axisymmetry would diminish the tendency for localization.

The relations (23) and (24) will hold at any point adjacent to the band if expressed in terms of the local normal and tangent directions. In particular, we note that the conditions at the flank of the

band (on the x_3 -axis at the band boundary; see Fig. 1) are

$$\sigma_{33}^{\text{flank}} = \sigma_{33}^B \quad (26a)$$

$$\varepsilon_{22}^{\text{flank}} = \varepsilon_{22}^B, \quad \varepsilon_{11}^{\text{flank}} = \varepsilon_{11}^B. \quad (26b)$$

These equations, together with equation (21), imply that for a thin (zero aspect ratio) band, the stress state at the flank is identical to that in the far field.

Similarly to the procedure in the preceding section, we will explore the effect of altering parameters on the stress state adjacent to the band for variations about a base set of parameters. This base set is only $\varepsilon_{33}^P \neq 0$ ($\varepsilon_{11}^P = \varepsilon_{22}^P = 0$), Poisson's ratio of the matrix $\nu = 0.2$, equal shear moduli for band and matrix, $\mu_B = \mu$, lateral far-field stress equal to half the normal stress, $\sigma_{11}^\infty = \sigma_{22}^\infty = 0.5\sigma_{33}^\infty$, and $\sigma_{33}^\infty/2\mu\varepsilon_{33}^P = 0.05$. Components of the stress in the band, divided by $2\mu\varepsilon_{33}^P$, are plotted against v_B , the Poisson's ratio in the band. For $\mu_B = \mu$, and $\nu = 0.2$, $v_B = 0$ corresponds to $\kappa_B/\kappa = 0.5$; for $\kappa_B/\kappa = 2, 3, 5, 10$, the corresponding values of v_B are 0.333, 0.385, 0.429 and 0.463, respectively. Because the porosity of the band material is reduced relative to the matrix, it is likely that the bulk modulus of the band material will exceed that of the matrix $\kappa_B/\kappa > 1$, but there are no quantitative estimates. Plotting results against v_B covers the entire range of possibilities.

Figure 4 shows σ_{33}^{tip} and σ_{11}^{tip} for values of $\sigma_{33}^\infty/2\mu\varepsilon_{33}^P$ an order of magnitude smaller (0.005) and larger (0.5) than for the base set (0.05). Values of $\sigma_{22}^{\text{tip}}/2\mu\varepsilon_{33}^P$ do not depend on v_B and equal 0.253, 0.275 and 0.5 for $\sigma_{33}^\infty/2\mu\varepsilon_{33}^P = 0.005, 0.05$, and 0.5, respectively. Only for $\sigma_{33}^\infty/2\mu\varepsilon_{33}^P = 0.5$ and small v_B does $\sigma_{33}^{\text{tip}}/2\mu\varepsilon_{33}^P$ rise significantly above unity (to about 1.9 for $v_B = 0$) and only for $\sigma_{33}^\infty/2\mu\varepsilon_{33}^P = 0.5$ and large v_B does $\sigma_{11}^{\text{tip}}/2\mu\varepsilon_{33}^P$ depart significantly from zero (to about 0.8 for $v_B = 0.5$). The ratio $\sigma_{33}^\infty/2\mu\varepsilon_{33}^P = 0.5$ corresponds to a relatively small compactive strain or relatively large far-field compressive stress normal to the plane of the band.

Figure 5 shows the effect of uniaxial ($\sigma_{11}^\infty/\sigma_{33}^\infty = 0.0$) and hydrostatic ($\sigma_{11}^\infty/\sigma_{33}^\infty = 1.0$) far-field stress in addition to the base value $\sigma_{11}^\infty/\sigma_{33}^\infty = 0.5$. The stress σ_{33}^{tip} increases with increasing triaxiality ($\sigma_{11}^\infty/\sigma_{33}^\infty$) for $v_B < \nu$ and decreases with increasing triaxiality for $v_B > \nu$. The stress σ_{11}^{tip} increases with triaxiality and v_B but, again, the variation is small ($c. 0.1 \times 2\mu\varepsilon_{33}^P$). The stress component σ_{22}^{tip} is again independent of v_B and equal to 0.25, 0.275 and 0.30 multiplied by $2\mu\varepsilon_{33}^P$ for $\sigma_{11}^\infty/\sigma_{33}^\infty = 0.0, 0.5$ and 1.0. An interesting feature

of Figure 5b is that for $\sigma_{11}^\infty/\sigma_{33}^\infty = 0$, σ_{11}^{tip} is negative (tensile) for $v_B < \nu$ and positive (compressive) for $v_B > \nu$, although the magnitude is small.

Figure 6 shows the effect of a band shear modulus that is an order of magnitude larger or smaller than the matrix modulus. Although, as argued above, it is likely that the bulk modulus of the band will exceed that of the matrix, the relative size of the shear moduli is not so clear. Greater density (as a result of decrease of porosity) might increase the shear modulus. More likely, decohesion and, sometimes, fragmentation of the band material would reduce the resistance to shear by facilitating particle rearrangement and rolling. Decreasing the ratio of the shear moduli to $\mu_B/\mu = 0.1$ increases σ_{33}^{tip} , except for v_B near 0.5. The effect is greatest for small values of v_B but the maximum increase is less than a factor of two. The variation of σ_{22}^{tip} with v_B is similar for $\mu_B/\mu = 0.1$, although the magnitude of the increase for a reduced shear modulus is smaller than for σ_{33}^{tip} . Although a value of band shear modulus much greater than the matrix modulus seems unlikely, the stresses are shown for $\mu_B/\mu = 10.0$. The increase in the ratio of shear modulus from one to 10 has little effect on σ_{33}^{tip} , reduces σ_{22}^{tip} slightly, more so for v_B near 0.5, and increases σ_{11}^{tip} from very small fractions of $2\mu\varepsilon_{33}^P$ to 0.1–0.32 $\mu\varepsilon_{33}^P$.

In summary, for a wide variation of parameters about the base set, σ_{33}^{tip} is about 1–2 times $2\mu\varepsilon_{33}^P$. The other stress components are typically around a few tenths to half of σ_{33}^{tip} . These results suggest that the stress state at the band tip is mainly controlled by $2\mu\varepsilon_{33}^P$ rather than the far-field stress, unless its magnitude is comparable with $2\mu\varepsilon_{33}^P$.

Energy release propagation criterion

The results of the preceding section have shown that when the aspect ratio of the bands is of the order of the values inferred from field observations by Sternlof *et al.* (2005), 10^{-3} – 10^{-4} , the actual value of the aspect ratio has little effect on the stress state at the band tip and can be taken as zero. Similarly, if the inelastic compactive strain $\varepsilon_{33}^B = 0.1$ and the ratio of the matrix shear modulus to remote stress (normal to the band) is of the order of 10^2 , even implausibly large variations of the contrast of elastic moduli have relatively little effect. In short, the ratio of the stress at the tip of the band to that in the far field is in the range 10–100 and is controlled primarily by the product of the magnitude of the inelastic compactive strain and the ratio of the shear modulus to remote stress. The ratio of stress at the tip of the band to remote stress does, however, increase with a reduction in the band

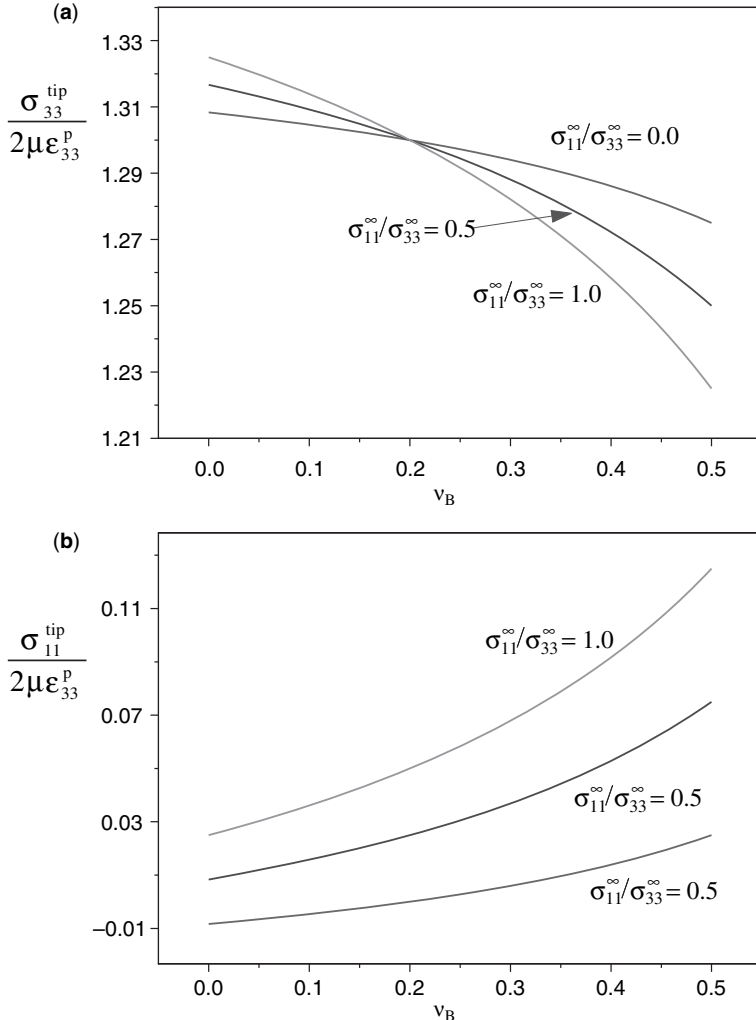


Fig. 5. Same as Figure 4 but with $\sigma_{33}^{\infty}/2\mu\varepsilon_{33}^p = 0.05$ and $\sigma_{11}^{\infty}/\sigma_{33}^{\infty} = 0.0, 0.5$ and 1.0 .

shear modulus and becomes unbounded in the limit $\mu_B \rightarrow 0$. The inferred level of stress elevation, 10–100 times the far-field stress, is consistent with the concept that band propagation occurs in a crack-like manner.

Although these results demonstrate that the normal stress just ahead of a compaction band is elevated, they give no indication of what level is needed for propagation. As the bands observed in the field have stopped propagating, we can only say that the current level is below that needed for propagation. A useful approach to the condition for propagation is to consider the energy released per unit band extension, as has been successfully applied to tensile and shear fractures. Vajdova & Wong (2003) and

Tembe *et al.* (2006) have used this approach to interpret the extension of compaction bands from circumferentially notched specimens of Bentheim and Berea sandstone. By estimating the compaction energy from the nominal stress v. displacement curves, Vajdova & Wong (2003) obtained a lower bound on the compaction energy for Bentheim sandstone of 16 kJ m^{-2} and Tembe *et al.* (2006) estimated values ranging from 6 to 43 kJ m^{-2} for Berea and Bentheim sandstones.

Rudnicki & Sternlof (2005) have developed the idea for compaction energy release using a simple model adapted from an example used by Rice (1968a) to illustrate the *J*-integral. They considered a long (semi-infinite) compaction band in an infinite

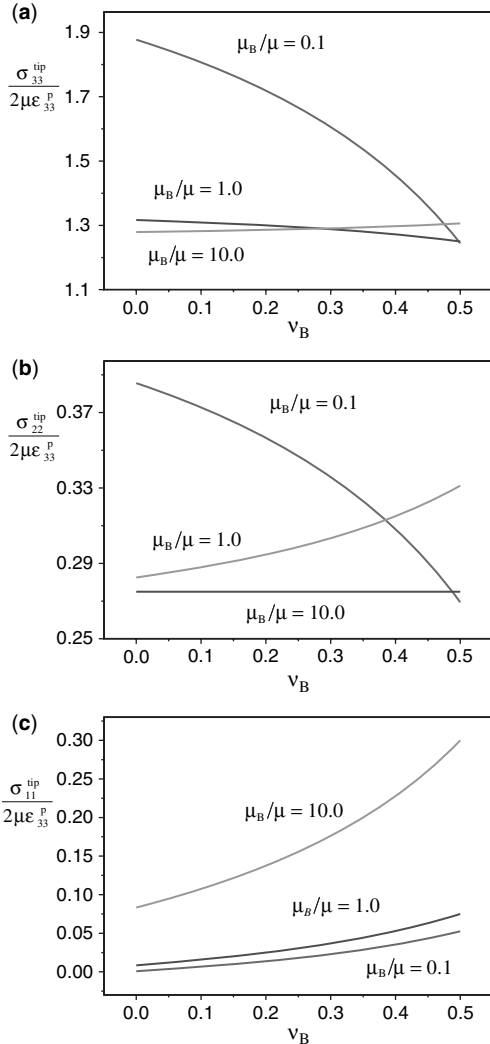


Fig. 6. Same as Figure 4 but with $\sigma_{33}^{\infty}/2\mu\epsilon_{33}^P = 0.05$ and $\mu_B/\mu = 0.1, 1.0$ and 10.0 and also showing $\sigma_{22}^{\infty}/2\mu\epsilon_{33}^P$ (b).

strip of width w (taken as representative of the distance between bands in application to the field data) with an elastic modulus for 1D strain of $M (=2\mu(1-v)/(1-2v))$ for an isotropic elastic material). The compaction band attains a constant thickness ξw far behind its tip where the elastic modulus in the band is M_B and the 1D inelastic compactive strain is ϵ^P . Because the configuration is translationally invariant in the direction of the band and strip, advance of the band a unit distance reduces the strain energy of a vertical slice of material far ahead of the band tip to that of a vertical slice far behind the band tip. Rudnicki & Sternlof

(2005) gave an exact result for this difference, but if the band thickness is very much less than w , $\xi \ll 1$, and the band modulus does not differ significantly from the modulus of the surrounding material, the energy release is given by the simple expression

$$\mathcal{G}_{\text{band}} = \sigma_+ \xi \epsilon^P w \quad (27)$$

to first order in ξ . In equation (27), $\sigma_+ = M(\Delta/w)$ is the uniform compressive stress far ahead of the band tip and Δ is the relative closure of the layer boundaries (so that Δ/w is the nominal strain in the absence of the band). Thus, the energy released (per unit area of band advance) has the interpretation of the stress multiplied by the compactive displacement in the band. For representative values of the parameters derived for the Aztec sandstone corresponding to 1 cm thick compaction bands spaced 1 m apart, and $\epsilon^P = 0.1$, corresponding to a porosity reduction of 10%, Sternlof *et al.* (2005) found $\mathcal{G}_{\text{band}} = 40 \text{ kJ m}^{-2}$. This result is surprisingly similar to the range of compaction energies estimated by Vajdova & Wong (2003) and Tembe *et al.* (2006) for different sandstones and laboratory conditions.

Combined anti-crack–dislocation model

As discussed above, the data on compaction band profiles from the Valley of Fire (Sternlof *et al.* 2005) are nearly elliptical. The ratio of midpoint thickness to band length is not, however, constant as would be the case for self-similar ellipses (or as predicted for the ratio of midpoint displacement to length for an anti-crack model with uniform surface tractions). Sternlof *et al.* (2005, Fig. 4b) showed that the midpoint thickness increases more slowly for the longer bands. For the shorter bands (less than about 10 m), the half-width increases roughly linearly with length. This suggests the possibility of self-similar extension, although the aspect ratios are so small that any lateral spreading must also be small. The widths of the three longest bands do not follow this trend but increase with length at a smaller rate. Sternlof (2006) suggested that the midpoint thickness reaches an asymptotic value for the longest bands, although the data are not unambiguous on this issue because of the difficulty of identifying very long, isolated bands. He suggested a conceptual model (see his fig. 4.23) that is similar to the simple plane strain (infinite in extent out of the plane of the sketch) model shown in Figure 7.

This configuration is identical to that for a tensile solution given by Tada *et al.* (1973) with the signs of the stress and displacement reversed.

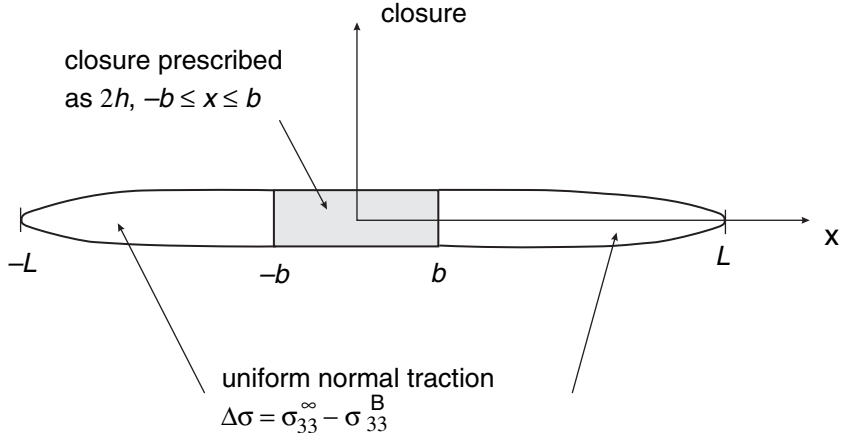


Fig. 7. Schematic illustration of a compaction band of total length $2L$. A uniform compactive displacement $2h$ is specified for $-b \leq x \leq b$ and a uniform closure traction, equal to the difference between the far-field compressive stress σ_{33}^{∞} and the resistive stress in the band σ_{33}^B , is specified for $|b| < x \leq |L|$. This is a plane strain model and, hence, extends indefinitely out of the plane of the sketch. Displacements are shown as opening for clarity but correspond to interpenetration (compaction) in the model.

(Again the interpenetration of the crack surfaces is interpreted as inelastic compactive displacement.) The compaction band has total length $2L$ with a uniform compactive displacement $2h$ specified for $-b \leq x \leq b$. For $|b| < |x| \leq |L|$ a uniform closure traction, equal to the difference between the far-field compressive stress σ_{33}^{∞} and the resistive stress in the band σ_{33}^B , is specified. The magnitude of this traction is chosen to eliminate the singularity in stress at $x = \pm b$, or equivalently, to ensure that the tangent to the profile of crack surface displacements is continuous. This traction is given by

$$\Delta\sigma = \frac{\mu h}{L(1-\nu)} \frac{1}{E_1(k) - (b/L)^2 E_2(k)} \quad (28)$$

where $k = \sqrt{1 - (b/L)^2}$ and E_1 and E_2 are the complete elliptic integrals of the first and second kinds, respectively. The stress intensity factor at the ends of the compaction band is given by

$$K = \sqrt{\frac{\pi}{L-b(1-\nu)}} \frac{\mu h}{\left\{ \frac{k\sqrt{1-b/L}}{E_1(k) - (1-k^2)E_2(k)} \right\}}. \quad (29)$$

The factor $\{\dots\}$ equals unity in the limit $b/L \rightarrow 0$ ($k \rightarrow 1$). In this limit $\Delta\sigma \rightarrow \mu h/L(1-\nu)$ so that the stress intensity factor reduces to $\Delta\sigma\sqrt{\pi L}$, the well-known expression for a crack of length $2L$ loaded by a stress $\Delta\sigma$. In the alternative limit, $b/L \rightarrow 1$ ($k \rightarrow 0$), $\{\dots\}$

equals $\sqrt{8}/\pi = 0.90$ and equation (29) reduces to

$$K = \sqrt{\frac{8}{\pi}} \frac{1}{\sqrt{(L-b)(1-\nu)}} \frac{\mu h}{\pi} \quad (30)$$

to first order in $1 - b/L$. Equation (30) is the stress intensity factor at the right end of a crack of length $L - b$ wedged open by a semi-infinite dislocation of magnitude $2h$ at the left end and uniform traction to ensure no singularity at the left end (Tada *et al.* 1973). This is identical to the solution for a crack of length $(L - b)$ enclosing a net entrapped dislocation $2h$ and traction chosen to negate the singularity at the left end (Rice 1968b). The traction in this case is $\Delta\sigma \rightarrow 2\mu h/\pi(L-b)(1-\nu)$, so that the stress intensity factor is twice that for a crack of length $2(L-b)$ with uniform traction $\Delta\sigma$ and no entrapped dislocation. As is evident from equation (30), the stress intensity factor becomes unbounded as $L \rightarrow b$ and so also does the traction required to eliminate the singularity at the edge of the dislocation. This behaviour reflects the stronger stress singularity at the edge of a uniform dislocation (reciprocal of distance from the edge) than at the edge of a crack (reciprocal of the square root of distance from the edge). Figure 8a plots the factor $\{\dots\}$ against b/L from zero to one (corresponding to k varying over the same range). Figure 8b plots the stress intensity factor from equation (29), divided by $\sqrt{\pi}\mu h/\sqrt{L(1-\nu)}$, against b/L . Also shown is $(1-b/L)^{-1/2}$, the approximate result obtained by setting the

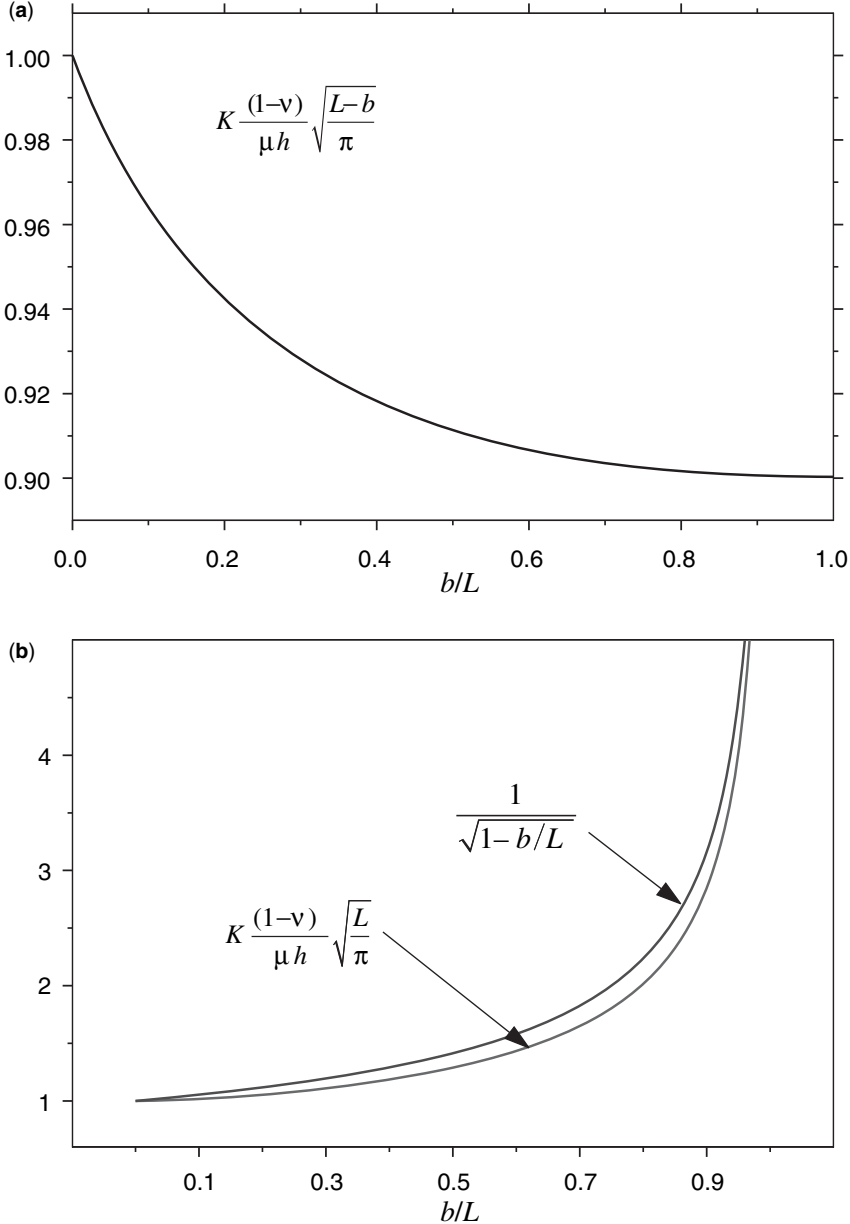


Fig. 8. (a) Plot of the stress intensity factor K at $x_1 = \pm L$ in Figure 7, divided by $\mu h \sqrt{\pi/(L-b)/(1-v)}$ against b/L .
(b) Comparison of K divided by $\mu h \sqrt{\pi/L/(1-v)}$ with $(1 - b/L)^{-1/2}$ against b/L .

factor $\{\dots\}$ in equation (29) equal to unity. As the plot shows, the stress intensity factor is well approximated by

$$K = \sqrt{\frac{\pi}{L-b}} \frac{\mu h}{(1-v)} \quad (31)$$

not only near $b/L \rightarrow 0$, where it is exact, but over most of the range of b/L .

Tada *et al.* (1973) also gave the expression for the crack surface displacements (here, closure or interpenetration). These are plotted in Figure 9 for b/L equal to 0, 0.25, 0.5, 0.75, and 0.9. For $b/L = 0$, there is no entrapped dislocation and the

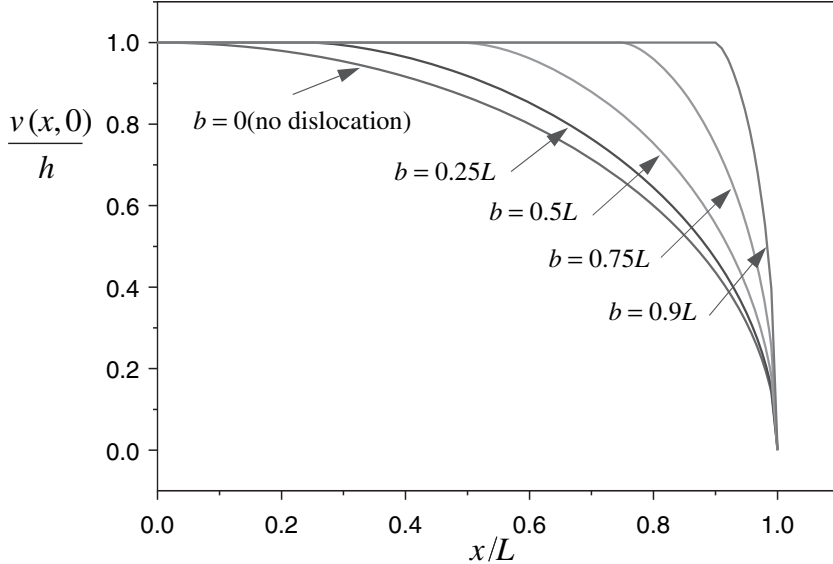


Fig. 9. Closing displacement divided by half the imposed closing dislocation h against distance from the centre divided by the band half-width L . Profiles are plotted for $b/L = 0, 0.25, 0.5, 0.75$ and 0.9 .

displacement profile is purely elliptical (as for a crack loaded by uniform surface tractions). As long as b/L is not too large, the profiles do not differ significantly from elliptical and probably fall within the scatter of data from figure 4a of Sternlof *et al.* (2005).

The roughly elliptic displacement profiles measured by Sternlof *et al.* (2005) suggest that b/L is small and the stress intensity factor can be approximated by equation (31) with $b = 0$. Substituting this value into the relation between the stress intensity factor and energy release rate \mathcal{G} ,

$$\mathcal{G} = (1 - \nu)K^2/2\mu \quad (32)$$

and rearranging yields

$$\frac{2h}{\sqrt{L}} = \sqrt{\frac{8\mathcal{G}(1 - \nu)}{\pi\mu}}. \quad (33)$$

Thus, if compaction bands are assumed to grow at a constant, critical value of the energy release rate, equation (33) implies that the band thickness (or midpoint closure) should scale as the square root of the band half-length. This predicted scaling is consistent with a recent analysis of compaction band data by Rudnicki *et al.* (2006). They replotted the data from Figure 4b of Sternlof *et al.* (2005) on a log-log scale, and added several

points from laboratory data and from field data of Hill (1989) and Mollema & Antonellini (1996). Fitting a straight line through the data yields a relationship of the form

$$2h = AL^B \quad (34)$$

where A and B are constants. The exponent B is roughly $1/2$: 0.42 , 0.5 , and 0.53 for fitting the entire dataset, all the field data and the Sternlof *et al.* (2005) data, respectively. (Fossen & Hesthammer (1997) have reported a similar scaling relation (width proportional to the square root of length) for deformation bands in Jurassic sandstone in southeastern Utah.) For $\mu = 8.33$ GPa and $\nu = 0.2$, values inferred for the Valley of Fire by Sternlof *et al.* (2005), the coefficient A corresponds to critical values of \mathcal{G} equal to 25 , 30 , and 37 kJ m $^{-2}$ for the same three fits. These values are slightly lower than the $\mathcal{G} = 40$ kJ m $^{-2}$ as estimated by Rudnicki & Sternlof (2005) and consistent with laboratory estimates (Vajdova & Wong 2003; Tembe *et al.* 2006). Using the individual values of $2h$ and L with the same values of μ and ν yields critical energy release rates ranging from 4 to 90 kJ m $^{-2}$ for the field data and 71 , 105 , and 111 kJ m $^{-2}$ for the three laboratory values. It is not surprising that the laboratory values are at the upper end of the range, as the approximation of $b/L \rightarrow 0$ is probably not very good for bands

that extend across the entire specimen. Despite the many uncertainties involved in this comparison, the agreement seems too good to be coincidental and suggests that the model depicted in Figure 7 and suggested by Sternlof (2006) has merit.

Discussion

We have modelled a compaction band as a thin ellipsoidal inhomogeneity subjected to an inelastic compactive strain and compressive stresses in the far field. The shape was strongly suggested by field observations of Sternlof *et al.* (2005) and Sternlof (2006) on the Aztec sandstone of the Valley of Fire, Nevada. For a range of parameters encompassing the field data and aspect ratios typical of the field data, 10^{-3} – 10^{-4} , the results show that the stress state in the band does not differ significantly from that for zero aspect ratio. The stress state within the band is primarily controlled by the ratio of the far-field compressive stress to twice the shear modulus of the matrix multiplied by the inelastic compactive strain. For the field data, this ratio is about 0.02–0.05, but it may be several times larger for laboratory experiments. For the approximation of a zero aspect ratio band, the stress state at the flank of the band is identical to the far-field stress state. The stress state at the tip of the band is fully 3D (all three principal stresses differ even when the far-field stress, imposed inelastic strain and band shape are axisymmetric). The calculations suggest that the ratio of the compressive stress ahead of the band and normal to the plane of the band to that in the far field is of the order of 10–100. This ratio is not significantly affected by elastic mismatch within even an implausibly wide range, although the ratio does become unbounded in the limit of the band shear modulus going to zero. Hence, elastic mismatch is not likely to be a major factor in compaction band extension. The stress elevation is dominated by the product of the inelastic compactive strain and the ratio of the shear modulus to far-field compressive normal stress.

Sternlof and Pollard (2002) and Sternlof *et al.* (2003) suggested that compaction bands can be modelled as anti-cracks. Anti-cracks are the compressive counterpart of a tensile crack: the stiffness of material in the band is neglected and the band is idealized as negligibly thin. The predicted interpenetration of anti-crack surfaces, although physically unrealistic, is interpreted as closure of the band boundaries as a result of inelastic compaction. The anti-crack approximation arises as a limit of the inhomogeneity model. As noted above, for zero aspect ratio, the compressive stress at the band tip does become unbounded as the shear

modulus within the band μ_B goes to zero. The correspondence between a crack with uniform crack-surface tractions and the limit of a flat ellipsoid is well known (Rudnicki 1977; Hoenig 1978). To obtain this limit properly, it is necessary to consider an ellipsoid with small but finite thickness c , in the limit $c \rightarrow 0$ with $c\epsilon_{33}^B$ remaining finite and equal to the relative crack surface displacements.

The calculations here have demonstrated that results for zero aspect ratios differ negligibly from those for the very small aspect ratios typical of field data, 10^{-3} – 10^{-4} , and that σ_{33}^{tip} is roughly one to two orders of magnitude larger than σ_{33}^{∞} for the parameters considered here. Furthermore, the results have been shown not to be strongly dependent on the elastic mismatch (which is not well constrained by observation). For these reasons, it is not unreasonable to idealize the ratio $\sigma_{33}^{\text{tip}}/\sigma_{33}^{\infty}$ as unbounded, as it is in the limit $\mu_B/\mu \rightarrow 0$ or for an ‘anti-crack’. Sternlof *et al.* (2005) used a MATLAB code (provided by P. Sharma of the University of Houston) to compute the variation of stress (σ_{33} in the notation here) with distance from the tip of an ellipsoidal inclusion. They showed (their fig. 15) that for very small distances the stress varies as $r^{-1/2}$, where r is distance from the tip, as it does near the tip of a crack in a linear elastic material, but that the stress at the interface between band and matrix remains finite (as long as the ellipsoid has finite aspect ratio and nonzero modulus). Sternlof *et al.* (2005) concluded that, at least for parameters representative of field data, the difference between the stress fields of the anti-crack and inclusion models is significant only very close to the tip and the anti-crack model is a reasonable approximation. This idealization of a compaction band as an anti-crack makes it possible to take advantage of the body of results for linear elastic fracture mechanics.

On the other hand, Katsman *et al.* (2006) used numerical calculations with a spring-network model and some analytical calculations for a tabular closing mode dislocation to conclude ‘that there is little similarity between stress distributions around CBs and cracks (or anticracks as extended from Fletcher & Pollard (1981))’ and proposed that compaction bands are better described as ‘anti-dislocations’. Their latter conclusion is supported by the results here in the sense that the ratio $\sigma_{33}^{\infty}/2\mu\epsilon_{33}^P$ is small, a few per cent, for field data and that the band and near-tip stress are primarily controlled by the inelastic compactive strain ϵ_{33}^P . Thus, the specified inelastic compactive strain imposes a displacement on the band boundaries rather than a traction, as is normally the case in crack problems.

The distinction between crack and dislocation models is not, however, a sharp one given the

well-known connection between them (Bilby & Eshelby 1968). A ‘crack’ model typically implies that the distribution of crack surface tractions is specified and the relative crack surface displacements are calculated, whereas a ‘dislocation’ model implies that the relative displacements are specified. Of course, for a distribution of crack surface tractions there is a corresponding distribution of crack surface displacements (dislocation) and vice versa. Although Sternlof *et al.* (2005) referred to their model as an ‘anti-crack’, they implemented it by specifying the relative crack surface displacements (dislocation) corresponding to the measured width profiles. Because the measured width profiles are elliptic, the resulting crack surface traction is uniform as for a simple crack model. (In this case, the far-field stress of Sternlof *et al.* (2005) should be regarded as the difference between the far-field stress and this uniform traction.)

As already noted, the stress ahead of a crack (or anti-crack) is singular at the tip and varies as $r^{-1/2}$, where r is distance from the tip. The stress at the edge of a uniform tabular dislocation is, however, also singular and, as noted by Katsman *et al.* (2006), varies as r^{-1} . Of course, the stress in any real material cannot be unbounded and will be alleviated by inelastic processes that are neglected in the linear elastic idealization. A more complex and realistic model might specify the relation between the relative displacements and the tractions in such a way as to reflect the inelastic processes at the tip. At present, however, such details are not constrained by observation. The advantage of the crack formulation is that the energy in finite volumes surrounding the tip is bounded. (This is not the case for a uniform tabular dislocation; this feature is reflected in that $K \rightarrow \infty$ in equation (30) when $L \rightarrow b$.) Consequently, a criterion for propagation can be expressed in terms of a critical value of the stress intensity factor (the coefficient of the inverse square root singular stress on the plane ahead of the crack, usually divided by $\sqrt{2\pi}$) or the energy released per unit area of band advance. In addition, a large body of evidence in fracture mechanics (e.g. Rudnicki 1980; Anderson 1995; Lawn 1983) has established that whenever the actual inelastic processes that occur in response to the high stress at the tip take place in a zone having a length scale much smaller than geometric lengths in the problem (small-scale yielding), the singular elastic field is a good description at distances several times the inelastic process zone size. In this sense, the stress intensity factor (or energy release rate) relates the intensity of the near tip field to the applied loads or displacements in a way that is insensitive to the detailed inelastic processes near the tip. The energy release model of Rudnicki & Sternlof (2005) takes advantage of

these features of linear elastic fracture mechanics to compare an estimate of critical energy release rate with values inferred from laboratory tests (Vajdova & Wong 2003; Tembe *et al.* 2006). Similarly, the combined anti-crack–dislocation model discussed here uses the estimated energy release rate to suggest an explanation for the variation of band width with length noted by Sternlof (2006) and elaborated by Rudnicki *et al.* (2006).

The variation and magnitude of the stress field near the band tip will, of course, depend on the inelastic microstructural processes that occur there, including grain decohesion and rearrangement and, possibly, cracking and fracture, as well as the elastic mismatch. If the band is modelled as having a finite stiffness (elastic constants), then it seems unlikely that the stress field will be dramatically altered by variations in the tip shape (as long as there are no corners or vertices, which would be expected to introduce weak singularities). If, however, the band stiffness is neglected and the band is assumed to be very narrow, then the stress at the band tip is approximately inversely proportional to the root radius of the band tip. An elliptical profile of displacements is associated with the inverse square root of distance singularity characteristic of linear elastic fracture mechanics and implies a very small inelastic process zone. The field observations of Sternlof *et al.* (2005) and Sternlof (2006) gave little or no indication of such a process zone at the band tip; their band profiles appeared to be very nearly elliptical as the end is approached. Nevertheless, there is likely to be increased uncertainty in measurements very close to the tip. On the other hand, Tembe *et al.* (2006) used microstructural observations to inelastic process zone sizes of 0.3–0.5 times the notch depth (2 mm) for samples with diameters of 18.4 mm and found that this agrees with predictions of a linear elastic fracture model. The implications of this for the different rock type, stress level and geometry of the field data are not clear, but further information on the details of the compaction processes near the tip of a band would provide insight into the interpretation of the critical energy release rate and its possible dependence on microstructural parameters.

Conclusion

We have used results from Eshelby (1957) to examine the stress state within and at the tip of a compaction band modelled as a thin, ellipsoidal inhomogeneity subjected to an inelastic compactive strain. For parameter values inferred for the field site of Sternlof *et al.* (2005), the compressive stress normal to the plane of the band just ahead

of the tip is of the order of 10–100 times the remote stress. Aspect ratios typical of field data, 10^{-3} – 10^{-4} , do not yield results significantly different from those for zero aspect ratio. Elastic mismatch between the band and the surrounding material has only a small effect on the stress ahead of the band for compactive strains, moduli and stresses typical of field values. The relatively minor effect of the elastic mismatch is also consistent with the results of an energy release model of propagation introduced by Rudnicki & Sternlof (2005). This model suggests the product of the remote stress and the relative inelastic compactive displacement as a quantity critical for propagation. An estimate for this product from the field data of Sternlof *et al.* (2005) yields a value of about 40 kJ m^{-2} , similar to values of compaction energies inferred from laboratory tests on circumferentially notched compression samples (Vajdova & Wong 2003; Tembe *et al.* 2006). A combined anti-crack-dislocation model yields quantitative results of the stress intensity factor and the closure distribution for a conceptual model proposed by Sternlof (2006). If the band is assumed to grow at a critical value of the energy release rate estimated by Rudnicki & Sternlof (2005) then the prediction of the variation of band width with length agrees well with that identified by Rudnicki *et al.* (2006).

Principal financial support for this work was provided by the US Department of Energy, Office of Basic Energy Science, Geosciences Research Program through grant DE-FG02-93ER14344/A016 to Northwestern University. I am grateful to K. Sternlof for many helpful discussions and explanations of the field observations, and to S. Tembe and T.-F. Wong for providing their extension and reanalysis of Sternlof's data and for many discussions.

Appendix

The Eshelby factors appearing in equations (15), (16) and (17) of the text are given by

$$\begin{aligned} S_{3333} &= 1 - \frac{(1-2v)}{2(1-v)} I(e) - \frac{e^2(2-3I(e))}{2(1-v)(1-e^2)} \\ S_{kk33} &= 1 - \frac{(1-2v)}{(1-v)} I(e) \\ S_{33kk} &= \frac{(1+v)}{(1-v)} (1 - I(e)) \end{aligned}$$

where

$$I(e) = \frac{e}{(1-e^2)^{3/2}} \left\{ \arccos(e) - e(1-e^2)^{1/2} \right\}$$

and, for axisymmetry, the indices '22' can be replaced by

'11' wherever they appear. The expression for $I(e)$ corrects a misprint in Rudnicki (2002), which has e^2 instead of e in the numerator of the first term multiplying $\{\dots\}$. The factor S_{3311} can be determined from

$$S_{3311} = \frac{1}{2} (S_{33kk} - S_{3333})$$

again noting that $S_{3311} = S_{3322}$. S_{1133} can be calculated in similar fashion.

References

- ANDERSON, T. L. 1995. *Fracture Mechanics, Fundamentals and Applications*, 2nd edn. CRC Press, Boca Raton, FL.
- ANTONELLINI, M. & AYDIN, A. 1994. Effect of faulting on fluid flow in porous sandstones: petrophysical properties. *AAPG Bulletin*, **78**, 355–377.
- ANTONELLINI, M. & AYDIN, A. 1995. Effect of faulting on fluid flow in porous sandstone: geometry and spatial distribution. *AAPG Bulletin*, **79**, 642–671.
- BASTAWROS, A.-F., BART-SMITH, H. & EVANS, A. G. 2000. Experimental analysis of deformation mechanisms in a closed-cell aluminum alloy foam. *Journal of the Mechanics and Physics of Solids*, **48**, 301–322.
- BAUD, P., KLEIN, E. & WONG, T.-F. 2004. Compaction localization in porous sandstones: spatial evolution of damage and acoustic emission activity. *Journal of Structural Geology*, **26**, 603–624.
- BÉSUELLE, P. & RUDNICKI, J. W. 2004. Localization: shear bands and compaction bands. In: GUÉGUEN, Y. & BOUTÉCA, M. (eds) *Mechanics of Fluid Saturated Rocks*. International Geophysics Series, **89**, 219–321.
- BILBY, B. A. & ESHELBY, J. D. 1968. *Dislocations and the Theory of Fracture*, Volume 1. Academic Press, New York, 99–182.
- CHALLA, V. & ISSEN, K. A. 2004. Conditions for compaction band formation in porous rock using a two-yield surface model. *Journal of Engineering Mechanics*, **130**, 1089–1097.
- COCCO, M. & RICE, J. R. 2002. Pore pressure and poro-elasticity effects in Coulomb stress analysis of earthquake interactions. *Journal of Geophysical Research*, **107**, doi:10.1029/2000JB000138.
- ESHELBY, J. D. 1957. The determination of the elastic field of an ellipsoidal inclusion and related problems. *Proceedings of the Royal Society of London, Series A*, **241**, 376–396.
- FLETCHER, R. C. & POLLARD, D. D. 1981. Anticrack model for pressure solution surfaces. *Geology*, **9**, 419–424.
- FORTIN, J., STANCHITS, S., DRESEN, G. & GUÉGUEN, Y. 2006. Acoustic emission and velocities associated with the formation of compaction bands in sandstone. *Journal of Geophysical Research*, **111**, B10203, doi:10.1029/2005JB003854.
- FOSSEN, H. & HESTHAMMER, J. 1997. Geometric analysis and scaling relations of deformation bands in porous sandstones. *Journal of Structural Geology*, **19**, 1479–1493.

- GRUESCHOW, E. & RUDNICKI, J. W. 2005. Elliptic yield cap constitutive modeling for high porosity sandstone. *International Journal of Solids and Structures*, **42**, 4574–4587.
- HAIMSON, B. C. 2001. Fracture-like borehole breakouts in high-porosity sandstone: are they caused by compaction bands? *Physics and Chemistry of the Earth (A)*, **26**, 15–20.
- HAIMSON, B. C. 2003. Borehole breakouts in Berea sandstone reveal a new fracture mechanism. *Pure and Applied Geophysics*, **160**, 813–831.
- HAIMSON, B. & LEE, H. 2004. Borehole breakouts and compaction bands in two high-porosity sandstones. *International Journal of Rock Mechanics & Mining Sciences*, **41**, 287–301.
- HAIMSON, B. C. & SONG, I. 1998. Borehole breakouts in Berea sandstone: two porosity-dependent distinct shapes and mechanisms of formation. In: *SPE/ISRM Rock Mechanics in Petroleum Engineering*. Society of Petroleum Engineers, Richardson, TX, 229–238.
- HILL, R. E. 1989. *Analysis of deformation bands in the Aztec sandstone, Valley of Fire State Park, Nevada*. Master's thesis, University of Nevada, Las Vegas.
- HOENIG, A. 1978. The behavior of a flat elliptical crack in an anisotropic elastic body. *International Journal of Solids and Structures*, **14**, 925–934.
- HOLCOMB, D. J. & OLSSON, W. A. 2003. Compaction localization and fluid flow. *Journal of Geophysical Research*, **108**, B6,2290, doi:10.1029/2001JB000813.
- ISSEN, K. A. & RUDNICKI, J. W. 2000. Conditions for compaction bands in porous rock. *Journal of Geophysical Research*, **105**, 21529–21536.
- KATSMAN, R., AHARONOV, E. & SCHER, H. 2006. Localized compaction in rocks: Eshelby's inclusion and the spring network model. *Geophysical Research Letters*, **33**, L10311, doi:10.1029/2005GL025628.
- KINNEY, J. H., MARSHALL, G. W., MARSHALL, S. J. & HAUPPT, D. L. 2001. Three dimensional imaging of large compressive deformations in elastomeric foams. *Journal of Applied Polymer Science*, **80**, 1746–1755.
- KIRBY, S., DURHAM, W. B. & STERN, L. 1992. The ice I-II transformation: mechanisms and kinetics under hydrostatic and nonhydrostatic conditions. In: MAENO, N. & HONDOH, T. (eds.) *Physics and Chemistry of Ice*. Hokkaido University Press, Sapporo, 456–462.
- KLAETSCH, A. R. & HAIMSON, B. C. 2002. Porosity-dependent fracture-like breakouts in St. Peter sandstone. In: HAMMAH, R., BADEN, W., CURRAN, J. & TELESNICKI, N. (eds) *Mining and Tunneling Innovation and Opportunity*, University of Toronto Press, Toronto, 1365–1371.
- LAWN, B. 1993. *Fracture of Brittle Solids* 2nd edn, Cambridge Solid State Science Series, Cambridge University Press, Cambridge.
- MOLLEMA, P. & ANTONELINI, M. A. 1987. Compaction bands: a structural analog for anti-mode I cracks in aeolian sandstone. *Tectonophysics*, **267**, 209–228.
- MURA, T. 1987. *Micromechanics of Defects in Solids*, 2nd, revised edn. Kluwer, Norwell, MA.
- OLSSON, W. A. 1999. Theoretical and experimental investigation of compaction bands. *Journal of Geophysical Research*, **104**, 7219–7228.
- OLSSON, W. A. & HOLCOMB, D. J. 2000. Compaction localization in porous rock. *Geophysical Research Letters*, **27**, 3537–3540.
- PAPKA, S. D. & KYRIAKIDES, S. 1998. Experiments and full-scale numerical simulations of in-plane crushing of a honeycomb. *Acta Metallurgica*, **46**, 2765–2776.
- PARK, C. & NUTT, S. R. 2001. Anisotropy and strain localization in steel foam. *Material Science and Engineering*, **A299**, 68–74.
- RICE, J. R. 1968a. A path independent integral and the approximate analysis of strain concentration by notches and cracks. *Journal of Applied Mechanics*, 379–386.
- RICE, J. R. 1968b. Mathematical analysis in the mechanics of fracture. In: LIEBOWITZ, H. (ed.) *Fracture: an Advanced Treatise*, Volume 2. Academic Press, New York, 191–311.
- RUDNICKI, J. W. 1977. The inception of faulting in a rock mass with a weakened zone. *Journal of Geophysical Research*, **82**, 844–854.
- RUDNICKI, J. W. 1980. Fracture mechanics applied to the Earth's crust. *Annual Review of Earth and Planetary Sciences*, **8**, 489–525.
- RUDNICKI, J. W. 2002. Alteration of regional stress by reservoirs and other inhomogeneities: stabilizing or destabilizing? In: VOUILLE, G & BEREST, P. (eds) *Proceedings of the Ninth International Congress on Rock Mechanics*, Paris, 25–29 August, 1999, Volume 3. Balkema, Rotterdam, 1629–1637.
- RUDNICKI, J. W. 2003. Compaction bands in porous rock. In: LABUZ, J. F. & DRESCHER, A. (eds) *Bifurcations and Instabilities in Geomechanics*. Proceedings of the International Workshop on Bifurcation and Instability 2002, St. Johns College 3–5 June, 2002. Swets & Zeitlinger, Lisse, 29–39.
- RUDNICKI, J. W. 2004. Shear and compaction band formation on an elliptic yield cap. *Journal of Geophysical Research*, **109**, B03402, doi:10.1029/2003JB002633.
- RUDNICKI, J. W. & STERNLOF, K. R. 2005. Energy release model of compaction band propagation. *Geophysical Research Letters*, **32**, L16303, doi:10.1029/2005GL023602.
- RUDNICKI, J. W., TEMBE, S. & WONG, T.-F. 2006. Relation between width and length of compaction bands in porous sandstones (abstract). *EOS Transactions, 87(52), American Geophysical Union, Fall Meeting Supplement*, Abstract T43A-1633.
- STERNLOF, K. R. 2006. *Structural geology, propagation mechanics and hydraulic effects of compaction bands in sandstone*. PhD thesis, Stanford University, Stanford.
- STERNLOF, K. & POLLARD, D. 2002. Numerical modeling of compactive deformation bands as granular anti-cracks. *EOS Transactions, American Geophysical Union*, **83**, F1347, Fall Meeting Supplement, Abstract T11F-10.
- STERNLOF, K., POLLARD, D. & CHOPRA, G. 2003. Compaction bands as anticracks in sandstone: taming complexity through integrated observation, experimentation and process based simulation. *Geological Society of America, Abstracts with Programs*, **35**, no. 6, 40.
- STERNLOF, K. R., CHAPIN, J. R., POLLARD, D. D. & DURLOFSKY, L. J. 2004. Permeability effects of systematic deformation band arrays in sandstone. *AAPG Bulletin*, **88**, 1315–1329.

- STERNLOF, K. R., RUDNICKI, J. W. & POLLARD, D. D. 2005. Anti-crack inclusion model for compaction bands in sandstone. *Journal of Geophysical Research*, **110**, B11403, doi: 10.1029/2005JB003764.
- TADA, H., PARIS, P. C. & IRWIN, G. R. 1973. *The Stress Analysis of Cracks Handbook*, Del Research, Hellertown, PA.
- TEMBE, S., VAJDOVA, V., WONG, T.-F. & ZHU, W. 2006. Initiation and propagation of strain localization in circumferentially notched samples of two porous sandstones. *Journal of Geophysical Research*, **111**, B02409, doi:10.1029/2005JB003611.
- VAJDOVA, V. & WONG, T.-F. 2003. Incremental propagation of discrete compaction bands and microstructural observations on circumferentially notched samples of Bentheim sandstone. *Geophysical Research Letters*, **30**, 1775, doi:10.1029/2003GL017750.
- VAJDOVA, V., BAUD, P. & WONG, T.-F. 2004. Permeability evolution during localized deformation in Bentheim sandstone. *Journal of Geophysical Research*, **109**, B10406, doi:10.1029/2003JB002942.
- WAWERSIK, W. R., RUDNICKI, J. W., DOVE, P. ET AL. 2001. Terrestrial sequestration of CO₂: an assessment of research needs. *Advances in Geophysics*, **43**, 97–177.
- WONG, T.-F., BAUD, P. & KLEIN, E. 2001. Localized failure modes in a compactant porous rock. *Geophysical Research Letters*, **28**, 2521–2524.

Characterization of pore-space heterogeneity in sandstone by X-ray computed tomography

L. LOUIS^{1,2}, P. BAUD³ & T.-F. WONG¹

¹*Department of Geosciences, State University of New York at Stony Brook, Stony Brook, NY 11794-2100, USA*

²*Present address: Département des Sciences de la Terre et de l'Environnement, Université de Cergy-Pontoise, CNRS UMR 7072, Bâtiment Neuville 3.1, Neuville-sur-Oise, F-95031 Cergy-Pontoise, France (e-mail: laurent.louis@u-cergy.fr)*

³*Institut de Physique du Globe (CNRS/ULP), 5 rue Descartes, 67084 Strasbourg, France*

Abstract: In this study we review some of the recent advances in the application of X-ray computed tomography (X-ray CT) to geomaterials. This non-destructive technique based on density contrasts provides 2D images comparable with micrographs and 3D reconstructions at various resolutions depending on the acquisition setup. Synchrotron images with resolution of a few microns allow for 3D mapping of the pore space and can be used to perform 3D fluid flow simulations. ‘Industrial’ CT systems can provide images of centimetre-sized samples with a resolution of *c.* 50 µm. This resolution is suitable for studying centimetre-scale structural heterogeneities and compaction localization, as illustrated in recent studies. Starting from images taken at both synchrotron and industrial resolutions in intact samples of porous sandstones, we show that important conclusions on pore-space heterogeneity can be drawn from global and local analysis of the distributions of X-ray attenuation values. The global analysis is used in particular to identify relatively homogeneous materials in which compaction bands are likely to develop. Local analysis performed over small clusters of voxels appears to have more potential for the geometric description of the pore space. We show the existence of a resolution at which the local coefficient of variation of the X-ray distributions reaches a maximum. This resolution, which is about an order of magnitude lower than synchrotron resolution, appears to be related to the pore size, and the corresponding coefficient of variation to the porosity.

Since its invention in the 1970s, X-ray computed tomography (CT) has spread and developed quickly, mostly stimulated by growing needs in medicine for diagnostics and interventional procedures. This technique, originally meant to provide high-resolution non-destructive 3D reconstructions of bones and soft tissues, eventually attracted interest from other domains such as industry and geosciences. Whereas medical applications require fast imaging and limited beam energy, industrial use allows systems to be optimized for penetration, resolution and long exposures. Non-destructive testing, chemical characterization, and monitoring of deformation or alteration over long periods of time are some examples of applications. Earth processes such as earthquakes, orogeny, basin tectonics or fluid circulation involve mechanisms down to the scale of individual grains (micrometer–millimeter) and the ability of X-ray CT to monitor these mechanisms non-invasively and in three dimensions in the laboratory makes it an ideal tool for geoscientists (Sutton *et al.* 2002). Implications for construction, oil recovery, soil contamination or waste repository are also

considerable, and numerous studies have been conducted to address both applied and theoretical issues (Van Kaick & Delorme 2005; Cnudde *et al.* 2006). For instance, understanding of fluid flow in porous rocks can be greatly improved by combining theoretical simulations with 3D imaging of the material studied (Schwartz *et al.* 1994). With synchrotron X-ray microtomography, which can image the porous network of a sandstone with a resolution of the order of 1 µm (Dunsmuir *et al.* 1992), accurate permeability and conductivity estimations are made possible (Fredrich *et al.* 1993, 2006; Spanne *et al.* 1994; Coker *et al.* 1996; Coles *et al.* 1998; Arns *et al.* 2001, 2004). Also, microscopic deformation mechanisms such as pressure solution can be monitored *in situ* (Renard *et al.* 2004).

The sensitivity of X-ray CT imaging to local density allows for mineral characterization and statistical pore-space analysis. Studies have been reported on meteorites (Arnold *et al.* 1983), soils (Warner *et al.* 1989; Anderson *et al.* 1990; Lontoc-Roy 2005; Nahmani 2005), garnet porphyroblasts (Carlson & Denison 1992; Ketcham & Carlson 2001; Ketcham 2005), sandstone and

carbonate rocks (Mogensen *et al.* 2001; Van Geet *et al.* 2001). In experimental soil and rock mechanics, density changes associated with strain localization during dilatant brittle failure have been captured in numerous studies (Roscoe 1970; Desrues 1984; Raynaud *et al.* 1989; Kawakata *et al.* 1999; Bésuelle *et al.* 2003). X-ray tomography was also used to image density contrasts caused by compaction localization in both tectonically and experimentally deformed sandstones (Antonellini *et al.* 1994; Bésuelle *et al.* 2003; Aydin *et al.* 2006). Although not as straightforward as in the case of dilatant failure, especially at high resolution, visualization of compaction localization can still be satisfactorily achieved by processing the image dataset (Louis *et al.* 2006, 2007).

The present study is focused on the use of X-ray CT data in relation to pore-space heterogeneity and strain localization in sandstone. First, we briefly review some applications of 3D synchrotron microtomography and X-ray microfocus tomography to rocks. We then consider the characterization of the density heterogeneity of five sandstones (Fontainebleau, Bentheim, Diemelstadt, Berea and Darley Dale) as seen by X-ray imaging, at the scale of a centimetre-size rock sample and at the scale of a grain. At the larger scale, we estimate global X-ray attenuation parameters (mean and standard deviation) in an entire CT image and we find that these characteristics are highly dependent on the image resolution. When comparing the values obtained for the five sandstones, we suggest that a first-order analysis of the X-ray CT data may help anticipate the occurrence of strain localization. At the scale of the grain, the observed density heterogeneities depend on the topology of the void space. We find that each sandstone possesses a characteristic elementary volume for which the local heterogeneity is maximized. Although this volume and associated heterogeneity can be related to the pore size, it also appears to provide an adequate resolution for the visualization of strain localization. Overall, it is demonstrated that images acquired at coarse resolution such that void and solid fraction cannot be isolated still contain characteristic information for every rock investigated.

X-ray CT applied to rocks

Principle of X-ray CT imaging and common setups

X-ray CT is a non-destructive imaging technique that provides point-wise estimation of X-ray attenuation values of a material traversed by an X-ray beam. For a monoenergetic X-ray beam passing

through a homogeneous material, incident and attenuated X-rays are related by Beer's law, $I = I_0 e^{-\mu h}$, where μ is the attenuation coefficient and h the thickness of the object. For energy levels below 200 keV, the attenuation coefficient μ is controlled by two dominant physical processes, the photoelectric effect and the Compton effect. The photoelectric effect, which is proportional to Z^{4-5} (Z being the atomic number), is the main attenuation mechanism at energy levels up to 50–100 keV. At higher energy levels up to 5–10 MeV, the Compton effect, proportional to Z , dominates. Therefore, whereas higher energy levels are suitable for quantifying material local density, lower energy levels are more sensitive to composition differences (Ketcham & Carlson 2001). Notwithstanding these differences, good local density estimations can in general be made, especially in monomineral porous assemblies.

A simple scheme of most common X-ray acquisition setups is given in Figure 1. The X-ray beam may consist of coherent light (synchrotron light sources, Fig. 1a) resulting in distortion-free images, or initiate from virtually a point source (microfocus X-ray tubes employed in medical or industrial systems, Fig. 1b). Although synchrotron and fan X-ray beams have a certain thickness, only rays passing through the scan plane are generally used in image reconstruction. After going through the sample, the planar set of attenuated X-rays is recorded via a linear or arcuate series of detectors. Rotation of either the sample or the source-detector assembly allows for generation of

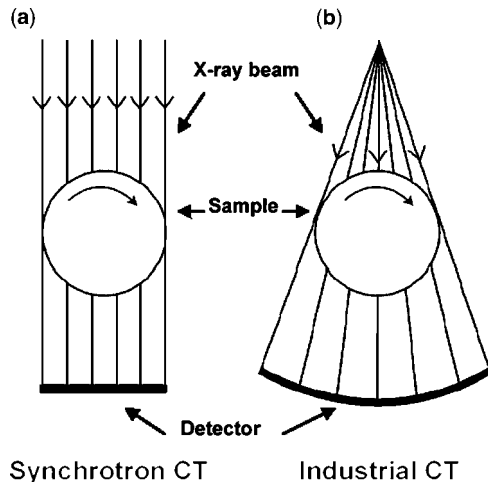


Fig. 1. (a) Principle of X-ray acquisition setup: X-ray beam made of parallel rays in synchrotron light sources. (b) X-ray beam initiates from virtually a point source in medical-industrial systems.

a set of views that are subsequently processed to recover a 2D slice mapping out the attenuation distribution of the sample. The final resolution of the X-ray images depends on the object size, the detector size and the focal spot size (medical and industrial systems only) (Van Geet *et al.* 2001). The detector size limits the total number of pixels recorded for each view and if the whole sample is illuminated at once, the larger the object, the larger the area represented by one pixel. In the case of fan beams, the best resolution that can be obtained is the focal spot size. In medical CT systems, the focal spot size is usually in the range 500–2000 μm , whereas industrial systems can be equipped with tubes with focal spot size as low as $<10 \mu\text{m}$ (Ketcham & Carlson 2001). In synchrotron X-ray sources, coherent light, which allows for non-ambiguous determination of the elementary volumes imaged, together with very high-resolution detectors can achieve resolutions as good as 1 μm for samples a few millimetres in size (Flannery *et al.* 1987; Lindquist *et al.* 2000).

Synchrotron based X-ray CT (1–10 μm spatial resolution)

In addition to using monochromatic light, which is very beneficial regarding effects such as beam hardening, microtomography with synchrotron X-ray sources can provide images of millimetre-sized samples with spatial resolution of the order of 1 μm . Following the first tomographic reconstruction from synchrotron-based images in a coal sample by Flannery *et al.* (1987), numerous analyses on geomaterials have been carried out. Most of these studies have taken advantage of the high-resolution capability of synchrotron X-ray imaging to reconstruct and describe the structure of porous materials. Coker *et al.* (1996) used synchrotron X-ray images to describe from a statistical point of view the pore space of a sample of Fontainebleau sandstone. The same rock was subsequently imaged by Lindquist *et al.* (1996, 2000) and the technique of medial axis analysis was introduced to extract geometric parameters such as pore and throat size distributions. A similar study was more recently conducted by Song *et al.* (2001) to describe the pore space of vesiculated basaltic rocks. The solid fraction from images of a Fontainebleau sandstone sample was used by Thovert *et al.* (2001) to achieve a grain reconstruction through a Poissonian generation of polydisperse spheres. Reconstruction of the pore space also allows for estimation of transport properties such as permeability and electrical conductivity (Spanne *et al.* 1994; Auzerais *et al.* 1996; Arns *et al.* 2001). Using synchrotron images of natural and

synthetic sandstones with a resolution of 1.67 μm , Fredrich *et al.* (2006) performed massively parallel lattice Boltzmann simulations of single-phase fluid flow. The macroscopic permeability computed from the image data agreed remarkably well in their study with experimental data over several orders of magnitude.

The formation of some geometric features associated with rock deformation has also been studied in synchrotron systems, such as the evolution of grain contact morphology during pressure solution creep in halite aggregates (Renard *et al.* 2004) and the inception of dilating shear bands in very fine-grained material (Viggiani *et al.* 2004). In the latter, the very small grain size of the clayey silt studied did not allow independent visualization of the pore space. However, the 14 μm resolution helped the same team to capture very accurately the overall strain evolution during the formation of a dilating shear band using digital image correlation (Lenoir 2006).

We show in Figure 2 a typical example of a 3D reconstruction from microtomographic images for a sample of Fontainebleau sandstone of 22% porosity. This dataset was acquired by Lindquist *et al.* (2000) at the X2-B tomographic facility of the Brookhaven National Synchrotron Light Source. Dunsmuir *et al.* (1992) provided a full description of this system. The Fontainebleau sandstone is an ideal rock for performing such imaging, as it is remarkably homogeneous in composition (>99% quartz) and has already been the focus of numerous studies (Bourbie & Zinszner 1985; Doyen 1988; Thiry *et al.* 1988; Zamora & Poirier 1990; Fredrich *et al.* 1993; Zhu *et al.* 1995). The reconstructions in Figure 2 represent exactly a 1 mm^3 volume. For better visualization, a parallelepiped has been cut out and the solid fraction and pore space have been isolated in Figure 1a and 1b, respectively. Such images clearly show, for instance, that much higher connectivity of the pore space is observed as compared with traditional 2D sectioning of rock samples.

'Industrial' high- and ultrahigh-resolution X-ray CT (10–100 μm spatial resolution)

Following the classification given by Ketcham & Carlson (2001), high- and ultrahigh-resolution CT systems are characterized by maximum resolutions of 100 μm and 10 μm (focal spot size), respectively. Usually, larger voxel sizes are accompanied by larger capacity of the imaging setup in terms of the size of the sample imaged. The type of applications that can be conducted with such versatile systems therefore depend highly on the size of the features investigated. For example, if the focus is

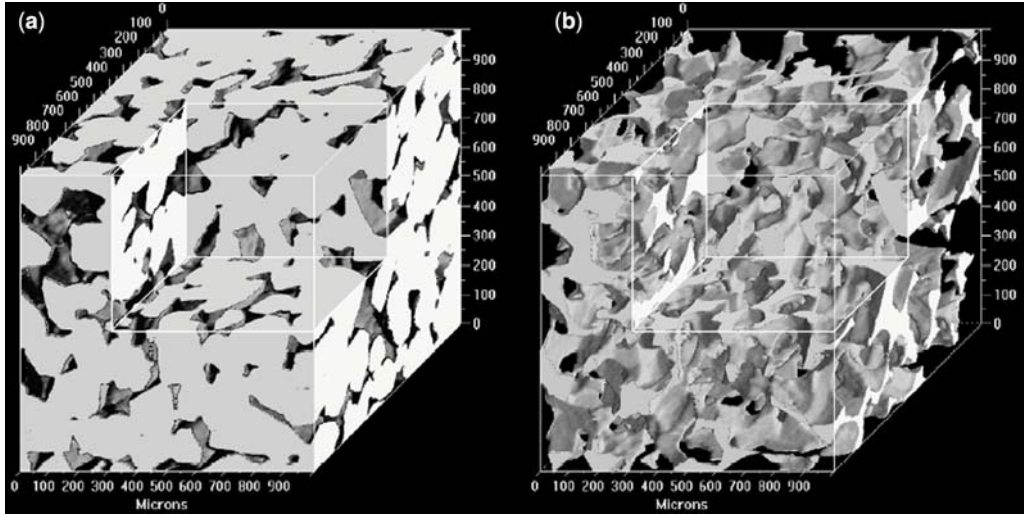


Fig. 2. A 3D reconstruction of a 22% porosity sample of Fontainebleau sandstone from microtomographic images of 5.7 μm resolution (Lindquist *et al.* 2000). The two images result from a thresholding at grey level value 140. (a) Solid fraction (pore space is made transparent). (b) Pore space (solid fraction is made transparent).

on determining the presence and geometric parameters of crystals, inclusions or pores that are large enough to enclose a significant amount of voxels, the same type of studies as those presented in the previous section can be conducted, and the only difference will be a change in absolute dimensions. Ketcham & Carlson (2001) provided a few examples of applications with the isolation of porphyroblasts in schist, diamonds and garnet in eclogites, and large-scale fracture networks in carbonate rock. Ketcham & Iturrino (2005) introduced new methods for imaging fracture networks in volcanic rocks based on subsequent imaging of dry and saturated samples. Ketcham (2005) conducted a full study of the location, size, shape and orientation of garnets in a garnet–kyanite schist. Veins in sandstone and stylolites in carbonate rock were also imaged using a laboratory X-ray CT system at c. 20 μm resolution by Van Geet *et al.* (2001). Ruiz de Argondona *et al.* (1999) monitored the progressive formation of macroscopic fissures in a dolomite during freeze–thaw cycles.

In the case of a sandstone, industrial CT resolution is such that the voxels of a CT slice usually return values reflecting various mixtures of solid matrix and void space. Depending on the resolution, this partial volume effect (Ketcham & Carlson 2001) can cause pore space to show higher attenuation values than the air outside the sample. On the other hand, voxels larger than grain and pore sizes allow for the inference of the spatial distribution of the porosity (Wellington & Vinegar 1987), and calibrations performed on porous rocks

and soils can establish a linear relationship between X-ray attenuation and local density (Vinegar *et al.* 1991; Desrues *et al.* 1996). Figure 3 presents a typical example of density heterogeneity within a CT slice of Rothbach sandstone cored at an oblique orientation with respect to the bedding plane. Differences in attenuation between sedimentary laminations reflect variations in porosity (Fig. 3a) as verified on photographs obtained from the corresponding thin section (Fig. 3b and c). Such variations in X-ray attenuation were used in a recent study as landmarks to perform digital image correlation on deformed samples and highlight zones of localized deformation (Louis *et al.* 2007).

Porosity contrasts between zones of a rock sample may also arise from mechanical deformation during strain localization, and numerous studies have focused on such features. The work of Desrues (1984) is probably one of the first attempts to use CT for imaging density variations associated with localized deformation in geomaterials. Local decrease in density associated with the formation of dilating shear bands in sand and sandstone have since then been reported in many X-ray CT studies (Vinegar *et al.* 1991; Bésuelle *et al.* 2000, 2003; Desrues 2004; Oda *et al.* 2004). Figure 4a shows an original CT image of a sample of Darley Dale sandstone deformed in triaxial compression at 20 MPa confining pressure and 10 MPa pore pressure. Dark zones in the upper part of the image are conjugate dilating shear bands that developed during brittle failure.

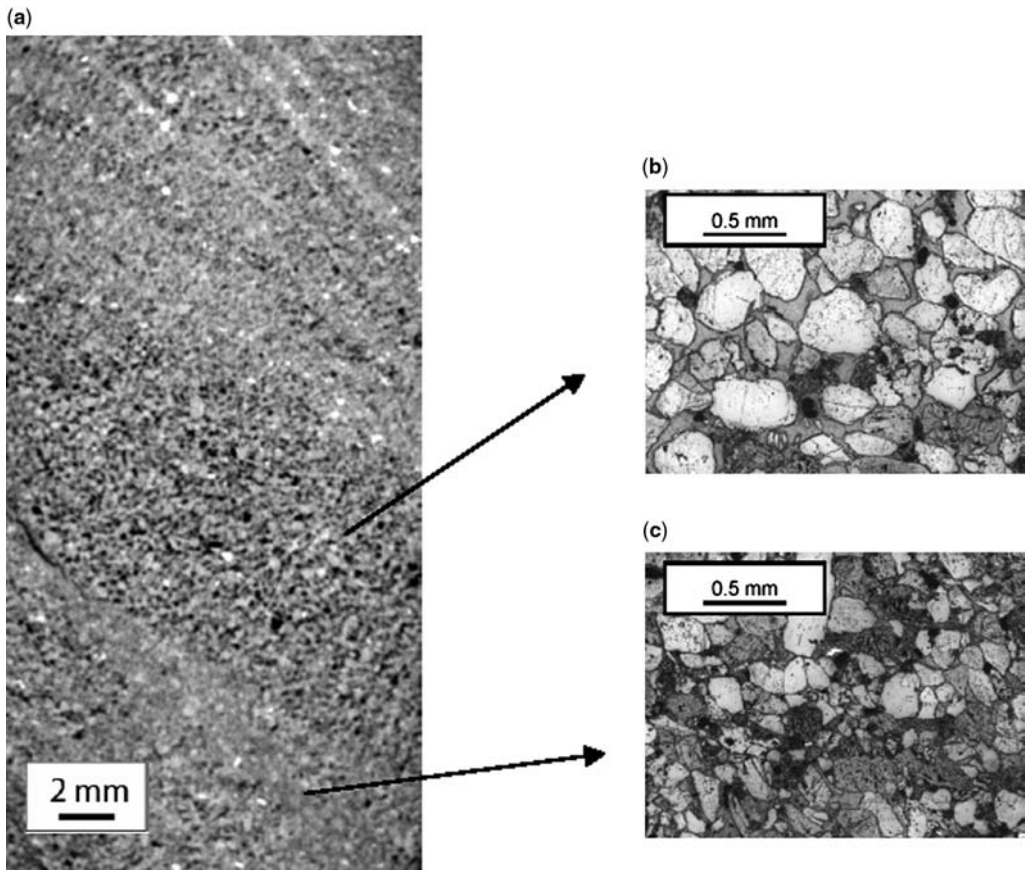


Fig. 3. (a) High-resolution CT scan of a sample of Rothbach sandstone at *c.* 50 μm resolution. This sample was cored at 45° to the sedimentary bedding. (b) Optical micrograph showing a high-porosity area of the sample, which appears darker (less dense) in the CT image. (c) A denser zone, which appears lighter in the CT image.

Compactive localized deformation in sandstone has also been recognized as an important failure mode both in the field (Antonellini *et al.* 1994; Aydin *et al.* 2006) and in the laboratory (Olsson 1999; Wong *et al.* 2001; Baud *et al.* 2004). However, CT imaging of such phenomenon is not as straightforward, because of the relatively low density contrast between compacted and undeformed zones (Louis *et al.* 2006). CT images of compaction localization in most previous studies were obtained at relatively poor resolution ($>1\text{ mm}$) and porosity contrasts between compacted and intact zones were observed through averaging of X-ray attenuation values over many grains and pores. At higher resolution (*c.* 50 μm in every direction), compaction localization was not observed in the images presented by Louis *et al.* (2006) in a recent study. In that study, the researchers deformed a sample of Diemelstadt sandstone at 150 MPa confining pressure and 10 MPa pore pressure, and a series of compaction

bands developed horizontally, perpendicular to the direction of major principal stress (see photograph in Fig. 4b). In the CT slice shown in Figure 4c, the presence of these bands did not result in a significant contrast in X-ray attenuation.

As compaction is likely to homogenize the distribution of X-ray attenuation values between neighbouring voxels through grain crushing and associated pore collapse, Otani *et al.* (2005) suggested the use of changes in overall homogeneity of X-ray CT images as a damage indicator in compacted sand piles. Otani *et al.* acquired X-ray CT scans at regular depth intervals and evaluated in each image the coefficient of variation δ or COV, which is defined as the ratio between the standard deviation σ and the mean X-ray attenuation μ such that $\delta = \sigma/\mu$. They were thus able to determine the specific depths at which particle crushing had occurred. In the Diemelstadt sandstone, Louis *et al.* (2006) showed that the spatial distribution

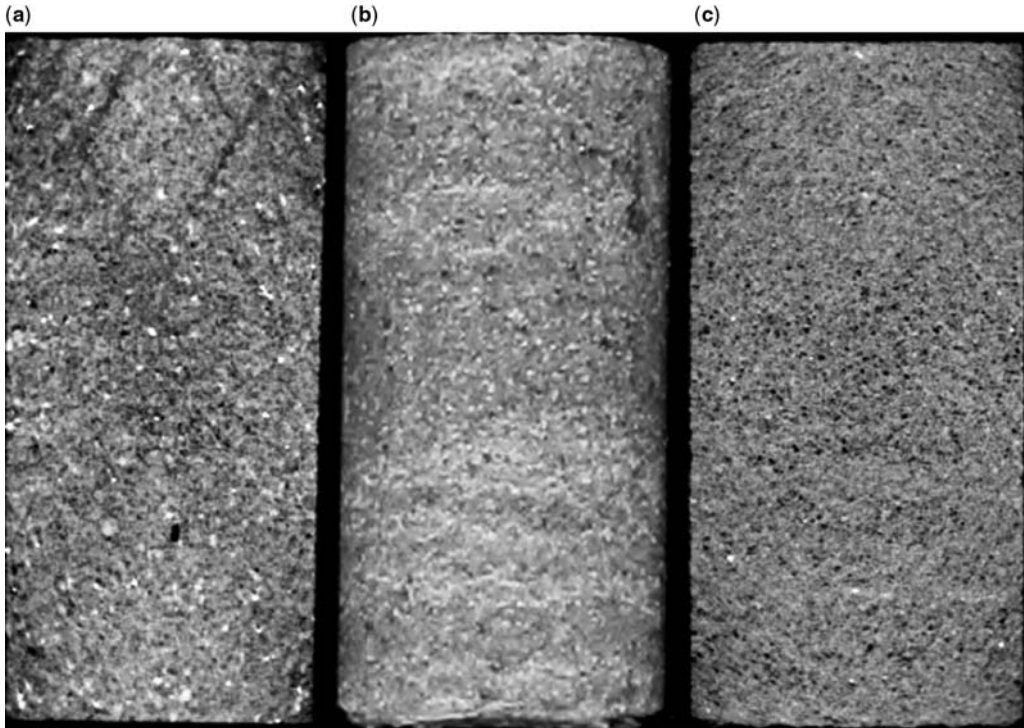


Fig. 4. (a) Original CT image of sample of Darley Dale sandstone deformed in the brittle regime. Dark zones visible at the upper end of the sample are conjugate dilating shear bands. (b) Photograph of a sample of Diemelstadt sandstone after triaxial compression experiment at 150 MPa effective pressure. Compaction bands (light) have developed on the exterior surface subperpendicular to the direction of the major principal stress. (c) CT data for a vertical slice passing through the central axis of the sample in (b) (Louis *et al.* 2006).

of δ_λ (coefficient of variation estimated among subsets of 27 neighbouring voxels, Fig. 5a) could be used to delineate compaction bands (Fig. 5b and c) that were invisible on the original images (Fig. 4b). Below, we will discuss the potential use of δ and δ_λ to obtain further insight into pore-space heterogeneity in porous sandstone.

Characterization of rock density heterogeneity: global estimations

In this study, we used two sets of X-ray CT data acquired in five sandstones. The first dataset, for Fontainebleau sandstone, was obtained by synchrotron X-ray microtomography and was previously presented by Lindquist *et al.* (2000). The second set of CT images was obtained at lower resolution on Darley Dale, Berea, Bentheim and Diemelstadt sandstones. The petrophysical description of these sandstones is given in Table 1.

A fundamental issue in the interpretation of CT images is the calibration that relates grey-level

values and actual densities. Grey-level values corresponding to the pore space and minerals vary from one setup to another and quantitative comparison between sandstones requires these values to be identical. The images of the Fontainebleau sandstone are encoded in 8 bits (0–255) whereas images for the four other sandstones are encoded in 16 bits (0–65535). Typically, the reconstruction parameters are optimized so that the data would fill up the available grey-scale range. To compare the calibration between sandstones, values obtained from 16 bit images were normalized to the 8 bit range (i.e. divided by 256). This comparison is presented in Figure 6. Respective grey-level values for grain and pore space in the Fontainebleau sandstone were extracted directly from the grey-level distributions. For the other sandstones, the grey level corresponding to zero density was obtained in dark areas imaged outside the samples and we used the average grey level and dry density as coordinates for the second pair of values. The calibration lines of Fontainebleau sandstone samples on one hand and of the four other sandstones on the other

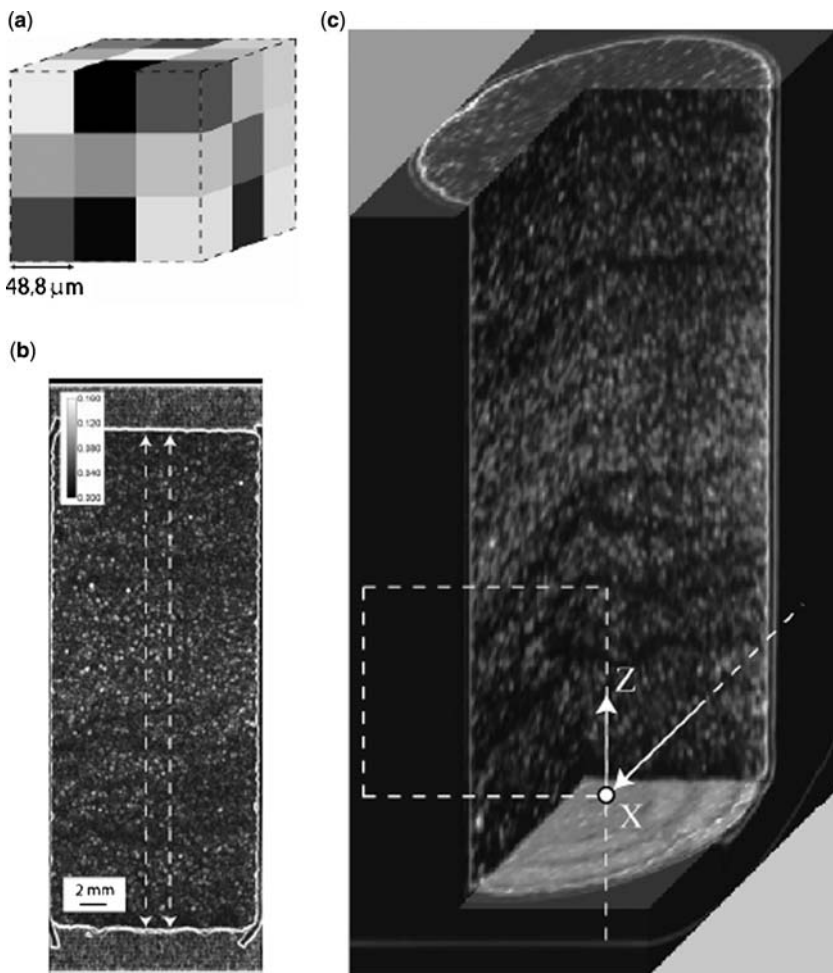


Fig. 5. (a) Elemental volume made up of 27 voxels used for the calculation of the local value of δ . Each side of the elemental volume has a length of 0.15 mm, which is almost identical to the average grain diameter of 0.16 mm. (b) Spatial distribution of δ for a vertical slice. The contrast between bands and relatively undamaged areas was significantly enhanced. (c) The 3D volume reconstructed after processing of all data.

hand are identical. The smaller slope of the calibration line for the latter can be explained by the presence of high-density minerals in some of the samples. Below, whereas quantitative comparison between Bentheim, Diemelstadt, Berea and Darley Dale sandstones is conducted, only qualitative comparison between these rocks and the Fontainebleau sandstone is possible, and the two datasets used will be studied on separate graphs.

Synchrotron imaging of Fontainebleau sandstone

Fontainebleau sandstone was chosen by Lindquist *et al.* (2000) because its modal composition is

>99% quartz (Bourbié & Zinszner 1985). Samples were extracted from four blocks with modal porosities 7.5, 13, 15 and 22%. Lindquist *et al.* (2000) noted that the 15% porosity sample was actually found to show considerably higher porosity (18%) than the average block, and this sample will be described below as the 18% porosity sample instead of 15%. Imaging on 4.52 mm diameter samples was performed at the X2-B tomographic facility of the National Synchrotron Light Source at Brookhaven National Laboratory to produce images with a linear voxel size of 5.7 μm in all three directions. Specific information concerning the X-ray imaging setup employed for acquiring this dataset has been given by Dunsmuir

Table 1. Petrophysical description of the five sandstones investigated in this study

Sandstone	Porosity (%)	Grain radius (mm)	Composition
Bentheim	23	0.105	Quartz 95%, kaolinite 3%, orthoclase 2%
Diemelstadt	25	0.08	Quartz 68%, feldspar 26%, oxides 4%, micas 2%
Berea	21	0.13	Quartz 71%, feldspar 10%, carbonate 5%, clay ~10%
Darley Dale	14	0.17	Quartz 66%, feldspar 21%, mica 3%, clay ~6%
Fontainebleau	7.5; 13; 18; 22	~0.125	Quartz >99%

Data from Baud *et al.* (2004), except those for Fontainebleau sandstone, from Lindquist *et al.* (2000).

et al. (1992). We will consider here only a single CT scan per block investigated.

Figure 7a–d shows the four images of Fontainebleau sandstone that were used in this work and the corresponding grey-level distributions. The total size of the inset images is 3.2 mm. In the distributions, pore and grain fractions are shown by two separate modes. The amplitude of the peak corresponding to the pore space increases significantly with porosity. Such images were used by Lindquist *et al.* (2000) to estimate geometric

properties of the pore space after the dataset had been binarized.

The distributions of X-ray attenuation data for this sandstone, which is mostly composed of quartz (*c.* 99%), depend almost exclusively on the size and topology of the pore space. Images such as those presented in Figure 7, acquired with a resolution high enough (5.7 µm through synchrotron imaging) to allow for unambiguous segmentation between solid and void fractions, provide a reference frame in which the structure

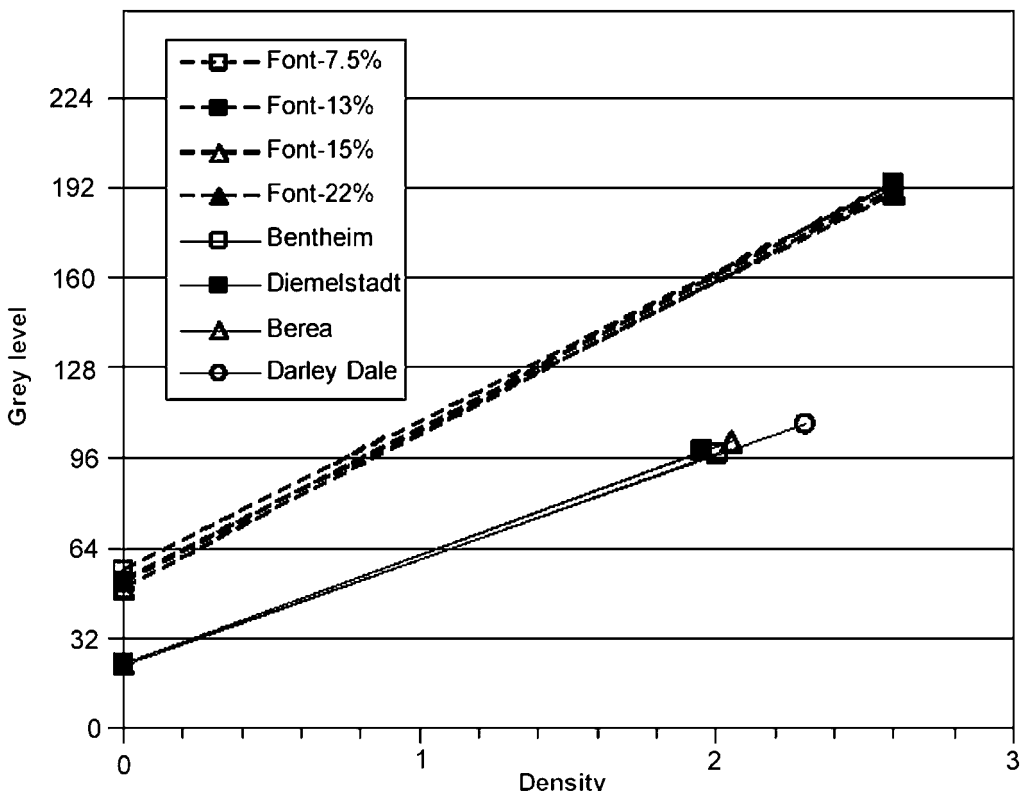


Fig. 6. Comparison of the grey-level calibrations for Fontainebleau sandstone samples imaged with synchrotron radiation at the National Synchrotron Light Source at Brookhaven National Laboratory and for samples of the other four sandstones studied imaged at the High Resolution X-ray CT Facility in Austin, Texas.

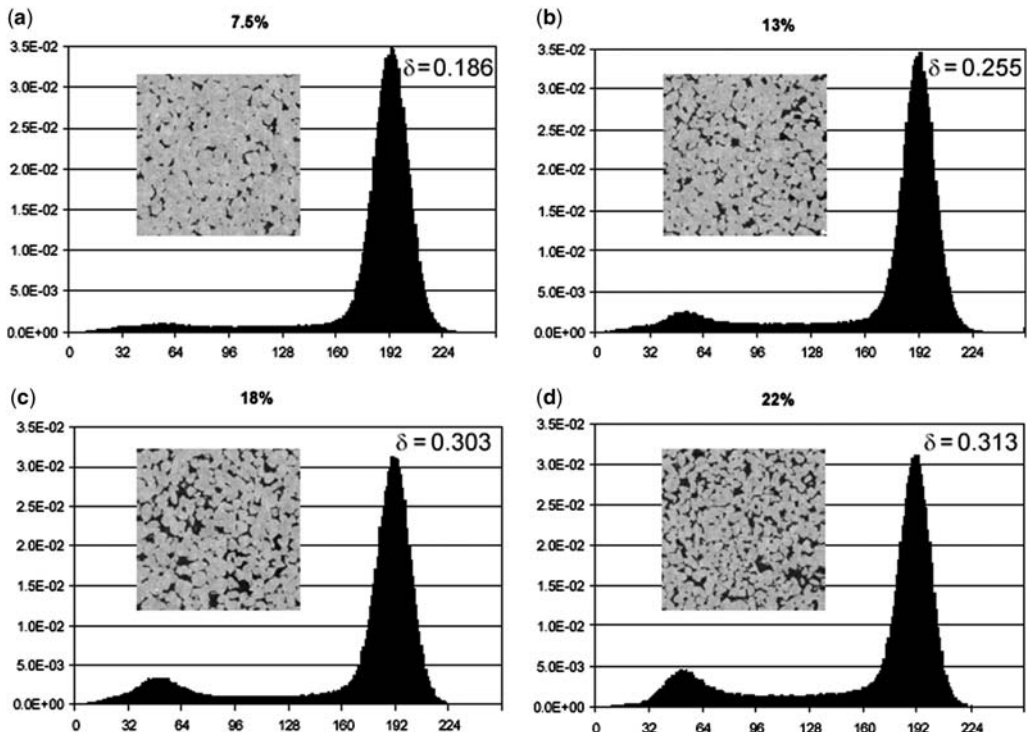


Fig. 7. Microtomographic image and distribution of X-ray attenuation values of four samples of Fontainebleau sandstone with porosity of 7.5% (a), 13% (b), 18% (c) and 22% (d). The images were taken at the National Synchrotron Light Source at Brookhaven with a resolution of 5.7 μm (Lindquist *et al.* 2000).

of the pore space is fully resolved. Data acquisition using a lower-resolution setup induces averaging over voxels and loss of sharpness in the definition of the void–solid boundaries until the pore space as an individual body (i.e. characterized by a single X-ray attenuation value) disappears. This partial volume effect can more generally lead to erroneous quantification in terms of shape and relative proportion of the rock constituents (Ketcham 2005). From the images of Figure 7, we can simulate a change in the resolution by averaging neighbouring pixels with a sliding window of the size of the new pixel and then reduce the image size accordingly. We show in Figure 8 the resulting image and associated distribution for a tenfold increase of the pixel size (57 μm per pixel) for the 22% porosity sample. The definition of the pore-space boundaries is clearly altered as values are averaged over many voxels, and the corresponding distribution changes from bimodal to unimodal. Merging of the two initial modes observed in Figure 7d results in a distribution highly skewed towards lower grey-level values, with a δ value (see previous section) reduced from 0.313 to 0.230.

The variety of setups available for X-ray CT imaging offer a range of resolutions (micrometre to millimetre) and it is important to understand the corresponding changes to be expected in the distribution of X-ray attenuation values for a

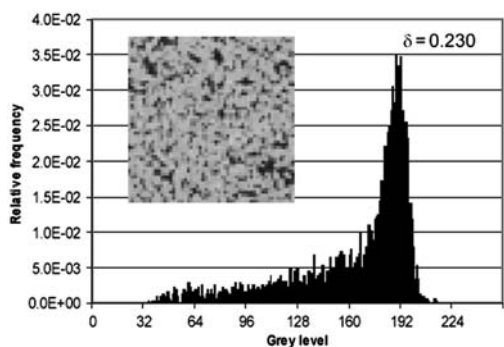


Fig. 8. Vertical image and distribution of X-ray attenuation values for the 22% porosity sample of Fontainebleau sandstone after alteration of the resolution from 5.7 μm to 57 μm .

given material. This can be done using the δ as an indicator. Repeating the same averaging procedure that simulates data acquisition at coarser resolution, we can obtain the evolution of δ as a function of the voxel size. This procedure is similar to the coarseness analysis performed by Coker *et al.* (1996) on binarized images of Fontainebleau sandstone. Figure 9a presents a typical 2D result for the sample of 22% porosity and for a pixel size varying from one to 100 times the original pixel size (i.e. from 5.7 to 570 μm). The resulting curve decreases asymptotically, and beyond 500 μm very little change in the value of δ is observed. Typically, synchrotron imaging provides the highest resolution and grey-level heterogeneities, as no contrast higher than that existing between a pore and a grain can possibly be observed. At higher voxel size, a very large range of resolutions (from a few microns to a few hundreds microns in width) can typically be obtained with versatile ultrahigh- and high-resolution systems such as those at the X-ray CT facility in Austin, Texas (industrial CT) (Ketcham & Carlson 2001). In this domain, which includes the 2D simulation shown in Figure 8, the distribution of X-ray attenuation values is unimodal and the change in δ as pixel size increases corresponds to the continuous reduction of the width of the tail (or skewness) related to the remaining pore space. Therefore, there is a one-to-one correspondence between δ and the resolution. At significantly lower resolutions (medical X-ray imaging resolution) the distribution of attenuation values becomes close to normal and variations of δ are negligible.

In Figure 9b, we present the evolution of δ with the pixel size for the four samples of Fontainebleau sandstone of different porosities. Overall, higher

porosity leads to higher values of δ . At coarser resolutions, porosity has less impact on the coefficient of variation and the curves tend to stabilize towards closer levels. The remaining differences at lower resolution (100 μm) could be linked to small differences in the pore-size distributions. A higher residual heterogeneity is observed in the sample with 18% porosity, which was also found by Lindquist *et al.* (2000) to have the larger pore throat average cross-sectional area. This suggests that the overall coefficient of variation δ at coarse resolution is particularly sensitive to this parameter. Because of the small size of the images used (3.2 mm), δ was not determined for pixel sizes larger than c. 500 μm .

High-resolution CT imaging of four porous sandstones

The four samples imaged were cylinders 18 mm wide and 38 mm long cored from blocks of Bentheim, Diemelstadt, Berea and Darley Dale sandstones. These sandstones have respective porosities of 23, 25, 21 and 14% and their modal composition is given in Table 1. The samples of this second dataset are plugs used for mechanical testing in the rock mechanics laboratory at Stony Brook (Wong *et al.* 1997; Baud *et al.* 2004). The images were obtained at the High-Resolution CT Facility at the University of Texas at Austin. The setup of the ultrahigh-resolution system has been fully described by Ketcham & Carlson (2001). This system employs a 200 kV microfocal X-ray source capable of a $<10 \mu\text{m}$ focal spot size. Although close to the synchrotron resolution in capacity, data for this group of sandstones were

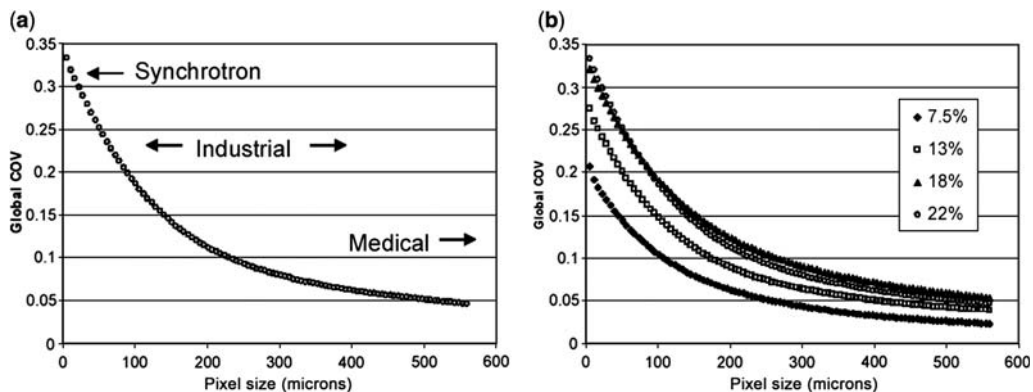


Fig. 9. (a) Evolution of the overall δ as a function of the pixel size for a sample of Fontainebleau sandstone of 22% porosity. The ranges of resolution corresponding to CT data acquisition using synchrotron, industrial and medical CT are indicated on the graph. (b) Comparison of the evolutions of δ with pixel size for the four samples of Fontainebleau sandstone of 7.5, 13, 18 and 22% porosity.

acquired at only $48.8 \mu\text{m}$ per voxel, the smallest resolution allowing for scanning our samples entirely along their long axis with the 1024-channel detector used. It is worth noting here that better resolution ($c. 15 \mu\text{m}$) could have been obtained by scanning the samples parallel to their diametric cross-section. However, given the size of the dataset that would have then been generated (about a sixfold increase) and since we were interested in observing larger-scale density changes, the $48.8 \mu\text{m}$ resolution used was considered suitable for this study.

The scan images used here are presented in Figure 10a–d. At this resolution ($c. 50 \mu\text{m}$), we cannot resolve the complexity of the pore space. The specimens of Bentheim and Diemelstadt sandstones appear homogeneous. The Darley Dale specimen and to a higher degree the Berea specimen present more heterogeneous structures. The lighter spots visible in the Berea sample correspond to denser areas (denser minerals and/or filled pores).

The overall distributions of X-ray CT attenuation values corresponding to the images of Figure 10 are presented for the four sandstones in Figure 11a. Average grey-level value and δ vary from one sandstone to another. Darley Dale sandstone, which has the lowest porosity (14%), has a higher average

grey-level value than other sandstones. The three remaining sandstones define two groups: Bentheim and Diemelstadt with relatively lower average and close δ values, and Berea with relatively higher average and higher coefficient of variation. The difference in the average value can be explained by the different porosities (23% and 25% for Bentheim and Diemelstadt; 20% for Berea).

Recent theoretical studies (Katsman *et al.* 2005; Wang *pers. com.* 2007) suggested that pore-space homogeneity promotes the development of discrete compaction bands in porous sandstone, whereas a more heterogeneous structure would favour a more diffuse development of damage. Tembe (*pers. com.* 2007) presented grain- and pore-size distributions as well as the distribution of inter-granular grain contact lengths in Berea, Bentheim and Diemelstadt sandstones, and reached similar conclusions. Figure 11b shows their grain contact statistics for these three rocks. Discrete compaction bands developed in Bentheim and Diemelstadt sandstones that showed comparable and relatively narrow distributions of grain contacts, and a wider distribution of grain contacts promoted the development of diffuse compaction bands in Berea sandstone (Baud *et al.* 2004).

The δ values of the distributions presented in Figure 11a also reflect a degree of heterogeneity

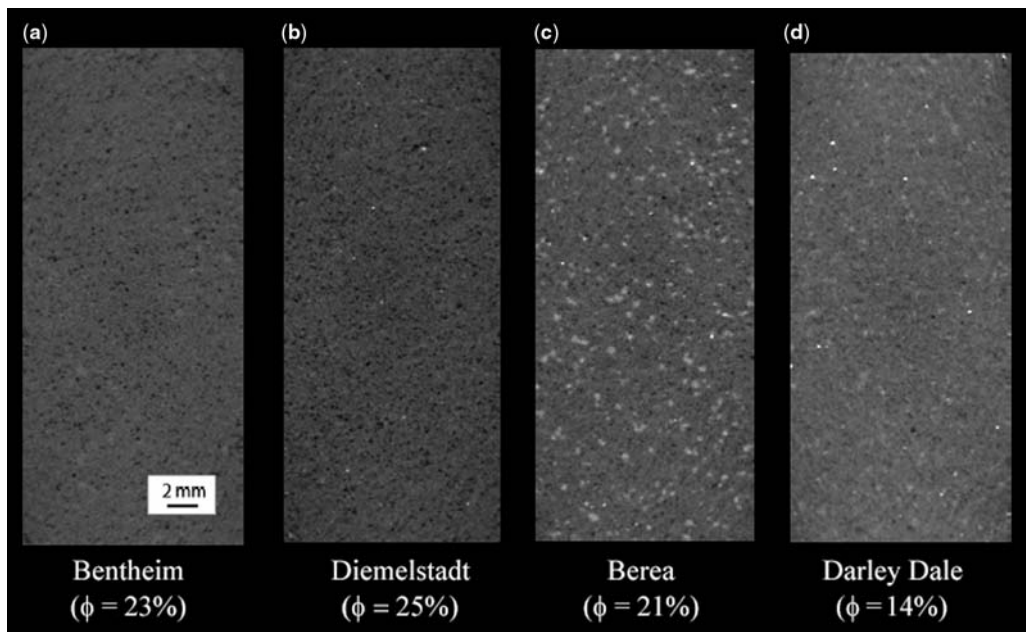


Fig. 10. X-ray CT images of intact samples of Bentheim (a), Diemelstadt (b), Berea (c) and Darley Dale (d) sandstones acquired at a resolution of $48.8 \mu\text{m}$.

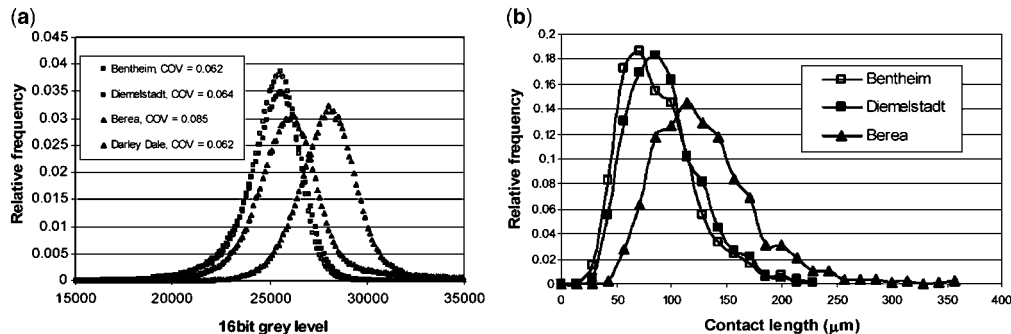


Fig. 11. (a) Distributions of X-ray attenuations for intact samples of Bentheim, Diemelstadt, Berea and Darley Dale sandstones. (b) Distributions of intergranular grain contact lengths in the Bentheim, Diemelstadt and Berea samples (from Tembe *et al.* 2007).

that is controlled at the same time by the pore-size distribution and mineral content. Bentheim and Diemelstadt sandstones have very similar density distributions with a relatively low δ . In contrast, the density distribution for Berea sandstone has a significantly higher δ . The distributions presented in Figure 11a and b are in excellent qualitative agreement. This suggests therefore that global CT analysis could be a useful tool to predict compaction localization in porous rocks.

Using the same procedure as applied on images of Fontainebleau sandstone (see previous section), we studied the effect of the resolution on δ . The starting resolution is in this case the resolution of the images presented in Figure 9 (*c.* 50 μm) and because of the larger dimensions of the samples we performed the simulations up to a much larger pixel size close to 5 mm (Fig. 12). Overall, the curves have the same shape as for the simulations performed on Fontainebleau sandstone images (Fig. 8b). The δ value decreases rapidly with the pixel size to reach a plateau at resolutions between 2 and 3 mm for the four sandstones. Because these sandstones have different microstructures and compositions, the interpretation of the observed differences in Figure 12 is not straightforward. However, several interesting features may be noted. First, the evolution of δ in the Diemelstadt and Bentheim sandstones is almost identical. These two sandstones have comparable porosities, similar intergranular grain contact distributions (Tembe *et al.* 2007) but significantly different mineralogical compositions (Table 1). Whereas the Bentheim sandstone is mostly made of quartz (95%), the Diemelstadt sandstone contains more than 30% of non-quartz phases. The similarity observed in Figure 12 for these two rocks suggests that a global analysis of the X-ray attenuations cannot resolve heterogeneity linked to mineralogy if the minerals do not have significant density

contrasts. The higher heterogeneity observed for the Berea and Darley Dale sandstones becomes less and less visible with increasing pixel sizes and δ for these two rocks reaches low values comparable with those for the Diemelstadt and Bentheim sandstones. The pixel size at which δ becomes constant could be interpreted as a representative volume beyond which the rocks could be considered homogeneous as far as the distribution of X-ray attenuation is concerned. Theoretically, δ should approach zero at large pixel sizes, with all the pixels having the same grey level. We suggest that the residual level observed in Figure 12 is the limit for a natural material.

Characterization of rock density heterogeneity: local estimations

In the previous section we evaluated the effect of a change in the image resolution on the overall value of δ . In this section we will examine the use of δ_λ , a local version of the coefficient of variation, for visualizing density contrasts within a sample. We performed 2D simulations including both resolution changes and calculations of δ_λ among nine neighbouring pixels, a 2D equivalent of the procedure used by Louis *et al.* (2006) to image compaction bands in Diemelstadt sandstone (Fig. 5). At each resolution, instead of calculating an overall value of the coefficient of variation as in Figures 9 and 12, we calculated all the δ_λ values and the average $\bar{\delta}_\lambda$. Figures 13a and b shows the evolution of $\bar{\delta}_\lambda$ as a function of the pixel size for the four samples of Fontainebleau sandstone studied by Lindquist *et al.* (2000) and for the four sandstones imaged at Austin, respectively. Despite the differences in structures and compositions, the curves are qualitatively similar for all sandstones and show important variations of $\bar{\delta}_\lambda$

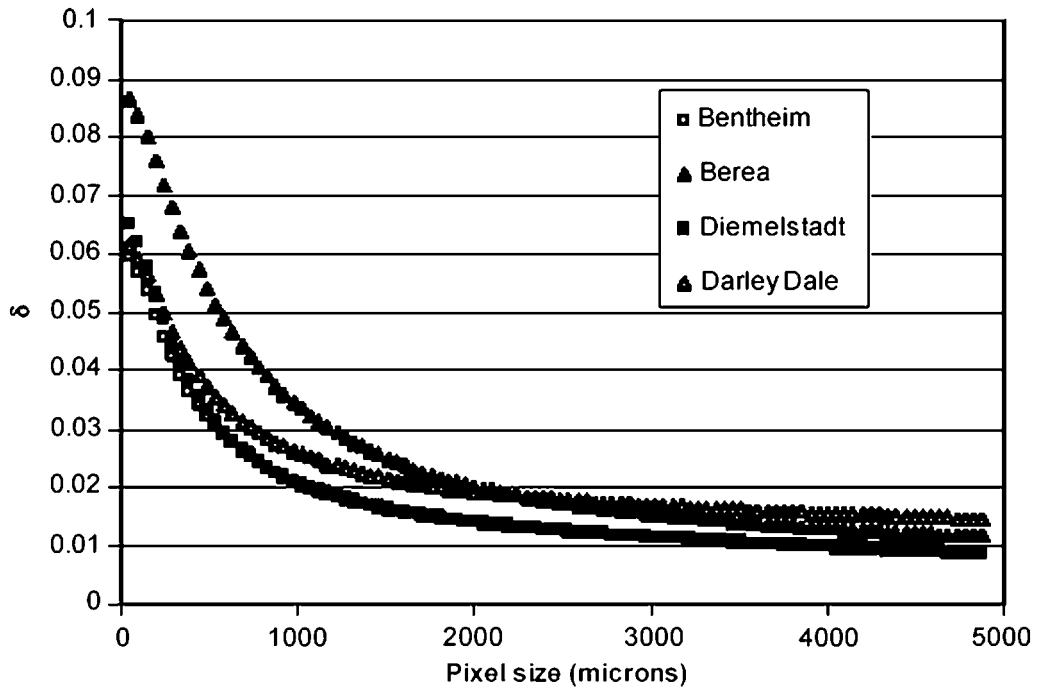


Fig. 12. Evolution of the overall δ as a function of the pixel size for intact samples of Bentheim, Diemelstadt, Berea and Darley Dale sandstones.

with pixel size. At small pixel sizes, $\bar{\delta}_\lambda$ is relatively low. As the pixel size increases, $\bar{\delta}_\lambda$ increases to a maximum, and then decreases asymptotically to very low values. In Figure 13a (Fontainebleau sandstone), $\bar{\delta}_\lambda$ increases with porosity at high resolutions. It is roughly the same at coarser resolutions, except for the 18% porosity sample, which has a higher $\bar{\delta}_\lambda$ than the 22% porosity sample. The values of $\bar{\delta}_\lambda$ calculated for the Bentheim, Diemelstadt and Darley Dale sandstones are similar and show comparable evolutions. Much larger values were obtained for Berea sandstone. In Figure 13c and d, we compare the global and local estimation of δ for Bentheim and Berea sandstones, respectively. To have comparable scales, we used the size of the averaging window for the local estimations ($3 \times$ pixel size). For Bentheim sandstone of relatively homogeneous structure (Fig. 13c), the local estimation can provide additional information only at resolutions better than 2 mm. Beyond this resolution, the rock appears homogeneous, and global and local analyses give the same value. For Berea sandstone, the local estimation is always significantly higher than the global one, confirming that this rock is significantly more heterogeneous over a wide range of scales. In all cases, the behaviour observed at high resolution differs

significantly from the evolution shown in global estimations and reveals the non-random nature of the grey-level distribution in the images analysed. In Figures 9 and 12, the statistics were achieved notwithstanding the spatial arrangement of all the pixels analysed. The estimation of $\bar{\delta}_\lambda$ shows the presence of a structure with characteristic size that is probably related to the pores. Figure 14 shows a simulation of the value of δ to be expected for a varying porosity within a 9 pixels evaluation window. Two cases with only pore and matrix phases are considered. In the first case, the pixels representing the porous space are given a non-zero value, whereas in the second one these pixels are set to zero (binary image). In the first case, independently of the values attributed to the pore and solid fractions respectively, δ is maximized when the porosity represents half of the surface of the evaluation window. In the binary case, the results are significantly different. If the evaluation window is made of pixels with values zero and one, the highest value of δ is attained when one pixel has value one and all the others are zero. Therefore, $\bar{\delta}_{\lambda,\max}$ is reached when a maximum amount of evaluation windows are almost totally filled with zero-value pixels. The presence of pores with very low X-ray attenuation leads to high $\bar{\delta}_\lambda$ values when compared with

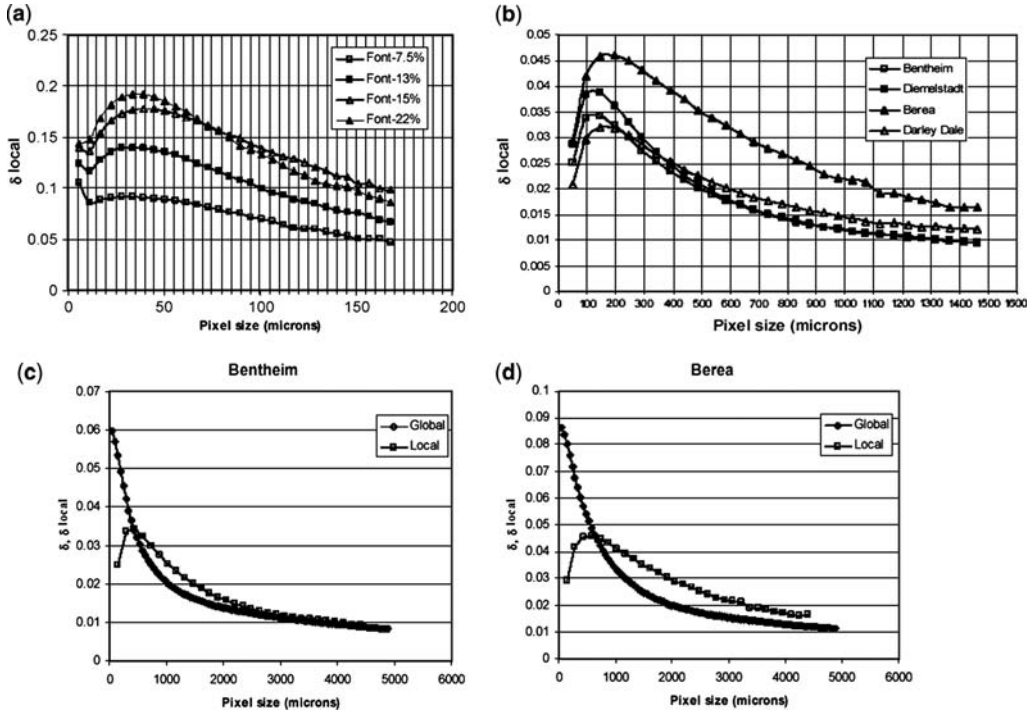


Fig. 13. Average of δ_λ calculated on windows made of nine pixels as a function of the pixel size for the four samples of Fontainebleau sandstone studied by Lindquist *et al.* (2000) (a), and for intact samples of Bentheim, Diemelstadt, Berea and Darley Dale sandstones (b). (c) and (d) show comparison between global (\blacklozenge) and local (\square) analysis of the coefficient of variation in intact samples of Bentheim and Berea sandstones, respectively.

pixels from the solid fraction. The larger the number of such pores in the studied material, the larger the number of evaluation windows that will return a high δ_λ , and therefore the higher the average $\bar{\delta}_\lambda$. This effect may be attenuated by a large pore-size distribution. At a given resolution, if some of the pores fall under the pixel size their effect will be considerably attenuated and the value $\bar{\delta}_\lambda$ will not be maximized. Consequently, the porosity effect is expected to fade away after the pixel size becomes larger than the average pore.

When $\bar{\delta}_\lambda$ reaches a maximum, we may suggest that a critical pixel size somehow related to the average pore size was reached, and that the associated value of $\bar{\delta}_{\lambda,\max}$ is proportional to the number of such pores (i.e. to the porosity). If the presence of peaks in $\bar{\delta}_\lambda$ reflects a characteristic dimension of the pore space, the exact nature of this dimension cannot be extracted directly from the data presented in Figure 13a and b because of the complexity of the information. To gain more insight with a somewhat simpler problem, we conducted the same simulation on binary images. The evolution of $\bar{\delta}_\lambda$ with pixel size was calculated in binarized images of

Fontainebleau sandstone in which the initial resolution allowed for a satisfactory mapping of the pore space. The images were thresholded at grey level 140, as was done by Lindquist *et al.* (2000).

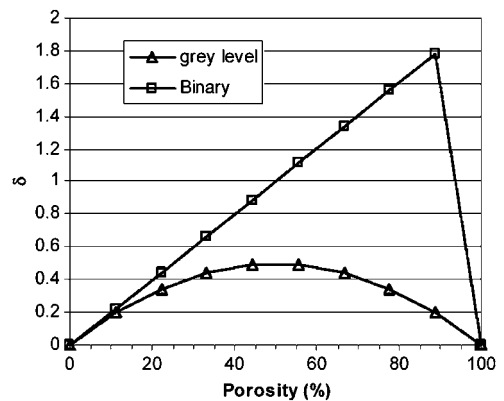


Fig. 14. δ_λ calculated on a single window made of nine pixels as a function of porosity for a binary image (\square) and for an image made of grey levels (Δ).

Figure 15a and b shows the raw image of the 22% porosity sample and the corresponding binarized image, respectively. As Fontainebleau sandstone is >99% quartz, the raw image and binarized one are very similar and the main difference is the disappearance of the ring artefacts (potentially leading to overestimations of the local heterogeneity at small scale) in the binary image. Results of the calculation of $\bar{\delta}_\lambda$ are presented in Figure 16. Because of the binary nature of the images, values calculated for $\bar{\delta}_\lambda$ are much higher than in Figure 13b. Values of $\bar{\delta}_{\lambda,\max}$ and the corresponding window size are given in Table 2. If we plot $\bar{\delta}_{\lambda,\max}$ as a function of porosity (Fig. 17), a very good linear trend arises, and the best fitting line passes almost through coordinate (0,0) (perfect homogeneity of a non-porous medium).

We have shown that for a binary image, $\bar{\delta}_{\lambda,\max}$ depends on the porosity. Figure 16 also suggests that more information can be extracted from the window size corresponding to this maximum. The size of this evaluation window may be related to the shape and size of the pores and/or pore throats. For instance, the larger evaluation window at $\bar{\delta}_{\lambda,\max}$ is observed in the sample of 18% porosity (see inset in Fig. 16), which was also found by Lindquist *et al.* (2000) to show the largest throat cross-sectional area out of the four porosities investigated. This correlation suggests that the window size corresponding to $\bar{\delta}_{\lambda,\max}$ could provide a measurement of the access radius of the pores. However, further analysis involving quantitative numerical simulations on model

materials of different microstructures, and comparison with CT data, is necessary to better interpret the simulations presented in Figure 16.

Notwithstanding the need for theoretical simulations for the geometric interpretation of $\bar{\delta}_{\lambda,\max}$, the existence of a resolution at which the local coefficient of variation is maximum can have interesting implications for the study of strain localization in porous rocks. The approach developed by Louis *et al.* (2006) to image discrete compaction bands was based on the contrast between a relatively heterogeneous intact zone of a sample, and the compaction bands, where grain crushing and pore collapse homogenized the material. The most relevant scale to look at the problem should therefore be the scale at which pore-scale heterogeneity is maximum; that is, the pixel size corresponding to $\bar{\delta}_{\lambda,\max}$. To check this assumption, we compare in Figure 18 one CT slice of the deformed sample of Diemelstadt sandstone analysed by Louis *et al.* (2006) at the resolution of industrial CT with a new calculation at a resolution of 150 μm corresponding to $\bar{\delta}_{\lambda,\max}$ for Diemelstadt sandstone in Figure 13b. For each calculation the respective distributions of δ_λ are provided. Both distributions are log-normal, as it is usually the case for pore- and grain-size distributions in granular rocks. As expected, in the undamaged areas (e.g. the centre of the sample) the heterogeneity has increased. Less expected is the δ_λ increase within the compaction bands, which is actually due to a ‘contamination’ of the intact surrounding areas facilitated by the thinness

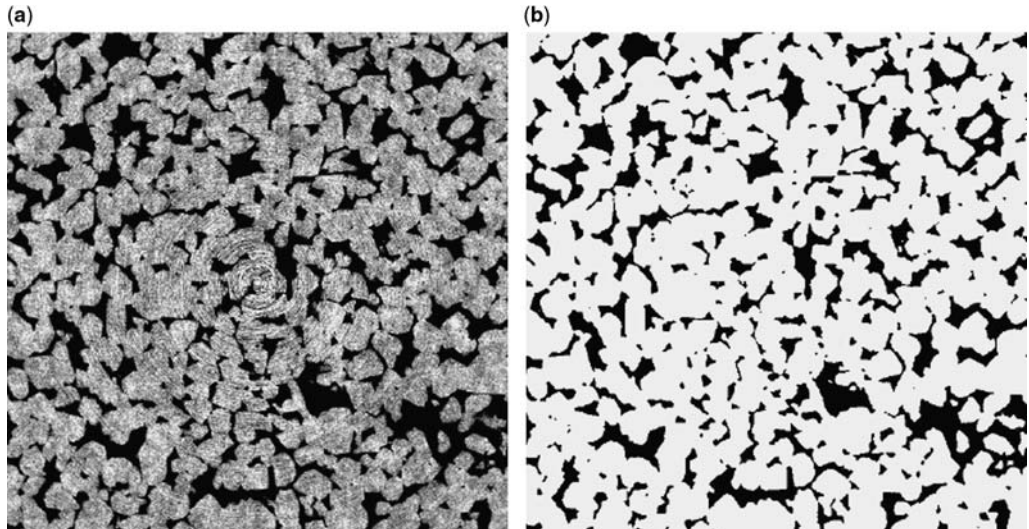


Fig. 15. (a) Example of CT image of the 22% porosity sample of Fontainebleau sandstone studied by Lindquist *et al.* (2000). (b) Same image after thresholding at a grey-level value of 140 and binarization.

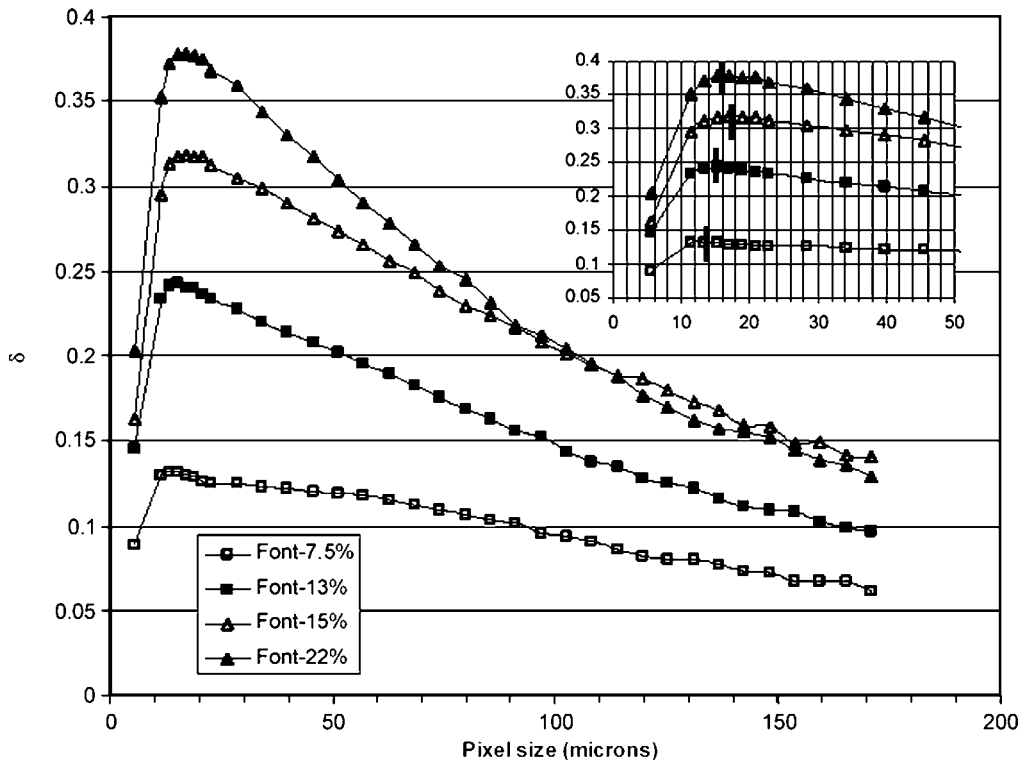


Fig. 16. Average of δ_λ calculated on windows made of 9 voxels as a function of the pixel size for binarized images of the four samples of Fontainebleau sandstone studied by Lindquist *et al.* (2000).

of the bands. Overall, the distributions illustrate a change in the sense of an improved contrast with a shift from 0.017 to 0.02 in the standard deviation. This preliminary result suggests that, in the context of density distribution analysis, it may be beneficial to decrease the spatial resolution to an extent that is constrained mostly by

the pore-size distribution, to increase the contrast on processed images.

Summary and conclusions

In this paper we have reviewed a number of applications of X-ray CT to rocks. The relevance of

Table 2. Maximum value of the average local coefficient of variation ($\bar{\delta}_{\lambda,\max}$) obtained during simulations of voxel size increase, and size of the corresponding evaluation window (three times the voxel size) for the grey-level case and after binarization (Fontainebleau only)

Sandstone	Grey level		Binary	
	$\delta_{\lambda,\text{mean}}$	Evaluation window (μm)	$\delta_{\lambda,\text{mean}}$	Evaluation window (μm)
Bentheim	0.039	360		
Diemelstadt	0.0345	360		
Berea	0.032	525		
Darley Dale	0.046	480		
Fontainebleau 7.5%	0.092	90	0.132	41.25
Fontainebleau 13%	0.14	105	0.243	45
Fontainebleau 18%	0.178	126	0.318	51
Fontainebleau 22%	0.192	105	0.378	49.5

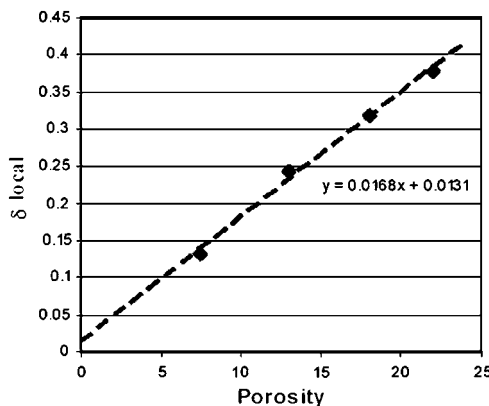


Fig. 17. Peak value of the average of δ_λ as a function of the porosity in binarized images of the four Fontainebleau sandstone samples studied by Lindquist *et al.* (2000).

this technique to various geophysical problems is in several ways a problem of scale: the scale of the studied object, the resolution of the images and the most relevant scale to look at the physics of the studied problem. Synchrotron images with resolution of several microns allow resolution of the

geometric complexity of the pore space and can be used for instance to perform fluid flow simulations. However, such high resolutions are mostly obtained on relatively a small sample (typically several millimetres). High-resolution ‘industrial’ CT with resolution of c. 50 μm is more appropriate to image entirely centimetre-sized samples such as those used in triaxial deformation experiments. Structural heterogeneities (such as bedding) and compaction localization can be studied using images taken at this resolution.

Starting from images taken both at synchrotron and industrial resolutions on intact samples of porous sandstones, we have shown that important conclusions on pore-space heterogeneity can be drawn from global and local analysis of the distributions of X-ray attenuations. The global analysis can be used, for instance, to identify relatively homogeneous geomaterials in which compaction bands are likely to develop. However, the amount of information that we can obtain from a global averaging of the CT signal decreases dramatically with the pixel size. Local estimation of the X-ray attenuation homogeneity appears to have considerable potential for the delineation of homogeneity contrasts as well as for the geometric description of the pore space. In particular, we have shown

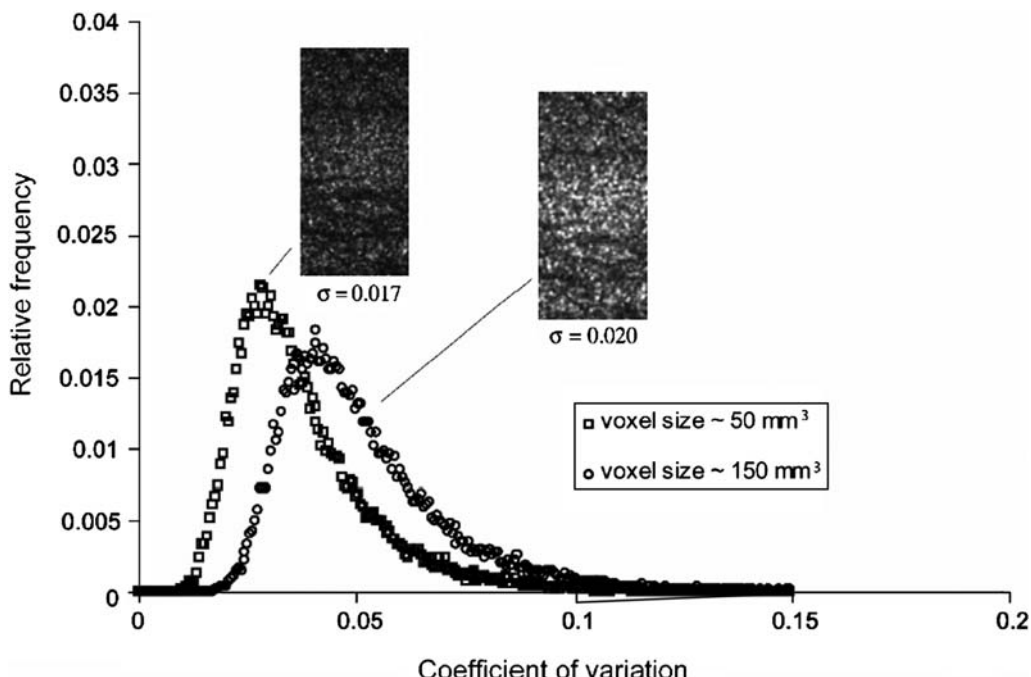


Fig. 18. Estimation of δ_λ in a single CT image of a sample of Diemelstadt sandstone deformed at 150 MPa effective pressure (Louis *et al.* 2006) at 50 μm resolution and after pixel size increase to 150 μm . The distributions show an overall increase of the contrast between the compaction bands and the relatively intact areas.

the existence of a scale at which the local coefficient of variation of the distributions reached a maximum. In the Fontainebleau sandstone, this value was found to be proportional to the porosity even though the resolution had been altered so that isolation of the pore space and solid fraction of the rock was not possible. In this study, we have mainly performed oversimplified 2D simulations, and more realistic 3D simulations, which should lead to a more accurate characterization of the pore space, will be conducted in the future.

We thank S. Tembe and J. Schmittbuhl for stimulating discussions. X-ray scanning was conducted by R. Ketcham at the High-Resolution X-ray Computed Tomography Facility of the University of Texas at Austin, an NSF-supported multi-user facility (grant EAR 0345710). The research at Stony Brook was partially supported by the National Science Foundation under grant EAR-0310087. This paper has been improved thanks to the careful reviews of J. Fredrich and G. Viggiani.

References

- ANDERSON, S. H., PEYTON, R. L. & GANTZER, C. J. 1990. Evaluation of constructed and natural soil macropores using X-ray computed-tomography. *Geoderma*, **46**, 13–29.
- ANTONELLINI, M., AYDIN, A., POLLARD, D. D. & D'ONFRO, P. 1994. Petrophysical study of faults in sandstone using petrographic image analysis and X-ray computerized tomography. *Pure and Applied Geophysics*, **143**, 181–201.
- ARNOLD, J. R., TESTA, J. P., FRIEDMAN, P. J. & KAMBIC, G. X. 1983. Computed tomographic analysis of meteorite inclusions. *Science*, **219**, 383–384.
- ARNS, C. H., KNACKSTEDT, M. A., PINCZEWSKI, W. V. & LINDQUIST, W. B. 2001. Accurate estimation of transport properties from microtomographic images. *Geophysical Research Letters*, **28**, 3361–3364.
- ARNS, C. H., KNACKSTEDT, M. A., PINCZEWSKI, W. V. & MARTYS, N. S. 2004. Virtual permeometry on microtomographic images. *Journal of Petroleum Science and Engineering*, **45**, 41–46.
- AUZERAIS, F. M., DUNSMUIR, J., FERREOL, B. B. ET AL. 1996. Transport in sandstone: a study based on three dimensional microtomography. *Geophysical Research Letters*, **23**, 705–708.
- AYDIN, A., BORJA, R. I. & EICHHUBL, P. 2006. Geological and mathematical framework for failure modes in granular rock. *Journal of Structural Geology*, **28**, 83–98.
- BAUD, P., KLEIN, E. & WONG, T.-F. 2004. Compaction localization in porous sandstones: spatial evolution of damage and acoustic emission activity. *Journal of Structural Geology*, **26**, 603–624.
- BÉSUELLE, P., DESRUES, J. & RAYNAUD, S. 2000. Experimental characterisation of the localisation phenomenon inside a Vosges sandstone in a triaxial cell. *International Journal of Rock Mechanics & Mining Sciences*, **37**, 1223–1237.
- BÉSUELLE, P., BAUD, P. & WONG, T.-F. 2003. Failure mode and spatial distribution of damage in Rothbach sandstone in the brittle–ductile transition. *Pure and Applied Geophysics*, **160**, 851–868.
- BOURBIE, T. & ZINSZNER, B. 1985. Hydraulic and acoustic properties as a function of porosity in Fontainebleau sandstone. *Journal of Geophysical Research*, **90**, 11524–11532.
- CARLSON, W. D. & DENISON, C. 1992. Mechanisms of porphyroblast crystallization—results from high-resolution computed X-ray tomography. *Science*, **257**, 1236–1239.
- CNUDDE, V., MASSCHAELE, B., DIERICK, M., VLASSENBOECK, J., VAN HOOREBEKE, L. & JACOBS, P. 2006. Recent progress in X-ray CT as a geosciences tool. *Applied Geochemistry*, **21**, 826–832.
- COKER, D. A., TORQUATO, S. & DUNSMUIR, J. H. 1996. Morphology and physical properties of Fontainebleau sandstone via a tomographic analysis. *Journal of Geophysical Research*, **101**, 17497–17506.
- COLES, M. E., HAZLETT, R. D., SPANNE, P., SOLL, W. E., MUEGGE, E. L. & JONES, K. W. 1998. Pore level imaging of fluid transport using synchrotron X-ray microtomography. *Journal of Petroleum Science and Engineering*, **19**, 55–63.
- DESRUES, J. 1984. *La localisation de la déformation dans les matériaux granulaires*. USMG-INPG, Grenoble.
- DESRUES, J. 2004. Tracking strain localization in geomaterials using computerized tomography. In: OTANI, J. & OBARA, Y. (eds) *International Workshop on X-ray CT for Geomaterials GeoX*. Balkema, Kumamoto, 15–41.
- DESRUES, J., CHAMBON, R., MOKNI, M. & MAZEROLLE, F. 1996. Void ratio evolution inside shear bands in triaxial sand specimens studied by computed tomography. *Géotechnique*, **46**, 529–546.
- DOYEN, P. M. 1988. Permeability, conductivity, and pore geometry of sandstone. *Journal of Geophysical Research*, **93**, 7729–7740.
- DUNSMUIR, J. H., FERGUSON, S. R. & DAMICO, K. L. 1992. Design and operation of an imaging X-ray-detector for microtomography. *Institute of Physics Conference Series*, **121**, 257–264.
- FLANNERY, B. P., DECKMAN, H. W., ROBERGE, W. G. & D'AMICO, K. L. 1987. Three dimensional X-ray microtomography. *Science*, **237**, 1439–1444.
- FREDRICH, J. T., GREAVES, R. H. & MARTIN, J. W. 1993. Pore geometry and transport properties of Fontainebleau sandstone. *International Journal of Rock Mechanics & Mining Sciences & Geomechanics Abstracts*, **30**, 691–697.
- FREDRICH, J. T., DI GIOVANNI, A. A. & NOBLE, D. R. 2006. Predicting macroscopic transport properties using microscale image data. *Journal of Geophysical Research*, **111**, B03201, doi:10.1029/2005JB003774.
- KATSMAN, R., AHARONOV, E. & SCHER, H. 2005. Numerical simulation of compaction bands in high-porosity sedimentary rock. *Mechanics of Materials*, **37**, 143–162.
- KAWAKATA, H., CHO, A., KIYAMA, T., YANAGIDANI, T., KUSUNOSE, K. & SHIMADA, M. 1999. Three-dimensional observations of faulting process in Westerly granite under uniaxial and triaxial conditions by X-ray CT scan. *Tectonophysics*, **313**, 293–305.

- KETCHAM, R. A. 2005. Three-dimensional grain fabric measurements using high-resolution X-ray computed tomography. *Journal of Structural Geology*, **27**, 1217–1228.
- KETCHAM, R. A. & CARLSON, W. D. 2001. Acquisition, optimization and interpretation of X-ray computed tomographic imagery: applications to the geosciences. *Computers & Geosciences*, **27**, 381–400.
- KETCHAM, R. A. & ITURRINO, G. J. 2005. Nondestructive high-resolution visualization and measurement of anisotropic effective porosity in complex lithologies using high-resolution X-ray computed tomography. *Journal of Hydrology*, **302**, 92–106.
- LENOIR, N. 2006. *Comportement mécanique et rupture dans les roches argileuses étudiés par microtomographie à rayons X*. PhD thesis, Université Joseph Fourier-Grenoble 1.
- LINDQUIST, W. B., LEE, S. M., COKER, D. A., JONES, K. W. & SPANNE, P. 1996. Medial axis analysis of void structure in three-dimensional tomographic images of porous media. *Journal of Geophysical Research, Solid Earth*, **101**, 8297–8310.
- LINDQUIST, W. B., VENKATARANGAN, A., DUNSMUIR, J. & WONG, T.-F. 2000. Pore and throat size distributions measured from synchrotron X-ray tomographic images of Fontainebleau sandstones. *Journal of Geophysical Research*, **105**, 21509–21527.
- LONTOC-ROY, M., DUTILLEUL, P., PRASHER, S. O., HAN, L. W. & SMITH, D. L. 2005. Computed tomography scanning for three-dimensional imaging and complexity analysis of developing root systems. *Canadian Journal of Botany*, **83**, 1434–1442.
- LOUIS, L., WONG, T.-F., BAUD, P. & TEMBE, S. 2006. Imaging strain localization by X-ray computed tomography: discrete compaction bands in Diemelstadt sandstone. *Journal of Structural Geology*, **28**, 762–775.
- LOUIS, L., WONG, T.-F. & BAUD, P. 2007. Imaging strain localization by X-ray radiography and digital image correlation: deformation bands in rothbach sandstone. *Journal of Structural Geology*, **29**, 129–140.
- MOGENSEN, K., STENBY, E. H. & ZHOU, D. E. 2001. Studies of waterflooding in low-permeable chalk by use of X-ray CT scanning. *Journal of Petroleum Science and Engineering*, **32**, 1–10.
- NAHMANI, J., CAPOWIEZ, Y. & LAVELLE, P. 2005. Effects of metal pollution on soil macroinvertebrate burrow systems. *Biology and Fertility of Soils*, **42**, 31–39.
- ODA, M., TAKEMURA, T. & TAKAHASHI, M. 2004. Microstructure in shear band observed by microfocus X-ray computed tomography. *Géotechnique*, **54**, 539–542.
- OLSSON, W. A. 1999. Theoretical and experimental investigation of compaction bands in porous rock. *Journal of Geophysical Research*, **104**, 7219–7228.
- OTANI, J., MUKUNOKI, T. & SUGAWARA, K. 2005. Evaluation of particle crushing in soils using X-ray CT data. *Soils and Foundations*, **45**, 99–108.
- RAYNAUD, S., FABRE, D., MAZEROLLE, F., GERAUD, Y. & LATIERE, H. J. 1989. Analysis of the internal structure of rocks and characterization of mechanical deformation by a non-destructive method: X-ray tomodensitometry. *Tectonophysics*, **159**, 149–159.
- RENARD, F., BERNARD, D., THIBAULT, X. & BOLLER, E. 2004. Synchrotron 3D microtomography of halite aggregates during experimental pressure solution creep and evolution of the permeability. *Geophysical Research Letters*, **31**, L07607, doi:10.1029/2004GL019605.
- ROSCOE, K. H. 1970. Influence of strains in soil mechanics. *Géotechnique*, **20**, 129–170.
- RUIZ DE ARGONDONA, V. G., RODRIGUEZ REY, A., CELORIO, C., SUÁREZ DEL RÍO, L. M., CALLEJA, L. & LLAVONA, J. 1999. Characterization by computed X-ray tomography of the evolution of the pore structure of a dolomite rock during freeze-thaw cyclic tests. *Physics and Chemistry of the Earth (A)*, **24**, 633–637.
- SCHWARTZ, L. M., AUZERAIS, F., DUNSMUIR, J., MARTYS, N., BENTZ, D. P. & TORQUATO, S. 1994. Transport and diffusion in 3-dimensional composite media. *Physica A*, **207**, 28–36.
- SONG, S. R., JONES, K. W., LINDQUIST, W. B., DOWD, B. A. & SAHAGIAN, D. L. 2001. Synchrotron X-ray computed microtomography: studies on vesiculated basaltic rocks. *Bulletin of Volcanology*, **63**, 252–263.
- SPANNE, P., THOVERT, J. F., JACQUIN, C. J., LINDQUIST, W. B., JONES, K. W. & ADLER, P. M. 1994. Synchrotron computed microtomography of porous media—topology and transport. *Physical Review Letters*, **73**, 2001–2004.
- SUTTON, S. R., BERTSCH, P. M., NEWVILLE, M., RIVERS, M., LANZIROTTI, A. & ENG, P. 2002. Microfluorescence and microtomography analyses of heterogeneous earth and environmental materials. In: FENTER, P., RIVERS, M., STURCHIO, N. & SUTTON, S. (eds), *Applications of Synchrotron Radiation in Low-Temperature Geochemistry and Environmental Sciences*. Reviews in Mineralogy and Geochemistry, **49**, 429–483.
- THIRY, G., BERTRAND AYRAULT, M. & GRISONI, J. C. 1988. Ground-water silicification and leaching in sands: example of the Fontainebleau sand (Oligocene) in the Paris basin. *Geological Society of America Bulletin*, **100**, 1283–1290.
- THOVERT, J. F., YOUSEFIAN, F., SPANNE, P., JACQUIN, C. J. & ADLER, P. M. 2001. Grain reconstruction in porous media: application to low-porosity Fontainebleau sandstone. *Physical Review*, **E63**, 061307.
- VAN GEET, M., SWENNEN, R. & WEVERS, M. 2001. Towards 3-D petrography: application of microfocus computer tomography in geological science. *Computers & Geosciences*, **27**, 1091–1099.
- VAN KAICK, G. & DELORME, S. 2005. Computed tomography in various fields outside medicine. *European Radiology*, **15**, pD74–D81.
- VIGGIANI, G., LENOIR, N., BÉSUERRE, P., DI MICHELI, M., MARELLO, S., DESRUES, J. & KRETZSCHMER, M. 2004. X-ray microtomography for studying localized deformation in fine-grained geomaterials under triaxial compression. *Comptes Rendus Mécanique*, **332**, 819–826.
- VINEGAR, H. J., DE WAAL, J. A. & WELLINGTON, S. L. 1991. CT studies of brittle failure in Castlegate sandstone. *International Journal of Rock Mechanics & Mining Science*, **28**, 441–448.

- WARNER, G. S., NIEBER, J. L., MOORE, I. D. & GEISE, R. A. 1989. Characterizing macropores in soil by computed-tomography. *Soil Science Society of America Journal*, **53**, 653–660.
- WELLINGTON, S. L. & VINEGAR, H. J. 1987. X-ray computerized tomography. *Journal of Petroleum Technology*, **39**, 885–898.
- WONG, T.-F., DAVID, C. & ZHU, W. 1997. The transition from brittle faulting to cataclastic flow in porous sandstones: mechanical deformation. *Journal of Geophysical Research*, **102**, 3009–3025.
- WONG, T.-F., BAUD, P. & KLEIN, E. 2001. Localized failure mode in a compactant porous rock. *Geophysical Research Letters*, **28**, 2521–2524.
- ZAMORA, M. & POIRIER, J. P. 1990. Experimental study of acoustic anisotropy and birefringence in dry and saturated Fontainebleau sandstone. *Geophysics*, **55**, 1455–1465.
- ZHU, W., DAVID, C. & WONG, T.-F. 1995. Network modeling of permeability evolution during cementation and hot isostatic pressing. *Journal of Geophysical Research*, **100**, 15451–15464.

Using production data and time domain seismic attributes for history matching

A. FORNEL¹, M. MEZGHANI^{1,2} & V. LANGLAIS³

¹*Institut Français du Pétrole, 1–4 avenue de Bois Préau, 92852 Rueil-Malmaison, France
(e-mail: Alexandre.FORNEL@ifp.fr)*

²*Present address: Saudi Aramco, PO Box 13765, 31311 Dhahran, Saudi Arabia
(e-mail: mokhles.mezghani@aramco.com)*

³*Present address: Areva NC, BUM/DT/SER, 4 rue Paul Dautier, 78141 Vélizy Cedex, France*

Abstract: A fundamental goal of oil and gas reservoir characterization is to enhance the reliability of dynamic fluid flow simulation studies through better description of geological heterogeneity. Ideally, the geological model should be updated in real time with all available data (especially information derived from seismic, production, well test and core studies) to achieve significant optimization of field management. Such an update can lead to much improved understanding of the dynamic reservoir production forecasting. To this end we propose an integrated technique for improved geological modelling and reservoir characterization, which is based on a non-linear optimization loop for quantitative use of 4D seismic data in combination with production data.

This paper describes an innovative integrated technique (see Fig. 1), based on a simulation workflow, which integrates geological modelling, upscaling, fluid flow simulation coupled with rock physics modelling, depth–time conversion and frequency filtering. Impedance data obtained from pre-stack seismic inversion (spatial information) in addition to production data (more localized information) are used to constrain and update the geological model. The reliability of the model is improved through the minimization of a weighted least-squares objective function, which measures the mismatch between the simulated results and the measured data (both production and 4D seismic).

We successfully applied this technique to a multi-scale reservoir characterization process using a 3D synthetic case. The model is constrained by the compressional and shear impedances and two-way travel times for compressional waves at the base seismic survey ($t = 0$ years, i.e. before production).

Pre-stack seismic data inversion

Reservoir geophysicists commonly use inversion to obtain compressional and shear impedances from pre-stack seismic amplitude data. Seismic amplitude is appropriate for structural interpretation because it reflects the presence of an interface between two layers of different elastic properties, but also carries information on elastic properties themselves (impedances) that can be extracted

from seismic amplitudes by means of stratigraphic inversion. Most algorithms and software solutions rely on the acoustic approximation of the elastic wave equation, which allows us to model seismic amplitudes with the convolution model (Tonellot *et al.* 2001). This approximation, which is based on Zoeppritz equations (Aki & Richards 1980), allows the direct estimation of an optimal elastic model in compressional and shear impedances, under the constraint of geological and petrophysical *a priori* information. In many cases, the *a priori* model is built from well data only, but can be improved by the addition of velocity data. Pre-stack seismic data inversion allows the direct estimation of an optimal elastic model in terms of compressional and shear impedances (I_P and I_S). These impedances derived from pre-stack seismic data are used to constrain and update the geological model.

Production and pre-stack 4D seismic data history matching

The advent of 4D seismic technology brings an additional challenge to industry, in terms of simultaneous integration of production and seismic-related data (Landa & Horne 1997; Gosselin *et al.* 2000; Guéritot & Pianello 2000; Kretz *et al.* 2002). The purpose of this study is to enhance the characterization of subsurface reservoirs by combining geological, geophysical and reservoir engineering data. This goal is fulfilled by developing a 4D workflow

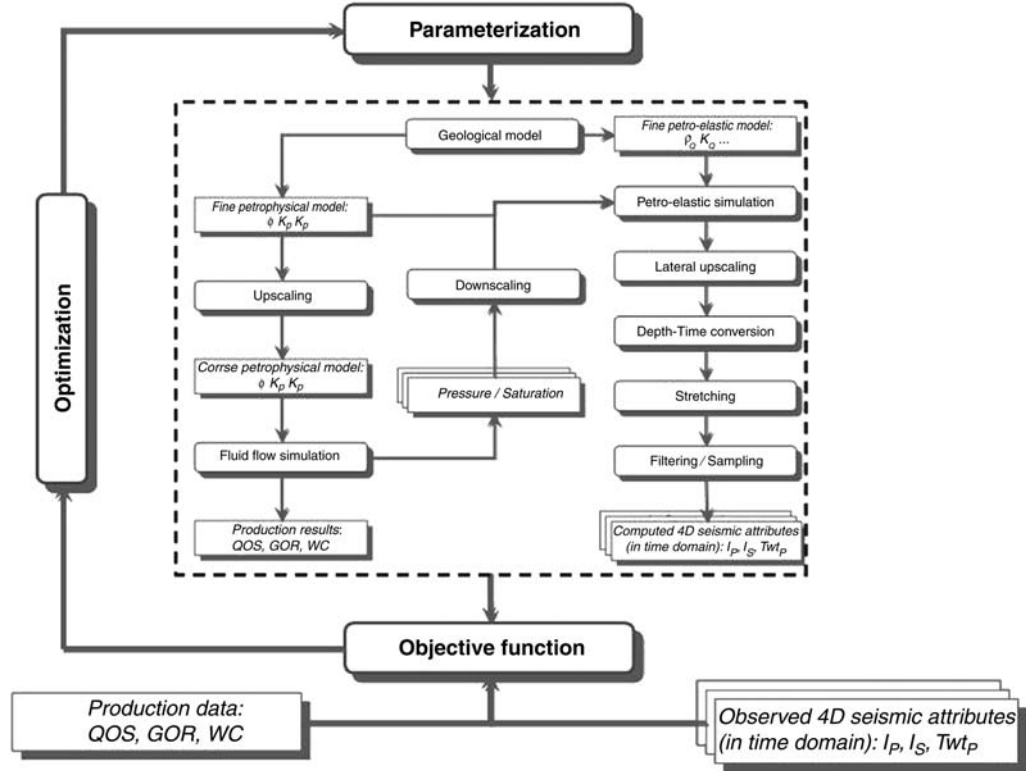


Fig. 1. Proposed technique to integrate production and 4D seismic attributes in history matching.

integrating 4D seismic and production-related data, through the application of the inversion framework. The main difficulty is to account for different scales in the proposed 4D workflow: the geological scale, the fluid flow simulation scale and the seismic scale (Mezghani & Roggero 2001).

The proposed approach (Mezghani *et al.* 2004a, b) includes the following aspects.

(1) Perturbation of the geostatistical model using the gradual deformation parameterization (Hu & Blanc 1998). The geostatistical model includes the facies distribution as well as the petrophysical property distributions (porosity and permeability). The gradual deformation method is a way to constrain the geostatistical model using production data, when deforming continuously one realization of this model. Furthermore, such a method ensures the preservation of the geostatistical properties of the model.

(2) Computation of the flow simulation model by upscaling the fine-scale geostatistical model.

(3) Simulation of the fluid flow model to generate synthetic production results as well as synthetic saturation and pressure distributions.

(4) Generation of fine-scale saturation-pressure distributions by downscaling fluid flow simulation results.

(5) Simulation of the petro-elastic model to generate synthetic compressional and shear impedances (I_p , I_s) and velocities (V_p , V_s) in the depth domain.

(6) Horizontal upscaling of seismic velocities and impedances.

(7) Conversion of depth coordinates in seismic two-way travel times.

(8) Filtering of the synthetic impedances in the band-width of the seismic data and sampling at the seismic resolution.

(9) Computation of the objective function.

(10) Updating of the fine-scale geostatistical model using the classical optimization process.

Geostatistical model perturbation

Most of the success in data integration for reservoir characterization purposes has been obtained with the application of geostatistical techniques. The

parameterization of the geostatistical model is fundamental, in order to honour geological information. This integration is carried out within the framework of an iterative scheme, based on an optimization process. It aims at perturbing an initial porosity–permeability field representative of the geostatistical model considered. Ideally, the final porosity–permeability field must honour not only the dynamic data (production and 4D seismic data), but also the geostatistical coherence of the model (average, variogram, etc). The match of the dynamic data is controlled by the objective function that measures the difference between simulated results and observed data. The gradual deformation method ensures the preservation of the geostatistical model properties.

The gradual deformation parameterization consists in writing a new realization of the porosity–permeability fields, assumed to be of Gaussian type, as a linear combination of independent realizations of a multi-Gaussian random function. The porosity–permeability fields are thus given by

$$\phi(\lambda) = \sum_{i=1}^n \lambda_i \phi_i \text{ and } k(\theta) = \sum_{i=1}^n \theta_i k_i \quad (1)$$

where λ_i and θ_i are the coefficient values of the linear combination (deformation parameters), and ϕ_i and k_i are the independent realizations of the multi-Gaussian random function for the porosity and the permeability.

To preserve the geostatistical properties of the model, the coefficients λ and θ must satisfy the following normality constraint:

$$\sum_{i=1}^n \lambda_i^2 = 1 \text{ and } \sum_{i=1}^n \theta_i^2 = 1. \quad (2)$$

The coefficients λ and θ are estimated so that the resulting porosity field $\phi(\lambda)$ and permeability field $k(\theta)$ reproduce the dynamic data as well as possible. If we use a ϕ – k correlation law describing the dependence of the permeability on the porosity, we simply apply the gradual deformation method to the porosity field and then update the permeability field using this correlation law.

Upscaling

An important issue regarding the role of flow simulation in seismic reservoir monitoring is the simulator grid size. It is always desirable to have the flow simulation grid as fine as possible to capture the details of reservoir heterogeneity and the spatial saturation distribution. For practical considerations, a compromise must be reached between

the desire to capture the details and the availability of computational resources. Consequently, flow simulation results are always spatial averages over relatively large blocks, in which fine-scale details have been transferred to a coarser scale through an upscaling process instigated to reduce the numerical cost of the flow simulation. State-of-the-art, flow-based upscaling techniques have been discussed by Wen & Hernandez (1996) and Renard & de Marsily (1997). The upscaling technique used here is a power-law method, with flexibility to select arithmetic, geometric or harmonic averaging of flow properties.

Fluid flow simulation

Fluid flow simulation is required to better constrain the geological model to production data measured at wells (bottom hole flow pressure, gas–oil ratio, water cut, etc.) derived from Darcy's law:

$$q = -\frac{k_r}{\mu} \bar{K} \nabla(P - \rho g z) \quad (3)$$

where q is the flow velocity, k_r the relative permeability, μ the viscosity, \bar{K} the permeability tensor, P the pressure, ρ the density, and g the gravity acceleration.

For seismic reservoir monitoring, the saturation–pressure patterns are also required as output from the fluid flow simulation.

Petro-elastic modelling

Converting fluid changes to seismic changes always requires the estimation of fluid changes at scales smaller than that of the fluid flow simulation. In our approach we propose performing the petro-elastic simulation at the geological model scale. This requires downscaling of the pressure and saturation distributions computed by the fluid flow simulator. The objective of the downscaling step is the mapping of physical properties such as pressures and saturations from a coarse grid (fluid flow simulation scale) to a fine grid (geological model scale). The proposed downscaling method is based on a simple mapping in the fine grid. More sophisticated downscaling techniques could be envisaged, but the calculation time could be prohibitive for the history matching purpose.

The saturation–pressure patterns obtained from the downscaling module are mapped onto compressional and shear velocities and impedances at each fine geostatistical cell. A number of quantitative relationships have been published in the open technical literature to link elastic properties of rocks with their pore space, pore fluid, fluid saturation, pore

pressure, and rock composition (Mavko *et al.* 1998). Many of these relationships are based on empirical correlation. Other relationships derive from effective medium theory and hence are subject to different types of operating assumptions (Gassmann's equations; Gassmann 1951).

Compressional impedance

The compressional impedance is defined as the product of the bulk density ρ_B and the compressional velocity V_P :

$$I_P = \rho_B V_P. \quad (4)$$

First, we need to compute the bulk density ρ_B , using the formula

$$\rho_B = (1 - \phi)\rho_{Gr} + \phi\rho_F \quad (5)$$

where ρ_{Gr} is the grain density, which is defined for each facies, ρ_F is the fluid density, and ϕ is the porosity: one constant value per facies or one value per pixel (3D cube).

The downscaling step allows us to compute the fluid density taking into account pressure effects:

$$\rho_F = \rho_O(P_O)S_O + \rho_W(P_W)S_W + \rho_G(P_G)S_G \quad (6)$$

where ρ_O , ρ_W and ρ_G are the phase densities, S_O , S_W and S_G are the phase saturations, P_O , P_W and P_G are the phase pressures, and subscripts O, W and G indicate oil, water and gas, respectively.

The phase pressures and saturations are computed by the fluid flow simulator then downscaled to a fine grid. Phase densities are inferred from pressure-density tables (one table for each fluid phase).

The second step is the computation of the compressional velocity V_P :

$$V_P = \sqrt{\frac{3K + 4\mu}{3\rho_B}} \quad (7)$$

where K is the bulk modulus and μ is the shear modulus.

Gassmann's equation (Gassmann 1951) allows us to compute the bulk modulus K :

$$K = K_M + \frac{\left[1 - \frac{K_M}{K_{Gr}}\right]^2}{\frac{\phi}{K_F} + \frac{1 - \phi}{K_{Gr}} - \frac{K_M}{K_{Gr}^2}} \quad (8)$$

where K_{Gr} is the bulk modulus of grain (one constant value per facies depending on the composition

of the basement), K_F is the bulk modulus of fluid, and K_M is the bulk modulus of the porous frame (one constant value per facies depending on the composition of the basement). However, if there is no available value for K_M , an experimental model (Ramamoorthy *et al.* 1995; Zinsner 2002), which takes into account porosity effects, is proposed:

$$K_M = K_{Gr}(3.88\phi^2 - 3.9\phi + 1). \quad (9)$$

The expression of the bulk modulus of fluid K_F is based on Gassmann's equation:

$$\frac{1}{K_F} = \frac{S_O}{K_O} + \frac{S_W}{K_W} + \frac{S_G}{K_G} \quad (10)$$

where K_O , K_W and K_G are fluid phase moduli based on pressure-modulus tables, and S_O , S_W and S_G are phase saturations computed by the fluid flow simulator and the downscaling module.

The Hertz–Mindlin model (Mindlin 1949) allows us to take into account pressure variation effects on V_P :

$$V_P(P_c - P_p) = V_P(\Delta P_a) \left(\frac{P_c - P_p}{\Delta P_a} \right)^{h_p} \quad (11)$$

Where P_c is the confining pressure, P_p is the pore pressure, ΔP_a is the asymptotic differential pressure, and h_p is the Hertz coefficient for compressional waves.

Shear impedance

$$I_S = \rho_B V_S \text{ with } V_S = \sqrt{\frac{\mu}{\rho_B}}. \quad (12)$$

Shear modulus of porous frame μ should be provided by the user: one constant μ per facies. However, if there is no available value for μ , the Ramamoorthy equation (Ramamoorthy *et al.* 1995; Zinsner 2002) is proposed:

$$\mu = \mu_{Gr}(2.19\phi^2 - 3.48\phi + 1) \quad (13)$$

where μ_{Gr} corresponds to the shear modulus of a grain. This experimental model describes the dependence of μ on the porosity ϕ . Furthermore, the impact of pressure variation on shear velocity can be modelled using the Hertz model:

$$V_S(P_c - P_p) = V_S(\Delta P_a) \left(\frac{P_c - P_p}{\Delta P_a} \right)^{h_S} \quad (14)$$

where h_S is the Hertz coefficient for shear waves.

Horizontal upscaling or downscaling

To be able to compare the computed impedances with the synthetic data, we must perform an upscaling or a downscaling to map the obtained data from the geological scale to the seismic data scale. Generally, we use a horizontal upscaling.

Depth–time conversion

Such a conversion is the key step of our technique. Using seismic velocity cubes given by the petro-elastic model, we are able to transform impedance cubes from the depth domain to the time domain. The main advantage is to build a velocity law cell by cell and to update it during the optimization process and through time. Therefore we always have travel times coherent with impedances. Generally, researchers use only one constant seismic velocity cube for the entire optimization and through time, or only averaged velocities between seismic markers.

Filtering

To obtain the synthetic impedances in the bandwidth of the seismic data, we need to filter compressional and shear impedances obtained by the seismic module, choosing a low pass, a high pass, a band pass or a band stop filter. Then we sample the obtained filtered impedances at the seismic resolution (generally 2 ms).

Objective function: least-squares criterion

The update of the geological model by the dynamic data depends on the minimization of an objective function that measures the mismatch between the observed data (production and 4D seismic-related data) and the obtained simulation results for a fixed value of the parameters θ . The least-squares formulation is frequently used in the oil industry:

$$\begin{aligned} J(\theta) = & \frac{1}{2} (P^{\text{obs}} - P(\theta))^T C_P^{-1} (P^{\text{obs}} - P(\theta)) \\ & + \frac{1}{2} (S^{\text{obs}} - S(\theta))^T C_S^{-1} (S^{\text{obs}} - S(\theta)) \end{aligned} \quad (15)$$

where P^{obs} is the production data, $P(\theta)$ is the simulated production results for the parameter value θ , C_P is the covariance matrix on the production data, S^{obs} is the 4D seismic-related data, $S(\theta)$ is the simulated seismic results for the parameter value θ , and C_S is the covariance matrix on the seismic data.

The covariance matrix represents the uncertainty on the residual between measured and simulated data. These errors are assumed independent in our case, therefore the covariance matrix is diagonal.

The minimization of the objective function requires the calculation of the derivatives of the

simulation results with respect to the parameters to estimate

$$\frac{\partial P}{\partial \theta}(\theta) \text{ and } \frac{\partial S}{\partial \theta}(\theta). \quad (16)$$

In this study, a finite-difference approximation is used for the calculation of the derivative of the simulation results with respect to the parameterization of the fine-scale geostatistical model. This choice allows a quick application of our 4D workflow without requiring any additional programming in the fluid flow simulator or the petro- elastic modelling.

Optimization techniques

The algorithms of non-linear optimization calculate, according to an iterative process, a value θ^{opt} of the parameters, which minimizes the objective function. An iteration of the optimization algorithm determines an estimate of the parameters according to this principle:

$$\theta^{(k+1)} = \theta^{(k)} + t^{(k)} s^{(k)}. \quad (17)$$

Calculation of a direction. The direction $s^{(k)}$ is the solution of a particular linearized problem. The formulation of this problem depends upon the simulation results as well as their derivative with respect to the parameterization.

Linear search. The step $t^{(k)}$ is calculated to satisfy the descent relation

$$J(\theta^{(k)} + t^{(k)} s^{(k)}) < J(\theta^{(k)}). \quad (18)$$

Various methods of optimization, such as the steepest descent, Fletcher–Powell, Levenberg–Marquardt and the Gauss–Newton, are implemented. In this study, we choose to work with the Fletcher–Powell algorithm, which offers the advantages of both the steepest-descent (stability and robustness far from the solution) and Gauss–Newton methods (fast convergence in the neighbourhood of the solution). A general overview of optimization methods has been given by Lions (1968).

Validation on synthetic test case

For a good observation of the impact 4D seismic data on reservoir characterization, the synthetic case should be designed to be favourable for a 4D seismic programme. The following criteria affected our choice of candidate reservoir.

(1) The studied reservoir must be a good representation of a real case, not only from a geological point of view, but also with respect to the fluids saturating the medium.

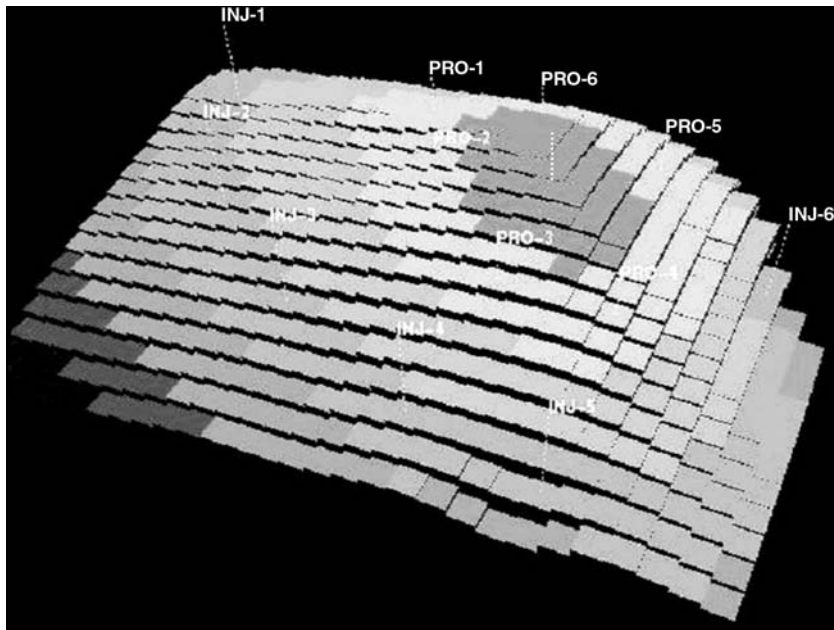


Fig. 2. Structure of the PUNQ-MONITOR test case.

(2) Most 4D seismic studies show that it is feasible to follow the gas–oil contact displacement because it causes important reflections. Indeed, the existence of gas causes a significant decrease of seismic velocities, leading to an impedance variation.

PUNQ-MONITOR case description

For our validation test, we are working with the PUNQ-MONITOR case (see Fig. 2), widely inspired by PUNQ-S3, a simplified case with a small-size reservoir model. The PUNQ-S3 model is a standard test case defined in the PUNQ project (Production forecasting with UNcertainty Quantification) for comparative studies of the inversion method.

Geological modelling

The geological model of the PUNQ-MONITOR case includes five geological units: units 1, 3 and 5 (sandstones) are of high reservoir quality; unit 4 (sandstones with lagoonal clays) is of intermediate reservoir quality; unit 2 (sandstones with lagoonal shales) is of low reservoir quality.

A geostatistical model based on Gaussian random realizations is used to generate the porosity and permeability fields. The structural parameters of the geological model are defined in Table 1.

Table 1. Structural parameters for the PUNQ-MONITOR test case

Unit:	Porosity				
	1	2	3	4	5
Average	0.30	0.16	0.30	0.20	0.30
Deviation	0.075	0.040	0.075	0.050	0.075
Correlation	1000	750	1500	750	1250
Anisotropy	3.5	1.0	4.0	2.0	3.0
Unit:	\log_{10} (horizontal permeability)				
	1	2	3	4	5
Average	2.00	1.20	2.00	1.60	2.00
Deviation	0.500	0.300	0.500	0.400	0.500
Correlation	1000	750	1500	750	1250
Anisotropy	3.5	1.0	4.0	2.0	3.0
Unit:	\log_{10} (vertical permeability)				
	1	2	3	4	5
Average	0.94	0.17	1.09	0.56	0.93
Deviation	0.583	0.391	0.424	0.453	0.577
Correlation	1000	750	1500	750	1250
Anisotropy	3.5	1.0	4.0	2.0	3.0

It should be noted that the correlation lengths, angles and anisotropy ratios are the same for porosity and permeability.

Geostatistical simulation

The geostatistical simulation proceeds unit by unit: the simulation grid size per unit is $171 \times 252 \times 6$; the simulation block size is $20 \text{ m} \times 20 \text{ m} \times 3 \text{ m}$. For each layer, the following steps were followed to generate the PUNQ-MONITOR reference case.

(1) Simulate a normalized Gaussian random field for porosity (ϕ).

(2) Co-simulate a normalized Gaussian random field for the logarithm of the horizontal permeability ($\log(k_h)$), based on the normalized porosity field. The correlation coefficient used between ϕ and $\log(k_h)$ is 0.8.

(3) Co-simulate a normalized Gaussian random field for the logarithm of the vertical permeability ($\log(k_v)$), based on the normalized horizontal permeability field ($\log(k_h)$). The correlation coefficient used between $\log(k_h)$ and $\log(k_v)$ is 0.8.

(4) Transform all normalized fields (porosity and permeability) to the mean and standard deviation defined in Table 1.

(5) Transform the log-permeability fields to permeability fields using a 10th power.

Fluid flow simulation

The geostatistical simulation model is composed of $171 \times 252 \times 30$ grids corresponding to 1292760 grid blocks with a block size of $20 \text{ m} \times 20 \text{ m} \times 3 \text{ m}$. The aggregation, whose rate is $9 \times 9 \times 6$, is performed by using power laws. The grid properties for the fluid flow simulation are as follows: simulation grid size is $19 \times 28 \times 5$ simulation block size is $180 \text{ m} \times 180 \text{ m} \times 18 \text{ m}$.

During the production phase (1967–1978), six production wells were drilled on units 1–3–5; during the injection phase (1967–1978), six water injection wells were drilled on units 3–4–5 and one gas injection well on unit 1.

Petro-elastic simulation (PEM)

A realistic petro-elastic model is used to generate compressional and shear impedances. For the PUNQ-MONITOR case, a PEM is defined for each unit, as shown in Table 2.

The petro-elastic simulation grid is identical to the geostatistical simulation grid: the simulation grid size is $171 \times 252 \times 30$; the simulation block size is $20 \text{ m} \times 20 \text{ m} \times 3 \text{ m}$. Therefore we need to downscale the flow simulation results (pressure and saturation) from the fluid flow simulation grid ($180 \text{ m} \times 180 \text{ m} \times 18 \text{ m}$) to the geostatistical simulation grid ($20 \text{ m} \times 20 \text{ m} \times 3 \text{ m}$).

Four surveys, consisting of base survey at T_0 ($t = 0$ years) and monitoring surveys at T_1 ($t = 6$ years), T_2 ($t = 12$ years) and T_3 ($t = 18$ years), of compressional and shear impedances for the PUNQ-MONITOR dataset are computed using the fine grid data of pressures and saturations after downscaling. To mimic a real dataset, a third scale is introduced in addition to the geostatistical and fluid flow scales, the seismic scale. The seismic grid size is $57 \times 84 \times n$, where n depends on the reservoir time thickness and is different for compressional and shear waves; the seismic grid block size is $60 \text{ m} \times 60 \text{ m} \times 2 \text{ ms}$. Therefore we must upscale the compressional and shear dataset to the seismic data scale: from ($20 \text{ m} \times 20 \text{ m} \times 3 \text{ m}$) to ($60 \text{ m} \times 60 \text{ m} \times 3 \text{ m}$). We then compute two-way travel times for each wave and for each seismic survey. Furthermore, we have chosen to filter the obtained dataset using the frequencies 0 Hz–0 Hz–100 Hz–120 Hz corresponding to a low-pass filter.

Base seismic survey history matching

We first perform a history match (Fornel 2006) using seismic data from the base survey T_0 alone (3D cubes of compressional and shear impedances, 2D map of travel time) to match porosity fields. We then use this as starting point for the history matching including production data and three seismic surveys (the last one will be used to verify the predictability of the geological model obtained after the optimization process).

Table 2. Petro-elastic parameters per geological unit

	Unit 1	Unit 2	Unit 3	Unit 4	Unit 5
Bulk modulus of grain K_{Gr} (GPa)	37	30	37	34	37
Bulk modulus of porous frame K_{M} (GPa)	8.70	11.00	8.86	12.90	8.62
Shear modulus of grain μ_{Gr} (GPa)	45	45	45	45	45
Shear modulus of porous frame μ_{dry} (GPa)	7.72	8.70	7.54	10.30	7.84
Hertz coefficient for compressional wave	0.08	0.08	0.08	0.08	0.08
Hertz coefficient for shear wave	0.12	0.12	0.12	0.12	0.12

Constrained datasets

Models have been constrained with two different datasets generated from the reference case: (1) static data, consisting of porosity profiles from production and injection wells to obtain initial values for the porosity means and standard deviations, and porosity values from production wells to constrain simulated porosity field using kriging; (2) dynamic data, consisting of compressional impedance $I_P(T_0)$, shear impedance $I_S(T_0)$, and compressional two-way travel time $T_{wtp}(T_0)$.

Parameters

We have chosen to use the gradual deformation method (10 parameters per unit) to update and characterize porosities. We note that it is not necessary to calculate permeability in this case. For each geological unit, porosity mean and standard deviation are also used as optimization parameters (two additional parameters per unit). Finally, we use 35 parameters. The optimization process is based on gradual deformation chains, as follows.

Step 1: we first choose 11 random geostatistical realizations.

Step 2: we apply the gradual deformation using 10 parameters.

Step 3: we run an optimization process to obtain 10 optimal parameters and thus an optimal geostatistical realization for the geological model.

Step 4: another 10 random realizations are then chosen and we go back to the second step, and so on until we have an acceptable objective function value (as low as possible).

Objective function and weights

The objective function includes three series related to the base seismic survey: one cube of compressional impedances $I_P(T_0)$, one cube of shear impedances $I_S(T_0)$, and one map of reservoir time thickness for compressional waves $T_{wtp}(T_0)$. Therefore the objective function can be written as follows:

$$F(\theta) = \sum_{i=1}^{nb_{I_p}} W_i^{I_p} \left(I_{P,i}^{\text{ref}} - I_{P,i}^{\text{sim}}(\theta) \right)^2 + \sum_{i=1}^{nb_{I_S}} W_i^{I_S} \left(I_{S,i}^{\text{ref}} - I_{S,i}^{\text{sim}}(\theta) \right)^2 + \sum_{i=1}^{nb_{T_{wtp}}} W_i^{T_{wtp}} \left(T_{wtp,i}^{\text{ref}} - T_{wtp,i}^{\text{sim}}(\theta) \right)^2 \quad (19)$$

where nb_{I_p} , nb_{I_S} and $nb_{T_{wtp}}$ are the numbers of measurements per data series, $W_i^{I_p} = 1/[nb_{\text{series}} nb_{I_p} (\sigma_{I_p^{\text{ref}}}^2)]$, $W_i^{I_S} = 1/[nb_{\text{series}} nb_{I_S} (\sigma_{I_S^{\text{ref}}}^2)]$ and $W_i^{T_{wtp}} = 1/[nb_{\text{series}} nb_{T_{wtp}} (\sigma_{T_{wtp}^{\text{ref}}}^2)]$ are the weights, $nb_{\text{series}} = 3$ is the number of data series, and $\sigma_{I_p^{\text{ref}}} = 2.83\% I_p^{\text{ref}}$, $\sigma_{I_S^{\text{ref}}} = 1.72\% I_S^{\text{ref}}$ and $\sigma_{T_{wtp}^{\text{ref}}} = 0.27\% T_{wtp}^{\text{ref}}$ are the standard deviations used related to the data.

History matching results

For the base seismic survey history matching, we have performed 220 simulations to reach a decrease in the objective function of 90.4%. Figure 3 shows the objective function evolution: light grey indicates the values at each iteration (220 iterations) of the optimization process and dark grey the

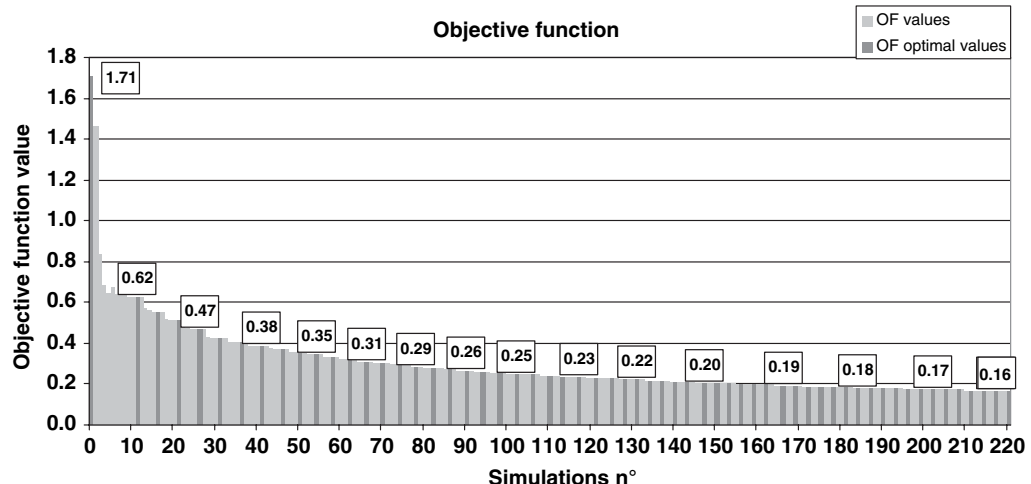


Fig. 3. Objective function evolution.

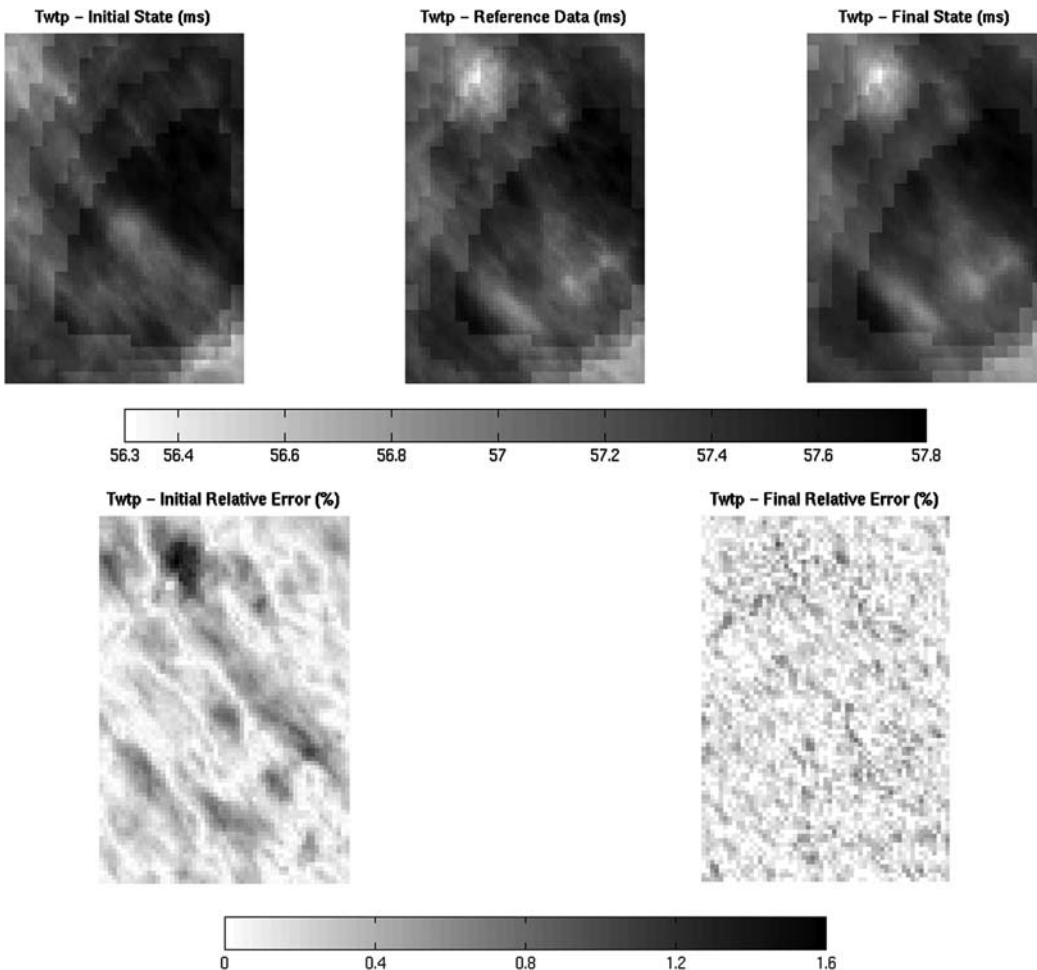


Fig. 4. Results obtained on the map of reservoir time thickness. At the top, the initial state, the reference data and the final state; at the bottom the initial and final relative errors.

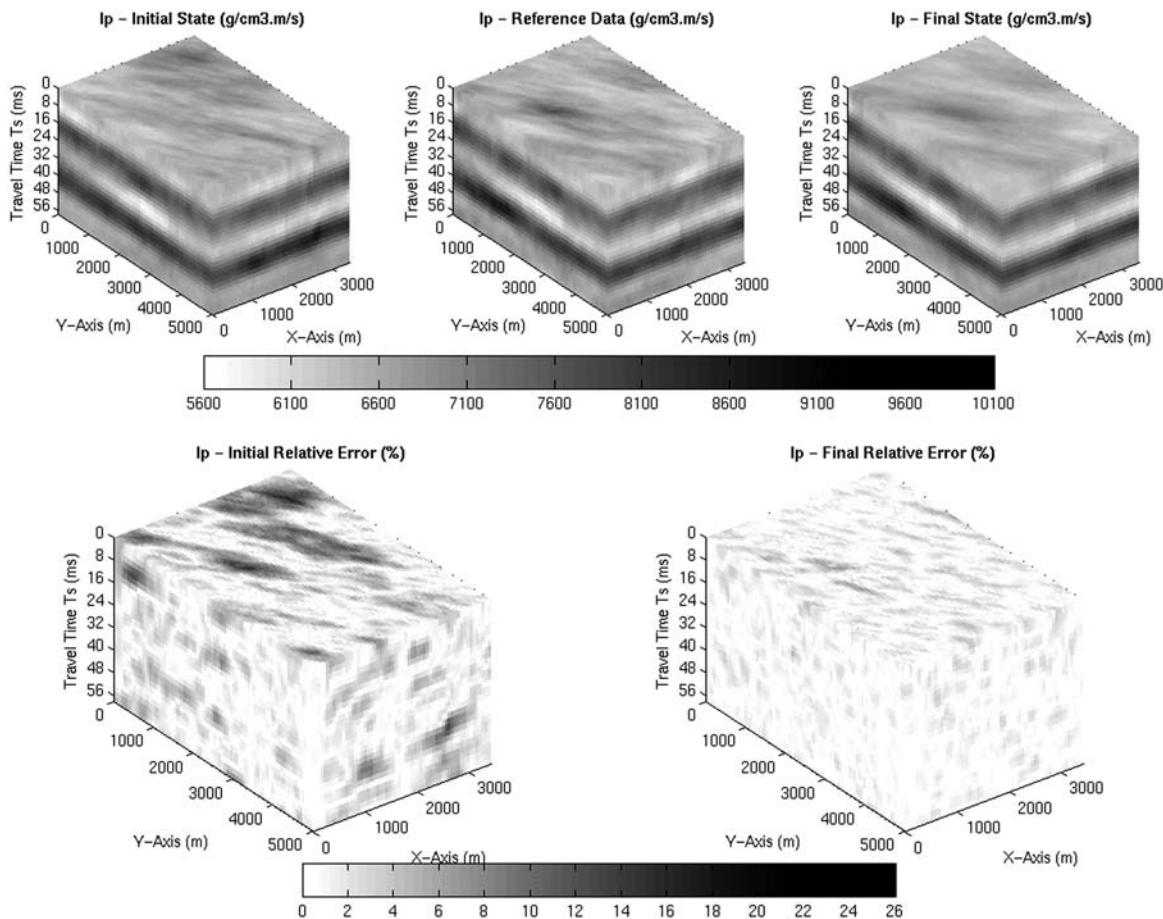


Fig. 5. Results obtained on the cube of compressional impedances I_p . At the top, the initial state, the reference data and the final state; at the bottom the initial and final relative errors.

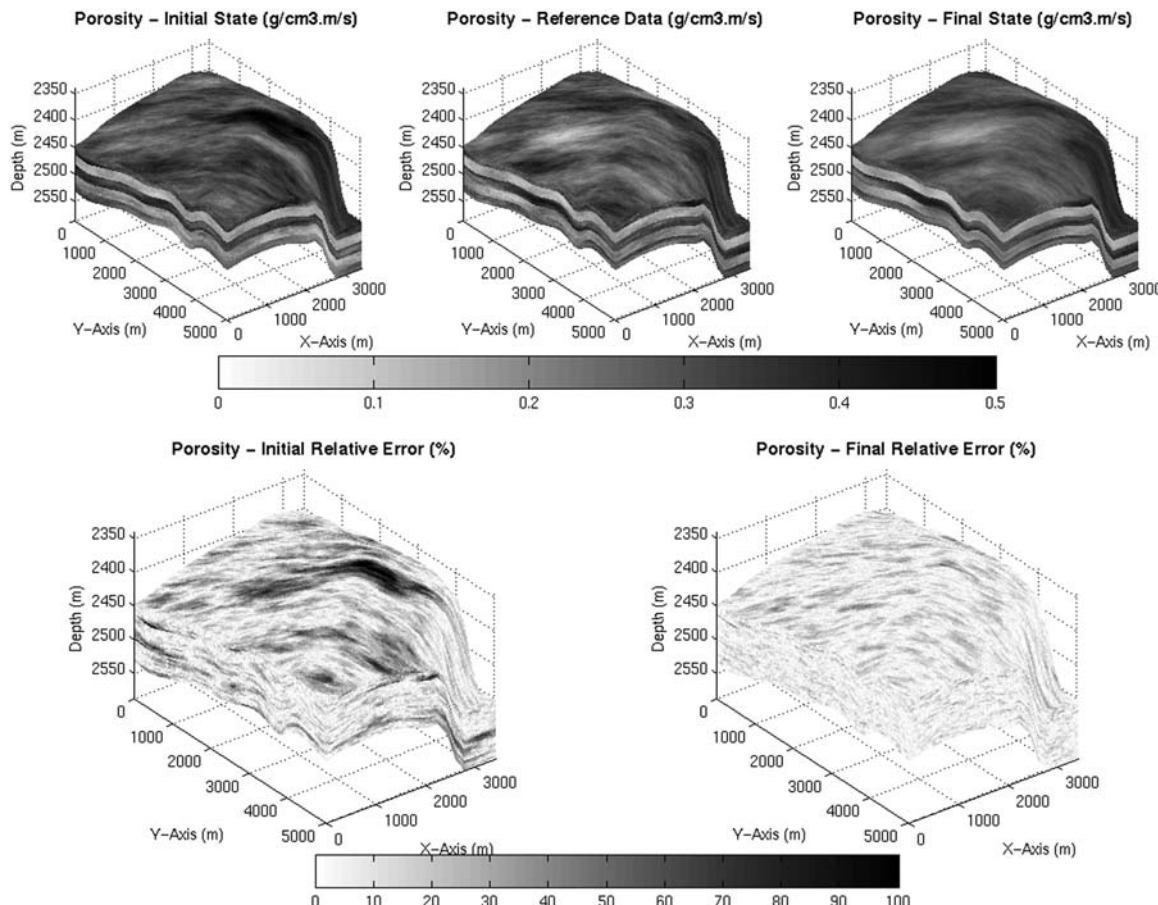


Fig. 6. Results obtained on the cube of porosity: initial state (top left), reference data (top middle), final state (top right), initial relative error (bottom left) and final relative error (bottom right).

optimal value for each gradual deformation chain (59 chains). We observe an exponential decrease of the objective function; this is typical when using the gradual deformation method.

Figure 4 shows the results obtained for the reservoir time thickness. At the top left we can see the initial state, in the top centre the reference data map to match and at the top right the final optimal map after 220 simulations. We find a very good match at the end of the optimization process because the final map reproduces not only trends but also some heterogeneity that appears on the referencedata map. Analysing the results obtained on the cube of compressional impedances $I_P(T_0)$ in Figure 5, we reach the same conclusions.

We note that, between the initial and final states, the means of the relative error have decreased by 66.6% for the compressional impedances (see Fig. 5), 61.3% for the shear impedances, and 77.7% for the reservoir time thickness (see Fig. 4).

As of the objectives of the base seismic survey history matching is to reproduce the porosity fields, we have compared the initial and final states with the reference cube in Figure 6. We note that the mean of the relative error decreases significantly (from 25.6% to 9.2%), which will be a good starting point for a complete history matching (i.e. integrating production and 4D seismic data).

Conclusions

The 4D workflow used in this work takes advantage of a powerful data integration scheme that involves both dynamic and static information, and delivers estimates that preserve the coherency of the geological model properties, guarantee the match of production and 4D seismic-related measurements, and benefit from models supported by the physics of fluid flow and acoustic wave propagation.

The proposed approach highlights the applicability of 4D seismic data in geological modelling and reservoir characterization. Interdisciplinary integration of seismic measurements and rock physics with multiphase fluid flow helps to reduce uncertainties in petrophysical property distributions, and as a result, also reduces uncertainties in interpreting seismic attributes for an optimal reservoir management.

Further work will involve making a complete history match using both production data (bottom hole pressure, gas–oil ratio, water cut) and 4D seismic data (compressional and shear impedances, reservoir time thickness). To do this, we will use the porosity field obtained by the inversion presented in this paper.

Such a test will be made in two parts: the first will involve an inversion of production data only, and the second will use both production and 4D seismic data, to quantify the impact of seismic attributes on the history matching process.

The authors thank IFP for its permission to publish this paper.

References

- AKI, K. & RICHARDS, P. G. 1980. *Quantitative Seismology: Theory and Methods*. Freeman, San Francisco, CA.
- FORNEL, A. 2006. *Monitoring de réservoirs: mise à jour du modèle géologique par les données de production et de sismique 4D*. IFP 59055. Institut Français du Pétrole, Rueil-Malmaison.
- GASSMANN, F. 1951. *Über die Elastizität Poröser Medien*. Vierteljahrsschrift Naturforschung Gesellschaft, Zurich, **96**, 1–23.
- GOSSELIN, O., COMINELLI, A., VAN DER BERG, S. & CHOWDHURY, S.-D. 2000. A gradient-based approach for history matching of both production and 4D seismic data. In: *ECMOR VII, Baveno, Lago Maggiore, Italy*.
- GUÉRILLOT, D. & PIANELO, L. 2000. Simultaneous matching of production data and seismic data for reducing uncertainty in production forecasts. In: *Proceedings of the SPE European Petroleum Conference, 24–25 October 2000, Paris, France*, SPE 65131.
- HU, L.-Y. & BLANC, G. 1998. Constraining a reservoir facies model to dynamic data using a gradual deformation method. In: *ECMOR VI, Peebles, Scotland*.
- KRETZ, V., LE RAVALEC-DUPIN, M. & ROGGERO, F. 2002. An integrated reservoir characterization study matching production data and 4D seismic. In: *Annual Technical Conference and Exhibition, San Antonio, TX*, SPE 77516.
- LANDA, J. & HORNE, R. 1997. A procedure to integrate well test data, reservoir performance history and 4D seismic information into a reservoir description. In: *Annual Technical Conference and Exhibition, San Antonio, TX*, SPE 38653.
- LIONS, J. L. 1968. *Contrôle optimal de systèmes gouvernés par des équations aux dérivées partielles*. Dunod, Paris.
- MAVKO, G., MUKERJI, T. & DVORKIN, J. 1998. *The Rock Physics Handbook: Tools for Seismic Analysis in Porous Media*. Cambridge University Press, Cambridge.
- MEZGHANI, M. & ROGGERO, F. 2001. Combining gradual deformation and upscaling techniques for direct conditioning of fine scale reservoir models to dynamic data. In: *Proceeding of the SPE Annual Technical Conference and Exhibition, New Orleans, LA*, SPE 71334.
- MEZGHANI, M., FORNEL, A., LANGLAIS, V. & LUCET, N. 2004a. History matching and quantitative use of 4D seismic data for an improved reservoir. In: *Annual Technical Conference and Exhibition, Houston, TX*, SPE 90420.
- MEZGHANI, M., FORNEL, A., LANGLAIS, V. & LUCET, N. 2004b. Multiscale reservoir characterization using production and time lapse seismic data. In: *ECMOR IX, Cannes*.

- MINDLIN, R. D. 1949. Compliance of elastic bodies in contact. *Journal of Applied Mechanics*, **16**, 259–268.
- RAMAMOORTHY, R., MURPHY, W. F. & COLL, C. 1995. Total porosity estimation in shaly sands from shear modulus. In: *Proceedings of SPWLA 36th Annual Logging Symposium Transactions*.
- RENARD, P. & DE MARSILY, G. 1997. Calculating equivalent permeability: a review. *Advances in Water Resources*, **20**, 253–278.
- TONELLOT, T., MACÉ, D. & RICHARD, V. 2001. Joint stratigraphic inversion of angle-limited stacks. In: *SEG 71st Annual International Meeting*.
- WEN, X. H. & HERNANDEZ, J. J. 1996. Upscaling hydraulic conductivities in heterogeneous media: an overview. *Journal of Hydrology*, **183**, 9–32.
- ZINSNER, B. 2002. *Modélisation de Monitoring Géophysique Saint-Clair sur Epte—caractérisation pétro-acoustique de roches réservoirs*. IFP 56867. Institut Français du Pétrole, Rueil-Malmaison.

Influence of persistence on behaviour of fractured rock masses

B. H. KIM, P. K. KAISER & G. GRASSELLI

Geomechanics Research Centre, MIRARCO, Laurentian University, Sudbury, 935 Ramsey Lake Road, Sudbury, Ont., Canada P3E 2C6 (e-mail: bkim@mirarco.org)

Abstract: Most of the models that simulate fractured rock masses assume fully persistent discontinuities, simplifying the fact that, in nature, fractured rock masses are made of non-continuous sets of joints. A rock bridge gives an effective cohesion to the fracture and a block of rock cannot fall or slide until all the rock bridges fail. This failure involves the failure of the intact rock, which can be orders of magnitude stronger than the shear strength of the rock joint. In this study we focus on how the distribution of rock bridges influences the overall rock mass behaviour, to contribute to the understanding of how the presence of rock bridges influences the 'scale' effect that is observed between strength values measured on intact rock in the laboratory and those observed at the rock mass scale. To estimate the influence of spatial fracture, parameters of the rock mass strength and deformation were determined, using the orthogonal arrays method, UDEC and variance analysis. The numerical model was first calibrated on shear tests of samples made of continuous joints, and then used to investigate the shear behaviour of a fractured rock mass with non-persistent joints. The 2D approach was successfully extended to 3D models using 3DEC with the aim of providing a better approach for simulating the stability of an underground cavern in a fractured rock mass.

Discontinuities or joints in the rock mass have various shapes and sizes. Along with the joint orientation and spacing, the joint persistence, or the relative size of the joint, is one of the most important factors in determining the block sizes of a jointed rock masses. Although the importance of joint persistence on the overall rock mass strength has long been known, the impact of persistence on rock strength is under-represented in most current rock mass classification systems (Kim 2002). In addition, joints are often assumed to be fully persistent for stability analysis of tunnels or slopes. This oversimplification may lead to an overestimation of the number of removable blocks near the excavated face, resulting in excessive expenditure on the rock support. On the other hand, if the joint persistence characteristics are properly considered and the block size can be accurately estimated, safe and economic design of the rock structure can be achieved.

For an optimum design of underground structures in rock, it is therefore important to estimate the size and distribution of the blocks that constitute the rock mass as close to reality as possible. For this purpose, using UDEC (Itasca 2004b) and 3DEC (Itasca 2004a) we have studied how joint persistence and block size are affected by variations in the geometry of discontinuities. To acquire a specific and statistically sound understanding of how the variation of a single parameter is reflected in the overall phenomenon, a large number of parametric analyses are generally necessary to evaluate the 'weight' of each single parameter. The number

of tests increases exponentially with the number of parameters and modification of the level of parameters to reduce test cases can result in false consequences as the weighted value of each parameter may be disregarded. To prevent this type of statistical error, combinations of joint spacing, dip direction, dip angle, and length have been statistically generated with the help of orthogonal arrays using the experimental design approach. Statistical analyses, analysis of variance and regression analysis were then performed to elucidate the influence of rock bridges obtained from the numerical modelling on both the shear behaviour of the rock mass and displacement around the underground cavern.

Discontinuity persistence and rock bridges

Fractures usually occupy only a part of the surface extended by the joint plane to a given rock volume. Persistence is the term used to describe the areal extent or size of a discontinuity within a plane (Brady & Brown 1992). In jointed rock masses, rock bridges exist because of the non-persistent nature of joints. A rock bridge is defined as a small bridge of intact rock separating coplanar or non-coplanar discontinuities. Persistence can be estimated by comparing either the sum of the trace length l_i relative to the length of a collinear scan line $L(\sum l_i/L)$ or the sum of individual joint surface areas a_i to the surface of a coplanar reference

area $A(\sum a_i/A)$ (Dershowitz & Einstein 1988). In practice, as it is almost impossible to accurately measure the true joint area, the persistence is often estimated based on the trace length. An illustration of persistent and non-persistent joints is presented in Figure 1.

Consensus exists on the fact that rock bridges play an important role in stabilizing a rock mass by the resistance to removal of blocks of rock. A rock block cannot fall or slide from an excavation or slope until the appropriate rock bridges have failed. The rock bridge failure involves the failure of the intact rock, which can be an order of magnitude stronger than the rock mass (Kemeny 2005). The importance of rock bridges or non-persistent joints on the stability of rock slopes has been studied by, among others, Einstein *et al.* (1983), Sjöberg (1996) and Nichol *et al.* (2002), and the effect of rock bridges on the strength or deformation properties of rock masses has been discussed by Kemeny & Cook (1986), Shen *et al.* (1995) and Kemeny (2003), among others.

If the joints are not persistent, the rock mass strength is higher and the global stability is enhanced. Diederichs & Kaiser (1999) demonstrated that the capacity of 1% rock bridge area equivalent to $100 \text{ cm}^2 \text{ m}^{-2}$ total joint area in a strong rock (uniaxial compressive strength, UCS > 200 MPa) is equivalent to the capacity of at least one cablebolt. Consequently, the apparent block volume should be larger for rock masses with non-persistent joints (Cai *et al.* 2004). Cai *et al.* proposed that if the joint lengths are only about 20% of the reference length, the equivalent block size is about five times larger than that with persistent joints. Thus, the presence of discontinuous joints has a significant effect on the properties and behaviour of rock masses and should be carefully considered for the engineering characterization of the rock masses.

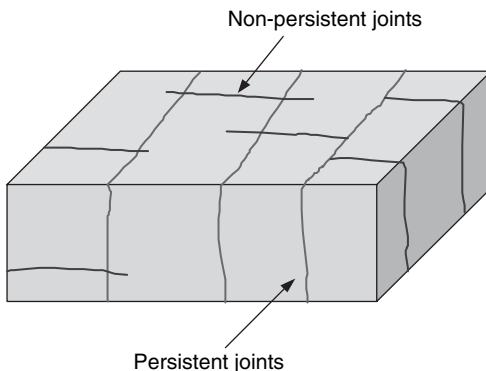


Fig. 1. Illustration of joint persistence.

The issue of joint persistence is important but, at the same time, it is one of the most difficult issues to address in rock mechanics. In the present study, we use the distinct element method, in combination with the experimental design technique, to systematically investigate the effect of joint persistence on the mechanical behaviour of jointed rock masses.

Experimental design and ANOVA

Because the inherent variability of the spatial characteristics of joints (e.g. orientation, length, spacing, etc.) is significant and the number of relevant parameters in determining a joint network is large, it is impractical to run a parametric study by varying each parameter individually. Therefore, to save time but simultaneously honour the statistical distributions of the parameters, it is necessary to develop an experimental design to collect sufficient sample data and develop a statistical analysis method to draw accurate conclusions from the collected sample data.

The specific questions that the experiment is intended to answer must be clearly identified before carrying out the experiment. We must also attempt to identify known or expected sources of variability in the experimental units, as one of the main aims of a designed experiment is to reduce the effect of these sources of variability on the result.

The experimental design technique is used to assist data acquisition, to decrease experiment error, and to provide statistical analysis tools to describe the degree of errors. Two basic principles guide statistical experimental design: replication and randomness. Replication means that the same results can be obtained using the same experimental conditions. Randomness is required to ensure objectivity by putting the experiment objects into different conditions or by randomly arranging their experimental order. Furthermore, it is necessary to have a homogeneous experimental environment when applying probability theory. The principle of orthogonal array design is to eliminate the inclination effect caused by other factors when the influence of a specific factor is investigated. When there are many parameters to be studied, the main effect of each parameter and some of the reciprocal actions are estimated, whereas other reciprocal actions are disregarded to reduce the number of tests. The benefit of orthogonal array design is that it calculates the parameter changes from experimental or field-mapping data, facilitates the easy preparation of input data for analysis of variance, and allows us to consider many parameters in experiment or simulation without

increasing the test scale (Mendenhall & Sincich 1995; Devore 2000).

Let us assume that there is an orthogonal array presented as $L_9(3^4)$. This means that four factors or parameters could be used in the experiment and there are three stages in which the parameters can change their values. Eighty-one experiments are required to obtain results that are statistically significant and representative. If the orthogonal array is used, however, only nine experiments are needed.

In experiments, a treatment is something that researchers administer to experimental units. For example, a rock mass with three joint sets may have a different orientation for each set. Treatments are administered to experimental units by 'level', where level implies an amount or magnitude. For example, if the experimental units had a dip angle of 15° , 45° , 60° and those amounts would be the three levels of the treatment. 'Level' is also used for categorical variables, such as joint set A, B and C, where the three are different kinds of joint set, not different levels of the same set.

A factor of an experiment is a controlled independent variable; a variable whose levels are set by the experimenter. A factor is a general type or category of treatments. Different treatments constitute different levels of a factor. For example, three different groups of runners may be subjected to different training methods. The runners are the experimental units, the training methods, the treatments; the three types of training methods constitute three levels of the factor 'type of training'.

The results of the test are usually reported in an analysis of variance (ANOVA) table. ANOVA is used to uncover the main and interaction effect of categorical independent variables on an interval dependent variable. The key statistic in the ANOVA is the F -test of the difference of group means. The F -test is intended to find out if the means of the groups formed by values of the independent variable (or combinations of values for multiple independent variables) are different enough not to have occurred by chance. If the group means do not differ significantly, then it is inferred that the independent variables do not have an effect on the dependent variable. If the F -test shows that the independent variables

are related to the dependent variable, then multiple comparison tests of significance are used to explore which value groups of the independent variables have the most influence on the relationship. Unlike regression, ANOVA does not assume linear relationships and it handles interaction effects automatically. It is not a test of difference in variances, but rather an assumption of relative homogeneity of variances. Thus, one of the key assumptions in ANOVA is that the groups formed by the independent variables are relatively equal in size and have similar variances to the dependent variable. Like regression, ANOVA is a parametric procedure that assumes multivariate normality (Mendenhall & Sincich 1995; Devore 2000).

Table 1 shows the general organization of the ANOVA table. The terminology used in the ANOVA table is based on the partitioning of the sum of squares. The variability of all of the observations is measured by SS (total), which is partitioned into two resources of variability. The sum of squares for treatments (SST) is the variation attributed to the differences between the treatment means, and the sum of squares for error (SSE) measures the amount of variability within the samples. The test is then based on comparing the relative sizes of SST and SSE after taking into consideration the degree of freedom.

For the application at hand, orthogonal arrays are used to define the combination of joint spacing, dip direction, angle, and length of different joint sets that simulate discontinuous blocks with various shapes and sizes in UDEC and 3DEC, respectively. In addition, we conducted ANOVA using calculated results from the orthogonal arrays to analyse the effect of joint spacing, angle, and length on shear behaviour of a fractured rock mass and wall displacement around a tunnel.

Parametric analysis using numerical simulation

UDEC modelling for shear tests

The aim of this study is to understand how persistence influences block size and distribution at rock

Table 1. Examples of results from ANOVA

Source of variation	Degree of freedom	Sum of square	Mean square	F
Treatments	$k - 1$	SST	$MST = SST/(k - 1)$	$F = MST/MSE$
Error	$n - k$	SSE	$MSE = SSE/(n - k)$	
Total	$n - 1$	SS(total)		

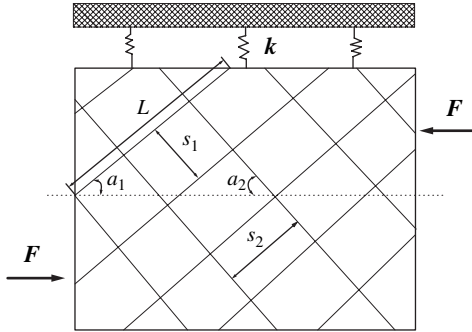


Fig. 2. Layout of the UDEC model.

mass scale, and how such distributions change the mechanical behaviour of the rock mass under direct shear conditions. UDEC (discrete element method) has been chosen to model direct shear tests of partially fractured large samples because of its capability to handle samples that contain discontinuous blocks. UDEC is a 2D program that treats the model as being in plane strain, with an out-of-plane thickness of 1 unit. The geometry of the numerical model and its boundary conditions are based on calibrated models published by Szymkowski (2003). We consider two joint sets in a region of 400 mm × 300 mm (width × length)

as shown in Figure 2. The rock mass is confined within a shear box. Each of the joint sets in the numerical model originates at the left-hand end of the shear plane. The main algorithm, once calibrated against the laboratory tests, was adopted to secure allegiance of the numerical model and then applied to solve several numerical models that we generated with different block size and joint network within the blocks. The UDEC models were used to calculate shear and normal displacements and stresses under constant normal stiffness conditions (CNS).

UDEC requires the following inputs to generate joint sets: average and standard deviation of the angle between the horizontal plane and the first joint set; average and standard deviation of spacing for each joint set; average and standard deviation for each joint length; average and standard deviation for the gap that represents the rock bridge length in each joint set (Fig. 3).

The joint spacings analysed with the orthogonal array have dimensions equal to 1, 2, 3, 5, 7, 10 and 20 cm. The average angles between the horizontal plane and the first joint set are assumed to be 5°, 15°, 45°, 60° and 85° for the orthogonal array. The two joint sets are first assumed perpendicular to each other, which is representative of several joint geometries observed in the field. At the same time, we also investigated joint geometries with two non-orthogonal joint sets. The angles between

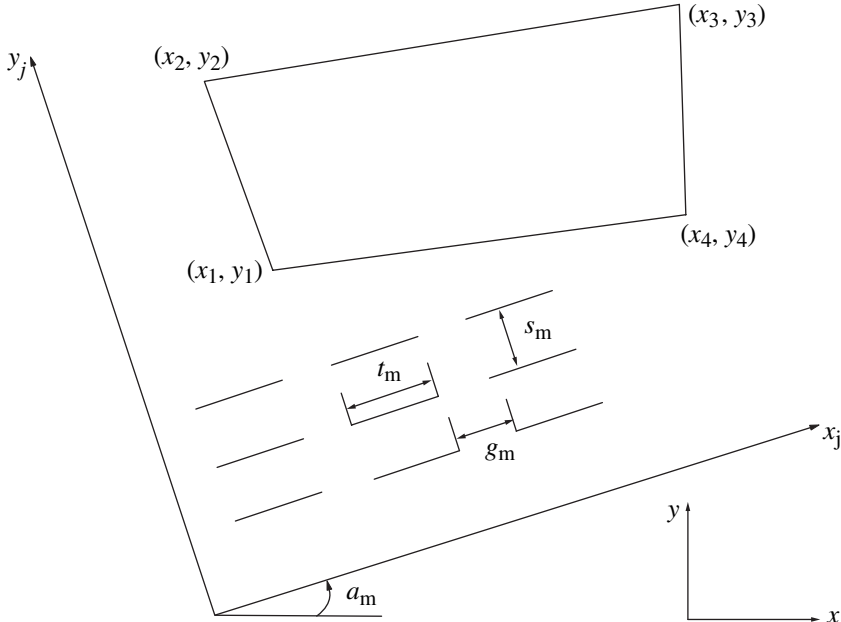


Fig. 3. Parameters used for generating joint sets in UDEC (Itasca 2004b).

the two joint sets are 30° , 45° , 60° , 75° , 90° , 105° , 120° , 135° and 150° . The results from our statistical analysis show that the gap proper of each joint sets has a negligible effect on the block area calculation if we do not consider the joint persistence. This result means that the persistence characteristics can be fully described by joint length alone. Consequently, joint average gaps can be discarded for the orthogonal array analysis. Following this consideration, for our simulation we selected six levels of factors for joint spacing, five levels of joint angle with respect to the horizontal plane, and three levels of joint length, resulting in a combination of 49 simulation cases in the orthogonal array as shown in Appendix 1.

The mechanical values for the intact rock and joint parameters adopted in our numerical model have been measured with standard laboratory tests carried out as part of the testing programme (Tables 2 and 3).

UDEC results

In engineering practice, the stability of a cavern or slope is controlled by the geometry of distinct rock blocks and by their interaction. The important concept that needs further explanation is the adoption of the distinct block system in design. Even though two models may have the same average joint orientation angles and spacing, the presence of rock bridges (modelled using non-persistent joint sets) totally changes the geometrical structure of the rock mass, and it can drastically increase the rock block size. The rock block sizes and shapes depend on the distribution variability of the input parameters.

Figure 4 presents one example, Case 10 in Appendix 1, showing the blocks generated by two persistent joint sets in two dimensions. Figure 5a presents the blocks delineated by two non-persistent joint sets whose average joint orientation angles and spacing are same as for Case 10

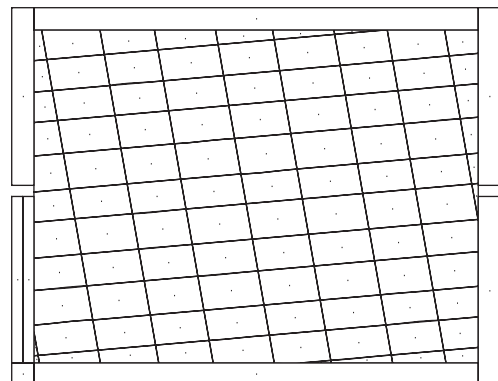


Fig. 4. Examples of the block system generated by two joint sets using UDEC.

shown in Figure 4. The standard deviations for the joint set orientations are 5° . As a result of the above procedure, some joints terminate in the intact rock, simulating rock bridges observed in rock masses. The block system shown in Figure 5b is generated by eliminating the incomplete joints (joints terminating inside intact rocks). Rock blocks show different sizes and shapes that are determined by the distributions of the variability of the input parameters. In this study, we have generated many block systems with different joint lengths according to the joint persistence characteristics.

The next step is the adoption of the distinct block system in rock engineering design. The deletion of the incomplete joints ignores fracture propagation near the joint tips. When only few joints are present in the rock mass, the effect of the rock bridge and the fracture propagation from the joint tips cannot be ignored. However, when there are many joints in the rock mass, as shown in Figure 5a, the distinct blocks shown in Figure 5b will dominate the behaviour of the rock

Table 2. Mechanical properties used in UDEC

Density	Bulk modulus	Shear modulus	Cohesion	Friction angle	Tensile strength	Dilation angle
2200 kg m^{-3}	265 MPa	160 MPa	1.0 MPa	37°	0.7 MPa	9°

Table 3. Joint properties used in UDEC

Normal stiffness	Shear stiffness	Cohesion	Friction angle	Tensile strength	Dilation angle
1000 MPa m^{-1}	100 MPa m^{-1}	0.0 MPa	27°	0.0 MPa	0°

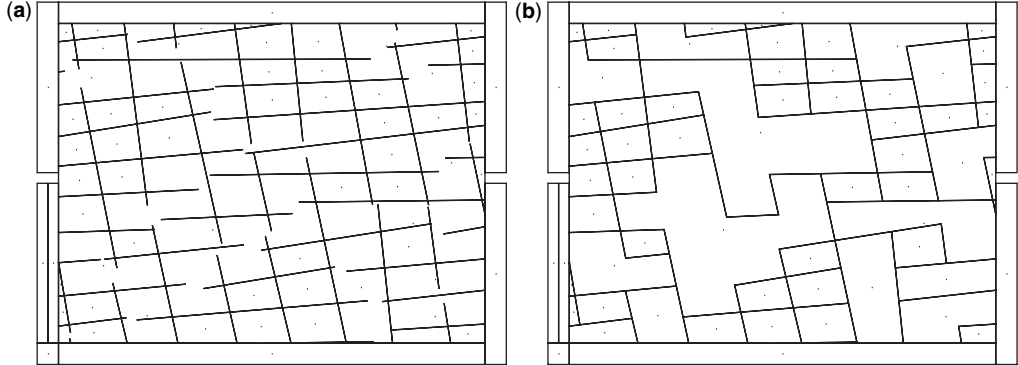


Fig. 5. Examples of block systems generated by two joint sets using UDEC.

masses when loaded because they provide the joint plane with macroscopic tensile strength. When the rock mass shown in Figure 5a is loaded, it will behave similarly to the rock mass shown in Figure 5b. With a degree of approximation, the contribution or influence from the isolated, incomplete joints, as they are called in UDEC, is negligible. For rock engineering application, this is sufficient in terms of defining the macroscopic strength and deformation parameters of a blocky to highly jointed rock masses.

The presence of rock bridges drastically influences the direct shear behaviour and results in an increased strength and ratio of strength development. Fully persistent joints allow the rock mass to deform principally along the joints, and only a few failures develop across the blocks. Consequently, the stress-strain curve is smooth and dominated

by the frictional law at the interfaces (see Fig. 6, blocks with persistent joints).

On the other hand, the presence of rock bridges (non-persistent joints) creates an imbricate structure that results in a stiffer and strong rock mass response. Under direct shear the system needs to break the asperities or block before any frictional behaviour is allowed or must dilate significantly. This results in higher strength of the rock mass and in a bi-linear stress-strain curve (see Fig. 6, blocks with non-persistent joints). The knee of the curve corresponds to the genesis of one continuous shear plane along which all the interlocking blocks that were present are failed. The higher strength of this system is due to the fact that more intact rock needs to fail before the system is free to move. As the presence of roughness locks the two walls of the joint and asperities need to fail (failure through intact rock) before the joint moves under shear or needs to dilate, similar to the behaviour of rock bridges at rock mass scale. They need to fail before any movement is allowed.

Figure 7 shows the regression analysis result of normalized block areas (horizontal axis) as a function of the corresponding calculated shear stress (vertical axis) for the case with non-persistent joints. In this paper we have chosen to normalize block areas and calculated shear strength with respect to the maximum value calculated in the modelling; that is, the normalized block area was calculated as

$$\frac{A}{A_{\max}}, \quad A = \frac{s_1 \times s_2}{\sin(a_1 + a_2)}. \quad (1)$$

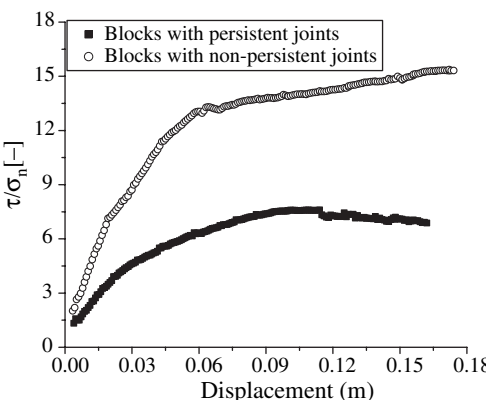


Fig. 6. Ratio of shear stress to normal load v. horizontal displacement for test result of blocks with persistent joints (■) and with non-persistent joints (○).

The correlation between normalized block size and normalized shear stress calculated from the UDEC

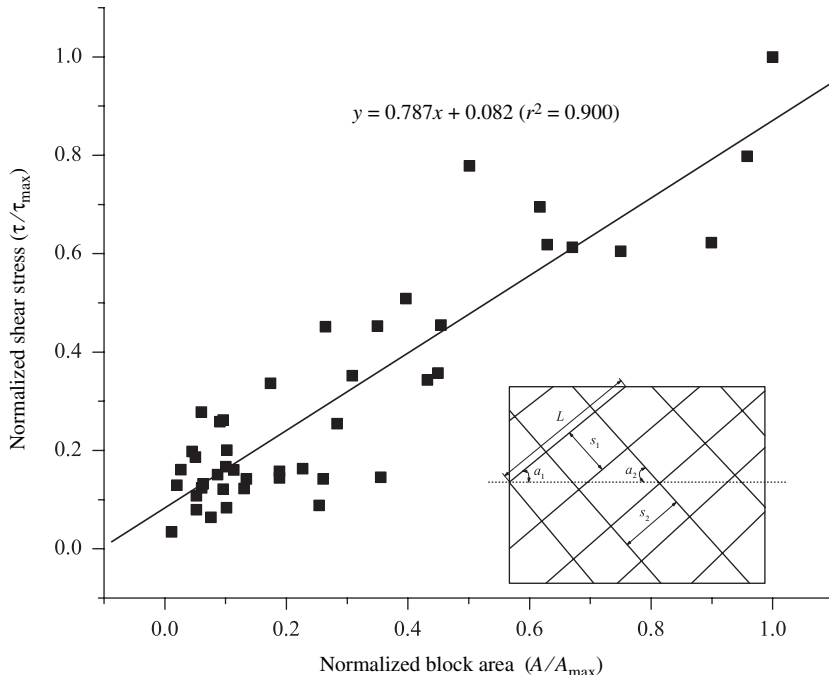


Fig. 7. Regression between normalized block size and calculated shear stress.

models results is equal to

$$y = 0.787x + 0.082 \quad (r^2 = 0.900). \quad (2)$$

It indicates that shear stress is generally directly proportional to block size; however, this correlation suggests that it is reasonable to suppose that the shear strength will be underestimated if joint persistence is not correctly accounted for.

With the aim of understanding how the variability of each geometric parameter affects the strength of a rock mass characterized by non-persistent joints, we have simulated, using UDEC, 49 different geometries, which have been created using the orthogonal array in Appendix 1.

Figure 8 shows how the adjusted persistence affects the strength of the rock mass. The adjusted persistence is the length of the joint projected on the shear plane and is expressed as

$$p_a = L \times \cos(a_1). \quad (3)$$

The stress ratio expresses the increment in strength as a result of the presence of interlocking, and it is defined as the ratio between the shear strength calculated with UDEC models with non-persistent

joint (τ) and the shear strength of the same model but with persistent joints (τ_0).

For every simulation the standard deviation of the angle between the two joint sets is 5° and all the standard deviations of joint spacing and length are 10% of the mean values. The ratio of shear strength is drastically decreased as persistence increases. This observation means that in practice, if persistence is not correctly accounted for, the mean block size and thus the strength of the rock mass would be underestimated.

Using SPSS (SPSS Inc. 2004) ANOVA was conducted to evaluate the influence of geometric characteristics of joints (i.e. joint spacing, angle between joint sets, and joint persistence) on the estimation of block size in UDEC simulation (see Table 4). The factor F is defined as the ratio of the mean square of treatment factor (sums of square errors for each treatment divided by the degree of freedom, which is the number of populations being tested minus one) and the mean square of error. The F value represents the contribution of each factor to the statistical significance of the calculation.

Results from statistical analysis show that the F value, in the case of fully persistent joints, is highest for normalized joint spacing (8.135), and

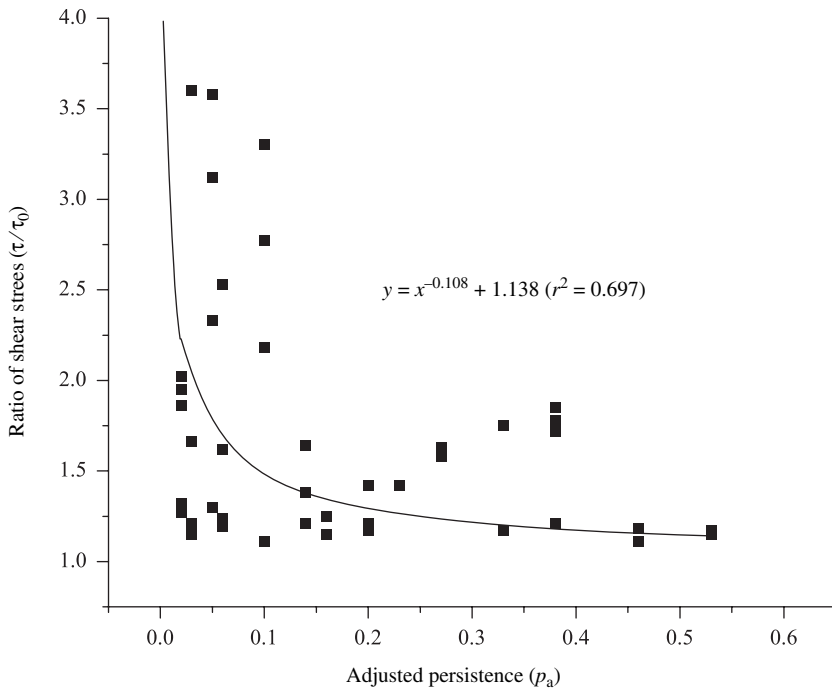


Fig. 8. Regression between adjusted persistence and ratio of shear stress.

lowest for the angle between joint sets (0.463). In the case of non-persistent joints the contribution of the persistence (10.022) is larger than those of spacing (5.749) and angle between joint sets (4.439). This means that persistence is ‘more important’ than joint spacing and the angle between joint sets when studying the mechanical behaviour of fractured rock masses. Therefore, as the contribution of joint persistence is greater than that of the spacing and the angle between joint sets,

the persistence characteristics should be considered very carefully when designing rock structures.

3D modelling for tunnel stability analysis

Rock blocks are 3D in nature. Based on the previous approach we have extended the analysis to the third dimension using 3DEC. With the help of the orthogonal arrays as shown in Appendix 2, several joint set models were generated to compare model

Table 4. Summary of the variance analysis results (UDEC)

Persistent			Non-persistent		
Source	F	Significance	Source	F	Significance
Spacing 1	10.427	0.000	Spacing 1	1.738	0.021
Spacing 2	8.032	0.000	Spacing 2	1.441	0.038
Angle 1	4.975	0.004	Angle 1	0.925	0.481
Angle 2	1.742	0.162	Angle 2	6.934	0.003
Length	n.a.	n.a.	Length	5.771	0.018
Normalized spacing	8.135	0.000	Normalized spacing	5.749	0.004
Normalized angle	0.463	0.000	Normalized angle	4.439	0.023
Persistence	n.a.	n.a.	Persistence	10.022	0.004

n.a., not applicable.

Table 5. Joint set characteristics

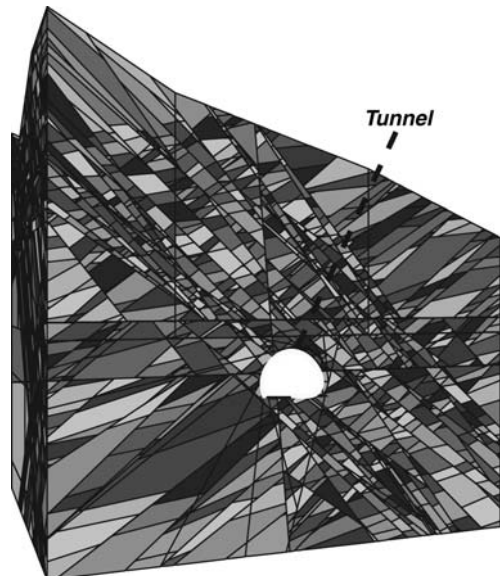
	Dip direction (deg.)	Dip angle (deg.)	Spacing (cm)
Joint Set 1	083	44	60
Joint Set 2	326	53	100
Joint Set 3	189	55	100

deformations for various geometries. As the UDEC models showed that persistence is the most influential parameter with respect to strength and deformation for the rock mass, this 3D analysis focuses only on how the presence of rock bridges formed by different length of joint influence the stability of an excavation. The main purpose of the modelling is to establish how joint persistence influences the overall behaviour of a tunnel and assess its importance when designing an underground rock structure.

Data from one road tunnel under construction in Korea were used in this analysis. The tunnel is located in the western part of South Korea and is constructed through mainly Mesozoic volcanic rocks and alkali feldspar granite. The alkali feldspar granite is the main rock type in the tunnel section analysed here, and it is characterized by the presence of three joint sets (Table 5).

Average persistences of joint sets measured in the field are all less than 0.5; however, they were all fixed to 0.5 to simplify the computational effort of 3D modelling used during the tunnel design phase. Rock mass quality (rating) ranged from poor (RMR 30) to fair (RMR 45).

The 3DEC model is 60 m wide, 50 m high and 80 m long, and all joints have persistence equal to 0.5 (Fig. 9). For the numerical calculation we applied displacement boundary conditions and initial isotropic stress state ($k = 1$) equal to $\sigma = 0.37$ MPa. Furthermore, no support system was installed during excavation to investigate the rock mass displacement around the tunnel.

**Fig. 9.** Layout of 3DEC model for parametric analysis.

Mechanical rock properties and joint properties for the analysis are listed in Tables 6 and 7.

3DEC results

Figure 10 presents different block volumes that were generated using the orthogonal arrays (see Appendix 2). Simulation 0 shows the block geometry adopted during the design of tunnel that considers all three sets of joint with persistence equal to 0.5. This hypothesis results in an average block volume of 2.61 m^3 . However, by simply accounting for the variability of joint persistence, several other scenarios where the calculated average block volume is greater than that used for tunnel design (simulation 0) were generated. For example, the block size of simulation 9 is five times larger than that of simulation 0.

Table 6. Mechanical properties used in 3DEC

Density	Bulk modulus	Shear modulus	Cohesion	Friction angle	Tensile strength	Dilation angle
2650 kg m^{-3}	7.0 GPa	2.8 GPa	32 MPa	40°	16 MPa	5°

Table 7. Joint properties used in 3DEC

Normal stiffness	Shear stiffness	Cohesion	Friction angle	Tensile strength	Dilation angle
1000 MPa m^{-1}	100 MPa m^{-1}	0.0 MPa	37°	0.0 MPa	3°

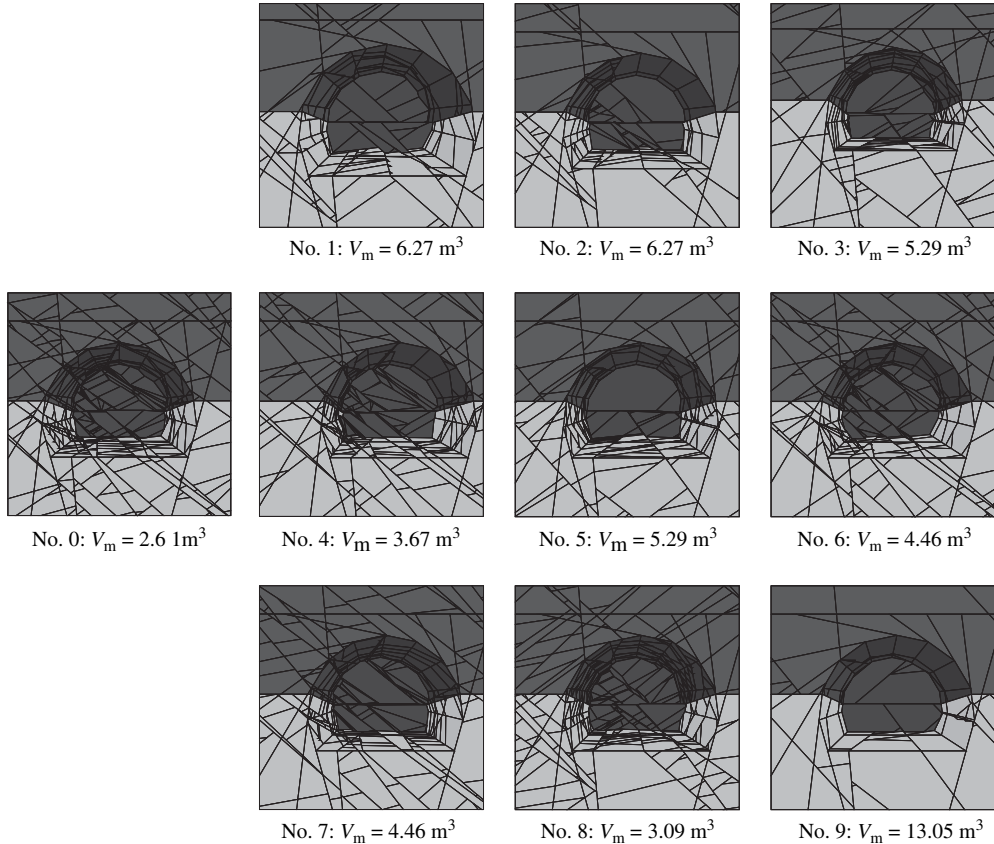


Fig. 10. Scenarios of block geometries generated using the orthogonal array in Appendix 2.

To better evaluate how persistence and, consequently, the calculated average block volume influence tunnel deformations, ANOVA was conducted to assess the effect of joint persistence on the calculated displacements at the crown (settlement S) and at the wall (convergence C) of the tunnel. Table 8 presents the result of the ANOVA.

According to the statistical analysis, the F value, which represents the contribution of persistence to each displacement, is much greater for the settlement (43.792) than for the convergence (7.215). This means that the influence of persistence affects settlement more than wall convergence for the gravitational failure of a rock tunnel in the rock mass.

Figure 11 presents the relationship between the normalized displacement and the combined joint persistence factor:

$$\frac{S}{S_{\max}} = 0.044 \exp\left(\frac{p_f}{0.157}\right) \quad (r^2 = 0.962) \quad (5)$$

where the average displacements at the roof and the walls obtained from our 3DEC simulations are normalized with respect to the maximum value calculated for each case, and the combined joint persistence factor, p_f , is defined as $p_f = \sqrt[3]{p_1 p_2 p_3}$.

When the persistence factor is smaller than 0.25, the normalized displacements are relatively small.

Table 8. Summary of the variance analysis results (3DEC)

Source	Dependence	Sum of square	Degree of freedom	Square of average	F	Significance
Persistence factor	Settlement	5.387E - 02	7	7.695E - 03	43.792	0.005
	Convergence	1.994E - 02	7	2.848E - 03	7.215	0.036

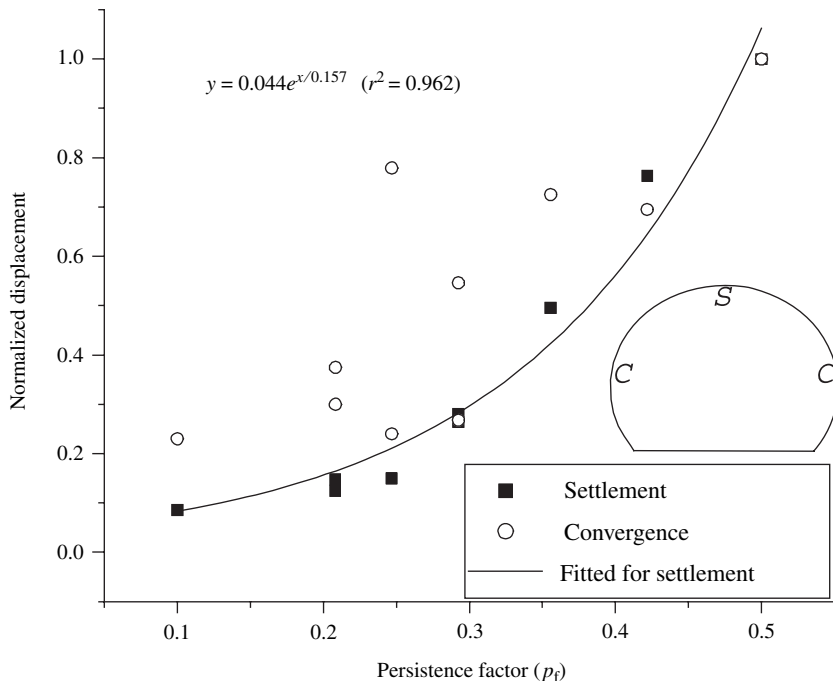


Fig. 11. Regression between persistence factor and normalized displacement of the tunnel (S, position of measured roof settlement; C, position of measured wall convergence).

Conclusions

Distinct element numerical codes (UDEC and 3DEC) were used to study the mechanical behaviour of a fractured rock mass (block system) characterized by the presence of several joint sets with varying persistence. The objective was to statistically analyse how joint persistence affects the mechanical response of the fractured rock mass.

With the aid of the experimental design statistical tool, block systems with various joint persistence factors, spacing and orientation have been generated. Orthogonal arrays using this experimental design approach have been adopted with the aim of reducing simulation effort, allowing an optimal selection for the combinations of input parameters that determine the geometry of a fractured rock mass. The numerical results have been statistically analysed using the analysis of variance (ANOVA) method. ANOVA results show that the F value for joint persistence, which represents the contribution of persistence to the statistical significance of the mechanical behaviour of the rock mass, is much

higher than those for other geometric characteristics of the joint such as spacing and angle between joint sets. This result strongly suggests that joint persistence is one of the most important parameters to be considered for engineering design of a rock structure.

The analysis of a tunnel under excavation in South Korea shows that the effect of persistence is much more important for crown settlement than for wall convergence (up to six times larger). Another important observation is that for a persistence factor <0.3 , the displacement at the tunnel face decreases drastically. It is also reasonable to suppose that by using the correct input value for the persistence, blocky rock mass could be turned into massive rock in extreme circumstance.

The results of this preliminary study suggest that joint persistence is one of the most important parameters to be considered for an accurate characterization of rock mass strength and thus should be carefully taken into account for a safe and economic design of underground rock structures.

Appendix 1

Orthogonal array for the input parameters for block system generation using UDEC

No.	a_1 (deg)	a_2 (deg)	L (cm)	s_1 (cm)	s_2 (cm)	No.	a_1 (deg)	a_2 (deg)	L (cm)	s_1 (cm)	s_2 (cm)
1	5	-5	29.4	5	3	26	5	-85	12.6	0	10
2	85	-15	21.0	5	7	27	15	-60	29.4	1	5
3	5	-15	12.6	2	5	28	15	-5	21.0	2	2
4	60	-60	12.6	3	2	29	5	-45	21.0	10	1
5	5	-45	12.6	3	3	30	5	-85	29.4	7	1
6	60	-15	29.4	10	10	31	15	-85	21.0	3	10
7	60	-60	21.0	1	5	32	5	-60	12.6	2	7
8	45	-60	29.4	3	7	33	45	-5	12.6	1	1
9	5	-15	29.4	7	2	34	15	-85	12.6	7	7
10	5	-85	12.6	3	5	35	15	-60	21.0	5	10
11	5	-60	21.0	1	10	36	45	-85	29.4	5	5
12	5	-60	29.4	10	10	37	15	-45	12.6	5	10
13	5	-5	21.0	1	7	38	15	-45	29.4	1	2
14	85	-60	12.6	1	1	39	15	-15	12.6	1	3
15	5	-60	12.6	5	2	40	85	-45	21.0	7	5
16	60	-5	12.6	7	10	41	85	-60	12.6	10	3
17	60	-85	21.0	2	3	42	45	-15	12.6	1	10
18	45	-85	21.0	10	2	43	45	-60	21.0	7	3
19	15	-15	21.0	3	1	44	15	-60	12.6	7	10
20	45	-45	12.6	2	10	45	85	-5	29.4	3	10
21	85	-85	19.4	2	10	46	15	-85	29.4	1	3
22	60	-85	12.6	5	1	47	60	-45	29.4	1	7
23	85	-85	12.6	1	2	48	5	-85	21.0	1	10
24	15	-85	12.6	10	7	49	15	-60	29.4	2	1
25	15	-5	12.6	10	5	-	-	-	-	-	-

a_1a_2 , joint inclination angle relative to x -axis, positive anticlockwise; L , joint length; s , joint spacing.

Appendix 2

Orthogonal array for the input persistence for block system generation using 3DEC

No.	p_1	p_2	p_3
0	0.5	0.5	0.5
1	0.3	0.3	0.1
2	0.3	0.1	0.3
3	0.1	0.3	0.5
4	0.5	0.3	0.3
5	0.1	0.5	0.3
6	0.5	0.5	0.1
7	0.5	0.1	0.5
8	0.3	0.5	0.5
9	0.1	0.1	0.1

References

- BRADY, B. H. G. & BROWN, E. T. 1992. *Rock Mechanics for Underground Mining*. Chapman & Hall, London.
- CAI, M., KAISER, P. K., UNO, H., TASAKA, Y. & MINAMI, M. 2004. Estimation of rock mass strength and deformation modulus of jointed hard rock masses using the GSI system. *International Journal of Rock Mechanics & Mining Sciences*, **41**, 3–19.
- DERSHOWITZ, W. S. & EINSTEIN, H. H. 1988. Characterizing rock joint geometry with joint system models. *Rock Mechanics & Rock Engineering*, **21**, 21–51.
- DEVORE, J. L. 2000. *Probability and Statistics for Engineering and Sciences*. Thomson Learning, Duxbury.
- DIEDERICHS, M. S. & KAISER, P. K. 1999. Tensile strength and abutment relaxation as failure control mechanisms in underground excavations. *International Journal of Rock Mechanics & Mining Sciences & Geomechanics Abstracts*, **36**, 69–96.
- EINSTEIN, H. H., VENEZIANO, D., BAECHER, G. & O'REILLY, K. 1983. The effect of discontinuity persistence on rock slope stability. *International Journal of Rock Mechanics & Mining Sciences & Geomechanics Abstracts*, **20**, 227–236.
- ITASCA 2004a. 3DEC, Version 3.0. Itasca Consulting Group Inc. Itasca, Minneapolis, MN.
- ITASCA 2004b. UDEC—Universal Distinct Element Code, Version 4.0. Itasca Consulting Group Inc. Itasca, Minneapolis, MN.
- KEMENY, J. M. 2003. The time-dependent reduction of sliding cohesion due to rock bridges along discontinuities: a fracture mechanics approach. *Rock Mechanics & Rock Engineering*, **36**, 27–38.
- KEMENY, J. M. 2005. Time-dependent drift degradation due to the progressive failure of rock bridges along discontinuities. *International Journal of Rock Mechanics & Mining Sciences*, **42**, 35–46.
- KEMENY, J. M. & COOK, N. G. W. 1986. Effective moduli, non-linear deformation and strength of cracked elastic solid. *International Journal of Rock Mechanics & Mining Sciences & Geomechanics Abstracts*, **23**, 107–118.
- KIM, B. H. 2002. *Revaluation of rock mass classification using multivariate analysis and estimation of the support on tunnel*. PhD thesis, Chonnam National University, Gwangju.
- MENDENHALL, W. & SINCICH, T. 1995. *Statistics for Engineering and Sciences*. Prentice-Hall, Englewood Cliffs, NJ.
- NICHOL, S. L., HUNGR, O. & EVANS, S. G. 2002. Large-scale brittle and ductile toppling of rock slopes. *Canadian Geotechnical Journal*, **39**, 773–788.
- REYES, O. & EINSTEIN, H. 1991. Failure mechanisms of fractured rock—a fracture coalescence model. In: WITTKE, W. (ed.) *Proceedings of the 7th ISRM, Aachen, Germany*, 333–339.
- SHEN, B., STEPHANSSON, O., EINSTEIN, H. & GHAHREMAN, B. 1995. Coalescence of fracture under shear stresses in experiments. *Journal of Geophysical Research*, **100**, 5975–5990.
- SJÖBERG, J. 1996. *Large scale slope stability in open pit mining—a review*. Technical Report, Lulea University of Technology, Division of Rock Mechanics.
- SPSS Inc. 2004. SPSS 12.0KOR for Windows. SPSS, Chicago, IL.
- SZYMAKOWSKI, J. 2003. *Direct shear test of jointed soft rock masses*. PhD thesis, Monash University, Clayton, Vic.

Using physical properties to understand the porosity network geometry evolution in gradually altered granites in damage zones

M. ROSENER & Y. GÉRAUD

IPGS UMR7516 EOST, 1 rue Blessig, 67084 Strasbourg cedex, France

(e-mail: mrosener@illite.u-strasbg.fr)

Abstract: This study, based on petrophysics, is linked to the geothermal project developed at Soultz-sous-Forêts, in northeastern France. In such a context, understanding and modelling the thermo-hydro-mechanical and chemical processes implies a good knowledge of the porosity network geometry and its evolution during alteration. Various physical properties (permeability, specific surface and porosity) were measured on samples from the protolith and damage zones of fault zones in the geothermal reservoir exploited at Soultz-sous-Forêts. Measured porosity values vary from 0.2 to 10%, and using structural parameters (threshold values, specific surface and porosity distribution), three groups are identified. Each of them shows a specific pore shape distribution and the porosity increase within a given group is assumed to be associated with an increase of pore number rather than an enlargement or shape modification.

It is now well accepted that the fault zone architecture follows the Caine *et al.* (1996) and Sibson (2003) models, with a highly cataclasized core zone surrounded by a damage zone and finally the non-affected protolith (Fig. 1). Fluid flow generated in such a system implies thermo-hydro-mechanical and chemical interactions, and these processes are controlled by external factors such as temperature (Lasaga 1984; Hellmann 1994; Baldeyrou *et al.* 2003), stress (Heuze 1983; Auradou *et al.* 2003, 2005; Berard & Cornet 2003) and fluid chemistry (Aquilina *et al.* 1997; Komninou & Yardley 1997), and by internal factors such as structure (Norton & Knapp 1977; Sausse *et al.* 2001; Sausse 2002; Cornet *et al.* 2003) and mineralogy of the rock (Komninou & Yardley 1997; Sausse *et al.* 1998).

All these interactions take place in the pore space, giving the porosity network geometry (i.e. the volume delimited by pores, throats, and their relative layout and connections) a non-negligible impact on transport and exchange processes. With that in mind, our attention turns to the matrix of the damage zone (see Fig. 1), where surrounding fractures and fluid flow generate alteration with a particular porous network, dominated by transport and reaction, and make the storage capacity and specific surface higher than in any other part of the fault zone (Aharonov *et al.* 1997; Sibson 2003).

Many from these fault zones and damage zones were identified in the granites from the EPS1 borehole, Soultz-sous-Forêts, France (Dezayes *et al.* 1995; Genter *et al.* 1995; Genter & Trainau 1996). Samples were cored in the matrix of different damage zones and in the protolith, and showed four alteration facies. The aim of this

study is to understand how the porosity network developed in the matrix evolves during alteration. To obtain this information, three physical properties were measured: permeability, specific surface and porosity. Several studies were performed on these three properties, to try to find a relation between them (Wienand & Huenges 1989), or to model one of them on the basis of the other two (Salem & Chilingarian 1999; Fischer & Gaupp 2004). In this paper, samples were sorted by porosity network geometry (i.e. mercury porosimetry results), then the other two properties were compared with their corresponding porosity values. The results show a particular behaviour within each group during alteration: increase of porosity can be explained by an increase of pore population, and the geometry of the new voids seems to be constant during the porosity development.

Techniques

Permeability measurement

Based on Fick's law and Darcy's theory linking pressure gradient and fluid flow through a permeable medium, permeability measurements were made using a gas permeameter (Klinkenberg 1941; Guéguen & Palciauskas 1992). The system operates with nitrogen and a 4 MPa confining pressure is applied on the samples. Then for different constant head pressures (maximum 3.5 MPa), and if the steady-state condition is reached, gas flow and pressures from both sides of the sample are measured. Finally, measurements are corrected for the Klinkenberg effect (Klinkenberg 1941) and

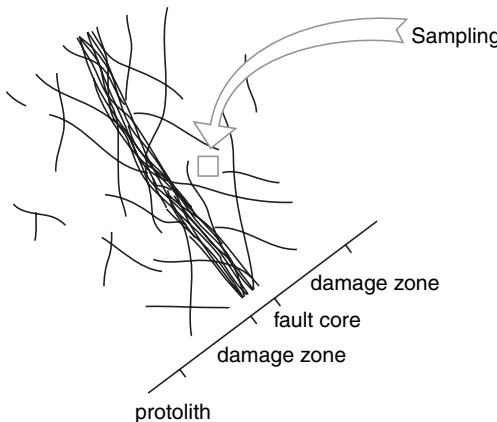


Fig. 1. The Caine *et al.* (1996) model of a fault zone.

the true permeability value is calculated (see also Scheidegger 1974; Debschütz *et al.* 1989).

Specific surface measurement

The method used for specific surface measurements is the BET (Brunnauer–Emmett–Teller) method (Brunnauer *et al.* 1938). At low temperature and low pressure, gas is adsorbed on the porosity network surface. By measuring the quantity of gas adsorbed at different pressures, it is possible to estimate the specific surface of the sample. Except for one sample with a very low specific surface, which required krypton, all the measurements were made using nitrogen (see also Gregg & Sing 1982).

Porosity measurement

Porosity measurement and porous network characterization were made using mercury injection (Guéguen & Palciauskas 1992). This method is based on the proposal by Washburn (1921), on the basis of the Young–Laplace equation for the displacement of a non-wetting fluid in a thin capillary tube, which gives the relationship between fluid pressure and throat size:

$$r = (-2\gamma \cos \theta)/p \quad (1)$$

where r is the radius of the capillary tube (Waschburn 1921), or the distance of the pore walls in slit-shaped pore (Lenormand *et al.* 1983), γ is the surfacial tension ($485 \times 10^{-3} \text{ N m}^{-1}$), θ is the contact angle between the non-wetting fluid, the wetting fluid and the solid (130°), and p is the capillary pressure applied on the liquid.

Generally, the results of this mercury injection test are presented as curves of injected volume v. capillary pressure (or the equivalent throat radius). These curves are known to be highly reproducible for a given material and differ widely between samples with different pore structures (van Brakel 1975; Wardlaw & Taylor 1976; Kloubek 1994).

As a result of large differences between pore and throat radius, it is possible that a part of the mercury remains in the sample when the capillary pressure is released to atmospheric pressure (Wardlaw & McKellar 1981; Li & Wardlaw 1986a, b). Therefore, the measurement involves three steps: (1) the pressure is increased to the maximum (300 MPa); (2) it returns to atmospheric pressure; (3) it is finally increased to the maximum again (Fig. 2a). The curve obtained at the first step gives the access to the total connected volume, and the maximum value is assumed to be the total connected porosity (Fig. 2b, continuous line). The volume that remains in the sample at the end of the second step is called the trapped porosity and is related to the heterogeneity of the network geometry (Li & Wardlaw 1986a, b; Wardlaw *et al.* 1987). During the last step, because the trapped porosity is still filled by mercury, the injection occurs only in the so-called free porosity, and the injection profile obtained shows the access to it only (Fig. 2b, bold line). Finally, looking at the difference between the total connected volume curve and the free porosity curve, it is possible to calculate the access to the trapped porosity (Fig. 2b, dashed line). From both free and trapped porosity cumulative curves, the corresponding incremental curves are deduced (Fig. 2c).

Petrography and sample location

Known as the European heat mining project, the Soultz-sous-Forêts geothermal exchanger was developed in deep hot fractured granites (at 5 km depth and 200°C) (Baria & Baumgärtner 1999). During the 1980s, this place was chosen because of a positive thermal anomaly linked to the graben's history (Villemin & Bergerat 1987; Le Carlier *et al.* 1994), and the EPS1 borehole, from which the samples come, was cored.

The thermal exchanger is based on a system of three wells. Fluid flow between the injection well and the two production wells is possible because of the inherited structure of the system, which is composed of many interconnected normal fault zones (Dezayes *et al.* 1995; Genter *et al.* 1995; Genter & Trainneau 1996; Gérard *et al.* 1998).

Circulation tests made in recent years showed a delay in the arrival time of the tracer and a high

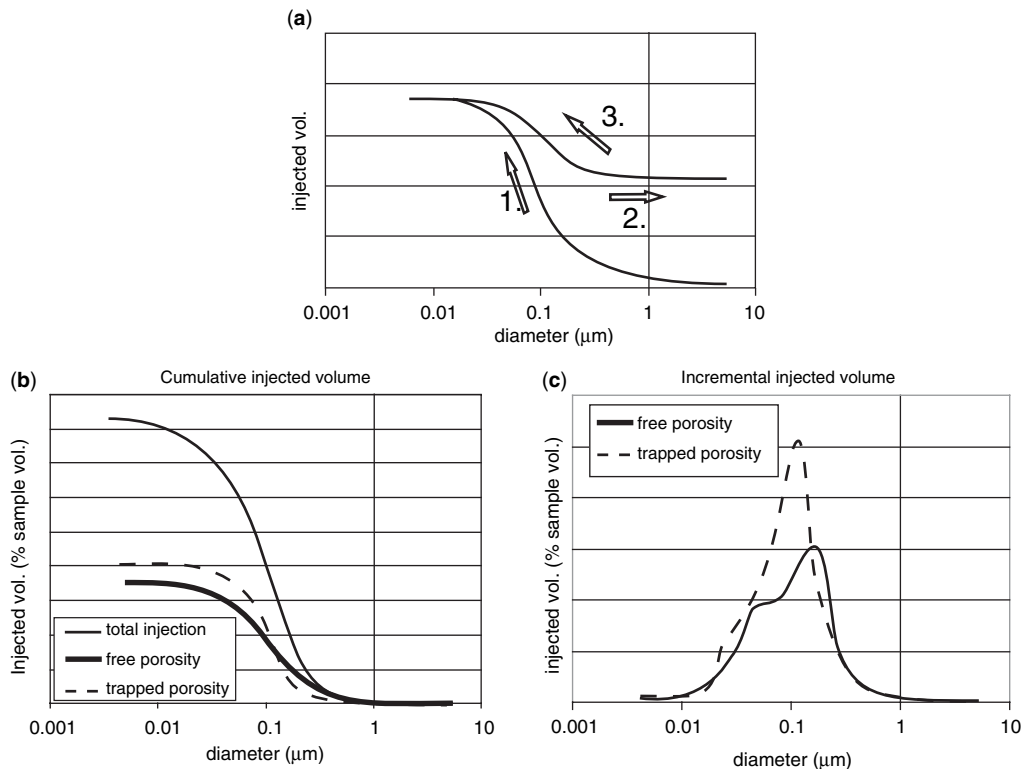


Fig. 2. Mercury porosimetry: (a) example of a mercury injection procedure; (b) mercury injection curve, with free and trapped porosity curves; (c) incremental injection curves.

dilution of the tracer (Gérard *et al.* 1998). These two observations can be explained by the complexity of the route taken by the fluid and the extent of the fault and fracture system; another explanation could be related to the effect of the damage zone. Width, porosity and surface reaction of this part

of the fault zone make it non-negligible in terms of storage and fluid circulation.

With that in mind, a total of 20 cylindrical samples (18 mm diameter and 15 mm length) were cored, parallel to the borehole axis, in the protolith and in different gradually altered matrices in

Table 1. Granite petrography, structure and alteration phases

Facies	Primary mineralogy	Structure	Alteration phases
Fresh granite			
Pervasive alteration		Microfractured	
Vein alteration with illite	Porphyritic granite with orthoclase phenocrysts (1–7 cm), quartz, plagioclase, biotite, chlorite and some hornblende		Some chloritized biotite Plagioclase and biotite are replaced by clays and carbonate; chlorite by illite
Vein alteration with hematite		Fractured to cataclasized	Plagioclase and biotite are replaced by clays and carbonate; chlorite by illite; high hematite concentration

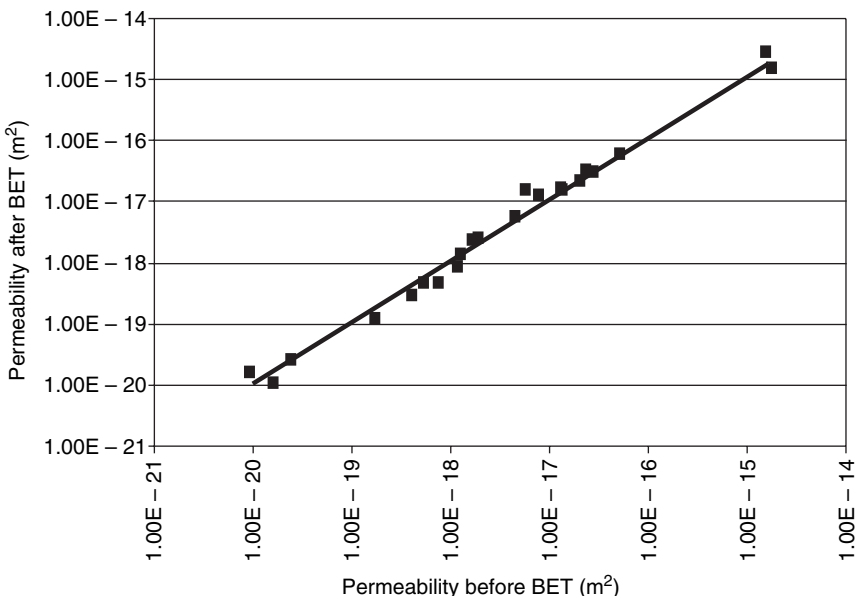
Table 2. Sample list, facies and measurement results

	Sample number	Depth (m)	Alteration facies	Permeability (m^2)	Specific surface ($\text{m}^2 \text{m}^{-3}$)	Porosity (%)
K79-2128	1	1455	Pervasive alteration	1.75E - 19	4.33E + 06	2.91
	2			9.18E - 21	5.07E + 06	3.33
K102	3	1602	Fresh granite	5.87E - 18	5.91E + 04	0.14
	4		Vein alteration with illite	n.a.	5.88E + 05	1.14
K108-2758	5	1631		4.57E - 18	1.84E + 06	1.59
	6			1.28E - 18	3.47E + 06	1.97
	7		Vein alteration with hematite	n.a.	7.41E + 06	3.93
K109-2795	8	1641		1.58E - 15	1.50E + 06	1.15
	9			2.08E - 17	3.52E + 06	0.81
	10		Fresh granite	1.82E - 15	1.65E + 06	0.27
K117-2900	11	1671	Fresh granite	2.36E - 17	1.70E + 06	0.22
K138-3318	12	1807	Low pervasive alteration	1.20E - 18	2.51E + 06	1.82
	13			1.32E - 17	2.90E + 05	0.82
K150-3645	14	1906	Low pervasive alteration	2.44E - 20	2.00E + 06	0.35
K177-4329	15	2053	Fault sealing (quartz + illite)	1.63E - 20	1.49E + 06	1.75
K193	16	2152	High pervasive alteration	7.37E - 18	4.26E + 06	3.92
	17			1.70E - 18	5.74E + 06	5.07
K195-4774	18	2161	High pervasive alteration	1.44E - 18	7.07E + 06	8.62
	19			7.59E - 19	1.01E + 07	7.83
	20			5.38E - 19	8.46E + 06	9.87

n.a., not applicable.

damage zones, showing four different facies. For each one, primary mineralogy, structures and alteration phases were described by Trainneau *et al.* (1991) and Genter & Trainneau (1992), and are summarized in Table 1. To obtain mercury porosimetry results as

representative as possible and limit the impact of local variations in porosity and mineralogy, it was attempted to core the samples in agreement with the rock mineralogical proportions. Permeability measurements were not possible on samples 6 and

**Fig. 3.** The limited impact of BET technique on permeability measurement.

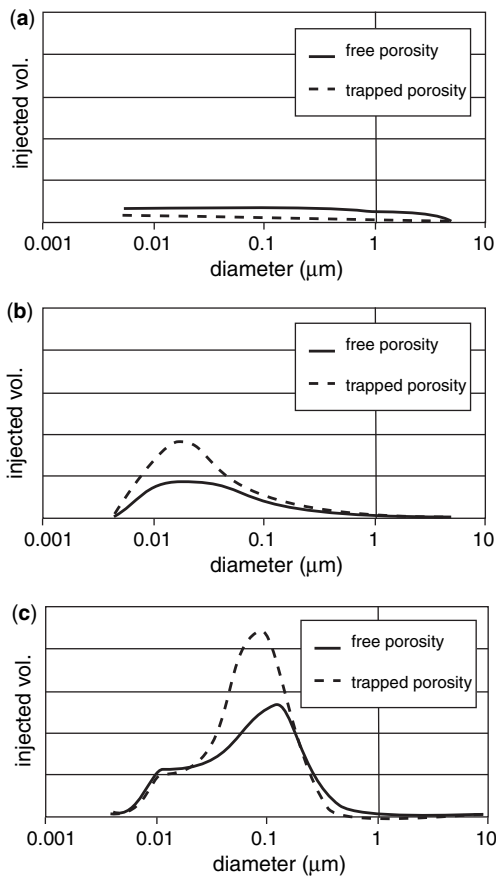


Fig. 4. Sample grouping based on the shape of the incremental injection curves: (a) group 1; (b) group 2; (c) group 3. Only the total shape of the curve is necessary to determine the group, and because porosity values vary within a given group, there is no vertical scale in the graphs (see text).

9 because their shapes were not totally cylindrical. Except these two samples, permeability, specific surface and porosity measurements were performed on all the samples. Results and alteration facies are summarized in Table 2.

Results

According to Brace (1980), granite permeability varies between 5×10^{-17} and 10^{-21} m^2 . In this study, measurements gave results over five orders of magnitude, from 1.57×10^{-15} to $1.56 \times 10^{-20} \text{ m}^2$, with the highest values attributed to fractured samples. The BET method showed specific surfaces between 5.91×10^4 and $1.01 \times 10^7 \text{ m}^2 \text{ m}^{-3}$. Porosity values varied from 0.13 to 9.87% (see Table 2).

During the specific surface measurement, the sample temperature decreases to the liquid nitrogen temperature (-196°C). To ensure that such a thermal shock has a limited effect on the porosity network geometry, two permeability measurements were made, one before and one after the specific surface measurement. Figure 3, which shows the permeability before specific surface measurement v. the permeability after specific surface measurement, shows that the BET technique has no major effect on the porosity network geometry; therefore the specific surface can directly be compared with the porosity.

Because this study is focused on the porosity network geometry and its evolution with increasing alteration, porosimetry results have a non-negligible weight. Looking at the incremental injection curves and particularly their general shape, it is possible to distinguish three groups.

Group 1

Samples 3, 10, 11 and 14 have similar injection curves. Porosity varies between 0.13 and 0.35%, and specific surface from 5.91×10^4 to $2.00 \times 10^6 \text{ m}^2 \text{ m}^{-3}$. Permeability ranges from 2.57×10^{-20} to $1.82 \times 10^{-15} \text{ m}^2$. Mercury injection tests show a porosity network geometry with no trapped porosity; all the porosity is assumed to be free (Fig. 4a).

Group 2

Porosity of samples 4–9, 12, 13 and 15 shows the same geometric properties and varies between 0.8 and 3.93%. Specific surface values vary from 3.52×10^5 to $7.41 \times 10^6 \text{ m}^2 \text{ m}^{-3}$, and permeability ranges from 1.63×10^{-20} to $1.57 \times 10^{-15} \text{ m}^2$. With mercury injection tests, it is possible to see that free porosity is still accessible through small diameters (between 0.07 and 0.006 μm), and that trapped porosity with the same thresholds is present too (Fig. 4b).

Group 3

Samples 1, 2 and 16–20 show the widest porosity range: from 2.91 to 9.87%. Specific surface measurement shows values from 4.26×10^6 to $1.01 \times 10^7 \text{ m}^2 \text{ m}^{-3}$, and permeability ranges from 1.56×10^{-20} to $7.37 \times 10^{-18} \text{ m}^2$. Mercury injection tests show a high volume of trapped porosity with access diameter between 0.3 and 0.03 μm, and a smaller volume controlled by access diameter between 0.03 and 0.006 μm. Free porosity is accessible through diameters between 0.3 and 0.006 μm, with a maximum of injection for access diameter around 0.15 μm (Fig. 4c).

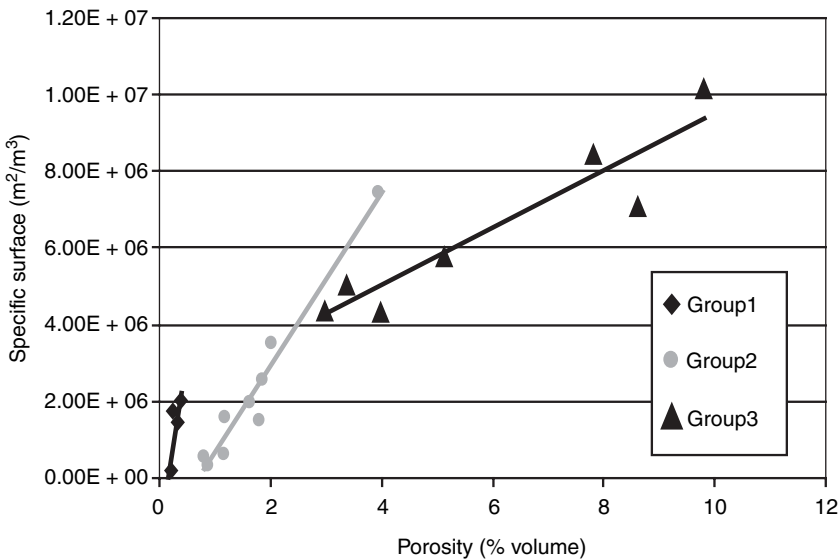


Fig. 5. Specific surface v. porosity: each group shows a specific linear relation, linked to the mean void shape (see text).

Discussion

The groups are based on samples presenting similar free porosity and trapped porosity injection curves. Samples of a single group have different porosity values but identical geometric properties (access diameter to the free and trapped porosity, relative volume distribution). Increase of porosity in a given group is associated with the development of porous volume without changes in the threshold values.

Figure 5 shows the relationship between specific surface (S) and porosity (V) for each sample. Looking at the three groups, it is possible to distinguish three linear relations (i.e. $\Delta S/\Delta V = \text{constant}$), with 9.87×10^8 , 2.29×10^8 and 7.41×10^7 slopes corresponding respectively to group 1, group 2 and group 3, and with correlation coefficient between 0.90 and 0.97. Therefore, in each group, the increase of porosity follows a geometric plan that makes the mean S/V ratio stay the same for each new-formed porous volume.

For agreement with these two observations, the porosity development within a given group must be explained by an increase of pore population rather than an increase of pore radius.

More information on transport properties and their evolution with alteration can be deduced from the permeability–porosity relation (Fig. 6). Because of low ranges of porosity, groups 1 and 2 show no particular trends, but samples from group

3 seem to show a remarkable behaviour (see Fig. 6, continuous line): the lowest permeability values correspond to the lowest porosity ones, and as a first step, porosity network development implies a high increase of connectivity, and therefore of permeability. Then, as the porosity increase continues, the porosity network geometry becomes more complex and the permeability decreases progressively because of tortuosity.

In a general way, except for samples 8 and 10, which are fractured, the maximum value of permeability decreases with the porosity increase (see Fig. 6, dashed line). Also, because mercury porosimetry shows a general increase of pore threshold from group 1 to group 3, this behaviour indicates the influence of tortuosity on the medium transport properties.

With that in mind, the following model of matrix porosity evolution during alteration can be proposed (see Fig. 7). During alteration, creation of new pores and dissolution imply that the porosity volume increases. At the same time, secondary mineral precipitations (especially clays) cover the surface of pores, progressively isolating primary minerals from the fluid. Finally, dissolution–precipitation stops, because it becomes easier for this phenomenon to operate on new sites. The final pore geometry will be an equilibrium between the mineralogical characteristics of primary minerals and secondary minerals (i.e. looking at all the pore population, statistically,

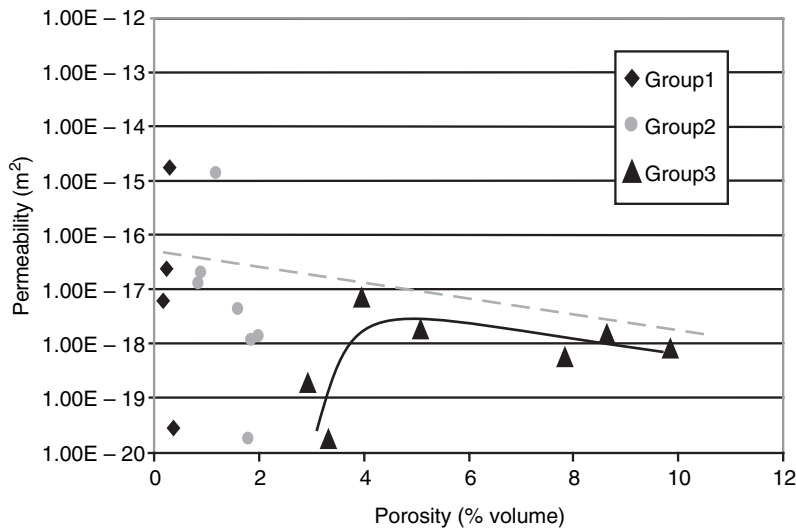


Fig. 6. Permeability v. porosity (see text).

$\Delta S/\Delta V = \text{constant}$). This kind of porosity development can also be related to the permeability behaviour, with an increase first of connectivity and then of tortuosity.

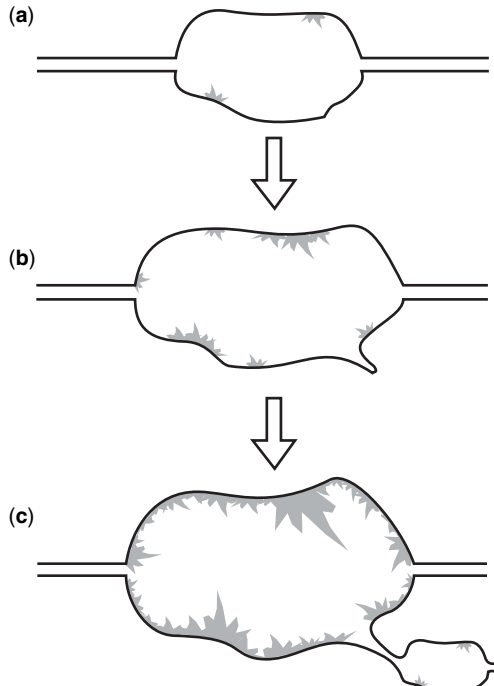


Fig. 7. Porosity development model at the pore scale.

A control of this assumption is obtained from SEM images of three samples of group 3, which show an increasing porosity (Fig. 8). New voids are principally created in plagioclase, but also, to a smaller extent, in the K-feldspar or at mineral borders. The images are at the same magnification; pore shape and pore threshold sizes remain the same, but the pore population is increasing, associated with the pore volume.

Because the S/V ratio (i.e. slope value) decreases progressively from group 1 to group 3 (see Fig. 5), possible relations between them must be considered. The S/V ratio depends partly on the void's shape: planar structures such as cracks imply a high surface development for small volumes (i.e. a high slope), whereas spherical structures offer the minimum S/V ratio (i.e. a low slope). But above all, it is inversely proportional to the mean pore radius (\neq pore threshold measured by mercury porosimetry). So in Figure 5, the decrease of slope values underlines an increase of the mean pore radius, including probably shape variations. Nevertheless, it is not certain that these groups form three steps of the same alteration process. In fact, if low-porosity samples from group 3 are compared with high-porosity samples from group 2, they show higher porosity and pore thresholds, but a lower permeability (see Fig. 6). Samples from group 2 therefore have a better connectivity. In principle, if the two groups are considered as steps of the same alteration process, samples from group 3 should inherit their connectivity from group 2 and have a higher permeability.

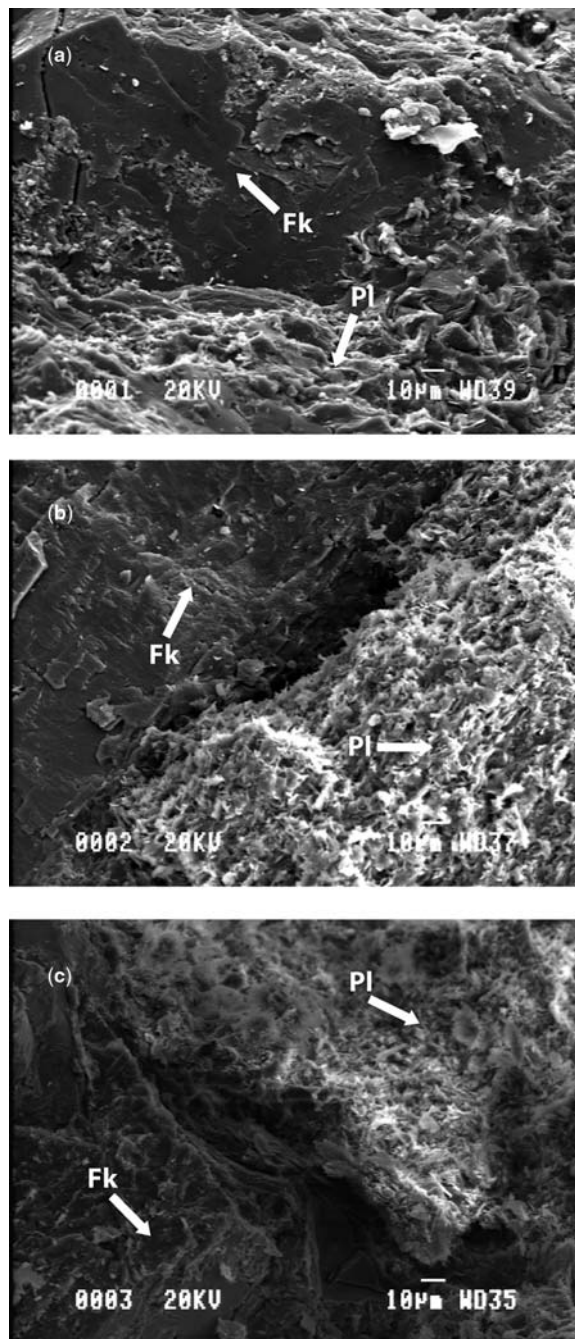


Fig. 8. SEM images from group 3 showing the evolution of alteration and the porosity development in plagioclases (Fk, K-feldspar; Pl, plagioclase).

Conclusion

Permeability, specific surface and porosimetry measurements were carried out on samples from the matrix of the damage zone and the protolith. Based on these results, especially porosimetry results, three groups were defined, which show distinctive porous network characteristics and behaviour during alteration. At present, it is not possible to define precisely if there is a relation between these groups. Further information from clay study and dating should clarify these relations.

High dilution of tracer and delay in arrival time during circulation tests performed in the Soultz-sous-Forêts geothermal exchanger (Gérard *et al.* 1998) suggest a non-negligible impact of the damage zone in terms of reservoir properties. Connections and exchanges with the fault core are probably favoured by matrix properties and fracture density, with some 'buffer effect' of the damage zone. At present, thermo-hydro-mechanical modelling taking into account all these properties is running to determine and understand the total behaviour of the damage zone during fluid circulations.

The authors would like to thank T. Reuschlé for helping with the specific surface measurements, and B. Ledesert and G. Zimmermann for their constructive remarks.

References

- AHARONOV, E., ROTHMAN, D. H. & THOMPSON, A. H. 1997. Transport properties and diagenesis in sedimentary rocks; the role of micro-scale geometry. *Geology*, **25**, 547–550.
- AQUILINA, L., PAUWELS, H., GENTER, A. & FOUILAC, C. 1997. Water–rock interaction processes in the Triassic sandstone and the granitic basement of the Rhine Graben: geochemical investigation of a geothermal reservoir. *Geochimica et Cosmochimica Acta*, **61**, 4281–4295.
- AURADOU, H., MALOY, K. J., SCHMITTBUHL, J. & HANSEN, A. 2003. Drainage in a rough gouge filled fracture. *Transport in Porous Media*, **50**, 267–305.
- AURADOU, H., DRAZER, G., HULIN, J. P. & KOPLIK, J. 2005. Permeability anisotropy induced by the shear displacement of rough fracture walls. *Water Resources Research*, **41**, W09423, doi:10.1029/2005WR003938.
- BALDEYROU, A., VIDAL, O. & FRITZ, B. 2003. Etude expérimentale des transformations de phase dans un gradient thermique: application au granite de Soultz-sous-Forêts, France. *Comptes Rendus de l'Académie des Sciences, Série II, Fascicule A*, **335**, 371–380.
- BARIA, R. & BAUMGÄRTNER, J. 1999. European HDR research programme at Soultz-sous-Forêts (France); 1987–1996. *Geothermics*, **28**, 655–669.
- BERARD, T. & CORNET, F. H. 2003. Evidence of thermally induced borehole elongation: a case study at Soultz, France. *International Journal of Rock Mechanics & Mining Sciences*, **40**, 1121–1140.
- BRACE, W. F. 1980. Permeability of crystalline and argilaceous rocks. *International Journal of Rock Mechanics & Mining Sciences & Geomechanics Abstracts*, **17**, 241–251.
- BRUNNAUER, S., EMMETT, P. H. & TELLER, E. 1938. Adsorption of gases in multimolecular layers. *Journal of the American Chemical Society*, **60**, 309–319.
- CAINE, J. S., EVANS, J. P. & FORSTER, C. B. 1996. Fault zone architecture and permeability structure. *Geology*, **24**, 1025–1028.
- CORNET, F. H., LI, L., IPPOLITO, I., KUROWSKI, P. & HULIN, J. P. 2003. The hydromechanical behaviour of a fracture: an in-situ experimental case study. *International Journal of Rock Mechanics & Mining Sciences*, **40**, 1257–1270.
- DEBSCHÜTZ, W., KRUCKEL, U. & SCHOPPER, J. R. 1989. Effects of geostatic stress and pore pressure on the Klinkenberg permeability factor and other fluid parameters. In: MAURY, V. & FOURMAINTRAUX, D. (eds) *Proceedings of the Symposium 'Rock at Great Depth'*. Balkema, Rotterdam, 179–185.
- DEZAYES, C., VILLEMIN, T., GENTER, A., TRAINEAU, H. & ANGELIER, J. 1995. Analysis of fractures in boreholes of the Hot Dry Rock project at Soultz-sous-Forêts (Rhine Graben, France). *Scientific Drilling*, **5**, 31–41.
- FISCHER, C. & GAUPP, R. 2004. Multi-scale rock surface area quantification—a systematic method to evaluate the reactive surface area of rocks. *Chemie der Erde, Geochemistry*, **64**, 241–256.
- GENTER, A. & TRAINEAU, H. 1992. Borehole EPS1, Alsace, France: preliminary geological results from granite core analysis for hot dry rock research. *Scientific Drilling*, **3**, 121–141.
- GENTER, A. & TRAINEAU, H. 1996. Analysis of macroscopic fractures in granite in the HDR geothermal well EPS-1, Soultz-sous-Forêts, France. *Journal of Volcanology and Geothermal Research*, **72**, 121–141.
- GENTER, A., TRAINEAU, H., DEZAYES, C., ELSASS, P., LEDESERT, B., MEUNIER, A. & VILLEMIN, T. 1995. Fracture analysis and reservoir characterization of the granitic basement in the HDR Soultz project (France). *Geothermal Science and Technology*, **4**, 205–214.
- GÉRARD, A., JUNG, R., BAUMGÄRTNER, J., BARIA, R., GANDY, T. & TRAN-VIET, T. 1998. *Essais de circulation moyenne durée conduits à Soultz-sous-Forêts en 1997*. Rapport SOCOMINE, Soultz-sous-Forêts.
- GREGG, S. J. & SING, K. S. W. 1982. *Adsorption, Surface Area and Porosity*, 2nd edn. Academic Press, London.
- GUEGUEN, Y. & PALCIAUSKAS, V. 1992. *Introduction à la Physique des Roches*. Hermann, Paris.
- HELLMANN, R. 1994. The albite–water system: Part I. The kinetics of dissolution as a function of pH at 100, 200 and 300 °C. *Geochimica et Cosmochimica Acta*, **58**, 595–611.
- HEUZE, F. E. 1983. High-temperature mechanical, physical, and thermal properties of granitic rocks; a review. *International Journal of Rock Mechanics & Mining Sciences*, **20**, 3–10.
- KLINKENBERG, L. J. 1941. Permeability of porous media to liquids and gases. *American Petroleum Institute, Drilling and Production Practice*, **2**, 200–213.

- KLOUBEK, J. 1994. Investigation of porous structures using mercury reintrusion and retention. *Journal of Colloid and Interface Science*, **163**, 10–18.
- KOMNINOU, A. & YARDLEY, B. W. 1997. Fluid–rock interaction in the Rhine Graben: a thermodynamic model of the hydrothermal alteration observed in deep drilling. *Geochimica et Cosmochimica Acta*, **61**, 515–531.
- LASAGA, A. C. 1984. Chemical kinetics of water–rock interactions. *Journal of Geophysical Research*, **86**, 4009–4025.
- LE CARLIER, C., ROYER, J. J. & FLORES, L. 1994. Convective heat transfer at the Soultz-sous-Forêts geothermal site—implication for oil potential. *First Break*, **12**, 555–560.
- LENORMAND, E., ZARCONE, C. & SARR, A. 1983. Mechanisms of the displacement of one fluid by another in a network of capillary ducts. *Journal of Fluid Mechanics*, **135**, 337–353.
- LI, Y. & WARDLAW, N. C. 1986a. The influence of wettability and critical pore-throat size ratio on snap-off. *Journal of Colloid and Interface Sciences*, **109**, 461–472.
- LI, Y. & WARDLAW, N. C. 1986b. Mechanism of non wetting phase trapping during imbibition at slow rates. *Journal of Colloid and Interface Sciences*, **109**, 473–486.
- NORTON, D. & KNAPP, R. 1977. Transport phenomena in hydrothermal system; the nature of porosity. *American Journal of Science*, **277**, 913–936.
- SALEM, H. S. & CHILINGARIAN, G. V. 1999. Determination of specific surface area and mean grain size from well-log data and their influence on the physical behaviour of offshore reservoirs. *Journal of Petroleum Science and Engineering*, **22**, 241–252.
- SAUSSE, J. 2002. Hydromechanical properties and alteration of natural fracture surfaces in the Soultz granite (Bas-Rhin, France). *Tectonophysics*, **348**, 169–185.
- SAUSSE, J., GENTER, A., LEROY, J. L. & LESPINASSE, M. 1998. Description et quantification des altérations filonniennes: paléoécoulements fluides dans le granite de Soultz-sous-Forêts (Bas-Rhin, France). *Bulletin de la Société Géologique de France*, **169**, 655–664.
- SAUSSE, J., JACQUOT, E., FRITZ, B., LEROY, J. & LESPINASSE, M. 2001. Evolution of crack permeability during fluid–rock interaction. Example of the Brézouard granite (Vosges, France). *Tectonophysics*, **336**, 199–214.
- SCHEIDECKER, A. E. 1974. *The Physics of Flow through Porous Media*, 3rd edn. University of Toronto Press, Toronto, Ont.
- SIBSON, R. H. 2003. Thickness of the seismic slip zone. *Bulletin of the Seismological Society of America*, **93**, 1169–1178.
- TRAINEAU, H., GENTER, A., CAUTRU, J. P., FABRIOL, H. & CHEVREMONT, P. 1991. Petrography of the granite massif from drill cutting analysis and well log interpretation in the geothermal HDR borehole GPK1 (Soultz, Alsace, France). *Geothermal Science & Technology*, **3**, 1–29.
- VAN BRAKEL, J. 1975. Pore space models for transport phenomena in porous media; review and evaluation with special emphasis on capillary liquid transport. *Powder Technology*, **11**, 205–236.
- VILLEMIN, T. & BERGERAT, F. 1987. L'évolution structurale du fossé rhénan au cours du Crétacé: un bilan de la déformation et des effets thermiques de l'extension. *Bulletin de la Société Géologique de France*, **8**, 245–255.
- WARDLAW, N. C. & MCKELLAR, M. 1981. Mercury porosimetry and interpretation of pore geometry in sedimentary rocks and artificial models. *Powder Technology*, **29**, 127–143.
- WARDLAW, N. C. & TAYLOR, R. P. 1976. Mercury capillary pressure curves and the interpretation of pore structure and capillary behaviour in reservoir rocks. *Bulletin of Canadian Petroleum Geology*, **24**, 225–262.
- WARDLAW, N. C., LI, Y. & FORBES, D. 1987. Pore-throat size correlation from capillary pressures curves. *Transport in Porous Media*, **2**, 597–614.
- WASHBURN, E. W. 1921. Note on a method of determining the distribution of pore sizes in a porous material. *Proceedings of the National Academy of Sciences of the USA*, **7**, 115–116.
- WIENAND, J. & HUENGES, E. 1989. Porositaet, innere Oberflaeche und Permeabilitaet von Kernen der Kontinentalen Tiefbohrung. In: *49. Jahrestagung der Deutschen Geophysikalischen Gesellschaft gemeinsam mit der Arbeitsgemeinschaft Extraterrestrische Physik—Abstracts*.

Numerical modelling of pressure solution deformation at axisymmetric asperities under normal load

Y. BERNABÉ¹ & B. EVANS²

¹*Ecole et Observatoire des Sciences de la Terre de Strasbourg, Université Louis Pasteur–CNRS, 5 rue René Descartes, 67084 Strasbourg Cedex, France (e-mail: ybernabe@eost.u-strasbg.fr)*

²*Department of Earth, Atmospheric and Planetary Sciences, Massachusetts Institute of Technology, 54-718, Cambridge, MA 02139, USA*

Abstract: We developed a numerical model of compression of asperities by pressure solution (PS). The dissolution rate along the contact was determined by (1) computing the normal stress distribution from the present shape of the asperities, and (2) solving the diffusion equation inside the fluid-saturated solid–solid interface, including local dissolution source terms corresponding to the stress field previously determined. The change in shape of the asperities during an infinitesimal time interval can then be calculated and the entire procedure repeated as many times as desired. We simulated PS compaction of axisymmetric asperities with different sizes and shapes under various temperatures and loads, and using different values of the interface diffusion coefficient. Our results show that as the contact flattens and grows during PS, the initial elastic deformation is partially relaxed and the stress transferred from the contact centre to the edge. Transient stress release remains significant during an extended period and could strongly influence the interpretation of laboratory experiments. In our model, dissolution and interface diffusion are not sequentially combined as is usually assumed, making it impossible to identify a single rate-limiting process. The convergence rate of the asperities was approximately proportional to the mean effective stress at the contact, and depended in a complex way on the contact radius, but was not sensitive to the asperity size. We also estimated the conditions under which undercutting at the contact edge is triggered.

Many structural features in natural granular rocks, occurring on scales from less than 1 mm to >100 m, strongly suggest that soluble minerals are transported from highly stressed grain-to-grain contacts to essentially unstressed sink regions. These field observations have led geologists to hypothesize that coupled chemical and mechanical mechanisms are important in controlling compaction and changes in transport properties in sedimentary basins (Durney 1972; Rutter 1976; Engelder *et al.* 1981; Angevine & Turcotte 1983; Gratier 1987, 1993a). Variously called solution–precipitation creep, solution–transfer creep or pressure solution (PS), this deformation mechanism has also been proposed as a healing mechanism in fault gouge (Sleep & Blanpied 1992; Karner *et al.* 1997) and is thought to affect the closure and, therefore, the hydraulic transmissivity of rough fractures at depth (Tsang 1991; Yasuhara *et al.* 2004). Despite over 20 years of careful experimentation and theoretical investigations, important questions about this process still remain.

The classic model of Paterson (1973, 1995) treats PS deformation of rocks as granular flow accommodated by material transfer through an intergranular fluid and does not include deformation accommodated by dislocation creep or by brittle

fracture. We shall adopt that description here, without making any judgement on which mechanisms will dominate under natural conditions. In Paterson's treatment, PS is decomposed into four distinct transfer paths depending on the source and sink positions: (1) pore surface to pore surface; (2) grain contact to grain contact; (3) pore surface to grain contact; (4) grain contact to pore surface. Each path is envisioned as a sequence of three steps: mobilization of solid material at the source, transport along the path and deposition at the sink. In this framework, it is possible to derive macroscopic rate laws, provided we can identify the predominant path and, along this path, the rate-controlling step (e.g. Rutter 1976; Paterson 1995; Shimizu 1995). We call these models macroscopic because they necessarily use average quantities such as characteristic path length, mean effective stress, and so forth. However, this approach is not as effective for the purpose of numerical modelling. It is more convenient to decompose PS into the elementary processes illustrated in Figure 1 (e.g. Renard *et al.* 1999, 2000; Gundersen *et al.* 2002; Yasuhara *et al.* 2003; Lehner & Leroy 2004): (1) transfer of material from the stressed mineral grains to the fluid saturating the solid–solid interface composing the grain contact; (2) diffusive

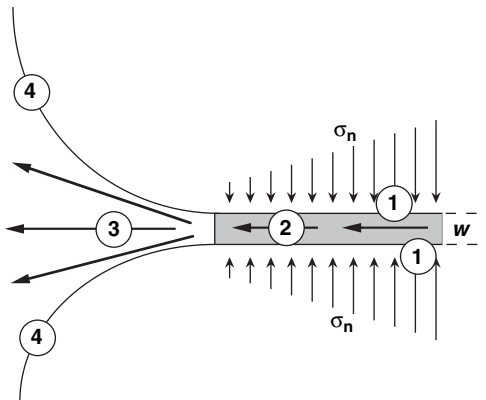


Fig. 1. A schematic illustration of the pressure solution processes at a single grain-to-grain contact subjected to a normal stress distribution σ_n : (1) dissolution at the solid–solid interface (characterized by rate constant K_{dis}); (2) diffusion along the interface (characterized by D^*); (3) diffusion in the ‘free’ pore fluid (characterized by D); (4) dissolution or precipitation along the unstressed fluid–solid surface (characterized by K_D or K_P). The solid–solid interface is represented as a thin layer of thickness w .

transport of solute along the contact region; (3) advective or diffusive transport within the ‘free’ pore space; (4) precipitation or dissolution along the free grain surface. These processes resemble Paterson’s steps but, as will be shown below, are not combined sequentially at the microscopic scale. Another advantage of this approach is that each elementary process is characterized by a specific phenomenological constant and is, therefore, directly identified in the mathematical treatment. For example, the bulk fluid coefficient of diffusion D corresponds to process (3) if solute transport in the ‘free’ pore space is diffusive (the description is more involved in the case of advective transport), whereas process (4) is described by K_D or K_P , the usual dissolution and precipitation rate constants. It should be noted that some of the numerical models mentioned above use average variables and parameters, and can therefore also be classified as macroscopic. In this paper, we follow the work of Lehner (1995) and Lehner & Leroy (2004) and construct a microscopic model, using local quantities and fully accounting for their spatial variations inside the contact region.

A number of important questions can only be addressed using a microscopic approach. In particular, in macroscopic models the mean driving force for PS is assumed to scale with the effective normal stress averaged over a characteristic grain contact area, although sometimes a critical stress magnitude is subtracted (Paterson 1995; Revil

1999; Bos & Spiers 2002; Gundersen *et al.* 2002; Yasuhara *et al.* 2003; Beeler & Hickman 2004). However, it has long been recognized that the actual stress distribution along the contact is probably complicated and may change in magnitude and shape during deformation (Rutter 1976). We addressed this issue by relaxing what we consider a severe constraint included in the Lehner & Leroy (2004) model; namely, that the dissolution rate is uniform over the entire grain contact at all times during PS. This hypothesis imposes a second-order polynomial stress distribution in the contact region. Instead, we determined the contact stress field at any given time by solving a Hertzian-type, elastic, contact problem using the current shapes of the contacting solids.

In this study, we focused exclusively on the interrelationships between the two elementary processes occurring at the intergranular contact region, namely, processes (1) and (2) in Figure 1, which, for convenience, are hereafter called contact dissolution and interface diffusion. This model, then, is predicated on the assumption that the ‘free’ pore surface geometry is not directly altered; that is, that free-surface dissolution and precipitation may be neglected. Such conditions might occur if fluid flow in the ‘free’ pore space transports any excess concentration away very rapidly or if the concentration of solute in the ‘free’ pore fluid is buffered in some other way. It is abundantly clear, however, that a full treatment of PS must also include descriptions of advective and diffusive transport of the mineral solute within the ‘free’ pore fluid and of dissolution and precipitation of the solute at source and sink regions within the ‘free’ pore space.

We applied our method to simulate deformation of axisymmetric quartz asperities in normal contact over a period of 6.3 years, a period far too short for interpretation of field observations, but much longer than laboratory experiments (to ensure accuracy a relatively small time increment of 1000 s had to be used, precluding simulation of geological time intervals). A generalization of the model to arbitrarily shaped asperities is straightforward in principle, but would be demanding in practice. We systematically varied the temperature, diffusion coefficient within the saturated solid–solid interface and externally applied normal load, and examined the behaviour of axisymmetric asperities with different sizes and shapes.

Pressure solution model

Let us consider a single, axisymmetric asperity in contact with a planar, semi-infinite, solid body as schematically shown in Figure 2a. This geometry

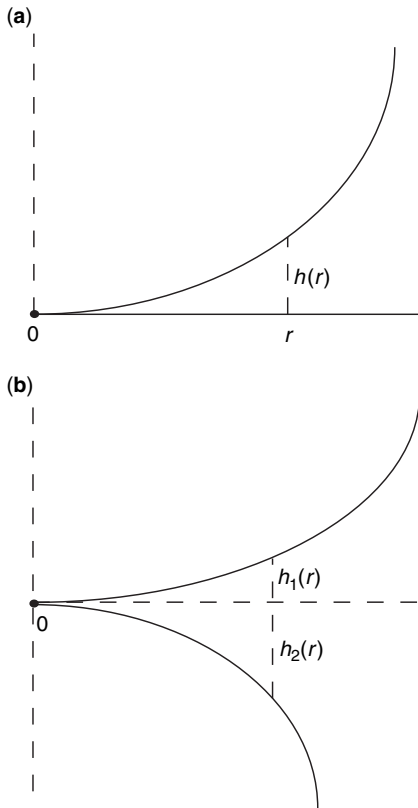


Fig. 2. Graphic definition of the relative separation $h(r)$ between (a) an axisymmetric asperity and a flat semi-infinite solid, and, (b) two different axisymmetric asperities, in which case we have $h(r) = h_1(r) + h_2(r)$. In both cases, the solids are unstressed but in contact at the point $r = 0$.

is not really restrictive, because, for elastic bodies, only the relative separation (defined as $h(r) = h_1(r) + h_2(r)$ in Fig. 2b) is mechanically important (Johnson 1985). Therefore, the model applies to any pair of axi-symmetric asperities in normal contact having the same relative separation, $h(r)$. In our simulations, both the asperity and the semi-infinite body are composed of quartz (but we neglect crystallographic anisotropy). The two solids are pressed together by remotely applied normal forces. The pore space around and inside the contact is saturated with an aqueous solution at temperature T and pressure p . The fluid in the ‘free’ pore space (i.e. outside the contact) is assumed to be in chemical equilibrium with the unstressed solids (i.e. under zero effective stress). We denote c_{eq} the equilibrium concentration of the solution in the ‘free’ pore space at the prescribed pressure p and temperature T . It should be noted that

the effect of surface curvature on dissolution–precipitation kinetics is not considered.

Following Paterson (1973) we assume that the solid–solid interface can be represented as an infinitesimally thin, dynamically stable, porous layer that remains fully saturated by the pore fluid at pressure p , but nevertheless transmits arbitrary normal and tangential tractions. The existence of an interface that provides a fast pathway for transport is essential for the activation of pressure solution, as vividly illustrated by the late B. Brether’s unpublished experiments (H. Pape, pers. comm.). In those experiments, grains of potassium alum ($\text{KAl}[\text{SO}_4]^2 \cdot 12\text{H}_2\text{O}$) were pressed against each other while immersed in water; no signs of pressure solution were observed unless a thin piece of filter paper was inserted at the contact, which provided the fully saturated, highly diffusive, stress-transmitting contact interface described above. The conditions under which such fluid-permeated, solid–solid interfaces exist in natural rocks are not known. If present, as is widely assumed, their internal structure may depend on mineralogy, geological history and fluid chemistry. In the laboratory, experimental results are known to be very sensitive to specimen preparation and to the identity of the minerals on either side of the interface (e.g. Hickman & Evans 1991, 1995), suggesting wide variations in interface and interphase boundary structures.

In natural systems, the scale of the internal structure of solid–solid interfaces is probably of the order of 10^{-8} m and is therefore very difficult to observe directly. Some attempts have been made by Hickman & Evans (1991, 1992, 1995), de Meer *et al.* (2002, 2005), and Karcz *et al.* (2005). Because of the lack of conclusive observations, several models are currently proposed: strongly adsorbed fluid films (e.g. Weyl 1959; Rutter 1983; Renard & Ortoleva 1997), a dynamic island–channel structure (e.g. Raj 1982; Lehner 1990; Paterson 1995; Ghoussoub & Leroy 2001), stress corrosion microcracks and fluid inclusions (Gratz 1991; den Brok 1998), and a hydrated gel or altered mineral layer (Revil 1999, 2001; A. Dimanov, pers. comm.). However, for the purpose of the present study, it is not necessary to specify the contact internal structure. The solid–solid interface need only be characterized by the product wD^* of its thickness w and an effective diffusion coefficient D^* . The activation energy for interface diffusion has been suggested to be similar to that for diffusion in the ‘free’ pore fluid (Renard *et al.* 2000). Until more detailed information is available, it is convenient to assume that w is insensitive to temperature and to express D^* as the product fD , where D is the (temperature-dependent) diffusion coefficient in the ‘free’ pore fluid and f is a

(temperature-independent) correction factor, $0 < f < 1$, intended to account for the difference between ‘free’ pore fluid and interface fluid, and other retardation effects (e.g. tortuous channels). It should be noted that f and w were additionally assumed here to be independent of stress.

Following Lehner & Leroy (LL) (2004), contact dissolution is modelled by expressing the mass of solid dissolved from the two bodies at any point along the contact interface per unit time and unit area (in $\text{kg m}^{-2} \text{s}^{-1}$), $J(r)$, as

$$J(r) = \rho_s K_{\text{dis}} \left(\frac{\rho_s \Omega_s}{kT} \right) [\mu_s(r) - \mu(r)] \quad (1)$$

where ρ_s denotes the solid density, Ω_s the molecular volume of the solid, $\mu_s(r)$ the chemical potential (in J kg^{-1}) in the stressed solid, $\mu(r)$ the chemical potential of the solute in the solution permeating the contact, k the Boltzmann constant ($1.38 \times 10^{-23} \text{ J K}^{-1}$) and K_{dis} a temperature-dependent, phenomenological rate coefficient for contact dissolution (in m s^{-1}). In the absence of conclusive experimental evidence, it is convenient to assume that K_{dis} is identical to K_D , the rate constant of dissolution for a solid immersed in a fluid. It should be noted also that, because precipitation is not considered here, we simply defined $J(r)$ as a positive quantity (when both precipitation and dissolution can occur a sign convention becomes necessary; e.g. Ghoussoub & Leroy 2001; Lehner & Leroy 2004). By definition, the chemical potential in the solution is given by

$$\mu(r) - \mu_0 = \frac{kT}{\rho_s \Omega_s} \ln \left(\frac{\gamma c(r)}{\gamma_0 c_0} \right) \quad (2)$$

where $c(r)$ is the concentration of the solution in the solid–solid interface, γ the activity coefficient (γ is approximately constant at moderate concentrations and will be omitted hereafter) and the subscript 0 refers to an unspecified reference state. In particular, the chemical potential in the equilibrium solution saturating the ‘free’ pore space is

$$\mu_{\text{eq}} - \mu_0 = \frac{kT}{\rho_s \Omega_s} \ln \left(\frac{c_{\text{eq}}}{c_0} \right) \quad (3)$$

where c_{eq} is the concentration of the equilibrium solution. Neglecting variations of the solid density, we can write (Paterson 1973)

$$\mu_s(r) - \mu_{\text{eq}} \approx \frac{\sigma_n(r) - p}{\rho_s} + (f_{\text{Hlm}}(r) - f_{\text{eq}}) \quad (4)$$

where $\sigma_n(r)$ is the normal stress (positive in compression), and, $f_{\text{Hlm}}(r)$ and f_{eq} the Helmholtz free

energy of the solid in stressed and unstressed conditions, respectively. It should be noted that the two terms on the right-hand side of equation (4) have the same sign and cannot cancel each other. Although the free energy term plays an important role in conditions leading to free surface dissolution and/or undercutting (Tada & Siever 1986; Tada *et al.* 1987; Gratier 1993b), it has been shown to be negligible inside a normally loaded contact (e.g. Paterson 1973; Rutter 1976; Lehner & Bataille 1984), leading to

$$\mu_s(r) - \mu_{\text{eq}} \approx \frac{\sigma_n(r) - p}{\rho_s}. \quad (5)$$

Combining equations (1), (2), (3) and (5), we obtain

$$J(r) = \rho_s K_{\text{dis}} \left[\frac{\Omega_s}{kT} \sigma_{\text{eff}}(r) - \ln \left(\frac{c(r)}{c_{\text{eq}}} \right) \right] \quad (6)$$

where $\sigma_{\text{eff}}(r) = \sigma_n(r) - p$ is the effective normal stress acting through the solid–solid interface.

During interface diffusion, the solute is transported outwards along the stressed solid–solid interface. To model this process, source terms must be added to the diffusion equation to allow for dissolution at each point along the interface:

$$\frac{\partial c(r)}{\partial t} - D^* \Delta c(r) = \frac{J(r)}{w \rho_F} \quad (7)$$

where ρ_F is the fluid density, Δ the Laplacian operator and t the time. As there is essentially no storage in the solid–solid interface, $\partial c / \partial t$ can be assumed to approach zero extremely fast. We can therefore consider PS to be a quasi-static compaction process. After using equation (6) and reorganizing the various terms, we obtain

$$\frac{d^2 c(r)}{dr^2} + \frac{1}{r} \frac{dc(r)}{dr} + \frac{K_{\text{dis}} \rho_s}{w D^* \rho_F} \times \left[\frac{\Omega_s}{kT} \sigma_{\text{eff}}(r) - \ln \left(\frac{c(r)}{c_{\text{eq}}} \right) \right] = 0. \quad (8)$$

This equation (with the appropriate boundary conditions) gives the distribution of concentration inside the contact interface for any stress field, $\sigma_{\text{eff}}(r)$. A very important remark needs to be made at this juncture: the solution of equation (8), $c(r)$, must lie between c_{eq} and a maximum concentration $c_{\text{max}}(r) = c_{\text{eq}} \exp(\sigma_{\text{eff}}(r) \Omega_s / kT)$. When diffusion along the interface is fast enough for $c(r)$ to reach c_{eq} , the dissolution rate depends only on $\sigma_{\text{eff}}(r)$ and we can conclude that the rate-limiting process is dissolution. Conversely, when diffusion is sufficiently slow, $c(r)$ approaches

$c_{\max}(r)$, effectively reducing the source term to nearly zero. In this case, the rate-limiting process is diffusion along the solid–solid interface. Between these two extreme behaviours, interface diffusion and dissolution appear to be so intricately coupled that it may be impossible to identify a single process as rate limiting. It should be noted that omitting the $\ln(c(r)/c_{\text{eq}})$ term in equation (6) automatically leads to dissolution-limited models of compaction by pressure solution. Indeed, in such models, the concentration gradient inside the solid–solid interface is free to grow boundlessly, allowing the diffusion rate to match any possible dissolution rate.

Then writing equation (8) in non-dimensional form yields

$$\frac{d^2C(R)}{dR^2} + \frac{1}{R} \frac{dC(R)}{dR} + \alpha[\beta\sigma^*(R) - \ln(C(R))] = 0 \quad (9)$$

where $R = r/a$, $C = c/c_{\text{eq}}$, $\sigma^*(R) = \sigma_{\text{eff}}(R)/\sigma_{\text{eff}}(0)$, $\alpha = (\rho_S/\rho_F) K_{\text{dis}} a^2 / wD^* c_{\text{eq}}$ and $\beta = \sigma_{\text{eff}}(0) \Omega_S/kT$. The appropriate boundary conditions are $C = 1$ for $R = 1$, and, $dC/dR = 0$ for $R = 0$. As shown in Appendix 1, if $\sigma^*(R)$, α and β are known, equation (9) can be numerically solved using the shooting method (Press *et al.* 1988). Thus, assuming that $\sigma^*(R)$, α and β remain constant during an infinitesimally small time interval δt , we can calculate the concentration profile $c(r)$ inside the contact and then, using equation (6), the thickness of solid dissolved $\delta h(r) = \delta t J(r)/\rho_S$ during the time interval δt . Therefore, dissolution produces changes in the relative separation $h(r)$, which, in turn, induce changes in $\sigma_{\text{eff}}(r)$ and a . If those changes can be evaluated, equation (9) can be solved and, by repeating the entire procedure as many times as desired, we can determine the evolution of the asperity under pressure solution.

Normal contact model

Under normal loading, the surfaces of both the asperity and the planar body deform and an axisymmetric (nearly planar) contact zone of radius a is produced. The relative normal displacement $u(r)$ of corresponding points on the surfaces of the asperity and planar body, and the effective normal stress $\sigma_{\text{eff}}(r)$ must verify the following conditions:

$$u(r) = u_{\text{el}} - h(r), \text{ and } \sigma_{\text{eff}}(r) \geq 0 \quad \text{for } r \leq a \quad (10a)$$

$$u(r) \geq u_{\text{el}} - h(r), \text{ and } \sigma_{\text{eff}}(r) = 0 \quad \text{for } r \geq a \quad (10b)$$

where u_{el} is the overall elastic displacement of the asperity with respect to the planar body.

To calculate $u(r)$ and $\sigma_{\text{eff}}(r)$, we will use the classic assumptions of Hertzian contact theory; namely, that the contact is frictionless, without adhesion, and that the asperity size is much larger than the contact radius (for a discussion of the limitations thus imposed see Johnson (1985)). Under these conditions, $u(r)$ is given for $r \leq a$ by the following expression (Li & Dempsey 1990):

$$u(r) = \frac{8(1-v^2)}{\pi E} \int_0^a \sigma_{\text{eff}}(s) \frac{s}{\max(s, r)} \times K\left(\frac{\min(s, r)}{\max(s, r)}\right) ds \quad (11)$$

where E denotes Young's modulus, v the Poisson's ratio, and $K(x)$ is a complete elliptical integral of the first kind; that is,

$$K(x) = \int_0^{\pi/2} \frac{d\theta}{\sqrt{(1-x^2\sin^2\theta)}}. \quad (12)$$

Equation (11) is complemented by the equilibrium condition

$$\int_0^a 2\pi s \sigma_{\text{eff}}(s) ds = F \quad (13)$$

where F is the effective normal load externally applied to the asperity.

Knowing $h(r)$ and F , and, using conditions (10a) and (10b), equations (11) and (13) can be numerically solved for a , u_{el} and $\sigma_{\text{eff}}(r)$ (Li & Dempsey 1990). For this purpose, we need first to write equations (11) and (13) in non-dimensional form:

$$\frac{4}{\pi} \int_0^1 \zeta(S) \frac{S}{\max(S, R)} K\left(\frac{\min(S, R)}{\max(S, R)}\right) ds = U_{\text{el}} - H(R) \quad (14)$$

and

$$\int_0^1 S \zeta(S) dS = F^* = \frac{F(1-v^2)}{\pi a^2 E} \quad (15)$$

where $U_{\text{el}} = u_{\text{el}}/a$, $H = h/a$, $S = s/a$, and $\zeta(S) = 2(1-v^2)\sigma_{\text{eff}}(S)/E$. The integral equations (14) and (15) can be discretized by representing the contact zone as a set of small annular regions, each with a constant ζ . It should be noted that, in this type of contact problem, the first spatial derivative of ζ is singular at the contact edge (i.e. at $R = 1$). We must therefore use the Gauss–Chebyshev

quadrature scheme (Li & Dempsey 1990), in which the width of the annular regions becomes increasingly smaller as the contact edge is approached. This procedure leads to a set of linear equations that can be solved as shown in Appendix 2.

Numerical simulations

We applied the method described above to a spherical asperity of radius r_c in contact with a semi-infinite planar body (in this case, $h(r) = r_c - (r_c^2 - r^2)^{1/2}$). For a given effective load F (its value was chosen so that the highest stress in the contact would remain below the plastic limit), the initial elastic displacement $u_{\text{el}}(0)$, contact radius $a(0)$ and effective stress field $\sigma_{\text{eff}}(r, 0)$ were calculated using Hertzian contact theory (Johnson 1985). From this starting state, the numerical simulation consisted in repeatedly performing the following three steps at any time t : (1) solve equation (9) knowing $u_{\text{el}}(t)$, $a(t)$ and $\sigma_{\text{eff}}(r, t)$; (2) calculate $\delta h(r)$ and update the relative separation $h(r)$; (3) solve equations (14) and (15) to obtain the new elastic displacement $u_{\text{el}}(t + \delta t)$, contact radius $a(t + \delta t)$ and stress field $\sigma_{\text{eff}}(r, t + \delta t)$. The implementation of step (2) requires some care, as $\delta h(r)$ is generally discontinuous at $r = a$ (indeed, the stress at the edge of the contact becomes finite during PS). We eliminated the discontinuity in δh and kept the relative separation $h(r)$ strictly monotonic by removing a small volume of solid material immediately outside the contact region as illustrated in Figure 3. This additional dissolved volume is very small compared with the total volume dissolved during δt and could be viewed as representing the

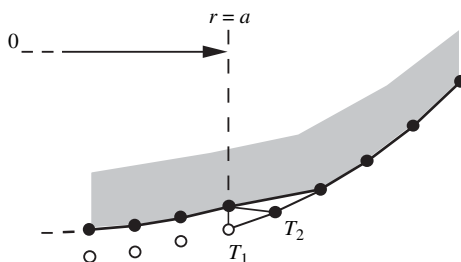


Fig. 3. A schematic illustration of the discretized asperity profile near the edge of the contact (i.e. at $r = a$) at times t (○) and $t + \delta t$ (●). Therefore, the distance separating ○ and ● measures the discretized thickness $\delta h(r)$ of dissolved solid during the interval of time δt . We see that the asperity profile becomes discontinuous at the contact edge. To eliminate the discontinuity, the small triangle T_1 is additionally dissolved. As illustrated here, a local minimum may then appear at the contact edge, possibly leading to a decrease of the contact radius. To avoid this problem, the small triangle T_2 is also removed.

Table 1. Numerical values and temperature dependence of the model parameters from Lehner & Leroy (2004)

Parameters	Values
c_{eq}	$0.055 \times 10^{-(0.254 + 1107.12/T)}$
D ($\text{m}^2 \text{s}^{-1}$)	$9 \times 10^{-7} \exp(-15000/8.31036T)$
E (MPa)	95600
K_{dis} (m s^{-1})	$2.27 \times 10^{-(3.826 + 0.002028T + 4158/T)}$
w (m)	10^{-8}
v	0.08
Ω_S (m^3)	3.7×10^{-29}
$\rho_s \rho_F$	2.65

The parameters considered are equilibrium concentration, diffusion coefficient in the 'free' fluid, quartz Young's modulus, contact dissolution constant for quartz, thickness of the solid–solid interface, quartz Poisson's ratio, quartz molecular volume, and ratio of solid to fluid densities. The temperature, T , is in K.

smoothing effect of the Helmholtz free energy term that is neglected in our model (however, the Helmholtz free energy term might be destabilizing in certain circumstances, in particular when undercutting occurs; Ghoussoub & Leroy 2001). We used numerical values appropriate for quartz (see Table 1). In particular, we included the temperature dependence of c_{eq} , K_{dis} (assumed equal to the free surface dissolution rate constant K_D) and D given by Lehner & Leroy (2004). Figure 4 shows an example of the evolution of the relative separation $h(r)$ and the associated stress field in the case of a spherical asperity with $r_c = 600 \mu\text{m}$. For this simulation, the parameters were $T = 574 \text{ K}$, $f = 0.001$, and $F = 2.89 \text{ N}$, and the time interval between two successive curves was 500 000 s. We can see that the asperity flattens with time and that the stress at the centre decreases while a stress discontinuity is formed at the edge (however, the first stress derivative at the contact edge, $\partial \sigma_{\text{eff}} / \partial r(a, t)$, remained negative at all times). During PS, normal stress is thus transferred from the centre to the edge of the contact.

A series of numerical simulations was performed to examine the effect of the following parameters: the temperature T , diffusion correction factor f , and effective load F . We varied these parameters one at a time (see Table 2), while holding the others constant at the pivot values shown in italics in Table 2 (the asperity was spherical with a radius $r_c = 600 \mu\text{m}$). In all cases investigated, a large portion of the initial elastic displacement was progressively recovered during PS (i.e. $u_{\text{el}}(t)$ decreased with time) as the dissolution displacement $u_{\text{dis}}(t)$ accumulated, the contact radius $a(t)$ grew, and the mean effective stress $\langle \sigma_{\text{eff}} \rangle(t)$ decreased. The release of stress is a consequence of contact growth and must, therefore, depend on

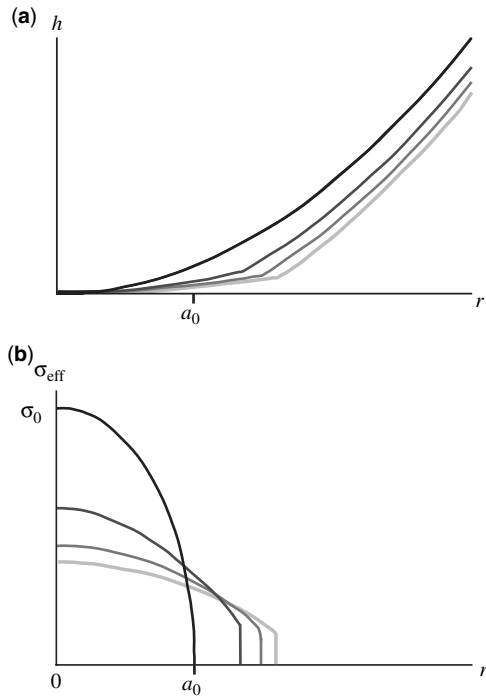


Fig. 4. An example of the evolution under PS of a quartz spherical asperity pressed against a planar quartz half-space: (a) four snapshots of the unstressed relative separation $h(r)$ at times $t = 0, 0.5 \times 10^6, 1.0 \times 10^6$ and 1.5×10^6 s; (b) the corresponding stress distribution in the contact region. In this simulation, we used $T = 574$ K, $f = 0.001$, $r_c = 600$ μm and $F = 2.89$ N. The initial contact radius is indicated by a_0 in both diagrams.

the geometry of the asperity (i.e. its size and shape). We see that, owing to decreasing mean stress and increasing diffusion distance, the local driving force and its gradient tend to decrease with time. Indeed, in all cases considered, the total displacement rate, $u'_{\text{tot}}(t)$, continuously decreased with time.

As expected, increasing the temperature accelerates dissolution, elastic stress relief and contact

growth, and, increases the total displacement rate (Figs 5 and 6), but the coupling of dissolution and diffusion has an interesting effect on the apparent activation energy. To estimate an effective activation energy, we constructed Arrhenius plots of the total displacement rate, $u'_{\text{tot}}(t)$, or dissolution displacement rate, $u'_{\text{dis}}(t)$, measured at times along the curves of Figure 5c corresponding to identical values of the mean effective stress (and of the contact radius, as $\langle \sigma_{\text{eff}} \rangle(t) \pi a(t)^2 = F$). The Arrhenius plots were not perfectly linear (particularly for u'_{tot}), but reducing the interval of time δt over which $u'_{\text{tot}} = \delta u_{\text{tot}} / \delta t$ and $u'_{\text{dis}} = \delta u_{\text{dis}} / \delta t$ were measured improved the linearity and yielded larger values of the activation energy. We found 45.4 and 45.9 kJ mol^{-1} for u'_{tot} , and, 58.0 and 45.8 kJ mol^{-1} for u'_{dis} at mean stress levels of 590 MPa (the initial state) and 110 MPa (the lowest stress reached in the 435 K simulation), respectively. These values fall between 72 and 15 kJ mol^{-1} , the values used here for K_{dis} and D , respectively. It should be noted that the activation energy values for u'_{dis} appear to decrease with time, suggesting that interface diffusion is more important in controlling rates at longer times. Also, the activation energy values for u'_{dis} and u'_{tot} tend to converge with increasing time, a consequence of the dominance of the dissolution displacement over the elastic displacement in the long time limit. We ran an additional series of very short simulations to investigate the effect of interface diffusion on the activation energy at $t = 0$ (the mean stress was 590 MPa). We obtained activation energies of 17.4, 32.7, 45.4, 50.7 and 51.8 kJ mol^{-1} for $u'_{\text{tot}}(0)$ and 33.3, 46.6, 58.0, 64.1 and 65.6 kJ mol^{-1} for $u'_{\text{dis}}(0)$ when f was taken to be equal to 0.00001, 0.0001, 0.001, 0.01 and 0.1, respectively. These values indicate that, although it may not be possible to identify a sole rate-limiting process, contact dissolution is more rate controlling (at least, at $t = 0$) for high f values (i.e. fast diffusion) than for low ones (i.e. slow diffusion). The fact that interface diffusion tends to inhibit contact dissolution is further illustrated in Figures 7 and 8. We observe that decreasing the

Table 2. Numerical values of parameters investigated in the spherical asperity simulations

Parameters	Values				
T (K)	435	472	508	542	574
f	0.00001	0.0001	0.001	0.01	0.1
F (N)	0.018	0.091	0.56	2.9	6.2
$\langle \sigma_{\text{eff}} \rangle$ (MPa)	190	320	590	1020	1320

The parameters considered are temperature T , diffusion correction factor f , load F and the initial mean stress $\langle \sigma_{\text{eff}} \rangle(0)$ (the mean stress values are given for the case $r_c = 600$ μm). The pivot values of the various parameters are shown in italics.

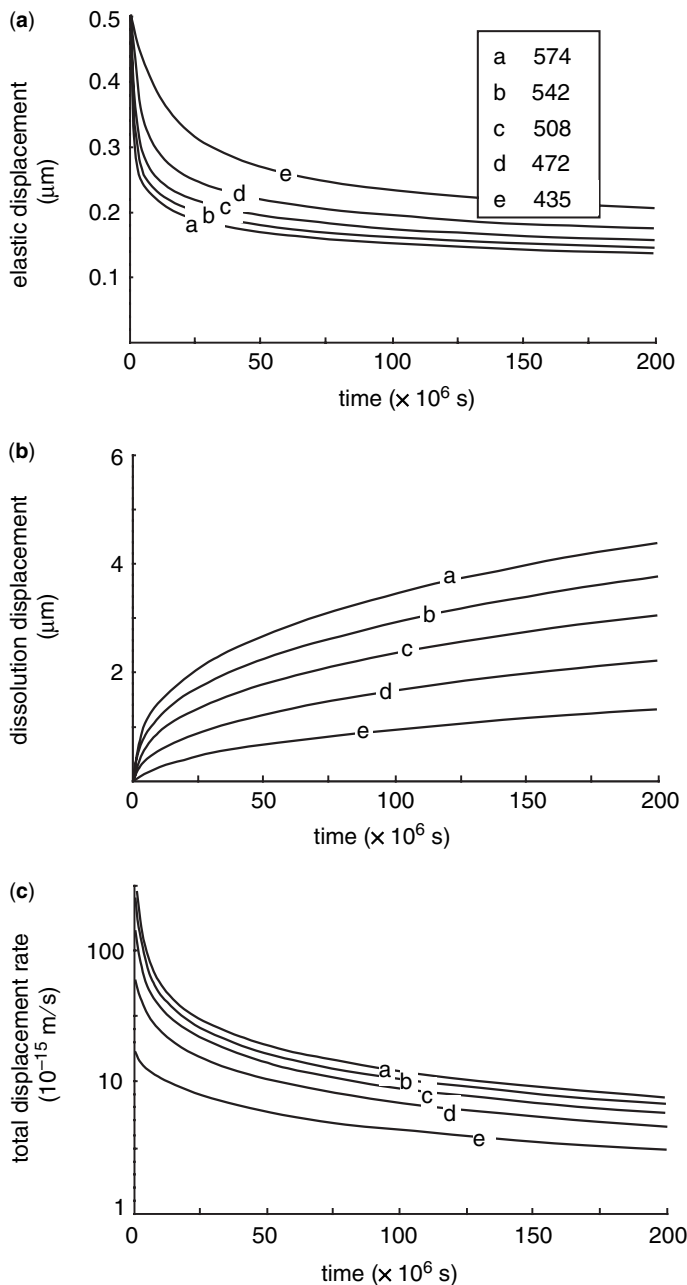


Fig. 5. Numerical results on the effect of temperature: the diagrams represent (a) the elastic displacement, (b) dissolution displacement, and (c) total displacement rate as functions of time. In these simulations, we used $T = 435, 472, 508, 542$ and 574 K (the various curves are labelled as indicated in the box), $f = 0.001$, $r_c = 600 \mu\text{m}$ and $F = 0.56 \text{ N}$.

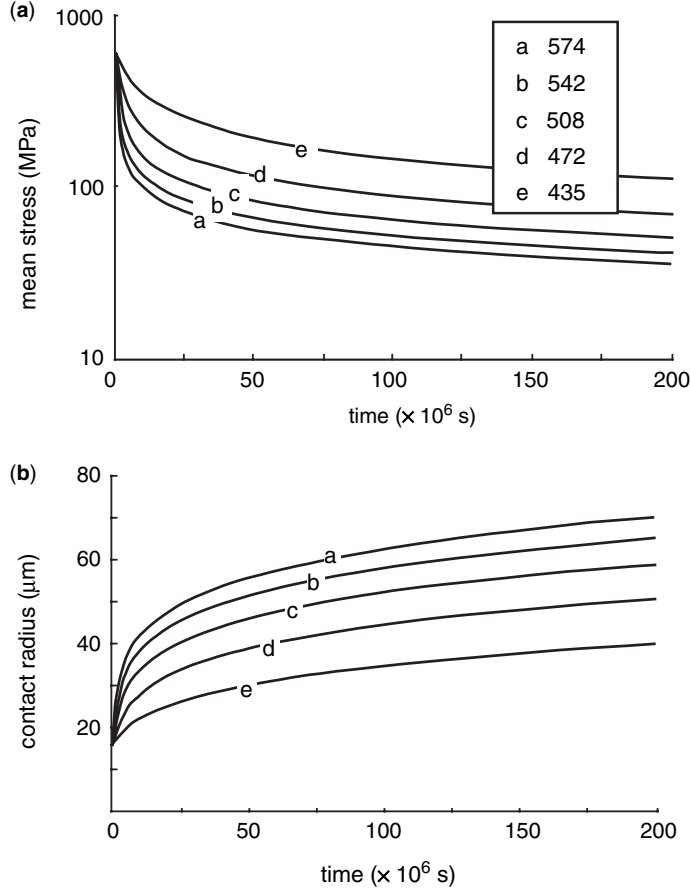


Fig. 6. Numerical results on the effect of temperature: (a) mean stress; (b) contact radius. These results correspond to the same simulations as shown in Figure 5.

diffusion correction factor f slows down dissolution, elastic stress relief and contact growth, and reduces the total displacement rate; also, PS appears to be less sensitive to diffusion for $f > 0.01$, confirming that the predominantly rate-controlling process switches from interface diffusion at low f to contact dissolution at high f values.

The effect of increasing load on displacement rates is shown in Figure 9a, for which the simulation parameters were $T = 508$ K, $f = 0.001$ and $r_c = 600 \mu\text{m}$. Interestingly, the plots of the normalized elastic displacement $u_{\text{el}}(t)/u_{\text{el}}(0)$ v. time (Fig. 9b) reveal that increasing the load (or, equivalently, the initial mean stress) tends to reduce the relative reduction of elastic strain. To test the relationship between load and displacement rate we plotted the ratios $u'_{\text{tot}}(t)/\langle\sigma_{\text{eff}}\rangle(t)$ (Fig. 9c) and $u'_{\text{dis}}(t)/\langle\sigma_{\text{eff}}\rangle(t)$ v. time for the five simulations of Figure 9a. We can see that these curves are not linear and do not overlap (even near $t = 0$). One

likely reason is that, according to Hertzian contact mechanics, different loads produced different initial values of the contact radius and the ensuing contact growth was different in each case considered. To test this idea we performed an additional series of simulations, in which we used different values of the asperity size r_c (i.e. 300, 600, 2000 and 6000 μm , respectively) for different loads (i.e. 1.1, 0.56, 0.17 and 0.056 N, respectively) so that the initial contact radius was the same in all cases (i.e. $a(0) = 17.3 \mu\text{m}$). In these simulations, although the curves of $u'_{\text{tot}}(t)/\langle\sigma_{\text{eff}}\rangle(t)$ (Fig. 10a) and $u'_{\text{dis}}(t)/\langle\sigma_{\text{eff}}\rangle(t)$ v. time were still not linear (owing to contact growth), they appeared to be nearly coincident. Indeed, the evolution of $a(t)$ was nearly identical in the four cases considered despite the large differences in r_c (Fig. 10b). We suspect that this effect is specifically related to the spherical shape and might not occur with another asperity shape.

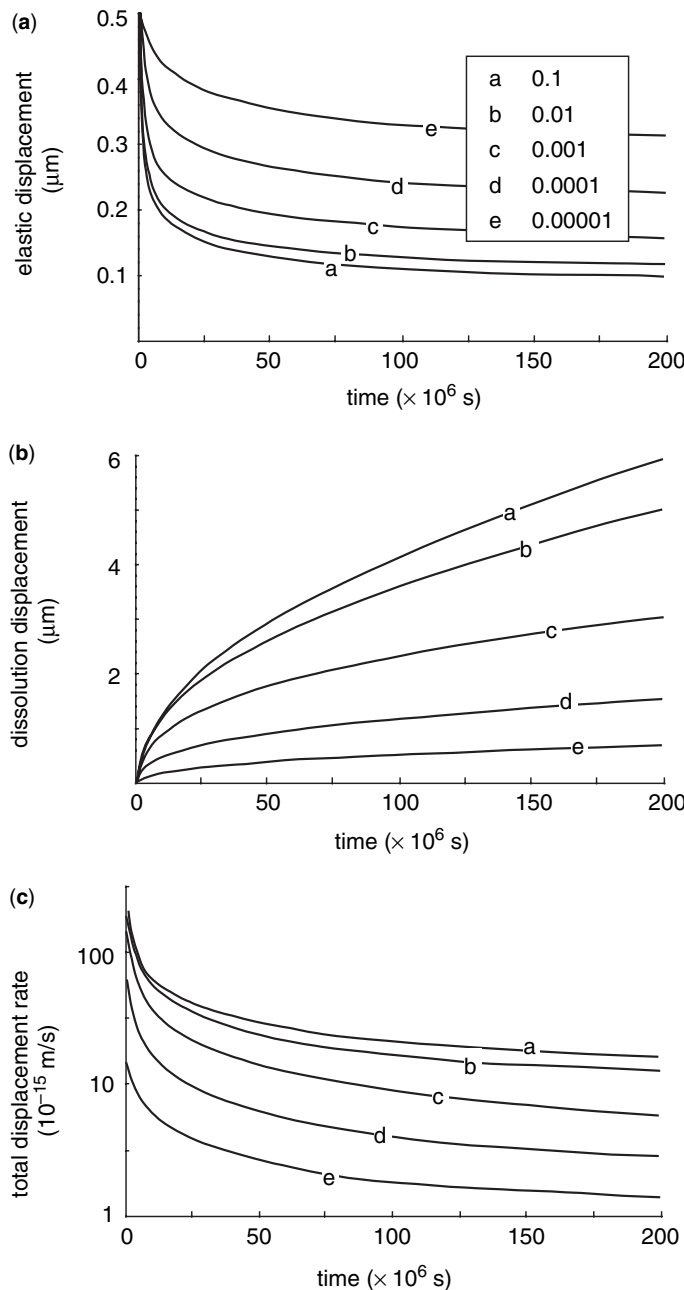


Fig. 7. Numerical results on the effect of interface diffusion: the diagrams represent (a) the elastic displacement, (b) dissolution displacement, and (c) total displacement rate as functions of time. In these simulations, we used $f = 0.00001, 0.0001, 0.001, 0.01$ and 0.1 (the various curves are labelled as indicated in the box), $T = 508 \text{ K}$, $r_c = 600 \mu\text{m}$ and $F = 0.56 \text{ N}$.

Because, as stated above, the asperity geometry (i.e. its size and shape) limits the contact growth during PS we performed a number of additional simulations on asperities with variable sizes and

shapes. To investigate the effect of asperity size we simply have to vary r_c while keeping all other parameters constant. It is logical to use the pivot values $T = 508 \text{ K}$ and $f = 0.001$, but a problem

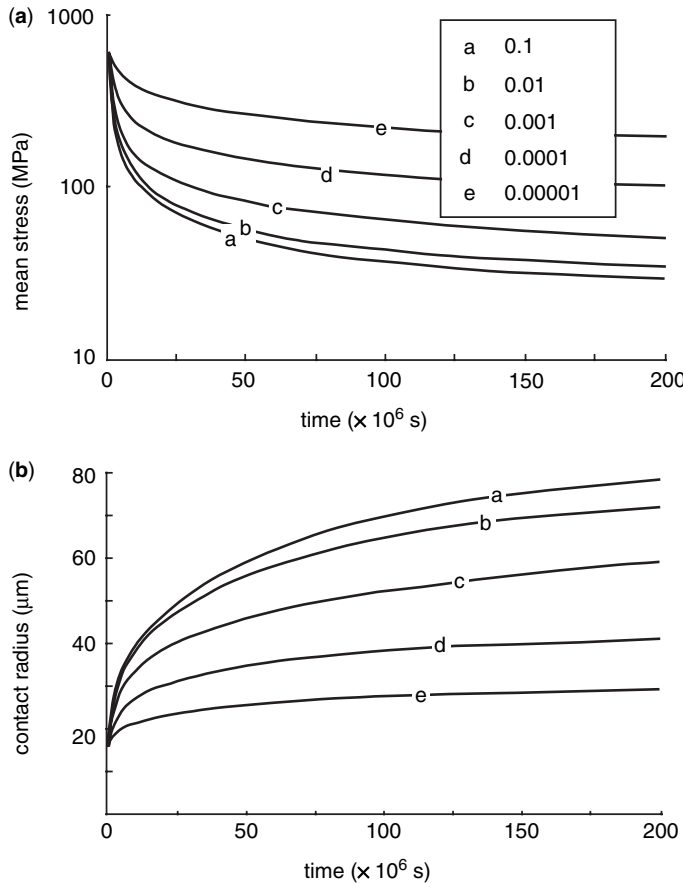


Fig. 8. Numerical results on the effect of interface diffusion: (a) mean stress; (b) contact radius. These results correspond to the same simulations as shown in Figure 7.

arises for our choice of a load parameter. According to Hertzian contact mechanics, varying r_c while keeping the effective load F constant yields different values of the initial mean stress $\langle\sigma_{\text{eff}}\rangle(0)$. Conversely, we must adjust F to generate an identical $\langle\sigma_{\text{eff}}\rangle(0)$ in asperities with different r_c . In our opinion, keeping $\langle\sigma_{\text{eff}}\rangle(0)$ constant rather than F is more meaningful for the following reason. In many PS experimental studies (e.g. Spiers & Schutjens 1990; Schutjens 1991; de Meer & Spiers 1995; Dewers & Hajash 1995; Hellmann *et al.* 2002; Niemeijer *et al.* 2002) fluid-saturated granular aggregates were isostatically (or uniaxially) compacted under constant temperature and constant effective confining pressure (or effective uniaxial stress). We therefore introduced the nominal effective confining pressure $p_c = F/(4r_c^2)$ and found from Hertzian contact theory that keeping p_c constant while varying r_c , as is experimentally done, is equivalent to holding $\langle\sigma_{\text{eff}}\rangle(0)$ constant in these

simulations. The relative elastic stress relief appeared to be inhibited by the asperity size (Fig. 11a). Interestingly, the total displacement rate was insensitive to r_c except during an initial transient probably linked to the early stage of elastic stress relief (Fig. 11b).

Finally, we ran simulations in identical conditions ($T = 508$ K, $f = 0.001$ and $F = 0.56$ N) on a spherical asperity ($r_c = 600 \mu\text{m}$) and on one with a spherical cap of radius 600 μm (for $r \leq 20 \mu\text{m}$) on top of a cone tangent to the spherical cap. Because a given amount of dissolution produces a much larger contact area for the conical asperity than the spherical one, the PS processes tend to slow down much faster for the former than for the latter. At late times, the total displacement rate for the conical asperity was less than 50% of that for the spherical one (Fig. 12). Even larger differences were obtained with an asperity with a concave shape (not shown here).

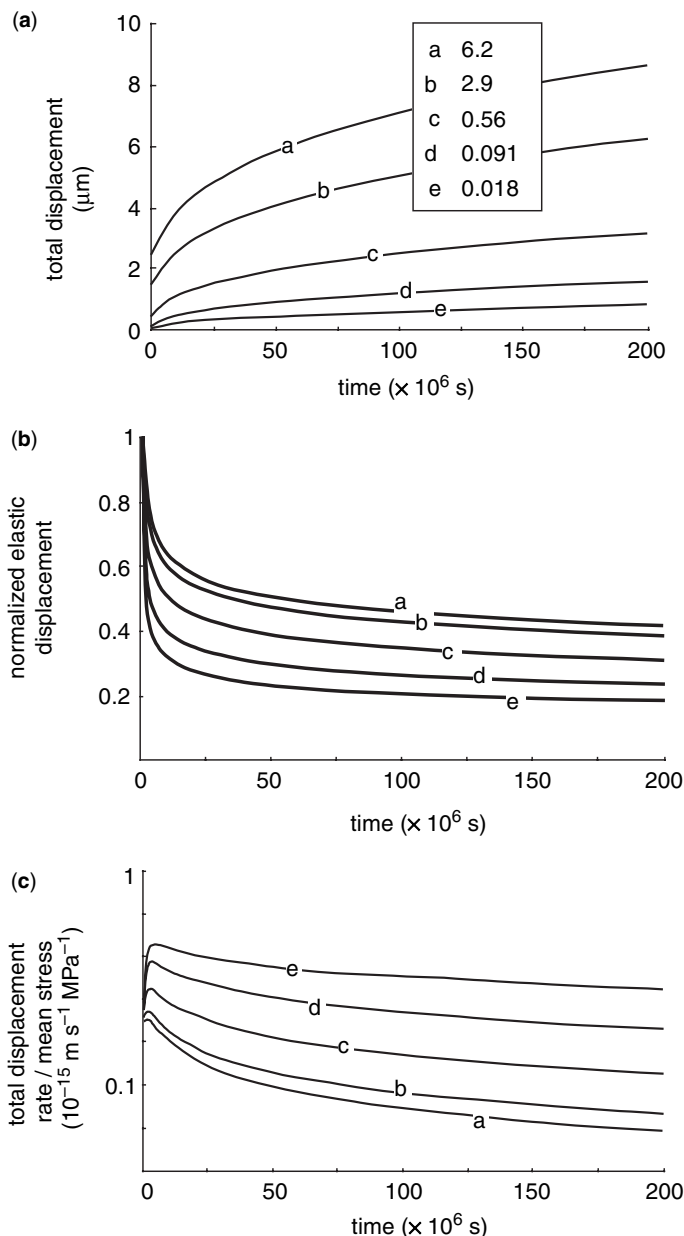


Fig. 9. Numerical results on the effect of the effective normal load: the diagrams represent (a) the total displacement, (b) elastic displacement normalized to its initial value, and (c) the ratio of total displacement rate by the mean stress as functions of time. In these simulations, we used $F = 0.018, 0.091, 0.56, 2.9$ and 6.2 N (the various curves are labelled as indicated in the box), $T = 508 \text{ K}$, $r_c = 600 \mu\text{m}$ and $f = 0.001$.

Discussion

Comparison with the LL model

The model described here is based on the LL model (Lehner & Leroy 2004). However, as those workers

were interested in estimating the very long-term PS behaviour, they made additional assumptions that allowed them to derive an analytical solution. Specifically, they neglected the elastic deformation and assumed that, in the long-time limit, the solid-solid contact evolved in such a way that the

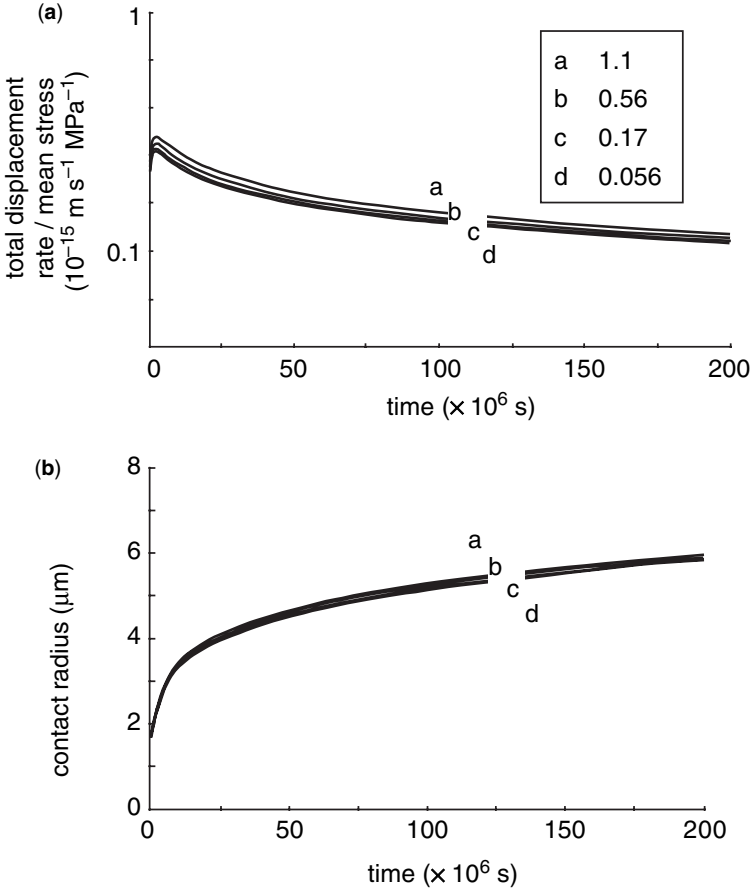


Fig. 10. Numerical results on the effect of the effective normal load: the diagrams represent (a) the ratio of total displacement rate by the mean stress, and (b) the contact radius as functions of time. In these simulations, we used $F = 0.056, 0.17, 0.56$ and 1.1 N (the various curves are labelled as indicated in the box), $T = 508 \text{ K}$ and $f = 0.001$, and the corresponding values of the asperity radius were $r_c = 6000, 2000, 600$ and $300 \mu\text{m}$, respectively. r_c was varied to produce a constant initial contact radius $a(0) = 17.3 \mu\text{m}$.

dissolution rate was uniform over the entire contact area, imposing a second-order polynomial stress field and leading to equation (3.25) in their paper. Incorporating a concentration equal to c_{eq} in that equation, we obtain the following expression for the LL dissolution displacement rate, $u'_{\text{LL}}(t)$:

$$u'_{\text{LL}}(t) = \frac{\frac{2}{kT} \langle \sigma_{\text{eff}} \rangle(t)}{\frac{2}{K_{\text{dis}}} + \frac{\rho_s}{\rho_f} \frac{a(t)^2}{4c_{\text{eq}}wD^*}}. \quad (16)$$

In equation (16), $u'_{\text{LL}}(t)$ is linearly related to $\langle \sigma_{\text{eff}} \rangle(t)$ but, in general, not to any specific, well-defined power of $a(t)$. However, it should be noted that, for $a(t) \gg a_{\text{crit}} = (8\rho_f c_{\text{eq}} w D^*/\rho_s K_{\text{dis}})^{1/2}$, $u'_{\text{LL}}(t)$ becomes inversely related to

the square of the contact radius, whereas, for $a(t)^2 \ll a_{\text{crit}}$, $u'_{\text{LL}}(t)$ is independent of it. For quartz, a_{crit} decreases with increasing temperature and decreasing diffusion correction factor f (e.g., $a_{\text{crit}} = 860, 29$ and $0.16 \mu\text{m}$ for $T = 400, 500$ and 600 K , and $f = 0.1, 0.001$ and 0.00001 , respectively). Using $\langle \sigma_{\text{eff}} \rangle(t) = F/\pi a(t)^2$ in equation (16), we infer that $u'_{\text{LL}}(t)$ is linearly related to F , but with a proportionality coefficient that depends on $a(t)$ and, therefore, varies with time.

To use equation (16), we must express the variation in contact radius corresponding to the dissolution of a layer of thickness δh during the infinitesimal time interval δt ($u'_{\text{LL}} \approx \delta h/\delta t$). For a spherical asperity we find

$$a(t + \delta t) = \sqrt{a(t)^2 - \delta h^2 + \delta h \sqrt{r_c^2 - a(t)^2}} \quad (17)$$

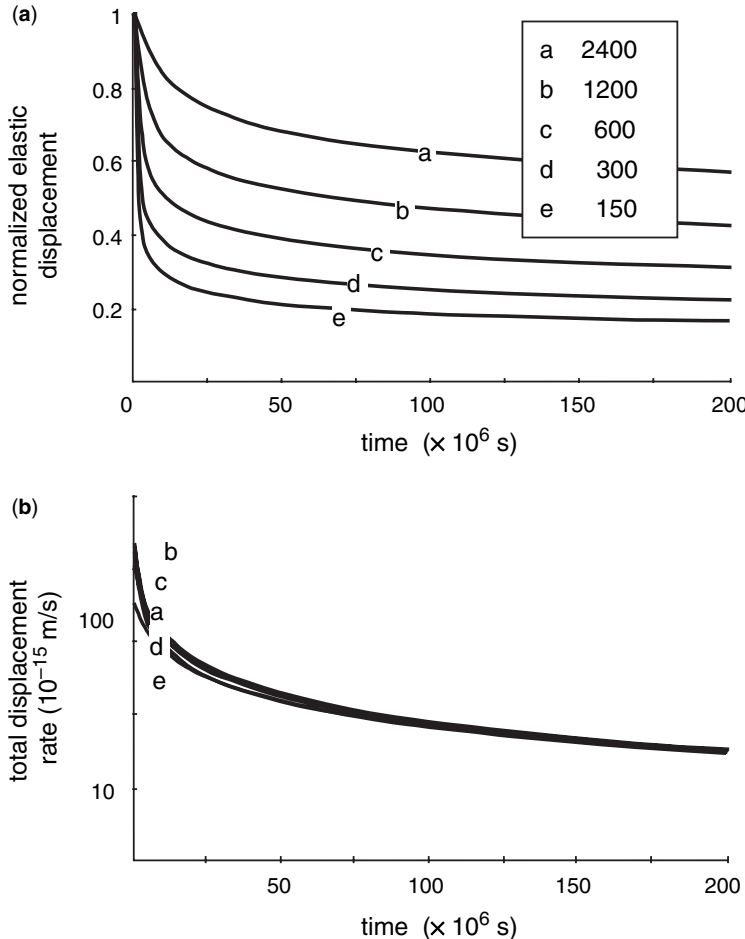


Fig. 11. Numerical results on the effect of the asperity radius: the diagrams represent (a) the elastic displacement normalized to its initial value, and (b) total displacement rate as functions of time. In these simulations, we used $r_c = 150, 300, 600, 1200$ and $2400 \mu\text{m}$ (the various curves are labelled as indicated in the box), $T = 508 \text{ K}$ and $f = 0.001$, and the corresponding values of F were $0.035, 0.14, 0.56, 2.2$ and 8.9 N , respectively.

As equations (16) and (17) are analytical, it is easy to repeat the entire set of simulations described in the previous section using the LL model and compare the new results with ours. We do not need to discuss the short-term discrepancies. They are not meaningful, as LL was designed to be a long-term model. For the longest period investigated here (6.3 years), the LL model tended to overestimate the dissolution displacement, mean stress and dissolution displacement rate (see Fig. 13) by up to 20, 50 and 30%, respectively, and underestimate the contact radius by 20%. The largest differences were obtained for high T , low f , large F and large r_c . The long-term discrepancies between the two models are relatively small but do not show

any sign of decreasing with time (at least, for times of the order of tens of years). This suggests that, although the asperity flattens during PS (see Fig. 4), the dissolution rate may never become completely uniform. In particular, the edge of the contact cannot become too sharply angular without leading to undercutting (the conditions of occurrence of undercutting will be discussed below).

We calculated effective activation energies for PS from the results of equations (16) and (17) and found values comparable with those reported earlier. We also reproduced the results of Figure 10 with an even tighter overlapping of the different curves. A perfect overlapping would indicate that the stress fields (not only the mean

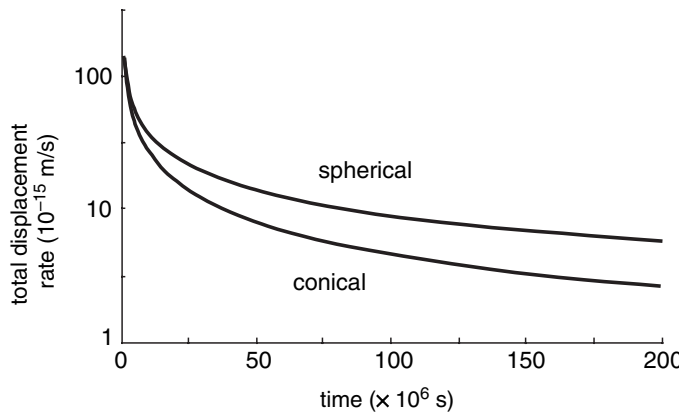


Fig. 12. Numerical results on the effect of the asperity shape. The diagram shows the total displacement rate as a function of time for a spherical and a conical asperity (see text for a more precise description). In these simulations, we used $T = 508\text{ K}$, $f = 0.001$ and $F = 0.56\text{ N}$.

stresses) calculated in different simulations are identical. Thus, we conclude that the contact stress field in our model has more variability than the quadratic stress field assumed in the LL model.

Rate-limiting process

Rate laws for compaction by PS have been derived assuming that the various processes involved during PS are sequential and can be treated independently (e.g. Rutter 1976; Paterson 1995; Shimizu 1995). The rate laws can be expressed in close form only if one of the processes involved (here, either interface diffusion or dissolution) is rate limiting (i.e. much slower than the other ones). The fact that different rate-limiting processes lead to different forms of the rate laws provides the basis for

identifying the most likely rate-limiting process in laboratory experiments (e.g. Gratier & Guiguet 1986; Schutjens 1991; Mullis 1993; Dewers & Hajash 1995; Niemeijer *et al.* 2002).

For example, it is a common technique to measure the effective activation energy for a suite of PS experiments and compare the observed value with the known activation energies of the various individual processes involved. In our simulations, apparent activation energies determined in that fashion ranged between 15 and 72 kJ mol^{-1} , the two activation energies used here for simulating the diffusion and dissolution end-members, respectively. The occurrence of intermediate values confirms that interface diffusion and contact dissolution are not simply sequentially combined in equation (8). We also observed that the apparent

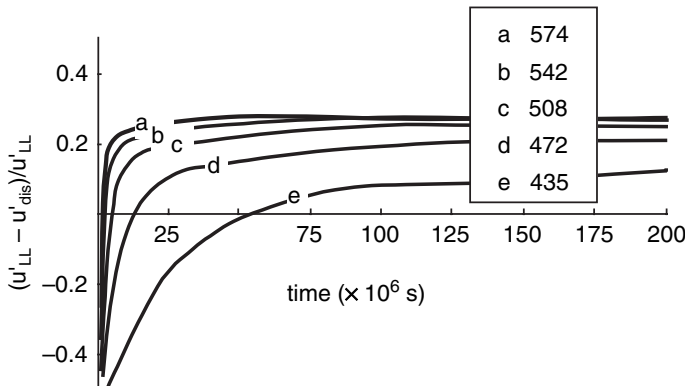


Fig. 13. Example of comparison of our numerical model with the LL model (Lehner & Leroy 2004). The diagram shows the normalized difference in dissolution rate, $(u'_\text{LL} - u'_\text{dis})/u'_\text{LL}$, for the five simulations of Figure 5.

activation energy tended to decrease with time, indicating that interface diffusion becomes dominant in the long-time limit. As explained above, if the concentration inside the solid–solid interface approaches c_{eq} , contact dissolution can be considered rate limiting, whereas, if it is close to c_{max} , the rate-limiting process must be interface diffusion. Figure 14a shows an example of the evolution with time of $(c_{\text{max}}(0, t) - c(0, t))/c_{\text{max}}(0, t)$, the normalized concentration difference at the centre of the contact ($T = 508$ K, $f = 0.001$, $F = 0.14$ N and $r_c = 300 \mu\text{m}$). We see that $(c_{\text{max}}(0, t) - c(0, t))/c_{\text{max}}(0, t)$ decreases monotonically with time, apparently asymptotically vanishing in the long-time limit. Thus, the concentration inside the solid–solid interface approaches c_{max} and we can again conclude that interface diffusion

becomes rate limiting in the long-time limit. It should be noted also that, as illustrated in Figure 14b, $c_{\text{max}}(0, t)$ decreases monotonically with time and appears to approach c_{eq} asymptotically at very long times. This indicates that the diffusion driving force continuously decreases with time. It is therefore possible that the displacement rate becomes vanishingly small without change in applied load if the contact area grows sufficiently large. PS might then appear to be effectively self-arresting as proposed by Stephenson *et al.* (1992) and Revil (1999, 2001), although there is no stress threshold included in equation (8). The self-arrest stress (i.e. stress occurring at very long times) is unlikely to be a constant as sometimes assumed (Stephenson *et al.* 1992; Revil 1999, 2001; Yasuhara *et al.* 2003) but should depend on the

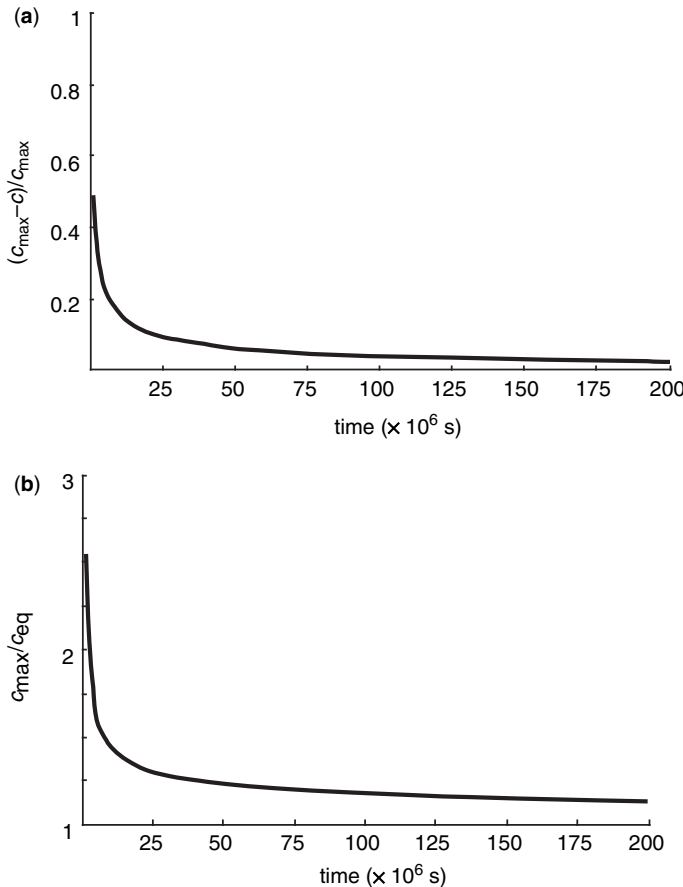


Fig. 14. Example of simulation results suggesting that interface diffusion becomes the rate-limiting process in the long-time limit. (a) Normalized difference between the concentration at the centre of the contact (i.e. at $r = 0$) and the maximum concentration allowed in equation (8), $(c_{\text{max}} - c)/c_{\text{max}}$; (b) maximum concentration allowed in equation (8) normalized to the equilibrium concentration in the ‘free’ pore space, $c_{\text{max}}/c_{\text{eq}}$.

asperity geometry as well as the physical parameters (i.e. temperature, interface diffusion coefficient, solubility, etc.).

Another idea, often used in experimental studies, is to test the dependence of the compaction rate on grain size. Here, we found that, although the contact size $a(t)$ is important, the asperity size r_c had no influence, except during a very short transient (Fig. 11b), suggesting that the grain size sensitivity observed in experimental studies might be caused by processes not included in our model (possibly, processes (3) and (4) in Fig. 1).

The stress dependence provides a way to check whether or not, in given experiments, PS was combined with other mechanical processes such as dislocation creep. We made log–log plots of $u'_{\text{tot}}(t)$ or $u'_{\text{dis}}(t)$ v. $\langle \sigma_{\text{eff}} \rangle(t)$ with the displacement rates measured at selected times from the results shown in Figures 9 and 10. We always found approximately linear relationships (i.e. power-law exponent between 0.9 and 1.1) when the measurement times were selected such that $a(t)$ was constant (the linear relationship is not exact because the entire stress field is involved in equation (8), not only the mean stress). If the measurement times corresponded to fixed total displacement (i.e. fixed compaction) instead of fixed radius of contact, power-law exponents around two were obtained. It is also important to use the local stress $\langle \sigma_{\text{eff}} \rangle(t)$ and not the nominal pressure p_c (using p_c , the simulations of Figure 9 yielded power-law exponents near three). The nearly linear relationship between displacement rate and mean stress (at fixed contact radius) observed here is consistent with equation (16). It should be noted, however, that the approximation $\log(c/c_{\text{eq}}) \approx (c - c_{\text{eq}})/c_{\text{eq}}$ is used in the LL model but not in ours, showing that this approximation is not responsible for the linear relationship.

One important consequence of the point-to-point coupling of the dissolution and diffusion processes considered in our simulations, then, is the introduction of more complex dependences of pressure solution rates on temperature, spatial scale and macroscopic loads than are present in macroscopic models, even when they include multiple transfer paths (Paterson 1995; Revil 1999; Bos & Spiers 2002; Gundersen *et al.* 2002; Yasuhara *et al.* 2003). Although we have considered only two mechanisms occurring along the contact interface, it is conceivable that coupling between and amongst the elementary processes along the other transfer paths and among elementary processes along different paths might also be significant. For example, it is possible that redistribution of stresses near the contact region might affect dissolution along Paterson's path C or precipitation along path D. Any alteration of the near-contact geometry

would then feed back into a new stress distribution at the contact itself. Further work needs to be done to determine if such couplings are important, if they can be detected in data from experiments or from field observations, or if they can be expected to persist to very long time scales.

Undercutting

During preliminary tests of our numerical method, we sometimes observed that the contact radius started to decrease at some point in the simulation. This anomalous behaviour seemed to be a computational artefact related to the numerical technique and did eventually disappear when time and distance increments were sufficiently reduced. However, this observation prompted us to investigate the conditions for which undercutting may arise in our model.

Undercutting occurs if, during the infinitesimal time interval δt , the thickness of solid dissolved is greater at the edge (i.e. $r = a$) than at a point infinitesimally close towards the interior of the contact (i.e. $r = a - dr$). This can be mathematically expressed as $\delta h(a, t) > \delta h(a - dr, t)$, leading to

$$\left(\frac{\Omega_s}{kT} \right) \sigma_{\text{eff}}(a, t) > \left(\frac{\Omega_s}{kT} \right) \sigma_{\text{eff}}(a - dr, t) - \ln \left\{ \frac{c(a - dr, t)}{c_{\text{eq}}} \right\} \quad (18)$$

and

$$\left(\frac{\Omega_s}{kT} \right) \frac{d\sigma_{\text{eff}}}{dr}(r = a, t) > \frac{d \ln(c)}{dr}(r = a, t). \quad (19)$$

Inequality (19) is the condition that the stress and concentration derivatives evaluated at the contact edge must verify for undercutting to occur. As $d \ln(c)/dr$ is everywhere negative, we find that the undercutting condition is always met if the first stress derivative is positive or zero at the edge of the contact. It is interesting to note that this type of stress field occurs when a rigid rectangular punch is pressed against a flat soluble substrate (see Tada & Siever (1986) or Gratier (1993b), who indeed observed undercutting). Thus, the advantage of using a rectangular punch (namely, to avoid contact growth and, thus, be able to produce steady-state PS creep) is compromised by the triggering of undercutting.

When undercutting occurs, we expect the displacement rates to be very different from those predicted by the present model. However, major modifications of our numerical method are required to investigate the kinetics of undercutting. The Helmholtz free energy term, which was neglected

here, must be incorporated and the contact mechanics problem must be formulated to include the existence of undercut cavities inside the grain-to-grain contact. The presence of undercut cavities also modifies the diffusion problem, whether or not the cavities are connected to the 'free' pore space.

Conclusion

By iteratively calculating the contact stress field and the resulting distribution of concentration inside the fluid-saturated solid–solid interface, we were able to simulate the evolution of axisymmetric asperities undergoing pressure solution without imposing excessive constraints on the stress field and/or the shape of the solid–solid contact.

Our numerical results confirmed, as intuitively expected from equation (8), that the two elementary processes, contact dissolution and interface diffusion, are combined in such an intricate way that it is not possible to identify a single rate-limiting process (e.g. we found activation energy values for PS in an intermediate range between the values for diffusion and for dissolution).

The simulations showed that, as dissolution accumulates, the tip of the contacting asperity flattens, the contact area grows, the mean stress decays, and the initial elastic displacement is partially released. The displacement rate decreases very quickly during the first stages of elastic stress relief, and then more and more slowly as the contact matures. For quartz, this transient can last up to several months and may have a significant impact on the results of PS experiments. Elastic stress relief is a consequence of contact growth and is, therefore, conditioned by the initial shape of the asperity. We also observed that contact growth was accompanied by a decrease in activation energy, suggesting that interface diffusion should become rate limiting at very long times if the contact area achieves enough growth.

During PS, stress is transferred from the centre of the contact to the edge. A stress discontinuity is thus produced at the contact edge, bringing the system closer to the undercutting condition. However, we eliminated any manifestation of undercutting in our simulations by decreasing the space and time increments, indicating that the simulated asperities did not develop excessively sharp angles at the contact edge. Of course, we cannot exclude that such sharp angles might appear at later times or under higher loads. Also, we are intuitively inclined to posit that the Helmholtz free energy term should tend to smooth the contact edge but we cannot know for sure until this term is fully included in the model.

Finally, in the long-time limit, our results approach agreement with those obtained from the

LL model (i.e. equation (16)), although relatively significant differences remain at the longest time considered here. Unfortunately, there is at present no practical way to find out whether these differences would vanish or not at even longer times. Nevertheless, this approximate agreement with equation (16) provides important insights and may be very helpful in constructing an effective rate law for pressure solution.

We are grateful to Y. Leroy, R. Katsman and E. Aharonov for their thoughtful reviews. This work was partially funded by the US Department of Energy under grant DE-FG02-97ER14760.

Appendix 1

To solve equation (9) numerically, we discretize the normalized contact area as a set of N small annular regions of equal width $1/N$, each with a constant C and a constant σ^* (Gauss–Chebyshev discretization is not necessary here and, in fact, is not easy to incorporate in the finite-difference scheme). Equation (9) is then transformed into the following set of finite-difference equations:

$$\begin{aligned} N^2(C_{i+1} - 2C_i + C_{i-1}) + \frac{N^2}{2i}(C_{i+1} - C_{i-1}) \\ + \alpha[\beta\sigma_i^* - \ln(C_i)] = 0 \end{aligned} \quad (A1)$$

where the index i (corresponding to $R = i/N$) ranges from one to N . For $i = 0$, we implement the symmetry condition $dC/dR = 0$ by writing equation (9) as

$$2N^2(C_1 - C_0) + \alpha[\beta\sigma_0^* - \ln(C_0)] = 0. \quad (A2)$$

In equations (A1) and (A2), the σ_i^* are linearly interpolated from the (appropriately normalized) stress values obtained by solving equations (14) and (15) (see Appendix 2). As explained above, we now apply the shooting method (Press *et al.* 1988). We start with a trial value of C_0 between one and $\exp(\beta\sigma_0^*)$, calculate C_i for $i = 1$ to N using equations (A1) and (A2) and compare C_N with one, its theoretical value. If C_N is lower (alternatively, higher) than one, we increase (alternatively, decrease) the trial value of C_0 until $C_N \approx 1$ to an acceptable precision. This algorithm is always successful because C is a monotonically decreasing function of R .

Appendix 2

First of all, we note that distances in equations (14) and (15) are normalized with respect to the contact radius a , which, unlike in Appendix 1, is one of the unknowns of the problem. We will therefore proceed iteratively. We start with a trial value of a , solve equations (14) and

(15), and, if the conditions (10a) and (10b) are not verified, modify a and repeat the procedure until these conditions are met. As will be explained below, it is easier to start with a value of a known to be too large.

To solve equations (14) and (15), we discretize the normalized contact area as a set of M small annular regions, each with a constant normalized stress ζ . Equation (14) is transformed into a system of M linear equations:

$$U_{\text{el}} - H_i = \frac{4}{\pi} \sum_{j=1}^M B_{ij} \zeta_j \quad (\text{A3})$$

where

$$B_{ij} = \int_{S_{j+1}}^{S_j} \frac{S}{\max(S, R_i)} K\left(\frac{\min(S, R_i)}{\max(S, R_i)}\right) dS \quad (\text{A4})$$

with $S_j = \cos((j-1)\pi/M)$ (note that $S_{M+1} = 0$) and $R_i = \cos((2i-1)\pi/4M)$. We can see that the width ($S_j - S_{j+1}$) of the annular regions is maximum at the centre and decreases monotonically towards the edge. The values of B_{ij} can be numerically determined. For the terms B_{ii} , the integral in equation (A4) converges because $K(x) \sim \ln(4/(1-x^2)^{1/2})$ for x approaching one. For the central terms B_{iM} , we use the properties of the elliptic integrals:

$$\int K\left(\frac{R}{S}\right) dS = SE(R/S) \quad \text{for } S \geq R \quad (\text{A5a})$$

$$\int \frac{S}{R} K\left(\frac{S}{R}\right) dS = R [E(S/R) - (1 - S^2/R^2) K(S/R)] \\ \text{for } S \geq R \quad (\text{A5b})$$

where $E(x)$ is a complete elliptic integral of the second kind:

$$E(x) = \int_0^{\pi/2} \sqrt{1-x^2 \sin^2 \theta} d\theta. \quad (\text{A6})$$

The equilibrium condition (15) becomes

$$\sum_{i=1}^M A_i \zeta_i = F^* \quad (\text{A7})$$

where

$$A_i = \int_{S_{i+1}}^{S_i} S dS = \frac{S_i^2 - S_{i+1}^2}{2}. \quad (\text{A8})$$

In matrix form, the system (A3) and the equation (A7) become

$$\frac{4}{\pi} \mathbf{B} \cdot \boldsymbol{\zeta} = U_{\text{el}} \mathbf{1} - \mathbf{H} \quad (\text{A9})$$

and

$$\mathbf{A}^T \cdot \boldsymbol{\zeta} = F^* \quad (\text{A10})$$

where the bold characters denote matrices, vectors ($\mathbf{1}$ is a vector whose components are all equal to one) and matrix product, and, the superscript T refers to the transposed vector. To solve equations (A9) and (A10) for U_{el} and $\boldsymbol{\zeta}$, we decompose $\boldsymbol{\zeta}$ as

$$\boldsymbol{\zeta} = U_{\text{el}} \boldsymbol{\zeta}_1 - \boldsymbol{\zeta}_2 \quad (\text{A11})$$

where $\boldsymbol{\zeta}_1$ and $\boldsymbol{\zeta}_2$ are solutions of $4/\pi \mathbf{B} \cdot \boldsymbol{\zeta}_1 = \mathbf{1}$ and $4/\pi \mathbf{B} \cdot \boldsymbol{\zeta}_2 = \mathbf{H}$, respectively. U_{el} is then obtained as

$$U_{\text{el}} = \frac{F^* + \mathbf{A}^T \cdot \boldsymbol{\zeta}_2}{\mathbf{A}^T \cdot \boldsymbol{\zeta}_1}. \quad (\text{A12})$$

References

- ANGEVINE, C. L. & TURCOTTE, D. L. 1983. Porosity reduction by pressure solution: a theoretical model for quartz arenites. *Geological Society of America Bulletin*, **94**, 1129–1134.
- BEELER, N. M. & HICKMAN, S. H. 2004. Stress-induced, time-dependent fracture closure at hydrothermal conditions. *Journal of Geophysical Research*, **109**, B02211, doi:10.1029/2002JB001782.
- BOS, B. & SPIERS, C. J. 2002. Frictional-viscous flow of phyllosilicate-bearing fault rock: microphysical model and implications for crustal strength profiles. *Journal of Geophysical Research*, **107**, 2028, doi:10.1029/2001JB000301.
- DE MEER, S. & SPIERS, C. J. 1995. Creep of wet gypsum aggregates under hydrostatic loading conditions. *Tectonophysics*, **245**, 171–183.
- DE MEER, S., SPIERS, C. J., PEACH, C. J. & WATANABE, T. 2002. Diffusive properties of fluid-filled grain boundaries measured electrically during active pressure solution. *Earth and Planetary Science Letters*, **200**, 147–157.
- DE MEER, S., SPIERS, C. J. & NAKASHIMA, S. 2005. Structure and diffusive properties of fluid-filled grain boundaries: an *in-situ* study using infrared (micro) spectroscopy. *Earth Planetary Science Letters*, **232**, 403–414.
- DEN BROK, S. W. J. 1998. Effect of microcracking on pressure-solution strain rate: the Gratz grain-boundary model. *Geology*, **26**, 915–918.
- DEWERS, T. & HAJASH, A. 1995. Rate laws for water-assisted compaction and stress-induced water–rock interaction in sandstones. *Journal of Geophysical Research*, **100**, 13093–13112.
- DURNEY, D. W. 1972. Solution transfer, an important geological deformation mechanism. *Nature*, **237**, 315–317.
- ENGELDER, T., GEISER, P. A. & ALVAREZ, W. 1981. Role of pressure solution and dissolution in geology. *Geology*, **9**, 44–45.
- GHOUSSOUB, J. & LEROY, Y. M. 2001. Solid–fluid phase transformation within grain boundaries during

- compaction by pressure solution. *Journal of Mechanics and Physics of Solids*, **49**, 2385–2430.
- GRATIER, J.-P. 1987. Pressure solution–deposition creep and associated tectonic differentiation in sedimentary rocks. In: JONES, M. E. & PRESTON, R. M. F. (eds) *Deformation of Sediments and Sedimentary Rocks*. Geological Society, London, Special Publications, **29**, 25–38.
- GRATIER, J.-P. 1993a. Pressure solution–deposition creep of rocks in the upper crust. *Bulletin de la Société Géologique de France*, **164**, 267–287.
- GRATIER, J.-P. 1993b. Experimental pressure solution of halite by an indenter technique. *Geophysical Researchers Letters*, **20**, 1647–1650.
- GRATIER, J.-P. & GUIGUET, R. 1986. Experimental pressure solution–deposition on quartz grains: the crucial effect of the nature of the fluid. *Journal of Structural Geology*, **8**, 845–856.
- GRATZ, A. J. 1991. Solution-transfer compaction of quartzites: progress toward a rate law. *Geology*, **19**, 901–904.
- GUNDERSEN, E., DYSTHE, D. K., RENARD, F., BJORLYKKE, K. & JAMTVEIT, B. 2002. Numerical modelling of pressure solution in sandstone, rate-limiting processes and the effect of clays. In: DE MEER, S., DRURY, M. R., DE BRESSER, J. H. P. & PENNOCK, G. M. (eds) *Deformation Mechanisms, Rheology and Tectonics: Current Status and Future Perspectives*. Geological Society, London, Special Publications, **200**, 41–56.
- HELLMANN, R., RENDER, P. J. N., GRATIER, J.-P. & GUIGUET, R. 2002. Experimental pressure solution compaction of chalk in aqueous solutions, I. Deformation behavior and chemistry. In: HELLMANN, R. & WOOD, S. A. (eds) *Water–Rock Interactions, Ore Deposits, and Environmental Geochemistry: a Tribute to David A. Crerar*. Geological Society, London, Special Publications, **7**, 129–152.
- HICKMAN, S. H. & EVANS, B. 1991. Experimental pressure solution in halite: the effect of grain/interphase boundary structure. *Journal of the Geological Society, London*, **148**, 549–560.
- HICKMAN, S. H. & EVANS, B. 1992. Growth of grain contacts in halite by solution transfer: implications for diagenesis, lithification, and strength recovery. In: EVANS, B. & WONG, T.-F. (eds) *Fault Mechanics and Transport Properties of Rocks*. Academic Press, San Diego, CA, 253–280.
- HICKMAN, S. H. & EVANS, B. 1995. Kinetics of pressure solution of halite–silica interfaces and intragranular clay films. *Journal of Geophysical Research*, **100**, 13113–13132.
- JOHNSON, K. L. 1985. *Contact Mechanics*. Cambridge University Press, New York.
- KARCZ, Z., AHARONOV, E., ERTAS, D., POLIZZOTTI, R. & SCHOLZ, C. H. 2005. The evolution of grain contacts undergoing pressure solution: unique insights from a confocal viewpoint (abstract). *Geochimica et Cosmochimica Acta*, **69**, A301.
- KARNER, S. L., MARONE, C. & EVANS, B. 1997. Laboratory study of fault healing and lithification in simulated fault gouge under hydrothermal conditions. *Tectonophysics*, **277**, 41–55.
- LEHNER, F. K. 1990. Thermodynamics of rock deformation by pressure solution. In: BARBER, D. J. & MEREDITH, P. G. (eds) *Deformation Processes in Minerals, Ceramics and Rocks*. Unwin Hyman, London, 296–333.
- LEHNER, F. K. 1995. A model for intergranular pressure solution in open systems. *Tectonophysics*, **245**, 153–170.
- LEHNER, F. K. & BATAILLE, J. 1984. Nonequilibrium thermodynamics of pressure solution. *Pure and Applied Geophysics*, **122**, 53–85.
- LEHNER, F. K. & LEROY, Y. 2004. Sandstone compaction by intergranular pressure solution. In: GUÉGUEN, Y. & BOUTÉCA, M. (eds) *Mechanics of Fluid-Saturated Rocks*. International Geophysics Series, **89**, 115–168.
- LI, H. & DEMPSEY, J. P. 1990. Axisymmetric contact of an elastic layer underlain by rigid base. *International Journal of Numerical Methods in Engineering*, **29**, 57–72.
- MULLIS, A. M. 1993. Determination of the rate-limiting mechanism for quartz pressure solution. *Geochimica et cosmochimica Acta*, **57**, 1499–1503.
- NIEMEIJER, A. R., SPIERS, C. J. & BOS, B. 2002. Compaction creep of quartz sand at 400–600 °C: experimental evidence for dissolution-controlled pressure solution. *Earth and Planetary Science Letters*, **195**, 261–275.
- PATERSON, M. S. 1973. Nonhydrostatic thermodynamics and its geologic applications. *Review of Geophysics and Space Physics*, **11**, 355–389.
- PATERSON, M. S. 1995. A theory for granular flow accommodated by material transfer via an intergranular fluid. *Tectonophysics*, **245**, 135–151.
- PRESS, W. H., FLANNERY, B. P., TEUKOLSKY, S. A. & VETTERLING, W. T. 1988. *Numerical Recipes in C: the Art of Scientific Computing*. Cambridge University Press, New York.
- RAJ, R. 1982. Creep in polycrystalline aggregates by matter transport through a liquid phase. *Journal of Geophysical Research*, **87**, 4731–4739.
- RENARD, F. & ORTOLEVA, P. 1997. Water films at grain–grain contacts: Debye–Hückel osmotic model of stress, salinity, and mineralogy dependence. *Geochimica et cosmochimica Acta*, **61**, 1963–1970.
- RENARD, F., PARK, A., ORTOLEVA, P. & GRATIER, J.-P. 1999. An integrated model for transitional pressure solution in sandstones. *Tectonophysics*, **312**, 97–115.
- RENARD, F., BROSSE, E. & GRATIER, J.-P. 2000. The different processes involved in the mechanism of pressure solution in quartz-rich rocks and their interactions. In: WORDEN, R. & MORAD, S. (eds) *Quartz Cement in Oil Field Sandstones*. Special Publication, International Association of Sedimentologists, **29**, 67–78.
- REVIL, A. 1999. Pervasive pressure-solution transfer: a poro-visco-plastic model. *Geophysical Researchers Letters*, **26**, 255–258.
- REVIL, A. 2001. Pervasive pressure-solution transfer in a quartz sand. *Journal of Geophysical Research*, **106**, 8665–8686.
- RUTTER, E. H. 1976. The kinetics of rock deformation by pressure solution. *Philosophical Transactions of the Royal Society of London Series A*, **283**, 203–219.

- RUTTER, E. H. 1983. Pressure solution in nature, theory and experiment. *Journal of the Geological Society, London*, **140**, 725–740.
- SCHUTJENS, P. M. T. M. 1991. Experimental compaction of quartz sand at low effective stress and temperature conditions. *Journal of the Geological Society, London*, **148**, 527–539.
- SHIMIZU, I. 1995. Kinetics of pressure solution creep in quartz: theoretical considerations. *Tectonophysics*, **245**, 121–134.
- SLEEP, N. H. & BLANPIED, M. L. 1992. Creep, compaction and the weak rheology of major faults. *Nature*, **359**, 687–692.
- SPIERS, C. J. & SCHUTJENS, P. M. T. M. 1990. Densification of crystalline aggregates by fluid-phase diffusional creep. In: BARBER, D. J. & MEREDITH, P. G. (eds) *Deformation Processes in Minerals, Ceramics and Rocks*. Unwin Hyman, London, 334–353.
- STEPHENSON, L. P., PLUMLEY, W. J. & PALCIAUSKAS, V. V. 1992. A model for sandstone Compaction by grain interpenetration. *Journal of Sedimentary Petrology*, **62**, 11–22.
- TADA, R. & SIEVER, R. 1986. Experimental knife-edge pressure solution of halite. *Geochimica et Cosmochimica Acta*, **50**, 29–36.
- TADA, R., MALIVA, R. & SIEVER, R. 1987. A new mechanism for pressure solution in porous quartzose sandstone. *Geochimica et Cosmochimica Acta*, **51**, 2295–2301.
- TSANG, C. F. 1991. Coupled hydromechanical-thermochemical processes in rock fractures. *Reviews of Geophysics*, **29**, 537–551.
- WEYL, P. K. 1959. Pressure solution and force for crystallization: a phenomenological theory. *Journal of Geophysical Research*, **64**, 2001–2005.
- YASUHARA, H., ELSWORTH, D. & POLAK, A. 2003. A mechanistic model for compaction of granular aggregates moderated by pressure solution. *Journal of Geophysical Research*, **108**, 2530, doi:10.1029/2003JB002536.
- YASUHARA, H., ELSWORTH, D. & POLAK, A. 2004. Evolution of permeability in a natural fracture: significant role of pressure solution. *Journal of Geophysical Research*, **109**, 3204, doi:10.1029/2003JB002663.

Weak elastic anisotropy in a cracked rock

T.-F. WONG & W. ZHU

Department of Geosciences, State University of New York at Stony Brook, Stony Brook,
NY 11794-2100, USA (e-mail: Teng-fong.Wong@stonybrook.edu)

Abstract: The elastic properties of a cracked rock are transversely isotropic if its crack density distribution is axisymmetric. The three Thomsen parameters ϵ , δ and γ are used to characterize the seismic properties of a weakly anisotropic rock. In this study we calculated these anisotropy parameters in such a cracked rock under dry and saturated conditions. We derived analytic expressions for a dry rock based on an approximate model proposed by earlier workers, which shows elliptically anisotropic behaviour. Guided by microstructural observations we adopted a two-parameter axisymmetric distribution to characterize the crack density, which predicts that in a fluid-saturated rock the parameters δ and γ are related to ϵ in a nonlinear manner. All three parameters considered are sensitively dependent on the difference in the densities of cracks with normals parallel and perpendicular to the symmetry axis. Theoretical predictions of the model are compared with laboratory and field measurements of seismic anisotropy.

Crack and textural fabrics have significant control over the development of mechanical anisotropy in a rock. Bedding in sedimentary rocks, cleavage in slates, preferred orientation of anisotropic minerals and anisotropic distribution of microcracks can all contribute to elastic anisotropy, a seismic manifestation of which is shear-wave splitting (Crampin 1981). Even though seismic anisotropy is often weak, the investigation of this phenomenon has evolved to become a useful tool for deciphering rock physics attributes in a reservoir (Helbig & Thomsen 2005).

Analysis of elastic-wave propagation in an anisotropic medium can be highly complex. In many geophysical applications the vertical direction can be considered to be a symmetry axis, so that the material anisotropy can be approximated as transversely isotropic. In a seminal paper, Thomsen (1986) proposed the use of three dimensionless parameters γ , δ and ϵ to characterize seismic anisotropy in a transversely isotropic rock, and demonstrated that in a weakly anisotropic rock the seismic velocities are given by relatively simple expressions in terms of these three parameters. Since then, extensive data on these three 'Thomsen parameters' have been acquired in the laboratory (Wang 2002), thus providing the rock physics basis for the analysis of seismic anisotropy phenomena in the field.

In many geological settings the orientations of microcracks in a rock and fractures in a rock mass are not randomly distributed. A preferred orientation may be associated with the tectonic stress field or pre-existing textural fabric. When such an anisotropic system of cracks is embedded in the rock matrix, the effective elastic properties will also be anisotropic. In particular, the elastic behaviour is transversely isotropic for an axisymmetric

crack system embedded in an isotropic rock matrix. A comprehensive analysis of such crack-induced elastic anisotropy was presented by Kachanov (1992, 1993), who derived explicit expressions for the elastic moduli of the cracked rock in terms of two tensors that characterize the crack fabric.

To our knowledge similar expressions have not been derived for the Thomsen anisotropy parameters, notwithstanding the many useful applications they have in the analysis of seismic anisotropy. An aim of this study is to establish the connection between these anisotropy parameters and the crack fabric tensors. The theoretical predictions are compared with laboratory and field data on seismic anisotropy, as well as microstructural characterization of microcrack density and orientation distribution in unstressed and stressed rocks.

Thomsen's parameters for elastic-wave propagation in a weakly anisotropic medium

The elastic stiffness tensor of a transversely isotropic material is specified by five independent constants (Nye 1985). If the axis of symmetry is aligned with the x_3 -axis, then the non-vanishing components are given by $C_{11} = C_{22}$, C_{33} , C_{12} , $C_{13} = C_{23}$, $C_{44} = C_{55}$ and $C_{66} = (C_{11} - C_{12})/2$, where we have adopted the Voigt (contracted matrix) notation to describe the stiffness tensor. To characterize the anisotropic behaviour of a transversely isotropic rock, Thomsen (1986) introduced three parameters γ , δ and ϵ , which, together with the velocities α and β for P and S waves can all be expressed in terms of the density ρ and the five

elastic stiffness components as

$$\alpha = \sqrt{\frac{C_{33}}{\rho}} \quad (1a)$$

$$\beta = \sqrt{\frac{C_{44}}{\rho}} \quad (1b)$$

$$\varepsilon = \frac{C_{11} - C_{33}}{2C_{33}} \quad (1c)$$

$$\gamma = \frac{C_{66} - C_{44}}{2C_{44}} \quad (1d)$$

$$\delta = \frac{(C_{13} + C_{44})^2 - (C_{33} - C_{44})^2}{2C_{33}(C_{33} - C_{44})}. \quad (1e)$$

In a transversely isotropic rock for which γ , δ and ε have magnitudes much less than one, terms of higher order involving these parameters can be neglected, and Thomsen (1986) showed that for such a weakly anisotropic rock the angular variations of the phase velocities (for the three modes of propagation with mutually orthogonal polarizations) in any plane containing the symmetry axis are given by the following relations:

$$V_P(\theta) \approx \alpha(1 + \delta \sin^2 \theta \cos^2 \theta + \varepsilon \sin^4 \theta) \quad (2a)$$

$$V_{SV}(\theta) \approx \beta \left(1 + \frac{\alpha^2}{\beta^2} (\varepsilon - \delta) \sin^2 \theta \cos^2 \theta \right) \quad (2b)$$

$$V_{SH}(\theta) \approx \beta(1 + \gamma \sin^2 \theta) \quad (2c)$$

where V_{SH} is the wave-front velocity of the pure shear wave (with polarized component in the x_3 direction), V_{SV} is the pseudo-shear wave polarized normal to the pure shear wave, and V_P is the pseudo-longitudinal wave. The phase angle between the wave-front normal and the symmetry axis x_3 is denoted by θ . These approximations are significantly simpler than the full expressions for a transversely isotropic rock (Mavko *et al.* 1998).

Crack fabric and elastic anisotropy

Our analysis closely follows Kachanov's (1992, 1993) formulation and comprehensive analysis of the effects of microcracks on the elastic moduli of a porous material. If a multiplicity of microcracks are embedded in its matrix, a rock will become more compliant, and accordingly its elastic compliance tensor will increase from the initial value S_{ijkl}^o (corresponding to that of the porosity-free solid matrix) to $S_{ijkl} = S_{ijkl}^o + \Delta S_{ijkl}$. In the Voigt matrix notation these quantities can alternatively be written as

$S_{ij} = S_{ij}^o + \Delta S_{ij}$. Here we will restrict our attention to the case when the rock matrix is isotropic, so that its elastic stiffness can be specified in terms of the Young's modulus E_o and Poisson's ratio v_o .

The perturbation of elastic compliance as a result of the introduction of a single planar crack into the solid matrix is described by the 'crack compliance tensor' B_{ij} , a symmetric second rank tensor that can conveniently be separated into a normal component B_N and tangential component B_T so that

$$B_{ij} = B_N n_i n_j + B_T (\delta_{ij} - n_i n_j) \quad (3)$$

where δ_{ij} is the Kronecker delta and n_i is the unit vector representing the outward normal to the crack plane. For a penny-shaped crack with radius c embedded in an isotropic elastic solid the shear and normal compliances are given by (Kachanov 1993)

$$B_T = \frac{32}{3\pi} \frac{(1 - v_o^2)c}{E_o(2 - v_o)} = \frac{gc}{\pi E_o} \quad (4a)$$

$$\frac{B_N}{B_T} = \left(1 - \frac{v_o}{2} \right) \left(\frac{\xi}{1 + \xi} \right) \quad (4b)$$

with the parameters g and ξ defined by

$$g = \frac{32}{3} \frac{(1 - v_o^2)}{(2 - v_o)} \quad (5a)$$

$$\xi = \frac{3\pi E_o \beta_f \langle w \rangle}{16(1 - v_o^2) c} \quad (5b)$$

where $\langle w \rangle$ and β_f denote the average half-aperture of the penny-shaped cracks and compressibility of the fluid, respectively.

Crack density tensors and elastic anisotropy

For a relatively dilute concentration of N cracks embedded in a volume V , their collective influence on the elastic compliance can be expressed in terms of two symmetric tensors: the second-rank tensor α_{ij} (or normalized tensor α_{ij}^*) dependent on the shear compliance

$$\alpha_{ij} = \frac{g}{E_o} \alpha_{ij}^* = \frac{1}{V} \sum_{r=1}^N B_T^r n_i^r n_j^r S_r \quad (6a)$$

and the fourth-rank tensor β_{ijkl} (or normalized tensor β_{ijkl}^*) dependent on the difference between the normal and shear compliance

$$\beta_{ijkl} = \frac{g}{E_o} \beta_{ijkl}^* = \frac{1}{V} \sum_{r=1}^N (B_N^r - B_T^r) n_i^r n_j^r n_k^r n_l^r S_r \quad (6b)$$

where S_r denotes the surface area of the r th crack. Specifically, the overall increase in elastic

compliance is given by

$$\Delta S_{ijkl} = \frac{1}{4} (\delta_{ik}\alpha_{jl} + \delta_{il}\alpha_{jk} + \delta_{jk}\alpha_{il} + \delta_{jl}\alpha_{ik}) + \beta_{ijkl} \quad (7)$$

with the assumption that the mechanical interaction among the N cracks is negligible.

If we focus on a transversely isotropic rock (with symmetry axis x_3) associated with an axisymmetric distribution of microcracks embedded in an isotropic elastic matrix, then the symmetry condition necessarily requires that $\alpha_{11} = \alpha_{22}$, $\beta_{1111} = \beta_{2222}$ and $\beta_{1122} = \beta_{1212} = \beta_{1111}/3$. Our aim is to calculate the Thomsen parameters, and before substituting into equations (1a)–(1e) we need to invert equation (7) to obtain the elastic stiffness tensor, which was given by Sayers & Kachanov (1995) in their equations (22)–(28). Using the Voigt notation and our normalization scheme, the non-vanishing components of the elastic stiffness of the cracked rock are given by

$$C_{11} + C_{12} = \frac{1 + g(\alpha_{33}^* + \beta_{3333}^*)}{E_o D} \quad (8a)$$

$$C_{11} - C_{12} = \frac{E_o}{(1 + v_o) + g(\alpha_{11}^* + 2\beta_{1111}^*/3)} \quad (8b)$$

$$C_{33} = \frac{(1 - v_o) + g(\alpha_{11}^* + 4\beta_{1111}^*/3)}{E_o D} \quad (8c)$$

$$C_{44} = \frac{E_o}{2(1 + v_o) + g(\alpha_{11}^* + \alpha_{33}^* + 4\beta_{1133}^*)} \quad (8d)$$

$$C_{13} = C_{23} = \frac{v_o - g\beta_{1133}^*}{E_o D} \quad (8e)$$

$$C_{66} = \frac{C_{11} - C_{12}}{2} = \frac{E_o}{2[(1 + v_o) + g(\alpha_{11}^* + 2\beta_{1111}^*/3)]} \quad (8f)$$

with $DE_o^2 = (1 + g(\alpha_{33}^* + \beta_{3333}^*)) \times (1 - v_o + g(\alpha_{11}^* + 4\beta_{1111}^*/3)) - 2(v_o - g\beta_{1133}^*)^2$.

Sayers & Kachanov's model for a dry rock

To analyse stress-induced anisotropy in a dry rock Sayers & Kachanov (1995) introduced an approximate model, which simplifies the mathematics considerably. It turns out that this approximation also allows us to arrive at some rather simple results for seismic anisotropy and provides a micro-mechanical basis for the end-member case of 'elliptic anisotropy' with $\delta = \epsilon$.

With reference to equation (5b) applied to a dry rock, the saturating fluid is air (which is highly compressible) and accordingly $\beta_f \gg 1$, $\xi \gg 1$, which implies that $\xi/(1 + \xi) \approx 1$. Sayers & Kachanov (1995) further argued that in most rocks Poisson's ratio $v_o \ll 2$, which implies that equations (4b) and (6b) can be simplified to $B_N \approx B_T$ and $\beta_{ijkl} = 0$. In this approximate model the microcrack anisotropy is specified by the second-rank tensor alone, and consequently the components of the elastic stiffness are simply given by

$$C_{11} + C_{12} = \frac{1 + g\alpha_{33}^*}{E_o D} \quad (9a)$$

$$C_{11} - C_{12} = \frac{E_o}{(1 + v_o) + g\alpha_{11}^*} \quad (9b)$$

$$C_{33} = \frac{(1 - v_o) + g\alpha_{11}^*}{E_o D} \quad (9c)$$

$$C_{44} = \frac{E_o}{2(1 + v_o) + g(\alpha_{11}^* + \alpha_{33}^*)} \quad (9d)$$

$$C_{13} = C_{23} = \frac{v_o}{E_o D} \quad (9e)$$

$$C_{66} = \frac{C_{11} - C_{12}}{2} = \frac{E_o}{2[(1 + v_o) + g\alpha_{11}^*]} \quad (9f)$$

with $DE_o^2 = (1 + g\alpha_{33}^*)(1 - v_o + g\alpha_{11}^*) - 2v_o^2$. On substituting these expressions into equations (1c), (1d) and (1e) and some algebra, we arrive at these relatively simple relations for the Thomsen anisotropy parameters:

$$\epsilon = \delta = \frac{g(\alpha_{33}^* - \alpha_{11}^*)(1 + g\alpha_{11}^*)}{2[(1 + g\alpha_{11}^*)^2 - v_o^2]} \quad (10a)$$

$$\gamma = \frac{g(\alpha_{33}^* - \alpha_{11}^*)}{4(1 + v_o + g\alpha_{11}^*)} = \frac{(1 - v_o + g\alpha_{11}^*)}{2(1 + g\alpha_{11}^*)} \epsilon \quad (10b)$$

Several features of these results are worth noting. First, the Thomsen parameters depend on only the crack density tensor and Poisson's ratio of the solid matrix. It will be shown below that whereas the anisotropy parameters would depend also on the fourth-rank tensor β_{ijkl} for the more exact analysis of both fluid-saturated and dry rocks, they remain independent of the Young's modulus of the matrix. A Poisson's ratio of $v_o = 0.2$ identical to the value used by Sayers & Kachanov (1995) will be assumed in all numerical calculations in this paper.

Second, the identity $\epsilon = \delta$ implies that only four independent components are required to characterize the stiffness of a transversely isotropic

rock, and it defines what is commonly referred to as 'elliptically anisotropic' behaviour (Thomsen 1986), which is associated with P wave-fronts emanating from a point source that are elliptical in shape (in any plane containing the symmetry axis of the transversely isotropic rock). Although this idealization is often invoked in the analysis of seismic propagation in an anisotropic medium, Berryman (1979) and Helbig (1979) have argued that elliptic anisotropy is not a good model for many scenarios, such as anisotropy induced by the alignment of fine layers of isotropic materials, for which one expects $\delta < \varepsilon$. However, the results here show that elliptic anisotropy would indeed develop in an axisymmetrically cracked rock under conditions as stipulated by Sayers & Kachanov (1995) in their dry rock model. It should also be noted that although the Thomsen parameters were proposed for a weakly anisotropic material, the conclusion on elliptic anisotropy here is valid even for large values of δ and ε , provided the assumption of Sayers & Kachanov (1995) that the cracks are non-interactive remains valid.

Third, the Thomsen parameters according to equations (10a) and (10b) increase linearly with the crack density difference $\alpha_{33}^* - \alpha_{11}^*$ (Fig. 1). The microstructural interpretation of this behaviour requires first specifying the geometric attributes of microcracks in the rock, which will be addressed in the next section. To consider the more general case of a fluid-saturated rock, we also need to include the fourth-rank tensor β_{ijkl} in the analysis.

An axisymmetric model of microcrack anisotropy

In selecting a statistical model for anisotropic distribution of microcracks we were guided by microstructural observations and quantitative characterization of microcrack density in rocks. Previous microstructural studies of triaxially compressed rocks show that the crack density distribution can be approximated by the superimposition of an isotropic distribution and a set of stress-induced cracks aligned subparallel to the maximum compression direction (e.g. Wong 1985; Hoxha & Homand 2000; Takemura & Oda 2005). In a rock with strong bedding anisotropy such as shale the cracks seem to align subparallel to the bedding planes (e.g. Johnston & Christensen 1995; Hornby 1998; Sayers 1999). With reference to the coordinate system shown in Figure 2a, these microstructural observations suggest the use of the following axisymmetric distribution of microcrack density:

$$f(\theta, \phi) = a + b\delta(\theta) \quad (11)$$

where $\delta(\theta)$ is the Dirac delta function, corresponding to a set of microcracks with normals preferentially aligned with the direction $\theta = 0$ (i.e. the x_3 -axis).

Both positive and negative values of b will be considered. If $b > 0$ the elastic anisotropy arises from arrays of cracks parallel to the $x_1 - x_2$ plane (Fig. 2b), and consequently the minimum elastic stiffness and seismic velocities are along the x_3 direction. If $b < 0$ the elastic anisotropy arises from arrays of cracks parallel to the x_3 direction (Fig. 2c), and consequently the maximum elastic stiffness and seismic velocities are along this direction.

Following Schubnel & Guéguen (2003) we will assume that the penny-shaped cracks have uniform radius c , and on substituting equations (4a) and (4b) into (6a) and (6b) we can relate the crack density tensors to geometric attributes of the cracks:

$$\alpha_{ij}^* = \frac{c^3}{V} \sum_{r=1}^N n_i^r n_j^r = \frac{Nc^3}{V} \langle n_i n_j \rangle = \alpha_{mm}^* \langle n_i n_j \rangle \quad (12a)$$

$$\begin{aligned} \beta_{ijkl}^* &= \frac{Nc^3}{V} \left[\left(1 - \frac{v_o}{2}\right) \frac{\xi}{1+\xi} - 1 \right] \sum_{r=1}^N n_i^r n_j^r n_k^r n_l^r \\ &= \left[\left(1 - \frac{v_o}{2}\right) \frac{\xi}{1+\xi} - 1 \right] \alpha_{mm}^* \langle n_i n_j n_k n_l \rangle. \end{aligned} \quad (12b)$$

The bracket $\langle \rangle$ is used here to denote the mean value of a quantity that varies with orientation. Given a continuous distribution such as (11) the mean value can be calculated as

$$\langle h \rangle = \frac{1}{2\pi} \int_0^{2\pi} d\phi \int_0^{\pi/2} hf(\theta, \phi) \sin \theta d\theta. \quad (13)$$

With reference to the coordinate system in Figure 2a, the outward normal can be expressed as functions of the angles θ and ϕ , and after calculating the mean values using (13) they were substituted into (12a) and (12b) to arrive at the following expressions for the second-rank tensor:

$$\alpha_{11}^* = \alpha_{22}^* = a/3 \quad (14a)$$

$$\alpha_{33}^* = a/3 + b \quad (14b)$$

with $\alpha_{ii}^* = Nc^3/V = a + b$, and therefore the angular distribution of crack density is

$$f(\theta, \phi) = \frac{Nc^3}{V} \left[\frac{a}{(a+b)} + \frac{b}{(a+b)} \delta(\theta) \right]. \quad (14c)$$

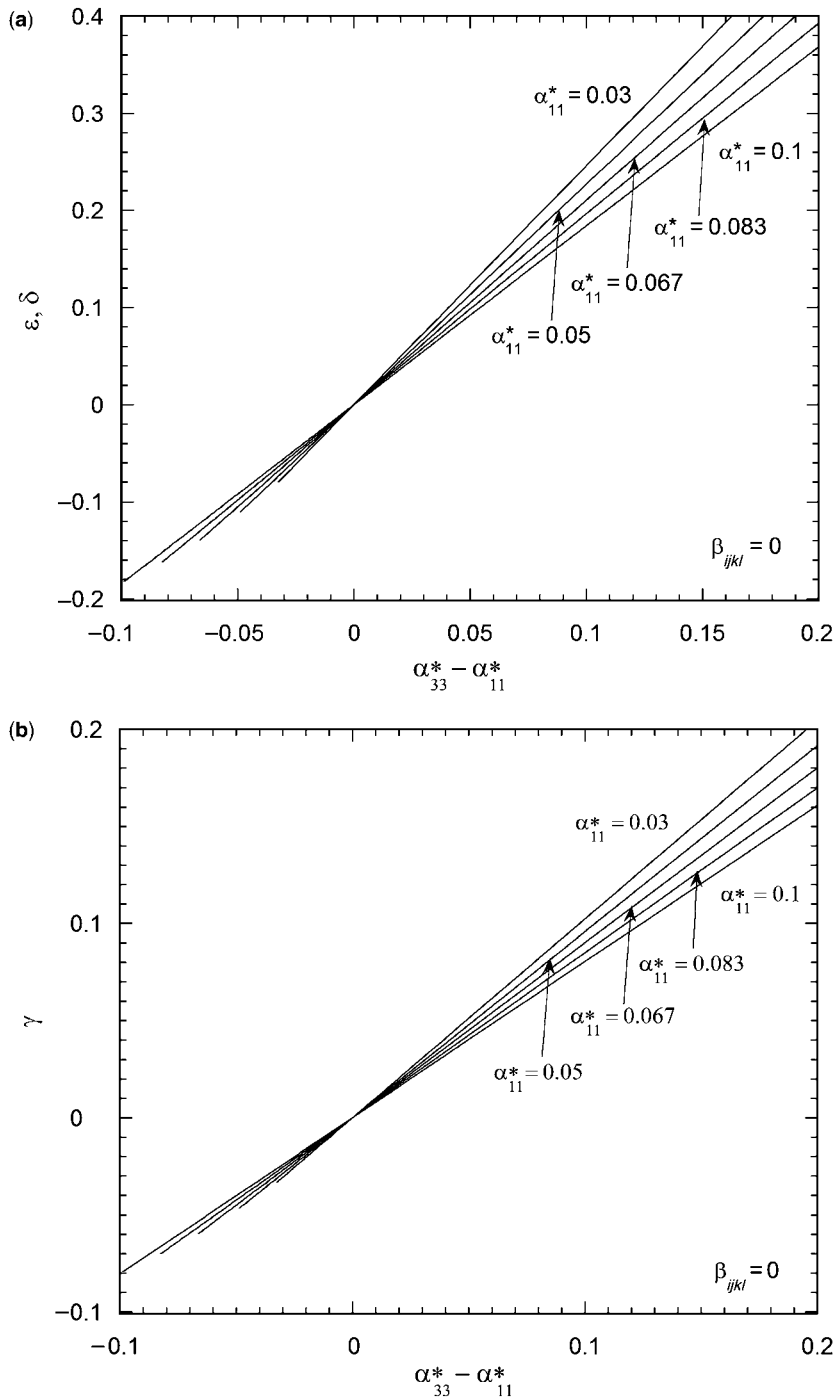


Fig. 1. The Thomsen parameters (a) ϵ and δ , (b) γ as functions of crack density difference $\alpha_{33}^* - \alpha_{11}^*$ for a dry rock with $\beta_{ijkl} = 0$ and α_{11}^* ranging from 0.03 to 0.1.

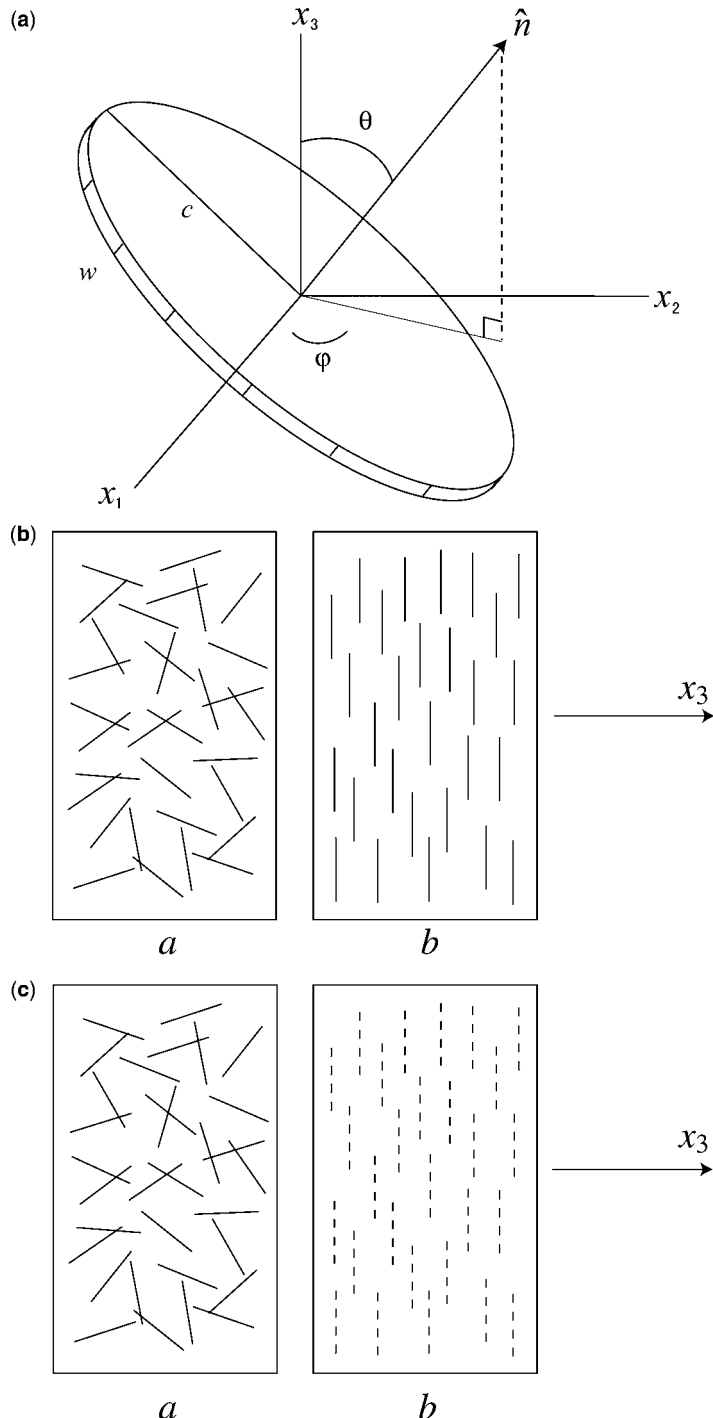


Fig. 2. (a) A penny-shaped crack with radius c and half-aperture w . The angle between the crack normal \hat{n} and axis x_3 is denoted by θ , and azimuthal angle is denoted by ϕ . (b) Conceptual model for the axisymmetric distribution of microcrack density given by equation (11) where a represents a system of randomly oriented cracks and $b > 0$ represents those at the preferred orientation parallel to the $x_1 - x_2$ -plane. (c) Same as (b) for $b < 0$ where dashed lines represent closed cracks in that direction.

The fourth-rank tensor is given by

$$\beta_{1111}^* = \beta_{2222}^* \\ = \left[\left(1 - \frac{v_o}{2} \right) \left(\frac{\xi}{1 + \xi} \right) - 1 \right] \frac{a(a+b)}{5} \quad (15a)$$

$$\beta_{3333}^* = \left[\left(1 - \frac{v_o}{2} \right) \left(\frac{\xi}{1 + \xi} \right) - 1 \right] \\ \times \frac{(a+5b)(a+b)}{5} \quad (15b)$$

$$\beta_{1133}^* = \left[\left(1 - \frac{v_o}{2} \right) \left(\frac{\xi}{1 + \xi} \right) - 1 \right] \frac{a(a+b)}{15}. \quad (15c)$$

Thomsen's parameters for a fluid-saturated rock

Equations (14a), (14b) and (15a)–(15c) can be substituted first into equations (8a)–(8f) to obtain the stiffness, and then into equations (1a)–(1e) to arrive at the Thomsen anisotropy parameters. In these calculations the values of ξ need to be specified first. To describe the influence of a saturating fluid on the elastic response of a cracked solid Kachanov (1992, 1993) introduced this parameter, which is related to the undrained response in an isolated crack to a stress perturbation. To evaluate ξ we can use (5b) and substitute into it appropriate values for the elastic moduli (Schubnel & Guéguel 2003). As noted above, although the expressions derived here depend on Poisson's ratio, the Young's modulus does not appear in most of them. Accordingly, we decided to express equation (5b) in a somewhat different form, circumventing the use of E_o and introducing instead a quantity that can be constrained by laboratory measurements.

A thin crack is readily closed when subjected to a sufficiently high hydrostatic pressure. For a penny-shaped crack of radius c and aspect ratio $\langle w \rangle/c$, this 'crack closure pressure' is given by (Walsh 1965)

$$P_{\text{cr}} = \frac{\pi E_o}{4(1 - v_o^2)} \frac{\langle w \rangle}{c} \quad (16a)$$

which, on substituting into (5b), gives the simple result

$$\xi = (3/4)P_{\text{cr}}\beta_f. \quad (16b)$$

The crack closure pressure can be inferred from the nonlinear elastic response of a rock to hydrostatic loading (Brace 1965). In a relatively compact rock

it has a value of the order of 100 MPa, and as the compressibility of water under room conditions is 4.4×10^{-4} MPa $^{-1}$ this would give an estimate of $\xi \approx 0.033$. In this case, we can neglect the contribution of ξ to the fourth-rank tensor and rewrite equation (12b) as

$$\beta_{ijkl}^* = -\alpha_{mm}^* \langle n_i n_j n_k n_l \rangle. \quad (17a)$$

However, it should be noted that porous sedimentary rocks often contain almost equant voids of relatively high aspect ratio, which may remain open even if the rock is subjected to a pressure of several hundred MPa. Indeed, Louis *et al.* (2003) recently inferred from the P-wave anisotropy measurements that the anisotropy in Bentheim sandstone arises from the elastic fabric related to such pores. In this case, a value of $P_{\text{cr}} \approx 100$ MPa would underestimate the fluid interaction effect, and it is then questionable whether ξ can be approximated as zero.

As noted above, the compressibility β_f for air is so high that in a dry rock the fourth-rank tensor is given by

$$\beta_{ijkl}^* = -(v_o/2)\alpha_{mm}^* \langle n_i n_j n_k n_l \rangle. \quad (17b)$$

We present here our calculations for the three Thomsen parameters using the axisymmetric crack distribution (11). Equations (12a) and (12b) were used to calculate the seismic anisotropy in a fluid-saturated rock and dry rock, respectively. Overall the results for the dry case (Fig. 3) are similar to those for Sayers & Kachanov's (1995) model (Fig. 1). The three parameters increase almost linearly with the crack density difference $\alpha_{33}^* - \alpha_{11}^* = b$. The two parameters ϵ and δ are almost equal, but at large values of crack density difference the latter deviates slightly from the linear trend so that we have $\epsilon > \delta$. In contrast, the results for the saturated case (Fig. 4) are different. As functions of the crack density difference, ϵ and δ do not follow linear trends. Both would initially increase to attain a peak and then decrease with increasing b .

Comparison with laboratory and field measurements

Our model makes rather specific predictions on the correlation between the three Thomsen parameters. In a dry cracked rock the ratios δ/ϵ and γ/ϵ are predicted to be close to one and $1/2$, respectively (equations (10a) and (10b) and Fig. 3). In a water-saturated rock these ratios are not constant, and therefore the parameters δ and γ as functions of ϵ are given by the nonlinear curves shown in

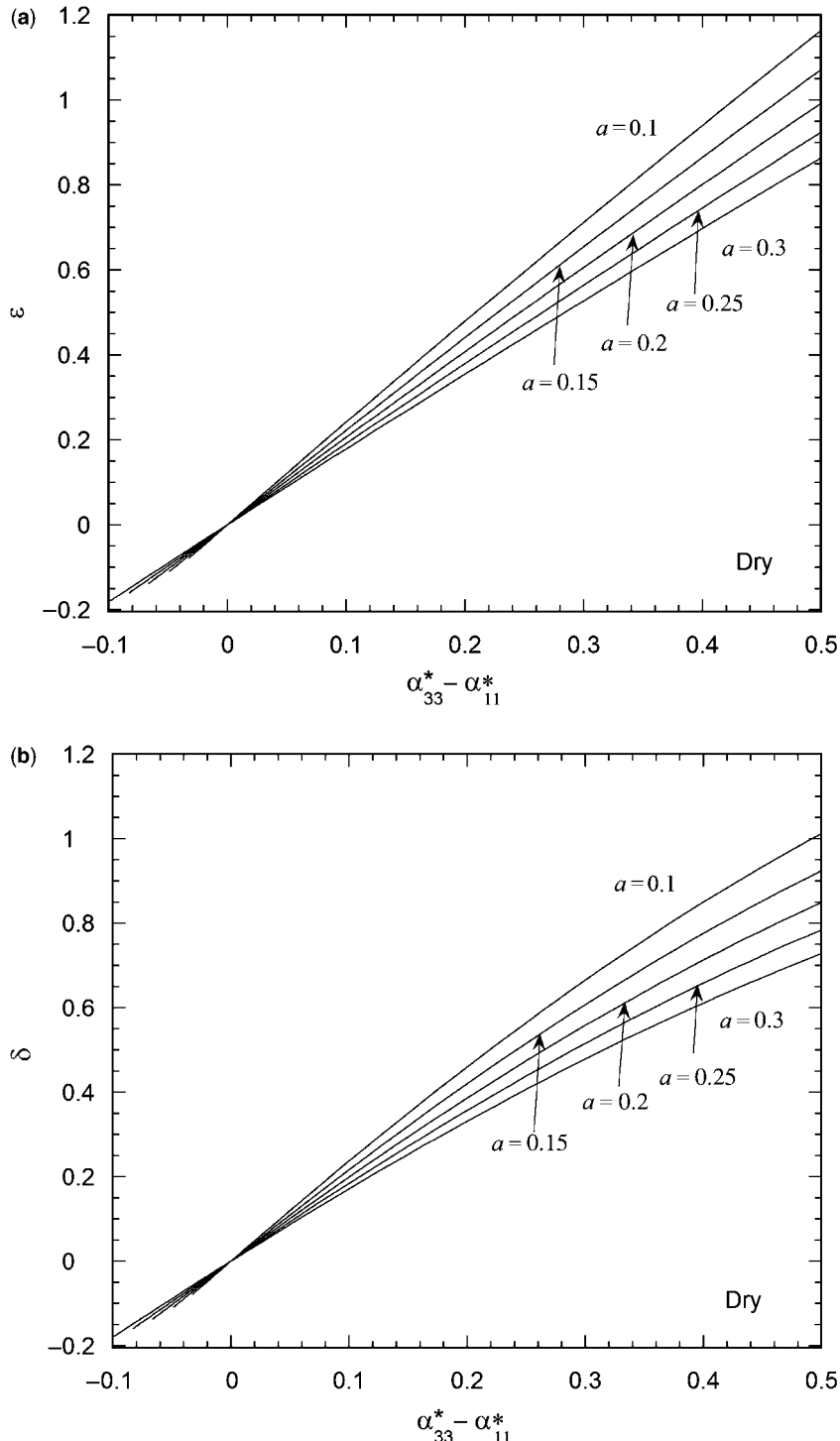


Fig. 3. The Thomsen parameters (a) ϵ , (b) δ and (c) γ as functions of crack density difference $\alpha_{33}^* - \alpha_{11}^*$ for a dry rock with a ranging from 0.1 to 0.3.

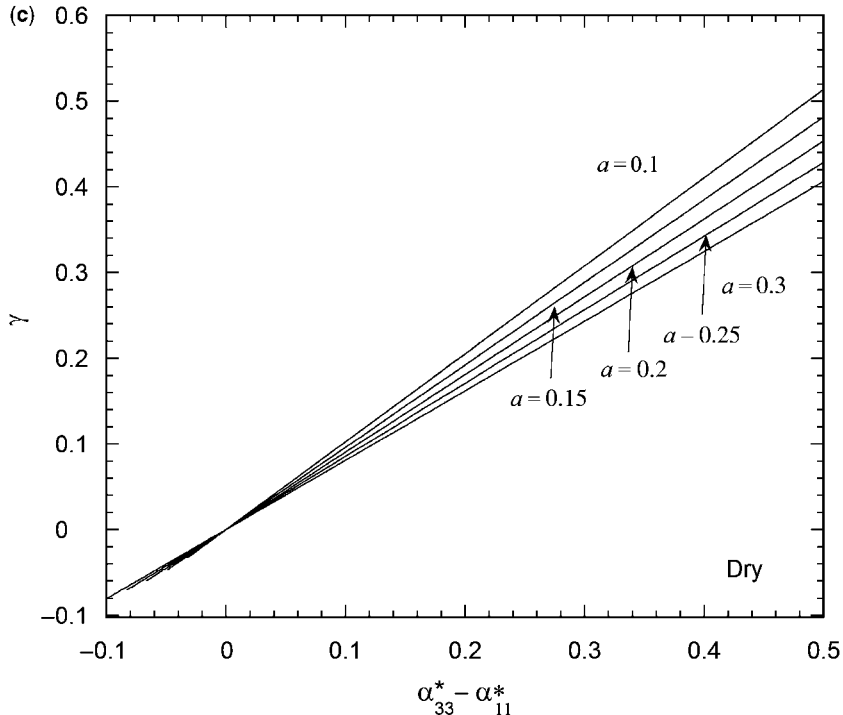


Fig. 3. (Continued)

Figure 5. Wang (2002) presented one of the most comprehensive sets of laboratory measurements on seismic anisotropy in sedimentary rocks. Most of his measurements show positive values of ε , δ and γ , indicating that if the anisotropy can be attributed to microcracks, the crack planes would be preferentially aligned with bedding corresponding to $b > 0$ in equation (11). Grouping all data for dry, water-saturated and brine-saturated samples, Wang (2002) observed that his data for sands and carbonates cluster along an approximately linear trend corresponding to the elliptic anisotropy condition $\varepsilon = \delta$, whereas the shale data indicate $\varepsilon > \delta$. As for the γ , his data show an overall trend for $\gamma = -0.01049 + 0.9560\varepsilon$ with a correlation coefficient squared (r^2) of 0.7463. This empirical fit is shown as the dashed line in Figure 5b, which has a slope significantly steeper than our predicted value of 1/2 for a dry cracked rock.

In Wang's (2002) study the shale data show the largest discrepancy from these overall trends. We selected a representative subset of his saturated shale data for comparison with our model. The data for δ as a function of ε consistently fall below the elliptic anisotropy line, whereas our model prediction (for a ranging up to 0.3) brackets

more than half of the data (Fig. 5a). Presumably the rest of his data can also be interpreted by a fluid-saturated crack model with $\alpha_{kk}^* \geq b > 0.3$, but we consider such a crack density value to be too high in an unstressed rock. There is a paucity of systematic microcrack density data on sedimentary rocks, but published data (mostly on crystalline rocks as function of stress) indicate that the crack density α_{kk}^* has a value of the order of 0.1 in an unstressed rock, which would increase to a value of c. 1 when stressed to failure (Madden 1983; Wong 1985; Guéguen *et al.* 1997; Hoxha & Homand 2000; Takemura & Oda 2005). Similarly, about half of the data for γ as a function of ε can be bracketed by our model results for saturated rock with a up to 0.3 (Fig. 5b). It should be noted that the model here focuses on the microcrack effect, thus neglecting the petrofabric effect associated with preferred orientation of anisotropic clay minerals. It is of interest to note that Sayers (1999) demonstrated that an approach similar to that of Sayers & Kachonov (1995) can be employed to analyse the effect of clay mineral alignment on elastic anisotropy. His analysis also underscored the necessity to model the matrix of a shale as elastically anisotropic. It is likely that the petrofabric

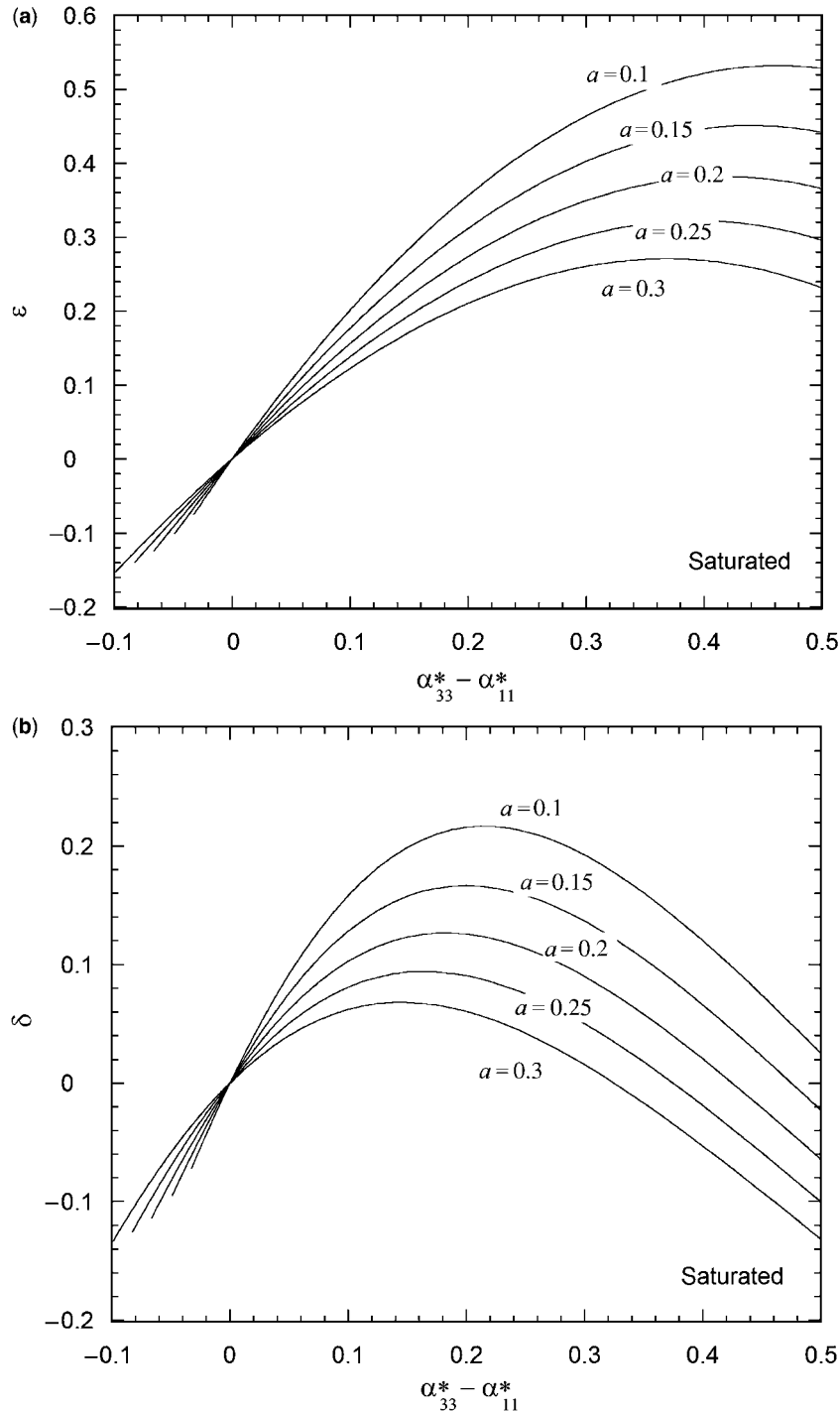


Fig. 4. The Thomsen parameters (a) ϵ , (b) δ and (c) γ as functions of crack density difference $\alpha_{33}^* - \alpha_{11}^*$ for a saturated rock with a ranging from 0.1 to 0.3.

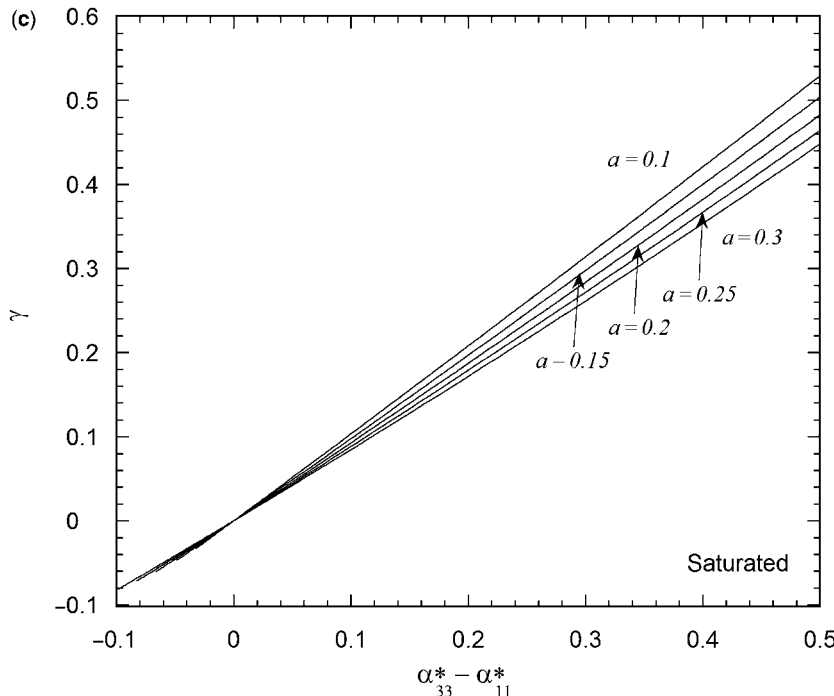


Fig. 4. (Continued)

associated with preferred orientation of clay minerals and elastic anisotropy of the rock matrix can influence the overall seismic anisotropy behaviour in a shaly rock (Cholach & Schmitt 2006; Sarout 2006; Valcke *et al.* 2006), which should be incorporated in the future in a more comprehensive analysis.

Wang (2002) also concluded that his data for (dry and saturated) shale show an overall trend for both ϵ and γ to decrease with increasing porosity. The calculations here show that at the same crack density difference ϵ and γ would decrease with increasing α_{kk}^* or a (Figs 3a, c, and 4a, c). If we make the plausible assumption that the crack density and porosity are positively correlated, then the experimental data and theoretical predictions are in agreement.

Shear-wave anisotropy is characterized by the parameter γ , which our model predicts to be approximately equal to the crack density difference $\alpha_{33}^* - \alpha_{11}^*$ for both dry and saturated rocks (Figs 3c and 4c). This can be used to constrain the micro-crack fabric and fracture anisotropy responsible for shear-wave anisotropy observed in borehole logs. Boness & Zoback (2004) recently analysed the shear-wave log from the San Andreas

Observatory at Depth (SAFOD) pilot hole, and they reported that the fast-wave velocity direction seems to correlate with the maximum horizontal stress direction (inferred from borehole breakout and other stress indicators). They attributed this correlation to stress-induced closure of fractures, which would be analogous to fracture orientation given by equation (11) with a negative b value. The shear-wave anisotropy of c. 10% observed was comparable with a value of γ up to 0.1, and from our calculations this would translate to a crack density difference $\alpha_{33}^* - \alpha_{11}^* \approx 0.1$, which may be manifested in the fracture anisotropy in the borehole log data. It should also be noted that dispersion effects in a fluid-saturated rock may be appreciable and should be accounted for in extrapolating laboratory data to field measurements (Schubnel & Guéguen 2003).

In contrast, Hung *et al.* (2007) concluded that unlike SAFOD, shear-wave anisotropy in their borehole log for the Taiwan Chelungpu Fault Drilling Project (TCDP) was not due to stress-induced closure of fractures, but rather was associated with microcrack fabric observed in laboratory measurements of P-wave anisotropy in TCDP sandstone cores of Louis *et al.* (2005),

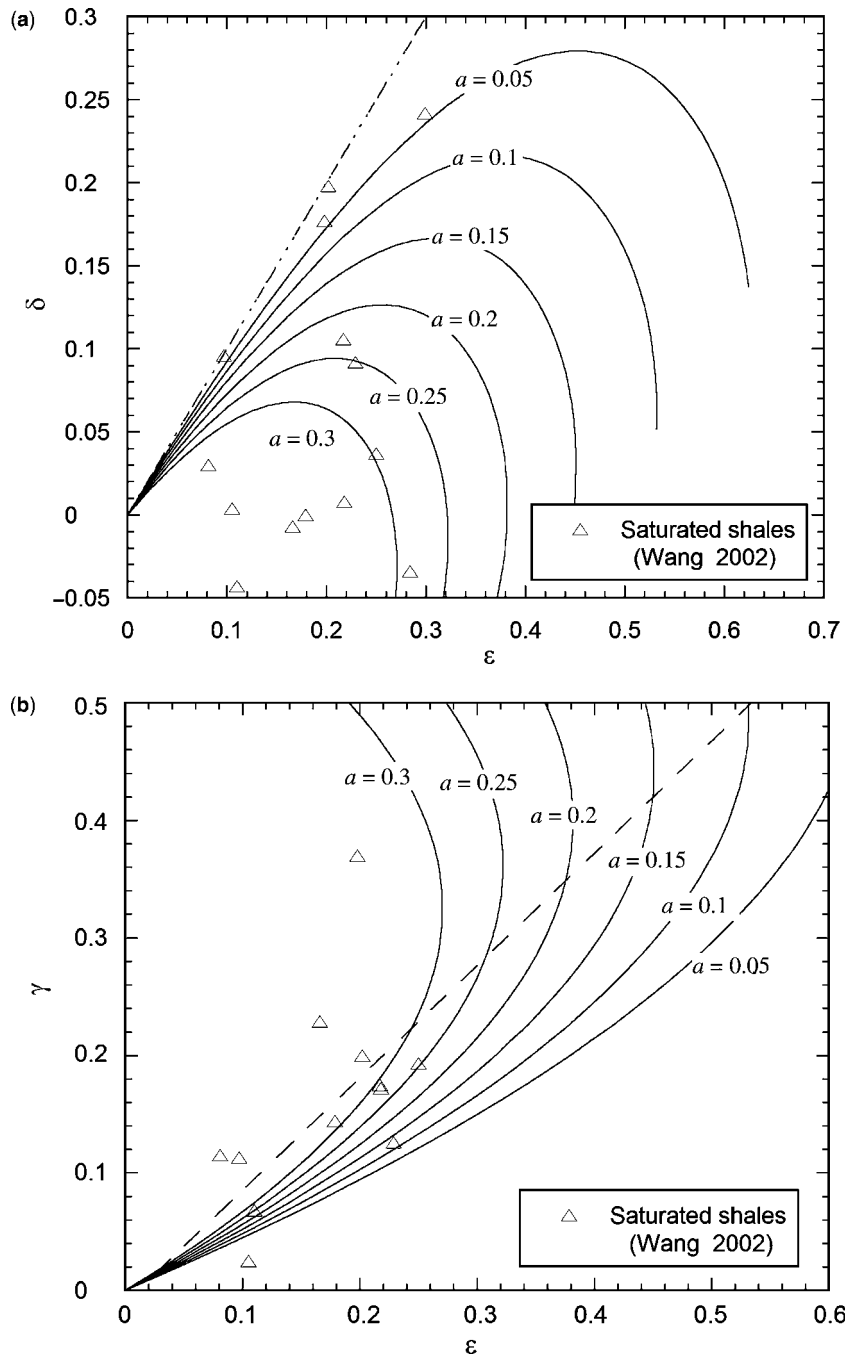


Fig. 5. Correlations between the Thomsen parameters for a saturated rock with a ranging from 0.05 to 0.3: (a) δ and (b) γ as functions of ϵ . Δ , selected experimental data for shales from Wang (2002).

who attributed the fabric to inelastic opening of microcracks as a result of the stress field associated with layer-parallel shortening in the fold-and-thrust belt. More thorough analysis of the SAFOD and TCDP logs in conjunction with systematic microstructural analysis would help resolve some of these questions. The analysis here helps to constrain the textural and crack anisotropies in relation to seismic anisotropy in laboratory and field measurements.

Conclusion

Using Kachanov's (1992, 1993) formulation we analysed the effects of an axisymmetric system of microcracks on seismic anisotropy. The elastic behaviour of such a cracked rock is transversely isotropic, and its seismic properties can be characterized by the three Thomsen parameters. In this study we calculated the parameters ϵ , δ and γ under dry and saturated conditions. We derived analytic expressions for the model proposed by Sayers & Kachanov (1995), which assumes that the contribution from the fourth-rank crack density tensor is negligible. This model predicts that the elliptic anisotropy condition $\epsilon = \delta$ is obeyed in a dry rock.

Guided by microstructural observations we adopted a two-parameter axisymmetric distribution to characterize the crack density, which predicts that δ and γ in a fluid-saturated rock are related to ϵ in a nonlinear manner. All three Thomsen parameters are sensitively dependent on the crack density difference. Although our model shows basic agreement with some of the laboratory data on seismic anisotropy in saturated shale, there are discrepancies, which suggest that the petrofabric associated with preferred orientation of clay minerals and elastic anisotropy of the rock matrix may have considerable influence, which should not be neglected in models. Preliminary comparison with borehole log data suggests rock physics tests that may be useful for interpreting the shear-wave anisotropy observations.

This study was motivated by the thesis research of A. Schubnel and L. Louis. We are grateful to the reviewers Y. Guéguen and J. Rudnicki for their comments and suggestions. We have also benefited from discussions with C. David, L. Louis and P. Baud. This research was partially supported by the National Science Foundation under grant EAR-0346022.

References

- BERRYMAN, J. G. 1979. Long-wave elastic anisotropy in transversely isotropic media. *Geophysics*, **44**, 896–917.
- BONESS, N. L. & ZOBACK, M. D. 2004. Stress-induced seismic velocity anisotropy and physical properties in the SAFOD Pilot Hole in Parkfield, CA. *Geophysical Research Letters*, **31**, L15S17, doi:10.1029/2003GL01290120.
- BRACE, W. F. 1965. Some new measurements of linear compressibility of rocks. *Journal of Geophysical Research*, **70**, 391–398.
- CHOLACH, P. Y. & SCHMITT, D. R. 2006. Intrinsic elasticity of a textured transversely isotropic muscovite aggregate: comparisons to the seismic anisotropy of schists and shales. *Journal of Geophysical Research*, **111**, B09410, doi:09410.01029/02005JB004158.
- CRAMPIN, S. 1981. A review of wave motion in anisotropic and cracked elastic media. *Wave Motion*, **3**, 343–391.
- GUÉGUEN, Y., CHELIDZE, T. & LE RAVALEC, M. 1997. Microstructures, percolation thresholds, and rock physical properties. *Tectonophysics*, **279**, 23–35.
- HELBIG, K. 1979. Discussion on 'The reflection, refraction and diffraction of waves in media with elliptical velocity dependence' by LEVIN, F. K. *Geophysics*, **44**, 987–990.
- HELBIG, K. & THOMSEN, L. 2005. 75-plus years of anisotropy in exploration and reservoir seismics: a historical review of concepts and methods. *Geophysics*, **70**, 9ND–23ND.
- HORNBY, B. E. 1998. Experimental laboratory determination of the dynamic elastic properties of wet, drained shales. *Journal of Geophysical Research*, **103**, 29945–29964.
- HOXHA, D. & HOMAND, F. 2000. Microstructural approach in damage modeling. *Mechanics of Materials*, **32**, 377–387.
- HUNG, J.-H., WU, Y.-H., YEH, E.-C., WU, J.-C. & TCDP SCIENTIFIC PARTY. 2007. Subsurface structure, physical properties, and fault zone characteristics in the scientific drill holes of Taiwan Chelungpu-fault Drilling Project. *Terrestrial Atmospheric and Oceanic Sciences*, **18**, 271–293.
- JOHNSTON, J. E. & CHRISTENSEN, N. I. 1995. Seismic anisotropy of shales. *Journal of Geophysical Research*, **100**, 5991–6003.
- KACHANOV, M. 1992. Effective elastic properties of cracked solids: critical review of some basic concepts. *Applied Mechanics Reviews*, **45**, 304–335.
- KACHANOV, M. 1993. Elastic solids with many cracks and related problems. *Advances in Applied Geophysics*, **30**, 259–445.
- LOUIS, L., DAVID, C. & ROBION, P. 2003. Comparison of the anisotropic behaviour of undeformed sandstones under dry and saturated conditions. *Tectonophysics*, **370**, 193–212.
- LOUIS, L., DAVID, C., ROBION, P., WONG, T.-F. & SONG, S.-R. 2007. Anisotropy of magnetic susceptibility and P-wave velocity in core samples from the Taiwan Chelungpu-fault Drilling Project (TCDP). *EOS Transactions, AGU* **86**(52), T51A-1319.
- MADDEN, T. R. 1983. Microcrack connectivity in rocks: a renormalization group approach to the critical phenomena of conduction and failure in crystalline rocks. *Journal of Geophysical Research*, **88**, 585–592.

- MAVKO, G., MUKERJI, T. & DVORKIN, J. 1998. *The Rock Physics Handbook—Tools for Seismic Analysis in Porous Media*. Cambridge University Press, Cambridge.
- NYE, J. F. 1985. *Physical Properties of Crystals*. Oxford University Press, Oxford.
- SAROUT, J. 2006. *Propriétés physique et anisotropie des roches argileuses: modélisation micromécanique et expériences triaxiales*. PhD thesis, Ecole Normale Supérieure, Paris.
- SAYERS, C. 1999. Stress-dependent seismic anisotropy of shales. *Geophysics*, **64**, 93–98.
- SAYERS, C. M. & KACHANOV, M. 1995. Microcrack-intruded elastic wave anisotropy of brittle rocks. *Journal of Geophysical Research*, **100**, 4149–4156.
- SCHUBNEL, A. & GUÉGUEN, Y. 2003. Dispersion and anisotropy of elastic waves in cracked rocks. *Journal of Geophysical Research*, **108**(B2), 2101, doi:10.1029/2002JB001824.
- TAKEMURA, T. & ODA, M. 2005. Changes in crack density and wave velocity in association with crack growth in triaxial tests of Inada granite. *Journal of Geophysical Research*, **110**, B05401, doi:10.1029/2004JB003395.
- THOMSEN, L. 1986. Weak elastic anisotropy. *Geophysics*, **51**, 1954–1966.
- VALCKE, S. L. A., CASEY, M., LLOYD, G. E., KENDALL, J.-M. & FISHER, Q. J. 2006. Lattice preferred orientation and seismic anisotropy in sedimentary rocks. *Geophysical Journal International*, **166**, 652–666.
- WANG, Z. 2002. Seismic anisotropy in sedimentary rocks, Part 2: laboratory data. *Geophysics*, **67**, 1423–1440.
- WALSH, J. B. 1965. The effect of cracks on the compressibility of rocks. *Journal of Geophysical Research*, **70**, 381–389.
- WONG, T.-F. 1985. Development of stress-induced anisotropy and localized deformation in brittle rock. In: BOEHLER, J.-P. (ed.) *Plastic Behavior of Anisotropic Solids*. Centre National de la Recherche Scientifique, Paris.

Index

Page numbers in italic, e.g., 153 refer to figures. Page numbers in bold, e.g., 110, signify entries in tables.

- activation energy 191, 198, 199–200, 202
advection 186
anti-crack dislocation model 107, 108, 117–21, 122, 123
aquifers, deep saline 26
argillite
 anisotropy factor 60, 61, 68
 constant temperature 58–60
 elastic anisotropy 57–69
 heating cooling cycles 60–3, 61, 64, 67
 increasing temperature 65, 66, 68
 magnetic anisotropy 57–69, 60
 magnetic mineralogy 63–4
 physical properties 57–8
 sample shape effect 58, 59
aspect ratio 107, 111, 112, 113, 115, 121, 123, 213
asperity
 axisymmetric 185–205
 contact zone 189–90
 convergence rate 185
 evolution 189, 191
 geometry 185, 191, 193–5, 197–8, 199, 201, 202
 normal contact model 189–95, 191
 profile 190
 radius 197, 198
 relative separation 187, 187, 189, 190, 191
backfill 37–8
Bentheim sandstone 72, 86, 132, 134, 213
 CT imaging 136–8, 137, 140
 FE model 78–83
 laboratory experiment 72–7, 82–3, 86
 micrograph 78
 model binary image 78, 79
 model boundary conditions 80, 80
 model mesh geometry 79, 80
 model vectorization 78, 79
 preconditioned 75–7, 76
 strain values 82–3, 83
bentonite 37, 38
Berea sandstone 89–90, 132, 134
 CT imaging 136–8, 137, 140
BET (Brunnauer–Emmett–Teller) method 176, 178, 179
Biot coefficient 71
Boltzmann constant 188
borehole testing 15–34, 92
breakouts 89–105
 formation mechanisms 90
 geometry 89–90, 93, 95, 99, 100
 initiation 93–5
micromechanics 93–7
stress conditions 93, 103–4
tip 93, 95, 95, 96
 see also slot excavation; slot
 shaped breakout;
 slot wall reloading
brittle fracture 185
bulk modulus 80–1, 84–5, 86, 109, 115
caprock 27, 28
 failure 29–30, 31
chemical equilibrium 187
chemical processes 175, 185
clay minerals 38, 180, 217, 219
 dewatering 57
 transformations 57
 CO_2
 brine formation storage 27, 28
 buoyancy flow 28
 chemical reactions 28
 hydromechanics 26–32
 injection pressure 28, 29, 29
 injection and storage 15–34, 28, 29
 leakage paths 31
 mineral trapping 28
coercivity 63–4
compaction bands 4, 89–105, 98, 99, 127, 132, 137–8
 adjacent stress 113–15, 114, 116, 117
 anti dislocations 121–2
 anti-crack 111, 121–2
 axial stress 112
 closing dislocation 120, 121
 crushed zone 101, 104
 definition 90, 95–6, 107
 dislocation model 111
 displacement 113, 118, 118, 119–20
 elastic properties 108–10
 ellipsoidal model 108–13, 109, 114, 117–21, 122
 empty 95
 energy release propagation 115–17, 123
 evolution 102–3, 104
 flow across 107
 formation 112, 114
 initiation 102–3, 104
 length 107
 porosity 89–105, 112
 propagation criteria 122
 propagation mechanisms 107–8
 propagation models 107–25
 scale 141–2, 143
semi infinite dislocation 118
spring network model 102–3, 121
stress state 108, 110–13
tip stress 115–16, 121
traction 113, 118, 118, 121–2
types 89, 102
compaction energy 116–17
contact dissolution 186, 188, 191, 199–200, 202
contact radius 190, 191, 193, 193, 195, 197–8, 197, 201–3
Coulomb failure criteria 30
cracked rock 207–20
 dry 207
 elastic properties 207
 saturated 207
cracks
 closure pressure 213
 compliance tensor 208
 density 207, 210–13, 211, 214–15, 215–17, 216–17
 density tensor 219
 elastic anisotropy 208–13
 fabric 208–13
 intragranular 89, 100–1
 planes 215
 see also fractures; microcrack
 anisotropy
creep 7–8, 38, 129
 see also dislocation creep; dissolution creep
Darcy's theory 175
Darley Dale sandstone 130, 132, 132, 134
 CT imaging 136–8, 137, 140
deformation, irreversible 73–4, 75, 81
density 130, 131, 137–8
 global heterogeneity 132–8
 grey levels 132–3, 134–6, 134, 137–8, 140–1, 140, 141, 142
 local heterogeneity 138–42
Diemelstadt sandstone 131, 132, 132, 134, 143
 CT imaging 136–8, 137, 140
diffusion 35, 38, 186
 coefficient 187–8
 correction factor 190–3, 197
 equation 185, 188
 rate 189
 see also interface diffusion
Dirac delta function 210
dislocation creep 185
displacement rate 191, 192, 193, 194, 195, 197, 198, 199, 200, 201, 202

- dissolution 180, 195
 creep 201
 displacement rate 190, 192, 194, 197–8
 rate 185, 186, 188–9, 197–8, 199
see also contact dissolution
- effective load 190–3, 195, 196, 197, 200
 elastic
 anisotropy 207–20
 behaviour 81
 compliance tensor 208–9
 deformation 73, 185, 196
 displacement 189, 190, 191, 192, 193, 194, 196, 198, 202
 linear elastic fracture model 122
 modulus 117, 213
 properties 147
 pure elastic fracture model 24, 27
 stiffness tensor 207–8, 209–10
 strain 4
 wave propagation 207–8
- elliptic anisotropy 209–10, 215, 219
 engineered barrier 37, 38
 Eshelby factors 123
 Eshelby inclusion model 111
 excavation 41
 excavation damaged zone (EDZ)
 7–8, 35, 57
 cut-off experiment 42–6, 42, 55
 evolution 55
 EZ-A 42–6, 43, 44
 locating 41, 55
 mechanical characterization 41
 reloading 41, 43–5, 45–6, 51–5, 51
 self sealing 35, 38
 stress redistribution 37
 velocity survey 41–55
- extensometer 72, 83
- fault slip 30, 33
 fault systems 42
 fault zone
 architecture 175
 model 176
- faults
 cataclasized zone 175
 damage zone 175–84
 reactivation 30–1
- FEBEX tunnel 19, 20–1
 Fick's law 175
 fluid
 circulating 95, 97, 101, 104, 183
 concentration 202
 pressure 18, 20, 22–3
 saturation 8
 supercritical 27
 tracers 176–7, 183
- fluid flow 9, 15, 175, 176, 186
 and alteration 175
 hydromechanics 23–6
- pathways 4
 rate 18, 26, 27
- fluid flow simulation 3, 147, 149
 3D 127
 coupling 5
 model 148
 PUNQ-MONITOR 153
 upscaling 149
- foliation index 62–3, 64, 68
 Fontainebleau sandstone 129,
 132, 134
 3D reconstruction 130
 CT imaging 136–8, 140, 141
 synchrotron imaging 133–6, 136
 X-ray attenuation 135
- fractured rock 161–73
 hydromechanics 15–34
- fractures 9
 acoustic emissions 9
 ANOVA 161, 162–3, 163, 167, 168, 171
 aperture 9, 15, 18, 23–4, 25–6
 conductivity 4
 connectivity 24
 continuous 161
 discrete network (DFN) 23, 23
 healing 7–8, 9
 hydromechanics 17
 interference between 33
 locked open 18
 network 23, 162
 nucleation and propagation 10
 orientation 24, 161, 207
 orthogonal arrays method 161,
 162–3
 persistence 161–73, 162, 166,
 167, 168
 persistence factor 171, 171
 pure elastic model 24, 27
 shear dilations 24–5
 shear reactivation 32
 spacing 161
 stress induced closure 217
 stress state 23–4, 24
 trace length 24
see also cracks
- France
 Bure underground research
 laboratory 57–69
 geothermal exchanger 175,
 176–7, 183
- gas flow 38
 gas permeameter 175
 Gauss–Chebyshev quadrature
 scheme 189–90
- geomechanics 1–14
 coupling 4–6
- geostatistical model 148
 perturbation 148–9
 PUNQ-MONITOR 153
- GeoSys/RockFlow 80
- grain contacts 93, 137–8, 138,
 185, 202
- interface 187
 stress distribution 186
- grains
 crushed 100–1, 102, 104
 debonded 93–5, 101–2, 104
 induced stress 81
 repacking 95, 97, 98, 104
 size 201
 structure 71, 75, 78
 sutures 89, 91, 100–1, 104
- granite 175–84, 177
 permeability 179
 sample list 178
 SEM images 181, 182
- Helmholtz free energy 188, 190, 201–2
- Hertzian contact theory 189, 190, 193, 195
- history matching 147–59
 data integration 158
 dynamic data 154
 porosity fields 158
 results 154–8
 static data 154
- hydraulic conductivity 4, 18
 hydraulic flat jack 46
 hydraulic jacking test 18, 18, 19
 hydrological processes 175
- hydromechanics
 coupled modelling 15–34
 injection well testing 17–18
- hydrostatic loading 213
- interface diffusion 186, 188–9, 191, 194, 195, 199–200, 200, 202
 coefficient 185
- isothermal remanent magnetisation
 (IRM) 63, 65
- joints *see* fractures
- Klinkenberg effect 175
 Kronecker delta 108, 208
- laboratory *see* underground research laboratory
- Lame's constants 80–1
- Laplacian operator 188
- Lehner & Leroy (2004) model 186, 188, 190, 196–9, 199, 201, 202
 parameters 190
- linear elastic fracture model 122
- loading *see* effective load; hydrostatic loading
- logging while drilling (LWD) 93
- magnetic susceptibility 8, 57–69, 60, 61, 64
 anisotropy 58
 Flinn diagram 62, 63
- magnetization
 isothermal remanent (IRM) 63, 65
 unblocking temperature 63–4, 65

- mechanical anisotropy 207
 mechanical deformation 15
 mechanical processes 175, 185
 mechanical stability 3
 mercury porosimetry 176, 177, 178, 180, 183
 microcrack anisotropy
 axisymmetric model 210–13, 212
 lab and field measurements 213–19
 model predictions 213
 microscopy
 scanning electron (SEM) 92, 95
 granite images 181, 182
 mineral precipitations 180
 mineral transformations 66–7, 68
 Mohr–Coulomb failure criteria 23, 27
 oil production 5
 Opalinus Clay 37, 41
P-wave, propagation 47–8
P-wave velocity 8, 48, 49, 50, 50, 55–69, 60, 61, 64, 67–8
 anisotropy 58
 ellipsoidal model 62, 62
 evolution 41, 52, 52–4
 Flinn diagram 62, 63
 permeability 3, 6, 8, 18, 31, 129, 149, 175, 179
 connectivity 181
 measurements 175–6, 178, 178, 179, 183
 porosity relation 180, 181
 stress dependent 15, 23, 24, 27, 29
 tortuosity 180, 181
 petro-elastic model 6, 148, 149–50
 compressional impedance 150, 156
 PUNQ-MONITOR 153
 shear impedance 150
 petrography 177
 sample location 176–9
 petrophysics 175
 Poisson's ratio 80, 84–6, 108, 109, 112, 114, 115, 116, 117, 189, 208, 209, 213
 pore pressure 3, 4, 6, 19–22, 20–1, 72, 73, 74, 76, 81, 82, 85
 changes 87
 evolution 22
 induced 73, 75, 81, 83
 undrained 71
 pore space
 3D mapping 127
 fluid 187
 free 202
 geometry 86–7, 127
 heterogeneity 127–46
 irregular 82, 82
 partial volume effect 135
 and porosity 133–5
 reconstruction 129
 pores
 connections 175
 geometry 128, 141, 175, 180
 number 175
 population 180, 181
 radius 180, 181
 throat 141, 175
 volume 71, 75, 78, 128, 141, 180, 181
 poroelastic numerical model 75
 poroelastic theory 6
 porosity 4, 94, 136, 137, 139–40, 140, 143, 144, 149, 157, 175, 180, 217
 2D 95, 98, 99, 104
 compaction bands 96–7, 112
 connected 176
 contrasts 130–1
 development model 180–1, 181, 182
 distribution 175
 free 176, 177, 179, 180
 gradual deformation method 154
 injection curves 176, 179, 179, 180
 measurement 176, 177, 178, 180, 183
 permeability relation 180, 181
 and pore space 133–5
 ranges 89
 trapped 176, 177, 179, 180
 X-ray attenuation 130
 porosity network
 geometry evolution 175–84
 sample list 178, 179
 precipitation rate constant 186
 pressure 6, 45, 45, 51–5, 52–4
 confining 71–87, 73, 74, 76–7, 81, 83, 85, 86, 195
 crack closure 213
 profile 18, 19
 pressure solution 9, 129
 compaction 185, 188–9
 compaction rate laws 199–201
 deformation modelling 185–205
 numerical simulations 190–5
 processes 185–6, 186
 rate limiting process 199–201, 200, 202
 self arrest stress 200–1
 stress dependence 201
 temperature 190–3, 192–3
 transfer paths 185
 pressure solution model 186–9
 undercutting 201–2
 production data 147–8
 PUNQ-MONITOR 152–8, 152, 152
 fluid flow simulation 153
 geological modelling 152–8
 geostatistical model 153
 petro-elastic model 153
 pure elastic fracture model 24, 27
- radioactive decay, host rock
 temperature 57
 radioactive tracers 38
 radioactive waste
 decay heat 35, 57
 diffusion 35
 solute transport 38
 storage 1, 5–10
 rate laws 185, 199–201
 repository 1–14
 characterisation 2
 characterization 35–40
 evolution 1, 10, 35, 36
 hard rock 9–10
 host formation 6
 long term monitoring 10, 37
 performance 35, 36
 radioactive waste storage 6–10, 35
 soft rock 7–9
 steel canister failure 35
 unsaturated zone 35
 reservoir simulations 1
 coupling 4–6
 overburden 6
 sideburden 6
 underburden 6
 reservoirs 1–14
 characterization 2, 147
 choice of candidate 151–2
 compartmentalization 4
 geomechanical effects 3–5
 geothermal 175
 highly compacted 4–5
 hydrocarbon recovery 3–6
 poorly compacted 4
 production forecasting 147
 rocks 107
 saturation 6, 8
 temperature 6
 rock bridges 161, 166
 failure 162
 and joint persistence 161–2
 rock compressibility factor 3
 rock laboratory 38–9, 39
 rock mass
 block size 161, 162, 165, 166–7, 167
 classification systems 161
 physical properties 175–84
 strength 1, 7–10, 166, 167, 171
 rock physics 1–14
 ROCMAS code 15, 16, 18, 19
 Rothbach sandstone 130, 131
- St Peter sandstone 89–105
 crushed zone 100–1, 102
 experiments 90–2
 high porosity 93–9, 94–8
 low porosity 99–101, 100–2
 properties 90
- sandstone
 orientation dependent anisotropy 72
 poroelastic response 71–87

- Sayer & Kachanov's model 219
 dry rock 209–10
 scale 2, 3, 33, 148, 149
 seismic amplitude 147
 seismic anisotropy 207, 209,
 213–17, 219
 seismic data
 4D 3, 6, 147–59
 optimization techniques 151
 pre-stack inversion 147
 and production data 148, 148
 seismic tomography 41, 42, 43, 44,
 47–9, 47, 48
 seismic velocity 207, 210
 depth-time conversion 151,
 155, 158
 EDZ survey 41–55
 filtering 151
 objective function 148, 151,
 154–8, 154
 shales
 anisotropy 8
 mechanical properties 7
 shear band, dilating 129, 130–1, 132
 shear compliance 208
 shear displacement 33
 shear modulus 80–1, 107, 109, 111,
 112, 115, 121
 shear slip 31, 31, 32
 shear strength 18
 shear stress 166–7, 167
 shear wave anisotropy 217, 219
 shear wave splitting 207
 Skempton coefficient 71, 73, 77,
 81–2, 82
 decrease 72, 75, 83, 86–7
 elastic hollow sphere 83–6, 84
 first derivative 86
 isotropic 74–5, 74, 75, 83, 85,
 86–7
 spherical fluid inclusion 84
 slot excavation 42–6, 45, 49
 velocity survey 43, 49–51, 50, 53
 slot shaped breakout 89–105
 advance rate 50
 conceptual model 101–4, 103
 formation 93–7, 94
 micromechanics 99–101, 100
 slot wall reloading 42–6, 45, 46
 velocity survey 43–5, 51–5, 51
 solute transport 15–34, 38
 solution, chemical potential 188
 solution–precipitation creep *see*
 pressure solution
 solution–transfer creep *see* pressure
 solution
 sorption 38
 specific surface 175
 measurements 176, 179,
 180, 183
 strain
 localization 128
 volumetric 73–4, 74, 75–6,
 76, 84–5
 stress 3, 5
 direction 8, 89, 93, 94
 evolution 30–1
 intensity factor 118, 119, 122
 principal 93, 94, 112, 114
 regional field 9
 stress field 22–3, 185, 190, 197,
 198–9, 201, 202
 anisotropy 30
 far 93, 99
 local 22, 23
 regional 9, 22, 23
 stress ratio 25–6, 27, 99, 100, 107,
 115–16, 167, 168
 stress regime
 isotropic 31
 normal faulting 32
 type 32
 stress-induced anisotropy 209
 Sweden, hard rock laboratory 17
 Switzerland
 Grimsel test site 19
 Mont Terri rock laboratory
 35–40, 41
 thermal cracking 57, 67, 68
 thermal processes 175
 Thomsen's parameters 207, 209–10,
 211, 219
 dry rock 214–15
 elastic wave propagation 207–8
 fluid saturated rock 213, 216–17,
 218
 Thomsen's weak anisotropy theory
 62, 62
 TOMSIS software 47–8
 TOUGH-FLAC code 15,
 16–17, 16
 TOUGH2-FLAC3D codes 27
 tracers 38, 176–7, 183
 transport processes, rate laws 185
 tunnel
 boring machine 19–22, 20
 closure 37
 construction 169
 drilling hydromechanics 19–23
 failure 170, 171
 self sealing 35, 37
 stability analysis 168–70
 UDEC model, 3DEC 161,
 168–70, 169
 ANOVA 170, 170
 block geometry 170
 fracture properties 169
 fracture sets 168, 169
 mechanical properties 169
 orthogonal array 168, 170, 172
 results 169–70
 UDEC model 161, 164
 ANOVA 167, 168
 block system 165–7, 165–7
 fracture properties 165
 inputs 164
 mechanical properties 165
 orthogonal array 172
 results 165–8
 shear tests 163–8
 underground research laboratory
 1–3, 6, 9
 Voigt notation 207–9
 X-ray attenuation 131, 135
 global 143
 local 143
 porosity 130
 X-ray computed tomography
 127–46
 acquisition setups 128–9
 applications 127–8, 130
 binary images 140–1, 141, 142,
 142, 143
 coefficient of variation 131–2,
 133, 136, 136, 137–8,
 139, 140, 144
 industrial 127, 129–32, 143
 local coefficient of variation 140,
 140, 142, 142, 143
 principle of 128–9
 resolution 127, 129, 135–7, 136,
 138, 139, 139, 141–2,
 143, 143
 synchrotron 127, 129, 143
 Young–Laplace equation 176
 Young's modulus 80, 84, 85, 86,
 112, 189, 208, 209

The study of reservoir and repository performance requires the integration of many different fields in Earth sciences, among them rock physics and geomechanics. The aim of this book is to emphasize how rock physics and geomechanics help to get a better insight into important issues linked to reservoir management for exploitation of natural resources, and to repository safety assessment for hazardous waste storage in geological environment. The studies presented here deal with the hydromechanical coupling in fractured rocks, the key experiments in safety assessment of repositories, the development of damaged zones during excavation in a shale formation, the influence of temperature on the properties of shales, the poroelastic response of sandstones, the development and propagation of compaction bands in reservoir rocks, imaging techniques of geomaterials, the characterization and modelling of reservoirs using 4D seismic data, the mechanical behaviour of fractured rock masses, the petrophysical properties of fault zones, models for rock deformation by pressure solution and the elastic anisotropy in cracked rocks.